materials

Special Issue Reprint

Hot Deformation and Microstructure Evolution of Metallic Materials

Edited by
Ivo Schindler

www.mdpi.com/journal/materials

MDPI

Hot Deformation and Microstructure Evolution of Metallic Materials

Hot Deformation and Microstructure Evolution of Metallic Materials

Editor

Ivo Schindler

MDPI • Basel • Beijing • Wuhan • Barcelona • Belgrade • Manchester • Tokyo • Cluj • Tianjin

Editor
Ivo Schindler
VSB – Technical University of Ostrava
Czech Republic

Editorial Office
MDPI
St. Alban-Anlage 66
4052 Basel, Switzerland

This is a reprint of articles from the Special Issue published online in the open access journal *Materials* (ISSN 1996-1944) (available at: https://www.mdpi.com/journal/materials/special_issues/deformation_metal).

For citation purposes, cite each article independently as indicated on the article page online and as indicated below:

LastName, A.A.; LastName, B.B.; LastName, C.C. Article Title. *Journal Name* **Year**, *Volume Number*, Page Range.

ISBN 978-3-0365-7744-9 (Hbk)
ISBN 978-3-0365-7745-6 (PDF)

Contents

materials

MDPI

Editorial

Hot Deformation and Microstructure Evolution of Metallic Materials

Ivo Schindler

Faculty of Materials Science and Technology, VŠB – Technical University of Ostrava, 17. listopadu 2172/15, 70800 Ostrava, Czech Republic; ivo.schindler@vsb.cz

Hot plastic deformation is a key method of processing metallic materials and controlling their final properties through structure-forming processes. The efficiency of the bulk forming processes contributes significantly to the environmental aspects of our civilization's sustainable development. The ability to exploit the structural potentiality of both traditional alloys and new, progressive materials is crucial in terms of economic growth.

Thus, the content of this Special Issue, "Hot Deformation and Microstructure Evolution of Metallic Materials", focused not only on common technologies (e.g., rolling or forging), but also on various types of complex thermomechanical processing. The strong physical basis of the research work, the application of advanced hot deformation simulators and structural analysis methods, and the optimization computer simulations of forming processes were emphasized. Much attention was paid to the structure-forming processes, which are connected with the bulk forming and controlled cooling of various types of metallic materials (steels, alloys of aluminum including composites, magnesium, titanium, copper, etc.). It is interesting that the experiments describe in almost half of the articles were based on the application of a compression test—either uniaxial or with plane strain.

Many authors devoted themselves to the analysis of flow stress curves and their use in the creation of constitutive models; the description of the dynamic recrystallization kinetics using the calculated value of the activation energy at hot forming; the construction of processing maps, etc. Łukaszek-Sołek et al. [1] focused on the hot deformation behavior of 4130 steel and the optimization of its processing parameters. The flow stress curves obtained during compression tests, as well as the processing maps which elaborated on the basis of various flow stability criteria, were discussed. Processing parameters developed according to Prasad's and Murty's criteria were recommended for designing the technology for forging the investigated steel. Such parameters ensure the homogeneity and stability of the material flow, which was confirmed by the successful forging of 4130 steel in industrial conditions. Chen et al. [2] developed a flow stress model of 300 M steel using hot uniaxial tensile tests. Compared with uniaxial compression, the tensile flow stress was 29.1% higher because dynamic recrystallization softening was less sufficient in the tensile stress state. To eliminate the influence of sample necking on the stress–strain relationship, both the stress and the strain were calibrated using the cross-sectional area of the neck zone. A constitutive model was established based on the modified Arrhenius model, in which the individual parameters were described as a functions of strain. Hot deformation behavior of selected non-alloyed carbon steels was investigated by Kawulok et al. [3]. Based on the analysis of experimentally determined flow stress curves, material constants suitable for predicting the peak flow stress, σp; peak strain, εp; and critical strain, $\varepsilon crDRX$, necessary to induce dynamic recrystallization were determined. The validity of the predicted critical strains, $\varepsilon crDRX$, was then experimentally verified. Equations describing a simple linear dependence of the critical strain $\varepsilon crDRX$ on the peak strain εp were derived for all investigated steels. The determined hot deformation activation energy Q decreased with increasing carbon content. Individual flow stress curves of the studied steels were mathematically described using the Cingara and McQueen model. Kittner, Ullmann, and

Citation: Schindler, I. Hot Deformation and Microstructure Evolution of Metallic Materials. *Materials* **2023**, *16*, 1602. https://doi.org/10.3390/ma16041602

Received: 20 January 2023
Accepted: 9 February 2023
Published: 14 February 2023

Ulrich [4] performed a comparative study on the hot deformation behavior of as-cast and twin-roll cast (TRC) Mg-6.8Y-2.5Zn-0.4Zr alloy. TRC resulted in a finer microstructure. In the conventional as-cast state, dynamic recrystallization (DRX) was delayed by the coarse, blocky, long-period stacking-order phases. Optimum deformation conditions for both states are temperatures from 500 °C to 520 °C, and strain rates ranging from 0.01 s^{-1} to 0.1 s^{-1} for the as-cast material as well as a strain rate of 1 s^{-1} for the TRC material. Wang et al. [5] proposed the cold radial forging method and semi-solid isothermal treatment in the semi-solid isothermal compression (SSIC) process to fabricate high-quality, semi-solid billets of 6063 aluminum alloy. Constitutive equations were established based on the experimental data to predict the flow stress. Four stages (i.e., sharp increase, decrease, steady state, and slow increase) were observed in the true stress–true strain curve. The deformation mechanism for SSIC of cold radial forged alloy 6063 mainly included four modes: the liquid phase flow, grain slide or grain rotation along with the liquid film, slide among solid grains, and the plastic deformation of solid grains. The strain compensation model and processing maps to describe the hot deformation behavior of a metastable β titanium alloy was developed by Lypchanskyi et al. [6] at near and above β transus temperatures. The strain-compensated constitutive model was developed using the Arrhenius-type equation. The dynamic material modeling in combination with Prasad's stability criterion made it possible to generate processing maps for the investigated deformation conditions. The high material flow stability under investigated deformation conditions was revealed. It was found that dynamic recovery was the main mechanism operating during the deformation of the investigated alloy. Zhang et al. [7] studied the DRX behavior of 47Zr-45Ti-5Al-3V alloy by using an experiment and numerical simulation method based on DEFORM-3D software and cellular automata (CA) over a range of deformation temperatures (850 to 1050 °C) and strain rates (10^{-3} to 100 s^{-1}). With the rising deformation temperature and decreasing strain rate, the grain size (dDRX) and volume fraction (XDRX) of DRX were dramatically boosted. According to the developed kinetics models, the distributions of the dDRX and XDRX for DRX grains were predicted by DEFORM-3D. DRX microstructure evolution is simulated by CA. The nucleation and growth of DRX grains in the tested alloy during hot working can be simulated more accurately by CA simulation compared with finite element analysis. In research presented by Opěla et al. [8], conventional hot processing maps superimposed over flow stress maps or activation energy maps were utilized to study the correlations among the efficiency of power dissipation, flow stress, and activation energy evolution in the case of Cr-Mo low-alloyed steel. All maps were assembled on the basis of two flow curve datasets. The experimental set is the result of a series of uniaxial hot compression tests. The predicted flow curve dataset was calculated on the basis of the subsequent approximation procedure via a well-adapted artificial neural network. It was found that both flow stress and activation energy evolution were able to express changes in the studied steel caused by the hot compression deformation. A direct association with the course of power dissipation efficiency is evident. It can be stated that the activation energy processing maps represent another tool for finding the appropriate forming conditions and can be utilized as a support feature for the conventionally-used processing maps to extend their informative ability.

The authors of a total of five papers focused on the study and modeling of microstructure development during hot rolling and subsequent cooling. The grain size models of Hanoglu and Šarler [9] were one-way coupled to the macro-scale calculations performed with the slice model assumption. The macroscale solution was based on a novel radial basis function collocation method. This numerical method was truly meshless, as it involved space discretization in arbitrarily distributed nodes without meshing. Austenite grain size at each rolling pass, as well as the ferrite grain size at the end of rolling, were predicted in this simulation. It was also shown that based on the rolling schedule, it was highly likely that recrystallization would take place at each pass throughout a continuous rolling mill. The simulation system was coded as a user-friendly computer application for industrial use and ran on regular personal computers. The computational time for a typical rolling simu-

lation is usually less than one hour. Lin et al. [10] studied a 6-pass continuous hot-rolling process followed by air cooling by means of a coupled multi-scale simulation approach. The finite element method was utilized to obtain macroscale thermomechanical parameters. The microstructure evolution during the recrystallization and austenite (γ)-to-ferrite (α) transformation was simulated by a mesoscale cellular automaton model. The driving force for α-phase nucleation and growth involved the contribution of the deformation stored energy inherited from hot-rolling. A detailed analysis demonstrated how the parameters, including strain rate, grain size, temperature, and inter-pass time, influenced the different mechanisms of recrystallization. Grain refinement induced by recrystallization and the γ→α phase transformation was also quantified. The simulated final α-fraction and the average α-grain size agreed reasonably well with the experimental microstructure. The kinetics of dynamic, meta-dynamic, and static recrystallization in high-carbon bainitic steel during hot deformation were described by Dembiczak and Knapiński [11]. The developed mathematical model takes into account the dependence of the changing kinetics on the structural size of the preliminary austenite grains, as well as the value of strain, strain rate, temperature, and time. Physical simulations were carried out by plain strain compression tests (PSCT). Based on dilatometric studies, growth of the austenite grain occurred under isothermal annealing conditions. The developed mathematical models were verified by a semi-industrial hot-rolling process. Sauer et al. [12] analyzed the microstructure development of Nb-microalloyed steel during rolling on a heavy-section mill. A modified microstructure evolution model was presented that better accounted for the influence of strain-induced precipitation (SIP) on the kinetics of static recrystallization. The model was verified using the plain strain compression simulations of rolling a round bar 100 mm in diameter. For indirect comparison with the model outputs, the SIP initiation time was determined based on the NbX precipitate size distribution obtained by transmission electron microscopy. Using the PSCT and the outputs from the microstructure evolution model, it was found that during conventional rolling, strain-induced precipitation occurred after the last pass and, thus, did not affect the austenite grain size. By lowering the rolling temperature, it was possible to reduce the grain size by up to 56 μm. Schindler et al. [13] studied the combined effect of austenitization temperature and pre-deformation on continuous cooling transformation (CCT) diagrams of 23MnNiCrMo5-3 steel. Based on the dilatometric tests and metallographic analyses, a total of five different diagrams were constructed and compared. Pre-deformation corresponding to the true strain of 0.35 or even 1.0 had no clear effect on the austenite decomposition kinetics at a deformation temperature of 880 °C. During the long-lasting cooling, recrystallization and, likely, coarsening of the new austenitic grains occurred, which almost eliminated the influence of pre-deformation on the temperatures of the diffusion-controlled phase transformations. Decreasing the deformation temperature to 830 °C led to a significant acceleration of the austenite→ferrite and austenite→pearlite transformations due to the applied strain of 1.0 only in the region of the cooling rate, between 3 and 35 $°C \cdot s^{-1}$. Acceleration of the diffusion-controlled phase transformations resulted from the formation of an austenitic microstructure with a mean grain size of approximately 4 μm. As the analysis of the stress–strain curves showed, grain refinement was carried out by dynamic and metadynamic recrystallization. At low cooling rates, the effect of plastic deformation on the kinetics of phase transformations was indistinct.

The other three articles also discuss the microstructure evolution. Zurutuza et al. [14] studied the effect of DRX in ultra-high strength boron-microalloyed steels optionally alloyed with niobium and molybdenum. Multi-pass torsion tests were performed to simulate plate rolling conditions, followed by direct quenching. For Nb-microalloyed steel, partial DRX occurred and resulted in local clusters of fine-sized equiaxed grains being dispersed within the pancaked austenitic structure. A recrystallized austenite fraction appeared and transformed into softer phase constituents after direct quenching. The addition of molybdenum suppressed DRX and ensured the formation of fully martensitic microstructures. Cojocaru et al. [15] analyzed the hot deformation behavior of UNS S32750 Super-Duplex

Stainless Steel during processing by upsetting. The resulting samples were examined by electron backscatter diffraction (EBSD) to establish the evolution of the phases present in the structure from several points of view: nature, distribution, morphology (size and shape), and their structural homogeneity. The GROD (Grain Reference Orientation Deviation) distribution map was also determined while taking into account the possible precipitation of the secondary austenite phase and DRX process, depending on deformation temperature. The main conclusion is that the studied steel can be safely deformed by upsetting between 1050 °C and 1275 °C. Warm compression tests were carried out by Xu et al. [16] on low carbon and low alloy steel at temperatures of 600–850 °C. The evolution of microstructure and texture was studied using EBSD. The results indicated that cementite spheroidization greatly reduced at 750 °C due to a phase transformation. Dynamic recrystallization led to a transition from {112}<110> texture to {111}<112> texture. The contents of {111}<110> texture and {111}<112> texture were equivalent above 800 °C, resulting in the better uniformity of the γ-fiber texture. A temperature of 800 °C is suitable for the warm forming application, where the investigated material is easy to deform and evolves into a uniform and refined microstructure.

The following works [17,18] are related to the study of formability. The research of Du et al. [17] aimed to investigate the formability of Al–Si alloys reinforced with different fractions and different sizes of SiC particles to create an efficient and lightweight composite brake disk. Lanthanum and cerium were added to strengthen the aluminum matrix alloy and to improve the capability of the brake discs to withstand elevated temperature conditions, such as more extended braking periods. These elements formed intermetallic phases that further strengthened the composite. The additions of Ce and La strengthened the softer matrix regions and resulted in a doubled compression peak strength of the material without affecting the formability, as demonstrated by the processing maps. Rodak, Kuc, and Mikuszewski [18] studied superplastic deformation of Al–Cu alloys after grain refinement by extrusion combined with reversible torsion (KoBo). The binary as-cast Al–Cu alloys Al-5%Cu, Al-25%Cu, and Al-33%Cu (in wt%), composed of the intermetallic θ-Al2Cu and α-Al phases, were severely plastically deformed using extrusion coefficients of up to 98. KoBo enabled large elongation for alloys Al-25%Cu and Al-33%Cu (with higher intermetallic phase values) in the range from 830% to 1100% to be obtained by tensile testing at a temperature of 400 °C and a strain rate of 10^{-4} s^{-1}. The degree of elongation depended on the extrusion coefficient and increased, as a result of α-Al and θ-Al2Cu phase refinement, to about 200–400 nm. A microstructural study showed that the mechanism of grain boundary sliding was responsible for superplastic deformation.

Several authors have dealt with both theoretical and technological aspects of forging. Banaszek et al. [19] investigated the influence of open-die forging parameters on the flow kinetics of AZ91 magnesium alloy. The paper presents the results of numerical simulations (using commercial Forge®NxT software) of the process of forging ingots on a hydraulic press with the use of flat and proprietary shaped anvils. The aim of this research was to reduce the number of forging passes. Analysis of the hydrostatic pressure distribution and of the equivalent strain was carried out. This is one of the elements used for determining the ability of forging technology to obtain a semi-finished product from the AZ91 alloy with good strength properties. An analysis of the formability, structure, and properties of the AZ61 cast magnesium alloy using the example of a new forging process of aircraft mount forgings was presented by Dziubińska, Surdacki, and Majerski [20]. It was assumed that their production process would be based on drop forging on a die hammer. Two geometries of preforms, differing in forging degree, were used as the billet for the forging process. Using a cast preform positively affected the formability and flow kinematics during forging and reduced the number of operations necessary to obtain the correct product. Numerical analysis of the proposed new technology was carried out using the commercial software DEFORM 3D v.11. The results obtained from numerical tests confirmed the possibility of forming the forgings of aviation mounts from the AZ61 cast alloy with the proposed technology. They also allowed information to be obtained regarding the kinematics of the

material flow during forming and process parameters, such as strain distribution, temperature, Cockcroft–Latham criterion, and forming energy. The proposed forging process was verified in industrial conditions. The article of Banaszek et al. [21] discusses the impact of hot forging elongation operations on the closure of metallurgical discontinuities, such as middle porosity in selected magnesium alloys, depending on the shape of the input used. Laboratory simulations and numerical modeling, using the Forge®NxT 2.1 program based on the finite element method, were carried out in order to bring about the closure of defects of metallurgical origin in deformed forging ingots. Optimal values of the main technological parameters of forging and appropriate groups of anvils to be used in the individual stages of forging were proposed in order to eliminate the metallurgical defects. Using ultrasonic waves, Moravec, Bury, and Černobila [22] investigated selected characteristics of forging steel specimens for various levels of their relative reduction. The experimental procedure, using both the attenuation and velocity measurements, verified that the reduction in specimens' material had an effect on the propagation of ultrasound waves passing through the body of the specimen. The increase in toughness after a relative reduction in forging in the range of 10–50% is, with highest probability, caused by the relatively important deformation hardening. The experiments were supplemented by Barkhausen's noise detection and metallographic analysis of the specimens.

The paper by Bajor et al. [23] presents an analysis of the results of numerical simulations of the extrusion process of structural panels made from the 5xxx and 6xxx series aluminum alloys. The obtained products are intended for innovative superstructures of special car bodies. The main purpose of the research was to design a split die and to determine the parameters of the extrusion process. The distribution of stress, strain, strain rate, and temperature in the extruded metal was analyzed for two different punch movement speeds. It was shown that panel sections can be produced from ingots with a length of 770 mm on a press with the force of 35 MN. Mittelman et al. [24] studied the possibility to produce composite components by joining using plastic deformation, which results in metallurgical bonding at the interface. Beams of 6061 aluminum alloy were bonded by hot compression at temperatures of 300–500 °C to different degrees of reduction. The compression was followed by tensile debonding experiments, and the revealed interface was microscopically characterized in order to determine the areas that were metallurgically bonded. The actual bonded area was much smaller than the interface contact area. Thermo-mechanical finite element models of the compression forming were used to investigate the thermo-mechanical fields, which developed along the interface and influenced the resulting bonding strength. A quantitative criterion for bonding quality was implemented and shown to correlate with the experimental findings.

Conflicts of Interest: The authors declare no conflict of interest.

References

1. Łukaszek-Sołek, A.; Śleboda, T.; Lisiecki, L.; Krawczyk, J. Hot deformation behavior of 4130 high-strength steel. *Materials* **2022**, *15*, 7817. [CrossRef] [PubMed]
2. Chen, R.; Zhang, S.; Liu, X.; Feng, F. A flow stress model of 300m steel for isothermal tension. *Materials* **2021**, *14*, 252. [CrossRef] [PubMed]
3. Kawulok, P.; Opěla, P.; Schindler, I.; Kawulok, R.; Rusz, S.; Sauer, M.; Konečná, K. Hot deformation behavior of non-alloyed carbon steels. *Materials* **2022**, *15*, 595. [CrossRef] [PubMed]
4. Kittner, K.; Ullmann, M.; Prahl, U. A comparative study on the hot deformation behavior of as-cast and twin-roll cast Mg-6.8Y-2.5Zn-0.4Zr alloy. *Materials* **2021**, *14*, 3628. [CrossRef]
5. Wang, Y.; Zhao, S.; Guo, Y.; Liu, K.; Zheng, S. Deformation characteristics and constitutive equations for the semi-solid isothermal compression of cold radial forged 6063 aluminium alloy. *Materials* **2021**, *14*, 194. [CrossRef]
6. Lypchanskyi, O.; Śleboda, T.; Łukaszek-Sołek, A.; Zyguła, K.; Wojtaszek, M. Application of the strain compensation model and processing maps for description of hot deformation behavior of metastable β titanium alloy. *Materials* **2021**, *14*, 2021. [CrossRef]
7. Zhang, W.; Yang, Q.; Tan, Y.; Yang, Y.; Xiang, S.; Zhao, F. Study on the dynamic recrystallization behavior of 47Zr-45Ti-5Al-3V alloy by CA–FE simulation. *Materials* **2021**, *14*, 2562. [CrossRef]
8. Opěla, P.; Schindler, I.; Kawulok, P.; Kawulok, R.; Rusz, S.; Navrátil, H.; Jurča, R. Correlation among the power dissipation efficiency, flow stress course, and activation energy evolution in Cr-Mo low-alloyed steel. *Materials* **2020**, *13*, 3480. [CrossRef]

9. Hanoglu, U.; Šarler, B. Developments towards a multiscale meshless rolling simulation system. *Materials* **2021**, *14*, 4277. [CrossRef]
10. Lin, X.; Zou, X.; An, D.; Krakauer, B.; Zhu, M. Multi-scale modeling of microstructure evolution during multi-pass hot-rolling and cooling process. *Materials* **2021**, *14*, 2947. [CrossRef]
11. Dembiczak, T.; Knapiński, M. Shaping microstructure and mechanical properties of high-carbon bainitic steel in hot-rolling and long-term low-temperature annealing. *Materials* **2021**, *14*, 384. [CrossRef]
12. Sauer, M.; Fabík, R.; Schindler, I.; Kawulok, P.; Opěla, P.; Kawulok, R.; Vodárek, V.; Rusz, S. Analysis of the microstructure development of Nb-microalloyed steel during rolling on a heavy-section mill. *Materials* **2023**, *16*, 288. [CrossRef] [PubMed]
13. Schindler, I.; Kawulok, R.; Opěla, P.; Kawulok, P.; Rusz, S.; Sojka, J.; Sauer, M.; Navrátil, H.; Pindor, L. Effects of austenitization temperature and pre-deformation on CCT diagrams of 23MnNiCrMo5-3 steel. *Materials* **2020**, *13*, 5116. [CrossRef] [PubMed]
14. Zurutuza, I.; Isasti, N.; Detemple, E.; Schwinn, V.; Mohrbacher, H.; Uranga, P. Effect of dynamic recrystallization on microstructural evolution in B steels microalloyed with Nb and/or Mo. *Materials* **2022**, *15*, 1424. [CrossRef] [PubMed]
15. Cojocaru, E.; Nocivin, A.; Răducanu, D.; Angelescu, M.; Cinca, I.; Balkan, I.; Şerban, N.; Cojocaru, V. Microstructure evolution during hot deformation of UNS S32750 super-duplex stainless steel alloy. *Materials* **2021**, *14*, 3916. [CrossRef]
16. Xu, S.; Xu, H.; Shu, X.; Li, S.; Shen, Z. Microstructure and texture evolution in low carbon and low alloy steel during warm deformation. *Materials* **2022**, *15*, 2702. [CrossRef]
17. Du, A.; Lattanzi, L.; Jarfors, A.E.W.; Zhou, J.; Zheng, J.; Wang, K.; Yu, G. The influence of Ce, La, and SiC particles addition on the formability of an Al-Si-Cu-Mg-Fe SiCp-MMC. *Materials* **2022**, *15*, 3789. [CrossRef]
18. Rodak, K.; Kuc, D.; Mikuszewski, T. Superplastic deformation of Al–Cu alloys after grain refinement by extrusion combined with reversible torsion. *Materials* **2020**, *13*, 5803. [CrossRef]
19. Banaszek, G.; Bajor, T.; Kawałek, A.; Garstka, T. Investigation of the influence of open-die forging parameters on the flow kinetics of AZ91 magnesium alloy. *Materials* **2021**, *14*, 4010. [CrossRef]
20. Dziubińska, A.; Surdacki, P.; Majerski, K. The analysis of deformability, structure and properties of AZ61 cast magnesium alloy in a new hammer forging process for aircraft mounts. *Materials* **2021**, *14*, 2593. [CrossRef]
21. Banaszek, G.; Bajor, T.; Kawałek, A.; Knapiński, M. Modeling of the closure of metallurgical defects in the magnesium alloy die forging process. *Materials* **2022**, *15*, 7465. [CrossRef] [PubMed]
22. Moravec, J.; Bury, P.; Černobila, F. Investigation of forging metal specimens of different relative reductions using ultrasonic waves. *Materials* **2021**, *14*, 2406. [CrossRef] [PubMed]
23. Bajor, T.; Kawałek, A.; Berski, S.; Jurczak, H.; Borowski, J. Analysis of the extrusion process of aluminium alloy profiles. *Materials* **2022**, *15*, 8311. [CrossRef]
24. Mittelman, B.; Ben-Haroush, M.; Aloush, I.; Mordechay, L.; Priel, E. Bonding of Al6061 by hot compression forming: A Computational and experimental study of interface conditions at bonded surfaces. *Materials* **2021**, *14*, 3598. [CrossRef] [PubMed]

materials

MDPI

Article

Hot Deformation Behavior of 4130 High-Strength Steel

Aneta Łukaszek-Sołek *, Tomasz Śleboda, Łukasz Lisiecki and Janusz Krawczyk

Faculty of Metals Engineering and Industrial Computer Science, AGH University of Science and Technology, Av. Mickiewicza 30, 30-059 Krakow, Poland

* Correspondence: alukasze@metal.agh.edu.pl; Tel.: +48-12-617-25-75

Abstract: Hot deformation behavior of 4130 steel and optimization of its processing parameters are presented in this paper. Compression tests were performed at temperatures ranging from 800 to 1200 °C and at the strain rates in the range from 0.01 to 100 s^{-1}. A comprehensive analysis of the material behavior at different temperature and strain-rate ranges was performed taking into account various criteria of stability and instability of the material flow under various thermomechanical conditions. The flow–stress curves obtained during compression tests, as well as the processing maps elaborated on the basis of various flow–stability criteria, are discussed. Processing parameters developed according to the Prasad's and Murty's criteria are recommended for designing the technology of forging of the investigated steel. Such parameters ensure the homogeneity and stability of the material flow in a forged part, what was confirmed by successful forging of 4130 steel in industrial conditions. The processing map developed according to Gegel's approach, as compared to the processing maps obtained in accordance with the Prasad's and Murty's criteria, should be treated as general support for determining the thermomechanical processing parameters.

Keywords: thermomechanical processing; steel; processing maps; microstructure; forging

Citation: Łukaszek-Sołek, A.; Śleboda, T.; Lisiecki, Ł.; Krawczyk, J. Hot Deformation Behavior of 4130 High-Strength Steel. *Materials* **2022**, *15*, 7817. https://doi.org/10.3390/ma15217817

Academic Editor: Ivo Schindler

Received: 19 September 2022
Accepted: 31 October 2022
Published: 5 November 2022

1. Introduction

The control of hot deformation behavior and the properly chosen processing parameters are essential for successful design of the technology of the production of high-strength steel parts [1–4]. Processing maps and dynamic material modeling [5–7] enable selecting appropriate parameters of thermomechanical processing of such steels and, as a result, obtaining good quality products having profitable mechanical properties and uniform microstructure. Much research in this area has been carried out in relation to aluminum alloys [8,9], titanium alloys [10,11], and nickel alloys [12,13]. In the design of structural parts widely used in the automotive and railroad industries, high-strength steels are becoming increasingly important [14,15].

Using the basic principles of continuum mechanics of large plastic flow and also modeling of physical systems and irreversible thermodynamics, a methodology called the dynamic material model was developed [16]. The workpiece is treated as the dissipator of power—the unit power (P) absorbed by the material during processing. It can be expressed as [17,18]:

$$P = \sigma \cdot \dot{\varepsilon} = G + J = \int_0^{\dot{\varepsilon}} \sigma_p d\dot{\varepsilon} + \int_0^{\sigma} \dot{\varepsilon} d\sigma \quad (1)$$

where $\dot{\varepsilon}$ = the strain rate, s^{-1}, σ = the flow stress, MPa, J = dissipator co-content, G = dissipator content.

The J co-content, associated with the power dissipation dynamic processes ongoing in the material being processed, can be expressed as follows [18]:

$$J = \int_0^{\sigma} \dot{\varepsilon} d\sigma = \frac{\sigma \cdot \dot{\varepsilon} \cdot m}{m+1} \quad (2)$$

where m is the strain-rate-sensitivity parameter.

The relationship between the heat generation (G) and the microstructural changes (J) is described by the strain-rate-sensitivity parameter (m) and can be calculated from the formula [17]:

$$m = \left(\frac{\partial J}{\partial G}\right)_{T,\,\varepsilon} = \left(\frac{\partial log\sigma}{\partial log\dot{\varepsilon}}\right)_{T,\,\varepsilon} \tag{3}$$

where ε = the constant true strain value, T = the temperature, °C.

Flow–stress data are used to derive the workability parameters by applying various criteria and developing processing maps from them. The processing maps as a function of temperature and log (strain rate) show the process conditions for stable and unstable hot deformation [19–22]. For the determination of the stability domains and the areas of flow instability based on the dynamic modeling of the material behavior in hot deformation processes, various criteria have been developed. The criteria for stability and instability of a material under different thermomechanical conditions make it possible to conduct research on the behavior of metallic materials in hot deformation processes. Such studies should also consider the comparison of existing criteria [23–25]. Nevertheless, the responsibility for selecting and evaluating the correctness of a given theory in modeling hot deformation behavior is within the scope of the designer or researcher responsibility.

In the first criterion (Prasad's approach), the efficiency of power dissipation-η, reflecting the material microstructure evolution, is determined by the following formula [7]:

$$\eta = \frac{J}{J_{max}} = \frac{2m}{m+1} \tag{4}$$

This criterion can be expressed as [7,26,27]:

$$\xi_1 = \frac{\partial log\left(\frac{m}{m+1}\right)}{\partial log\dot{\varepsilon}} + m \leq 0 \tag{5}$$

It is used to identify instabilities in the material flow during hot working.

In the second criterion, according to Murty's approach, the expression of the power dissipation efficiency η is defined by the use of the $J/Jmax$ ratio, and provided by [28,29]:

$$\eta = \frac{J}{J_{max}} = 2\left(1 - \frac{1}{\sigma\dot{\varepsilon}}\int_0^{\dot{\varepsilon}} \sigma\, d\dot{\varepsilon}\right) \tag{6}$$

The Murty's instability parameter can be calculated as [28–30]:

$$\xi_2 = \frac{2m}{\eta} - 1 < 0 \tag{7}$$

Applying the second law of thermodynamics, the extremal principles of irreversible thermodynamics as applied to large plastic flow and the stability theory, Gegel [23,29] constructed two Liapunov functions that applied the efficiency of the power dissipation η and the temperature sensitivity s with the independence variable as log$\dot{\varepsilon}$:

$$V_1 = \eta\left(log\dot{\varepsilon}\right) \tag{8}$$

$$V_2 = s\left(log\dot{\varepsilon}\right) \tag{9}$$

The temperature-sensitivity parameter of the flow stress can be calculated from the equation [29]:

$$s = \frac{1}{T}\cdot\frac{\partial ln\sigma}{\partial\left(\frac{1}{T}\right)} \tag{10}$$

The parameters η and s are determined as the strain rate and temperature function.

In the third criterion, according to Gegel's approach, the criteria for ensuring the stable material flow could be given as:

$$0 < m \leq 1 \tag{11}$$

$$\eta_{criterion} = \frac{\partial \eta}{\partial \left(ln\dot{\varepsilon} \right)} < 0 \tag{12}$$

$$s \geq 1 \tag{13}$$

$$s_{criterion} = \frac{\partial s}{\partial \left(ln\dot{\varepsilon} \right)} < 0 \tag{14}$$

The Gegel's instability parameters are:

$$\xi_3 = m < 0 \tag{15}$$

$$\xi_4 = -\frac{\partial \eta}{\partial \left(ln\dot{\varepsilon} \right)} < 0 \tag{16}$$

$$\xi_5 = s - 1 < 0 \tag{17}$$

$$\xi_6 = -\frac{\partial s}{\partial \left(ln\dot{\varepsilon} \right)} < 0 \tag{18}$$

Considering Gegel's criterion, the strain-rate-sensitivity parameter m can be related to the mechanical stability and the temperature-sensitivity parameter s to the material or structural stability [23]. In order to ensure stable material flow, it is important that the stress increases with the strain rate (and the curves have a convex shape), and the flow stress should decrease with respect to the temperature [28]. According to the second law of thermodynamics, if the temperature-sensitivity parameter s is greater than 1, then the stable material flow will be ensured [29]. In order to gain a power dissipation map, the stability parameters should be presented as a contour map taking into account temperature and log (strain rate). With such a map, it is possible to observe the proportion of power dissipated by the microstructure as a function of strain rate, strain, and temperature. It is assumed that the higher the value of the power dissipation efficiency (30–60%), the higher the probability of dynamic recrystallization (DRX), while at the lower values of the power dissipation efficiency (20–30%) DRV-related processes can be expected [12]. It happens that high values of the parameter η do not always correspond to domains that are safe for the workability of the material, and therefore the criterion for the occurrence of flow instability (η_i) must also be taken into account. In the result, changes in the instability parameter η_i as a function of strain rate and temperature enable instability maps to be plotted. The areas where $\eta_i < 0$ correspond to microstructural instabilities in the material. In these areas, defects can be expected in the form of void formation, wedge cracking, intercrystalline fracture and other types of fracture processes, as well as adiabatic shear bands, Lüder bands, kink bands and mechanical twinning [21,31,32]. When designing the forming technology for a specific material, the information gained from the processing map is very useful. The process windows describe the most favorable forming parameters (in terms of temperature and strain rate) and also allow the control of the microstructure. The range of strain and strain rates under which the processing tests are conducted are also of great importance. Bulk metal forming processes are characterized by the wide range of deformation velocity and the corresponding wide range of the strain rates. In the case of structural parts with complex geometries, it seems worthwhile to undertake the studies comparing the accuracy of the criteria for identifying areas of the flow instability on the processing maps obtained according to Prasad's, Murty's, and Gegel's criteria for the different strains and the highest possible strain rates. An interesting approach to analyze the deformation behaviour and microstructure evolution in isothermal compression of 300M steel was presented by Sun et al. [33]. The development of processing maps coupled with grain size was proposed using the physics-based visco-plastic constitutive equations and adopting a dynamic material model. For the different strains, the efficiency of the power dissipation

and the instability parameters coupled with the material grain size were calculated. It was found that, in the case of isothermal compression of 300M steel, the grain size-coupled processing maps differ from the traditional processing maps in terms of Prasad's theory, and that, in parallel with the microstructure observations, they can more accurately describe the deformation behavior of the material at elevated temperatures. Zhou et al. [34] studied the hot forging behavior of 25CrMo4 steel and developed a constitutive model. Moreover, the optimum parameters for the forging process were determined from the throughput maps and, using a kinetic model, the effect of strain on the efficiency of the power dissipation was discussed. However, the study was conducted for a true strain of 0.7 and a maximum strain rate of 10 s^{-1}. Usually, processing maps are produced for only one, and a small, strain value. Only few works present processing maps developed for strains of, for example, 0.8 and higher [35–38]. For example, Liu et al. [39] studied the hot deformation behavior of 25CrMo4 steel based on the processing maps but only for the strain of 0.8 and strain rate of 1 s^{-1}. Such a low strain rate does not correspond to the strain rates commonly used in industrial conditions in the majority of forging machines. In the majority of papers, the highest strain rate for which research is conducted is 10 s^{-1} [34,40], sometimes 50 s^{-1} [41], and infrequently 80 s^{-1} [25]. In turn, the strain rate of 100 s^{-1} was taken under consideration, for example, by Sescharyulu et al. [42], but only for the true strain of 0.5, Sui et al. [43] for the true strain of 0.7, Łukaszek-Sołek et al. [35,36] for the true strain of 0.9, and by Pu et al. [44] for the strain of 1. Few works deal with the comparison of different criteria and the development of comprehensive processing maps. For the high-Mn TWIP austenitic steel [37] instability maps based on different stability and instability criteria (i.e., Gegel's and Alexander-Malas's stability criterion, Prasad's, Murty's and Babu's instability criterion) were developed and compared. On the basis of the deformation maps based on microstructural observation, it was found that instability maps differed to some extent from each other and that the instability criteria were more suitable in terms of predicting the occurrence of flow instabilities, which manifest themselves as heterogeneous flow and localized deformation bands.

This paper presents a comprehensive analysis of the hot deformation behavior of the 4130 steel under test at different temperature ranges and strain rates up to 100 s^{-1}. The flow–stress curves obtained from the compression tests were used to develop processing maps developed on the basis of different flow–stability criteria for different strains up to that equal to 1. As a result, the hot deformation behavior of the investigated steel for a wide range of strain rates corresponding to the characteristics of most machines used in industrial forging conditions and a wide range of strains is discussed and, furthermore, favorable hot working parameters were proposed and verified in an industrial forging test.

2. Experimental Procedure

4130 steel was selected for the investigation. Table 1 presents the chemical composition of the investigated steel.

Table 1. The chemical composition of the investigated steel.

Chemical Composition, wt. %												
Fe	**C**	**Mn**	**Ni**	**Cr**	**P**	**Si**	**Mo**	**S**	**V**	**Sn**	**Al**	**N**
Bal.	0.29	0.55	0.11	1.10	0.007	0.17	0.22	0.012	0.004	0.007	0.027	0.008

The investigated material was supplied by a commercial manufacturer (FRY Steel Company, Chicago, USA) in a form of a Ø50 bar in a heat-treated state. All test samples were cut out from a 4130-steel rod, in the direction parallel to the rod axis at a distance of approx. 2/3 of the radius from the center of the rod cross-section. The samples having 12 mm in height and 10 mm in diameter were machined by electrical discharge machining (EDM) and polished before compression tests. A compression testing was then performed on the Gleeble 3800 thermomechanical simulator (Dynamic Systems Inc., Poestenkill, NY, USA)

until a total true strain was 1. The isothermal tests were carried out in an argon atmosphere at the temperature range from 800 to 1200 °C, and at the strain-rate range from 0.01–100 s^{-1}. A graphite foil was used as a lubricant to minimize the friction between the samples and anvils. The samples were homogenized in 10 s prior to deformation and the resistance heating rate of 2.5 °C/s was applied. After the compression test, the specimens were cooled with compressed air (10 °C/s) and machined along the axial direction to observe the microstructure. Microstructural investigations were performed using an Axiovert 200MAT optical microscope, manufactured by the Zeiss company (Oberkochen, Germany), and also using a scanning microscope, FEI VERSA 3D (FEI—ThermoFisher Scientific, Waltham, MA, USA),, for obtaining images with the application of the BSE technique (the detector of reversely dissipated electrons). Analytical modeling was performed using Matlab software (version R2022a, MathWorks, Natick, MA, USA) in order to calculate the workability parameters such as the strain-rate-sensitivity parameter m, the efficiency of power dissipation, and etc. The various parameters needed for designing processing maps were calculated based on the flow–stress data. A cubic spline fit for the test data was applied to generate the greater number of data points. The Surfer software (version 23.3.202, Golden Software, LLC, Golden, USA) was used for generating the processing maps. Industrial drop forging tests were conducted for selected model forging made of the 4130 steels under the conditions determined for processing windows on developed processing maps.

3. Results and Discussion

The microstructure of the investigated steel in as-delivered (hot-rolled and normalized) condition is presented in Figure 1.

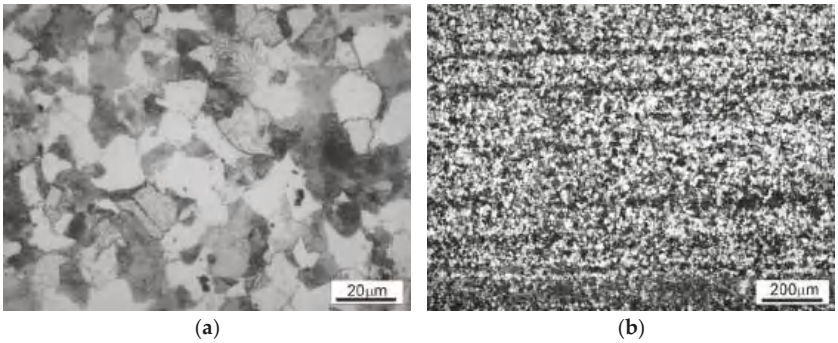

(**a**) (**b**)

Figure 1. The microstructures of the 4130 steel in as-delivered condition: (**a**) transverse cross-section, (**b**) longitudinal cross-section.

The microstructure of the starting material (annealed 4130 steel bar) consists of ferrite and pearlite (Figure 1a,b). In the longitudinal section, banding resulting from interdendritic microsegregation and subsequent hot forming can be observed (Figure 1b). The homogeneity of the material on the rod cross-section allowed for the preparation of samples with a similar initial microstructure for the plastometric tests. Additionally, the presence of weak banding allowed the assessment of the influence of deformation on the material flow and the influence of deformation conditions on the homogenization of the microstructure.

3.1. Flow Behaviour

True stress–strain curves for the investigated steel deformed to a true strain of 1 at the temperature range from 800–1200 °C and strain-rate range from 0.01–100 s^{-1} are presented in Figure 2.

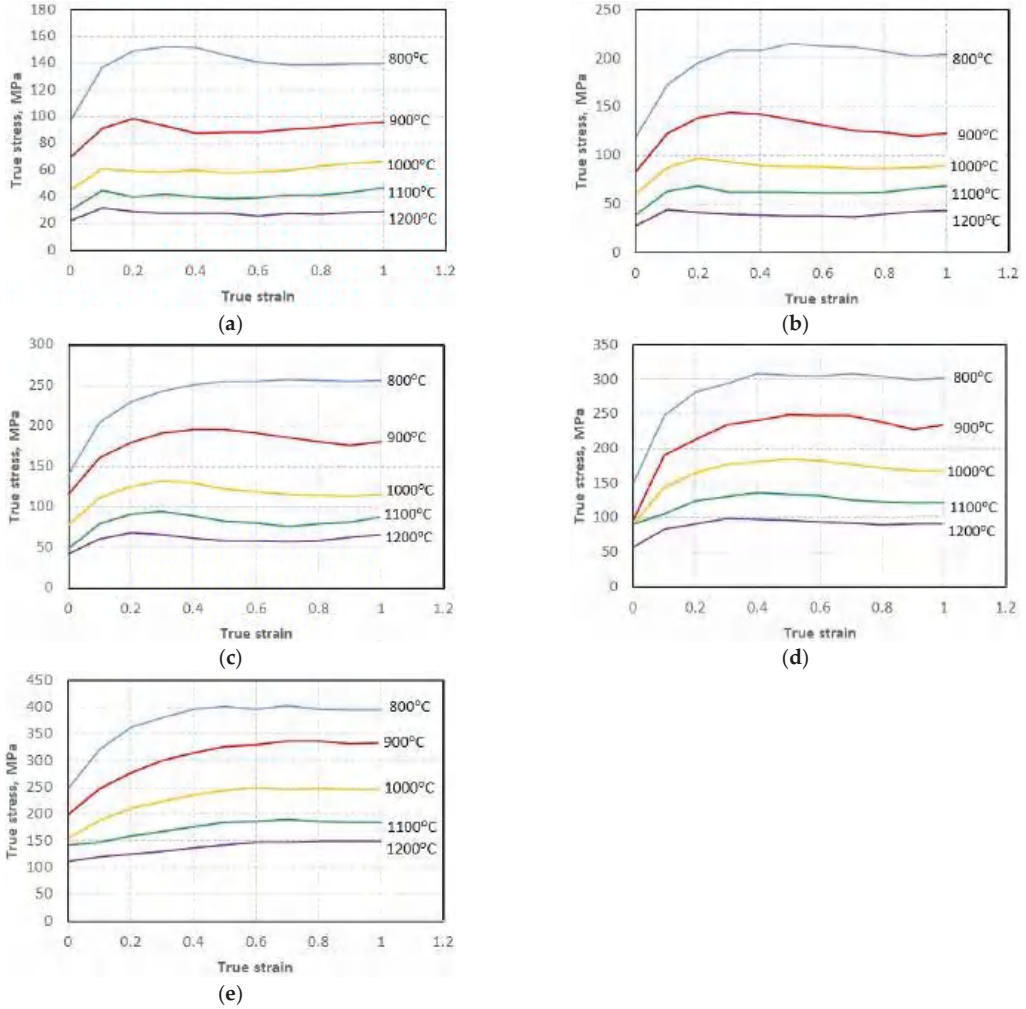

Figure 2. The true stress-true strain curves for the investigated 4130 steel deformed in compression at the true strain rate of 0.01 s^{-1} (**a**), 0.1 s^{-1} (**b**), 1 s^{-1} (**c**), 10 s^{-1} (**d**), 100 s^{-1} (**e**).

The expected decrease in flow stress with increasing temperature and decreasing strain rate was observed, which signifies that, in the case of the investigated steel processing, the deformation temperature and strain rate have great effect on its hot deformation behavior. Stress rising to a peak followed by softening toward a steady state region signifies typical DRX behavior under higher temperatures (1000–1200 °C) regardless of strain rate. The flow–stress curves for the lower deformation temperatures (800 °C and 900 °C) indicate that, at those temperatures, the investigated material underwent recrystallization to a limited extent also regardless of the applied strain rate.

3.2. Processing Maps

Basing on the obtained flow–stress curves, the processing maps for various temperatures and for the true strains of ε = 0.4, 0.6, 0.8, and 1 were elaborated (Figure 3). The numbers on the contour lines signifies the percent efficiency of the power dissipation η. They are directly related to the process of microstructural evolution of the material, such as

DRX, grain coarsening or DRV [45–47]. The areas of the flow instability characterize inhomogeneous deformation, which should be avoided when designing hot processing conditions.

(**a**) (**b**)

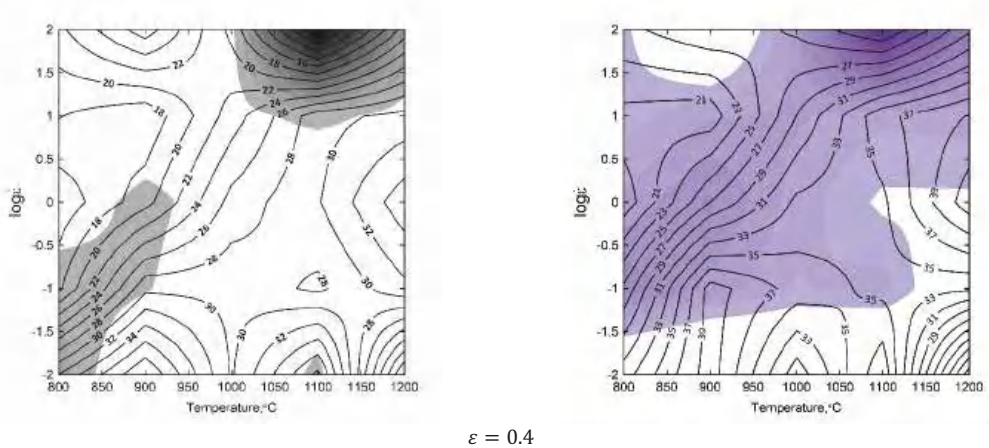

$\varepsilon = 0.4$

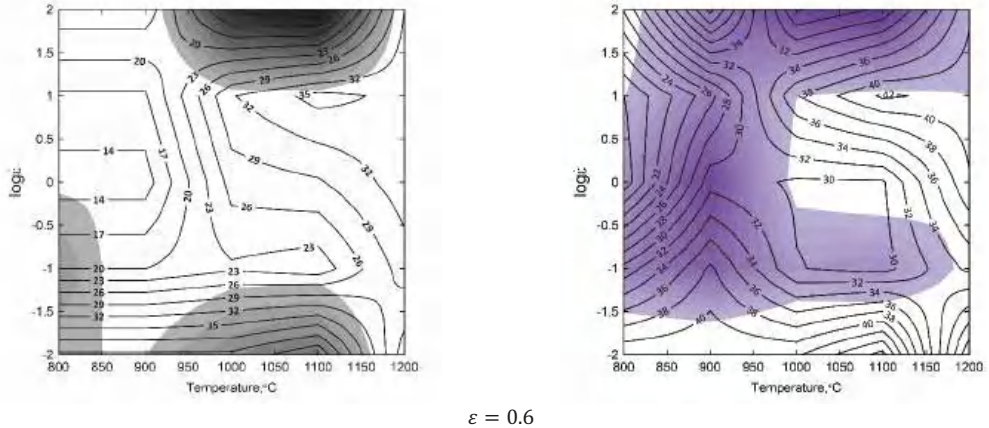

$\varepsilon = 0.6$

Figure 3. *Cont.*

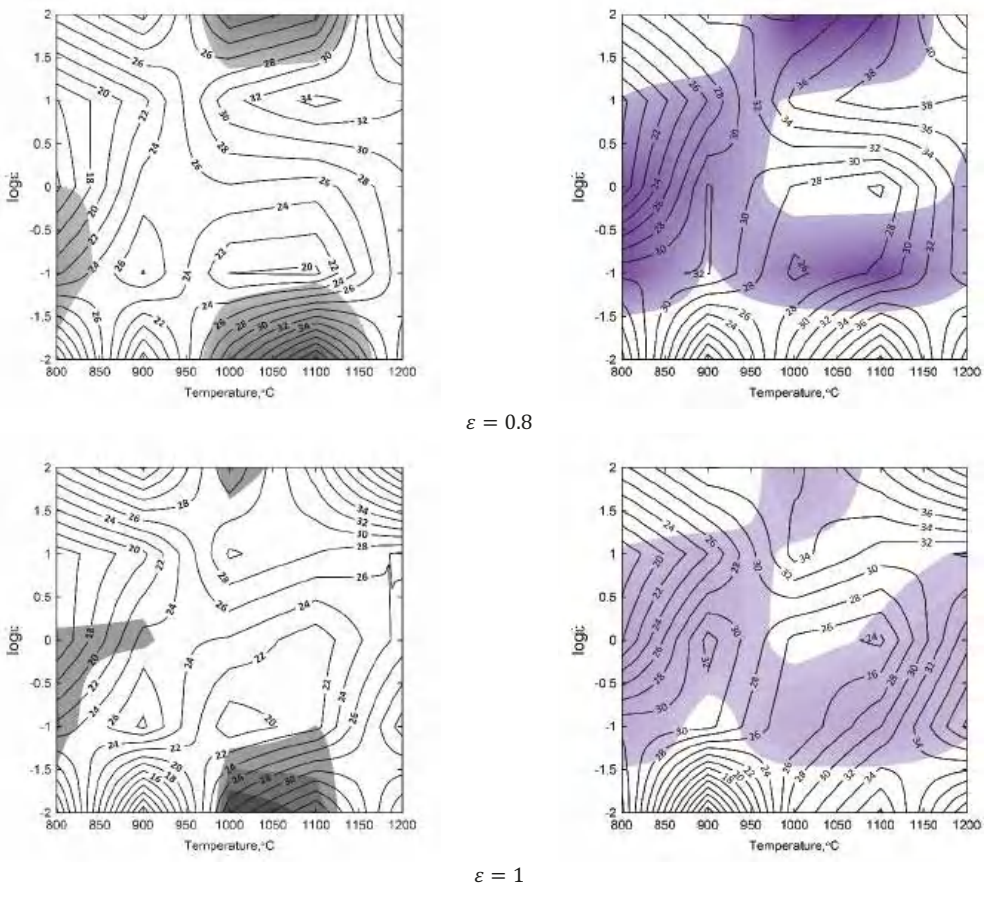

Figure 3. 4130 steel processing maps based on the Prasad's (**a**) and Murty's (**b**) criterion for the true strain of: 0.4, 0.6, 0.8, 1.

The areas of material flow instability shown on the processing maps were elaborated for a true strain of 1 (Figure 3). The preferred processing windows include the significant parameters of the process and design recommendations for the thermomechanical forging processes. In the processing maps drawn up upon the basis of Prasad's criterion, three processing windows were differentiated and upon the basis of Murty's criterion, there were four processing windows. Processing window 1 is characterized by the similar location on the processing map comparing Prasad's with Murty's approach within the range of η%, which represents the temperature and strain rate, and constitutes the contour of the dissipation efficiency parameter:

- η_P = 18–36% in the range of temperatures from T = 800–975 °C, and a strain rate of $\dot{\varepsilon}$ = 12.5–100 s^{-1}. The isoclines of η%, retaining fairly uniform variability, have a regular oval shape and indicate an increasing workability of the material with an increasing strain rate.
- η_M = 18–32% in the range of temperatures from T = 800–950 °C, and a strain rate $\dot{\varepsilon}$ = 12.5–100 s^{-1}. The isoclines of parameter η have a similar course, a small amplitude of changes, and they increase simultaneously with the temperature. The changing frequency of the course of the isoclines indicates the certain stability of material flow during deformation.

It may be recommended for the processes of small forgings with the application of the forging devices of the following types: horizontal forging machines, hydraulic screw presses, screw presses and double-action air-steam hammers.

The comparison of processing window 2 developed in accordance with Prasad's and Murty's criterion makes it possible to see their similarity (shape and parameters). It is situated within the contour of isoclines:

- η_P = 30–46% in the range of temperatures from T = 1075–1200 °C and strain rate of $\dot{\varepsilon}$ = 15.8–100 s^{-1}.
- η_M = 32–44% for T = 1075–1200 °C and $\dot{\varepsilon}$ = 15.8–100 s^{-1}.

The isoclines of the dissipation efficiency parameter η% have a very regular shape. That window reflects the optimum conditions for the material workability at the temperature of 1200 °C and a strain rate 100 s^{-1}. It may be recommended for conducting the conventional processes of die impression forging for a wide assortment of forgings with the application of the Maxi-type mechanical presses, screw presses and double-action air-steam hammers. For that group of forging devices, the deformation velocity converted into the strain rate fluctuates within a very wide range ($\dot{\varepsilon} = 0.03 - 1400\ s^{-1}$).

Processing window 3 is characterized by the following parameters:

- η_P = 10–24%, $\dot{\varepsilon}$ = 0.01 – 0.06 s^{-1}, and T = 800–980 °C. The values of the η% isoclines may prove the uniformity of the material flow in the range of small strain rates, and possibly that window may be recommended for the purpose of hot forging small drop forgings with the application of a hydraulic press.
- η_M = 10 –30% in the range of temperatures from T = 800–980 °C, and strain rate $\dot{\varepsilon}$ = 0.01 – 0.06 s^{-1}. The course of the isoclines maintains a uniform growth tendency of the values of η% with the decrease in temperature down to 800 °C. The window is dedicated for hot forging small and very small, compact and elongated die forgings with the application of hydraulic presses, and the open die forgings in flat or shaped anvils.

Processing window 4 in accordance with Murty's criterion includes the following parameters:

- η_M = 28–38%, T = 1000–1200 °C and $\dot{\varepsilon}$ = 0.01–0.03 s^{-1}. The window characterizes the optimal level of susceptibility to plastic deformation, reaching the maximum of the values of power dissipation amounting to 38%. The isoclines of the process efficiency η have a regular course and a small curvature in its shape, proving the uniform kinetics of the material plastic flow, and homogeneous deformation. The parameters of this window are appropriate for the forging of relatively small die forgings with the application of Maxi mechanical, hydraulic and hydraulic–mechanical presses.

The shape and size of the processing windows for ε = 0.8 are similar to the windows for ε = 1 and undergo the substantial differentiation of the significant parameters of the process.

In the case of the true strain of 0.6, the areas of instability undergo extension and are not in agreement with processing window 3 obtained according to Prasad's approach. The processing map generated for the true strain of 0.6, taking into consideration Murty's approach, shows one very extensive area of instability, which is not in agreement with processing windows 1 and 2. Processing windows 3 and 4 change their parameters, because in this case the stability areas insignificantly change their size—they are flattened and elongated in their shape.

For the true strain of 0.4 on the processing map, there are only two processing windows according to Prasad's approach: 1, and also 3 (but having slightly different position). Processing window 2 was excluded from consideration because of the increased area of instability. Taking into account the processing windows created on the processing map obtained according to Murty criterion, the position of windows 3 and 4 is not changed. The efficiency of power dissipation parameter η% has much lower values.

The processing parameters presented in processing window 2 are recommended for designing the technology of forging. They should ensure the homogeneity and stability of the material flow in a forged part.

Table 2 shows a summary of the parameters for the determined processing windows for the true strain of 1 according to the approach of Prasad and Murty.

Table 2. Suggested thermomechanical processing parameters for the investigated steel, determined in processing windows for a true strain of 1 according to Prasad's and Murty's criterion.

Window		Prasad's Approach	Murty's Approach
1	The efficiency of power dissipation	η_P = 18–36%	η_M = 18–32%
	The range of temperatures	T = 800–975 °C	T = 800–950 °C
	The range of strain rate	$\dot{\varepsilon}$ = 12.5–100 s^{-1}	
2	The efficiency of power dissipation	η_P = 30–46%	η_M = 32–44%
	The range of temperatures	T = 1075–1200 °C	
	The range of strain rate	$\dot{\varepsilon}$ = 15.8–100 s^{-1}	
3	The efficiency of power dissipation	η_P = 10–24%	η_M = 10–30%
	The range of temperatures	T = 800–980 °C	
	The range of strain rate	$\dot{\varepsilon}$ = 0.01–0.06 s^{-1}	
4	The efficiency of power dissipation	-	η_M = 28–38%
	The range of temperatures	-	T = 1000–1200 °C
	The range of strain rate	-	$\dot{\varepsilon}$ = 0.01–0.03 s^{-1}

The analysis of the processing maps in accordance with Prasad's and Murty's criterion makes it possible to ascertain that Murty's criterion presents deformation mechanisms set against energy-focused ways of seeing the process in a more comprehensive way, in particular, within the range of changes in the course, and in the values of the efficiency of the power dissipation parameter η%, and also in that of the material structure. The differences between the predicted results for the processing windows and the location of them are small, and the precision of predictions in accordance with Murty's criterion is more stable, and, ipso facto, superior. Murty's criterion presents the regimes of process instability in accordance with the equation (7) more broadly, because it includes the values of the efficiency of the power dissipation parameter η and the strain-rate-sensitivity parameter m for verifying the metallurgical process instability. Upon the basis of the processing maps for the investigated steels (Figure 3), it is possible to observe that the amount of deformation exerts a significant influence upon identifying the processing windows and the area of instability. Processing maps provide valuable technological information for designing the bulk metal working process, such as the forging of drop forgings having diversified surfaces (in terms of cavities, ribs or splines), and the degree of the difficulty of processing. That is relevant to, in particular, the assessment of the intensiveness of the material forming process and in determining the level of the influence of the set of intermediate strains for achieving the correct die impression, filling and obtaining the presumed shape of a good quality forged part. Taking advantage of the method of intermediate stages may constitute a significant cognitive contribution to the assessment of the material forming design correctness.

The complex maps, presented in Figure 4, were developed as the result of superimposing four inequalities describing the stability criteria in accordance with Gegel's approach for the true strain of 1. The map shows the stable domains (white areas) and the instability regimes (colored). Three stability areas, marked as A, B and C, having the most advantageous combination of the parameters m, $\eta_{\text{criterion}}$, s and $s_{\text{criterion}}$ were identified for the 4130 steel.

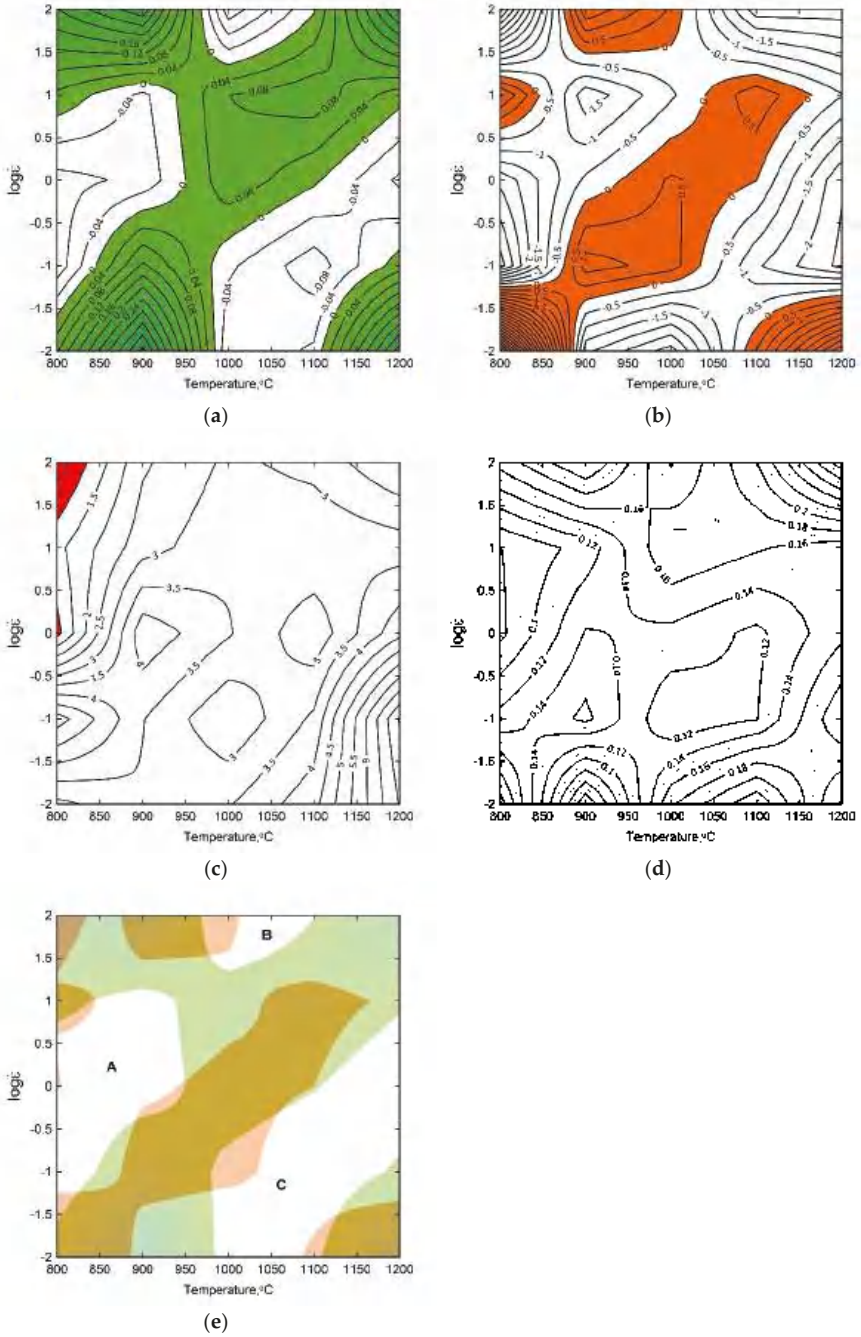

Figure 4. Contour map for the $\eta_{\text{criterion}}$ (**a**), contour map for the $s_{\text{criterion}}$ (**b**), contour map for the temperature-sensitivity parameter of flow stress s (**c**), the maps of changes in the strain-rate-sensitivity parameter m (**d**) and the processing map based upon Gegel's stability criterion (**e**) for the 4130 steel for the true strain of 1, A, B, C-domains of flow stability.

3.3. Processing Maps Combined with the Analysis of the Microstructure of the Investigated Steel

The analysis of the microstructures of the samples deformed in the compression on the Gleeble 3800 simulator was performed. The microstructure of the investigated steel developed as the result of intense cooling after deformation in the austenite region. The applied cooling resulted in a diffusion-free transformation of the austenite into martensite or in intermediate transformation into bainitic structures.

It can be observed that increasing the deformation temperature and strain rate favor the homogenization of the tested steel, causing the banded structure to disappear (Figure 5). However, even at higher strain rates at a deformation temperature of 1200 °C, banding in the microstructure of the samples can still be noticed. This proves the important role of temperature and annealing time for the austenitic range in the diffusion of alloying elements and carbon, favoring the homogenization of the chemical composition of austenite. Figure 5 presents the complex processing map combining all the analyzed flow–stability criteria correlated with the characteristic microstructural changes observed in the deformed samples. The left-hand upper corner of the processing map has the parameter value of $s < 1$, and therefore, the temperature and microstructure instability of the material. The right-hand upper corner of the map (strain rate increasing up to 100 s^{-1}) indicates an increase in material strength resulting from work hardening. The left-hand bottom corner of the complex processing map indicates the deformation heterogeneity, often connected with transition bands between two parts of austenite grains (banding). The right-hand bottom corner of the map is characterized by microstructural instability connected with the growth of the austenite grains in the matrix of a deformed material.

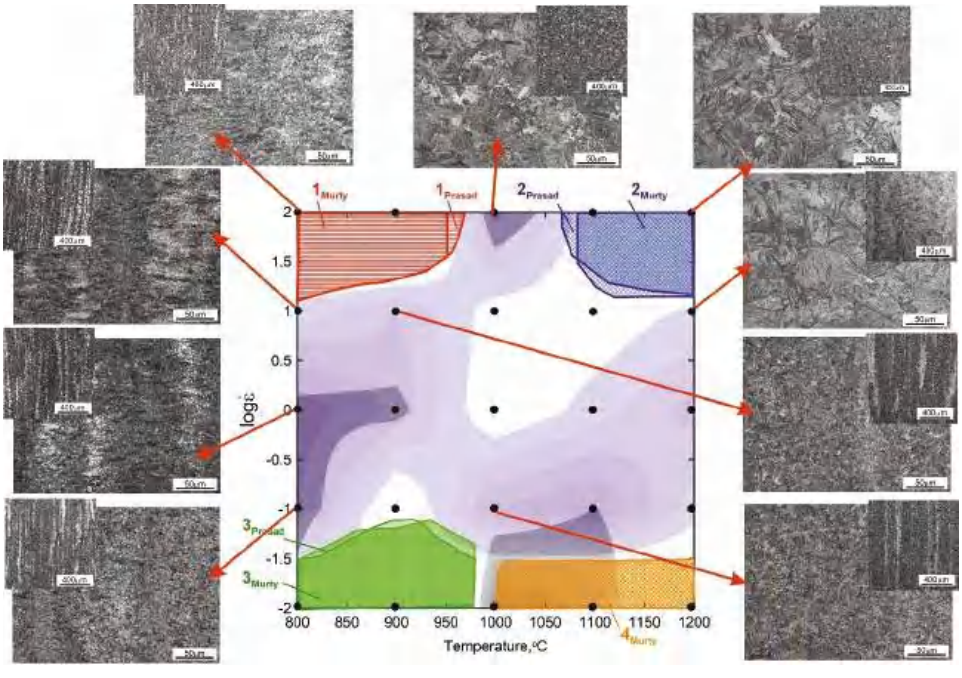

Figure 5. Complex processing map combining all the analyzed flow–stability criteria correlated with characteristic microstructural changes observed in the deformed samples. The areas in gray shades correspond to the material flow instability parameters. White areas correspond to processing parameters leading to stable material flow.

The banding visible in the microstructure of the deformed compression samples is the result of microsegregation of the chemical composition (mainly phosphorus and manganese). In the normalized (initial) state, it is faintly visible; however, accelerated cooling from the austenite range (austenitic structure was deformed) resulted in a bainitic transformation, which made again the areas of chemical composition segregation visible due to the formation of the different bainite morphologies as a result of the different hardening of micro-areas of the different chemical composition.

3.4. Industrial Forging Test and the Analysis of the Microstructure of Forged Part

A comprehensive approach to the issue of die forging enables a multi-criteria analysis of the thermomechanical process of forging complex-shaped forgings—the typical representative of which is the flange-type forging—according to the parameters determined on the basis of the processing maps ensuring the desired microstructure and mechanical properties. The forging of 4130 steel in industrial conditions was carried out on a double-action hammer in accordance with the established parameters of the forming process related to the processing window 2 according to Prasad's and Murty's criteria. The billet was heated up to the temperature of 1200 °C in an electrical furnace and forged in two operations: initial upset forging and forging in a finishing impression. After the forging process, the forged part was cooled with forced air. A flange forged on hammer is presented in Figure 6a. The samples for the metallographic investigations were taken from the cross-section of the forged part (Figure 6b).

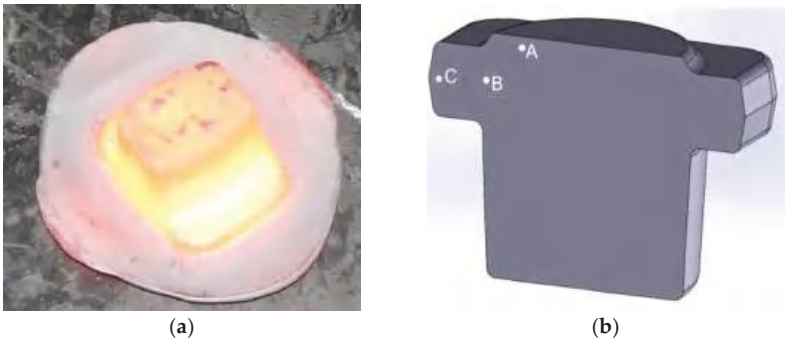

(**a**) (**b**)

Figure 6. The flange forged on hammer (**a**), the flange model with areas of metallographic investigations marked (**b**). A, B, C – areas of metallographic observations on the forged part cross-section.

Figure 7 shows selected optical (a) and scanning electron micrographs (b) at the points selected for the analysis (see Figure 6b) of the microstructure of the flange forging. The mean primary austenite grain sizes were calculated using Jeffries method. The microstructure has the largest grains in area B (2956 μm^2), smaller in area A (2888 μm^2), and the smallest in area C (1769 μm^2). This corresponds to the areas of increasing strain in the forged part. The characteristic features of the pearlitic structure indicate its more intense supercooling in the areas of more intense cooling of the forged part, where the microstructure has the morphology of the upper bainite. The microstructure indicates the least intense cooling at area B and the most intense cooling at areas A and C.

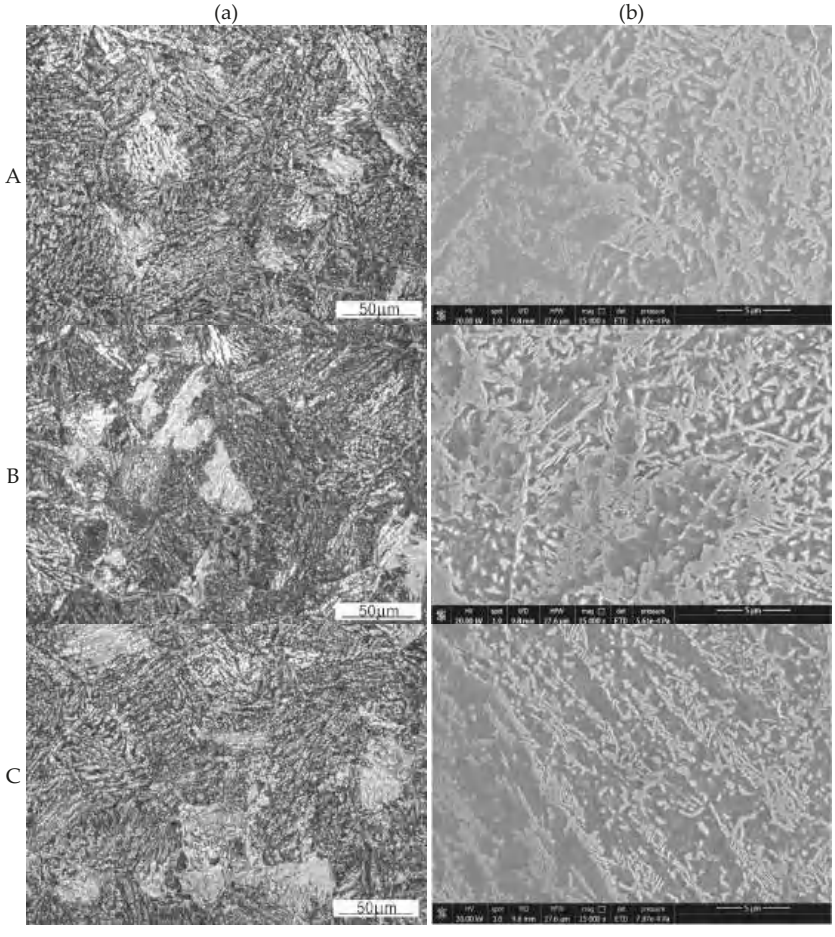

Figure 7. The microstructure of the 4130-steel flange in pre-selected points of the microstructure observations (**A**–**C**): (**a**) light microscope, (**b**) scanning microscope.

The transformation of austenite to fine pearlite (fine-plate structure) is more diffusive in nature than the transformation of austenite to upper bainite. The diffusive nature of these transformations (in the case of pearlite nucleating mainly at austenite grain boundaries) makes it difficult to reconstruct the austenitic structure formed in this case by the plastic deformation of austenite and the processes of its recovery and dynamic recrystallization. However, these transformations are often similar in temperature range (always, however, perlite is formed at higher temperatures than bainite), which often results, as in the present case, in the absence of a clear distinction between the areas of fine perlite and upper bainite. Increasing the cooling rate facilitates a less diffusive transformation (in this case, resulting in formation of upper bainite) and limits the extent to which a more diffusive pearlitic transformation occurs. However, the austenite grain refinement (area C in Figure 6b), introducing more high-energy grain boundaries, promotes the diffusion that is facilitated along these boundaries. This leads to reducing the hardenability, which favors the occurrence of pearlitic transformation and therefore a mainly diffusive transformation. Therefore, considering area C shown in Figure 6b, two opposite phenomena (accelerated cooling and grain refinement) result in a similar character of the morphology of cementite precipitates (Figure 7b) at this area of the forged part cross-section as well as at areas B and C.

4. Conclusions

The main conclusions of this study can be summarized as follows:

- The conducted assessment of process stability and instability in accordance with Prasad's and Murty's criterion for the true strain of 1 showed three processing windows developed in accordance with Prasad's criterion and four processing windows developed in accordance with Murty's criterion.
- Upon the basis of the processing maps of the investigated steel, it is possible to observe that the level of strain has a significant influence on identifying the processing windows and the area of instability.
- The processing map developed according to Gegel's approach, as compared to the processing maps obtained in accordance with Prasad's and Murty's criteria, showed three stability areas. It is, however, difficult to clearly identify the most favorable combinations of the processing parameters based on them. This map should be treated as general support for determining thermomechanical processing parameters.
- Processing parameters presented in processing window 2, developed according to Prasad's and Murty's criteria, are recommended for designing the technology of forging of the investigated steel. Industrial forging tests should be carried out under the following thermomechanical conditions: $T = 1075$–$1200\ ^{\circ}C$ and $\dot{\varepsilon} = 15.8$–$100\ s^{-1}$ on hammers or other high-strain-rate forging machines. Such parameters ensure the homogeneity and stability of the material flow in a forged part, which was confirmed by the successful forging of 4130 steel in industrial conditions.

Author Contributions: Conceptualization, A.Ł.-S. and T.Ś.; methodology, A.Ł.-S., T.Ś. and J.K.; validation, A.Ł.-S., T.Ś., Ł.L. and J.K.; formal analysis, A.Ł.-S., T.Ś., Ł.L. and J.K.; investigation, A.Ł.-S., T.Ś. and J.K.; writing—original draft preparation, A.Ł.-S. and T.Ś.; writing—review and editing, A.Ł.-S. and T.Ś. All authors have read and agreed to the published version of the manuscript.

Funding: The research project was financed by the Ministry of Education and Science (AGH —research subsidy No. 16.16.110.663).

Institutional Review Board Statement: Not applicable.

Informed Consent Statement: Not applicable.

Data Availability Statement: Not applicable.

Conflicts of Interest: The authors declare no conflict of interest.

References

1. Xu, L.; Chen, L.; Chen, G.; Wang, M. Hot deformation behavior and microstructure analysis of 25Cr3Mo3NiNb steel during hot compression tests. *Vacuum* **2018**, *147*, 8–17. [CrossRef]
2. Chakravarthi, K.V.A.; Koundinya, N.T.B.N.; Narayana Murty, S.V.S.; Nageswara Rao, B. Microstructure, properties and hot workability of M300 grade maraging steel. *Def. Technol.* **2018**, *14*, 51–58. [CrossRef]
3. Sajadi Far, S.V.; Ketabchi, M.; Nourani, M.R. Hot Deformation Characteristics of 34CrMo4 Steel. *J. Iron Steel Res. Int.* **2010**, *17*, 65–69. [CrossRef]
4. Łukaszek-Sołek, A.; Krawczyk, J.; Śleboda, T.; Grelowski, J. Optimization of the hot forging parameters for 4340 steel by processing maps. *J. Mater. Res. Technol.* **2019**, *8*, 3281–3290. [CrossRef]
5. Anoop, C.R.; Prakash, A.; Giri, S.K.; Narayana Murty, S.V.S.; Samajdar, I. Optimization of hot workability and microstructure control in a 12Cr-10Ni precipitation hardenable stainless steel: An approach using processing maps. *Mater. Charcter.* **2018**, *141*, 97–107. [CrossRef]
6. Ren, F.; Chen, F.; Chen, J.; Tang, X. Hot deformation behavior and processing maps of AISI 420 martensitic stainless steel. *J. Manuf. Process.* **2018**, *31*, 640–649. [CrossRef]
7. Prasad, Y.V.R.K.; Sasidhara, S. *Hot Working Guide: A Compendium of Processing Maps*; ASM International: Novelty, OH, USA, 1997.
8. Lin, Y.C.; Luo, S.; Jiang, X.; Tang, Y.; Chen, M. Hot deformation behavior of a Sr-modified Al–Si–Mg alloy: Constitutive model and processing maps. *Trans. Nonferrous Met. Soc. China* **2018**, *28*, 592–603. [CrossRef]
9. Wang, S.; Hou, L.G.; Luo, J.R.; Zhang, J.S.; Zhuang, L.Z. Characterization of hot workability in AA 7050 aluminum alloy using activation energy and 3-D processing map. *J. Mater. Process. Technol.* **2015**, *225*, 110–121. [CrossRef]
10. Lypchanskyi, O.; Śleboda, T.; Wojtaszek, M.; Muszka, K.; Łukaszek-Sołek, A.; Stanik, R.; Gude, M. The analysis of flow behavior of Ti-6Al-2Sn-4Zr-6Mo alloy based on the processing maps. *Int. J. Mater. Form.* **2021**, *14*, 523–532. [CrossRef]

11. Prasad, Y.V.R.K.; Seshacharyulu, T. Processing maps for hot working of titanium alloys. *Mater. Sci. Eng. A* **1998**, *243*, 82–88. [CrossRef]
12. Lypchanskyi, O.; Śleboda, T.; Zyguła, K.; Łukaszek-Sołek, A.; Wojtaszek, M. Evaluation of hot workability of nickel-based superalloy using activation energy map and processing maps. *Materials* **2020**, *13*, 3629. [CrossRef] [PubMed]
13. Wan, Z.; Hua, L.; Sun, Y.; Wang, T.; Li, Z. Hot deformation behavior and processing workability of a Ni-based alloy. *J. Alloys Compd.* **2018**, *769*, 367–375. [CrossRef]
14. Huo, Y.; Lin, J.; Bai, Q.; Wang, B.; Tang, X.; Ji, H. Prediction of microstructure and ductile damage of a high-speed railway axle steel during cross wedge rolling. *J. Mater. Process. Technol.* **2017**, *239*, 359–369. [CrossRef]
15. Barbier, D.; Guérin, J.D.; Dubar, M.; Bénard, T.; Bonneau, S.; Cabrera, E.S.P. Hot ductility and flow stress of AISI 4130 and 52100-type steels. *Mater. Sci. Eng. A* **2017**, *690*, 37–43. [CrossRef]
16. Prasad, Y.V.R.K.; Seshacharyulu, T. Modelling of hot deformation for microstructural control. *Int. Mater. Rev.* **1998**, *43*, 243–258. [CrossRef]
17. Prasad, Y.V.R.K.; Gegel, H.L.; Doraivelu, S.M.; Malas, J.C.; Morgan, J.T.; Lark, K.A.; Barker, D.R. Modeling of dynamic material behavior in hot deformation: Forging of Ti-6242. *Metall. Mater. Trans. A* **1984**, *15*, 1883–1892. [CrossRef]
18. Prasad, Y.V.R.K. Processing maps: A status report. *J. Mater. Eng. Perform.* **2003**, *12*, 638–645. [CrossRef]
19. Wen, D.X.; Lin, Y.C.; Li, H.B.; Chen, X.M.; Deng, J.; Li, L.T. Hot deformation and processing map of a typical Ni–based superalloy. *Mater. Sci. Eng. A* **2014**, *591*, 183–192. [CrossRef]
20. Momeni, A.; Dehghani, K. Hot working behavior of 2205 austenite–ferrite duplex stainless steel characterized by constitutive equations and processing maps. *Mater. Sci. Eng. A* **2011**, *528*, 1448–1454. [CrossRef]
21. Momeni, A.; Dehghani, K. Characterization of hot deformation behavior of 410 martensitic stainless steel using constitutive equations and processing maps. *Mater. Sci. Eng. A* **2010**, *527*, 5467–5473. [CrossRef]
22. Lin, Y.C.; Liu, G. Effects of strain on the workability of a high strength low alloy steel in hot compression. *Mater. Sci. Eng. A* **2009**, *523*, 139–144. [CrossRef]
23. Li, X.; Lu, S.; Wang, K.; Fu, M.W.; Cao, C. Analysis and comparison of the instability regimes in the processing maps generated using different instability criteria for Ti–6.5Al–3.5Mo–1.5Zr–0.3Si alloy. *Mater. Sci. Eng. A* **2013**, *576*, 259–266. [CrossRef]
24. Zhou, G.; Ding, H.; Cao, F.; Zhang, B. A comparative study of various flow instability criteria in processing map of superalloy GH4742. *J. Mater. Sci. Technol.* **2014**, *30*, 217–222. [CrossRef]
25. Rajput, S.K.; Dikovits, M.; Chaudhari, G.P.; Poletti, C.; Warchomicka, F.; Pancholi, V.; Nath, S.K. Physical simulation of hot deformation and microstructural evolution of AISI 1016 steel using processing maps. *Mater. Sci. Eng. A* **2013**, *587*, 291–300. [CrossRef]
26. Lukaszek-Solek, A.; Krawczyk, J. The analysis of the hot deformation behaviour of the Ti-3Al-8V-6Cr-4Zr-4Mo alloy, using processing maps, a map of microstructure and of hardness. *Mater. Des.* **2015**, *65*, 165–173. [CrossRef]
27. Murty, N.S.V.S.; Rao, N.B.; Kashyap, B.P. Identification of flow instabilities in the processing maps of AISI 304 stainless steel. *J. Mater. Process. Technol.* **2005**, *166*, 268–278. [CrossRef]
28. Murty, N.S.V.S.; Rao, N.B.; Kashyap, B.P. Instability criteria for hot deformation of materials. *Inter. Mater. Rev.* **2000**, *45*, 15–26. [CrossRef]
29. Al Omar, A.; Prado, J.M. Criteria for prediction of plastic instabilities for hot working processes (part I: Theoretical review). *Weld. Int.* **2012**, *26*, 921–934. [CrossRef]
30. Rieiro, I.; Carsí, M.; Ruano, O.A. Comparison of efficiency and stability maps obtained by various methods. *Adv. Mater. Process. Technol.* **2018**, *4*, 132–141. [CrossRef]
31. Wang, J.; Dong, J.; Zhang, M.; Xie, X. Hot working characteristics of nickel–base superalloy 740H during compression. *Mater. Sci. Eng. A* **2013**, *566*, 61–70. [CrossRef]
32. Momeni, A.; Dehghani, K.; Reza Ebrahimi, G.; Kazemi, S. Developing the processing maps using the hyperbolic sine constitutive equation. *Metall. Mater. Trans. A* **2013**, *44*, 5567–5576. [CrossRef]
33. Sun, H.M.; Li, M.Q.; Liu, Y.G. Development of processing map coupling grain size for isothermal compression of 300M steel. *Mater. Sci. Eng. A* **2014**, *595*, 77–85. [CrossRef]
34. Zhou, P.; Ma, Q.-X. Dynamic Recrystallization Behavior and Processing Map Development of 25CrMo4 Mirror Plate Steel During Hot Deformation. *Acta Metall.Sin. (Engl. Lett.)* **2017**, *30*, 907–920. [CrossRef]
35. Łukaszek–Sołek, A. Technological aspect of processing maps for the AA2099 alloy. *Acta Metall. Sin. (Engl. Lett.)* **2015**, *28*, 22–31. [CrossRef]
36. Łukaszek–Sołek, A.; Śleboda, T.; Krawczyk, J.; Bednarek, S.; Wojtaszek, M. Characterization of the workability of Ni-Fe-Mo alloy by complex processing maps. *J. Alloys Compd.* **2019**, *797*, 174–184. [CrossRef]
37. Zhang, J.; Di, H.; Mao, K.; Wang, X.; Han, Z.; Ma, T. Processing maps for hot deformation of a high–Mn TWIP steel: A comparative study of various criteria based on dynamic materials model. *Mater. Sci. Eng. A* **2013**, *587*, 110–122. [CrossRef]
38. Bruschi, S.; Poggio, S.; Quadrini, F.; Tata, M.E. Workability of Ti–6Al–4V alloy at high temperatures and strain rates. *Mater. Lett.* **2004**, *58*, 3622–3629. [CrossRef]
39. Liu, K.; Huo, Y.; He, T.; Huo, C.; Jia, C.; Du, X.; Wang, B. High-temperature deformation behavior and hot-processing map of 25CrMo4 axle steel based on friction correction. *Mater. Technol.* **2021**, *55*, 843–850. [CrossRef]

40. Xi, S.; Gao, X.; Liu, W.; Lu, Y.; Fu, G.; Tao, H.; Zang, Y. Hot deformation behavior and processing map of low-alloy offshore steel. *J. Iron Steel Res. Int.* **2022**, *29*, 474–483. [CrossRef]
41. Zhao, Z.L.; Ning, Y.Q.; Guo, H.Z.; Yao, Z.K.; Fu, M.W. Discontinuous yielding in Ni–base superalloys during high–speed deformation. *Mater. Sci. Eng. A* **2014**, *620*, 383–389. [CrossRef]
42. Seshacharyulu, T.; Medeiros, S.C.; Frazier, W.G.; Prasad, Y.V.R.K. Hot working of commercial Ti–6Al–4V with an equiaxed α–β microstructure: Materials modeling considerations. *Mater. Sci. Eng. A* **2000**, *284*, 184–194. [CrossRef]
43. Sui, F.L.; Xu, L.X.; Chen, L.Q.; Liu, X.H. Processing map for hot working of Inconel 718 alloy. *J. Mater. Process. Technol.* **2011**, *211*, 433–440. [CrossRef]
44. Pu, E.; Zheng, W.; Xiang, J.; Song, Z.; Li, J. Hot deformation characteristic and processing map of superaustenitic stainless steel S32654. *Mater. Sci. Eng. A* **2014**, *598*, 174–182. [CrossRef]
45. Al Omar, A.; Alcelay, I.; Prado, J.M. Criteria for prediction of plastic instabilities for hot working processes: Part II. Characterization of plastic flow of medium carbon microalloyed steel using phenomenological and continuum criteria. *Weld. Int.* **2009**, *26*, 935–943. [CrossRef]
46. Quan, G.Z.; Zhao, L.; Chen, T.; Wang, Y.; Mao, Y.P.; Lv, W.Q.; Zhou, J. Identification for the optimal working parameters of as-extruded 42CrMo high-strength steel from a large range of strain, strain rate and temperature. *Mater. Sci. Eng.* **2012**, *538*, 364–373. [CrossRef]
47. Rao, K.P.; Prasad, Y.V.R.K. Advanced Forming Technologies: Advanced techniques to evaluate hot workability of materials. *Compr. Mater. Process.* **2014**, *3*, 397–426. [CrossRef]

materials

MDPI

Article

A Flow Stress Model of 300M Steel for Isothermal Tension

Rongchuang Chen [1,*], Shiyang Zhang [1], Xianlong Liu [1] and Fei Feng [2,3]

[1] School of Materials Science & Engineering, Hubei University of Automotive Technology, Shiyan 442002, China; 202011104@huat.edu.cn (S.Z.); liuxianlong@huat.edu.cn (X.L.)
[2] State Key Laboratory of Materials Processing and Die & Mould Technology, Huazhong University of Science and Technology, Wuhan 430074, China; fengfei@hust.edu.cn
[3] School of Mechanical & Electrical Engineering, Wuhan Institute of Technology, Wuhan 430205, China
* Correspondence: crc@huat.edu.cn; Tel.: +86-134-7628-4413

Abstract: To investigate the effect of hot working parameters on the flow behavior of 300M steel under tension, hot uniaxial tensile tests were implemented under different temperatures (950 °C, 1000 °C, 1050 °C, 1100 °C, 1150 °C) and strain rates (0.01 s^{-1}, 0.1 s^{-1}, 1 s^{-1}, 10 s^{-1}). Compared with uniaxial compression, the tensile flow stress was 29.1% higher because dynamic recrystallization softening was less sufficient in the tensile stress state. The ultimate elongation of 300M steel increased with the decrease of temperature and the increase of strain rate. To eliminate the influence of sample necking on stress-strain relationship, both the stress and the strain were calibrated using the cross-sectional area of the neck zone. A constitutive model for tensile deformation was established based on the modified Arrhenius model, in which the model parameters (n, α, Q, $\ln(A)$) were described as a function of strain. The average deviation was 6.81 MPa (6.23%), showing good accuracy of the constitutive model.

Keywords: flow stress model; tensile deformation; constitutive model; stress correction

Citation: Chen, R.; Zhang, S.; Liu, X.; Feng, F. A Flow Stress Model of 300M Steel for Isothermal Tension. *Materials* **2021**, *14*, 252. https://doi.org/10.3390/ma14020252

Received: 24 November 2020
Accepted: 4 January 2021
Published: 7 January 2021

1. Introduction

The 300M steel (yield strength $\geq$ 1800 MPa), a kind of low-alloyed ultra-high strength steel, is an important structural material used for large parts in aircrafts, ships, and nuclear power plants. To improve service performance, those large structural parts are often hot forged. However, in the forming of large parts, folding defects usually occur due to the failure of precise material control because of inaccurate flow stress prediction. Thus, establishment of an accurate flow stress model is a key issue in forging.

The understanding of the effects of hot working parameters (e.g., forging temperature, strain rate, strain) on flow behavior is vital for precise constitutive modelling. The strain rate and temperature effects were investigated by Ghavam et al. [1] and Huang et al. [2], and tensile flow stress models for IMI834 titanium alloy and 42CrMo steel were proposed. Lin et al. [3] constructed a phenomenological model to describe the influence of hot working parameters on flow stress in hot tension of Al-Cu-Mg alloy. Besides, the microstructure evolution (e.g., average dislocation density, average grain size, damage) plays an important role in flow stress evolution. The material flow behavior of 304HCu stainless steel under various temperatures and strain rates in tensile deformation was investigated by Yadav et al. [4], and a tensile flow stress model considering the evolution of mobile and forest dislocations was established. The grain evolution of C-Mn steel in hot tensile deformation was studied by Dolzhenko et al. [5], and result showed the average grain size and tensile yield stress followed the Hall-Petch relationship. Moreover, an accurate flow stress model should eliminate the experimental error due to necking in tension. In the hot tension experiment of Murata et al. [6], the necking image of notched specimen was recorded, and the flow stress–strain curve of SS400 steel was corrected with the help of image analysis and inverse analysis of finite element simulation. By a similar technique, Zhao et al. [7] successfully calibrated the flow stress of Q195 steel, HSLA350 aluminum

alloy, and AL6061 aluminum alloy. Gain et al. [8] proposed a flow stress model of AlSi9Cu3 alloy taking into account the stress triaxiality and damage evolution, and the model was applicable in various stress states (uniaxial tension, uniaxial compression, and Astakhov test). Until now, precise modelling of tensile flow stress is still facing difficulty due to the lack of knowledge about how stress states affect flow behaviors of metal materials.

Specifically, for 300M steel, a dislocation–based constitutive model considering dynamic, meta–dynamic, and static recrystallization in both single and multiple pass compression has been established by our group [9–11]. The softening behavior of 300M steel between passes was investigated by Liu et al., and models quantifying the meta–dynamic [12] and static recrystallization softening [13] were built. Recently, the fracture behavior of 300M steel in tensile deformation was studied by Wen et al. [14], but the tensile flow stress model of 300M steel has not been established so far.

Accordingly, as an essential part of precise prediction of flow stress and microstructure evolution of 300M steel in high temperature deformation, the present research aims to establish an accurate model to describe the flow stress evolution in tension. The flow stress and logarithmic strain will be corrected using the minimum area in the necking zone of specimen. A tensile flow stress model will be constructed.

2. Materials and Experiments

The 300M steel ingot (Φ300 mm × 1000 mm) was received in the as-forged state from China Erzhong Group Cooperation (Deyang, China). The chemical composition (weight percentage) was 93.982Fe-2.562Si-0.896Cr-0.824Ni-0.808Mn-0.435Mo-0.39C-0.086V-0.017S. All samples used in this research were taken from the half radius of the ingot. The initial microstructure was martensite (Figure 1a). In order to show the original austenite grain boundaries, the samples were tempered at 560 °C for 2 h, polished according to the standard metallographic procedure, and etched in the solution (1.7% hydrochloric acid, 22% detergent, 22% carbon tetrachloride, and balanced saturated picric acid) [15]. The microstruture was tempered martensite after tempering (Figure 1b), and the initial average grain size was 37.5 μm.

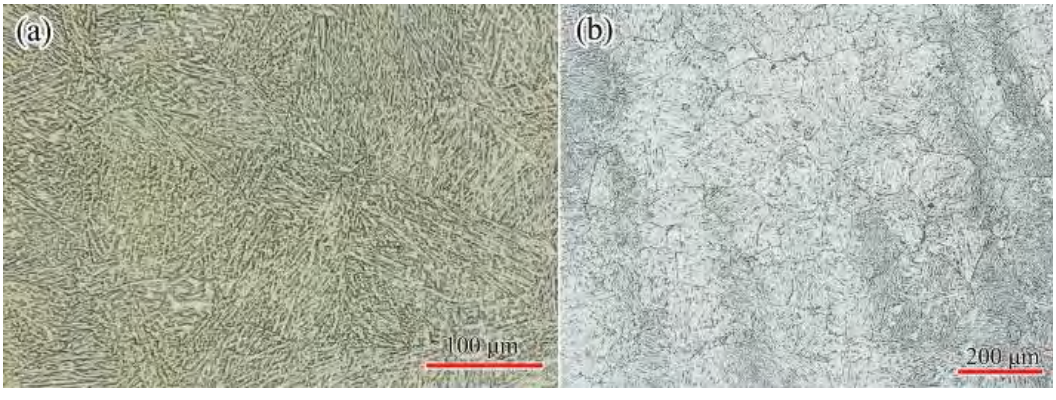

Figure 1. Microstructure of 300M steel in (**a**) as-received state, and (**b**) after tempering at 560 °C for 2 h.

Hot tensile tests were carried out on a thermal deformation simulator (Gleeble 3500, Dynamic Systems Inc., New York, NY, USA) at five temperatures (950 °C, 1000 °C, 1050 °C, 1100 °C, 1150 °C) and four speeds (0.174 mm/s, 1.74 mm/s, 17.4 mm/s, 174 mm/s). The temperature range corresponded to the usual hot working temperature of this material. The deformation speed corresponded to 0.01 s^{-1}, 0.1 s^{-1}, 1 s^{-1}, and 10 s^{-1}, respectively. In order to control the position of the necking zone, a notch (Φ8 mm × 12 mm) was turned in the middle of the specimen. A dilatometer was clipped in the middle of the specimen to measure the neck diameter. The force and elongation of specimens were automatically

measured by the machine. During the experiment, specimen was electrically heated, and a thermal couple welded in the notching area was able to measure the specimen temperature and transfer the data to a computer. The heating power could be automatically adjusted by a computer program to obtain specific temperatures.

The thermal-mechanical process is shown in Figure 2a. The test sample was heated at a heating rate of 200 °C/min to 1200 °C, held at 1200 °C for 4 min to complete austenization, and cooled to deformation temperature for another holding of 4 min. In total, twenty tests were carried out, and the experimental parameters are shown in Table 1. Once the specimen cracked, test was ceased and specimen was water quenched. The specimen photos are shown in Figure 2b. It should be noted that the length of the sample deformation area was 12 mm, and the chamfer length was 1 mm.

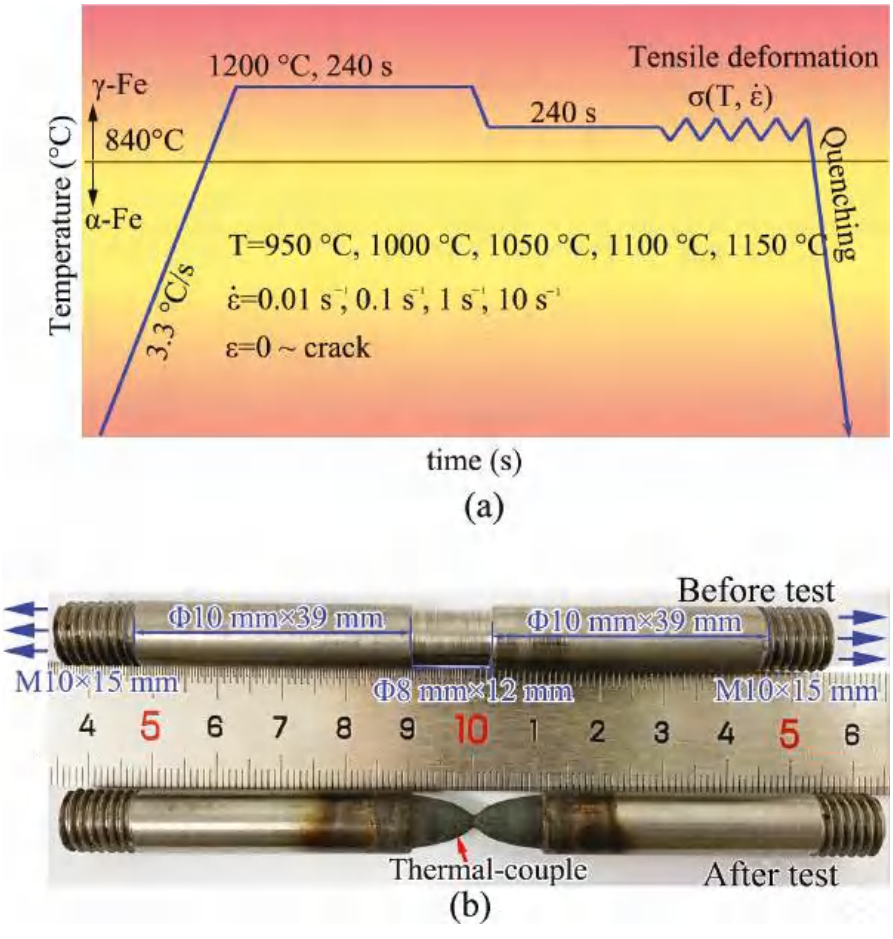

Figure 2. Experimental procedure. (**a**) thermal-mechanical process, (**b**) specimen photos before and after deformation.

Table 1. Experimental parameters.

Test No.	Temperature(°C)	Strain Rate (s^{-1})
1	950	0.01
2	950	0.1
3	950	1
4	950	10
5	1000	0.01
6	1000	0.1
7	1000	1
8	1000	10
9	1050	0.01
10	1050	0.1
11	1050	1
12	1050	10
13	1100	0.01
14	1100	0.1
15	1100	1
16	1100	10
17	1150	0.01
18	1150	0.1
19	1150	1
20	1150	10

3. Results and Discussion

3.1. Force-Stroke Curve

The force-stroke curves obtained in the tensile tests are shown in Figure 3. The deformation process was divided into four stages: the elastic stage, the stable deformation stage, the necking stage, and the fracture stage. Force increased linearly as the stroke increased in the elastic stage. When the strain exceeded the elastic limit, the stable deformation stage began. Since the strain was too low to trigger dynamic recrystallization, only work-hardening and dynamic recovery occurred. Under a high temperature and a low strain rate, the peak force was low, because dislocation annihilation was more complete. As the stroke increased further, necking gradually appeared. The loading force decreased due to the combing effect of the reduction of cross-sectional area and the dynamic recrystallization softening. In order to eliminate the influence of necking on the flow behavior in tensile deformation, the true stress and the logarithmic strain could be corrected by measuring the cross-sectional area of the necking zone of the specimen. In the fracture stage, micro-void formed and grew near the necking zone, leading to breakage [16]. It can be seen that the ultimate elongation was greater under a higher strain rate and at a lower temperature, and the cross-sectional area of the specimen slowly reduced to zero, indicating that the ductile fracture occurred.

3.2. Stress and Strain Correction

The true stress (σ) was defined by:

$$\sigma = \frac{F}{A} \tag{1}$$

Here, F was the loading force (N), and A was the cross-section area (m^2). In the present investigation, F was the tensile force, and A was the minimum cross-sectional area of the necking zone of the specimen. The cross-section of the specimen in this test was round, so $A = \pi d^2/4$, where d was the minimum cross-sectional diameter (m). The value of F was an exported data of the experiment equipment. The value of d was measured by a dilatometer.

The logarithmic strain, ε, was calculated by:

$$\varepsilon = \ln\left(\frac{l}{l_0}\right) \tag{2}$$

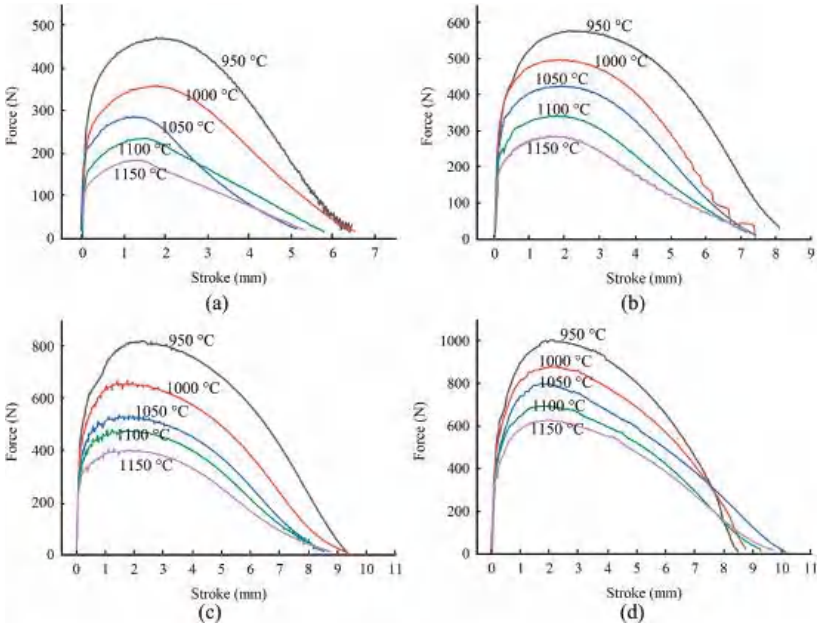

Figure 3. Force–stroke curve during tensile test. (**a**) 0.01 s^{-1}, (**b**) 0.1 s^{-1}, (**c**) 1 s^{-1}, (**d**) 10 s^{-1}.

Here, l_0 was the initial gauge length, and l was the gauge length after deformation. In this investigation, considering that the sample volume remained constant, l/l_0 equaled A_0/A, so:

$$\varepsilon = \ln\left(\frac{A_0}{A}\right) \tag{3}$$

Here, A_0 and A were calculated by the cross-sectional diameter of the specimen.

Strains and stresses were calculated according to Equations (1) and (3). The comparison of engineering stress and true stress is shown in Figure 4. In the elastic stage and the stable deformation stage, the engineering stress curve and the true stress curve were almost the same. But in the necking stage, an obvious difference of the two curves was shown.

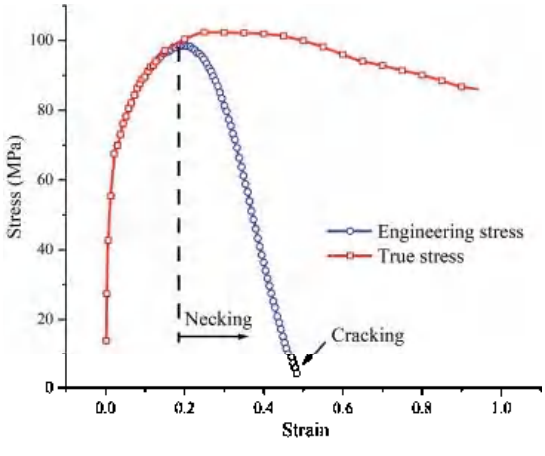

Figure 4. Comparison of engineering stress and true stress of 300M steel under 1050 °C 0.1 s^{-1}.

3.3. Tensile Flow Behavior

The true stress-logarithmic strain curves of 300M steel calculated by the above method are shown in Figure 5. Under a high temperature and a low strain rate, the true stress was low due to a low dislocation motion barrier. This phenomenon was also found in the compression of 300M steel [11], GH4169 alloy [17], GH4698 alloy [18], etc. The previous result in Figure 3, that the ultimate elongation was greater under a higher strain rate and a lower temperature, could be interpreted by the flow stress curves in Figure 5. Under a higher strain rate, work-hardening-shaped stress-strain curve was obtained, and the work-hardening led to the strengthening of the necking zone, causing deformation of the adjacent zones of specimen, and making the ultimate elongation greater. The flow stress curve shapes gradually transited from single peaked to exponential hardened when the strain rate increased. This was because the dynamic recrystallization was more easily to complete at a lower strain rate, while work-hardening played a more important role at a higher strain rate. Compared with Figure 6c, much more small recrystallized grains were found in Figure 6a. But only a few small recrystallized grains could be seen in Figure 6e, because under a low strain rate (0.01 s^{-1}) and high temperature (1150 °C), small recrystallized grains gradually coarsened. The grains in Figure 6g were relatively small because the deformation time was short, and the grains did not have enough time to grow [19].

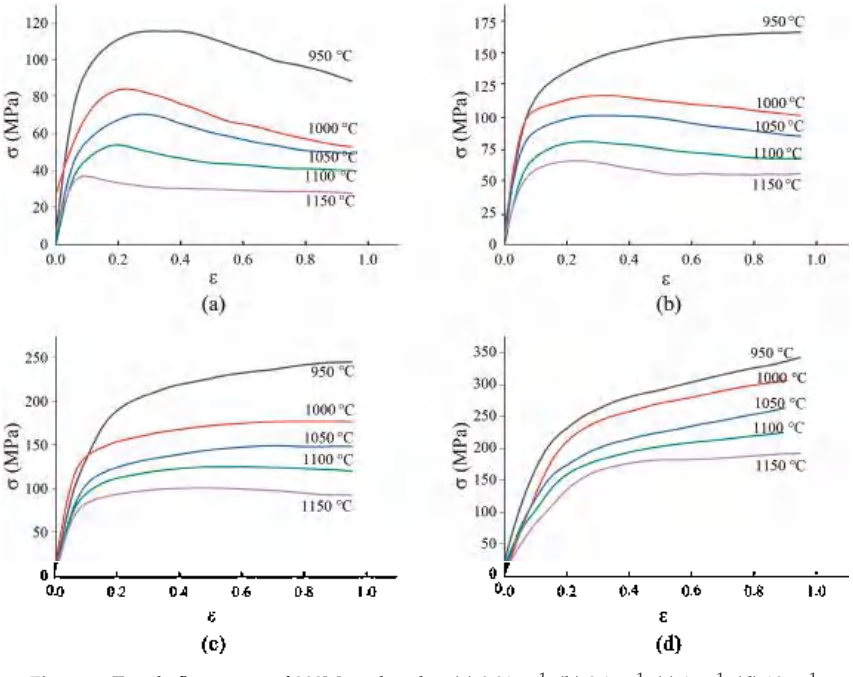

Figure 5. Tensile flow stress of 300M steel under: (**a**) 0.01 s^{-1}, (**b**) 0.1 s^{-1}, (**c**) 1 s^{-1}, (**d**) 10 s^{-1}.

Comparing the tensile flow stresses with the compressive flow stresses, it was found that the tensile flow stresses were 29.1% (27.8 MPa) greater, as shown in Figure 7. The flow stress difference could be explained by: (a) the flow stress was influenced by the stress state [8]. (b) the dynamic recrystallization in the tension was less sufficient, and the dynamic recrystallization softening was weakened by the work-hardening, resulting in a higher flow stress. This could be demonstrated by the comparison of the microstructures of 300M steel after tension and after compression. It could be seen in Figure 6 that more small recrystallized grains could be found after compression. Thus, the compressive flow stress

model could not be applied in the tensile deformation of 300M steel, and it was necessary to establish the constitutive model for the high temperature tension of 300M steel.

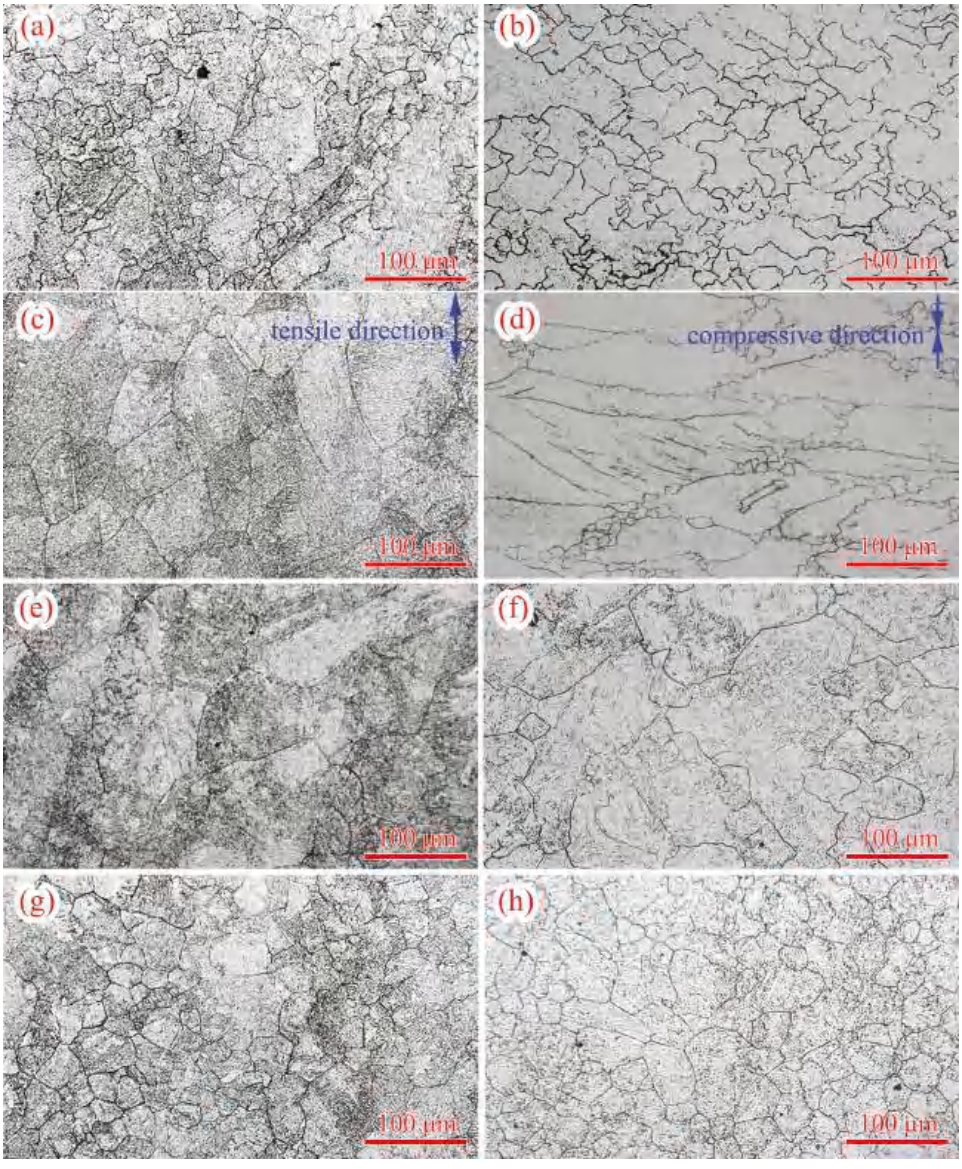

Figure 6. Microstructures of 300M steel after tension at (**a**) 950 °C 0.01 s^{-1}, (**c**) 950 °C 10 s^{-1}, (**e**) 1150 °C 0.01 s^{-1}, (**g**) 1150 °C 10 s^{-1}, and after compression at (**b**) 950 °C 0.01 s^{-1}, (**d**) 950 °C 10 s^{-1}, (**f**) 1150 °C 0.01 s^{-1}, (**h**) 1150 °C 10 s^{-1}.

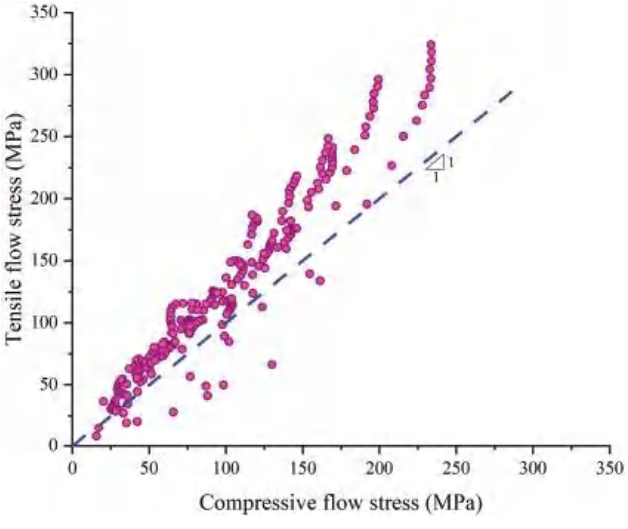

Figure 7. Comparison of tensile and compressive flow stress.

3.4. Constitutive Model

Some constitutive models are frequently used in modeling of steels, for example, the Johnson-Cook model [20], the Zerilli-Armstrong model [21], the artificial neural network model [22], the dislocation based model [4], the damage based model [8], etc. In the present investigation, the modified Arrhenius model was chosen to establish the stress (σ) and strain (ε) relation under various strain rates ($\dot{\varepsilon}$) and temperatures (T) because of the advantage in convenience and accuracy. The modified Arrhenius model was expressed as follows [23,24]:

$$\dot{\varepsilon} \cdot \exp\left(\frac{Q}{RT}\right) = A(\sinh(\alpha\sigma))^n \tag{4}$$

Here, R was the gas constant (8.314 J/(mol·K)). Q was the thermal activation energy (J/mol). n was the stress index. A and α were material constants. In the modified Arrhenius model, Q, A, n, and α could all be expressed as a polynomial function of strain (ε). In the present investigation, sixth-order polynomial function was used:

$$\Theta = c_0 + c_1\varepsilon + c_2\varepsilon^2 + c_3\varepsilon^3 + c_4\varepsilon^4 + c_5\varepsilon^5 + c_6\varepsilon^6 \tag{5}$$

Here, Θ denoted model parameters (Q, A, n, α); c_0~c_5 denoted sixth-order polynomial function coefficients. The key step for model construction was to obtain the model parameters (Q, A, n, and α) under different strains. Under a specific strain, the following calculation procedure was employed: (a) n was obtained by the slope of $\ln\sigma$ versus $\ln\dot{\varepsilon}$ curve. (b) α was calculated by the division of the slope of σ versus $\ln\dot{\varepsilon}$ curve and n. (c) Q was calculated by the slope of $\frac{1}{T}$ versus $\ln(\sinh(\alpha\sigma))$ curve. (d) $\ln A$ was calculated by the intercept of $\ln(\sinh(\alpha\sigma))$ versus $\ln\ \dot{\varepsilon} + Q/RT$ curve. The calculation was performed on *Matlab* software (R2016a). The calculation results of the coefficients in Equation (5) are shown in Table 2.

Table 2. Coefficients of the polynomials.

Coefficients	n	α	Q	ln$A$
c_0	34.414	0.022	1.167×10^6	2.700
c_1	−380.819	−0.165	-1.081×10^7	64.484
c_2	2198.841	0.809	5.820×10^7	509.409
c_3	−6344.018	−2.072	-1.604×10^8	1816.843
c_4	9592.681	2.894	2.353×10^8	3222.050
c_5	−7269.985	−2.080	-1.746×10^8	2771.555
c_6	2177.324	0.601	5.150×10^7	921.238

The variations of model parameters with strain are shown in Figure 8. Basically, the variations of the model parameters followed a similar trend with increasing strain. When the strain was smaller than ~0.2, the stress index (n) decreased rapidly from 18.5 to 6.6 as the strain increased, which indicated that dislocation cross-slips and dynamic recovery were the main deformation mechanisms [25]. Meanwhile, the thermal activation energy decreased from 760.6 kJ/mol to 375.9 kJ/mol because the atom motion barrier was lowered by dynamic recovery. When the thermal activation energy dropped below the activation energy required for dynamic recrystallization, dynamic recrystallization occurred. The stress index varied between 6.6 and 4.3, indicating that recrystallization was dominant in material softening [26,27]. The thermal activation energy gradually dropped from 375.9 kJ/mol to 270.8 kJ/mol, because the thermal activation energy barrier was reduced due to the combining effect of dynamic recrystallization and dynamic recovery.

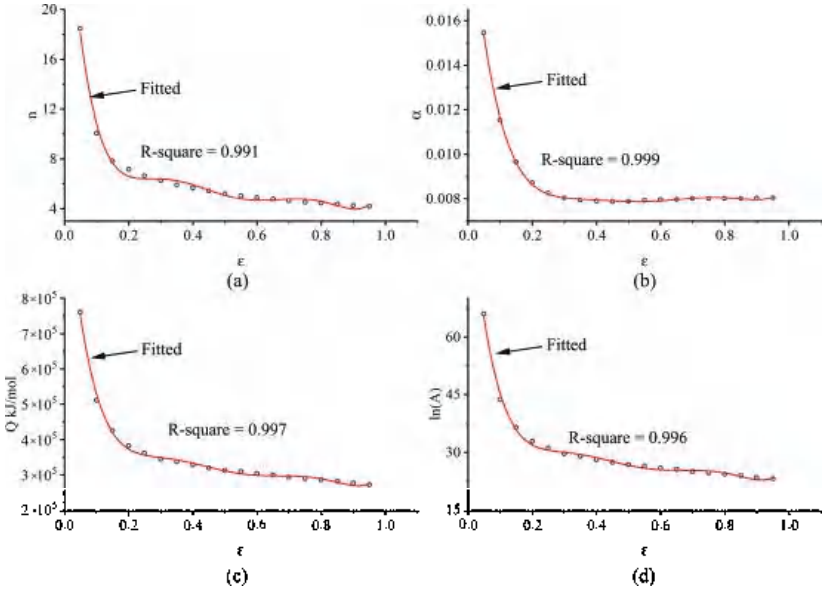

Figure 8. The polynomial fitting process of model parameters. (**a**) n, (**b**) β, (**c**) Q, (**d**) ln$A$.

A comparison was made between the experimental stresses and the calculated stresses, as shown in Figure 9. The confidence level evaluating the accuracy of the model, R, was expressed as:

$$R = \sqrt{1 - \frac{\sum_{i=1}^{n}(\hat{\sigma}_i - \sigma_i)^2}{\sum_{i=1}^{n}(\sigma_i - \overline{\sigma})^2}} \quad (6)$$

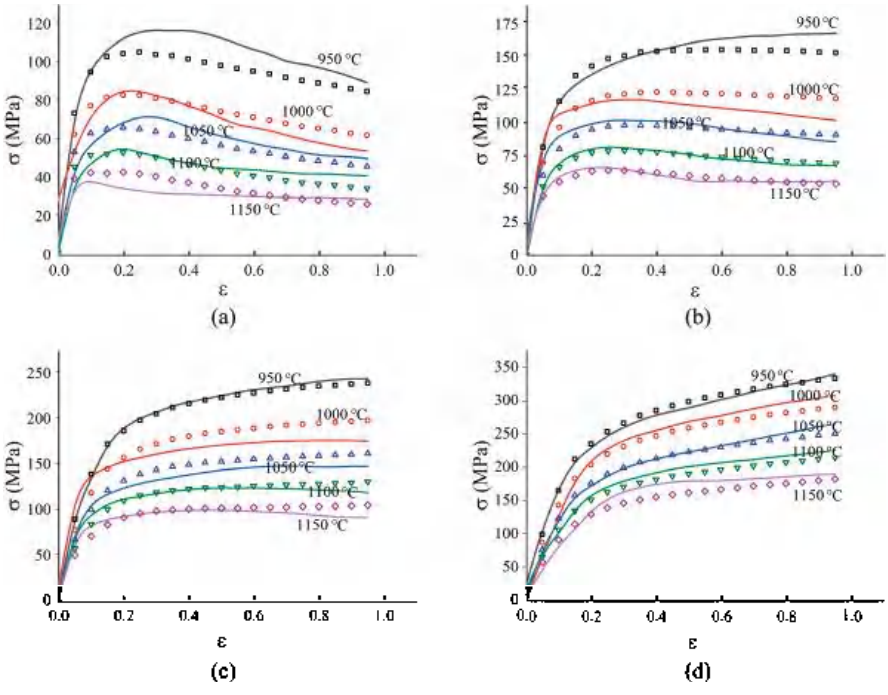

Figure 9. Comparisons of the calculated (dots) and experimental (lines) flow stress at the strain rates of (**a**) 0.01 s^{-1}, (**b**) 0. 1 s^{-1}, (**c**) 1 s^{-1}, (**d**) 10 s^{-1}.

Here, n was the sample number, $\hat{\sigma}_i$ the calculated flow stress of the *i*th sample, $\overline{\sigma}$ the average flow stress, and σ_i the experimental flow stress of the *i*th sample. The value of *R* was calculated to be 0.987. It could also be seen that the flow stress model was able to describe both the single peaked curve shape and the exponential hardened curve shape. Figure 10 was drawn by dots whose *x* ordinates and *y* ordinates were the experimental and calculated flow stresses, respectively. Figure 11 showed the mean percentage error of model prediction under each experiment condition. The maximum percentage error (12.3%) occurred at 1150 °C and 0.01s^{-1}, and the minimum error (1.85%) occurred at 950 °C and 1 s^{-1}. The average error under all test conditions was 6.23% (6.81 MPa). The error was induced by polynomial fitting and experimental error. Increasing the order of polynomial fitting on the one hand improve the accuracy of the model, on the other hand, increased the number of model parameters and deter the convenience of usage of the model. Experimental error could also be decreased by increasing the number of experimental repetitions. In general, the error was acceptable, and the model was overall accurate in describing the constitutive relationship of 300M steel in isothermal tension.

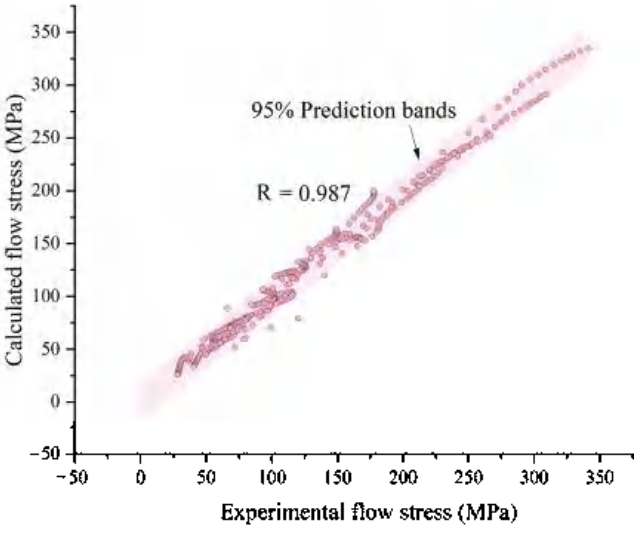

Figure 10. Scatter plots of the calculated flow stress versus experimental flow stress.

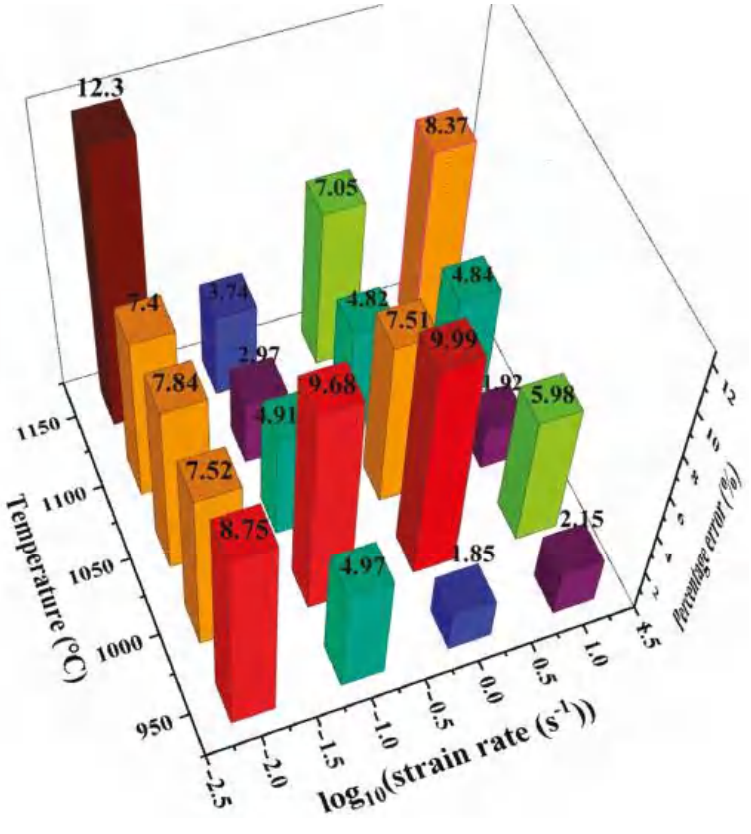

Figure 11. Percentage error of predicted flow stress under various tensile conditions.

4. Conclusions

The following conclusions could be drawn from this investigation:

(1) Under a higher temperature and a lower strain rate, the tensile force was lower and the ultimate elongation was shorter. The flow stress curve shape gradually transited from single peaked to exponential hardened when the strain rate increased.

(2) The tensile flow stresses were 29.1% (27.8 MPa) greater than the compressive flow stresses. The difference of the flow stress was caused by the difference of the stress state and the microstructure changes in dynamic recrystallization.

(3) The Arrhenius based flow stress model was able to accurately describe both the single peaked curve shape and the exponential hardened curve shape. The average deviation of the model calculation was 6.81 MPa (6.23%), and the value of R was 0.987.

Author Contributions: Conceptualization, R.C. and S.Z.; methodology, R.C.; software, X.L.; validation, F.F.; formal analysis, X.L.; investigation, R.C.; Investigation, R.C. and X.L.; Writing-original draft preparation, R.C. and S.Z.; writing-review & editing, S.Z. and F.F.; funding acquisition, X.L. and F.F. All authors have read and agreed to the published version of the manuscript.

Funding: This work was funded by the National Natural Science Foundation of China (51705169), the Key Laboratory of Automotive Power Train and Electronic in Hubei University of Automotive Technology (ZDK1201903, ZDK1202005), the Hubei Provincial Natural Science Foundation (2020CFB374), the State Key Laboratory of Materials Processing and Die & Mould Technology in Huazhong University of Science and Technology (P2020-015, P2020-05), and the Doctoral Scientific Research Fund of Hubei University of Automotive Technology (BK202005).

Institutional Review Board Statement: Not applicable.

Informed Consent Statement: Not applicable.

Data Availability Statement: Data available in a publicly accessible repository.

Conflicts of Interest: The authors declare that they have no conflict of interest.

References

1. Ghavam, M.H.; Morakabati, M.; Abbasi, S.M.; Badri, H. Flow behavior modeling of IMI834 titanium alloy during hot tensile deformation. *Trans. Nonferr. Met. Soc. China* **2015**, *25*, 748–758. [CrossRef]
2. Huang, Y.C.; Lin, Y.C.; Deng, J. Hot tensile deformation behaviors and constitutive model of 42CrMo steel. *Mater. Des.* **2014**, *53*, 349–356. [CrossRef]
3. Lin, Y.C.; Ding, Y.; Chen, M.S.; Deng, J. A new phenomenological constitutive model for hot tensile deformation behaviors of a typical Al–Cu–Mg alloy. *Mater. Des.* **2013**, *52*, 118–127. [CrossRef]
4. Yadav, S.D.; Vijayanand, V.D.; Nandgopal, M.; Reddy, G.V.P. On the tensile flow stress response of 304 hcu stainless steel employing a dislocation density based model and electron backscatter diffraction measurements. *Philos. Mag.* **2019**, *100*, 1–25. [CrossRef]
5. Dolzhenko, P.; Tikhonov, M.; Kaibyshev, R.; Belyakov, A. Dynamically Recrystallized Microstructures, Textures, and Tensile Properties of a Hot Worked High-Mn Steel. *Metals* **2019**, *9*, 30. [CrossRef]
6. Murata, M.; Yoshida, Y.; Nishiwaki, T. Stress correction method for flow stress identification by tensile test using notched round bar. *J. Mater. Process. Tech.* **2018**, *251*, 65–72. [CrossRef]
7. Zhao, K.; Wang, L.; Chang, Y. Identification of post-necking stress-strain curve for sheet metals by inverse method. *Mech. Mater.* **2016**, *92*, 107–118. [CrossRef]
8. Gain, S.; Silva, T.E.F.; Jesus, A.M.P. Mechanical characterization of the AlSi9Cu3 cast alloy under distinct stress states and thermal conditions. *Eng. Fract. Mech.* **2019**, *216*, 106499. [CrossRef]
9. Chen, R.; Xiao, H.; Wang, M. Hot Workability of 300M Steel Investigated by In Situ and Ex Situ Compression Tests. *Metals* **2019**, *9*, 880. [CrossRef]
10. Chen, R.; Guo, P.; Zheng, Z. Dislocation Based Flow Stress Model of 300M Steel in Isothermal Compression Process. *Materials* **2018**, *11*, 972. [CrossRef]
11. Zeng, R.; Huang, L.; Li, J. Quantification of multiple softening processes occurring during multi-stage thermoforming of high-strength steel. *Int. J. Plast.* **2019**, *120*, 64–87. [CrossRef]
12. Liu, J.; Liu, Y.G.; Lin, H. The metadynamic recrystallization in the two-stage isothermal compression of 300M steel. *Mater. Sci. Eng. A* **2013**, *565*, 126–131. [CrossRef]
13. Liu, Y.G.; Liu, J.; Li, M.Q. The study on kinetics of static recrystallization in the two-stage isothermal compression of 300M steel. *Comp. Mater. Sci.* **2014**, *84*, 115–121. [CrossRef]

14. Wen, D.X.; Wang, J.K.; Wang, K. Hot tensile deformation and fracture behaviors of a typical ultrahigh strength steel. *Vacuum* **2019**, *169*, 108863. [CrossRef]
15. Chen, R.; Zheng, Z.; Li, N. In-situ investigation of phase transformation behaviors of 300M steel in continuous cooling process. *Mater. Charact.* **2018**, *144*, 400–410. [CrossRef]
16. Feng, F.; Li, J.; Yuan, P. Application of a GTN Damage Model Predicting the Fracture of 5052-O Aluminum Alloy High-Speed Electromagnetic Impaction. *Metals* **2018**, *8*, 761. [CrossRef]
17. Chen, R.; Zheng, Z.; Li, J. Constitutive Modelling and Hot Workability Analysis by Microstructure Examination of GH4169 Alloy. *Crystals* **2018**, *8*, 282. [CrossRef]
18. Chen, R.; Xiao, H.; Wang, M.; Li, J. Flow Behavior and Hot Processing Map of GH4698 for Isothermal Compression Process. *Processes* **2019**, *7*, 491. [CrossRef]
19. Chen, R.; Zheng, Z.; Li, J. In situ investigation of grain evolution of 300M steel in isothermal holding process. *Materials* **2018**, *11*, 10. [CrossRef]
20. Wang, J.; Guo, W.; Li, P. Modified Johnson-Cook description of wide temperature and strain rate measurements made on a nickel-base superalloy. *Mater. High Temp.* **2017**, *34*, 157–165. [CrossRef]
21. Shamsolhodaei, A.; Zarei-Hanzaki, A.; Ghambari, M. The high temperature flow behavior modeling of NiTi shape memory alloy employing phenomenological and physical based constitutive models: A comparative study. *Intermetallics* **2014**, *53*, 140–149. [CrossRef]
22. Quan, G.Z.; Zou, Z.Y.; Wang, T.; Liu, B.; Li, J.C. Modeling the Hot Deformation Behaviors of As-Extruded 7075 Aluminum Alloy by an Artificial Neural Network with Back-Propagation Algorithm. *High Temp. Mater. Process.* **2016**, *36*, 1–13. [CrossRef]
23. Opěla, P.; Kawulok, P.; Schindler, I.; Kawulok, R.; Rusz, S.; Navrátil, H. On the Zener-Hollomon Parameter, Multi-Layer Perceptron and Multivariate Polynomials in the Struggle for the Peak and Steady-State Description. *Metals* **2020**, *10*, 1413. [CrossRef]
24. Prasad, Y.V.R.K.; Gegel, H.L.; Doraivelu, S.M. Modeling of dynamic material behavior in hot deformation: Forging of Ti6242. *Metall. Trans. A* **1984**, *15*, 1883–1892. [CrossRef]
25. Chaoyang, S.; Bing, S.; Chuanbiao, W.; Naiwei, Y.; Tianjun, M.; Wenliang, X.; Jing, Y. Experimental Investigation on High Temperature Creep Deformation Mechanism of BSTMUF601 Superalloy. *Acta Metall. Sin.* **2015**, *51*, 349–356.
26. Yin, F.; Hua, L.; Mao, H.; Han, X. Constitutive modeling for flow behavior of GCr15 steel under hot compression experiments. *Mater. Des.* **2013**, *43*, 393–401. [CrossRef]
27. Zhang, X.; Huang, L.; Li, J.; Li, P. Flow behaviors and constitutive model of 300M high strength steel at elevated temperature. *J. Cent. South Univ.* **2017**, *48*, 1439–1447.

materials

MDPI

Article

Hot Deformation Behavior of Non-Alloyed Carbon Steels

Petr Kawulok *, Petr Opěla, Ivo Schindler, Rostislav Kawulok, Stanislav Rusz, Michal Sauer and Kateřina Konečná

Faculty of Materials Science and Technology, VŠB–Technical University of Ostrava, 17. Listopadu 2172/15, 70800 Ostrava, Czech Republic; petr.opela@vsb.cz (P.O.); ivo.schindler@vsb.cz (I.S.); rostislav.kawulok@vsb.cz (R.K.); stanislav.rusz2@vsb.cz (S.R.); michal.sauer@vsb.cz (M.S.); katerina.konecna@vsb.cz (K.K.)

* Correspondence: petr.kawulok@vsb.cz; Tel.: +420-597-324-309

Abstract: The hot deformation behavior of selected non-alloyed carbon steels was investigated by isothermal continuous uniaxial compression tests. Based on the analysis of experimentally determined flow stress curves, material constants suitable for predicting peak flow stress σ_p, peak strain ε_p and critical strain ε_{crDRX} necessary to induce dynamic recrystallization and the corresponding critical flow stresses σ_{crDRX} were determined. The validity of the predicted critical strains ε_{crDRX} was then experimentally verified. Fine dynamically recrystallized grains, which formed at the boundaries of the original austenitic grains, were detected in the microstructure of additionally deformed specimens from low-carbon investigated steels. Furthermore, equations describing with perfect accuracy a simple linear dependence of the critical strain ε_{crDRX} on peak strain ε_p were derived for all investigated steels. The determined hot deformation activation energy Q decreased with increasing carbon content (also with increasing carbon equivalent value) in all investigated steels. A logarithmic equation described this dependency with reasonable accuracy. Individual flow stress curves of the investigated steels were mathematically described using the Cingara and McQueen model, while the predicted flow stresses showed excellent accuracy, especially in the strains ranging from 0 to ε_p.

Keywords: carbon steels; hot flow stress curves; dynamic recrystallization; peak flow stress; peak strain; critical strain for induce of dynamic recrystallization; activation energy at hot forming

Citation: Kawulok, P.; Opěla, P.; Schindler, I.; Kawulok, R.; Rusz, S.; Sauer, M.; Konečná, K. Hot Deformation Behavior of Non-Alloyed Carbon Steels. *Materials* **2022**, *15*, 595. https://doi.org/10.3390/ma15020595

Academic Editor: Federico Mazzucato

Received: 6 December 2021
Accepted: 11 January 2022
Published: 13 January 2022

1. Introduction

Dynamic recrystallization (DRX) is an important structure-forming process that occurs under the hot forming of metallic materials with low stacking fault energy [1–5]. This process is important, especially at the continuous hot rolling of steel strips, bars or wires [6–11]. The critical value of internal energy is required for the dynamic recrystallization initiation in the formed material, which corresponds to the achievement of critical strain ε_{crDRX} (—) [12–14]. As a result, a favorable state is created for the nucleation of new grain nuclei and their growth already during the deformation of the given material. After exceeding the critical strain ε_{crDRX}, the density of dislocations in the formed material increases, which is reflected in the flow stress increase up to a certain maximum (referred to as a peak flow stress σ_p (MPa)—see Figure 1). However, a flow stress rate increment gradually decreases due to the effects of dynamic softening processes. The critical strain required to induce the dynamic recrystallization ε_{crDRX} is thus lower than the peak strain ε_p, which corresponds to the peak flow stress σ_p in the flow stress–strain curve (see Figure 1). At strains higher than ε_p, dynamic recrystallization prevails over the strengthening processes during the deformation, which is reflected in a decrease in flow stress until the strain corresponds to steady state ε_{ss} (III.rd region in Figure 1). After reaching the steady state, i.e., the stress σ_{ss}, there is a balance between the softening and strengthening processes, and with increasing strain, the stress in the area IV.th does not change (see Figure 1) [12,14,15].

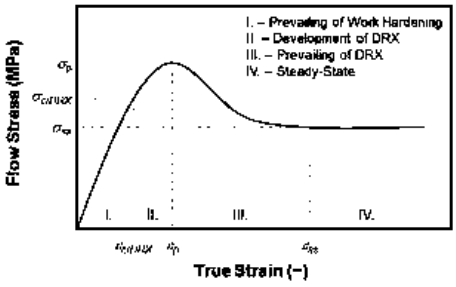

Figure 1. The schematic representation of flow stress curve influenced by dynamic recrystallization [12].

Depending on the chemical composition of the investigated materials and the chosen method of calculating the critical strain ε_{crDRX}, it should apply that $\varepsilon_{crDRX} = (0.09 \div 0.8) \cdot \varepsilon_p$ [13,16–18]. The critical strain required to induce dynamic recrystallization increases with increasing strain rate and decreasing temperature [12–14,16]. The kinetics of dynamic recrystallization is also affected by the grain size of the investigated steel. The initial finer grain-sized structure significantly accelerates the occurrence of DRX because the existing fraction of grain boundaries already determine the density of nucleation sites. The number of available nucleation sites will be reduced by reducing the total area of grain boundaries in a given material volume, which will be reflected in the course of DRX [4,16,17,19,20]. Coarse-grained structure materials (e.g., in the as-cast state) show a small total grain boundary area (compared to fine-grained materials), and thus, intragranular nucleation becomes the prevailing process. Structural heterogeneities, such as deformation bands, high angle grain boundaries, and twins formed during plastic deformation also serve as sites for the formation and growth of new grain nuclei [4,17,21].

For the purposes of research of the deformation behavior of metallic materials, continuous isothermal uniaxial compression tests are very suitable, which are most often performed on the Gleeble type simulators, whose products are flow stress curves [22–24]. The information about maximum flow stress and kinetics of dynamic recrystallization of a given material can be obtained from these flow stress curves [2,4,16,22,25,26]. In addition, these flow stress curves can be described by mathematical models, which can then be used as one of the material's input characteristics for a mathematical simulation using the finite element method. Several types of mathematical models have been developed for these purposes that can describe flow stress curves at high temperatures in areas of low strains (i.e., until the peak stress σ_p) [27–29], in areas of high strains (i.e., behind the peak stress) [30–32] or in the whole range of applied strains (i.e., including the area of hardening and the area where dynamic recrystallization occurs) [33–35]. Flow stress curves can also be obtained by torsion tests, but their disadvantage is the low applicable strain rates (usually up to approx. 10 s^{-1}) [36–38]. Higher strain rates (up to 100 s^{-1}) can be achieved in the case of compression tests performed on Gleeble simulators [2,13,24,39,40]. Tensile tests are also used in some cases to determine flow stress–strain curves [41–43]. In these cases, however, it must be considered that during tensile deformation, a characteristic neck with difficult-to-predict geometry and complicated stress develops on the deformed specimen due to the progressive non-uniform strain. Therefore, the flow stress values determined by this method are highly inaccurate.

The main aim of the performed experiments was to study the influence of carbon content on the flow stress and kinetics of dynamic recrystallization of selected non-alloyed carbon steels. These important attainments are valuable especially from the point of view of optimization of the hot forming processes of the investigated steels, especially with respect to a continuous hot rolling. Within the presented research, the prediction of peak flow stress, peak strain, critical strain necessary to induce dynamic recrystallization (also related

to peak strain), critical flow stress of the corresponding critical strain and prediction of hot deformation activation energy depending on the carbon content of non-alloyed carbon steels is solved. The secondary aim is to establish equations by which it will be possible to simply predict a critical strain for induce of dynamic recrystallization ε_{crDRX}, directly in dependence on the peak strain ε_p and also to simply predict the hot deformation activation energy only in dependence on the carbon content in the investigated steels. In addition, the approximation of measured flow stress curves of all investigated steels is also addressed.

2. Experiment Description

Four unalloyed carbon steels in the original as-cast state were selected for the above purposes, which differed mainly in carbon content (from 0.036 to 0.733 wt %) or carbon equivalent values (from 0.101 to 0.830)—see Table 1. In addition, steel C had a higher chromium content compared to other steels. To calculate the carbon equivalent C_{ekv} (−), given in Table 1, the relationship proposed by the International Welding Institute was used [44]:

$$C_{ekv} = \mathrm{C} + \frac{\mathrm{Mn}}{6} + \frac{\mathrm{Cr} + \mathrm{Mo} + \mathrm{V}}{5} + \frac{\mathrm{Cu} + \mathrm{Ni}}{15} \quad (1)$$

which takes into account the content of individual elements in wt %.

Table 1. Chemical composition of investigated steels in wt %.

	Steel A	Steel B	Steel C	Steel D
C	0.036	0.160	0.458	0.733
Mn	0.290	0.370	0.710	0.530
Si	0.036	0.055	0.291	0.220
P	0.009	0.017	0.013	0.009
S	0.010	0.006	0.023	0.013
Cu	0.040	0.040	0.040	0.010
Cr	0.050	0.060	0.270	0.030
Ni	0.030	0.030	0.030	0.010
Mo	0.007	0.011	0.013	0.003
V	0.003	0.005	0.002	0.003
C_{ekv} (−)	0.101	0.242	0.638	0.830

The initial structural state of the investigated steels was as-cast—the steels were delivered in the form of continuously cast billets of a square cross-section of 150 × 150 mm. The initial structure of the investigated steels A, B and D (analyzed by traditional optical microscopy with use of the Olympus GX51 microscope) is shown in Figure 2. In the structure of the steel A predominates mostly massive ferrite (MF) (locally Widmanstatten ferrite (WF)) with an abnormally wide range of grain size and shape—see Figure 2a,b. The share of pearlite is very low and corresponds to the carbon content in the steel A. The structure of the steel B consists of ferrite with different morphology (including acicular ferrite (AF)) and pearlite, in some places the casting structure in the form of dendrites (D) is visible—see Figure 2c,d. The coarse pearlitic blocks in the structure of steel D are partially lined with predominantly allotriomorphic ferrite (ATF) along the boundaries of the original austenitic grains—see Figure 2e,f.

It should be noted that the steel C was not tested in this work, but for purposes of this paper, the flow stress curves obtained by isothermal compression tests carried out in the work [45] were used.

The surface layer (solidified shell) with a thickness of 10 mm was removed from the continuously cast billets. Subsequently, prisms of square cross-section (15 × 15 mm) were cut around the circumference of the continuously cast billet, from which cylindrical specimens with a diameter of 10 mm and a height of 15 mm were made, which were used for continuous isothermal compression tests.

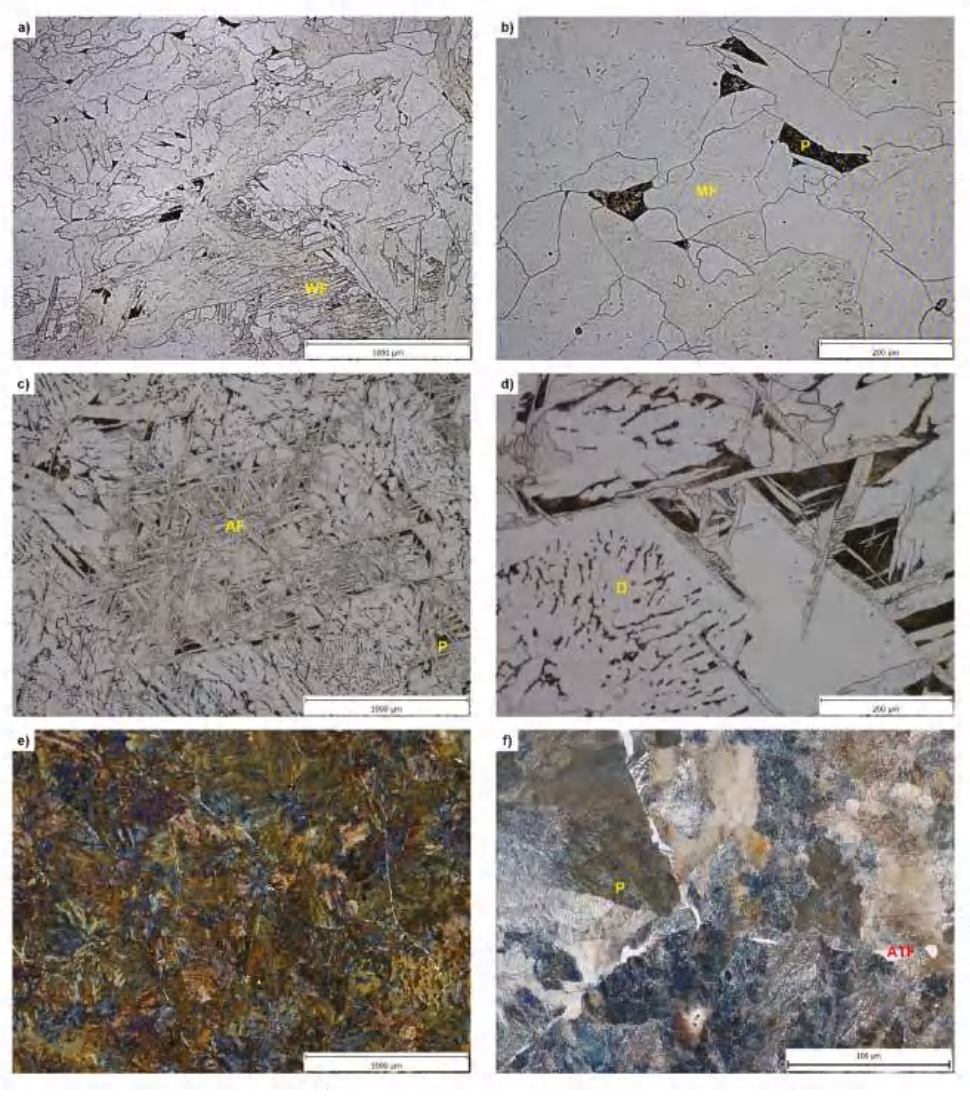

Figure 2. Initial structure of investigated steels A, B and D (dendrites—D, acicular ferrite—AF, allotriomorphic ferrite—ATF, massive ferrite—MF, Widmanstatten ferrite—WF, pearlite—P): (**a**,**b**) steel A; (**c**,**d**) steel B; (**e**,**f**) steel D.

The deformation temperatures were determined to be in the single-phase austenitic region and, at the same time, reflected the decrease of the solidus temperature and the Ac_3 temperature with increasing carbon content in the investigated steels. For these reasons, with using of parametric equations [46,47], the temperature of the finish transformation ferrite to austenite Ac_3 (°C) and the solidus temperature T_S (°C) were first determined:

$$\begin{aligned} Ac_3 = \; & 912 - 370{\cdot}C - 27.4{\cdot}Mn + 27.3{\cdot}Si - 6.35{\cdot}Cr - 32.7{\cdot}Ni + 95.2{\cdot}V + 190{\cdot}Ti + 72.0{\cdot}Al + 64.5{\cdot}Nb \\ & + 5.57{\cdot}W + 332{\cdot}S + 276{\cdot}P + 485{\cdot}N - 900{\cdot}B + 16.2{\cdot}C{\cdot}Mn + 32.3{\cdot}C{\cdot}Si \\ & + 15.4{\cdot}C{\cdot}Cr + 48.0{\cdot}C{\cdot}Ni + 4.32{\cdot}Si{\cdot}Cr - 17.3{\cdot}Si{\cdot}Mo - 18.6{\cdot}Si{\cdot}Ni + 4.80{\cdot}Mn{\cdot}Ni \\ & + 40.5{\cdot}Mo{\cdot}V + 174{\cdot}C^2 + 2.46{\cdot}Mn^2 - 6.86{\cdot}Si^2 + 0.322{\cdot}Cr^2 + 9.90{\cdot}Mo^2 + 1.24{\cdot}Ni^2 \\ & - 60.2{\cdot}V^2 \end{aligned} \quad (2)$$

$$T_S = 1535 - 200{\cdot}C - 183.9{\cdot}S - 124.5{\cdot}P \; - 6.8{\cdot}Mn - 12.3{\cdot}Si - 4.1{\cdot}Al - 1.4{\cdot}Cr - 4.3{\cdot}Ni \quad (3)$$

The determined temperatures Ac_3 and T_S of the steels A, B and D are given in Table 2. The lowest deformation temperature was chosen so that about 40–50 °C was added to the calculated temperature Ac_3 (see Table 2). The highest deformation temperature was determined by subtracting about 270–300 °C from the T_S solidus temperature (see Table 2). The remaining deformation temperatures T_d (°C), were chosen with a temperature step of 100 °C. The highest deformation temperature then represented the temperature of uniform austenitization of the specimens for the given investigated steel.

Table 2. Determined temperatures Ac_3, T_S and deformation temperatures T_d.

	Steel A	**Steel B**	**Steel D**
T_S (°C)	1522	1496	1379
Ac_3 (°C)	902	862	746
T_d (°C)	1250	1200	1100
	1150	1100	1000
	1050	1000	900
	950	900	800

Uniaxial continuous isothermal compression tests were performed on a Gleeble 3800-GTC universal hot deformation simulator using a Hydrawedge II unit (Dynamic Systems Inc., Poestenkill, NY, USA [48]).

The prepared cylindrical specimens were uniformly electrically resistance preheated (at a heating rate of 10 °C·s^{-1}) to the selected austenitization temperatures (steel A—1250 °C, steel B—1200 °C, steel D—1100 °C). After 60 s holding time they were cooled at a rate of 5 °C·s^{-1} to selected deformation temperatures (see Table 2), after which a 30 s holding time was included due to homogenization of the temperature in the specimen volume. Subsequently, the specimens were deformed by uniaxial compression to a true strain of 1.0 at constant strain rates of 0.05 s^{-1}, 1 s^{-1} and 20 s^{-1}.

Steel C in the initial as-cast state was deformed in work [45] by uniaxial compression on the same equipment at the same deformation parameters (true strain of 1.0 at constant strain rates 0.05 s^{-1}, 1 s^{-1} and 20 s^{-1}), but deformation temperatures were chosen differently. The steel C specimens were uniformly preheated to 1250 °C and after a subsequent 60 s holding were cooled at a rate of 5 °C·s^{-1} to the selected deformation temperatures (900 °C, 1000 °C, 1120 °C, 1250 °C), after which it was reached before deformation also 30 s holding time [45].

The temperature of the specimens was measured during the compression tests with one pair of K-type thermocouple wires, which were surface welded to the center of the height of the tested specimen. All compression tests were performed in a vacuum to eliminate the oxidation of specimens.

3. Calculation Methods

The Zener–Hollomon parameter Z (s^{-1}), which is defined as the temperature-compensated strain rate, can be used to predict σ_p and ε_p [4,24,26,49]:

$$Z = \dot{\varepsilon} \cdot \exp\left(\frac{Q}{R \cdot T}\right) \quad (4)$$

$$\sigma_p = \frac{1}{\alpha} \cdot \operatorname{arcsinh} \sqrt[n]{\frac{Z}{A}} \tag{5}$$

$$\varepsilon_p = U \cdot Z^W \tag{6}$$

where $\dot{\varepsilon}$ (s^{-1}) is the strain rate, Q ($J \cdot mol^{-1}$) is the hot deformation activation energy, R is the molar gas constant (8.314 $J \cdot mol^{-1} \cdot K^{-1}$), T (K) is the deformation temperature, α (MPa^{-1}), A (s^{-1}), n (−), U (s) a W (−) are the material constants.

The activation energy brings the material factor into relation (4), i.e., the influence of chemical composition, structure, etc. The value of the activation energy Q, together with other material constants α (MPa^{-1}), A (s^{-1}), n (−) suitable for prediction of the peak flow stress according to Equation (5), can be determined by regression analysis of the known Garofalo sinus-hyperbolic relation [50]:

$$\dot{\varepsilon} = A \cdot \exp\left(-\frac{Q}{R \cdot T}\right) \cdot \left[\sin h\left(\alpha \cdot \sigma_p\right)\right]^n \tag{7}$$

where σ_p (MPa) is peak flow stress, which corresponds to ε_p. Equation (7) is often solved by a simple graphical method based on repeatedly used linear regression [24,26,51]. For high deformation temperatures or low values of flow stress, relation (7) can be adjusted to the power function:

$$\dot{\varepsilon} = A_1 \cdot \exp\left(-\frac{Q}{R \cdot T}\right) \cdot {\sigma_p}^n \tag{8}$$

For low deformation temperatures or high values of flow stress, relation (7) can be transformed into the exponential form:

$$\dot{\varepsilon} = A_2 \cdot \exp\left(-\frac{Q}{R \cdot T}\right) \cdot \exp\left(\beta \cdot \sigma_p\right) \tag{9}$$

where A_1, A_2 a β are the material constants. The following relation gives the constant α from Equation (7):

$$\alpha = \frac{\beta}{n} \tag{10}$$

To determine the values of material constants n, α, A, Q, U and W of all investigated steels, the verified software ENERGY 4.0 was used. The software ENERGY 4.0 works on the basis of a combination of partial linear regressions and final complex nonlinear regression, thanks to which these constants determined in the previous step by linear regressions, are further specified [4,24–26,52]. In several works, only the simplified power Equation (8) was used to determine the activation energy and subsequently to predict peak flow stress σ_p, and the calculation was, therefore, significantly simpler—see, e.g., [53–55]. However, this simplification has been shown to lead to inaccurate results [24]. The calculation of hot deformation activation energy from experimental values by solving the sinushyperbolic Equation (7) is a proven method that has been successfully applied to several types of materials, e.g., steels [4,5,24,37,40], alloys based on copper [25], aluminum [26,56], magnesium [24,52] or nickel [2,57,58].

The critical strain ε_{crDRX} (−) necessary to induce dynamic recrystallization can be determined metallographically; however, this approach is extremely long, and the results are inaccurate. It is more appropriate to use a mathematical approach based on the analysis of the dependence of the work hardening rate on the stress in the range of strains from zero to peak. The work hardening rate θ (MPa) is defined as stress derivation according to deformation [18]:

$$\theta = \frac{d\sigma}{d\varepsilon} \tag{11}$$

The inflexion point of the curve $\theta \sim \sigma$ corresponds to the onset of DRX. The global minimum on the curve expressing the dependence $d\theta/d\sigma \sim \sigma$ corresponds to the inflexion point of the curve $\theta \sim \sigma$ and thus corresponds to the beginning of DRX [13,18,59,60]. From a

mathematical point of view, this global minimum (on the curve $d\theta/d\sigma \sim \sigma$) is the zero value of the second derivative θ according to σ [18]:

$$\frac{\partial^2 \theta_c}{\partial \sigma^2} = 0 \tag{12}$$

where θ_c is the work hardening rate in the critical state for the onset of DRX. The inflexion point of the curve $\theta \sim \sigma$ is the same as the inflexion point on the curve expressing the dependence $\ln \theta \sim \varepsilon$ and, therefore, must apply [18]:

$$\left.\frac{\partial^2 \theta_c}{\partial \sigma^2}\right|_{\sigma=\sigma_{crDRX}} = \left.\frac{\partial^2 \ln \theta_c}{\partial \varepsilon^2}\right|_{\varepsilon=\varepsilon_{crDRX}} = 0 \tag{13}$$

To derive an equation suitable for the prediction of critical strain ε_{crDRX}, a model by Cingara and McQueen was chosen in this case, which allows a mathematical description of flow stress curves up to the peak point (up to the strain of ε_p) [27]:

$$\sigma = \sigma_p \cdot \left[\frac{\varepsilon}{\varepsilon_p} \cdot \exp\left(1 - \frac{\varepsilon}{\varepsilon_p}\right)\right]^C \tag{14}$$

where ε $(-)$ is a value of true strain, and C $(-)$ is the strain hardening exponent. The logarithm of both sides of Equation (14) leads to the following linear equation [18]

$$\ln\left(\frac{\sigma}{\sigma_p}\right) = C \cdot \left[\ln\left(\frac{\varepsilon}{\varepsilon_p}\right) + \left(1 - \frac{\varepsilon}{\varepsilon_p}\right)\right] \tag{15}$$

Linear regression can then be used to determine the required values of the hardening exponent C separately from Equation (15) for each combination of temperature and strain rate (for one flow stress curve). For practical use, it is still necessary to compile a mathematical description of the exponent C, which will be described later. By deriving relation (14) according to the strain ε, the expression for determining θ can be obtained. By substituting the expression θ into Equation (13) and its subsequent solution, it is possible to arrive at a final expression, which allows the determination of the critical strain ε_{crDRX} [13,18]:

$$\varepsilon_{crDRX} = \varepsilon_p \cdot \frac{\sqrt{1 - C} + C - 1}{C} \tag{16}$$

Therefore, Equation (16), intended for the prediction ε_{crDRX}, depends on the peak strain ε_p and on the strain hardening exponent C.

4. Analysis of Measured Data

4.1. Prediction of Peak Flow Stress and Peak Strain

Flow stress curves were obtained by continuous isothermal uniaxial compression tests (see example in Figure 3). The coordinates of stress peaks were determined from these flow stress curves, which were then used as input data to calculate activation energy and other material constants suitable for predicting peak flow stress σ_p and peak strain ε_p during hot forming of the investigated steels.

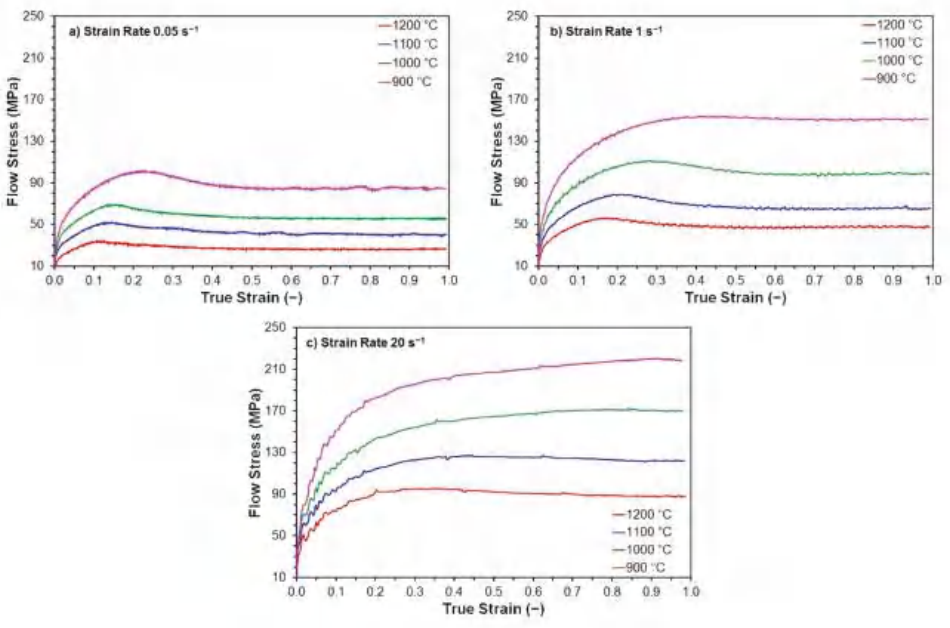

Figure 3. The measured flow stress curves of steel B: (**a**) strain rate 0.05 s^{-1}; (**b**) strain rate 1 s^{-1}; (**c**) strain rate 20 s^{-1}.

The constant n (see Equation (8)) for the selected high-temperature level is determined by the linear regression of the experimentally determined values of σ_p in the coordinates ln $\dot{\varepsilon}$~ln σ_p (see Figure 4a). For the selected low-temperature level, the constant β is determined by linear regression in the coordinates ln $\dot{\varepsilon}$~σ_p (see Equation (9) and Figure 4b). After calculating the material constant α according to Equation (10), the final linear regression of all measured data plotted in the coordinates ln $\dot{\varepsilon} - n$ ln [sinh $(\alpha \cdot \sigma_p)$]~T, material constants Q and A can be determined (see Figure 4c). The determined material constants are then refined by the final gradient optimization algorithm by solving Equation (7) via nonlinear regression analysis, which includes two mutually independent variables (temperature and strain rate). The material constants U and W are then determined using the activation energy by linear regression of the experimentally determined ε_p values in the coordinates ln ε_p~ln Z (see Figure 4d). The values of material constants of the examined steels, determined by regression analysis in the ENERGY 4.0 program, are given in Table 3.

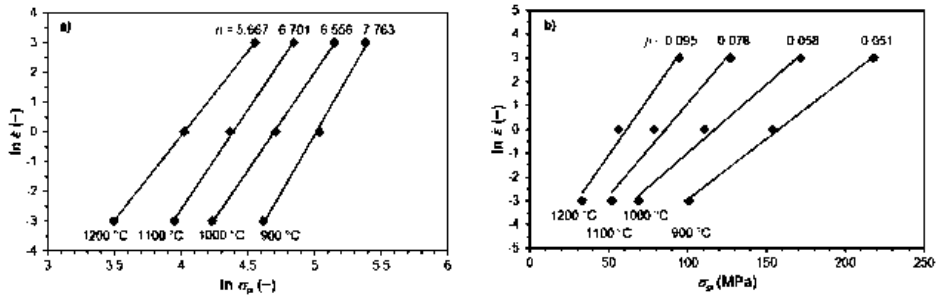

Figure 4. *Cont.*

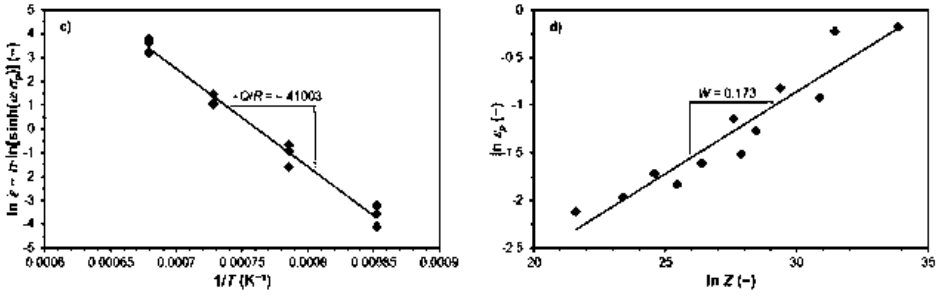

Figure 4. Calculation of material constants in Equations (7) and (6) for steel B: (**a**) calculation of n = 5.667; (**b**) calculation of β = 0.051; (**c**) calculation of Q = 341 kJ·mol^{-1}; (**d**) determination of W = 0.173.

Table 3. Determined material constants intended for prediction of σ_p and ε_p of investigated steels according to Equations (5) and (6).

	Steel A	Steel B	Steel C	Steel D
Q (kJ·mol^{-1})	321.37	301.12	293.63	271.42
n (−)	5.4113	5.3034	4.7085	4.6809
α (MPa^{-1})	0.0083	0.0080	0.0088	0.0075
A (s^{-1})	9.59×10^{12}	2.23×10^{12}	3.80×10^{11}	3.81×10^{11}
U (s)	0.00081	0.00240	0.00532	0.00505
W (−)	0.198	0.173	0.148	0147

The determined material constants Q, n, α, A, U and W (see Table 3) can be used for the given thermomechanical forming parameters for the prediction of peak flow stress σ_p and peak strain ε_p of investigated steels according to Equations (5) and (6). The accuracy of the predicted values σ_p and ε_p was simply evaluated using the correlation coefficient R (−), the relative calculation error Δ (%) and its mean values Δ_{mean} (%)—see Tables 4 and 5. The relative error values were determined according to the following relationships:

$$\Delta = \frac{\left(\sigma_{p(measured)} - \sigma_{p(predicted)}\right)}{\sigma_{p(measured)}} \cdot 100 \quad (17)$$

$$\Delta = \frac{\left(\varepsilon_{p(measured)} - \varepsilon_{p(predicted)}\right)}{\varepsilon_{p((measured)}} \cdot 100 \quad (18)$$

Table 4. Accuracy of σ_p values predicted according to Equation (5).

	Steel A	Steel B	Steel C	Steel D
R (−)	0.9998	0.9989	0.9993	0.9995
Δ_{mean} (%)	−0.05	−0.04	−0.53	−0.02

Table 5. Accuracy of ε_p values predicted according to Equation (6).

	Steel A	Steel B	Steel C	Steel D
R (−)	0.9690	0.9352	0.9494	0.8512
Δ_{mean} (%)	−2.53	−4.80	−1.60	−2.39

The excellent agreement of the calculated and measured values of the peak flow stress σ_p is confirmed by high values of correlation coefficients R and very low values of mean

calculation error Δ_{mean} given in Table 4. In the case of the peak strain ε_p the accuracy of back-calculation was lower but entirely sufficient—see Table 5. A comparison of experimentally determined and according to Equations (5) and (6) predicted values of σ_p a ε_p depending on the Zener–Hollomon parameter of all investigated steels is shown in Figure 5. The results shown in Figure 5, Tables 4 and 5 thus confirm that the chosen procedure for predicting the values of σ_p and ε_p was correct, respectively that Equations (5) and (6) (together with the constants shown in Table 3) can be used to predict the σ_p and ε_p of all investigated steels at given thermomechanical conditions of forming.

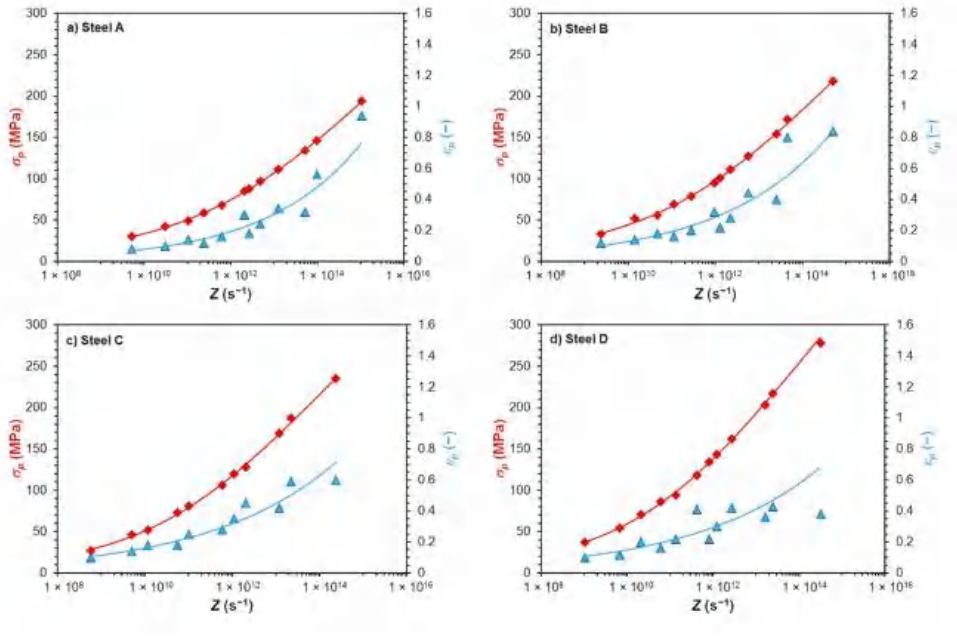

Figure 5. Comparison of measured and predicted values of σ_p and ε depending on the parameter Z (points—measured values; lines—predicted values): (**a**) steel A; (**b**) steel B; (**c**) steel C; (**d**) steel D.

4.2. Prediction of Critical Flow Stress and Critical Strain for Induce of DRX

To predict the critical strain ε_{crDRX} (−) necessary to induce dynamic recrystallization, it is necessary to derive a relationship that will allow the prediction of strain hardening exponent C (see Equation (16)). The value of the strain hardening exponent C is determined for each measured flow stress curve (i.e., for each combination of temperature and strain rate) as the line slope (dependence (15)), considering the zero value of the intersection with the vertical axis. An example of determining the constant C by linear regression of the measured data for one combination of temperature and strain rate (1000 °C and 20 s^{-1}) for steel B is shown in Figure 6.

The prediction of the strain hardening exponent C is possible based on its functional dependence on the Zener–Hollomon parameter Z (4), which includes the interaction effects of strain rate and temperature. The dependence of exponent C on parameter Z has a power character for a constant value of a strain rate and a variable deformation temperature [13]:

$$C = C_1 \cdot Z^{C_2} \tag{19}$$

where C_1 (s) and C_2 (−) are the material parameters, which are determined by regression separately for each strain rate $\dot{\varepsilon}$ (as line slope and the intersection of the given dependence with the y-axis), by converting relation (19) into a linear form—see Figure 7a (for steel

B). The parameters obtained in this way are further linearly dependent on the strain rate $\dot{\varepsilon}$ [30]—see Figure 7b (for steel B). The resulting relationship for the prediction of the strain hardening exponent C will, therefore, have the general form:

$$C = \left(a \cdot \dot{\varepsilon} + b\right) \cdot Z^{(c \cdot \dot{\varepsilon} + d)} \tag{20}$$

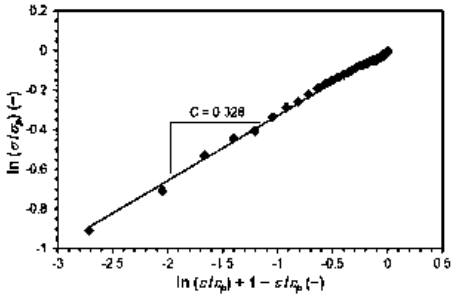

Figure 6. Determining the constant C for steel B (temperature 1000 °C, strain rate 20 s^{-1}).

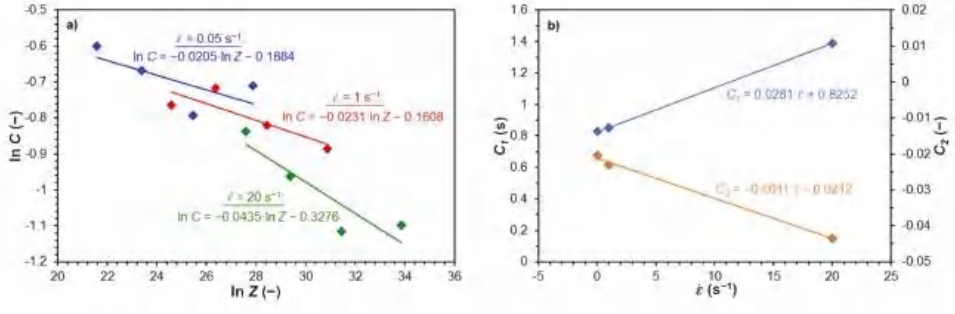

Figure 7. Determination of constants C_1 and C_2 for steel B: (**a**) determination of parameters C_1 and C_2 according to the Equation (19); (**b**) dependence of parameters C_1 and C_2 on strain rate.

The values of material constants a (s^2), b (−), c (s) and d (−) intended for the prediction of the strain hardening exponent C of all investigated steels (according to relation (20)) are given in Table 6.

Table 6. The material constants intended for prediction of strain hardening exponent C of investigated steels according to Equation (20).

	Steel A	Steel B	Steel C	Steel D
a (s^2)	0.0729	0.0281	−0.0572	−0.0600
b (−)	0.9348	0.8252	1.8288	1.4904
c (s)	−0.0018	−0.0011	0.0004	0.0020
d (−)	−0.0203	−0.0212	−0.0578	−0.0420

Using Equations (4), (6), (16) and (20) and using the material constants listed in Tables 3 and 6. It can be predicted the critical ε_{crDRX} strains necessary to induce dynamic recrystallization of all investigated non-alloyed carbon steels for the given thermomechanical forming conditions. The critical flow stress σ_{crDRX} (MPa), corresponding to the onset of dynamic recrystallization, can then be relatively easily determined using a modified

Cingara and McQueen relationship (14), in which the strain ε is replaced by the critical strain required to induce dynamic recrystallization ε_{crDRX}:

$$\sigma_{crDRX} = \sigma_p \cdot \left[\frac{\varepsilon_{crDRX}}{\varepsilon_p} \cdot \exp\left(1 - \frac{\varepsilon_{crDRX}}{\varepsilon_p}\right) \right]^C \quad (21)$$

The course of the determined values σ_{crDRX} and ε_{crDRX} depending on the Zener–Hollomon parameter of all investigated steels is shown in Figure 8.

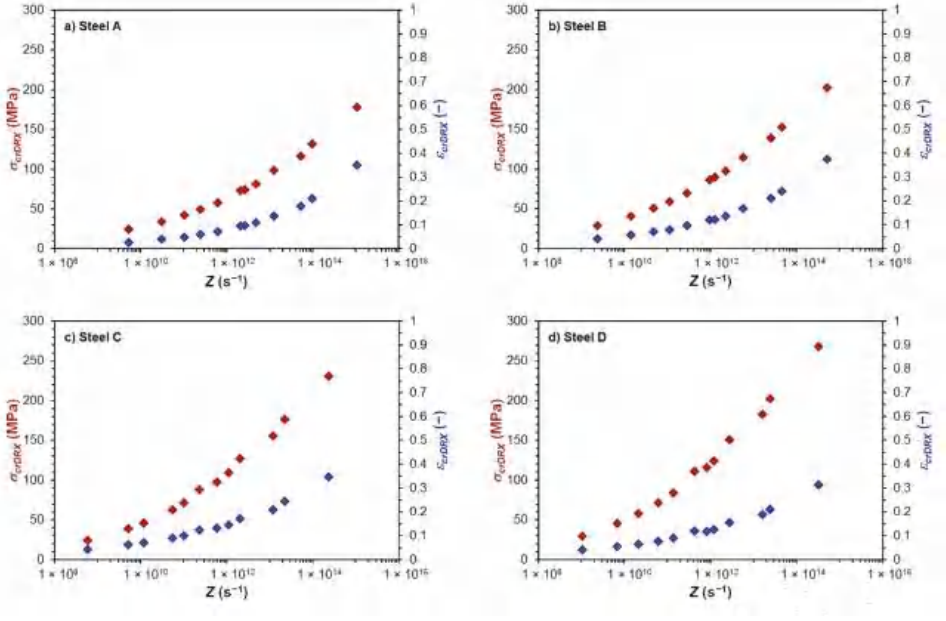

Figure 8. Dependence of determined values σ_{crDRX} and ε_{crDRX} on parameter Z: (**a**) steel A; (**b**) steel B; (**c**) steel C; (**d**) steel D.

5. Verification of Determined Critical Strains ε_{crDRX}

To verify the validity of the determined critical strains necessary to induce dynamic recrystallization ε_{crDRX}, additional isothermal uniaxial compression tests were performed on steels A, B and D at selected temperature and strain rate combinations. These additional experiments are aimed to detect dynamically recrystallized grains in the microstructure of the investigated steels. The heating mode of individual steels, or cylindrical specimens with a diameter of 10 mm and a height of 15 mm, corresponded to the description given in Section 2. After heating and defined holding time at the deformation temperature, the specimens were deformed by uniaxial compression. The strain value was determined to be a multiple of $1.3 \cdot \varepsilon_{crDRX}$, while the critical strain necessary to induce dynamic recrystallization of ε_{crDRX} was determined according to relation (16), resp. according to the procedure described in Section 4.2. In order to preserve the structure, the specimens were quenched in water immediately after deformation. The thermomechanical parameters of the individual supplementary uniaxial compression tests are given in Table 7.

Table 7. Parameters of additional uniaxial compression tests of steels A, B and D.

	Specimen	T_d (°C)	$\dot{\varepsilon}$	ε (−)
Steel A	A1	950	0.05	0.13
	A2	1050	1	0.14
	A3	1150	20	0.18
Steel B	B1	900	0.05	0.16
	B2	1000	1	0.18
	B3	1100	20	0.22
Steel D	D1	900	0.05	0.10
	D2	1000	1	0.12
	D3	1100	20	0.16

The deformed and quenched specimens were then tempered at 300 °C. The specimens were cut in the middle of their diameter (in the direction of their height) into two halves for metallographic analysis. The specimens prepared in this way were then etched with Alkilo with the addition of HCl to highlight the boundaries of the original austenitic grains. The microstructure in the middle of the height of these specimens was documented by SEM analysis on a JEOL JSM-6490LV microscope under BES imaging (combination of backscattered and secondary electrons, i.e., material and topographic contrast). Documentation of the microstructure of the examined specimens from steels A and B is given in Figures 9 and 10.

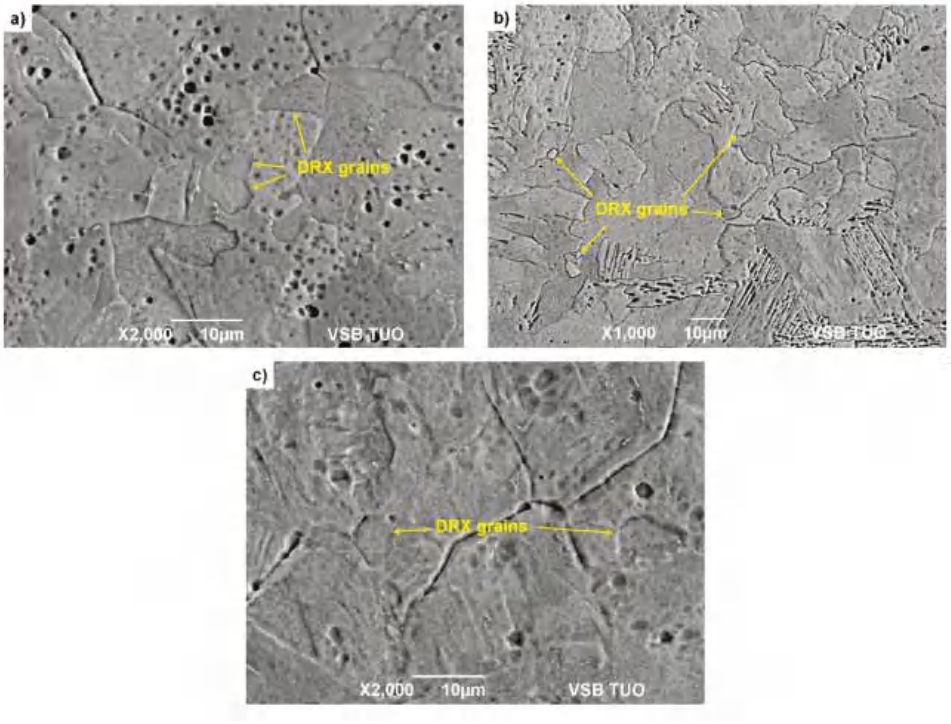

Figure 9. Metallographic images with etched boundaries of original austenitic grains of steel A: (**a**) T_d = 950 °C, $\dot{\varepsilon}$ = 0.05 s^{-1}, ε = 0.13; (**b**) T_d = 1050 °C, $\dot{\varepsilon}$ = 1 s^{-1}, ε = 0.14; (**c**) T_d = 1150 °C, $\dot{\varepsilon}$ = 20 s^{-1}, ε = 0.18.

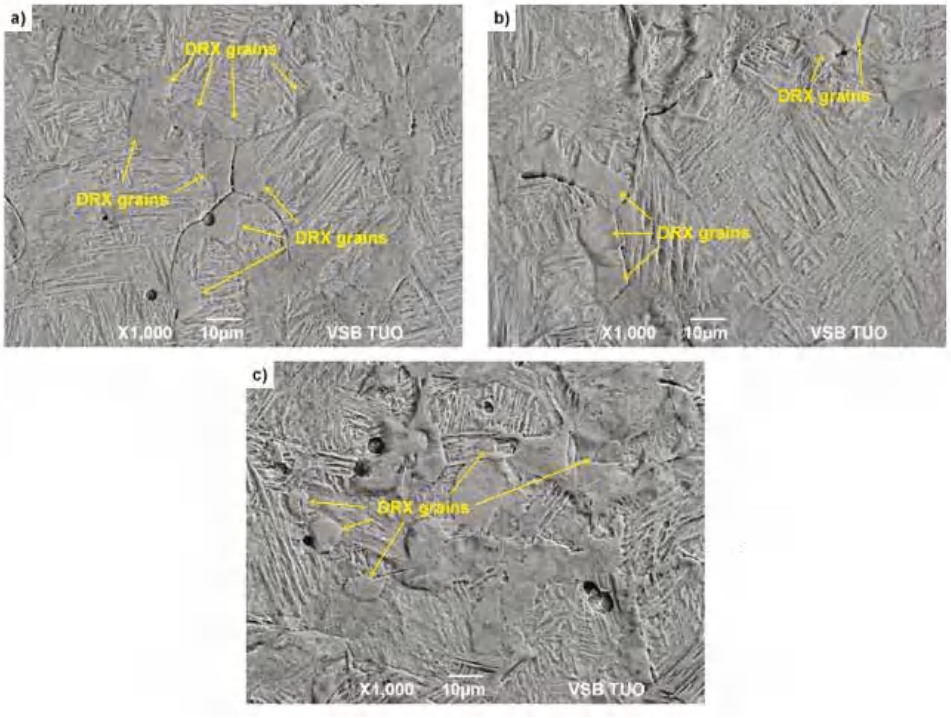

Figure 10. Metallographic images with etched boundaries of original austenitic grains of steel B: (**a**) T_d = 900 °C, $\dot{\varepsilon}$ = 0.05 s^{-1}, ε = 0.16; (**b**) T_d = 1000 °C, $\dot{\varepsilon}$ = 1 s^{-1}, ε = 0.18; (**c**) T_d = 1100 °C, $\dot{\varepsilon}$ = 20 s^{-1}, ε = 0.22.

Using SEM analysis of uniaxial compression tested specimens, fine dynamically recrystallized grains were detected in the microstructure of the steels A and B in all investigated cases—see Figures 9 and 10. These dynamically recrystallized grains, in most cases, are formed at the boundaries of the original austenitic grains (see for example, Figure 9b, Figure 10a or Figure 10b). In the case of the steel B, the differences between the original and dynamically recrystallized grains are clearly visible—see Figure 10. Due to the quenching of the deformed specimens with water, martensite with relatively coarse lath was formed in the original austenitic grains. The new dynamically recrystallized grains, formed at the boundaries of the original austenitic grains, contained martensite with a finer morphology. This additional experiment thus confirmed the validity of the determined critical strains ε_{crDRX}, which are necessary to induce dynamic recrystallization of steels A and B.

Unfortunately, in the case of the steel D, the boundaries of the original austenitic grains could not be clearly etched, not even with the use of other etchants. Signs of the boundaries of the original austenitic grains could only be seen in specimen D3 (see Figure 11), but it is not possible to reliably determine whether these are dynamically recrystallized grains.

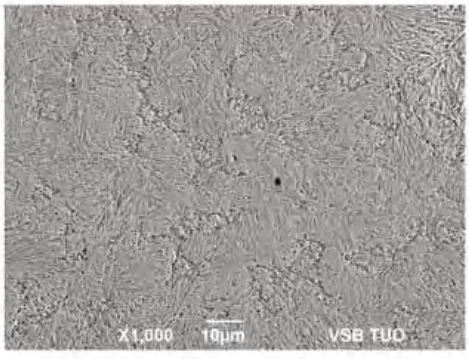

Figure 11. Metallographic image with uncertain etched boundaries of the original austenitic grains of steel D—T_d = 1100 °C, $\dot{\varepsilon}$ = 20 s^{-1}, ε = 0.16.

6. Discussion of Results

6.1. Predicted Peak Flow Stress and Peak Strain

Using Equations (4) and (6) and using the material constants listed in Table 3, peak flow stress σ_p and peak strain ε_p of the investigated steels for the given thermomechanical forming conditions can be predicted—see Figure 12. The peak flow stress σ_p and the peak strain ε_p of the investigated steels increases with the increasing value of the Zener–Hollomon parameter—see Figure 12. Steels with a higher carbon content or a higher carbon equivalent value showed greater maximum flow stress for a given size of the Zener–Hollomon parameter—see Figure 12a. In the case of the influence of carbon content or carbon equivalent on the value of the peak strain ε_p, the situation is more complicated. The low carbon steel A showed the lowest peak strain ε_p of all investigated steels—see Figure 12b. Thus, it can be assumed that for these conditions, the lowest strain will be needed to induce dynamic recrystallization of this low carbon steel compared to other investigated steels. In the case of the medium carbon steel C, for high values of the parameter Z (above 1 × 10^{14} s^{-1}), smaller strains are needed to achieve peak flow stress than in the case of the low carbon steel B—see Figure 12b. In the case of the high carbon steel D, the values of predicted peak strain ε_p in the whole range of the parameter Z are slightly lower than in medium carbon steel C. At values of the Z parameter above 4 × 10^{12} s^{-1}, the predicted peak strain ε_p of the steel D is also lower than in the low carbon steel B—see Figure 12b.

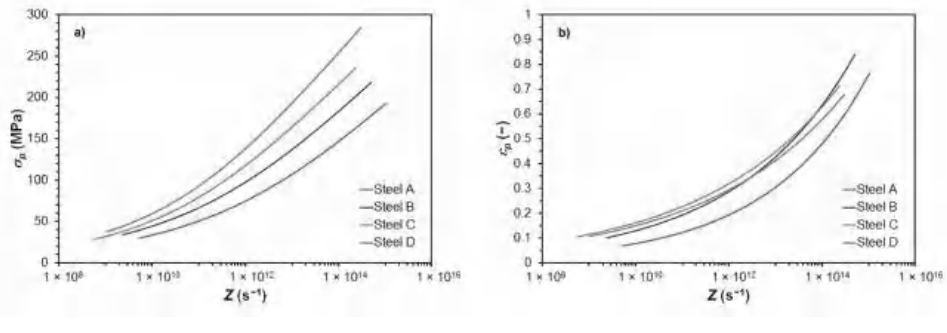

Figure 12. The effect of Zener–Hollomon parameter Z to the predicted values of σ_p and of ε_p of investigated steels: (**a**) peak flow stress σ_p; (**b**) peak strain ε_p.

6.2. Predicted Critical Flow Stress and Critical Strain for Induce of DRX

The comparison of the determined critical flow stresses σ_{crDRX} and critical strains ε_{crDRX} necessary to induce dynamic recrystallization, depending on the Zener–Hollomon parameter Z, is shown for all investigated steels in Figure 13. Steels with higher carbon content or a higher value of carbon equivalent for a given size of the Zener–Hollomon parameter, showed larger values of critical flow stress σ_{crDRX}—see Figure 13a, similar to the case of peak flow stress σ_p. Influence of carbon content or carbon equivalent to the value of the critical strain ε_{crDRX} was, except for the high carbon steel D, similar to the critical flow stress σ_{crDRX}. For a similar size of the Zener–Hollomon parameter, smaller critical strains ε_{crDRX} are required to induce dynamic recrystallization of the high carbon steel D than in the case of the medium carbon steel C—see Figure 13b.

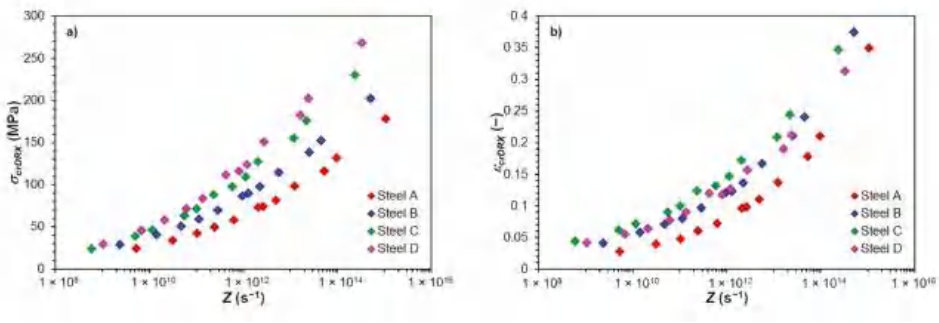

Figure 13. The effect of Zener–Hollomon parameter Z to determined critical stresses σ_{crDRX} and critical strains ε_{crDRX} for induce of dynamic recrystallization of investigated steels: (**a**) critical flow stress σ_{crDRX}; (**b**) critical strain ε_{crDRX}.

Figures 12b and 13b document that in the case of the steels B, C and D, in comparison to the steel A, larger strains are needed to induce the dynamic recrystallization. This would suggest that a higher carbon content in the investigated steels should lead to a retardation of dynamic softening processes. However, when comparing the B, C and D steels only among themselves, the effect of the carbon content on the kinetics of dynamic recrystallization is not convincingly clear because the corresponding values of the critical strain ε_{crDRX} as well as the values of the peak strain ε_p are very similar (for given values of the parameter Z).

The graphical dependencies shown in Figures 12 and 13 confirm that the stress σ_p or σ_{crDRX} and the strain ε_p or ε_{crDRX} increase in all investigated steels, with the increasing value of the parameter Z. This confirms the well-known fact that it is necessary to apply larger strains to induce dynamic recrystallization of the material at high values of the parameter Z [2,4,5,40,57], or it is necessary to ensure their accumulation during very short inter-pass times (for example, during rolling strips or in finishing blocks in wire rolling) [7,10].

Figure 14 shows 3D column charts documenting the dependence of the difference between peak strain ε_p and critical strain ε_{crDRX} for the given thermomechanical forming conditions of all investigated steels. It is clear from Figure 14 that the difference between ε_p and ε_{crDRX} increases as the deformation temperature decreases and the strain rate increases. At high deformation temperatures and low strain rates, the difference between ε_p and ε_{crDRX} is small (approx. 0.04 to 0.07). However, in the case of a combination of low deformation temperatures and high strain rates, the difference between ε_p and ε_{crDRX} reaches values up to 0.46, which is a significant fact, especially from the point of view of operating conditions. However, the ratio between ε_{crDRX} and ε_p is very similar for all combinations of thermomechanical forming conditions of all investigated steels—i.e., ranging from 38% to 48%.

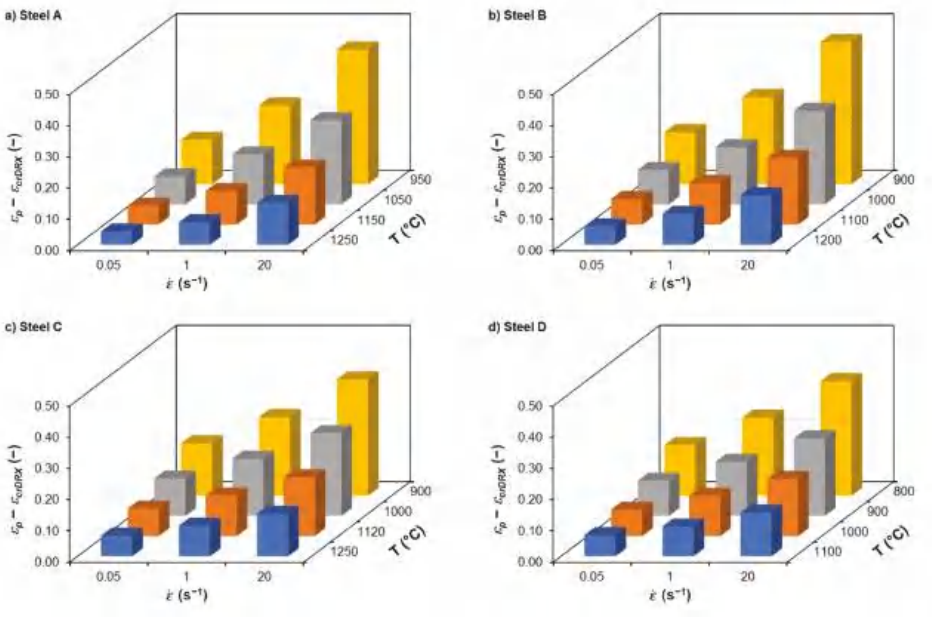

Figure 14. Graphical comparison of the difference between the peak strain ε_p and the critical strain ε_{crDRX} of the investigated steels: (**a**) steel A; (**b**) steel B; (**c**) steel C; (**d**) steel D.

The procedure for determining the critical strains ε_{crDRX} required to induce dynamic recrystallization, which is given in Section 4.2, is relatively time-consuming. However, the determined critical strains ε_{crDRX} can be related to the predicted peak strain ε_p—see Figure 15. It is, therefore, clear from the Figure 15 that the predicted critical strain ε_{crDRX} depends linearly on the peak strain ε_p. Thus, for the investigated non-alloyed carbon steels, it is possible, very simply and at the same time with very good accuracy, to determine the value of the critical strain ε_{crDRX} only via relation to the value of the peak strain ε_p:

$$\text{for steel A}: \ \varepsilon_{crDRX} = 0.4326 \cdot \varepsilon_p \tag{22}$$

$$\text{for steel B}: \ \varepsilon_{crDRX} = 0.4402 \cdot \varepsilon_p \tag{23}$$

$$\text{for steel C}: \ \varepsilon_{crDRX} = 0.466 \cdot \varepsilon_p \tag{24}$$

$$\text{for steel D}: \ \varepsilon_{crDRX} = 0.4454 \cdot \varepsilon_p \tag{25}$$

The very good accuracy of the above listed equations is documented by the high values of the coefficients of determination: for Equation (22) $R^2 = 0.9955$; for Equation (23) $R^2 = 0.9975$; for Equation (24) $R^2 = 0.9922$ and for Equation (25) $R^2 = 0.9912$.

Since, in Equations (22)–(25), the intersection with the y-axis is equal to 0, and the slope of the above linear dependencies of the critical strain ε_{crDRX} on the peak strain ε_p of all investigated steels are very similar (see Equations (22)–(25)), it is possible to compile a relationship that would describe this dependence (see Figure 16a) comprehensively for all investigated steels:

$$\varepsilon_{crDRX} = 0.4462 \cdot \varepsilon_p \tag{26}$$

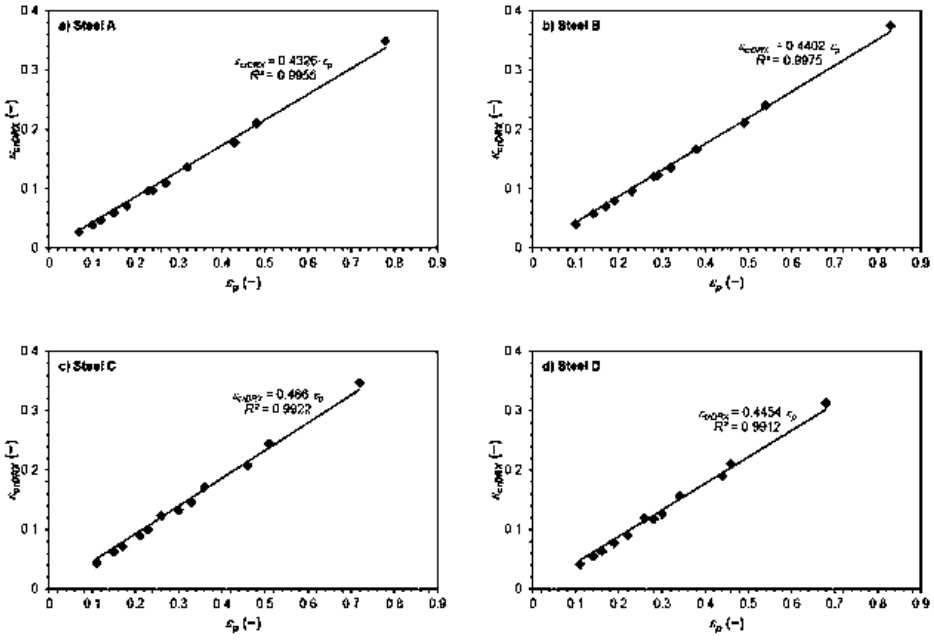

Figure 15. Relationship between critical strain ε_{crDRX} and peak strainε_p of investigated steels: (**a**) steel A; (**b**) steel B; (**c**) steel C; (**d**) steel D.

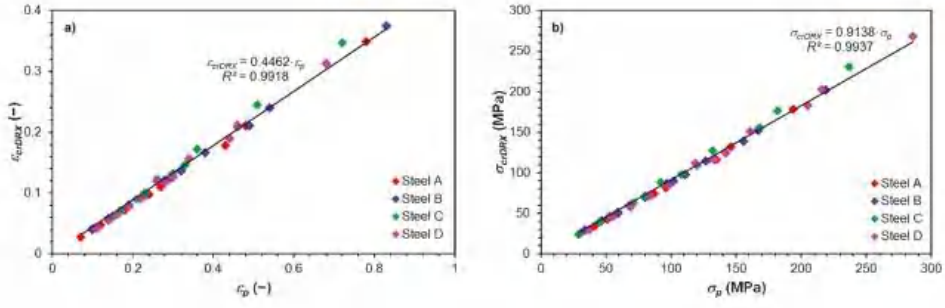

Figure 16. Dependence of the critical strain ε_{crDRX} and the critical flow stress σ_{crDRX} on the corresponding coordinates of the peak stress of all investigated steels: (**a**) critical strain ε_{crDRX}; (**b**) critical flow stress σ_{crDRX}.

Similarly, it is also possible to approach the simplified prediction of critical flow stress σ_{crDRX} in dependence on the peak flow stress σ_p for all investigated steels using a single complex equation (see Figure 16b):

$$\sigma_{crDRX} = 0.9138 \cdot \sigma_p \tag{27}$$

The excellent accuracy of Equation (26) is documented by the high value of the corresponding coefficient of determination $R^2 = 0.9918$ and graphically in Figure 16a. In the case of Equation (27), its excellent accuracy is again documented by the high value of the corresponding coefficient of determination $R^2 = 0.9937$, as well as graphically in Figure 16b.

Linear dependence of the critical strain ε_{crDRX} on the peak strain ε_p of all investigated steels is expressed with excellent accuracy by Equations (22)–(26). Equation (24), which expresses the linear dependence of ε_{crDRX} on ε_p of the medium carbon steel C, corresponds very well to the analogous dependence derived in [13] for C45 medium carbon steel (with similar chemical composition), which, however, was deformed in a wider range of deformation temperatures and strain rates:

$$\varepsilon_{crDRX} = 0.48 \cdot \varepsilon_p \tag{28}$$

The relationship expressing the dependence of critical strain ε_{crDRX} on peak strain ε_p was also derived by Liu et al. [18] for 316LN high-alloy steel:

$$\varepsilon_{crDRX} = 0.6 \cdot \varepsilon_p \tag{29}$$

The 316LN steel used in [18] contained 0.12 C, 1.28 Mn, 13.2 Ni, 17.2 Cr and 2.4 Mo (all in wt %). Fernández et al. in [17] also derived a relation describing the linear dependence of critical strain ε_{crDRX} on peak strain ε_p for low carbon micro-alloyed steels:

$$\varepsilon_{crDRX} = 0.77 \cdot \varepsilon_p \tag{30}$$

The micro-alloyed steels used in [17] contained 0.1 C, 1.28 Mn, 0.035 Nb, 0.0053 N and 0.07 C, 0.62 Mn, 0.034 Nb, 0.067 Ti, 0.0043 N (all in wt %). According to the general assumptions, the high content of alloying elements (e.g., Cr and Mo) in steels results in their strengthening and slowing down the kinetics of softening processes because these elements increase the activation energy of recrystallization. It should also be the case that microalloying elements (e.g., Nb and Ti) bind to carbon or nitrogen in steels and form precipitates (carbides, nitrides or carbonitrides Nb, Ti, etc.). These precipitates are formed at grain boundaries and slip planes, i.e., in places potentially suitable for the nucleation of new nuclei formed by recrystallization. Microalloying elements precipitated in solid solution or precipitates then inhibit recrystallization, increase flow stress and significantly reduce the plastic properties of steels [1,5,37,61,62]. Thus, it can be concluded that a higher strain is required to initiate the dynamic recrystallization of 316LN high alloy steel compared to unalloyed low carbon steel B (with a similar carbon content of 0.16 C), which corresponds to Equations (29) and (23). Similarly, it can also be concluded that in the case of micro-alloyed steels, higher strain is required to initiate dynamic recrystallization than in the case of non-alloyed carbon steels with similar carbon content (0.036 wt % for steel A, 0.16 wt % for steel B), which corresponds to Equations (30), (22) and (23).

6.3. Hot Deformation Activation Energy

The determined values of the hot deformation activation energy Q decrease with increasing carbon content or with an increasing value of carbon equivalent in the investigated steels, as also documented in Figure 17a:

$$Q = -14.7 \cdot \ln(C) + 273.93 \tag{31}$$

$$Q = -20.11 \cdot \ln(C_{ekv}) + 275.03 \tag{32}$$

where C is the carbon content (wt %) and C_{ekv} (−) is the carbon equivalent of the investigated steels. The accuracy of Equations (31) and (32), documented by the relevant coefficients of determination R^2 = 0.9062 for Equation (31), or R^2 = 0.8813 for Equation (32) is sufficient. Suppose that from graphical dependence of the activation energy on the carbon content or on the size of the carbon equivalent is excluded activation energy of medium carbon steel C, because the deformation temperatures of this steel were chosen by a different methodology than in the present work. Thus, the accuracy of simple prediction of the hot

deformation activation energy Q depending on the carbon content will increase significantly (see Figure 17b):

$$Q = -16.58 \cdot \ln(\mathrm{C}) + 267.74 \quad (33)$$

$$Q = -23.74 \cdot \ln(C_{ekv}) + 267.13 \quad (34)$$

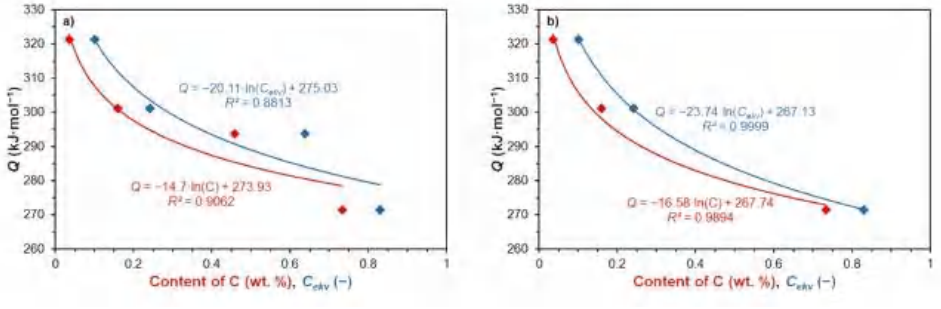

Figure 17. Dependence of hot deformation activation energy Q on carbon content and carbon equivalent of investigated steels: (**a**) for all investigated steels; (**b**) for the investigated steels A, B and D.

Excellent accuracy of Equation (33) is documented by the high value of the coefficient of determination R^2 = 0.9894. In the case of Equation (34), the coefficient of determination reaches the value R^2 = 0.9999.

The values of hot deformation activation energy Q of similar non-alloyed carbon steels can be found in the literature [63,64]. These were subsequently graphically compared with the hot deformation activation energy values determined by analyzing measured data in the ENERGY 4.0 software—see Figure 18. According to Figure 18, the activation energy decrease with increasing carbon content in the investigated steels is in accordance with the work results [61,63–66]. Mead and Birchenall reported in [67] that the activation energy of iron self-diffusion decreases with increasing carbon content. Carbon increases the self-diffusion coefficient of iron due to the expansion of the lattice that causes it. Thus, the rate of atomic mechanisms controlled by iron self-diffusion may increase with increasing carbon content, such as dislocation climbing, which reduces hot deformation activation energy. Although the exact experimental conditions of the used steels are not clear from the works [63,64], the graph in Figure 18 confirms the logarithmic dependence of the hot deformation activation energy Q on the carbon content in non-alloy steels.

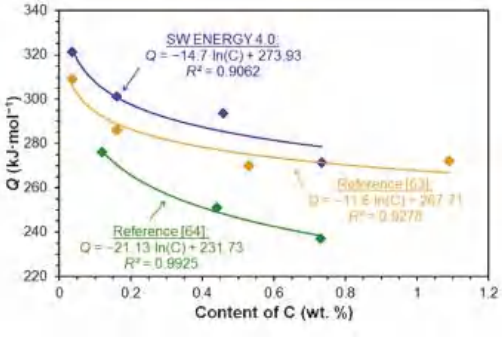

Figure 18. Comparison of values of hot deformation activation energy of non-alloyed carbon steels obtained in the literature research.

Parametric equations expressing the dependence of hot deformation activation energy on the chemical composition of steels can also be found in the literature. In work [64], Elfmark presented a simple equation describing the dependence of activation energy only on the carbon content in non-alloy steels:

$$Q = 288.8 - 28.6 \cdot C \tag{35}$$

In [62], Medina and Hernandez presented a relationship describing the dependence of hot deformation activation energy on the mass content of carbon, manganese, silicon, molybdenum, titanium, vanadium and niobium:

$$\begin{aligned} Q = 267000 - 2535.52 \cdot C + 1010 \cdot Mn + 33620.76 \cdot Si + 35651.28 \cdot Mo \\ + 93680.52 \cdot Ti^{0.5919} + 31673.46 \cdot V + 70729.85 \cdot Nb^{0.5649} \end{aligned} \tag{36}$$

In [68], Colas presented an equation for calculation the value of the hot deformation activation energy of non-alloy steels with a carbon content of 0.03–0.30 wt % C; 0.20–1.70 wt % Mn and max. 0.60 wt % Si:

$$Q = 282.7 + 92.4 \cdot C + 6.57 \cdot (Mn + Si) \tag{37}$$

A comparison of the activation energy values determined by the analysis of the measured data in the ENERGY 4.0 software and calculated using Equations (31) and (35)–(37) are documented in Figure 19.

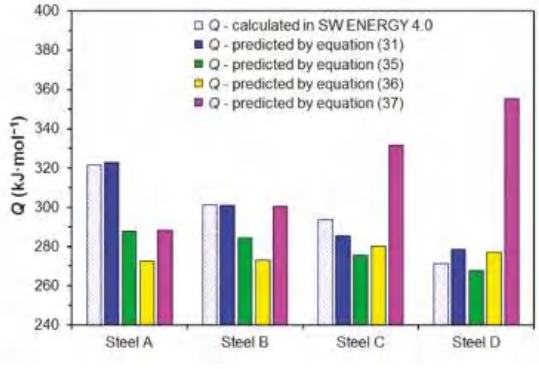

Figure 19. Comparison of values of the hot deformation activation energy Q of investigated steels determined by the ENERGY 4.0 software and using Equations (31) and (35)–(37).

Equations (31) and (35) and the results of the analysis of the measured data in the ENERGY 4.0 software reflect the decrease of the hot deformation activation energy Q with increasing carbon content in the investigated steels. However, the activation energy determined according to Equation (35) is significantly lower in the case of the investigated low carbon steels—see Figure 19. Medina and Hernandez [62] also included the influence of alloying elements in calculating the hot deformation activation energy Q—see Equation (36). This equation was determined by analyzing data measured by torsion tests performed for a wide range of non-alloyed and alloyed steels in strain rates 0.54–5.22 s^{-1} and deformation temperatures 850–1100 °C. The values of activation energy determined according to relation (36) did not differ significantly depending on the carbon content of the non-alloy carbon steels we examined—see Figure 19. According to the comparison chart shown in Figure 19, Equation (36) can only be used for medium and high carbon steel. Colas [68], on the other hand, presented the opposite trend, depending on the carbon content of hot deformation activation energy Q—see Equation (37). Unfortunately, work [68] does

not mention the thermomechanical forming conditions and chemical composition of the investigated steels, for which the relation (37) was constructed. However, it is clear from the graphical comparison in Figure 19 that relation (37) can only be used to predict the activation energy of non-alloyed carbon steels with a carbon content of about 0.15 wt % C. It follows from the above that parametric Equations (35)–(37) cannot accurately predict the hot deformation activation energy Q value for all the steels examined in this paper. For this purpose, the newly introduced relation (31), which expresses the logarithmic dependence of the activation energy on the carbon content in the investigated steels, seems to be more appropriate.

6.4. Mathematical Description of Flow Stress Curves of Investigated Steels

The model by authors Cingara and McQueen (14) [27], which was used to derive an equation suitable for predicting critical strain ε_{crDRX}, can also be used to approximate the flow stress curves of investigated steels. Of course, other models can be used for these purposes, which allow the approximation of the measured flow stress curves in the whole range of strains, such as the model by authors Hensel and Spittel [35], etc.

In this case, however, it is easier to use the Cingara and McQueen model (14) because the values of all relevant material constants are already determined for all investigated steels. Using the predicted values of peak flow stress σ_p, peak strain ε_p, strain hardening exponent C, or using the relations (4), (5), (6), (14), (20) and the corresponding material constants (see Tables 3 and 6), it is, therefore, possible to mathematically describe the individual flow stress curves of investigated steels—see Figure 20. The horizontal axis in Figure 20 is the true strain ranging from 0.02 to 0.94 for each flow stress curve. Individual flow stress curves correspond (for given deformation temperatures) from left to right with strain rates 0.05–1.0–20 s^{-1}. If there is no transition to steady state flow (steady state), the model of Cingara and McQueen (14) can be used to approximate flow stress curves with very good accuracy, not only for the range of strains from 0 up to the ε_p (or up to stress σ_p), but also in the area of the prevailing decrease in flow stress—see Figure 20.

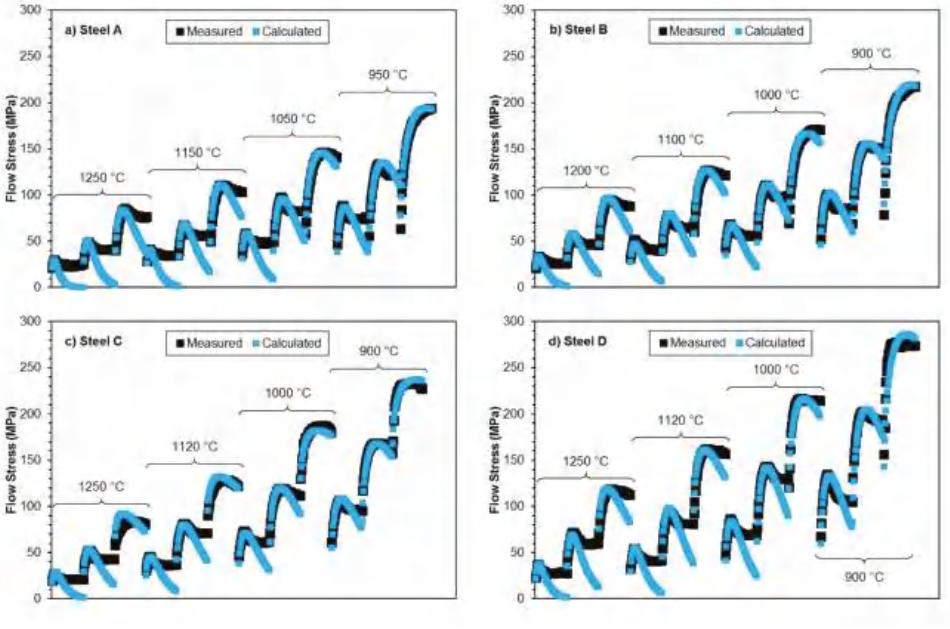

Figure 20. Comparison of measured (black points) and by Equation (14) predicted (blue points) individual flow stress curves of investigated steels: (**a**) steel A; (**b**) steel B; (**c**) steel C; (**d**) steel D.

The accuracy of predicted flow stress curves can be evaluated using the root mean square error RMSE (MPa) [57,69]:

$$\mathrm{RMSE} = \sqrt{\frac{1}{n} \cdot \sum_{i=1}^{n} [\sigma_i - \sigma(\varepsilon_i)]^2} \tag{38}$$

where n $(-)$ represents the number of points of the flow stress curves of particular steel included in the calculations (together for all combinations of temperature and strain rate). The values of σ_i (MPa) then represent the experimentally obtained values of flow stresses and $\sigma(\varepsilon_i)$ (MPa) are the values of flow stresses obtained by prediction through the model (14). The RMSE value then acquires a specific dimension (MPa). Since the model (14) [27] was originally designed to mathematically describe the flow stress curves up to the peak point (up to the strain of ε_p), the RMSE values were determined only for the predicted flow stress curves in the range of strains from 0 do ε_p. The excellent accuracy of the predicted flow stress curves (using Equation (14)) of all examined steels in the range of strains from 0 to ε_p is documented by low RMSE values (see Figure 21), which were up to 10 MPa for all investigated steels. The lowest RMSEs (only about of 4 MPa) are then associated with the steels A and B.

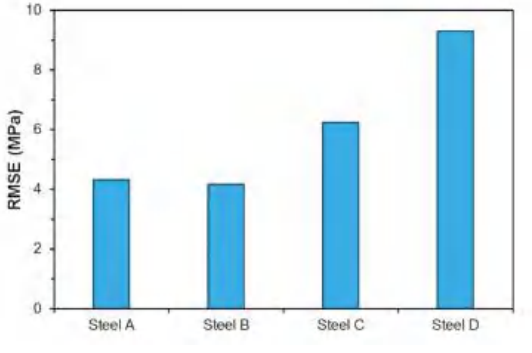

Figure 21. Root mean square error (RMSE) of predicted flow stress curves (by Equation (14)) in range of low strains (from 0 to ε_p) of investigated steels.

7. Conclusions

The stress–strain curves of selected non-alloy carbon steels were investigated using isothermal continuous uniaxial compression tests performed on a Gleeble 3800-GTC simulator.

The obtained stress–strain curves were analyzed in the ENERGY 4.0 software to determine the hot deformation activation energy and other material constants suitable for predicting the peak flow stress σ_p and the peak strain ε_p. The critical strains ε_{crDRX} required to induce dynamic recrystallization were then determined by analyzing the stress dependence of the work hardening rate on peak stress, using model Cingara and McQueen. In addition, the critical flow stresses σ_{crDRX} were also determined using this model, which corresponds to the critical strains ε_{crDRX} of all investigated steels. Based on the achieved results, it was confirmed that for a given size of the Zener–Hollomon parameter, with increasing carbon content (or with increasing value of carbon equivalent) in the investigated steels, their peak flow stress and critical flow stress also increase. In the case of carbon content or carbon equivalent influence, the peak strain and critical strain size made the situation more complicated. However, for all investigated steels, it was confirmed that the difference between the peak strain ε_p and the critical strain ε_{crDRX} increased with decreasing deformation temperature and increasing strain rate.

Based on the critical strains ε_{crDRX}, determined according to Equation (14) and subsequently experimentally verified, equations describing with excellent accuracy the simple linear dependence of ε_{crDRX} on the peak strain ε_p were derived for all investigated steels. In

addition, equations comprehensively describing the linear dependence of the critical strain ε_{crDRX} on the peak strain ε_p and the critical flow stresses σ_{crDRX} on the peak flow stress σ_p were derived as well.

The determined hot deformation activation energy Q decreased with increasing carbon content (or increasing value of carbon equivalent) in the investigated steels, and this dependence was described with good accuracy by a logarithmic equation.

Using the model Cingara and McQueen individual flow stress curves of investigated steels were mathematically described. The excellent accuracy of the predicted flow stress curves of all investigated steels, especially in the range of strains from 0 to ε_p, was documented by the low determined values of root mean square error.

Author Contributions: Conceptualization, P.K. and P.O.; methodology, P.K., P.O. and I.S.; validation, P.K., P.O., R.K. and K.K.; formal analysis, P.K., P.O. and M.S.; investigation, P.K., R.K., S.R. and K.K.; resources, P.K., P.O., I.S. and R.K.; data curation, P.K., P.O. and S.R.; writing—original draft preparation, P.K. and P.O.; visualization, P.K., P.O. and M.S.; supervision, P.K.; project administration, I.S. and S.R.; funding acquisition, I.S. and S.R. All authors have read and agreed to the published version of the manuscript.

Funding: The article was created thanks to the project No. CZ.02.1.01/0.0/0.0/17_049/0008399 from the EU and CR financial funds provided by the Operational Programme Research, Development and Education, Call 02_17_049 Long-Term Intersectoral Cooperation for ITI, Managing Authority: Czech Republic—Ministry of Education, Youth and Sports and within the students' grant projects SP2021/41 and SP2021/73 supported at the VŠB–TU Ostrava by the Ministry of Education, Youth and Sports of the Czech Republic.

Institutional Review Board Statement: Not applicable.

Informed Consent Statement: Not applicable.

Data Availability Statement: Not applicable.

Acknowledgments: The authors would like to thank to Petr Vašíček and Miroslav Šula (Department of Materials Forming, Faculty of Materials Science and Technology, VŠB–Technical University of Ostrava) for the preparation of compression test samples and also to Ivana Malá (Department of Material Engineering, Faculty of Materials Science and Technology, VŠB–Technical University of Ostrava) for the preparation of deformed samples to metallographic analysis.

Conflicts of Interest: The authors declare no conflict of interest.

References

1. Zhang, H.K.; Xiao, H.; Fang, X.W.; Zhang, Q.; Logé, R.E.; Huang, K. A critical assessment of experimental investigation of dynamic recrystallization of metallic materials. *Mater. Design.* **2020**, *193*, 108873. [CrossRef]
2. Wang, M.; Wang, W.; Liu, Z.; Sun, C.; Qian, L. Hot workability integrating processing and activation energy maps of Inconel 740 superalloy. *Mater. Today. Commun.* **2018**, *14*, 188–198. [CrossRef]
3. Qiang, F.; Bouzy, E.; Kou, H.; Zhang, Y.; Wang, L.; Li, J. Grain fragmentation associated continuous dynamic recrystallization (CDRX) of hexagonal structure during uniaxial isothermal compression: High-temperature α phase in TiAl alloys. *Intermetallics* **2021**, *129*, 107028. [CrossRef]
4. Kawulok, P.; Schindler, I.; Kawulok, R.; Opěla, P.; Sedláček, R. Influence of heating parameters on flow stress curves of low-alloy Mn-Ti-B steel. *Arch. Metall. Mater.* **2018**, *63*, 1785–1792. [CrossRef]
5. Zheng, S.J.; Yuan, X.H.; Gong, X.; Le, T.; Ravindra, A.V. Hot deformation behavior and microstructural evolution of an Fe-Cr-W-Mo-V-C steel. *Metall. Mater. Trans. A* **2019**, *50*, 2342–2355. [CrossRef]
6. Wang, M.T.; Zang, X.L.; Li, X.T.; Du, F.S. Finite Element Simulation of Hot Strip Continuous Rolling Process Coupling Microstructural Evolution. *J. Iron Steel Res. Int.* **2007**, *14*, 30–36. [CrossRef]
7. Siciliano, F.; Jonas, J.J. Mathematical Modeling of the Hot Strip Rolling of Microalloyed Nb, Multiply-Alloyed Cr-Mo, and Plain C-Mn Steels. *Metall. Mater. Trans. A* **2012**, *31*, 511–530. [CrossRef]
8. Gu, S.D.; Zhang, L.W.; Yue, C.X.; Ruan, J.H.; Zhang, J.L.; Gao, H.J. Multi-field coupled numerical simulation of microstructure evolution during the hot rolling process of GCr15 steel rod. *Comp. Mater. Sci.* **2011**, *50*, 1951–1957. [CrossRef]
9. Siciliano, F.; Rodrigues, S.F.; Aranas, C.; Jonas, J.J. The dynamic transformation of ferrite above Ae3 and the consequences on hot rolling of steels. *Tecnol. Metal. Mater. Miner.* **2020**, *17*, 90–95. [CrossRef]
10. Fu, Y.; Yu, H. Application of mathematical modeling in two-stage rolling of hot rolled wire rods. *J. Mater. Process. Tech.* **2014**, *214*, 1962–1970. [CrossRef]

11. Gu, B.; Chekhonin, P.; Schaarschuch, R.; Oertel, C.G.; Xin, S.W.; Ma, C.L.; Zhou, L.; Gan, W.M.; Skrotzki, W. Microstructure, texture and hardness of a metastable β-titanium alloy after bar-rolling and annealing. *J. Alloy. Compd.* **2020**, *825*, 154082. [CrossRef]
12. Ebrahimi, R.; Solhjoo, S. Characteristic Points of Stress-Strain Curve at High Temperature. *Int. J. ISSI* **2007**, *4*, 24–27.
13. Opěla, P.; Schindler, I.; Rusz, S.; Vančura, F. Determination of the critical strain for the onset of dynamic recrystallization of C45 carbon steel using flow stress models. In Proceedings of the 26th International Conference on Metallurgy and Materials Metal 2017, Brno, Czech Republic, 24–26 May 2017; pp. 496–501.
14. Solhjoo, S. Determination of critical strain for initiation of dynamic recrystallization. *Mater. Design.* **2010**, *31*, 1360–1364. [CrossRef]
15. Liu, Y.H.; Liu, Z.Z.; Wang, M. Gradient microstructure evolution under thermo-mechanical coupling effects for a nickel-based powder metallurgy superalloy—Dynamic recrystallization coexist with static recrystallization. *J. Mater. Process. Tech.* **2021**, *294*, 117142. [CrossRef]
16. Zhu, L.M.; Li, Q.A.; Chen, X.Y.; Zhang, Q. Effect of Sm on dynamic recrystallization of Mg-8Gd-0.5Zr alloy during hot compression. *J. Alloy. Compd.* **2021**, *865*, 158648. [CrossRef]
17. Fernández, A.I.; Uranga, P.; López, B.; Ródrigez-Ibabe, J.M. Dynamic recrystallization behavior covering a wide austenite grain size range in Nb and Nb–Ti microalloyed steels. *Mater. Sci. Eng. A* **2003**, *361*, 367–376. [CrossRef]
18. Liu, X.G.; Zhang, L.G.; Qi, R.S.; Chen, L.; Jin, M.; Guo, B.F. Prediction of critical conditions for dynamic recrystallization in 316LN austenitic steel. *J. Iron Steel Res. Int.* **2016**, *23*, 238–243. [CrossRef]
19. Ohadi, D.; Parsa, M.H.; Mirzadeh, H. Development of dynamic recrystallization maps based on the initial grain size. *Mater. Sci. Eng. A* **2013**, *565*, 90–95. [CrossRef]
20. Wang, Z.H.; Sun, S.H.; Wang, B.; Shi, Z.P.; Zhang, R.H.; Fu, W.T. Effect of grain size on dynamic recrystallization and hot-ductility behaviors in high-nitrogen CrMn austenitic stainless steel. *Metall. Mater. Trans. A* **2014**, *45*, 3631–3639. [CrossRef]
21. El Wahabi, M.; Gavard, L.; Montheillet, F.; Cabrera, J.M.; Prado, J.M. Effect of initial grain size on dynamic recrystallization in high purity austenitic stainless steels. *Acta Mater.* **2005**, *53*, 4605–4612. [CrossRef]
22. Chamanfar, A.; Alamoudi, M.T.; Nanninga, N.E.; Misiolek, W.Z. Analysis of flow stress and microstructure during hot compression of 6099 aluminum alloy (AA6099). *Mater. Sci. Eng. A* **2019**, *743*, 684–696. [CrossRef]
23. Guo, L.G.; Wang, F.Q.; Zhen, P.L.; Li, X.C.; Zhan, M. A novel unified model predicting flow stress and grain size evolutions during hot working of non-uniform as-cast 42CrMo billets. *Chin. J. Aeronaut.* **2019**, *32*, 531–545. [CrossRef]
24. Schindler, I.; Kawulok, P.; Kawulok, R.; Hadasik, E.; Kuc, D. Influence of calculation method on value of activation energy in hot forming. *High Temp. Mater. Processes* **2013**, *32*, 149–155. [CrossRef]
25. Schindler, I.; Sauer, M.; Kawulok, P.; Rodak, K.; Hadasik, E.; Jabłońska, M.B.; Rusz, S.; Ševčák, V. Study of hot deformation behavior of CuFe2 alloy. *Arch. Metall. Mater.* **2019**, *64*, 701–706. [CrossRef]
26. Schindler, I.; Kawulok, P.; Očenášek, V.; Opěla, P.; Kawulok, R.; Rusz, S. Flow stress and hot deformation activation energy of 6082 aluminium alloy influenced by initial structural state. *Metals* **2019**, *9*, 1248. [CrossRef]
27. Cingara, A.; McQueen, H.J. New formula for calculating flow curves from high temperature constitutive data for 300 austenitic steels. *J. Mater. Process. Tech.* **1992**, *36*, 31–42. [CrossRef]
28. Ghazani, M.S.; Eghbali, B. Modeling the flow behavior of AISI 321 austenitic stainless steel using a simple combined phenomenological method. *Mech. Mater.* **2019**, *137*, 103108. [CrossRef]
29. Abarghooee, H.; Arabi, H.; Seyedein, S.H.; Mirzakhani, B. Modelling of hot flow behavior of API-X70 microalloyed steel by genetic algorithm and comparison with experiments. *Int. J. Pres. Ves. Pip.* **2021**, *189*, 104261. [CrossRef]
30. Shafaat, M.A.; Omidvar, H.; Fallah, B. Prediction of hot compression flow curves of Ti–6Al–4V alloy in α + β phase region. *Mater. Design.* **2011**, *32*, 4689–4695. [CrossRef]
31. Najafizadeh, A.; Jonas, J.J. Predicting the critical stress for initiation of dynamic recrystallization. *ISIJ Int.* **2006**, *46*, 1679–1684. [CrossRef]
32. Johnson, G.R.; Cook, W.H. Fracture characteristics of three metals subjected to various strains, strain rates, temperatures and pressures. *Eng. Fract. Mech.* **1985**, *21*, 31–48. [CrossRef]
33. Quan, G.Z.; Tong, Y.; Luo, G.; Zhou, J. A characterization for the flow behavior of 42CrMo steel. *Comp. Mater. Sci.* **2010**, *50*, 167–171. [CrossRef]
34. Xiao, Y.H.; Guo, C. Constitutive modelling for high temperature behavior of 1Cr12Ni3Mo2VNbN martensitic steel. *Mater. Sci. Eng. A* **2011**, *528*, 5081–5087. [CrossRef]
35. Hensel, A.; Spittel, T. *Kraft- und Arbeitsbedarf Bildsamer Formgebungsverfahren*, 1st ed.; Deutscher Verlag für Grundstoffindustrie: Leipzig, Germany, 1978.
36. Yu, J.M.; Zhang, Z.M.; Xu, P.; Dong, B.B.; Wang, Q.; Meng, M.; Hao, H.Y.; Li, X.B.; Yin, X.Y. Dynamic recrystallization behavior of Gd-containing Mg alloy under torsion deformation. *J. Alloy. Compd.* **2019**, *787*, 239–253. [CrossRef]
37. Lino, R.; Guadanini, L.G.L.; Silva, L.B.; Neto, J.G.C.; Barbosa, R. Effect of Nb and Ti addition on activation energy for austenite hot deformation. *J. Mater. Res. Technol.* **2019**, *8*, 180–188. [CrossRef]
38. Marques, A.; Souza, R.A.; Pinto, G.A.M.; Galdino, A.G.S.; Machado, M.L.P. Evaluation of the softening mechanisms of AISI 4340 structural steel using hot torsion test. *J. Mater. Res. Technol.* **2020**, *9*, 10886–10900. [CrossRef]
39. Mandziej, S.T. Physical simulation of metallurgical processes. *Mater. Tech.* **2010**, *44*, 105–119.
40. Zhao, H.T.; Qi, J.J.; Liu, G.Q.; Su, R.; Sun, Z.H. A comparative study on hot deformation behaviours of low-carbon and medium-carbon vanadium microalloyed steels. *J. Mater. Res. Technol.* **2020**, *9*, 11319–11331. [CrossRef]

41. Murata, M.; Yoshida, Y.; Nishiwaki, T. Stress correction method for flow stress identification by tensile test using notched round bar. *J. Mater. Process. Tech.* **2018**, *251*, 65–72. [CrossRef]
42. Wen, D.X.; Gao, C.X.; Zheng, Z.Z.; Wang, K.; Xiong, Y.B.; Wang, J.K.; Li, J.J. Hot tensile behavior of a low-alloyed ultrahigh strength steel: Fracture mechanism and physically-based constitutive model. *J. Mater. Res. Technol.* **2021**, *13*, 1684–1697. [CrossRef]
43. Li, Z.; Zhao, J.W.; Jia, F.H.; Lu, Y.; Zhang, Q.F.; Jiao, S.H.; Jiang, Z.Y. Analysis of flow behaviour and strain partitioning mechanism of bimetal composite under hot tensile conditions. *Int. J. Mech. Sci.* **2019**, *169*, 105317. [CrossRef]
44. Žídek, M. *Metalurgická tvařitelnost ocelí za tepla a za studena [Metallurgical Formability of Steels at Hot and Cold Conditions]*, 1st ed.; Aleko: Praha, Czech Republic, 1995. (In Czech)
45. Rusz, S.; Němec, J.; Schindler, I.; Opěla, P.; Solowski, Z. Influence of initial structure on stress-strain curves of medium-carbon steel. In Proceedings of the 26th International Conference on Metallurgy and Materials Metal 2017, Brno, Czech Republic, 24–26 May 2017; pp. 533–538.
46. Thomas, B.G.; Samarasekera, I.V.; Brimacombe, J.K. Mathematical model of the thermal processing of steel ingots 1. heat flow model. *Met. Tran B* **1987**, *18*, 119–130. [CrossRef]
47. Kasatkin, O.G.; Vinokur, B.B.; Pilyushenko, V.L. Calculation models for determining the critical points of steel. *Met. Sci. Heat Treat.* **1984**, *26*, 27–31. [CrossRef]
48. GLEEBLE: Gleeble®Thermal-Mechanical Simulators. Available online: https://gleeble.com/ (accessed on 8 November 2021).
49. Zener, C.; Hollomon, J.H. Effect of Strain Rate Upon Plastic Flow of Steel. *J. Appl. Phys.* **1944**, *15*, 22–32. [CrossRef]
50. Garofalo, F. An empirical relation defining the stress dependence of minimum creep rate in metals. *Trans. Metall. Soc. AIME* **1963**, *227*, 351–356.
51. McQueen, H.J.; Yue, S.; Ryan, N.D.; Fry, E. Hot working characteristics of steels in austenitic state. *J. Mater. Process. Tech.* **1995**, *53*, 293–310. [CrossRef]
52. Legerski, M.; Plura, J.; Schindler, I.; Rusz, S.; Kawulok, P.; Kulveitová, H.; Hadasik, E.; Kuc, D.; Niewielski, G. Complex flow stress model for a magnesium alloy AZ31 at hot forming. *High Temp. Mater. Processes* **2011**, *30*, 63–69. [CrossRef]
53. Malas, J.C.; Venugopal, S.; Seshacharyulu, T. Effect of microstructural complexity on the hot deformation behavior of aluminum alloy 2024. *Mater. Sci. Eng. A* **2004**, *368*, 41–47. [CrossRef]
54. Huang, X.D.; Zhang, H.; Han, Y.; Wu, W.X.; Chen, J.H. Hot deformation behavior of 2026 aluminum alloy during compression at elevated temperature. *Mater. Sci. Eng. A* **2010**, *527*, 485–490. [CrossRef]
55. Quan, G.Z.; Mao, Y.P.; Li, G.S.; Lv, W.Q.; Wang, Y.; Zhou, J. A characterization for the dynamic recrystallization kinetics of as-extruded 7075 aluminum alloy based on true stress-strain curves. *Comp. Mater. Sci.* **2012**, *55*, 65–72. [CrossRef]
56. Bembalge, O.B.; Panigrahi, S.K. Hot deformation behavior and processing map development of cryorolled AA6063 alloy under compression and tension. *Int. J. Mech. Sci.* **2021**, *191*, 106100. [CrossRef]
57. Opěla, P.; Kawulok, P.; Schindler, I.; Kawulok, R.; Rusz, S.; Navrátil, H. On the Zener-Hollomon Parameter, Multi-Layer Perceptron and Multivariate Polynomials in the Struggle for the Peak and Steady-State Description. *Metals* **2020**, *10*, 1413. [CrossRef]
58. Yang., P.R.; Liu, C.X.; Guo, Q.Y.; Liu, Y.C. Variation of activation energy determined by a modified Arrhenius approach: Roles of dynamic recrystallization on the hot deformation of Ni-based superalloy. *J. Mater. Sci. Technol.* **2021**, *72*, 162–171. [CrossRef]
59. Ryan, N.D.; McQueen, H.J. Flow stress, dynamic restoration, strain hardening and ductility in hot workability of 316 steel. *J. Mater. Process. Tech.* **1990**, *21*, 177–199. [CrossRef]
60. Poliak, E.I.; Jonas, J.J. Initiation of dynamic recrystallization in constant strain rate hot deformation. *ISIJ Int.* **2003**, *43*, 684–691. [CrossRef]
61. Schindler, I.; Opěla, P.; Kawulok, P.; Sauer, M.; Rusz, S.; Kuc, D.; Rodak, K. Hot deformation activation energy of metallic materials influenced by strain value. *Arch. Metall. Mater.* **2021**, *66*, 223–228. [CrossRef]
62. Medina, S.F.; Hernandez, C.A. General expression of the Zener-Hollomon parameter as a function of the chemical composition of low alloy and microalloyed steels. *Acta Mater.* **1996**, *44*, 137–148. [CrossRef]
63. Sakai, T.; Ohashmi, M. The effect of temperature, strain rate and carbon content on hot deformation of carbon steels. *Tetsu–Hagané* **1981**, *67*, 2000–2009. [CrossRef]
64. Elfmark, J. Parametrické vyjádření kinetiky dynamické rekrystalizace při deformaci za tepla [Parametric expression of the kinetics of dynamic recrystallization during hot deformation]. *Hut. Listy* **1982**, *37*, 564–568. (In Czech)
65. Serajzadeh, S.; Taheri, A.K. An investigation on the effect of carbon and silicon on flow behavior of steel. *Mater. Design.* **2002**, *23*, 271–276. [CrossRef]
66. Saadatkia, S.; Mirzadeh, H.; Cabrera, J.M. Hot deformation behavior, dynamic recrystallization, and physically-based constitutive modeling of plain carbon steels. *Mater. Sci. Eng. A* **2015**, *636*, 196–202. [CrossRef]
67. Mead, H.W.; Birchenall, C.E. Self-diffusion of iron in austenite. *JOM* **1956**, *8*, 1336–1339. [CrossRef]
68. Colas, R. A model for the hot deformation of low-carbon steel. *J. Mater. Process. Tech.* **1996**, *62*, 180–184. [CrossRef]
69. Gauss, J.C.F. *Theoria Combinationis Observationum Erroribus Minimis Obnoxiae [Theory of the Combination of Observations Least Subject to Errors]*; Henricum Dieterich: Göttingen, Germany, 1823.

materials

MDPI

Article

A Comparative Study on the Hot Deformation Behavior of As-Cast and Twin-Roll Cast Mg-6.8Y-2.5Zn-0.4Zr Alloy

Kristina Kittner, Madlen Ullmann * and Ulrich Prahl

Institute of Metal Forming, Technische Universität Bergakademie Freiberg, Bernhard-von-Cotta-Straße 4, 09599 Freiberg, Germany; kristina.kittner@imf.tu-freiberg.de (K.K.); ulrich.prahl@imf.tu-freiberg.de (U.P.)
* Correspondence: madlen.ullmann@imf.tu-freiberg.de; Tel.: +49-3731-39-3095

Abstract: The Mg-6.8Y-2.5Zn-0.4Zr (WZ73) alloy exhibits different microstructure characteristic after conventional casting compared to the twin-roll cast (TRC) state. Twin-roll casting results in a finer microstructure, where the LPSO phases are more finely distributed and less strongly connected. A transfer of the hot deformation behavior from the as-cast condition to the TRC condition is only possible to a limited extent due to the microstructural differences. Both states show differences in the recrystallization behavior during hot deformation. In the conventional cast state, dynamic recrystallization (DRX) is assumed to be delayed by the occurrence of coarse blocky LPSO phases. Main DRX mechanisms are continuous dynamic recrystallization (CDRX), particle stimulated nucleation (PSN) and twin induced dynamic recrystallization (TDRX). The deformed TRC sample showed pronounced DRX at almost all deformation conditions. Besides the TDRX and the PSN mechanism, kink induced dynamic recrystallization (KDRX) can be observed. Optimum deformation conditions for both states are temperatures from 500 °C to 520 °C, and strain rates ranging from 0.01 s^{-1} to 0.1 s^{-1} for the as-cast material as well as a strain rate of 1 s^{-1} for the TRC material.

Keywords: flow curve; dynamic recrystallisation; processing map; LPSO phase; Mg-6.8Y-2.5Zn-0.4Zr; twin-roll casting; hot deformation behavior

Citation: Kittner, K.; Ullmann, M.; Prahl, U. A Comparative Study on the Hot Deformation Behavior of As-Cast and Twin-Roll Cast Mg-6.8Y-2.5Zn-0.4Zr Alloy. *Materials* **2021**, *14*, 3628. https://doi.org/10.3390/ma14133628

Academic Editor: Ivo Schindler

Received: 31 March 2021
Accepted: 25 June 2021
Published: 29 June 2021

1. Introduction

Within the last few years, there has been increased research on magnesium alloys with LPSO (long period stacking ordered) phases. These are known to provide alloys with a good mechanical property profile. The LPSO phases are characterized by excellent strength, unique crystal structure and good thermal stability. The good strength properties are retained even at elevated temperatures due to the high melting temperature of 545 °C. The high strength is mainly attributed to the formation of kink bands in the LPSO phase. Several studies have reported the formation of kink bands during plastic deformation for different initial states, such as as-cast or twin-roll cast. Predominantly, LPSO phases with an 18R or a 14H structure occur after conventional casting as well as after twin-roll casting (TRC) [1–7].

Many factors, such as temperature, strain rate and strain, are associated with the hot deformation behavior of metallic metals. For magnesium alloys containing LPSO phases, several papers are focused on the effect of such factors on workability and recrystallization behavior. Li et al. (2020) [8] investigated the hot deformation behavior of a $Mg_{95.21}Zn_{1.44}Y_{2.86}Mn_{0.49}$ magnesium alloy after homogenization. They have reported that at low temperatures (250 °C–300 °C), kink band formation in connection with low strain rates (0.01 s^{-1}) twinning are the main deformation mechanisms. The beginning of dynamic recrystallization (DRX) at the original grain boundaries was shown at temperatures between 350 °C and 400 °C, which remains incomplete. Increasing temperatures up to 500 °C results in a complete DRX. Comparable results are presented by Zhang et al. (2018) [9] for a homogenized Mg-Gd-Y-Zn-Zr alloy. Kink deformation mainly occurs at low temperatures, where sliding systems of magnesium can hardly be activated. Fekete et al. (2020) [10]

showed that twinning is still active at 300 °C during plastic deformation of a $Mg_{98.5}Y_1Zn_{0.5}$ magnesium alloy. The investigations of Li et al. (2019) [11] revealed that twinning acts as an additional deformation mode even at high strain rates (0.1–1 s^{-1}) during deformation of a Mg-5.6Gd-0.8Zn (wt.%) alloy. Dynamic recrystallization preferably starts at the twin boundaries (TDRX), at temperatures between 350 °C and 400 °C. Increasing temperatures lead to a change in the DRX mechanism, as new grains mainly originate at the original grain boundaries. At 500 °C the degree of DRX is considerably high. Other studies indicate that DRX starts at the primary LPSO phase [12]. It is reported that the formation of the lamellar LPSO phase can increase the critical resolved shear stress (CRSS) of the basal plane and improve the sliding of non-basal planes. Furthermore, regarding the interaction of LPSO phase and twins, Shao et al. (2020) [13] indicate that thin LPSO lamella allow the propagation of twins, while thick LPSO phases impede the twin propagation. However, the significance of the LPSO phase during hot deformation of magnesium alloys remains still unclear [10].

Based on our previous studies, this paper compares the hot deformation behavior of the Mg-6.8Y-2.5Zn-0.4Zr (WZ73) alloy in the as-cast and the twin-roll cast condition. In addition to the more economical and resource-saving production by reducing the forming and annealing effort during TRC, the quality of the cast strips can basically be improved in terms of homogeneity. The cooling rates (up to 2 106 K/s according to Allen et al. (2001) [14], i.e., about ten times faster than in slab casting), which depend on the strip thickness, have a positive effect on the microstructure and macrostructure of the strip during solidification, as well as on the precipitation state [15]. A transfer of the hot deformation behavior from the as-cast condition to the TRC condition is only possible to a limited extent, due to the microstructural differences. The purpose of this paper is to show these differences.

2. Materials and Methods

Cast ingots of the WZ73 alloy (Mg-6.8Y-.5Zn-0.4Zr) acquired from XI'AN YUECHEN Metal Products Co., Ltd., China, were used in this study. The chemical composition is shown in Table 1. Samples for plane strain compression tests with dimensions of 20 mm × 30 mm × 5.3 mm (length × width × height) were cut from these ingots. This condition is referred to as 'as-cast'. The cast ingots were also used as initial material for the twin-roll casting process. TRC was conducted on the industrial pilot plant (Pechiney, France) of the Institute of Metal Forming, using a hybrid casting nozzle consisting of steel and ceramic. Important casting parameters applied were line speed of 1.625 m/min, casting temperature of 730 °C and maximum roll force of 290 kN. Detailed description of the TRC of the WZ73 strips can be found in [4]. This condition is referred to as 'TRC'. Thickness of the TRC strip was 5.3 mm.

Table 1. Chemical composition of Mg-6.8Y-2.5Zn-0.4Zr (wt.%) alloy as determined by means of optical emission spectrometry (OES, Spectro/Ametek, Germany).

Y	Zn	Zr	Si	Fe	Cu	Ni	Others	Mg
6.8	2.5	0.4	0.01	0.005	0.001	0.001	0.01	Balance

The plane strain compression tests were performed under process-oriented conditions using a servo-hydraulic hot forming simulator. Samples were heat treated in an air circulation furnace at a temperature of 500 °C for a holding time of 2 h. Subsequent to the heat treatment, samples were compressed or cooled down (in the furnace) to the deformation temperatures between 350 °C and 450 °C and kept at these temperatures for 15 min in order to achieve a homogeneous temperature distribution over the cross section. To reduce friction between the samples surface and the tool, a graphite/oil mixture was used. Isothermal flow curves were obtained based on the recorded force-displacement data. Dissipation energy and friction were considered by the correction function according to Siebel (1932) [16], with $\mu = 0.12$. Softening effects as a result of dissipation energy were

considered numerically by using the thermodynamic temperature factor $K_\vartheta = \exp(-m_1 \cdot \vartheta)$ with $m_1 = -0.00427\ ^\circ C^{-1}$ for both as-cast and TRC conditions. Continuous compression was performed at strain rates of 0.01 s^{-1}, 0.1 s^{-1}, 1 s^{-1} and 10 s^{-1} (Figure 1). The samples were deformed to an equivalent logarithmic strain of $\varphi_v = 1$. Immediately after compression, samples were quenched into water to impede softening processes during cooling. Based on the flow curve data, processing maps are described as a function of temperature and strain rate, using the dynamic material model (DMM). The detailed approach can be found in [1,17].

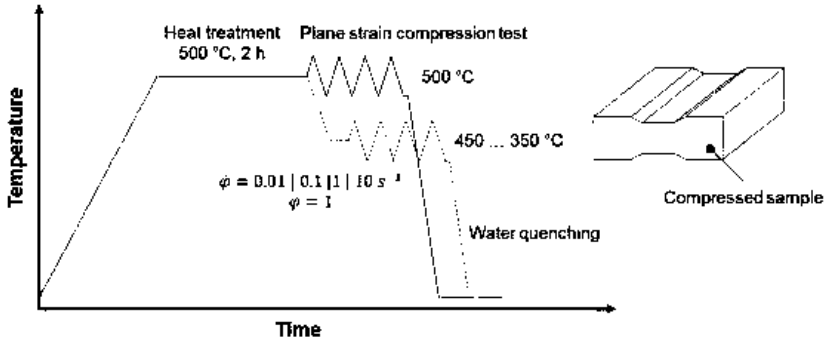

Figure 1. Schematic diagram of plane strain compression test.

From the compressed samples, longitudinal sections across the cross-section were cut and metallographically prepared for microstructural characterization. The samples were ground and then polished with an oxide polishing suspension. Etching was carried out in two steps. After brief rinsing with a 3% initial solution, the sample was etched with a picric acid solution consisting of 70 mL ethanol, 10 mL distilled water, 10 mL glacial acetic acid and 4.2 g picric acid. Light microscopic images were taken on a Keyence VHX 6000 microscope at the Institute of Metal Forming, Freiberg, Germany. Scanning electron microscopic (SEM) evaluation was performed on a ZEISS GeminiSEM 450 device at the Institute of Metal Forming, Freiberg, Germany. Different detectors were used for SEM: angular selective back-scatter (AsB), back-scatter (BSE) and secondary electron detector (SE). X-ray diffraction analysis (XRD) was performed on Empyrean Cu LFF HR at the Academic Centre for Materials and Nanotechnology, University of Science and Technology, Krakow, Poland using CuK radiation (λ = 1.540598 Å). Diffraction patterns were recorded within the 2θ-range of 30 to 60 with a step size of 0.026. For phase identification, the ICDD database was used. The diffraction peaks from Mg were identified based on ICDD 01-089-5003. However, as the existence of 18R and 14H LPSO structures cannot be unambiguously confirmed by the ICDD database, the final identification was only supported by ICDD and was evaluated based on the studies form Luo et al. (2000) [18], Onorbe et al. (2012) [19] and Wen et al. (2016) [20].

3. Results

3.1. Characterization of Initial States

Figure 2 showed the SEM-images of the microstructure of the homogenized (500 °C, 2 h) Mg-6.8Y-2.5Zn-0.4Zr alloy after conventional and after twin-roll casting. The microstructure of both conditions mainly consists of the α-magnesium matrix (dark grey) and network-like LPSO phases (light grey) located along the grain boundaries. Twin-roll casting leads to a finer microstructure compared to conventional casting. Thickness of the blocky LPSO phases within the network varies from 2 µm to 5 µm in the TRC (Figure 2d), while it rises up to 20 µm in the as-cast state (Figure 2c). According to the results of the X-ray diffraction analysis (Figure 3) and EDX analysis (Table 2), LPSO phases could be

assigned to an 18R or 14H structure. The exact distinction of both kinds of LPSO phases requires transmission electron microscopy. Based on the literature, the results are consistent with those of other research groups investigating magnesium alloys consisting of LPSO phases [21–23]. A detailed view into the microstructure (Figure 4) reveals another substantial difference between both initial states. After conventional casting, thin lamellar LPSO phases arise within the α-magnesium grains (Figure 4a). It is reported that those lamellae are enriched with Y and Zn [24], and can be assigned to the 14H structure [6,25]. It is assumed that the 14H LPSO lamellae can grow from stacking faults (SF) which precipitated from a supersaturated Mg matrix. During twin-roll casting and subsequent annealing, the formation of lamellar LPSO phases cannot be observed (Figure 4b). It is therefore assumed that the high cooling rate during TRC and the characteristic solidification conditions have a major impact on the precipitation kinetics of the LPSO phases. The amount of Y and Zn within the magnesium matrix after conventional casting is 3.6 wt.% and 1.4 wt.%, respectively, while it is 2.2 wt.% and 0.7 wt.% in the TRC state. Higher amounts of solute atoms in the magnesium matrix after TRC can be achieved by heat treatments at high temperatures above 500 °C and long holding times above 6 h. Previous studies showed that the amount of Y and Zn increased to 3.8 wt.% Y and 1.4 wt.% Zn after homogenization at 525 °C for 6 h. Followed by a low cooling rate, thin lamellar LPSO phases precipitate within the magnesium matrix [4].

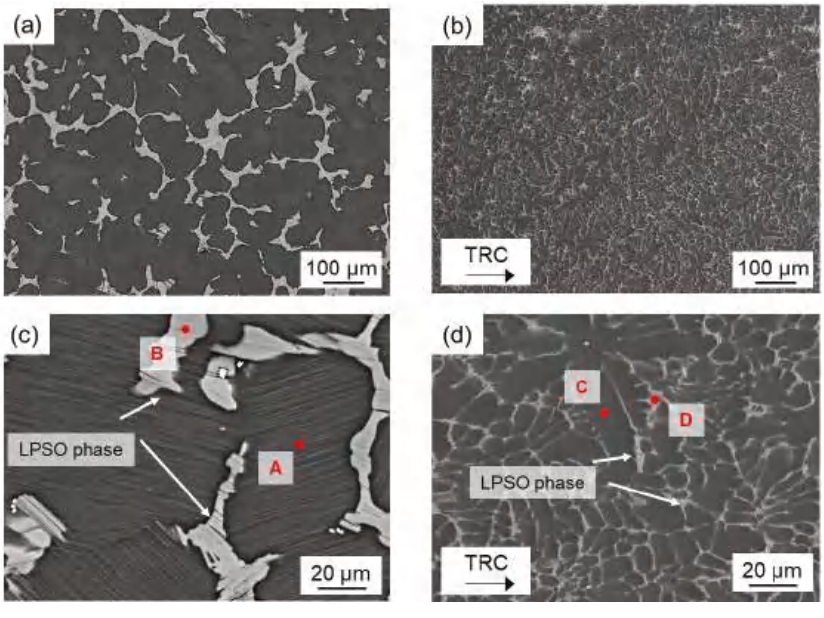

Figure 2. SEM images of the homogenized (500 °C, 2 h) Mg-6.8Y-2.5Zn-0.4Zr alloy: as-cast (**a**,**c**), (20 kV, AsB) and the TRC (**b**,**d**), (15 kV, SE) initial states: red points indicate EDX point measurement of the Mg matrix (A,C) and network-like LPSO structures (B,D).

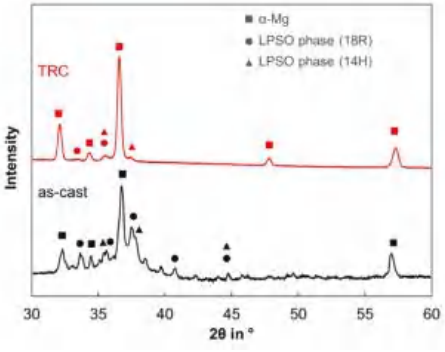

Figure 3. Results of the X-ray diffraction analysis (XRD) of the homogenized (500 °C, 2 h) Mg-6.8Y-2.5Zn-0.4Zr alloy after conventional and after twin-roll casting.

Table 2. Chemical composition of microstructural constituents from the as-cast and the TRC condition in Figure 2 (A, C—magnesium matrix, B, D—network-like LPSO structures) determined by means of energy dispersive X-ray spectroscopy (EDX)-analysis (wt.%).

Name		Mg	Y	Zn
A	matrix as-cast	95.0	3.6	1.4
B	LPSO as-cast	73.2	17.2	9.6
C	matrix TRC	97.1	2.2	0.7
D	LPSO TRC	74.2	15.6	10.2

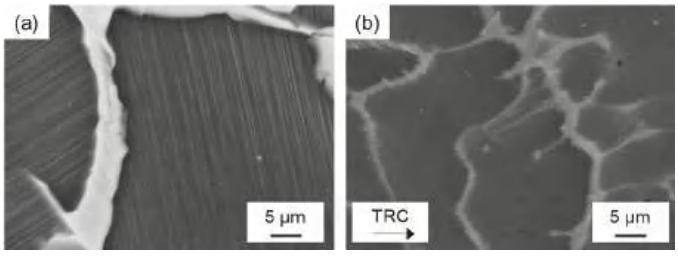

Figure 4. SEM images of the homogenized (500 °C, 2 h) Mg-6.8Y-2.5Zn-0.4Zr alloy after (**a**) conventional (20 kV, AsB) and after (**b**) twin-roll casting (15 kV, SE), detailed view.

3.2. Hot Deformation Behavior

3.2.1. Flow Stress Behavior

Figure 5 shows the flow stress–strain curves of the homogenized Mg-6.8Y-2.5Zn-0.4Zr after conventional and twin-roll casting deformed under different temperatures (350 °C, 400 °C, 450 °C, 500 °C) and strain rates (0.01, 0.1, 1, 10 s^{-1}) during hot compression. At a deformation temperature of 450 °C (Figure 5a) the flow stress–strain curves offer similar characteristics and the curves can be separated in three distinct regions. According to the occurring deformation mechanisms these regions correspond to hardening, transition and softening [26]. At the beginning of the flow, curve strain hardening is dominant and depends on the dislocation structure originating from plastic deformation. The increasing flow stress results from the dislocation storage, for example at the interface of α-Mg and LPSO phase. At low strain rates (<1 s^{-1}), the beginning of the plastic flow is accompanied by higher flow stresses in the as-cast condition, while at 10 s^{-1} the TRC and as-cast condition exhibit the same flow stress at the beginning of the plastic flow. Maximum flow stress in the as-cast state is higher compared to the TRC state. It is assumed that at

the large-scale LPSO phases in the as-cast state the dislocation density is higher because dislocations can hardly overcome or circumvent those LPSO phases compared to the finer phases after TRC. Therefore, in the as-cast condition, the flow curve exhibits higher flow stresses at 450 °C.

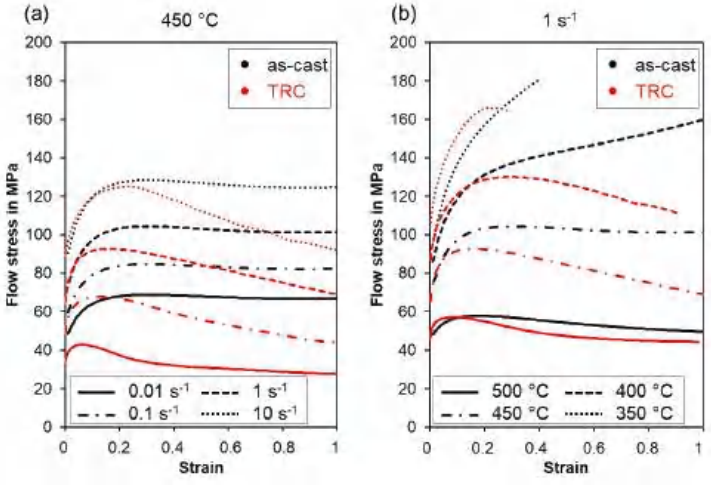

Figure 5. Flow stress-strain curves of the homogenized Mg-6.8Y-2.5Zn-0.4Zr alloy after conventional and twin-roll casting, deformed at (**a**) a temperature of 450 °C and different strain rates (0.01, 0.1, 1, 10 s^{-1}), and at (**b**) a strain rate of 1 s^{-1} and different temperatures (350, 400, 450, 500 °C).

After reaching the peak stress, the flow decreases or remains at a certain level because of softening processes, which take place when plastic deformation is maintained. During softening, dislocation movement is enabled by cross-slip and climbing processes, which result in the annihilation of dislocations and in a decreasing dislocation density. Both lead to a decrease of the flow stress. The flow curves of the as-cast condition reveal only a slight decrease of the flow stress, and then it is in a quasi-steady state, where hardening and softening counteract each other. It is assumed that at 450 °C dynamic recovery is the dominant softening mechanism. Only a small amount of dynamic recrystallization can be observed, indicating that the DRX remains incomplete even at high strains and low strain rates (Figure 6a,c). After twin-roll casting, the softening behavior deviates from the above. Once the maximum flow stress is exceeded, the flow curve drops significantly, which could be attributed to dynamic recrystallization (Figure 6b,d). The micrographs show an almost completely recrystallized structure at both high (10 s^{-1}) and low (0.01 s^{-1}) strain rates.

Decreasing forming temperatures result in increasing flow stress, which is shown in a temperature range from 350 °C to 500 °C and a strain rate of 1 s^{-1} in Figure 5b. The Mg-6.8Y-2.5Zn-0.4Zr alloy in the as-cast state exhibits an enhanced hardening behavior during plastic deformation at 350 °C and 400 °C. Softening during compression could not be obtained, and the samples deformed at 350 °C failed at a strain of 0.4. The TRC material revealed that softening occurred after reaching the peak stress even at low deformation temperatures (350 °C–400 °C). However, at 350 °C sample failed at a strain of 0.3, because enhanced hardening in the early stage of deformation results in the formation of microcracks, which provided the starting point for the material failure. From temperatures up to 400 °C, the flow curves show a characteristic progression of hardening and softening, with DRX predominating. Differences in temperature-dependent hardening and softening behavior between as-cast and TRC conditions almost disappear at 500 °C. At 500 °C, the flow curve of the conventional cast material also shows a softening behavior typical of dynamic recrystallization. For magnesium alloys containing LPSO phases, several research groups investigated the hot deformation behavior and presented comparable

results. Li et al. (2020) [8] showed flow stress-strain curves for a $Mg_{95.21}Zn_{1.44}Y_{2.86}Mn_{0.49}$ magnesium alloy, which are typical for DRX during hot compression. Main deformation mechanisms were kink deformation and twinning, while dynamic recrystallization occurred along the original grain boundaries and in the vicinity of the LPSO phases. Flow curves of the Mg-5.6GD-0.8Zn (wt.%) alloy reveal DRX characteristics expect hot deformation at 350 °C and 0.1 s^{-1} to 1 s^{-1}. At higher strain rates, twinning is an additional deformation mode and DRX takes place at the twin boundaries [11]. Lv et al. (2014) [27] investigated the hot deformation behavior of a Mg-2.0Zn-0.3Zr-5.8Y (wt.%) alloy in the temperature range from 300 °C to 500 °C and strain rates from 0.001 s^{-1} to 1 s^{-1}. The material showed a characteristic behavior of strain hardening and flow softening at low temperatures and high strain rates, while the flow stress decreases to a steady state at high temperatures and low strain rates.

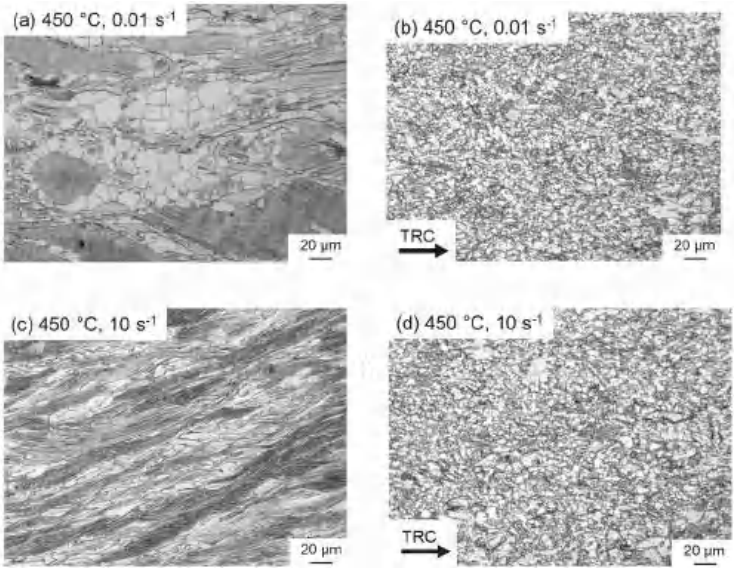

Figure 6. Optical micrographs of the deformed samples of the Mg-6.8Y-2.5Zn-0.4Zr alloy after conventional (**a**,**c**) and after twin-roll casting (**b**,**d**) at 450 °C and strain rates of 0.01 s^{-1} (**a**,**b**) and 10 s^{-1} (**c**,**d**).

3.2.2. Constitutive Equation

The activation energy is an important material parameter for determining the critical conditions for initiating dynamic recrystallization. In determining the model coefficients, it is assumed that the processes taking place during hot deformation are diffusion-controlled and thus strain rate- and temperature-dependent. The calculated flow curves form the basis for determining the dynamic recrystallization processes. From the flow stress maxima determined, the Zener–Hollomon parameter Z is established, considering the model coefficients A, α and n as well as the activation energy Q, using Equation (1) according to Sellars (1966) [28,29]:

$$Z = \dot{\varepsilon} \exp\left\{\frac{Q}{R \cdot T}\right\} = A[\sin(\alpha\sigma)]^n \quad (1)$$

where $\dot{\varepsilon}$ is the strain rate (s^{-1}), σ is the flow stress (MPa), A and α are material constants, n is the stress exponent, R is the universal gas constant (8.314 $J \cdot K^{-1}mol^{-1}$), and T is the absolute deformation temperature (K). Values for A, α and n for the as-cast and the TRC states can be found in Table 3. The parameters of the equation were determined using the

mean values from the increases in the graphs, which represented the linear relationship of the flow stress to the comparative strain rate and temperature.

Table 3. Model coefficients for determination of Z according to Equation (1).

Model Coefficient	As-Cast State	TRC State
A in s^{-1}	5.33817×10^{19}	2.61662×10^{19}
α in MPa^{-1}	0.010677	0.010849
n	6.6051	7.4871

The activation energy describes the difficulty of initiating deformation during hot working and is simultaneously affected by dynamic precipitation formation, pinning effects of dislocations, and the occurrence of secondary phases. The activation energy for dynamic recrystallization of LPSO containing magnesium alloys derived by different scientists is very different and varies between 182 kJ/mol and 276 kJ/mol, according to Gonzales et al. (2016) [30]. These values are significantly higher than the activation energy for self-diffusion in magnesium (135 kJ/mol [31]). Figure 7 shows the activation energies for various Mg alloys with LPSO phases. Only Mg-Y-Zn-Mn [8] and Mg-Gd-Zn [11] offer higher values with 393 kJ/mol and 289 kJ/mol, respectively. The activation energy for the Mg-6.8Y-2.5Zn-0.4Zr alloy investigated in this work is 279 kJ/mol for as-cast and 270 kJ/mol for the TRC conditions, and is thus in the upper range. Possible origins of the high Q-values for the Mg-Y-Zn alloys lie in the presence of the LPSO phase, which can occupy a proportion of up to 20% [4], depending on the alloy composition. The LPSO phases impede dislocation movement during deformation and cause self-diffusion within the crystal lattice to be suppressed. The influence of the proportion of alloying elements becomes clear when comparing the activation energy with twin-roll cast AZ31. Investigations by [32] show a value of Q = 178 kJ/mol.

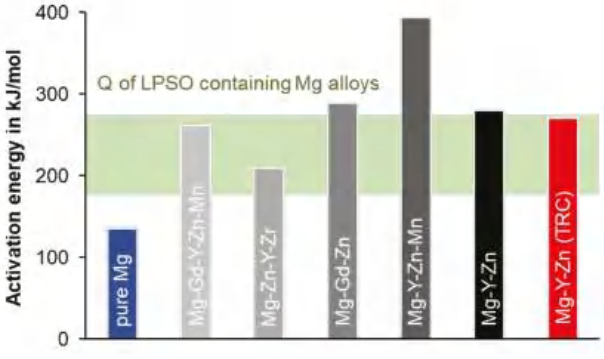

Figure 7. Activation energy Q of LPSO containing magnesium alloys compared to pure Mg [8,11,30,31,33,34].

3.2.3. Deformation and Recrystallization Behavior

The LPSO phases occur in different forms, block-like, connected to networks or isolated as well as in lamellar form. Due to their high thermal stability, a high density of LPSO phases remains in the microstructure even after hot deformation at temperatures between 350 °C and 500 °C. Figure 8 shows SEM images of the as-cast and the TRC condition after hot deformation, revealing differences in the nature of the LPSO phases that significantly affect recrystallization behavior. In the deformed sample after conventional casting (Figure 8a), the LPSO phases appear predominantly as coarse block-like structures that are interconnected in a network. These consecutive LPSO phases disrupt the boundary

migration of the DRX nuclei and have a hindering effect on the dynamic recrystallization. Simultaneously, lamellar LPSO phases occur within the magnesium matrix grains. As a result of hot deformation, the lamellae were kinked (Figure 9) and exhibit zigzag-like morphologies (Figure 10b,d). The initiation and arrangement of basal pairs of dislocations that align perpendicular to the slip plane are suggested to be the origin for the formation of kink boundaries [35]. The stacking sequence of the lamellar 14 H LPSO phase is suggested to restrict dynamic recrystallization and the occurrence of twinning within the matrix grains [36]. Therefore, in the as-cast state, fine DRXed grains are mainly formed at the initial grain boundaries as a result of continuous dynamic recrystallization (CDRX), and in the vicinity of the block-shaped LPSO phase via particle stimulated nucleation (PSN). However, PSN is less pronounced due to the suppressive effect caused by the nature of the blocky LPSO phases. Consequently, a bimodal microstructure consisting of coarse deformed original grains as well as fine dynamic recrystallized grains develops (Figure 10b,c). Contrary to the assumption of Hagihara et al. (2010) [36], twins can be observed within the magnesium matrix despite the presence of the lamellar LPSO phase (Figure 10a). These also serve as starting points for the dynamic recrystallization (TDRX, Figure 10c). Based on these results, DRX is assumed to be delayed and the main recrystallization mechanisms of the as-cast conditions are CDRX, PSN and TDRX. Kink-aided dynamic recrystallization (KDRX), like it was reported by Chen et al. (2020) [37] can hardly be detected. They showed that KDRX mainly occurs, where the LPSO phase is fairly fragmented. In this work, at low temperatures (350 °C) LPSO lamellae are kinked but not fragmented (Figure 9a). As can be seen from Figure 9a, kinking only takes place when lamellae are aligned parallel to compression direction. Fragmentation of lamellar LPSO phases can only be observed at temperatures above 450 °C (Figure 9b), and KDRX can be found. However, only a few grains exhibit lamellae in the compression direction and, at the same time, fragmentation of the lamellae, so the number of grains in which KDRX takes place is limited.

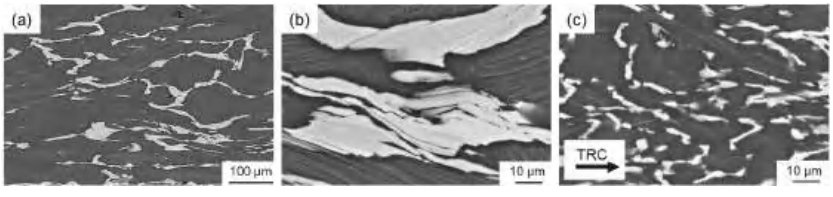

Figure 8. SEM images (15 kV, SE) of the deformed samples (**a**) as-cast condition, overview, (**b**) as-cast condition, detail and (**c**) TRC condition, detail.

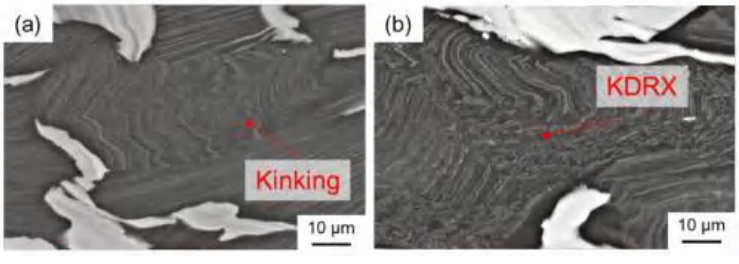

Figure 9. SEM images (20 kV, BSD) of deformed samples of the as-cast condition: (**a**) kinking at 350 °C and (**b**) kink-aided dynamic recrystallization at 450 °C.

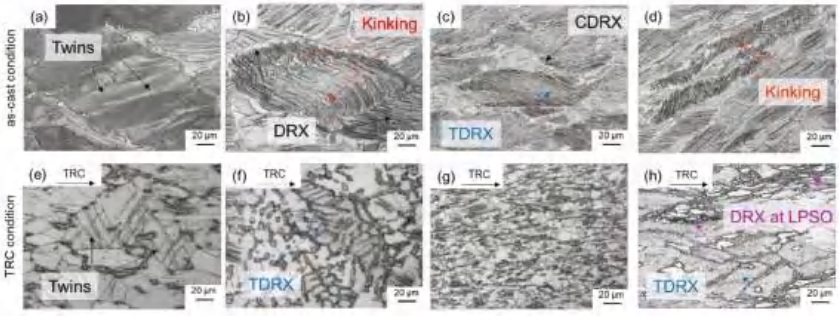

Figure 10. Optical micrographs of the deformed samples after conventional casting (**a**–**d**) and TRC (**e**–**h**) showing different deformation and recrystallization mechanisms.

In the TRC initial state, the block-like LPSO phase is more finely distributed and, above all, less strongly connected. The deformed specimen shows that the blocky LPSO phase is aligned in the flow direction of the material. At the same time, previous investigations [4] show that, depending on the deformation temperature, lamellar LPSO phases are precipitated within the Mg matrix during cooling from the heat treatment (Figure 11). It can be clearly seen that at 350 °C almost the entire Mg matrix is equipped with lamellae (Figure 11a), while at 450 °C only a few grains have lamellar LPSO phases (Figure 11b). This results in different recrystallization mechanisms depending on the deformation temperature.

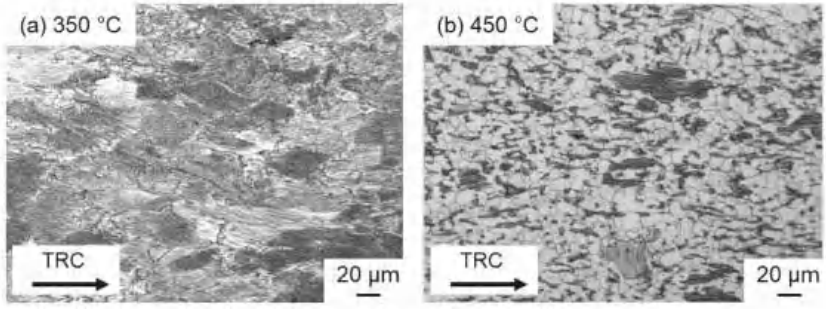

Figure 11. Optical micrographs of the deformed samples after twin-roll casting compressed at different temperatures (**a**) 350 °C and (**b**) 450 °C and a strain rate of 10 s^{-1}.

When deformation takes place at 350 °C, hardly any DRX occurs. However, it was also found in previous investigations [38] that twin and lamellar LPSO phases occur simultaneously. As the deformation temperature increases, the number of grains exhibiting lamellar LPSO phases decreases. Twins continue to occur (Figure 10e). Twin boundaries serve as starting points for dynamic recrystallization (TDRX) during hot deformation (Figure 10f,h). In the TRC initial state, DRX at the blocky LPSO phases plays a more important role. Their fine distribution and less network-like nature favor DRX by PSN (Figure 10h). Comparable results are also reported by Onorbe et al. (2012) [19]. Thus, a uniformly recrystallized microstructure can be achieved (Figure 10g). In deformed specimens exhibiting lamellar LPSO phases and kinking, DRX can be observed sporadically at the kink boundaries. Comparable to the studies of Chen et al. (2020) [37], KDRX occurs when the lamellae are fragmented (Figure 12a). However, this phenomenon occurs rather rarely. Figure 12b shows that LPSO lamellae without kinking have a rather unfavorable effect on the DRX. The grains with lamellae remain in the almost completely recrystallized microstructure.

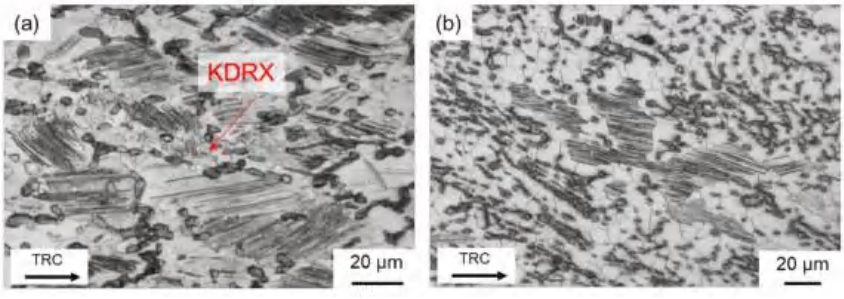

Figure 12. Optical micrographs of the deformed samples after twin-roll casting: (**a**) KDRX at fragmented lamellar LPSO phases and (**b**) grains with lamellar LPSO phases remain, while the surrounding microstructure is almost completely recrystallized.

3.2.4. Processing Maps

The DMM processing maps at a moderate strain of 0.4 are shown in Figure 13a for the as-cast, and in Figure 13b, for the TRC condition. Processing maps are based on an overlap of the power dissipation maps with the instability one according to [39]. The yellow regions possess high power dissipation efficiency of about 27% to 30% for the as-cast and 34% to 44% for the TRC condition. Both conditions offer a high efficiency at high strain rates (5 s^{-1}) in a temperature range of 400 °C to 440 °C for TRC condition, while for as-cast conditions higher temperatures of 450 °C to 470 °C are required for higher power dissipation efficiency. At higher temperatures (500 °C to 520 °C) moderate strain rates of 1 s^{-1} (TRC condition) and low strain rates of 0.1 s^{-1} to 0.01 s^{-1} (as-cast condition) are preferable for hot deformation. Under these conditions, dynamic recrystallisation is assumed to occur preferentially during hot deformation.

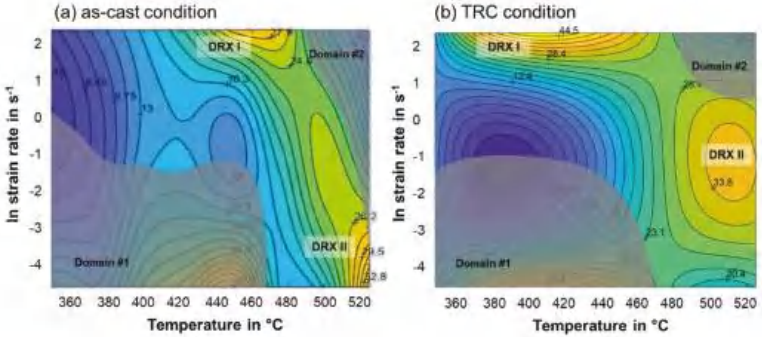

Figure 13. Processing maps of the (**a**) as-cast condition and (**b**) TRC condition in the temperature range from 350 °C to 525 °C at a strain of 0.4 [1,38].

Literature data on suitable hot deformation conditions for comparable alloys containing LPSO phases are presented in Figure 14. High efficiency regions are located at temperatures below 500 °C and strain rates lower than 1 s^{-1}. The conventionally cast and TRC Mg-6.8Y-2.5Zn-0.4Zr alloy both show flow instabilities in this parameter range. A second instability domain occurs at high temperatures (>500 °C). For the TRC condition unstable flow is restricted to high strain rates (10 s^{-1}), while it is broadened for the as-cast condition to lower strain rates (0.01 s^{-1}). In these zones, where the corresponding power dissipation coefficient is comparatively low, microcracks nucleate and propagate along the interface of the grain boundaries and the network-like LPSO phase. At low temperature and/or high strain rates, a large quantity of dislocations could pile-up at the interface of the magnesium matrix and the LPSO phase. The instability of adiabatic shear bands or

local plastic flow tends to occur rather than dynamic recrystallization. Consequently, these instabilities result in the formation of microcracks [1,38]. Optimum deformation conditions are temperatures from 500 °C to 520 °C at strain rates ranging from 0.01 s^{-1} to 0.1 s^{-1} for the as-cast material and a strain rate of 1 s^{-1} for the TRC material.

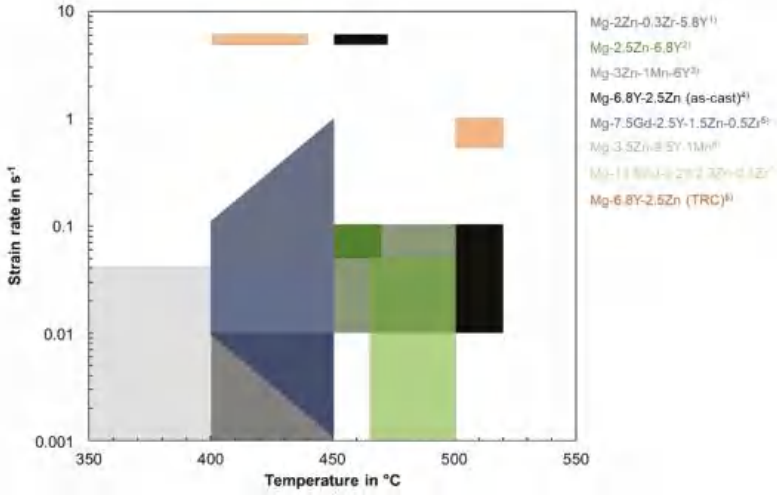

Figure 14. Process windows for several LPSO containing magnesium alloys based on processing maps: (1) [27] (2) [40] (3) [41] (4) [1] (5) [42] (6) [8] (7) [9] (8) [38].

4. Conclusions

This paper compares the hot deformation behavior of the Mg-6.8Y-2.5Zn-0.4Zr (WZ73) alloy in the as-cast and the twin-roll cast condition. The main findings can be summarized as follows:

- The microstructure of both conditions mainly consists of the α-magnesium matrix and network-like LPSO phases located along the grain boundaries. LPSO phases could be assigned to 18R or 14H structures. Twin-roll casting leads to a finer microstructure compared to conventional casting. After conventional casting, thin lamellar LPSO phases arise within the α-magnesium grains, which can be assigned to the 14H structure. In the TRC condition, lamellar LPSO phases are not observed.
- During hot deformation of the conventionally cast material, it is assumed that at 450 °C dynamic recovery is the dominant softening mechanism. Only a small amount of dynamic recrystallization can be observed, indicating that the DRX remains incomplete even at high strains and low strain rates. The TRC samples showed softening via dynamic recrystallization, where an almost completely recrystallized structure developed at both high (10 s^{-1}) and low (0.01 s^{-1}) strain rates.
- At higher temperatures (500 °C), DRX occurs in both conditions. The as-cast state exhibits a high amount of network-like and lamellar LPSO phases, which are assumed to be responsible for a delayed DRX. The main recrystallization mechanisms of the as-cast condition are CDRX, PSN and TDRX. Kink-aided dynamic recrystallization can hardly be detected. In the TRC initial state, the block-like LPSO phase is more finely distributed and, above all, less strongly connected. Lamellar LPSO phases are precipitated within the Mg matrix during cooling and different DRX mechanism take place depending on deformation temperature. The fine distribution of the LPSO phase and less network-like nature favor DRX by PSN. Besides this, TDRX and KDRX can be observed.

- Optimum deformation conditions are temperatures from 500 °C to 520 °C and strain rates ranging from 0.01 s^{-1} to 0.1 s^{-1} for the as-cast material as well as a strain rate of 1 s^{-1} for the TRC material.

Author Contributions: Conceptualization, K.K. and M.U.; methodology, M.U.; formal analysis, M.U.; investigation, K.K.; resources, U.P.; data curation, M.U.; writing—original draft preparation, K.K.; writing—review and editing, M.U.; visualization, U.P.; supervision, U.P.; project administration, U.P.; funding acquisition, M.U. and U.P. All authors have read and agreed to the published version of the manuscript.

Funding: The project "Saxon Alliance for Material- and Resource-Efficient Technologies (AMARETO)" is funded by the European Union (European Regional Development Fund) and by the Free State of Saxony. Grant Number: 100291457.

Institutional Review Board Statement: Not applicable.

Informed Consent Statement: Not applicable.

Acknowledgments: We thank Susanne Berndorf from the Institute of Metal Forming for microstructure characterization via SEM.

Conflicts of Interest: The authors declare no conflict of interest. The funders had no role in the design of the study; in the collection, analyses, or interpretation of data; in the writing of the manuscript, or in the decision to publish the results.

References

1. Ullmann, M.; Schmidtchen, M.; Kittner, K.; Henseler, T.; Kawalla, R.; Prahl, U. Hot Deformation Behaviour and Processing Maps of an as-Cast Mg-6.8Y-2.5Zn-0.4Zr Alloy. *Mater. Sci. Forum* **2019**, *949*, 57–65. [CrossRef]
2. Zhu, Y.; Morton, A.; Nie, J. The 18R and 14H long-period stacking ordered structures in Mg–Y–Zn alloys. *Acta Mater.* **2010**, *58*, 2936–2947. [CrossRef]
3. Kawamura, Y.; Hayashi, K.; Inoue, A.; Masumoto, T. Rapidly Solidified Powder Metallurgy Mg97Zn1Y2Alloys with Excellent Tensile Yield Strength above 600 MPa. *Mater. Trans.* **2001**, *42*, 1172–1176. [CrossRef]
4. Kittner, K.; Ullmann, M.; Arndt, F.; Kawalla, R.; Prahl, U. Microstructure and Texture Evolution during Twin-Roll Casting and Annealing of a Mg–6.8Y2.5Zn–0.4Zr Alloy (WZ73). *Crystals* **2020**, *10*, 513. [CrossRef]
5. Kittner, K.; Ullmann, M.; Arndt, F.; Berndorf, S.; Henseler, T.; Prahl, U. Analysis of defects in a twin roll cast Mg-Y-Zn magnesium alloy. *Eng. Rep.* **2021**, *17*, e12394. [CrossRef]
6. Liu, H.; Yan, K.; Yan, J.-L.; Xue, F.; Sun, J.-P.; Jiang, J.-H.; Ma, A.-B. Precipitation behavior of 14H LPSO structure in single 18R phase Mg–Y–Zn alloy during annealing at 773 K. *Trans. Nonferrous Met. Soc. China* **2017**, *27*, 63–72. [CrossRef]
7. Zhu, Y.; Morton, A.; Nie, J. Growth and transformation mechanisms of 18R and 14H in Mg–Y–Zn alloys. *Acta Mater.* **2012**, *60*, 6562–6572. [CrossRef]
8. Li, L.; Qi, F.; Wang, Q.; Hou, C.; Zhao, N.; Yang, Y.; Chai, S.; Ouyang, X. Hot deformation behavior of Mg95.21Zn1.44Y2.86Mn0.49 alloy containing LPSO phase. *Mater. Charact.* **2020**, *169*, 110649. [CrossRef]
9. Zhang, Z.; Yan, Z.; Du, Y.; Zhang, G.; Zhu, J.; Ren, L.; Wang, Y. Hot Deformation Behavior of Homogenized Mg-13.5Gd-3.2Y-2.3Zn-0.5Zr Alloy via Hot Compression Tests. *Materials* **2018**, *11*, 2282. [CrossRef]
10. Fekete, K.H.; Drozdenko, D.; Čapek, J.; Máthis, K.; Tolnai, D.; Stark, A.; Garcés, G.; Dobron, P. Hot deformation of Mg-Y-Zn alloy with a low content of the LPSO phase studied by in-situ synchrotron radiation diffraction. *J. Magnes. Alloy.* **2020**, *8*, 199–209. [CrossRef]
11. Li, K.; Chen, Z.; Chen, T.; Shao, J.; Wang, R.; Liu, C. Hot deformation and dynamic recrystallization behaviors of Mg-Gd-Zn alloy with LPSO phases. *J. Alloy. Compd.* **2019**, *792*, 894–906. [CrossRef]
12. Li, Y.; Xiao, W.; Wang, F.; Hu, T.; Ma, C. The roles of long period stacking ordered structure and Zn solute in the hot deformation behavior of Mg-Gd-Zn alloys. *J. Alloy. Compd.* **2018**, *745*, 33–43. [CrossRef]
13. Shao, X.; Jin, Q.; Zhou, Y.; Yang, H.; Zheng, S.; Zhang, B.; Chen, Q.; Ma, X. Basal shearing of twinned stacking faults and its effect on mechanical properties in an Mg–Zn–Y alloy with LPSO phase. *Mater. Sci. Eng. A* **2020**, *779*, 139109. [CrossRef]

14. Allen, R.V.; East, D.; Johnson, T.J.; Borbidge, W.E.; Liang, D. Magnesium Alloy Sheet Produced by Twin Roll Casting. *Magnes. Technol.* **2001**, *2013*, 74–79.
15. Kawalla, R.; Ullmann, M.; Schmidt, C.; Dembińska, J.; Vogt, H.P. Properties of Magnesium Strips Produced by Twin-Roll-Casting and Hot Rolling. *Mater. Sci. Forum* **2011**, *690*, 21–24. [CrossRef]
16. Siebel, E. *Die Formgebung im Bildsamen Zustande, Theoretische Grundlagen der Technischen Formgebungsverfahren*; Verlag Stahleisen: Düsseldorf, Germany, 1932.
17. Kittner, K.; Ullmann, M.; Henseler, T.; Kawalla, R.; Prahl, U. Microstructure and Hot Deformation Behavior of Twin Roll Cast Mg-2Zn-1Al-0.3Ca Alloy. *Materials* **2019**, *12*, 1020. [CrossRef]
18. Luo, Z.P.; Zhang, S.Q. High-resolution electron microscopy on the X-Mg12ZnY phase in a high strength Mg-Zn-Zr-Y magnesium alloy. *J. Mater. Sci. Lett.* **2000**, *19*, 813–815. [CrossRef]
19. Oñorbe, E.; Garces, G.; Pérez, P.; Adeva, P. Effect of the LPSO volume fraction on the microstructure and mechanical properties of Mg–Y2X –Zn X alloys. *J. Mater. Sci.* **2012**, *47*, 1085–1093. [CrossRef]
20. Wen, K.; Du, W.-B.; Liu, K.; Wang, Z.-H.; Li, S.-B. Precipitation behavior of 14H-LPSO structure in Mg–12Gd–2Er–1Zn–0.6Zr Alloy. *Rare Met.* **2016**, *35*, 367–373. [CrossRef]
21. Wang, L.; Jiang, J.; Liu, H.; Saleh, B.; Ma, A. Microstructure characterization and corrosion behavior of Mg–Y–Zn alloys with different long period stacking ordered structures. *J. Magnes. Alloy.* **2020**, *8*, 1208–1220. [CrossRef]
22. Shi, B.-Q.; Chen, R.-S.; Ke, W. Effects of processing route on texture and mechanical properties of WZ62 alloy. *Trans. Nonferr. Met. Soc. China* **2011**, *21*, 830–835. [CrossRef]
23. Suzawa, K.; Inoue, S.-I.; Nishimoto, S.; Fuchigami, S.; Yamasaki, M.; Kawamura, Y.; Yoshida, K.; Kawabe, N. High-strain-rate superplasticity and tensile behavior of fine-grained Mg97Zn1Y2 alloys fabricated by chip/ribbon-consolidation. *Mater. Sci. Eng. A* **2019**, *764*, 138179. [CrossRef]
24. Zhang, J.; Chen, C.; Que, Z.; Cheng, W.; Xu, J.; Kang, J. 18R and 14H long-period stacking ordered structures in the Mg93.96Zn2Y4Sr0.04 alloy and the modification effect of Sr on X-phase. *Mater. Sci. Eng. A* **2012**, *552*, 81–88. [CrossRef]
25. Wu, Y.; Zeng, X.; Lin, D.; Peng, L.; Ding, W. The microstructure evolution with lamellar 14H-type LPSO structure in an Mg96.5Gd2.5Zn1 alloy during solid solution heat treatment at 773K. *J. Alloy. Compd.* **2009**, *477*, 193–197. [CrossRef]
26. Trojanova, Z.; Lukac, P. Hardening and Softening in Magnesium Alloys. In *Magnesium Alloys—Design, Processing and Properties*; Czerwinski, F., Ed.; InTech: Rijeka, Croatia, 2011.
27. Lv, B.-J.; Peng, J.; Zhu, L.-L.; Wang, Y.-J.; Tang, A.-T. The effect of 14H LPSO phase on dynamic recrystallization behavior and hot workability of Mg–2.0Zn–0.3Zr–5.8Y alloy. *Mater. Sci. Eng. A* **2014**, *599*, 150–159. [CrossRef]
28. Garofalo, F. *Fundamentals of Creep and Creep-Rupture in Metals*; McMillan Series in Materials Science: New York, NY, USA, 1965; p. 258.
29. Weertman, J. Dislocation climb theory of steady-state creep. *ASM Trans. Quart. Metal Sci.* **1968**, *61*, 681–694. [CrossRef]
30. González, S.; Pérez, P.; Garcés, G.; Adeva, P. Influence of the processing route on the mechanical properties at high temperatures of Mg-Ni-Y-RE alloys containing LPSO-phases. *Mater. Sci. Eng. A* **2016**, *673*, 266–279. [CrossRef]
31. Vagarali, S.S.; Langdon, T.G. Deformation mechanims in H.C.P. metals at eleveted temperatures—II. Creep behavior of a Mg-0.8%Al solid solution alloy. *Acta Metall.* **1982**, *30*, 1157–1170. [CrossRef]
32. Ullmann, M. Rekristallisationsverhalten von Geglühtem AZ31-Gießwalzband Beim Warmwalzen. Ph.D. Thesis, Technische Universität Bergakademie Freiberg, Freiberg, Germany, 2014.
33. Jingfeng, W.; Feizhou, X.; Shijie, L.; Song, H.; Fusheng, P. Hot Deformation Behavior and Processing Maps of As-Homogenized Mg-Gd-Y-Zn-Mn Alloy. *Rare Met. Mater. Eng.* **2018**, *47*, 1700–1707. [CrossRef]
34. Chen, Q.; Xia, X.; Yuan, B.; Shu, D.; Zhao, Z.; Han, J. Hot workfability behavior of as-cast Mg–Zn–Y–Zr alloy. *Mater. Sci. Eng. A* **2014**, *593*, 38–47. [CrossRef]
35. Hagihara, K.; Okamoto, T.; Izuno, H.; Yamasaki, M.; Matsushita, M.; Nakano, T.; Kawamura, Y. Plastic deformation behavior of 10H-type synchronized LPSO phase in a Mg–Zn–Y system. *Acta Mater.* **2016**, *109*, 90–102. [CrossRef]
36. Hagihara, K.; Yokotani, N.; Umakoshi, Y. Plastic deformation behavior of Mg12YZn with 18R long-period stacking ordered structure. *Intermetallics* **2010**, *18*, 267–276. [CrossRef]
37. Chen, T.; Chen, Z.; Shao, J.; Wang, R.; Mao, L.; Liu, C. The role of long period stacking ordered phase in dynamic recrystallization of a Mg–Zn–Y alloy during hot compression. *J. Alloy. Compd.* **2020**, *818*, 152814. [CrossRef]
38. Ullmann, M.; Kittner, K.; Prahl, U. Hot Deformation and Dynamic Recrystallisation Behaviour of Twin-Roll Cast Mg-6.8Y-2.5Zn-0.4Zr Magnesium Alloy. *Materials* **2021**, *14*, 307. [CrossRef]
39. Prasad, Y.; Rao, K. Processing maps for hot deformation of rolled AZ31 magnesium alloy plate: Anisotropy of hot workability. *Mater. Sci. Eng. A* **2008**, *487*, 316–327. [CrossRef]
40. Zhou, X.; Yao, Y.; Zhang, J.; Lu, X.; Xu, K.; Liu, H.; Wu, Z. Improved workability for Mg-Y-Zn alloys via increased volume fraction of block LPSO phases. *Mater. Sci. Eng. A* **2020**, *794*, 139934. [CrossRef]
41. Tahreen, N.; Zhang, D.; Pan, F.; Jiang, X.; Li, D.; Chen, D. Strengthening mechanisms in magnesium alloys containing ternary I, W and LPSO phases. *J. Mater. Sci. Technol.* **2018**, *34*, 1110–1118. [CrossRef]
42. Xue, Z.; Luo, W.; Zhao, Z.; Ren, Y. Thermal compression, processing maps and microstructural evolution of as-cast Mg-Gd-Y-Zn-Zr alloy with long period stacking ordered phase. *Mater. Res. Express* **2020**, *7*, 056512. [CrossRef]

materials

MDPI

Article

Deformation Characteristics and Constitutive Equations for the Semi-Solid Isothermal Compression of Cold Radial Forged 6063 Aluminium Alloy

Yongfei Wang [1,2], Shengdun Zhao [1], Yi Guo [3,*], Kuanxin Liu [4] and Shunqi Zheng [4]

[1] School of Mechanical Engineering, Xi'an Jiaotong University, Xi'an 710049, China; wangyongfei324@mail.xjtu.edu.cn (Y.W.); sdzhao@mail.xjtu.edu.cn (S.Z.)
[2] State Key Laboratory of Materials Processing and Die & Mould Technology, Huazhong University of Science and Technology, Wuhan 430074, China
[3] School of Energy and Power Engineering, Xi'an Jiaotong University, Xi'an 710049, China
[4] Ningbo Branch of China Ordance Academy, Ningbo 315103, China; liukuanxin@cmari.com (K.L.); 2010010024@mail.hfut.edu.cn (S.Z.)
* Correspondence: yiguo666@mail.xjtu.edu.cn; Tel.: +86-13201848800

Abstract: Al-Mg-Si based alloys are popular alloys used in the automotive industry. However, limited studies have been performed to investigate the microstructure, deformation characteristics, and deformation mechanism for the semi-solid 6063 alloys. In this study, the cold radial forging method and semi-solid isothermal treatment (SSIT) are proposed in the semi-solid isothermal compression (SSIC) process to fabricate high-quality semi-solid 6063 billets. The effects of deformation temperature, strain rate, and strain on the microstructure, deformation characteristics, and deformation mechanism of the SSIC of cold radial forged 6063 alloys were investigated experimentally. Constitutive equations were established based on the measured data in experiments to predict the flow stress. Results show that an average grain size in the range from 59.22 to 73.02 μm and an average shape factor in the range from 071 to 078 can be obtained in the microstructure after the cold radial forged 6063 alloys were treated with SSIT process. Four stages (i.e., sharp increase, decrease, steady state, and slow increase) were observed in the true stress- true strain curve. The correlation coefficient of the constitutive equation was obtained as 0.9796 while the average relative error was 5.01%. The deformation mechanism for SSIC of cold radial forged aluminum alloy 6063 mainly included four modes: The liquid phase flow, grain slide or grain rotation along with the liquid film, slide among solid grains, and the plastic deformation of solid grains.

Keywords: semi-solid isothermal compression; aluminum alloy; microstructure; deformation characteristics; deformation mechanism; constitutive equations

Citation: Wang, Y.; Zhao, S.; Guo, Y.; Liu, K.; Zheng, S. Deformation Characteristics and Constitutive Equations for the Semi-Solid Isothermal Compression of Cold Radial Forged 6063 Aluminium Alloy. *Materials* **2021**, *14*, 194. https://doi.org/10.3390/ma14010194

Received: 30 November 2020
Accepted: 29 December 2020
Published: 3 January 2021

1. Introduction

Al-Mg-Si based aluminium alloys are popular materials applied in various engineering applications due to their outstanding physical properties, which are usually used to fabricate products via hot forging and machining processes. However, some drawbacks are observed during the hot forging manufacturing process, which includes low efficiency, high production cost, and low material usage coefficient [1–3]. The high-pressure die casting process has also been applied for the fabrication of aluminium alloy components, but the turbulent flow in this process causes the gas and shrinkage porosity [4], due to the high filling rate [5].

These disadvantages including low efficiency, high production cost, and low material usage coefficient, gas and shrinkage porosity, can be effectively eliminated by the semi-solid metal forming (SSMF) process, which integrates the easy fluidity of liquid casting process and the high mechanical properties of solid-state plastic forming and is considered one of the most promising metal processing technologies in the 21st century [6–8]. In the SSMF

process, the semi-solid billet, which has small- and near-spherical microstructures, is used to fabricate high-quality components with a dense internal structure, accurate size, few macro defects, and few micro defects [9].

In the SSMF process, the deformation characteristics and mechanism of the semi-solid billets are vital for the prediction of the flow stress, based on the temperature, material structure, and strain rate, through which the optimisation of the process parameters can be achieved [10,11]. Therefore, a lot of research has been performed to study the deformation characteristics and mechanisms in recent decades of various aluminium alloys [11–16]. Xu et al. [7] investigated the compression behaviour of the semi-solid AZ91D magnesium alloy. The semi-solid billets were prepared by the strain-induced melt activation (SIMA) process for the isothermal compression test by employing the repetitive upsetting-extrusion (RUE) method. Three stages were observed in experiments in the compression process. The predominant mechanism in each of these three stages was identified through the microstructure analysis. Chen et al. [11] discussed the deformation characteristics of the extruded 7075 aluminum alloy processed in the temperature range from 350 to 600 °C. It was found that the constitutive characteristics in the studied temperature range up the semi-solid temperature could be classified as plastic (350 to 490 °C) and thixotropic (above 490 °C) deformations. Binesh and Aghaie-Khafri [12] reported the mechanical properties of the 7075 aluminum alloy processed by the semi-solid SIMA. The semi-solid billet was prepared by applying the compression at ambient temperature and then at 600–620 °C (semi-solid temperature) for 5–10 min. It was revealed that the sample processed by SIMA at 600 °C for 10 min exhibited the largest values of both peak and steady-state stresses during the compression test. Wang et al. [13] studied the deformation characteristic of semi-solid ZCuSn10 copper alloy during the isothermal compression. The semi-solid billet used in this work was fabricated by the SIMA method including the rolling and remelting process. It was concluded that the resistance to deformation for the ZCuSn10 alloy under the semi-solid condition decreased with the increase in the process temperature. These studies indicate that the deformation characteristics of semi-solid materials are of importance for optimizing the semi-solid isothermal compression (SSIC) process.

The preparation of the semisolid billet is an indispensable step for the SSIC process. The SIMA, as one of the most popularly studied process methods for the preparation of the billet with fine and spheroidal solid particles, includes two stages namely the plastic deformation and the semi-solid isothermal treatment (SSIT). In the SIMA process, plastic deformation is the most critical stage as it significantly influences the grain size and grain distribution uniformity in the microstructure of the semi-solid alloy. Therefore, different deformation methods applied in the SIMA process, such as compression [12,17], rolling [13], repetitive upsetting-extrusion [18], equal channel angular extrusion [19,20], has attracted the attention of researchers in recent decades. Compared to the traditional deformation methods used in the SIMA process, several benefits to the industrial application can be obtained by adopting the cold radial forging technique in the SIMA process, such as large semi-solid billet, high level of automation, and easy operation [21–23].

However, to the best knowledge of the authors, the aluminium alloy directly treated by cold radial forging in the SSIC process has not been reported. Moreover, little research has been performed on the microstructure, deformation characteristics, and deformation mechanism for the semi-solid 6063 alloys. In this study, the cold radial forging method is proposed in the SIMA process for the preparation of high-quality semi-solid 6063 billets for the SSIC process. The effects of deformation temperature (i.e., isothermal temperature), strain rate, and strain on the microstructure, deformation characteristics, and deformation mechanism of the cold radial forged 6063 alloys were investigated experimentally. Furthermore, the constitutive equation of the semi-solid 6063 alloys was established based on the experimental results to predict the flow stress based on the effective liquid phase fraction, the deformation temperature, strain rate, and strain.

2. Materials and Experimental Procedure

The chemical composition of 6063 aluminium alloy investigated in this study is summarized in Table 1. The solidus and liquidus temperatures of this alloy were identified by the heat flow-temperature curve, which was obtained by using an 'STA 449F5' differential scanning calorimeter (DSC) (Netzsch, Selb, Germany). The samples with the dimension of 6 mm × 6 mm × 5 mm were heated from room temperature to 750 °C at 10 °C/min under a nitrogen atmosphere and analyzed by DSC. The results show that the solidus and liquidus temperatures of this alloy are 615 °C, and 655 °C, respectively. The largest weight proportion of the chemical composition is Mg, which accounts for 0.51% and is followed by Si and Mn. Ti and Cr are less than 0.001%, and 0.005% in weight percentage, respectively.

Table 1. Chemical composition of the 6063 aluminium alloy (wt.%).

Mg	Si	Mn	Zn	Fe	Cu	Ti	Cr	Al
0.51	0.39	0.03	0.02	0.15	0.01	<0.001	<0.005	Bal.

The SSIC process of the cold radial forged 6063 aluminium alloy in this paper mainly includes three stages as shown in Figure 1. Stage I: The barstock of 6063 alloys with a diameter of 100 mm was deformed by the cold radial forging process until the reduction in the area reached 64% (i.e., ϕ60 mm). The reduction in the area is calculated by the ratio of (A0–A1) to A0, where A0 and A1 are the cross-sectional area of the initial alloy, and the deformed alloy, respectively. Then, the action of sampling was finished from the cold radial forged alloy along the direction of radial forging, which had the diameter and height of 10 mm and 15 mm, respectively. Stage II: The SSIC process including SSIT and the deformation of isothermal compression were carried out with the SSIC- equipment which mainly included the top pressing head, bottom pressing head, insulation material, resistance furnace, and thermocouples. During the SSIC process, the resistance furnace was heated up to the setting deformation temperature, and then the cold radial forged sample was placed between the top and bottom pressing head for SSIT. The semi-solid samples can be obtained when the SSIT process had been executed for 10 min at different isothermal temperatures. After that, these samples were compressed with the true strain of 0.7 to obtain the compressed semi-solid sample by the top and bottom pressing head at different deformation temperatures and different strain rates. For all the experiments, the deformation temperature was selected the same as the isothermal temperature in SSIT. Stage III: The compressed semi-solid sample was cooled rapidly by water quenching for preserving the microstructures of the sample.

In this paper, there was a total of 12 semi-solid isothermal compression experiments performed to examine the effects of the operating parameters on the microstructure, deformation characteristics, and the deformation mechanism of the cold radial forged 6063 aluminum alloy. The details of the experiments are summarized in Table 2. The operating parameters studied in this paper contained the isothermal temperature, the strain rate, and the strain in Stage II. The isothermal holding time in all experiments was set as 10 min. In Experiments 1–3, the isothermal temperatures varied from 625 to 635 °C with no deformation supplied. The strains in Experiments 4–12 were all set as 0.7. In Experiments 4–6, the isothermal temperatures were all selected as 625 °C at the strain rate of 0.01, 0.1, and 1 s^{-1}, respectively. Similarly, in Experiments 7–9 and Experiments 10–12, the isothermal temperatures were the same in each group with the strain rate varying from 0.01 to 1 s^{-1}.

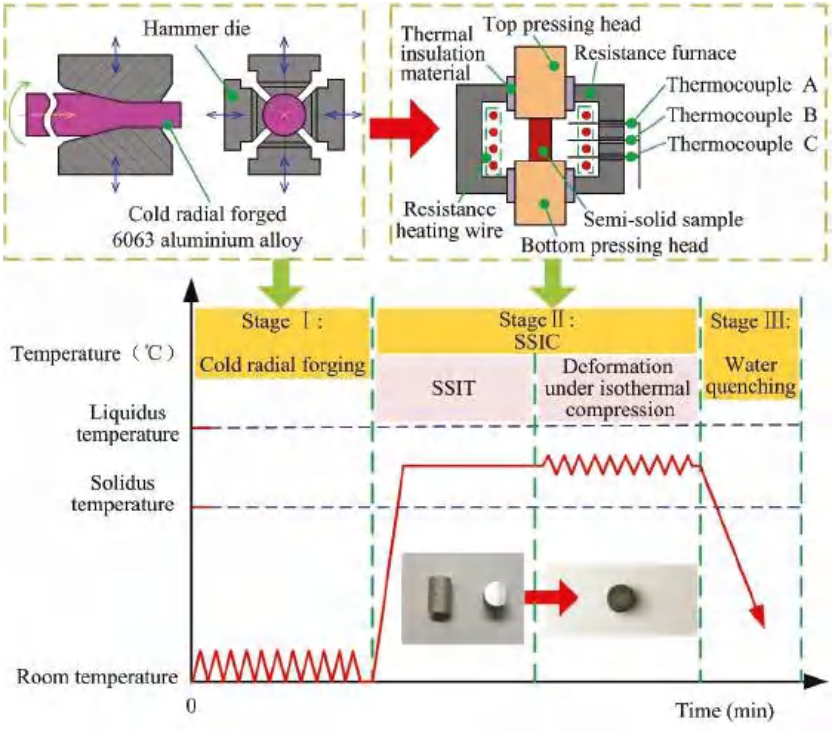

Figure 1. Schematic illustration of the SSIC process of the cold radial forged 6063 aluminium alloy.

Table 2. Experimental process parameters.

Experimental Number	Isothermal Temperature (°C)	Strain Rate (s^{-1})	Strain	Isothermal Holding Time (min)
1	625	0	0	10
2	630	0	0	10
3	635	0	0	10
4	625	0.01	0.7	10
5	625	0.1	0.7	10
6	625	1	0.7	10
7	630	0.01	0.7	10
8	630	0.1	0.7	10
9	630	1	0.7	10
10	635	0.01	0.7	10
11	635	0.1	0.7	10
12	635	1	0.7	10

During the semi-solid isothermal compression experiments, the true stress and true strain are determined in-situ by the SSIC-equipment (Xi'an Jiaotong University, Xi'an, China). Samples were taken along the axial direction, first ground through the sandpapers with the grits of 200, 400, 600, 800, 1000, 1200, and 1500 in sequence and then polished through the diamond paste with the particle size of 0.1 μm. Samples were etched in the aqueous HF solution with a concentration of 5% for about 90 s at room temperature. Finally, the observation of sample microstructure was carried out by optical microscope (NIKON ECLIPSE LV 150N, Nikoon, Tokyo, Japan). The average grain size (D) of solid grains can be calculated by Equation (1) while the shape factor (F) can be obtained by Equation (2) based on the number, area, and perimeter of solid grains, which were measured and calculated

by the Image-Pro Plus 6.0 software (Media Cybernetics, Rockville, MD, USA) [24–27]. The effective liquid phase fraction in semi-solid samples f_{EL} was calculated by Equation (3) [27],

$$D = \frac{\sum_{N=1}^{N} \sqrt{4A/\pi}}{N} \quad (1)$$

$$F = \frac{\sum_{N=1}^{N} 4\pi A/P^2}{N} \quad (2)$$

$$f_{EL} = \frac{A_L}{A_L + A_S} \quad (3)$$

where A, N, P are the area, number, perimeter of solid grains, respectively; A_L and A_S are the area of the liquid phase, and the area of the solid phase, respectively.

3. Results and Discussion

3.1. Effects of SSIT on the Microstructure

The microstructures of the radially forged 6063 aluminum alloy without and with SSIT are shown in Figure 2. It can be seen from Figure 2a that an obvious texture can be observed in the microstructure. The grains were elongated along the radial forging direction. Figure 2b–d show the semi-solid microstructures obtained after the radial forged alloy processed by SSIT at the isothermal temperature of 625 °C, 630 °C, and 635 °C for 10 min, respectively. Under the isothermal temperature condition of 625 °C, the semi-solid material of 6063 aluminum alloy was prepared with the fine, nearly spheroidized, uniform solid grains, but the liquid film between the solid grains in the microstructure was relatively thin, which can be seen in Figure 2b. Comparing Figure 2c,d, the solid grains gradually grew and nearly spheroidized, and a thicker liquid film was observed separating these solid grains as the isothermal temperature increased from 630 to 635 °C.

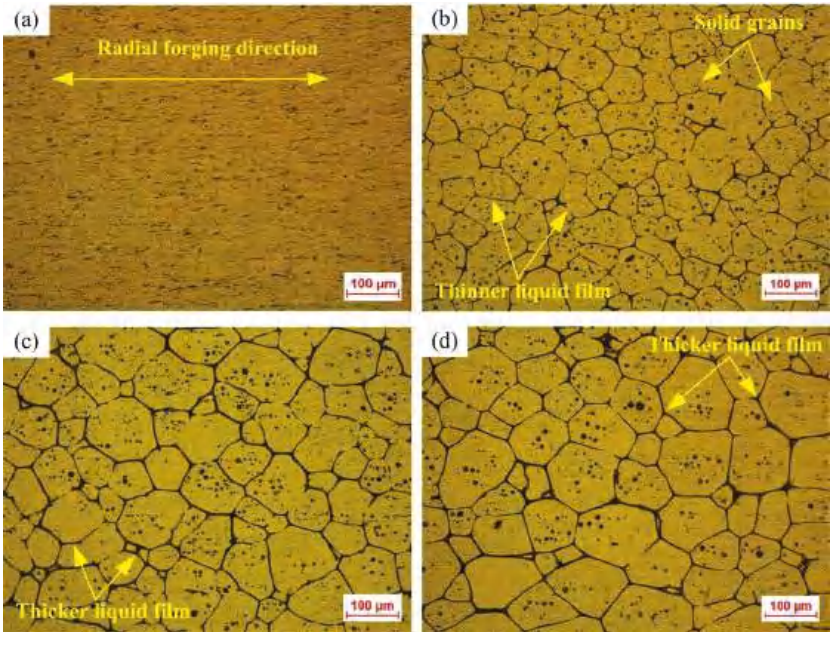

Figure 2. Microstructure of; (**a**) the cold radial forged 6063 aluminium alloy without SSIT, and semi-solid 6063 aluminium alloy after SSIT with the isothermal temperatures of; (**b**) 625 °C, (**c**) 630 °C, and (**d**) 635 °C.

The characteristics of the microstructure can be obtained by the quantitative analysis of samples processed at different isothermal temperatures, which includes the average grain size, the shape factor of solid grains, and the effective liquid fraction. As shown in Table 3, it was found that the average grain size, shape factor, and effective liquid fraction of solid grains increased with the enlargement in the isothermal temperature. During the SSIT process, the protruding edges and corners of solid grains will dissolve and subsequently precipitate at the sunken regions due to the difference in curvatures of different parts of the single solid grain [21]. Therefore, the shape factor further improves when the isothermal temperature increases from 630 °C to 635 °C. The largest average grain size and the smallest average shape factor were found as 73.02 μm and 0.71 μm, respectively. The maximum and minimum effective liquid fractions were obtained as 11.10%, and 14.42%, respectively. This means that the semi-solid material obtained from the radial forged 6063 aluminium alloy applied in this study after the SSIT is qualified for the semi-solid forming as the semi-solid materials with microstructure characteristics with the average grain size blow 100 μm and a shape factor above 0.6 is suitable for the semi-solid forming [28,29].

Table 3. Microstructural characteristics of 6063 alloy microstructure processed by SSIT at different isothermal temperatures.

Isothermal Temperature (°C)	Average Grain Size (μm)	Average Shape Factor	Effective Iiquid Fraction
625	59.22	0.71	11.10%
630	64.11	0.75	13.29%
635	73.02	0.78	14.42%

3.2. True Stress-True Strain Curves and the Deformation Pattern

The true stress-true strain curves of the radial wrought aluminium alloy 6063 during the semi-solid isothermal compression deformation procedure at different isothermal temperatures (i.e., deformation temperatures) are shown in Figure 3. It was revealed that at the same value of true strain, the true stress reduced when the deformation temperature increased. This was because different solid-phase fractions were obtained at different deformation temperatures. At the relatively low deformation temperature, the solid fraction in the sample was high, and the solid grains in the microstructure contacted each other to form a spatial framework structure. This framework structure hindered the slip and rotation of the solid grains. Therefore, the deformation of the sample mainly included the deformation of the spatial framework structure and the squeeze flow of the liquid phase. However, when the deformation temperature increased, the solid phase fraction in the sample decreased with the liquid phase continually surrounding the solid grains, which provided the beneficial condition to the slip and rotation of the solid phase grains. Therefore, the true stress required for the deformation was reduced. Moreover, the true strain required for the stabilization of the true stress was relatively low at a high deformation temperature and a certain strain rate. This was because there were more solid grain agglomerates in the sample when the deformation temperature was relatively low, which required a great amount of deformation to disaggregate these agglomerates. On the contrary, when the deformation temperature was relatively high, fewer agglomerates of the larger solid grains were generated in the sample, which was helpful for the completion of the disaggregation without the disaggregation process of the agglomerates or with only a small amount of deformation to achieve the stabilization of the true stress [30].

It can be concluded from Figure 3a–c that as the true strain increased, the true stress first increased rapidly, then decreased and stabilized, and finally increased slowly. This means that four stages can be observed in the variation of true stress when the true strain increases as shown in Figure 4, which are sharp increase (Stage I), decrease (Stage II), steady state (Stage III), and slow increase (Stage IV).

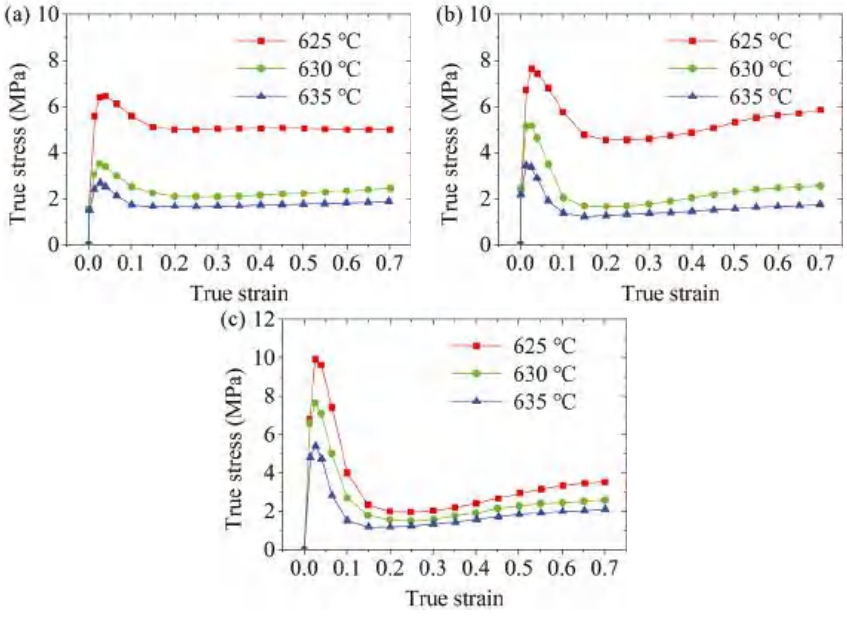

Figure 3. Ture stress-true strain curves of the cold radial forged 6063 aluminium alloy processed by the semi-solid isothermal compression at different temperatures with strain rates of (**a**) 0.01 s^{-1}, (**b**) 0.1 s^{-1}, and (**c**) 1 s^{-1}.

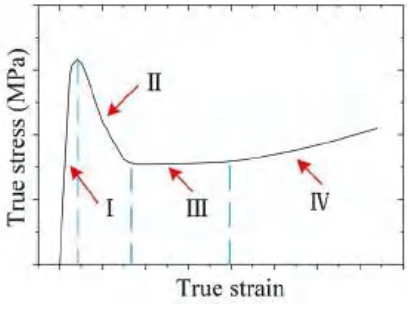

Figure 4. The deformation pattern of the cold radial forged 6063 aluminium alloy processed by SSIC.

Stage I: Sharp increase. Semi-solid materials can be regarded as the material with solid grains suspended in the liquid phase, where the solid phase grains or solid-phase grain aggregates contact locally to form a spatial framework structure when the solid phase ratio is large [7,10,30]. At the beginning of the SSIC, the central isostatic stress of the cylindrical compression sample is large, which will force the liquid phase to be squeezed and flowed from the central area to the peripheral area. However, the spatial framework structure, formed by the solid grains, would not be destroyed owing to the small deformation degree, and the deformation of the sample can be recovered if the load is removed. Therefore, the elastic deformation of the spatial framework structure takes place in the sample, namely, the true stress is increased when the true train increased.

Stage II: Decrease. As the SSIC continues, when the space framework structure reaches a certain degree of deformation, its deformation cannot be restored even if the load is removed. In other words, plastic deformation is achieved in the sample. At this stage, the spatial framework structure begins to be destroyed and is gradually and completely

surrounded by the liquid phase when the deformation degree increased. The slip and partial rotation of the solid grains then occur at this time. The slip among the solid grains is realized by the shearing force, which promotes the occurrence of holes at the boundary of the grains. These holes would expand rapidly along with the liquid phase, resulting in the damage of samples. This sample damage causes the flow stress to drop rapidly, that is, the true stress drops.

Furthermore, the plastic deformation will also promote the disaggregation of larger solid grain agglomerates, so that the liquid phase wrapped by the agglomerates is released, thereby increasing the liquid content inside the sample. This is helpful for the slippage and rotation of the solid grains, thereby contributing to the reduction of true stress.

Stage III: Steady state. At this stage, the spatial framework structure formed by the solid grains is basically destroyed. The solid particles in the semi-solid material are surrounded by the liquid phase and undergo plastic flow. The deformation resistance is mainly attributed to the slippage and rotation among the solid grains as well as the liquid phase flow. Therefore, the deformation resistance remains basically unchanged, that is, the true stress is at a steady state as the displacement increases.

Stage IV: Slow increase. The main reason for the increase in true stress at this stage is that the true strain is too large, which causes the semi-solid material to roll over during the SSIC process, gradually increasing the contact surface between the pressing head and the sample. This in turn increases the friction between the pressing head and the sample. Furthermore, during the SSIC process of the sample, as the true strain increases, most of the liquid is separated from the solid phases inside the sample and squeezed to the edge of the sample, resulting in an increase in the local solid fraction of the sample. This consequently causes the solid grains to be squeezed and bonded together and therefore generates the plastic deformation [12]. The pressure required to deform the solid grains is greater than the liquid phase flow, thus, it causes the augmentation in the true stress, that is, the true stress gradually enlarges when the true strain is elevated.

The effects of the deformation temperature on the peak stress and steady-state stress are shown in Figure 5. It can be seen that both the peak and steady-state stresses of the aluminum alloy 6063 semi-solid material significantly reduced when the deformation temperature increased at a certain strain rate. This phenomenon indicated that the SSIC of aluminium alloy 6063 was sensitive to the temperature, which is also found by reference [31]. This was because, in the initial stage of SSIC, the liquid fraction in the sample augmented with the increase in the deformation temperature, which increased the thickness of the liquid phase film between the solid grains and reduced the apparent viscosity. This resulted in reduction decrease in the connection strength between the solid grain aggregates. The spatial framework structure can be more easily destroyed, so the peak stress decreased. When it entered the steady state stage, more liquid phase helped the slippage and rotation among the solid grains easier to occur due to the high deformation temperature, leading to a reduction in the steady-state stress. Moreover, the aluminium alloy 6063 semi-solid material was more sensitive to the deformation temperature at the initial stage of SSIC. This was mainly because the peak stress reduced significantly with the elevation in the deformation temperature under different conditions of strain rate. But when the semi-solid 6063 alloys entered the steady-state flow, the steady-state stress tended to stabilize with the enlargement in the deformation temperature when the strain rate increased, which means that the steady-state stress was less sensitive to the deformation temperature under this condition.

The effects of the strain rate on the peak and steady-state stresses of the semi-solid isothermal compression curve of aluminum alloy 6063 are presented in Figure 6. It was found that the peak stress of the semi-solid material increased significantly with the increase in the strain rate at a certain deformation temperature. Nevertheless, a reduction tendency was observed in the steady-state stress with the increase in the strain rate. The explanation for this phenomenon is as follows.

(a) At the beginning of the SSIC deformation process, the deformation speed of the sample was small because the strain rate was low, which provided enough time for the liquid phase to participate in repairing the liquid phase film among the deformed solid grains. The deformation of the spatial framework structure of the sample can take place with the slippage and rotation among the solid grains, resulting in a small deformation resistance and small peak stress. On the contrary, the liquid phase did not have enough time to repair the liquid film among the deformed solid grains when the strain rate was high, which caused the difficulty of solid grains to slip and rotate. The solid grains squeezed with each other in this early stage, which hindered the deformation of the sample, thereby, increasing the peak stress.

(b) The spatial framework structure of the sample was gradually and completely destroyed with the increase in the semi-solid isothermal compression deformation displacement, which formed solid grains or solid grain agglomerates wrapped by the liquid phase. This influence of the liquid phase on the solid grains or solid grain agglomerates contributed to the occurrence of compression deformation, so the true stress gradually decreased and stabilized. When the strain rate was low, the movement speed of the liquid phase film among the solid grains was small, resulting in the weak shearing effect among the solid grains. Consequently, it was difficult to achieve the disaggregation and destruction of solid grain aggregates. Therefore, higher steady-state stress was required to promote the coordinated deformation between the solid grain agglomerates after entering the steady state flow. On the contrary, when the strain rate was high, the strong shearing effect between the solid grains can promote the disaggregation and destruction of some solid grain aggregates, so that the liquid phase wrapped by the aggregates was released. The liquid content inside the sample, thereby, increased, which was beneficial for the slippage and rotation of the solid grains, so the steady-state stress was observed relatively low.

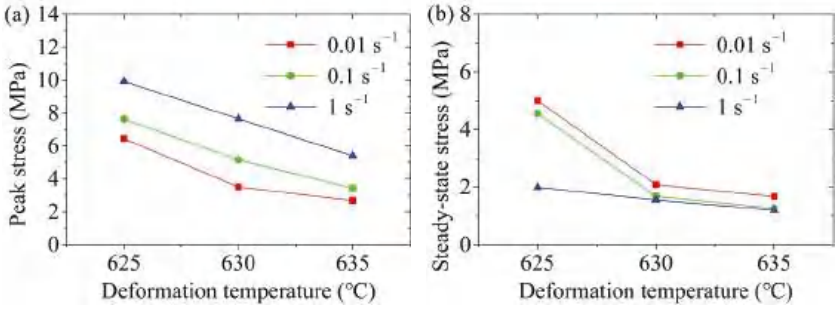

Figure 5. Influence of the deformation temperature in SSIC on the (**a**) peak stress, and (**b**) steady-state stress.

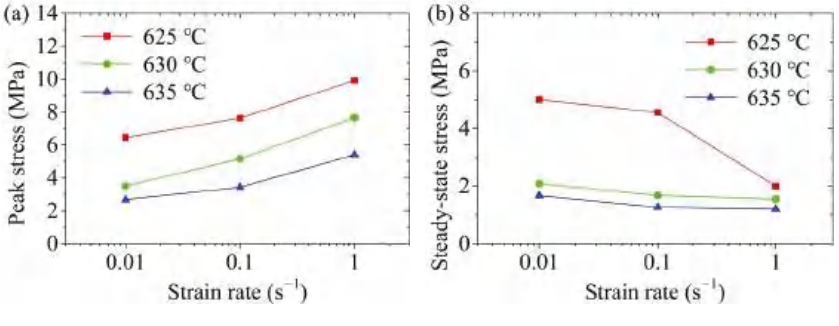

Figure 6. Influence of the strain rate in SSIC on the (**a**) peak stress; and (**b**) steady-state stress.

3.3. Constitutive Equations

The constitutive model expresses the material's dynamic response to the deformation amount, deformation temperature, and the strain rate during the plastic processing, which is crucial for the numerical simulation of the plastic deformation process using the finite element method and can be illustrated by Equation (4) [32],

$$\sigma = f(\varepsilon, \dot{\varepsilon}, T) \tag{4}$$

where, σ is the flow stress, MPa; ε is the strain of the material; $\dot{\varepsilon}$ is the strain rate, s^{-1}.

Semi-solid forming is carried out in the semi-solid temperature range of the metal, where both liquid and solid phases exist. Therefore its deformation behaviour is different from the solid state and the effect of the liquid fraction on the flow stress needs to be considered in the constitutive model [11]. Introducing the liquid phase fraction into Equation (4) to characterize the influence of it, the constitutive model of semi-solid thixotropy of the metal can be expressed as Equation (5),

$$\sigma = f(\varepsilon, \dot{\varepsilon}, T, f_L) \tag{5}$$

where f_L is the liquid phase fraction, %.

In the high-temperature hot forming process of the metal, the relationship between its flow stress and the operating parameters including the deformation temperature, strain, and strain rate can be expressed by the Arrhenius equation. The Arrhenius equation can characterize the sensitivity of flow stress to strain rate and deformation temperature as well as having the advantages of concision and a high degree of agreement with actual deformation. Its expressions are shown in Equations (6)–(8) [32–34]. In general, the exponential law expressed in Equation (6) is suitable for the stresses low-level values while the exponential law expressed by Equation (7) is applicable for stresses at high-level values. The hyperbolic sine law shown in Equation (8) can be applied to the entire stress range [35–37],

$$\dot{\varepsilon} = A_1 \sigma^{n_1} \exp\left(-\frac{Q}{RT}\right) \quad (\alpha\sigma < 0.8) \tag{6}$$

$$\dot{\varepsilon} = A_2 \exp(\beta\sigma) \exp\left(-\frac{Q}{RT}\right) \quad (\alpha\sigma > 1.2) \tag{7}$$

$$\dot{\varepsilon} = A[\sin h(\alpha\sigma)]^n \exp\left(-\frac{Q}{RT}\right) \quad (\text{all } \sigma) \tag{8}$$

where Q is the deformation activation energy, J/mol; R is the molar gas constant; T is the deformation temperature, K; n and n_1 are the stress exponent; A, A_1, and A_2 are factors of the material structure; α and β are stress level parameters, $\alpha = \beta/n_1$.

The magnitude of the peak stress is related to the selection of processing equipment and moulds in the semi-solid forming process. In this study, the peak stress is taken as the research object, the liquid phase correction term is introduced into the Arrhenius equation to modify Equation (8). Consequently, the Arrhenius equation adapted to the semi-solid temperature zone can be obtained as Equation (9),

$$(1 - 1.5 f_L)^L \dot{\varepsilon} = A[\sin h(\alpha\sigma)]^n \exp\left(-\frac{Q}{RT}\right) \tag{9}$$

where L is the liquid phase factor; $(1 - 1.5 f_L)^L$ shows that the tendency of the increase in the flow stress due to the enlargement in the strain rate when the liquid phase fraction increases.

In order to obtain the value of α, take the logarithm of Equations (6) and (7) to convert into the linear Equations (10), and (11), respectively:

$$\ln \dot{\varepsilon} = n_1 \ln \sigma + \ln A_1 - \frac{Q}{RT} \quad (\alpha\sigma < 0.8) \tag{10}$$

$$\ln \dot{\varepsilon} = \beta\sigma + \ln A_2 - \frac{Q}{RT} (\alpha\sigma > 1.2). \tag{11}$$

Introducing the peak stress and the corresponding strain rate at different deformation temperatures into Equations (10) and (11), the relationship between the strain rate and the peak stress at different deformation temperatures can be obtained, as shown in Figure 7. By linearly fitting the relationship between $\ln \dot{\varepsilon}$ and $\ln \sigma$ as well as that between $\ln \dot{\varepsilon}$ and σ at each deformation temperature shown in Figure 7, the slope of each straight line can be obtained. After calculating the mean value of slopes, it can be obtained that $n_1 = 7.61$ while $\beta = 1.32$, and consequently $\alpha = \frac{\beta}{n_1} = 0.1735$.

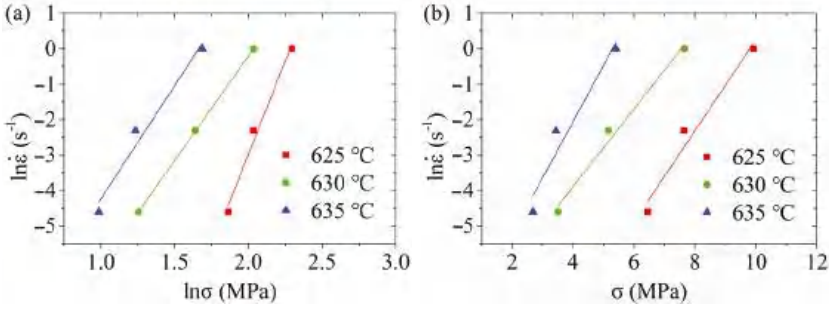

Figure 7. Relationship between the natural logarithm of the strain rate, and (**a**) the natural logarithm of the peak stress, and (**b**) the peak stress.

In order to calculate n, Equation (12) can be obtained by taking the logarithm of both sides of Equation (9):

$$\ln \dot{\varepsilon} = n \ln[\sin h(\alpha\sigma)] + \ln A - \frac{Q}{RT} - L \ln(1 - 1.5 f_L). \tag{12}$$

Importing the peak stress and the corresponding strain rate at different deformation temperatures into Equation (12), the relationship between $\ln \dot{\varepsilon}$ and $\ln[\sin h(\alpha\sigma)]$ was obtained and illustrated in Figure 8. The straight lines of the relationship and their slopes can be obtained through the linear fitting method. By calculating the mean value of slopes, it was obtained that $n = 5.5609$.

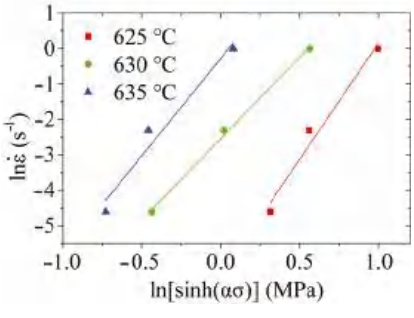

Figure 8. Relationship between $\ln \dot{\varepsilon}$ and $\ln[\sin h(\alpha\sigma)]$.

Based on the results in Section 3.1 as presented in Table 2, the effective liquid fractions at the deformation temperatures of 625 °C, 630 °C, and 635 °C were 11.10%, 13.29%, and 14.42%, respectively. Transforming Equation (12), Equation (13) can be obtained as follows:

$$n \ln[\sin h(\alpha\sigma)] - \ln \dot{\varepsilon} = -\ln A + \frac{Q}{RT} + L \ln(1 - 1.5 f_L). \quad (13)$$

Therefore, one Equation (13) can be obtained at a certain deformation temperature and a certain strain rate. Correspondingly, 9 equations can be obtained for 3 deformation temperatures and 3 strain rates, where only three parameters A, L, and Q are unknown. The least-squares solution was used to solve the overdetermined equation in this study. These 9 equations can then be written as the following matrix illustrated by Equation (14),

$$\boldsymbol{DX} = \begin{bmatrix} 1 & 1000/T & \ln(1 - 1.5 f_L) \end{bmatrix} \boldsymbol{X} = \boldsymbol{Y} \quad (14)$$

where $\boldsymbol{X}$, $\boldsymbol{Y}$, $\boldsymbol{D}$ are the 3*1, 9*1, and 9*3 matrixes, respectively. In the matrix $\boldsymbol{X}$, its elements are $X_1 = -\ln A$, $X_2 = \frac{Q}{1000R}$, and $X_3 = L$. In the matrix $\boldsymbol{Y}$, $Y_i = n \ln[\sin h(\alpha\sigma)] - \ln \dot{\varepsilon}$, where $i = 1, 2, \cdots 9$.

To calculate the values of parameters A, L, and Q, Equation (14) is multiplied by $\boldsymbol{D}^{\mathrm{T}}$ at both sides. Equations (15) and (16) can be obtained by performing the equivalent transformations:

$$\boldsymbol{D}^{\mathrm{T}}\boldsymbol{DX} = \boldsymbol{D}^{\mathrm{T}}\boldsymbol{Y} \quad (15)$$

$$\boldsymbol{X} = \left(\boldsymbol{D}^{\mathrm{T}}\boldsymbol{D}\right)^{-1}\boldsymbol{D}^{\mathrm{T}}\boldsymbol{Y}. \quad (16)$$

Introducing the corresponding parameters into Equation (13), matrixes $\boldsymbol{D}$, $\boldsymbol{X}$, and $\boldsymbol{Y}$ can be obtained as follows.

$$\boldsymbol{D} = \begin{bmatrix} 1 & 1.6 & -0.1821 \\ 1 & 1.6 & -0.1821 \\ 1 & 1.6 & -0.1821 \\ 1 & 1.5873 & -0.2223 \\ 1 & 1.5873 & -0.2223 \\ 1 & 1.5873 & -0.2223 \\ 1 & 1.5748 & -0.2437 \\ 1 & 1.5748 & -0.2437 \\ 1 & 1.5748 & -0.2437 \end{bmatrix}, \boldsymbol{X} = \begin{bmatrix} X_1 \\ X_2 \\ X_3 \end{bmatrix}, \boldsymbol{Y} = \begin{bmatrix} 6.3522 \\ 5.4162 \\ 5.5404 \\ 2.1848 \\ 2.4127 \\ 3.1344 \\ 0.5525 \\ -0.2494 \\ 0.4351 \end{bmatrix}$$

Introducing the above matrixes into Equation (16), the matrix $\boldsymbol{X}$ can be obtained by performing transposition and inverse matrix operations using Matlab software, which is $\boldsymbol{X} = \begin{bmatrix} 60.7210 \\ -16.5502 \\ 116.0644 \end{bmatrix}$. Consequently, the values of parameters were obtained as $A = 2.9602 \times 10^{70}$, $Q = 895.641$ kJ/mol, $L = 44.6267$. Importing the results of parameters into Equation (9), the peak stress equation of the aluminum alloy in the semi-solid region can be obtained as shown by Equation (17):

$$(1 - 1.5 f_L)^{44.6267} \dot{\varepsilon} = 2.9602 \times 10^{70} [\sin h(0.1735\sigma)]^{5.5609} \exp\left(-\frac{895641.8}{RT}\right) \quad (17)$$

It is worth noting that the applicable range of $(1 - 1.5 f_L)^{44.6267}$ in Equation (17) is $(1 - 1.5 f_L) > 0$, that is $f_L < 66.67\%$. This means that Equation (17) is applicable to the semi-solid thixotropic extrusion process when the liquid fraction is less than 66.67%.

The correlation coefficient R and the average absolute relative error (AARE) were used in the study to indicate the accuracy performance of the established peak stress equation

of the aluminium alloy in the semi-solid region, which are expressed by Equations (18), and (19), respectively,

$$R_c = \frac{\sum_{i=1}^{N}(\alpha_e - \overline{\alpha}_e)(\alpha_p - \overline{\alpha}_p)}{\sqrt{\sum_{i=1}^{N}(\alpha_e - \overline{\alpha}_e)^2 \cdot \sum_{i=1}^{N}(\alpha_p - \overline{\alpha}_p)^2}} \quad (18)$$

$$\mathrm{AARE}(\%) = \frac{1}{N}\sum_{i=1}^{N}\left|\frac{\alpha_e - \alpha_p}{\alpha_e}\right| \times 100\% \quad (19)$$

where α_e is the test value of the peak stress, MPa; $\overline{\alpha}_e$ is the average value of the tested peak stress, MPa; α_p is the predicted value of peak stress, MPa; $\overline{\alpha}_p$ is the average value of the predicted peak stress, MPa; N is the statistical number of data points.

As shown in Figure 9, the correlation coefficient between the predicted value of the peak stress and the experimentally tested value was found as 0.9796. The average relative error was obtained as 5.01% based on Equation (19), reflecting a high accuracy. This means that the constitutive equation can accurately express the change in the peak stress of aluminium alloy 6063 in the semi-solid region, which can be used for selecting the forming equipment of the semi-solid metal forming process.

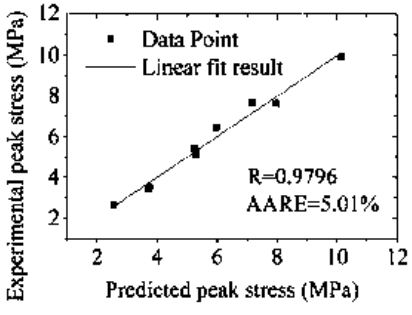

Figure 9. Relationship between the experimental and calculated peak stress of the cold radial forged 6063 aluminum alloy processed by SSIC.

3.4. Deformation Mechanism

3.4.1. Macroscopic Results and Analysis

The macroscopic photo of the radially forged aluminium alloy 6063 semi-solid isothermal compression samples is shown in Figure 10. Figure 10a presents the macroscopic photo of the samples processed at the strain rate of 0.1 s^{-1} with different deformation temperatures. It was found that the compressed sample gradually broke with the elevation in the deformation temperature. The higher the deformation temperature, the more obvious the degree of crushing of the compressed sample. This was because, at the beginning of the semi-solid isothermal compression deformation, the liquid phase already existed in the aluminium alloy 6063 semi-solid material, the fraction of which elevated with the enlargement in the deformation temperature. The liquid phase in the compressed sample was squeezed and flew to the sidewall of the sample at the central region and caused the sidewall to rupture during the SSIC deformation process. This liquid phase in the compressed sample continued to flow along the rupture of the sidewall in the final stage of the SSIC deformation, resulting in the fragmentation of the entire compressed sample. Nevertheless, the phenomenon aforementioned did not occur in the actual SSMF process. This was mainly because the mould cavity in the actual SSMF process was closed, which consequently avoided the outflow of the liquid phase [38,39].

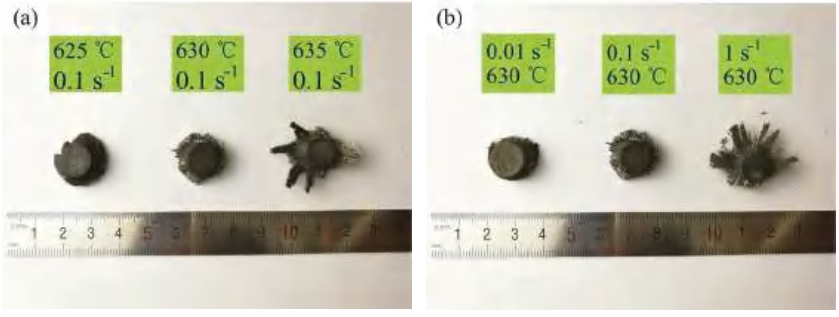

Figure 10. Macroscopic photo of samples after the SSIC at different, (**a**) deformation temperatures, and (**b**) strain rates.

The macroscopic photo of the samples processed at the deformation temperature of 630 °C under different strain rates is shown in Figure 10b. It was found that the macroscopic photo of the compressed sample changed significantly when the strain rate increased. The integrity of the compressed sample was relatively high at a relatively small strain rate, while the compressed sample was broken as the strain rate increased. This was because the flow of the liquid phase inside the semi-solid material became more intense with the elevation in the strain rate, so the degree of crushing increased.

According to the principle of pressure processing [13,32], the amount of deformation inside the sample is uneven in the process of material compression and deformation. The deformation area can be divided into hard deformation region, huge deformation region, and free deformation region, as shown in Figure 11a. The macroscopic photo of the section view along the longitudinal direction of the sample processed by the SSIC deformation is presented in Figure 11b, where the strain rate was 0.1 s^{-1}, the deformation temperature was set as 630 °C, and the strain was 0.7. It was found that similar to the compression deformation of solid metal, the semi-solid isothermal compression deformation sample also exhibited three different deformation regions, which are the hard deformation area near the end (Region A), the huge deformation area in the centre (Region B), and the free deformation region (Region C) in the convex region.

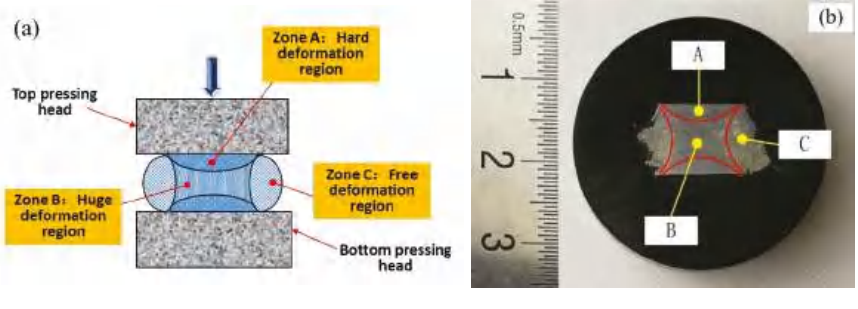

Figure 11. Deformation characteristics of the compressed samples: (**a**) Deformation region division, and (**b**) the longitudinal macroscopic photo of samples after the semi-solid isothermal compression (deformation temperature: 630 °C, strain rate: 0.1 s^{-1}).

3.4.2. Microstructure and Deformation Mechanism Analysis

The microstructures from different positions of the semi-solid compressed sample are shown in Figure 12. Comparing Figure 12b–f, the liquid fraction in the structure

tends to increase from the hard deformation region (Region A) to the huge deformation region (Region B), then to the free deformation region (Region C). A large increase in the liquid fraction was found in the free deformation region (Region C), compared to the huge deformation region (Region B). The most serious liquid segregates were observed in the free deformation region (Region C). This was because the liquid phase in the microstructure at Position 1 as shown in Figure 12a was squeezed out from the space among solid grains and in turn, flew to Positions 2 and 3 forced by the compression of the deformation as the amount of compression deformation continued to increase. Furthermore, under the action of the deformation force, the liquid phase at the centre of the sample (Positions 2 and 3) gradually flew to the edge position (Position 4 or 5), resulting in the uneven distribution of solid and liquid phases in each deformation region in the compressed sample.

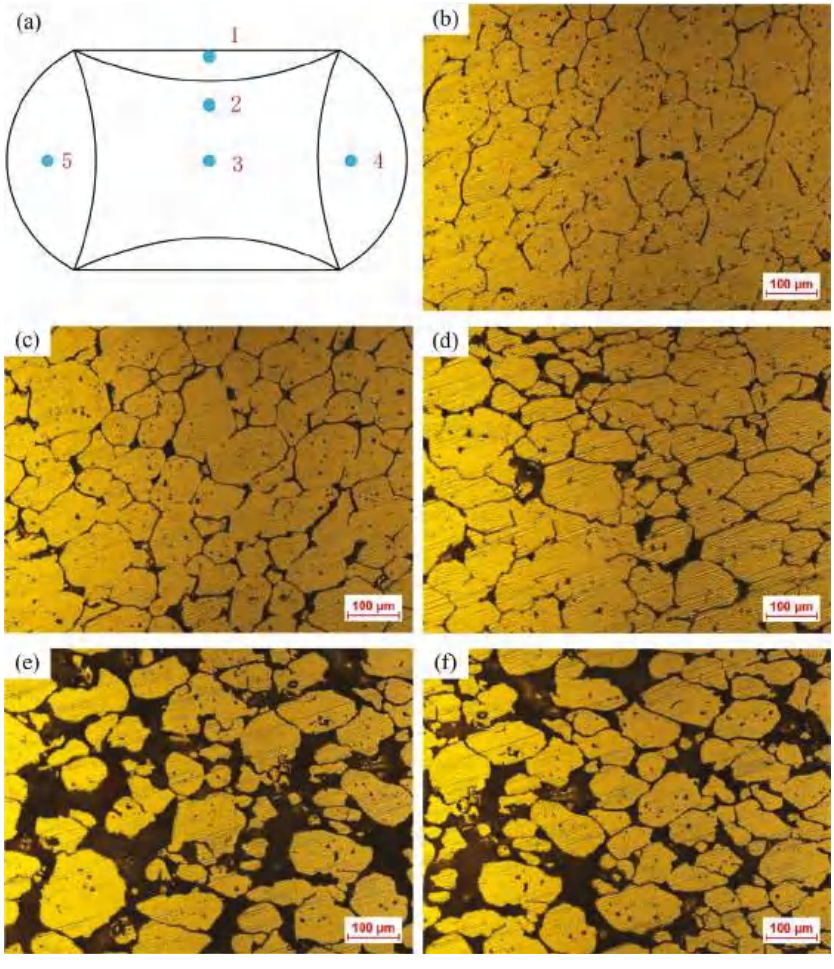

Figure 12. Microstructures of the cold radial forged 6063 alloy processed by SSIC (deformation temperature: 630 °C, strain rate: 0.1 s^{-1}): (**a**) Sample positions, (**b**) Position 1 in Region A, (**c**) Position 2 in Region B, (**d**) Position 3 in Region B, (**e**)Position 4 in Region C, and (**f**) Position 5 in Region C.

The liquid phase of the semi-solid material was mainly distributed at the boundary of the solid grains, which has the effect of isolating solid grains. When the compression force was applied to the semi-solid material, the separated flow of liquid and solid phases

would take place. Generally, the liquid content has a tendency to move before the solid grains. The reduction of the liquid phase would cause the subsequent flow of solid grains to contact with each other. If the deformation continues, severe plastic deformation would take place in the solid grains. Furthermore, the flow of the liquid phase would also cause the liquid phase segregation. The deformation was restricted in the deformation region. Therefore, the microstructure basically remained the original semi-solid microstructure without obvious segregation, as shown in Figure 12b. However, the liquid fraction was observed slightly reduced and the bonding phenomenon was found among part of the solid grains. This means that in the process of compression deformation, the mixed flow of solid grains and the liquid phase was the main phenomenon (i.e., the grain sliding or the grain rotation along with the liquid phase) in the hard deformation region. Partial liquid phase flow also occurred in Region A under the squeeze action of the deformation force. The deformation amount in Region B was observed relatively large, as shown in Figure 12c,d. In Region B, the solid grains appeared to be squashed with liquid phase segregation observed in some regions. Therefore, the liquid flow is the major phenomenon in the huge deformation region (i.e., Region B) at the beginning of SSIC. This liquid content was squeezed out with the increase in the compression deformation. The solid grains contacted each other and were squeezed by the deformation force, resulting in the plastic deformation of the solid grains. Meanwhile, a certain degree of slip and rotation appeared among the solid grains.

The nearly spherical phenomenon was observed in solid grains in the free deformation region (see Positions 4 and 5), but a more serious liquid phase segregation was also found as shown in Figure 12e,f. This was mainly because the liquid phase from the hard and huge deformation regions flew into the free deformation region, resulting in the macroscopic transfer of the liquid. Therefore, the closer to the free-deformation region, the more liquid phase there was, the more serious the liquid phase segregation. Moreover, the thorough partial solid-liquid separation was also observed in the free deformation region because of the movement of the liquid phase, where pores would be generated if the surrounding liquid or solid phase cannot be replenished in time. Therefore, liquid flow and the sliding or rotation of solid grains along the liquid phase are the deformation modes in the free deformation region.

Based on the analysis mentioned above, the deformation mechanism of the radially forged aluminium alloy 6063 material during the SSIC mainly included the grain slide or grain rotation along with the liquid film, the sliding among solid grains, and the plastic deformation of solid grains. Moreover, according to the analysis of the microstructure in different deformation regions, during the SSIC, different degrees of liquid phase flow occurred in all these three deformation regions. Considering this liquid phase flow, there were four deformation mechanisms in SSIC, which is presented in Figure 13, where the large blue arrow shows the compression direction during the SSIC deformation process, the little red arrow indicates the direction of grain movement, while the square and the rectangle indicates the deformation area before, and after, the deformation, respectively.

As presented in Figure 13a, the highest liquid phase fraction can be obtained in the liquid phase flow mechanism. The thick liquid film wraps the solid-phase grains and no contact existed among the solid grains. Consequently, the flow channel for the liquid phase is unobstructed. The liquid phase flows perpendicular to the compression direction while the solid grains mostly flow parallel to the compression direction when compression deformation is performed. The liquid phase segregation would then take place after the deformation. As illustrated in Figure 13b, the liquid fraction reduces and the nearly spherical solid particles are enfolded by a relatively thin liquid film in the mechanism of grain slide or grain rotation along with the liquid film. When the compression deformation is carried out, solid grains flow both perpendicular and parallel to the direction of the compression force. This means that the solid grains slide or rotate along with the liquid film, forming a mixed flow of solid grains and liquid phase.

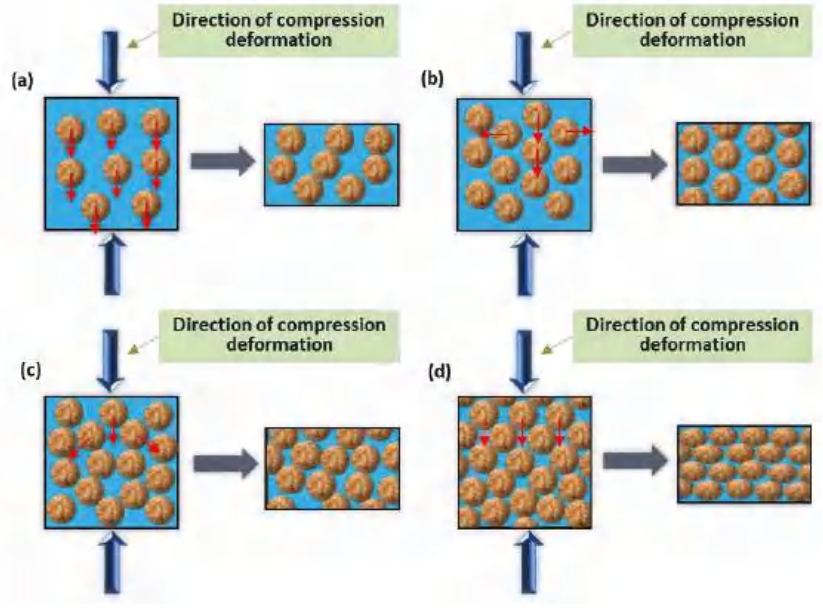

Figure 13. Schematic diagram of deformation mechanisms: (**a**) Liquid phase flow, (**b**) solid grains slip or rotate along the liquid film, (**c**) slipping among solid grains, and (**d**) plastic deformation of solid grains.

It can be found in Figure 13c that, in the sliding mechanism, the liquid phase fraction further decreased while the thickness of the liquid film among the solid grains continued to reduce. Solid grain clusters were formed as some solid grains contact each other, which blocks the flow channel for the liquid phase. Under the compression deformation, the solid grains inside the solid grain cluster would slide relative to the adjacent solid grains due to the shear force [7,12,40,41]. As presented in Figure 13d, a low phase fraction of the liquid phase is observed in the mechanism of the plastic deformation of solid grains while little liquid film among the solid grains can also be observed. In this mechanism, most of the solid grains contact each other, forming the solid grain clusters. The sliding among the solid grains is not intense enough to generate a large plastic deformation during the compression deformation process. Therefore, the plastic deformation would take place on the solid grains to achieve a large SSIC deformation of the metal material.

In summary, the phase fraction of liquid determines the deformation mode of the semi-solid material during the isothermal compression deformation process. When the phase fraction of liquid is large, the content of the liquid phase in the microstructure is high and thus, solid grains would not completely contact each other. The flow channel of the liquid phase is therefore unobstructed. The deformation mode mainly contains the liquid phase flow and the sliding or rotation of the solid grain along with the liquid film. When the phase fraction of liquid is small, the content of the liquid phase in the microstructure reduces, resulting in the local contact of solid grains. The flow channel of the liquid phase is then hindered. The deformation mode then mainly includes the sliding among solid grains and the plastic deformation of solid grains. Furthermore, the order of the main deformation mechanism with the decrease in the liquid phase fraction is from the liquid phase flow to the grain slide or grain rotation along with the liquid film, then to the sliding among the solid grains, and finally to the plastic deformation of solid particles. In terms of a specific compressed sample, the grain slide or grain rotation along the liquid phase is the main deformation mode in the hard deformation region (Region A); the plastic deformation of solid grains is the main deformation mode in the huge deformation region (Region B),

while a certain degree of sliding among the solid grains also appears in this region; the liquid phase flow and the grain slide or grain rotation along the liquid film are the main deformation modes in the free deformation region (Region C).

4. Conclusions

In this work, SSIC is proposed to investigate the microstructure, deformation characteristics, and deformation mechanism of semi-solid alloy, where the cold radial forging is introduced in the SIMA process to prepare the high-quality semi-solid billet. The main conclusions drawn from this study are shown as follows.

(1) The average grain size, shape factor, and effective liquid phase fraction increase with the enhancement in the deformation temperature. The high-quality semi-solid alloy, which has the average grain size in the range of 59.22–73.02 μm while the average shape factor in the range of 0.71–0.78, can be obtained when the cold radial forged 6063 aluminum alloy is treated by SSIT process at the deformation temperature in the range of 625–635 °C.

(2) The true stress-true strain curve of the cold radial forged 6063 aluminium alloy SSIC mainly includes four deformation stages: sharp increase stage, decrease stage, steady state stage, and slow increase stage. The true stress decreases when the deformation temperature increases at a certain strain rate, which means that both the peak and steady-state stresses decrease with the enlargement in the deformation temperature. The peak stress elevates while the steady-state stress decreases with the enlargement in the strain rate at a certain deformation temperature.

(3) Introducing the liquid phase correction term $S = (1 - 1.5f_L)^L$ into the Arrhenius equation, the peak stress constitutive equation of the semi-solid region of aluminium alloy 6063 in the semi-solid deformation temperature range is calculated and established as $(1 - 1.5f_L)^{44.6267}\dot{\varepsilon} = 2.9602 \times 10^{70}[\sin h(0.1735\sigma)]^{5.5609} \exp\left(-\frac{895641.8}{RT}\right)$. The correlation coefficient between the predicted value of the peak stress by the constitutive equation and the experimental result is 0.9796 while the average relative error is 5.01%, which means that the constitutive equation established in this study can accurately express the change in the peak stress of aluminium alloy 6063 in the semi-solid temperature region with the variation of the effective liquid phase fraction, deformation temperature, strain rate, and the strain.

(4) The deformation mechanisms of cold radial forged aluminium alloy 6063 during SSIC mainly include four modes: liquid phase flow, grain slide or grain rotation along with the liquid film, sliding among solid grains, and the plastic deformation of solid grains. For a specific sample, the grain slide or grain rotation along the liquid film is the main deformation mode in the hard deformation region. In the huge deformation region, the plastic deformation of solid grains is the main deformation mode while a certain degree of sliding among solid grains also exists. The liquid phase flow and the grain slide or grain rotation along the liquid film are the main deformation mode in the free deformation region.

Author Contributions: Conceptualization, Y.G. and S.Z. (Shengdun Zhao); methodology, Y.G.; formal analysis, Y.W., S.Z. (Shunqi Zheng) and Y.G.; investigation, Y.W. and K.L.; data curation, Y.W. and Y.G.; writing–original draft preparation, Y.W.; writing–review and editing, Y.G. and S.Z. (Shengdun Zhao); visualization, Y.W., K.L. and S.Z. (Shunqi Zheng); supervision, S.Z. (Shengdun Zhao). All authors have read and agreed to the published version of the manuscript.

Funding: This research was funded by the State Key Laboratory of Materials Processing and Die & Mould Technology (Grant No. P2021-005), the Fundamental Research Funds for the Central Universities (Grant No. XZY012019003/XJH012019010), the Natural Science Basic Research Program of Shaanxi (Grant No. 2020JQ-067), and the Nature Science Foundation of Zhejiang Province (Grant No. LQ18E040002).

Data Availability Statement: The data presented in this study are available on request from the corresponding author. The data are not publicly available due to project confidentiality requirements.

Conflicts of Interest: The authors declare no conflict of interest.

References

1. Yoshimura, H.; Tanaka, K. Precision forging of aluminum and steel. *J. Mater. Process. Tech.* **2000**, *98*, 196–204. [CrossRef]
2. Shan, D.B.; Xu, W.C.; Lu, Y. Study on precision forging technology for a complex-shaped light alloy forging. *J. Mater. Process. Tech.* **2004**, *151*, 289–293. [CrossRef]
3. Bayramoglu, M.; Polat, H.; Geren, N. Cost and performance evaluation of different surface treated dies for hot forging process. *J. Mater. Process. Tech.* **2008**, *205*, 394–403. [CrossRef]
4. Li, X.; Xiong, S.M.; Guo, Z. Correlation between Porosity and Fracture Mechanism in High Pressure Die Casting of AM60B Alloy. *J. Mater. Sci. Technol.* **2016**, *32*, 54–61. [CrossRef]
5. Zhang, P.; Li, Z.; Liu, B.; Ding, W.; Peng, L. Improved tensile properties of a new aluminum alloy for high pressure die casting. *Mat. Sci. Eng. A* **2016**, *651*, 376–390. [CrossRef]
6. Wang, Y.; Zhao, S.; Zhao, X.; Zhao, Y. Microstructural coarsening of 6061 aluminum alloy semi-solid billets prepared via recrystallization and partial melting. *J. Mech. Sci. Technol.* **2017**, *31*, 3917–3923. [CrossRef]
7. Xu, Y.; Chen, C.; Jia, J.; Zhang, X.; Dai, H.; Yang, Y. Constitutive behavior of a SIMA processed magnesium alloy by employing repetitive upsetting-extrusion (RUE). *J. Alloys Compd.* **2018**, *748*, 694–705. [CrossRef]
8. Fu, J.L.; Jiang, H.J.; Wang, K.K. Influence of Processing Parameters on Microstructural Evolution and Tensile Properties for 7075 Al Alloy Prepared by an ECAPBased SIMA Process. *Acta Metall. Sin.* **2018**, *31*, 337–350. [CrossRef]
9. Dao, V.; Zhao, S.; Lin, W.; Zhang, C. Effect of process parameters on microstructure and mechanical properties in AlSi9Mg connecting-rod fabricated by semi-solid squeeze casting. *Mat. Sci. Eng. A* **2012**, *558*, 95–102. [CrossRef]
10. Chen, X.H.; Yan, H. Constitutive behavior of Al 2 O 3np /Al7075 composites with a high solid fraction for thixoforming. *J. Alloys Compd.* **2017**, *708*, 751–762. [CrossRef]
11. Chen, G.; Lin, F.; Yao, S.; Han, F.; Wei, B.; Zhang, Y. Constitutive behavior of aluminum alloy in a wide temperature range from warm to semi-solid regions. *J. Alloys Compd.* **2016**, *674*, 26–36. [CrossRef]
12. Binesh, B.; Aghaie-Khafri, M. Phase Evolution and Mechanical Behavior of the Semi-Solid SIMA Processed 7075 Aluminum Alloy. *Metals* **2016**, *6*, 42. [CrossRef]
13. Wang, J.; Xiao, H.; Wu, L.B.; Hu, H.L.; Lu, D.H.; Zhou, R.F.; Zhou, R. Deformation characteristic of semi-solid ZCuSn10 copper alloy during isothermal compression. *Rare Met.* **2016**, *8*, 620–626. [CrossRef]
14. Meshkabadi, R.; Pouyafar, V.; Javdani, A.; Faraji, G. An Enhanced Steady-State Constitutive Model for Semi-solid Forming of Al7075 Based on Cross Model. *Metall. Mater. Trans. A* **2017**, *48*, 4275–4285. [CrossRef]
15. Wang, J.J.; Phillion, A.B.; Lu, G.M. Development of a visco-plastic constitutive modeling for thixoforming of AA6061 in semi-solid state. *J. Alloys Compd.* **2014**, *609*, 290–295. [CrossRef]
16. Lu, Y.l.; Li, M.Q.; Li, X.C. Deformation Behavior and Constitutive Equation Coupled the Grain Size of Semi-Solid Aluminum Alloy. *J. Mater. Eng. Perform.* **2010**, *19*, 1337–1343. [CrossRef]
17. Bolouri, A.; Shahmiri, M.; Cheshmeh, E.N.H. Microstructural evolution during semisolid state strain induced melt activation process of aluminum 7075 alloy. *T. Nonferr. Metal. Soc.* **2010**, *20*, 1663–1671. [CrossRef]
18. Xu, Y.; Hu, L.; Jia, J.; Xu, B. Microstructure evolution of a SIMA processed AZ91D magnesium alloy based on repetitive upsetting-extrusion (RUE) process. *Mater. Charact.* **2016**, *118*, 309–323. [CrossRef]
19. Jiang, J.; Wang, Y.; Liu, J.; Qu, J.-J.; Du, Z.-M.; Luo, S.-J. Microstructure and mechanical properties of AZ61 magnesium alloy parts achieved by thixo-extruding semisolid billets prepared by new SIMA. *T. Nonferr. Metal. Soc.* **2013**, *23*, 576–585. [CrossRef]
20. Jiang, J.; Wang, Y.; Xiao, G.; Nie, X. Comparison of microstructural evolution of 7075 aluminum alloy fabricated by SIMA and RAP. *J. Mater. Process. Tech.* **2016**, *238*, 361–372. [CrossRef]
21. Wang, Y.; Zhao, S.; Zhang, C. Microstructural evolution of semisolid 6063 aluminum alloy prepared by recrystallization and partial melting process. *J. Mater. Eng. Perform.* **2017**, *26*, 4354–4363. [CrossRef]
22. Wu, Y.J.; Dong, X.H.; Yu, Q. Upper bound analysis of axial metal flow inhomogeneity in radial forging process. *Int. J. Mech. Sci.* **2015**, *93*, 102–110. [CrossRef]
23. Yang, Y.; Zhang, X.; Fan, L.; Xu, C. Mechanical properties of steel gun barrel processed by cold radial forging with stepped mandrel under different forgingratios. *J. Phys. Conf. Ser.* **2020**, *1507*, 042004. [CrossRef]
24. Atkinson, H. Modelling the semisolid processing of metallic alloys. *Prog. Mater. Sci.* **2005**, *50*, 341–412. [CrossRef]
25. Orgéas, L.; Gabathuler, J.P.; Imwinkelried, T.; Paradies, C.; Rappaz, M. Modelling of semi-solid processing using a modified temperature-dependent power-law model. *Model. Simul. Mater. Sci. Eng.* **2003**, *11*, 553–574. [CrossRef]
26. Chen, G.; Zhang, S.; Zhang, H.; Han, F.; Wang, G.; Chen, Q.; Zhao, Z. Controlling liquid segregation of semi-solid AZ80 magnesium alloy by back pressure thixoextruding. *J. Mater. Process. Tech.* **2018**, *259*, 88–95. [CrossRef]
27. Wang, Y.; Zhao, S.; Zhao, X.; Zhao, Y. Effects of isothermal treatment parameters on the microstructure of semisolid alloys. *Mater. Sci. Tech. Lond.* **2017**, *34*, 104–110. [CrossRef]
28. Kim, H.H.; Lee, S.M.; Kang, C.G. Reduction in Liquid Segregation and Microstructure Improvement in a Semisolid Die Casting Process by Varying Injection Velocity. *Metall. Mater. Trans. B* **2011**, *42*, 156–170. [CrossRef]
29. Wang, Y.; Guo, Y.; Zhao, S. Effects of Process Parameters on the Microstructure and Hardness of Semi-Solid AlSi9Mg Aluminum Alloy Prepared by RAP Process. *Mater. Trans.* **2020**, *61*, 1731–1739. [CrossRef]
30. Zhang, C.; Zhao, S.; Yan, G.; Wang, Y. Deformation behaviour and microstructures of semi-solid A356.2 alloy prepared by radial forging process during high solid fraction compression. *Proc. Inst. Mech. Eng. B J. Eng.* **2018**, *232*, 487–498. [CrossRef]

31. Wu, M.; Liu, Y.; Wang, T.; Yu, K. Deformation Behavior and Characteristics of Sintered Porous 2024 Aluminum Alloy Compressed in a Semisolid State. *Mat. Sci. Eng. A* **2016**, *674*, 144–150. [CrossRef]
32. Kang, W.; Yang, Y.; Cao, S.; Li, L.; Xin, S.; Wang, H.; Cao, Z.; Liang, E.; Zhang, X.; Huang, A. Hot Deformation Behavior of a New Al–Mn–Sc Alloy. *Materials* **2019**, *13*, 22. [CrossRef] [PubMed]
33. Mirzadeh, H.; Cabrera, J.M.; Najafizadeh, A. Constitutive relationships for hot deformation of austenite. *Acta Mater.* **2011**, *59*, 6441–6448. [CrossRef]
34. Sellars, C.M.; Mctegart, W.J. On the mechanism of hot deformation. *Acta Mater.* **1966**, *14*, 1136–1138. [CrossRef]
35. Li, Y.; Zhao, S.; Fan, S.; Yan, G. Study on the material characteristic and process parameters of the open-die warm extrusion process of spline shaft with 42CrMo steel. *J. Alloys Compd.* **2013**, *571*, 12–20. [CrossRef]
36. Changizian, P.; Zarei-Hanzaki, A.; Roostaei, A.A. The high temperature flow behavior modeling of AZ81 magnesium alloy considering strain effects. *Mater. Des.* **2012**, *39*, 384–389. [CrossRef]
37. Ashtiani, H.R.R.; Parsa, M.H.; Bisadi, H. Constitutive equations for elevated temperature flow behavior of commercial purity aluminum. *Mater. Eng. A* **2012**, *545*, 61–67. [CrossRef]
38. Hassas-Irani, S.B.; Zarei-Hanzaki, A.; Bazaz, B.; Roostaei, A.A. Microstructure evolution and semi-solid deformation behavior of an A356 aluminum alloy processed by strain induced melt activated method. *Mater. Des.* **2013**, *46*, 579–587. [CrossRef]
39. Ning, Z.L.; Wang, H.; Sun, J.F. Deformation Behavior of Semisolid A356 Alloy Prepared by Low Temperature Pouring. *Mater. Manuf. Process.* **2010**, *25*, 648–653. [CrossRef]
40. Fadavi Boostani, A.; Tahamtan, S. Effect of a novel thixoforming process on the microstructure and fracture behavior of A356 aluminum alloy. *Mater. Des.* **2010**, *31*, 3769–3776. [CrossRef]
41. Meng, Y.; Sugiyama, S.; Yanagimoto, J. Microstructural evolution during partial melting and semisolid forming behaviors of two hot-rolled Cr-V-Mo tool steels. *J. Mater. Process. Tech.* **2015**, *225*, 203–212. [CrossRef]

materials

MDPI

Article

Application of the Strain Compensation Model and Processing Maps for Description of Hot Deformation Behavior of Metastable β Titanium Alloy

Oleksandr Lypchanskyi *, Tomasz Śleboda, Aneta Łukaszek-Sołek, Krystian Zyguła and Marek Wojtaszek

Faculty of Metals Engineering and Industrial Computer Science, AGH University of Science and Technology, Av. Mickiewicza 30, 30-059 Krakow, Poland; sleboda@agh.edu.pl (T.Ś.); alukasze@metal.agh.edu.pl (A.Ł.-S.); kzygula@agh.edu.pl (K.Z.); mwojtasz@metal.agh.edu.pl (M.W.)
* Correspondence: lypchans@agh.edu.pl; Tel.: +48-12-617-29-16

Abstract: The flow behavior of metastable β titanium alloy was investigated basing on isothermal hot compression tests performed on Gleeble 3800 thermomechanical simulator at near and above β transus temperatures. The flow stress curves were obtained for deformation temperature range of 800–1100 °C and strain rate range of 0.01–100 s^{-1}. The strain compensated constitutive model was developed using the Arrhenius-type equation. The high correlation coefficient (R) as well as low average absolute relative error (AARE) between the experimental and the calculated data confirmed a high accuracy of the developed model. The dynamic material modeling in combination with the Prasad stability criterion made it possible to generate processing maps for the investigated processing temperature, strain and strain rate ranges. The high material flow stability under investigated deformation conditions was revealed. The microstructural analysis provided additional information regarding the flow behavior and predominant deformation mechanism. It was found that dynamic recovery (DRV) was the main mechanism operating during the deformation of the investigated β titanium alloy.

Keywords: β titanium alloy; constitutive model; flow behavior; processing maps

Citation: Lypchanskyi, O.; Śleboda, T.; Łukaszek-Sołek, A.; Zyguła, K.; Wojtaszek, M. Application of the Strain Compensation Model and Processing Maps for Description of Hot Deformation Behavior of Metastable β Titanium Alloy. *Materials* **2021**, *14*, 2021. https://doi.org/10.3390/ma14082021

Academic Editor: Ivo Schindler

Received: 30 March 2021
Accepted: 15 April 2021
Published: 17 April 2021

1. Introduction

In recent years, the use of metastable β titanium alloys has grown steadily due to their ability to process at lower temperatures, good corrosion resistance, higher fatigue strengths, as well as the possibility of increasing the level of yield strength by hardening. Because of such a set of properties, this type of alloy is widely used in the aerospace industry [1]. Among the β alloys, the high strength Ti-10V-2Fe-3Al (Ti-1023) alloy should be noted due to its high combination of mechanical properties and good workability, which has influenced its widespread use in aircraft landing gear components [1,2].

Two of the most expedient methods of hot plastic deformation for ensuring the necessary mechanical properties of critical parts made of titanium alloys are hot die forging and isothermal forging. In addition, in recent years, methods based on powder metallurgy have become widespread for obtaining finished products from titanium alloys [3,4]. The main parameters of plastic deformation, determining the changes in the microstructure and deformation behavior of titanium alloys during processing, are temperature, strain, and strain rate. In addition, significant influence of the initial microstructure on the flow behavior during hot forming of the Ti-1023 alloy was noted [2,5,6]. The initial morphology of the globular α phase has a less effect on the increase in flow stress during isothermal forging below β transus temperature, as compared to α lamellae with a high aspect ratio. The increased sensitivity of the microstructure of the Ti-1023 alloy in near β transus (about 800 °C) temperature [2] should also be noted.

Thermomechanical processing parameters have a significant impact on the changes occurring in the microstructure during deformation of the materials that show susceptibility

to dynamic recrystallization (DRX) or dynamic recovery (DRV). The identification of these changes in the microstructure has been the aim of many studies in the field of constitutive and dynamic material modeling for describing the hot deformation behavior of both metallic materials and in particular β titanium alloys [7–15]. Xiao et al. [7] investigated the hot deformation flow behavior of a Ti-55511 alloy during hot compression using dislocation density-based constitutive model as well as processing maps. Moreover, Lin et al. [11] showed a comparative analysis of artificial neural network, Hensel-Spittel, and strain-compensated Arrhenius-type models to describe the flow behavior of Ti-55511 titanium alloy. Fan et al. [9] and Wu et al. [12] described the deformation mechanisms of Ti-7Mo-3Nb-3Cr-3Al and Ti-4Al-1Sn-2Zr-5Mo-8V-2.5Cr alloys, respectively, based on processing maps and constitutive equations. Zhao et al. [13] and OuYang et al. [14] analyzed the deformation mechanisms of Ti-1023 alloy during hot compression at supertransus temperatures using activation energy and DRX kinetics model, respectively. The hot flow behavior of Ti-1023 alloy has also been analyzed by the artificial neural network model, the constitutive model using regression method, and the physically-based constitutive model [15,16]. Besides, one of the hot deformation optimization approaches for Ti-1023 alloy was the use of processing maps based on dynamic materials modeling (DMM) [17,18]. Superimposing hot processing maps over flow stress maps as well as overactivation of energy values to evaluate the hot workability of the investigated materials is quite often applied [19,20].

The models based on Arrhenius-type constitutive equation are the most widely used phenomenological constitutive models that have been successfully used for descriptions of the flow behavior during hot deformation of alloys and metals [8,11,21–25]. The constitutive equation describing the flow behavior of Ti-1023 alloy obtained by the blended elemental powder metallurgy technique was elaborated and presented in [26]. The highest accuracy of the Arrhenius-type equation in the form of a hyperbolic sine law was confirmed in this respect. However, it should be noted that this equation does not take into account the influence of the strain level on the flow behavior of the material, which is an important factor for designing the technological parameters of hot working. It is worth emphasizing that most of the research works were focused on the hot deformation behavior of Ti-1023 below or near β transus temperature ranges. On the other hand, the flow behavior of this alloy in β region is not fully understood, which makes this issue worthy of deeper analysis. It is known that deformation above β transus temperature leads to DRX and prior refinement of β grains, and therefore finer lamella microstructure increasing the ductility as well as strength of this alloy [14,27].

For a deeper understanding of the high-temperature workability of Ti-1023 alloy, the results of flow behavior at near and above β transus temperature range are presented in this paper. Based on hot compression tests, the strain compensated Arrhenius-type model and processing maps were developed and discussed with regard to changes in the microstructure of the Ti-1023 alloy.

2. Materials and Methods

The chemical composition of the investigated titanium alloy was Ti-9.76V-1.84Fe-3.37Al (wt.%). The size of cylindrical specimens for hot compression tests was 10 mm in diameter and 12 mm in height. The specimens were machined from cast alloy rod (ϕ76 mm) and deformed in compression on the Gleeble 3800 thermomechanical simulator (Dynamic Systems, Inc., Poestenkill, NY, USA) to a total true strain of 1. The specimens were cut along the rod axis at a distance of approx. 2/3 of the radius from the center of the rod cross-section. The isothermal tests were performed under an argon atmosphere at the temperature varying from 800 °C to 1100 °C, and at strain rates of 0.01 s^{-1}, 0.1 s^{-1}, 1 s^{-1}, 10 s^{-1}, and 100 s^{-1}. A graphite foil was used as a lubricant in order to minimize the friction effect between the specimen and anvils. The samples were homogenized in 10 s prior to deformation and the resistance heating rate of 2.5 °C/s was applied. After compression, the samples were cooled in air and machined along the axial direction for microstructure observation.

The microstructure of Ti-1023 alloy in the as-received condition (Figure 1) consists of original β grains, intragranular lamellar α colonies with high volume fraction and continuous α layers on the β grains boundaries.

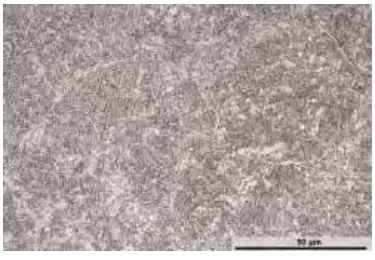

Figure 1. Starting microstructure of Ti-1023 alloy.

3. Results and Discussion

3.1. Flow Behaviour

It is well known that the influence of friction as well as adiabatic heating on flow stresses during compression tests leads to deviations in flow stress and difficulties associated with their interpretation. Taking into account this fact, the correction for friction and heating during deformation in order to precisely describe flow behavior of the material is an important factor. In the presented studies, the inverse analysis technique [28,29] was used in order to correct the data obtained on the basis of compression tests.

Based on the isothermal hot compression tests, true stress-strain curves for Ti-1023 alloy deformed to a true strain of 1 at the temperature range of 800–100 °C, and strain rate range of 0.01–100 s^{-1} (Figure 2) were obtained.

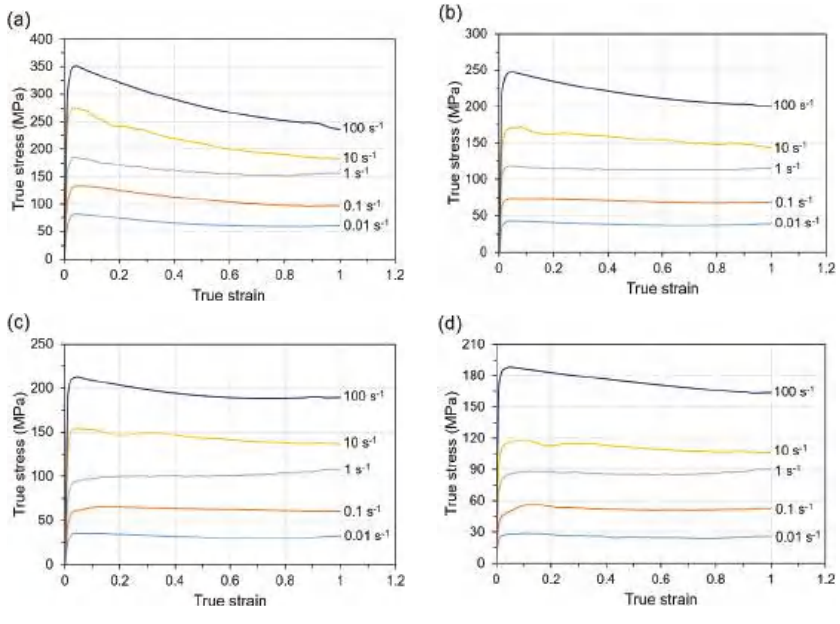

Figure 2. *Cont.*

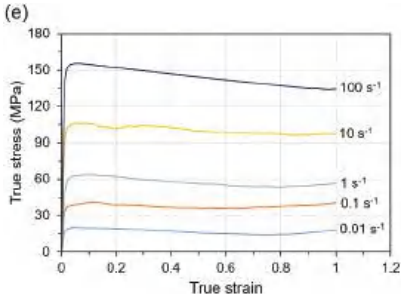

Figure 2. The true stress-true strain curves for Ti-1023 alloy deformed in compression at the temperature of (**a**) 800 °C, (**b**) 900 °C, (**c**) 950 °C, (**d**) 1000 °C, (**e**) 1100 °C and at various strain rates.

Generally, the expected decrease of flow stress with increasing temperature and decreasing strain rate was observed. As can be seen from the obtained curves, they are characterized in most of the cases by steady state flow after reaching a peak value at the initial stage. This type of material flow behavior can mostly be noticed in the case of materials subjected to deformation at the temperatures higher than supertransus temperature and is quite typical for β titanium alloys processed at this temperature range [30,31]. Rapid work hardening and subsequent flow softening effects during deformation at the temperature below β transus temperature (Figure 2a) indicated the occurrence of DRX or DRV. However, in this case, it should be noted that the flow curves obtained for the material deformed at strain rate of 10 s^{-1} and 100 s^{-1} show flow softening followed by continuous decrease of the flow stress without steady state flow region, and can indicate flow instability under such deformation conditions. It should also be noted that most of the curves, especially obtained at low strain rates ($\geq$1 s^{-1}), do not have distinct dynamic softening effects, which indicate the occurrence of the predominant DRV mechanism during deformation.

3.2. Development of the Constitutive Equation

The high-temperature deformation behavior of the material can be described by the relationships of the strain rate, temperature and flow stress, e.g., by the Arrhenius-type equation [25,32]:

$$\dot{\varepsilon} = AF(\sigma)\exp\left(-\frac{Q}{RT}\right) \quad (1)$$

where σ is the flow stress (MPa), $\dot{\varepsilon}$ is the strain rate (s^{-1}), R is the universal gas constant (8.314 $J{\cdot}mol^{-1}{\cdot}K^{-1}$), A is the material constant, Q is the deformation activation energy ($kJ{\cdot}mol^{-1}$), T is the deformation temperature (K), and $F(\sigma)$ is the flow stress function.

Depending on the stress levels, the flow stress function in Equation (1) can be expressed as given in [21]:

$$\dot{\varepsilon} = A_1\sigma^{n_1}\exp\left(-\frac{Q}{RT}\right), \text{ for } \alpha\sigma < 0.8 \quad (2)$$

$$\dot{\varepsilon} = A_2\exp(\beta\sigma)\exp\left(-\frac{Q}{RT}\right), \text{ for } \alpha\sigma > 1.2 \quad (3)$$

$$\dot{\varepsilon} = A[\sin h(\alpha\sigma)]^n\exp\left(-\frac{Q}{RT}\right), \text{for all } \sigma \quad (4)$$

where A, A_1, A_2, n_1, β, n and α are the material constants, $\alpha = \beta/n_1$.

The relationship between the strain rate and temperature is described by the Zener-Hollomon parameter (Z) [33]:

$$Z = \dot{\varepsilon}\exp\left(\frac{Q}{RT}\right) \quad (5)$$

After transformation of Equations (2)–(4) into the natural logarithm, they allow to calculate the materials' constants:

$$\ln \dot{\varepsilon} = \ln A_1 - \frac{Q}{RT} + n_1 \ln \sigma \tag{6}$$

$$\ln \dot{\varepsilon} = \ln A_2 - \frac{Q}{RT} + \beta\sigma \tag{7}$$

$$\ln \dot{\varepsilon} = \ln A - \frac{Q}{RT} + n \ln[\sin h(\alpha\sigma)] \tag{8}$$

According to Equations (6)–(8), using the corresponding strain rates and peak flow stresses data, the relationships of ln$\dot{\varepsilon}$-lnσ (Figure 3a), ln$\dot{\varepsilon}$-σ (Figure 3b) as well as ln$\dot{\varepsilon}$-ln[sinh($\alpha\sigma$)] (Figure 3c) can be plotted. The average linear slopes on the obtained diagrams allow determining the material constants n_1, β, and n as 5.405, 0.0626, and 3.942, respectively, as well as α parameter (0.0116). Based on the transformation of Equation (8) and the subsequent average slopes of linear regression lines of ln[sinh($\alpha\sigma$)]-($1/T$) relationships presented in Figure 3d, the deformation activation energy Q can be determined as 195.682 kJ/mol. The presented activation energy value for Ti-1023 alloy deformed near and above β transus temperatures is quite close to the activation energy presented for that type of titanium alloy deformed in compression at β phase temperature ranges noted in other studies 172 kJ/mol [13] and 210.45 kJ/mol [15] for Ti-1023 alloy or 222.173 kJ/mol for Ti-555211 alloy [34]. It should be noted that the calculated activation energy for the β phase region is significantly lower as compared to the α + β phase region for β titanium alloys. In addition, the obtained calculated Q value for the investigated alloy is slightly higher as compared to the self-diffusion activation energy for β titanium (153 kJ/mol) or α titanium (169 kJ/mol) [35,36]. It is generally accepted that the calculated Q value is much higher than the value of self-diffusion energy, indicating the presence of globularization or DRX as a predominant mechanism during deformation, while closer activation energy value is a characteristic feature for DRV [37]. In this regard, it should be considered that DRV is the predominant deformation mechanism for Ti-1023 alloy at temperatures above β transus temperature. This fact is also confirmed by the analysis of the flow stress curves (Figure 2), which in most of the cases showed steady state flow of the material without distinct dynamic softening effects.

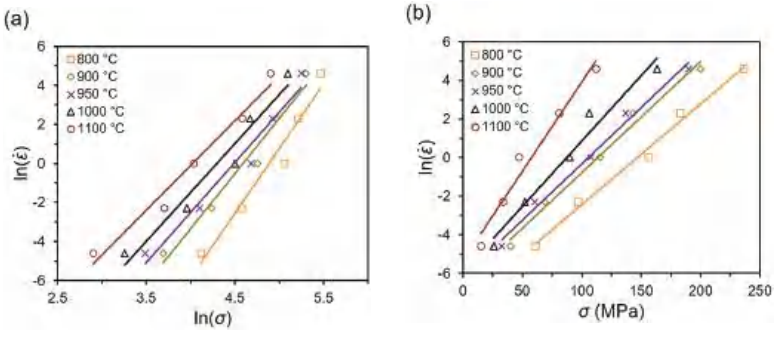

Figure 3. *Cont.*

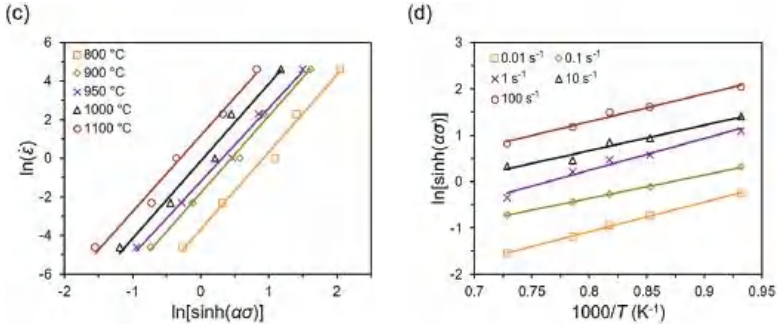

Figure 3. Relationships between (**a**) $\ln\dot{\varepsilon}$ and $\ln\sigma$, (**b**) $\ln\dot{\varepsilon}$ and σ, (**c**) $\ln\dot{\varepsilon}$ and $\ln[\sinh(\alpha\sigma)]$, (**d**) $\ln[\sinh(\alpha\sigma)]$ and $(1/T)$ for a true strain of 1.

After the conversion to logarithmic form, Equation (5) can be written as:

$$\ln Z = \ln A + n \ln[\sin h(\alpha\sigma)] \tag{9}$$

From the relationship between ln*Z* and $\ln[\sinh(\alpha\sigma)]$ (Figure 4) obtained using Equations (5) and (9), the ln*A* (18.243) was calculated by linear regression with high correlation coefficient (R = 0.989). In addition, the obtained fitting curve also allows to determine the n value as 3.934, and the small deviations between both presented values confirms the accuracy of both calculation methods.

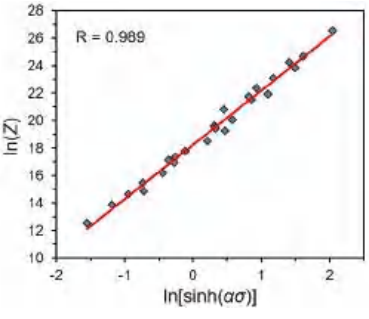

Figure 4. The relationship between ln*Z* and $\ln[\sinh(\alpha\sigma)]$.

Basing on the hyperbolic law, the flow stress as a function of the Zener-Hollomon parameter variable can be expressed as:

$$\sigma = \frac{1}{\alpha} \ln\left\{ \left(\frac{Z}{A}\right)^{\frac{1}{n}} + \left[\left(\frac{Z}{A}\right)^{\frac{2}{n}} + 1\right]^{\frac{1}{2}} \right\} \tag{10}$$

Taking into account the previously calculated material constants n, α, and A, the equation describing the flow stress at a constant true strain value can be given as:

$$\sigma = \frac{1}{0.0116} \ln\left\{ \left(\frac{Z}{8.372 \times 10^7}\right)^{\frac{1}{3.942}} + \left[\left(\frac{Z}{8.372 \times 10^7}\right)^{\frac{2}{3.942}} + 1\right]^{\frac{1}{2}} \right\} \tag{11}$$

3.3. Strain Compensated Constitutive Model

One of the main deformation parameters that affect the DRV and DRX mechanisms is a true strain. During hot compression, the true stress-true strain relationship describes the flow behavior of the material, inter alia work hardening, and flow softening effects. It is also known that the material parameters also depend on strain level, which was not taken into account before this stage of this research. The compensation of strain for description of hot deformation behavior can be considered basing on the polynomial functions of the strain for the given material parameters [25,38]. In these studies, the polynomial function was used to describe the influence of α, n, Q, and A material parameters on true strain range of 0.1 to 1, at 0.1 interval (Figure 5), for the investigated temperatures and strain rates. It was determined that the 6th-order polynomial function (Equation (12)) is the most optimal for describing variable material parameters as a function of true strain.

$$\begin{cases} \alpha = B_0 + B_1\varepsilon + B_2\varepsilon^2 + B_3\varepsilon^3 + B_4\varepsilon^4 + B_5\varepsilon^5 + B_6\varepsilon^6 \\ n = C_0 + C_1\varepsilon + C_2\varepsilon^2 + C_3\varepsilon^3 + C_4\varepsilon^4 + C_5\varepsilon^5 + C_6\varepsilon^6 \\ Q = D_0 + D_1\varepsilon + D_2\varepsilon^2 + D_3\varepsilon^3 + D_4\varepsilon^4 + D_5\varepsilon^5 + D_6\varepsilon^6 \\ lnA = F_0 + F_1\varepsilon + F_2\varepsilon^2 + F_3\varepsilon^3 + F_4\varepsilon^4 + F_5\varepsilon^5 + F_6\varepsilon^6 \end{cases} \quad (12)$$

The coefficients (B_i, C_i, D_i and F_i, for i = 0–6) for Equation (12) were obtained from the polynomial approximation (red lines) of the material parameters presented in Figure 5, and are given in Table 1.

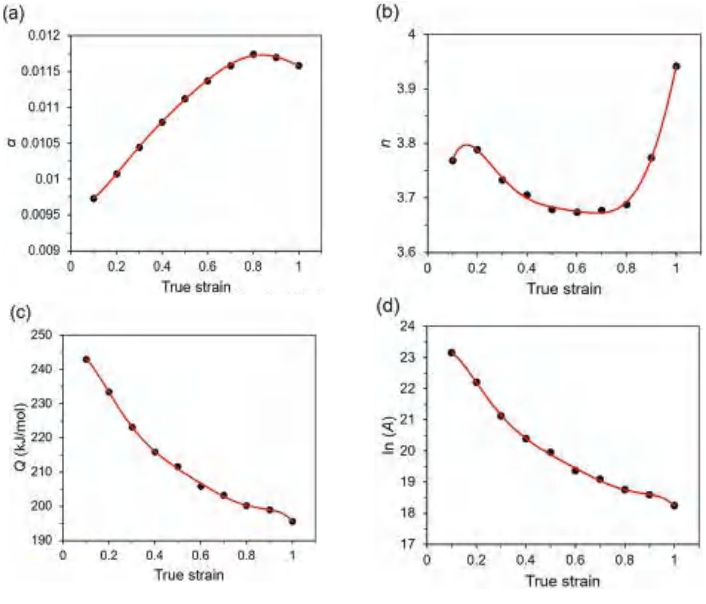

Figure 5. Material parameters (**a**) α, (**b**) n, (**c**) Q, and (**d**) ln$A$ for various true strain levels.

Table 1. The coefficients of material parameters α, n, Q, and A obtained basing on polynomial fitting.

α	n	Q, kJ/mol	ln$A$
$B_0 = 0.0097$	$C_0 = 3.4595$	$D_0 = 240.38$	$F_0 = 22.69$
$B_1 = -0.0027$	$C_1 = 5.8104$	$D_1 = 161.47$	$F_1 = 20.393$
$B_2 = 0.0411$	$C_2 = -35.627$	$D_2 = -1874.9$	$F_2 = -215.18$
$B_3 = -0.1249$	$C_3 = 97.715$	$D_3 = 6089.3$	$F_3 = 687.83$
$B_4 = 0.1933$	$C_4 = -136.94$	$D_4 = -9574.8$	$F_4 = -1070.8$
$B_5 = -0.1502$	$C_5 = 94.922$	$D_5 = 7379.5$	$F_5 = 817.86$
$B_6 = 0.0453$	$C_6 = -25.4$	$D_6 = -2225.2$	$F_6 = -244.58$

After determining the material parameters as a function of true strain, flow stresses were calculated taking into account the strain compensated constitutive model adopted for description of hot deformation behavior of Ti-1023 alloy at the investigated temperatures, strain and strain rate ranges. Figure 6 presents the experimental flow stresses obtained during hot compression tests and the flow stresses calculated on the basis of the constitutive equations and also taking into account various strain levels. As can be seen in Figure 6, there is a high correlation between the calculated and experimental flow stress values.

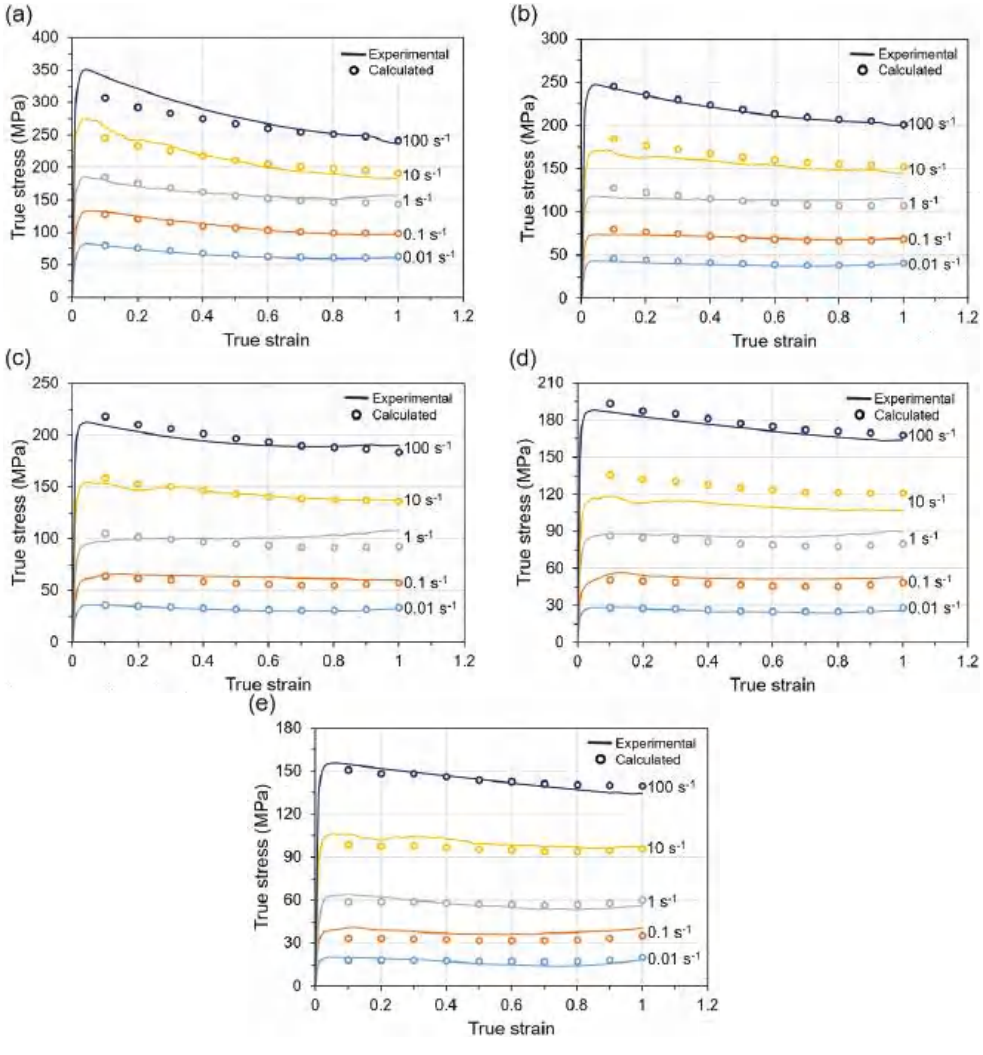

Figure 6. Experimental and calculated flow stresses for Ti-1023 alloy for deformation temperatures of (**a**) 800 °C, (**b**) 900 °C, (**c**) 950 °C, (**d**) 1000 °C, (**e**) 1100 °C.

The verification of the developed strain compensated model is based on discrepancies between experimental and calculated flow stress data. The most indicative parameters of

data prediction are the correlation coefficient (R) and an average absolute relative error ($AARE$, %), that can be determined by Equations (13) and (14), respectively [11].

$$R = \frac{\sum_{i=1}^{N}(E_i - \overline{E})(P_i - \overline{P})}{\sqrt{\sum_{i}^{N}(E_i - \overline{E})^2 (P_i - \overline{P})^2}} \quad (13)$$

$$AARE = \frac{1}{N}\sum_{i=1}^{N}\left|\frac{E_i - P_i}{E_i}\right| \times 100\% \quad (14)$$

where E_i is experimental flow stress and P_i is calculated flow stress, $\overline{E}$ and $\overline{P}$ are the mean values betwen experimental and calculated flow stress, N is the total number of data.

It is generally accepted that when the value of R coefficient is closer to 1 with small $AARE$ value, then higher accuracy of flow stress calculations can be obtained. The developed strain compensated constitutive model describing flow behavior of Ti-1023 alloy is characterized by R value of 0.9905 and the low $AARE$ (5.07%) level. As can be seen in Figure 7, the relationship between calculated and experimental data points is almost linear, which confirms the high accuracy of the developed model.

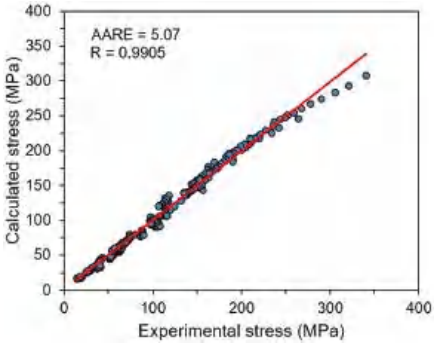

Figure 7. The correlation between calculated and experimental flow stresses for Ti-1023 alloy.

3.4. Processing Maps

The approaches based on DMM theory using criteria determining the material flow instability are an effective tool for describing the hot workability of the materials. The stability criterion developed by Prasad has shown its effectiveness in predicting the deformation behavior of many alloys [4,39–44]. The distribution of power dissipation and flow instability parameters in the form of maps allows controlling changes in microstructure during the deformation of the investigated material. The fundamental parameter in DMM is the efficiency of power dissipation (η), which indicates the power dissipated through microstructural development mechanisms such as phase transformations, DRV or DRX [40,42,45] and can be determined as:

$$\eta = \frac{2m}{m+1} \quad (15)$$

where m is the strain rate sensitivity parameter, which can be defined as a function of strain rate $\dot{\varepsilon}$ ($m = \partial \log\sigma / \partial \log \dot{\varepsilon}$).

It is well known that a higher value of the η parameter corresponds to a better hot workability of the material due to a larger share of the power dissipated resulting from changes in the material microstructure. On the other hand, the flow instability during hot deformation of the material can be described using the criterion (ξ) proposed by Prasad [42,44]:

$$\xi(\dot{\varepsilon}) = \frac{\partial \ln\left(\frac{m}{m+1}\right)}{\partial \ln \dot{\varepsilon}} + m \leq 0 \tag{16}$$

Negative vales of instability criterion parameter ξ reflects the instability of the material flow that can be characterized by adiabatic shear bands, kink bands, Lüders bands, flow localization, or cracking [43,46]. The superimposition of power dissipation map on instability map allows to develop the processing map for the investigated deformation parameters. Basing on the processing maps, it is possible to optimize the thermomechanical processing parameters and the material flow behavior can be predicted.

Basing on the DMM as well as on Prasad stability criterion, the processing maps for the deformation temperature range from 800 °C to 1100 °C and strain rate range of 0.01–100 s^{-1}, and for true strains 0.2, 0.6 and 1 (Figure 8) were developed. These maps represent the distribution of η parameter expressed as a percentage (black isoclines) and instability criterion $\xi \leq 0$ (gray shaded areas with red borders). The nature of the distribution of the efficiency of power dissipation indicates that the hot workability of the investigated titanium alloy is better at lower strain rates, which is typical for many titanium alloys and particularly for β titanium alloys [7,9,47,48]. As can be seen in Figure 8, the tendency of the distribution of the efficiency of power dissipation does not change with the change of the true strain value. It is generally accepted that the value of the efficiency of power dissipation in the range of 20–35% indicates DRV, while more than 35% is associated with DRX or superplasticity [7]. The high values of the η parameter can also indicate high ductility of large grains caused by substructure formation mechanisms [49,50]. As can be seen from the distribution of power dissipation, the DRV is the predominant deformation mechanism at the investigated deformation conditions.

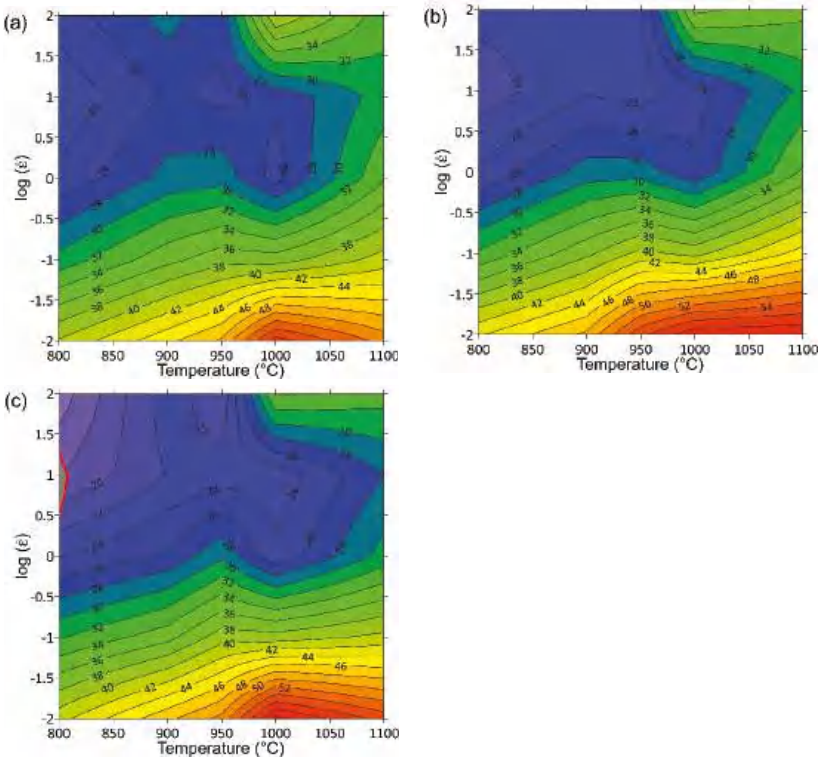

Figure 8. Processing maps for Ti-1023 alloy developed for true strains of (**a**) 0.2, (**b**) 0.6, and (**c**) 1.

The distribution of criterion ξ shows that the flow instability (a negative values of ξ) appears only in a small area for the true strain of 1 (Figure 8c), at strain rates from 3 s^{-1} to 6 s^{-1} and deformation temperatures in the range of 800–810 °C. This means that the flow behavior of Ti-1023 is quite stable under the investigated deformation conditions. It should also be emphasized that the noted instability area is characterized by the low efficiency of power dissipation (21–17%), and it is also one of the reasons not to recommend the hot deformation under parameters corresponding to this range of processing parameters.

Based on the distribution of flow instability parameter ξ as well as the η parameter, the processing windows describing the most useful combinations of hot deformation parameters can be determined. First of all, a domain should be distinguished (first processing window), with peak values of the efficiency of power dissipation in the range from 56% to 60%, in the temperature range from 950 °C to 1050 °C and low ($\geq$0.04 s^{-1}) strain rates. The second processing window is located in the domain at the temperature range of 980–1050 °C and strain rates $\leq$ 60 s^{-1} with peak value of parameter η in the range of 38–34%. The hot workability of Ti-1023 alloy can be improved by the application of deformation conditions corresponding to the proposed process windows.

3.5. The Microstructure Evolution

Figure 9 presents the microstructures of the specimens deformed in compression under various deformation temperatures and strain rates. The microstructure of the material deformed at temperature of 800 °C and strain rate of 0.01 s^{-1} (Figure 9a) is characterized by fine α phase precipitates, still remaining in the microstructure of the original β grains. An increase in the deformation temperature to 1000 °C (Figure 9b) leads to the complete dissolution of the α phase precipitates and to the effects associated with the DRV. The grain growth and deformation of the original β grains as well as the subsequent formation of the substructure as a result of deformation are observed. Such changes in the microstructure can be associated with superplasticity of large grains at low deformation strain rates, which was also reported in other studies [49,51]. In addition, the high value of parameter η (56–60%) indicates better workability during such deformation conditions as a result of a greater power dissipated due to the microstructural changes. The microstructure of the material deformed in the β phase region at temperature of 900 °C and strain rate of 1 s^{-1} is presented in Figure 9c. An increase in strain rate causes the original β grains to elongate in the direction of the material flow and the β grains boundaries are serrated. This effect is associated with DRV and affects the further nucleation of grains at the prior β phase boundaries, which is also visible in Figure 9c and is typical for DRX. At the highest deformation temperature and highest strain rate (Figure 9d), recrystallized grains and partial recrystallization of the microstructure can be observed.

As can be seen in Figure 10, the microstructure of the material deformed at 800 °C and under strain rate of 10 s^{-1} (conditions corresponding to instability area at processing map developed according to the Prasad criterion) indicates instability of the material flow (flow localization). It should be noted that the microstructure also contains, in addition to β grains, small particles of the α phase. It is known that inhomogeneous deformation of β grains can be associated with dislocations stuck at the interface between the α + β and β phases at high strain rates [47]. Taking into account the above analysis, the hot workability of Ti-1023 alloy under processing parameters corresponding to the presented flow instability is not recommended.

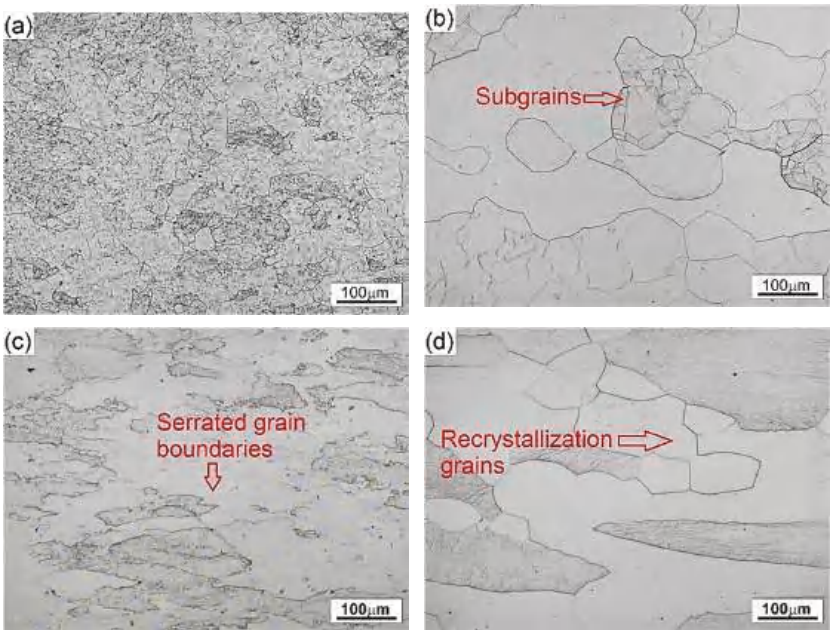

Figure 9. The microstructures of Ti-1023 alloy deformed under chosen processing conditions: (**a**) 800 °C and 0.01 s^{-1}, (**b**) 1000 °C and 0.01 s^{-1}, (**c**) 900 °C and 1 s^{-1}, (**d**) 1100 °C and 100 s^{-1}.

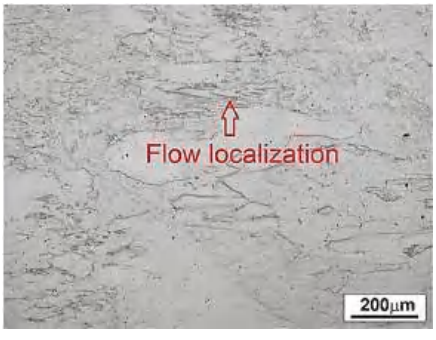

Figure 10. The microstructure of Ti-1023 alloy deformed under thermomechanical parameters corresponding to flow instability area.

4. Conclusions

The analysis of deformation behavior of β Ti-1023 alloy at temperatures near and above β transus temperature leads to the following conclusions:

- Basing on the Arrhenius-type equation, the strain compensated constitutive model was developed for the description of the flow behavior of the investigated alloy during high-temperature deformation. Very low value of average absolute relative error and high correlation between calculated values of flow stress and experimentally obtained flow stresses confirmed a high accuracy of the developed model.
- The processing maps were generated upon the Prasad stability criterion for the investigated deformation conditions. The most favorable parameters of the alloy processing, as well as the areas of instability of the material flow, have been established. Generally, the high material flow stability was revealed.

- It was confirmed that the dynamic recovery is the main mechanism operating during the high-temperature deformation of Ti-1023 alloy. The analysis of the microstructure of the material deformed under the assumed thermomechanical conditions showed that DRV mechanisms, such as formation of subgrains or formation of serrated grain boundaries, play an important role in deformation behavior of this alloy.

Author Contributions: Conceptualization, O.L. and T.Ś.; methodology, O.L., T.Ś., and A.Ł.-S.; validation, O.L., T.Ś., and A.Ł.-S.; formal analysis, K.Z. and M.W.; investigation, O.L., T.Ś., A.Ł.-S., and M.W.; writing—original draft preparation, O.L., T.Ś., A.Ł.-S., and K.Z.; writing—review and editing, O.L. and T.Ś. All authors have read and agreed to the published version of the manuscript.

Funding: The research project was financed by the Ministry of Science and Higher Education (AGH—research subsidy No. 16.16.110.663).

Institutional Review Board Statement: Not applicable.

Informed Consent Statement: Not applicable.

Data Availability Statement: Data sharing is not applicable to this article.

Conflicts of Interest: The authors confirm that they have no conflict of interest.

References

1. Boyer, R.R.; Briggs, R.D. The use of β titanium alloys in the aerospace industry. *J. Mater. Eng. Perform.* **2005**, *14*, 681–685. [CrossRef]
2. Jackson, M.; Dashwood, R.; Flower, H.; Christodoulou, L. The microstructural evolution of near beta alloy Ti-10V-2Fe-3Al during subtransus forging. *Metall. Mater. Trans. A* **2005**, *36*, 1317–1327. [CrossRef]
3. Zyguła, K.; Wojtaszek, M.; Lypchanskyi, O.; Śleboda, T.; Korpała, G.; Prahl, U. The Investigation on Flow Behavior of Powder Metallurgy Ti-10V-2Fe-3Al Alloy Using the Prasad Stability Criterion. *Metall. Mater. Trans. A* **2019**, *50*, 5314–5323. [CrossRef]
4. Zyguła, K.; Wojtaszek, M.; Śleboda, T.; Lech, S.; Lypchanskyi, O.; Korpała, G.; Prahl, U. The Influence of Induction Sintering on Microstructure and Deformation Behavior of Ti-5Al-5Mo-5V-3Cr Alloy. *Metall. Mater. Trans. A* **2021**. [CrossRef]
5. Jackson, M.; Jones, N.G.; Dye, D.; Dashwood, R.J. Effect of initial microstructure on plastic flow behaviour during isothermal forging of Ti-10V-2Fe-3Al. *Mater. Sci. Eng. A* **2009**, *501*, 248–254. [CrossRef]
6. Zhao, J.; Zhong, J.; Zhou, M.; Chai, F.; Yan, F. The effect of alpha phase on flow softening and deformation of Ti-10V-2Fe-3Al. *Mater. Sci. Technol.* **2017**, *33*, 1993–2003. [CrossRef]
7. Xiao, Y.-W.; Lin, Y.C.; Jiang, Y.-Q.; Zhang, X.-Y.; Pang, G.-D.; Wang, D.; Zhou, K.-C. A dislocation density-based model and processing maps of Ti-55511 alloy with bimodal microstructures during hot compression in α + β region. *Mater. Sci. Eng. A* **2020**, *790*, 139692. [CrossRef]
8. Liu, Q.; Wang, Z.; Yang, H.; Ning, Y. Hot Deformation Behavior and Processing Maps of Ti-6554 Alloy for Aviation Key Structural Parts. *Metals* **2020**, *10*, 828. [CrossRef]
9. Fan, J.K.; Kou, H.C.; Lai, M.J.; Tang, B.; Chang, H.; Li, J.S. Characterization of hot deformation behavior of a new near beta titanium alloy: Ti-7333. *Mater. Des.* **2013**, *49*, 945–952. [CrossRef]
10. Zhan, H.; Wang, G.; Kent, D.; Dargusch, M. Constitutive modelling of the flow behaviour of a β titanium alloy at high strain rates and elevated temperatures using the Johnson–Cook and modified Zerilli–Armstrong models. *Mater. Sci. Eng. A* **2014**, *612*, 71–79. [CrossRef]
11. Lin, Y.C.; Huang, J.; Li, H.-B.; Chen, D.-D. Phase transformation and constitutive models of a hot compressed TC18 titanium alloy in the α+β regime. *Vacuum* **2018**, *157*, 83–91. [CrossRef]
12. Wu, J.; Lü, Z.; Zhang, C.; Han, J.; Zhang, H.; Zhang, S.; Hayat, M.; Cao, P. Investigation of the Deformation Mechanism of a near β Titanium Alloy through Isothermal Compression. *Metals* **2017**, *7*, 498. [CrossRef]
13. Zhao, J.; Zhong, J.; Yan, F.; Chai, F.; Dargusch, M. Deformation behaviour and mechanisms during hot compression at supertransus temperatures in Ti-10V-2Fe-3Al. *J. Alloys Compd.* **2017**, *710*, 616–627. [CrossRef]
14. OuYang, D.L.; Fu, M.W.; Lu, S.Q. Study on the dynamic recrystallization behavior of Ti-alloy Ti-10V-2Fe-3V in β processing via experiment and simulation. *Mater. Sci. Eng. A* **2014**, *619*, 26–34. [CrossRef]
15. Quan, G.-Z.; Zou, Z.-Y.; Wen, H.-R.; Pu, S.-A.; Lv, W.-Q. A Characterization of Hot Flow Behaviors Involving Different Softening Mechanisms by ANN for As-Forged Ti-10V-2Fe-3Al Alloy. *High Temp. Mater. Proc.* **2015**, *34*, 651–665. [CrossRef]
16. Bobbili, R.; Ramudu, B.V.; Madhu, V. A physically-based constitutive model for hot deformation of Ti-10-2-3 alloy. *J. Alloys Compd.* **2017**, *696*, 295–303. [CrossRef]
17. Bao, R.Q.; Huang, X.; Huang, L.J.; Cao, C.X. Optimisation of hot die forging processes of Ti-10V-2Fe-3Al alloy. *Mater. Sci. Technol.* **2005**, *21*, 451–458. [CrossRef]

18. Quan, G.-Z.; Lv, W.-Q.; Liang, J.-T.; Pu, S.-A.; Luo, G.-C.; Liu, Q. Evaluation of the hot workability corresponding to complex deformation mechanism evolution for Ti-10V-2Fe-3Al alloy in a wide condition range. *J. Mater. Process. Tech.* **2015**, *221*, 66–79. [CrossRef]
19. Opěla, P.; Schindler, I.; Kawulok, P.; Kawulok, R.; Rusz, S.; Navrátil, H.; Jurča, R. Correlation among the Power Dissipation Efficiency, Flow Stress Course, and Activation Energy Evolution in Cr-Mo Low-Alloyed Steel. *Materials* **2020**, *13*, 3480. [CrossRef]
20. Zhou, P.; Deng, L.; Zhang, M.; Gong, P.; Wang, X. Characterization of Hot Workability of 5052 Aluminum Alloy Based on Activation Energy-Processing Map. *J. Mater. Eng. Perform.* **2019**, *28*, 6209–6218. [CrossRef]
21. Duan, Y.; Ma, L.; Qi, H.; Li, R.; Li, P. Developed constitutive models, processing maps and microstructural evolution of Pb-Mg-10Al-0.5B alloy. *Mater. Charact.* **2017**, *129*, 353–366. [CrossRef]
22. Cai, Z.; Ji, H.; Pei, W.; Tang, X.; Huang, X.; Liu, J. Hot workability, constitutive model and processing map of 3Cr23Ni8Mn3N heat resistant steel. *Vacuum* **2019**, *165*, 324–336. [CrossRef]
23. Wang, Y.; Zhao, G.; Xu, X.; Chen, X.; Zhang, C. Constitutive modeling, processing map establishment and microstructure analysis of spray deposited Al-Cu-Li alloy 2195. *J. Alloys Compd.* **2019**, *779*, 735–751. [CrossRef]
24. Jia, W.; Xu, S.; Le, Q.; Fu, L.; Ma, L.; Tang, Y. Modified Fields–Backofen model for constitutive behavior of as-cast AZ31B magnesium alloy during hot deformation. *Mater. Des.* **2016**, *106*, 120–132. [CrossRef]
25. Lin, Y.C.; Chen, X.-M. A critical review of experimental results and constitutive descriptions for metals and alloys in hot working. *Mater. Des.* **2011**, *32*, 1733–1759. [CrossRef]
26. Zyguła, K.; Wojtaszek, M.; Śleboda, T.; Lypchanskyi, O.; Rumiński, M.; Korpała, G.; Prahl, U. The analysis of hot deformation behavior of powder metallurgy Ti-10V-2Fe-3Al alloy using activation energy and Zener-Hollomon parameter. *Proc. Manuf.* **2020**, *50*, 546–551. [CrossRef]
27. Peng, X.; Guo, H.; Wang, T.; Yao, Z. Effects of β treatments on microstructures and mechanical properties of TC4-DT titanium alloy. *Mater. Sci. Eng. A* **2012**, *533*, 55–63. [CrossRef]
28. Gawad, J.; Kuziak, R.; Madej, L.; Szeliga, D.; Pietrzyk, M. Identification of rheological parameters on the basis of various types of compression and tension tests. *Steel Res. Int.* **2005**, *2*, 131–137. [CrossRef]
29. Plumeri, J.E.; Madej, Ł.; Misiolek, W.Z. Constitutive modeling and inverse analysis of the flow stress evolution during high temperature compression of a new ZE20 magnesium alloy for extrusion applications. *Mater. Sci. Eng. A* **2019**, *740-741*, 174–181. [CrossRef]
30. Warchomicka, F.; Poletti, C.; Stockinger, M. Study of the hot deformation behaviour in Ti-5Al-5Mo-5V-3Cr-1Zr. *Mater. Sci. Eng. A* **2011**, *528*, 8277–8285. [CrossRef]
31. Yang, X.; Wang, Y.; Dong, X.; Peng, C.; Ji, B.; Xu, Y.; Li, W. Hot deformation behavior and microstructure evolution of the laser solid formed TC4 titanium alloy. *Chin. J. Aeronaut.* **2021**, *34*, 163–182. [CrossRef]
32. Sellars, C.M.; McTegart, W.J. On the mechanism of hot deformation. *Acta Metall.* **1966**, *14*, 1136–1138. [CrossRef]
33. Zener, C.; Hollomon, J.H. Effect of strain rate upon plastic flow of steel. *J. Appl. Phys.* **1944**, *15*, 22–32. [CrossRef]
34. An, Z.; Li, J.; Feng, Y.; Liu, X.; Du, Y. Characterization of Hot Deformation Behavior of a New Near-β Titanium Alloy: Ti555211. *High Temp. Mater. Proc.* **2016**, *35*, 913–928. [CrossRef]
35. Sargent, P.M.; Ashby, M.F. Deformation maps for titanium and zirconium. *Scr. Metall.* **1982**, *16*, 1415–1422. [CrossRef]
36. Flower, H.M. Microstructural development in relation to hot working of titanium alloys. *Mater. Sci. Technol.* **1990**, *6*, 1082–1092. [CrossRef]
37. Chen, C.C.; Coyne, J.E. Deformation characteristics of Ti-6Al-4V alloy under isothermal forging conditions. *Metall. Mater. Trans. A* **1976**, *7*, 1931–1941. [CrossRef]
38. Lin, Y.C.; Chen, M.S.; Zhang, J. Constitutive modeling for elevated temperature flow behavior of 42CrMo steel. *Comput. Mater. Sci.* **2008**, *424*, 470–477. [CrossRef]
39. Lypchanskyi, O.; Śleboda, T.; Zyguła, K.; Łukaszek-Sołek, A.; Wojtaszek, M. Evaluation of Hot Workability of Nickel-Based Superalloy Using Activation Energy Map and Processing Maps. *Materials* **2020**, *13*, 3629. [CrossRef]
40. Prasad, Y.; Seshacharyulu, T. Processing maps for hot working of titanium alloys. *Mater. Sci. Eng. A* **1998**, *243*, 82–88. [CrossRef]
41. Lypchanskyi, O.; Śleboda, T.; Wojtaszek, M.; Muszka, K.; Łukaszek-Sołek, A.; Stanik, R.; Gude, M. The analysis of flow behavior of Ti-6Al-2Sn-4Zr-6Mo alloy based on the processing maps. *Int. J. Mater. Form.* **2020**. [CrossRef]
42. Srinivasan, N.; Prasad, Y.; Rao, P.R. Hot deformation behaviour of Mg-3Al alloy-A study using processing map. *Mater. Sci. Eng. A* **2008**, *476*, 146–156. [CrossRef]
43. Prasad, Y. Processing maps: A status report. *J. Mater. Eng. Perform.* **2003**, *12*, 638–645. [CrossRef]
44. Prasad, Y.; Sastry, D.H.; Deevi, S.C. Processing maps for hot working of a P/M iron aluminide alloy. *Intermetallics* **2000**, *8*, 1067–1074. [CrossRef]
45. Prasad, Y.V.R.K.; Gegel, H.L.; Doraivelu, S.M.; Malas, J.C.; Morgan, J.T.; Lark, K.A.; Barker, D.R. Modeling of dynamic material behavior in hot deformation: Forging of Ti-6242. *Metall. Mater. Trans. A* **1984**, *15*, 1883–1892. [CrossRef]
46. Łukaszek-Sołek, A.; Śleboda, T.; Krawczyk, J.; Bednarek, S.; Wojtaszek, M. Characterization of the workability of Ni-Fe-Mo alloy by complex processing maps. *J. Alloys Compd.* **2019**, *797*, 174–184. [CrossRef]
47. Wang, Z.; Wang, X.; Zhu, Z. Characterization of high-temperature deformation behavior and processing map of TB17 titanium alloy. *J. Alloys Compd.* **2017**, *692*, 149–154. [CrossRef]

48. Balasubrahmanyam, V.V.; Prasad, Y.V.R.K. Deformation behaviour of beta titanium alloy Ti-10V-4.5Fe-1.5Al in hot upset forging. *Mater. Sci. Eng. A* **2002**, *336*, 150–158. [CrossRef]
49. Morgan, G.C.; Hammond, C. Superplastic deformation properties of β-Ti alloys. *Mater. Sci. Eng.* **1987**, *86*, 159–177. [CrossRef]
50. Prasad, Y.V.R.K.; Seshacharyulu, T.; Medeiors, S.C.; Frazier, W.G. Effect of preform microstructure on the hot working mechanisms in ELI grade Ti-6Al-4V: Transformed β v. equiaxed (α+β). *Mater. Sci. Technol.* **2000**, *16*, 511–516. [CrossRef]
51. Bao, R.-Q.; Huang, X.; Cao, C.-X. Deformation behavior and mechanisms of Ti-1023 alloy. *Trans. Nonferrous Met. Soc. China* **2006**, *16*, 274–280. [CrossRef]

materials

MDPI

Article

Study on the Dynamic Recrystallization Behavior of 47Zr-45Ti-5Al-3V Alloy by CA–FE Simulation

Wenwei Zhang, Qiuyue Yang, Yuanbiao Tan *, Ya Yang *, Song Xiang and Fei Zhao

Guizhou Key Laboratory of Materials Mechanical Behavior and Microstructure, College of Materials and Metallurgy, Guizhou University, Guiyang 550025, China; Zww19960916@163.com (W.Z.); yangqy979@126.com (Q.Y.); sxiang@gzu.edu.cn (S.X.); fzhao@gzu.edu.cn (F.Z.)
* Correspondence: ybtan1@gzu.edu.cn (Y.T.); yangyaing@126.com (Y.Y.); Tel.: +86-147-8515-8006 (Y.T.)

Abstract: The dynamic recrystallization (DRX) behavior of 47Zr-45Ti-5Al-3V alloy was studied by using the experiment and numerical simulation method based on DEFORM-3D software and cellular automata (CA) over a range of deformation temperatures (850 to 1050 °C) and strain rates (10^{-3} to 10^{0} s^{-1}). The results reveal that the DRX behavior of 47Zr-45Ti-5Al-3V alloy strongly depends on hot-working parameters. With rising deformation temperature (T) and decreasing strain rate ($\dot{\varepsilon}$), the grain size (d_{DRX}) and volume fraction (X_{DRX}) of DRX dramatically boost. The kinetics models of the d_{DRX} and X_{DRX} of DRX grains were established. According to the developed kinetics models for DRX of 47Zr-45Ti-5Al-3V alloy, the distributions of the d_{DRX} and X_{DRX} for DRX grains were predicted by DEFORM-3D. DRX microstructure evolution is simulated by CA. The correlation of the kinetics model is verified by comparing the d_{DRX} and X_{DRX} between the experimental and finite element simulation (FEM) results. The nucleation and growth of dynamic recrystallization grains in 47Zr-45Ti-5Al-3V alloy during hot-working can be simulated accurately by CA simulation, comparing with FEM.

Keywords: 47Zr-45Ti-5Al-3V alloy; hot-working; DRX behavior; FEM; CA

Citation: Zhang, W.; Yang, Q.; Tan, Y.; Yang, Y.; Xiang, S.; Zhao, F. Study on the Dynamic Recrystallization Behavior of 47Zr-45Ti-5Al-3V Alloy by CA–FE Simulation. *Materials* **2021**, *14*, 2562. https://doi.org/10.3390/ma14102562

Academic Editor: Ivo Schindler

Received: 17 April 2021
Accepted: 7 May 2021
Published: 14 May 2021

1. Introduction

Zirconium alloys owns low thermal neutron absorption cross-section, superior mechanical properties for long term operations in high pressure and adequate corrosion resistance in contact with high-temperature water, which plays a significant role in structural materials of the aerospace field [1–3]. With the rapid development of the aviation industry, the increasing requirement in the mechanical properties was needed for the structural materials of the aerospace field. Recently, a series of new ZrTiAlV alloys with an ultrahigh strength were designed [4–9]. The mechanical properties of key components were depended on the microstructure produced during hot-working of the ZrTiAlV alloys, which was effected by hot processing parameters. Therefore, it is essential to deeply reveal the microstructure evolution and deformation mechanism of ZrTiAlV alloys at various hot-processing conditions. In the previous work, the hot-deformation behavior of ZrTiAlV alloys was investigated, and the constitutive equation and processing maps have established [7–11]. The hot-deformation behavior of new 47Zr-45Ti-5Al-3V alloy is significantly different from that of traditional zirconium alloys [12–15]. For the 47Zr-45Ti-5Al-3V alloy, the dynamic recrystallization is not easily occurred at low deformation temperature and high strain rate. Generally, DRX is regarded as an excellent way to refine the grain size of metals during the hot-working. However, no published investigation on the DRX kinetics behavior of 47Zr-45Ti-5Al-3V alloys has been carried out. Thus, it is critical to understand the microstructure evolution in the process of DRX and construct the DRX kinetics model for improving the mechanical properties of 47Zr-45Ti-5Al-3V alloy.

Recently, with the rapid increase in computer performance, the DRX kinetics of metals during hot-working has been qualitatively studied by using the software of FEM and

CA [16–24]. Irani et al. [16] investigated the DRX kinetics of the AA6060 aluminum alloy by the FEM method. The results demonstrated that controlling the number of element points can effectively improve efficiency and increase the accuracy of FEM. Ji et al. [17] embed the DRX kinetics model for 33Cr23Ni8Mn3N alloy into the DEFORM-3D software to characterize the relationship between hot-working parameters and the d_{DRX} and X_{DRX} of DRX grains. The result manifests a good consistent between the simulation and experimental results. Wu et al. [18] utilized a cellular automaton (CA) coupled with FEM by means of ABAQUS software to study the DRX microstructure evolution of AZ61 alloy. The simulation results correspond well to the experimental results. NithinBaler et al. [19] revealed the DRX mechanism of γ'-L12 alloy by the FEM methods, which was discontinuous dynamic recrystallization (DDRX). Geng et al. [20] also reported that the DRX evolution of GH4169 superalloy during hot-working can be better predicted by FEM software integrated with the developed kinetics model. Zhang et al. [21] studied the microstructure evolution of 7055 aluminum alloy in the rolling process by using FEM and CA methods, and found that CA method can more accurately simulate the evolution of DRX. Li et al. [22] utilized the 3D-CA method to describe the DRX behavior and mechanical response of the titanium alloy during the uneven deformation, which showed a good consistency with the results obtained by experimental test. All in all, the CA and FEM methods have been widely regarded as valid ways to predict the microstructure evolution in the DRX process of metals and alloys.

In order to reveal the DRX behavior and construct the DRX kinetics model of 47Zr-45Ti-5Al-3V alloy, in this present work, the CA–FE method is used to study the DRX behavior of 47Zr-45Ti-5Al-3V alloy from the macro- and micro-scales. A developed kinetics model of the DRX for 47Zr-45Ti-5Al-3V alloy was established. The microstructure evolution of the alloy in the process of DRX was analyzed by DEFORM-3D software and CA integrated with the developed kinetics and dislocation models. Additionally, a comparison of the difference between the experimental and simulated results has been carried out to testify the validity of FE–CA simulation.

2. Experiment

A forged 47Zr-45Ti-5Al-3V alloy (wt.%) was employed in this work. The specific preparation process has been introduced in the previous work [8]. The phase transformation temperature of $\beta \rightarrow \alpha + \beta$ for 47Zr-45Ti-5Al-3V alloy is 703 °C [5]. The forged alloy was solution-treatment at 1050 °C for 0.5 h and subsequently water-quench. Figure 1a depicts the initial microstructure of the solution-treated alloy with an average grain size of about 450 μm.

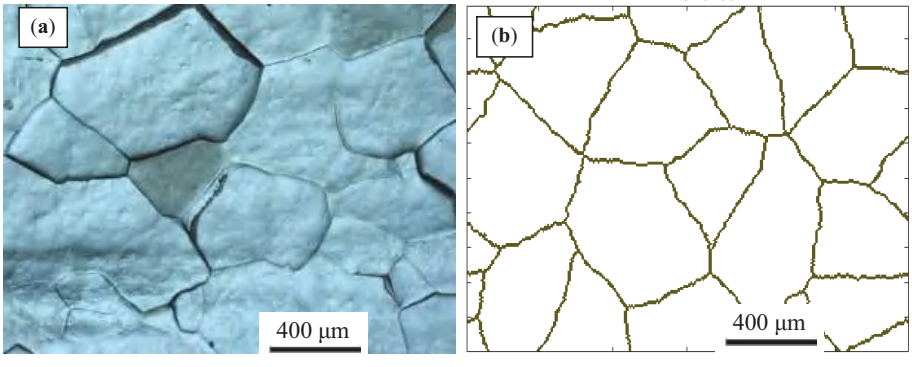

Figure 1. (**a**) Microstructure of the 47Zr-45Ti-5Al-3V alloy solution-treatment at 1050 °C for 0.5 h. (**b**) Initial microstructure simulated by CA.

Cylindrical samples of ø8 × 12 mm were prepared by the wire cutting. To analyze the DRX behavior and construct the DRX kinetics model of 47Zr-45Ti-5Al-3V alloy, hot compression test was conducted on a Gleeble 3500 at various testing conditions. The deformation temperature was set in the range of 850 to 1050 °C, and the strain rate was set in the range of 10^{-3} to 10^{0} s^{-1}. The schematic diagram of the experimental tests is shown in Figure 2. The testing samples were compressed to a true strain of 0.7. For preserving the microstructure of the deformed samples, the deformed samples were rapidly water-quenched to 20 °C.

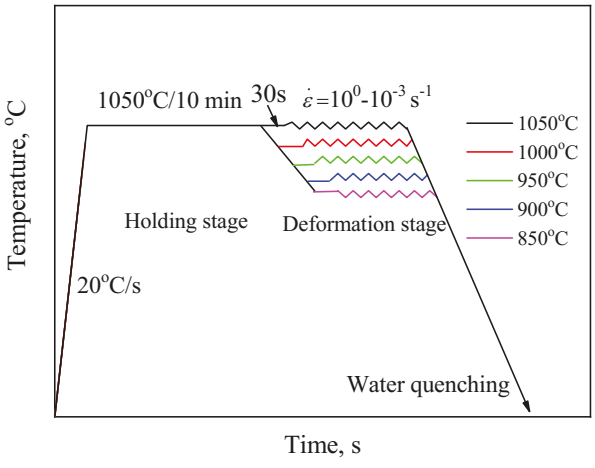

Figure 2. Schematic diagram of the experimental tests in this work.

For optical microstructure observation (OM) by using Leica DMI5000M, the deformed samples were ground and then etched by chemical means. The etching solution is a Kroll reagent of 15% HF, 40% HNO_3 and 45% H_2O (Vol.%). The value of the d_{DRX} and X_{DRX} of DRX grains was counted by the Image-Pro software (Media Cybernetics, Silver Spring, MD, USA).

3. Results and Discussion

3.1. Hot-Deformed Microstructure

Figure 3 presents typical stress–strain curves for the ZrTiAlV alloy at different temperatures. It is seen that the stress–strain curves illustrate a dynamic recovery characteristic at a low deformation temperature and high strain rate, while showing a dynamic recrystallization characteristic at a high deformation temperature and low strain rate. Figure 4 displays the representative deformed microstructures of the 47Zr-45Ti-5Al-3V alloy. At the strain rate of 1 s^{-1}, the initial grains of the samples deformed at the temperatures of 850 and 900 °C were elongated perpendicular to the compression direction of deformed samples, indicating that only DRV occurred. When the samples deformed at 950 °C/1 s^{-1}, a few fine grains of DRX formed at the grain boundaries of deformed grains, showing that dynamic recrystallization firstly took place under this deformation condition. As the deformation temperature increases and the $\dot{\varepsilon}$ decreases, the grain boundary migration rate is accelerated and the X_{DRX} and d_{DRX} of DRX grains increase. At the hot-working parameters of 1000 °C and 0.001 s^{-1}, the microstructure with uniform equiaxed grains can be achieved, revealing that a full DRX occurred during hot-working. When the T further raised to 1050 °C, there were obvious coarsening for the DRX grains. It is attributed to a fact that high deformation temperature and low $\dot{\varepsilon}$ provide enough energy and sufficient time for dynamic recrystallization to nucleate and grow, so the dynamic recrystallization is more sufficient under this condition.

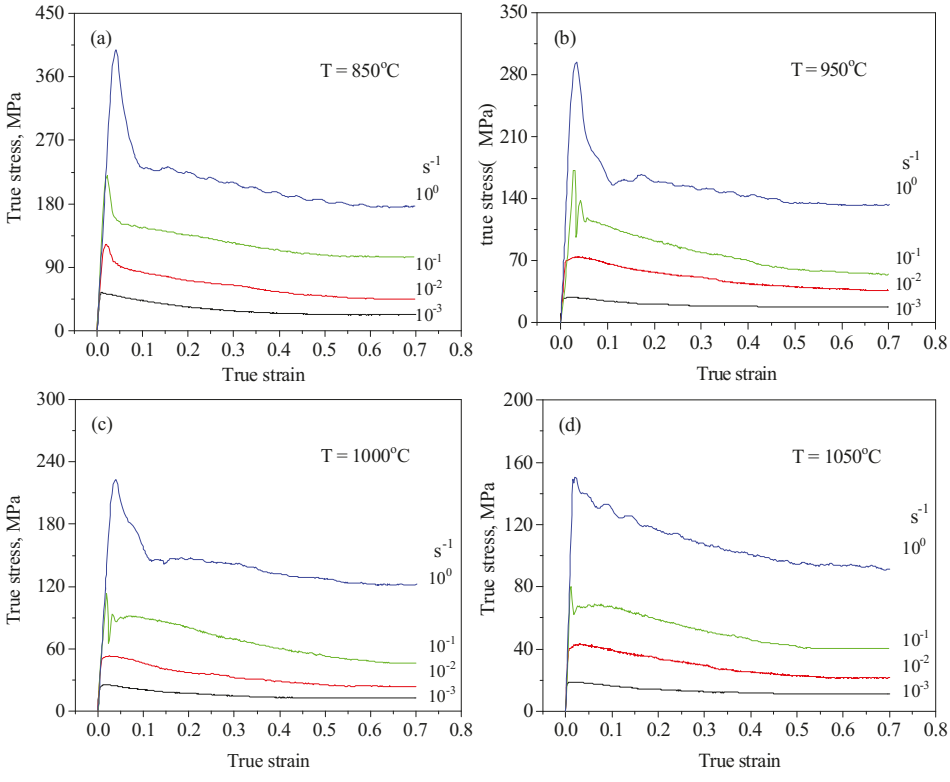

Figure 3. Typical stress–strain curves for the ZrTiAlV alloy at different temperatures [11]. (**a**) T = 850 °C; (**b**) T = 950 °C; (**c**) T = 1000 °C; (**d**) T = 1050 °C.

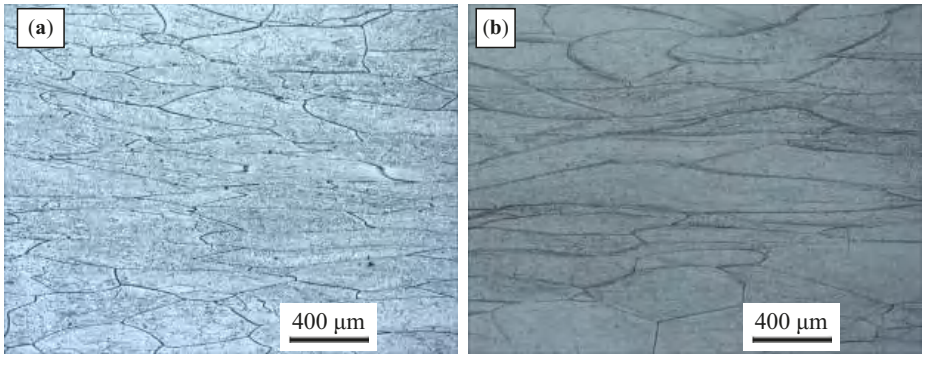

Figure 4. *Cont.*

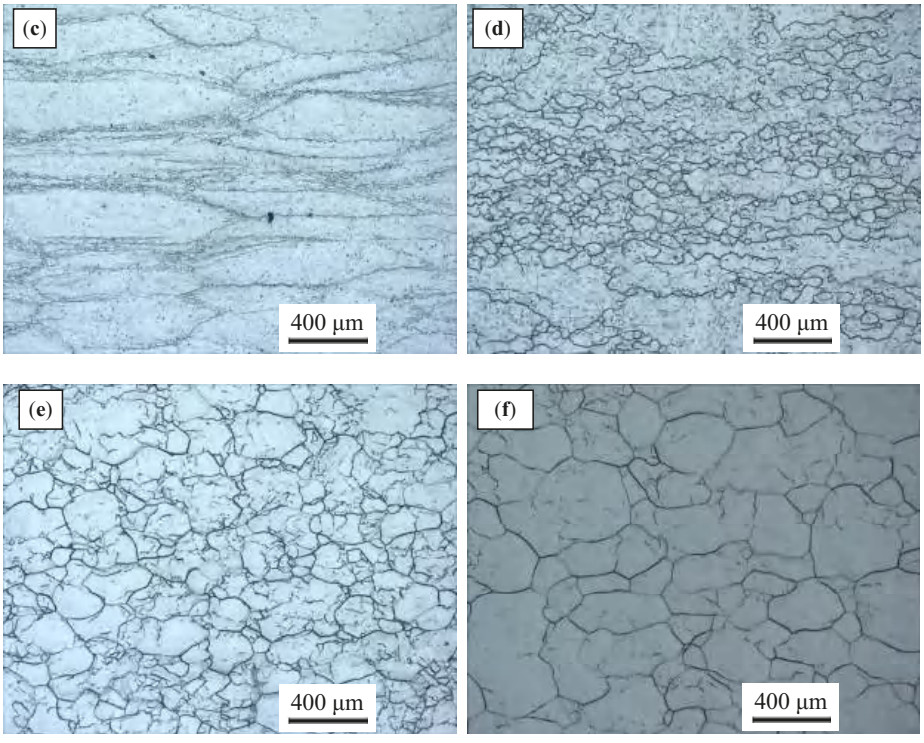

Figure 4. Optical microstructures of ZrTiAlV alloy under different hot-working conditions at the true strain of 0.7: (**a**) 850 °C, 1 s^{-1}; (**b**) 900 °C, 1 s^{-1}; (**c**) 950 °C, 0.1 s^{-1}; (**d**) 1000 °C, 0.01 s^{-1}; (**e**) 1000 °C, 0.001 s^{-1}; and (**f**) 1050 °C, 0.001 s^{-1}.

3.2. Peak Strain and Critical Strain

According to the flow curves obtained from hot-working, the peak strain (ε_p) of each flow curve is as listed in Table 1. It was observed that the ε_p gradually declined with the increment deformation temperature of at a given strain rate.

In previous work, the value of deformation activation energy (Q) was calculated to be 207.7 kJ/mol. The constitutive equation of the 47Zr-45Ti-5Al-3V alloy has been established according to the hyperbolic-sine Arrhenius-type equation as follows [11]:

$$\dot{\varepsilon} = 6.7 \times 10^8 [\sinh(\alpha\sigma_p)]^{3.09} \exp(-\frac{207700}{RT}) \quad (1)$$

Hence, the relationship between the ε_p and Zener–Hollomon parameter ($Z = \dot{\varepsilon} \exp(\frac{Q}{RT})$) can be characterized, as shown in Figure 5. The relation between the ε_p and Z can be written as the following formula [25–28]:

$$\varepsilon_p = 8.61 \times 10^{-5} Z^{0.39} \quad (2)$$

Generally, when the strain reaches a critical strain (ε_c) during hot-working, the DRX can occur due to the driving of dislocation accumulation and entanglement [29]. The critical strain (ε_c) is corresponding to the start point of DRX, which can be achieved by a turning point ($\partial(\partial\theta/\partial\sigma)/\partial\sigma = 0$) gained from the curve of strain hardening rate (θ) corresponding to the true stress (σ) [30,31]. In this present study, the values of ε_c at various hot-working

parameters were listed in Table 1. The relation between ε_c and ε_p can be expressed by the following [32]:

$$\varepsilon_c = \beta\varepsilon_p \quad (3)$$

where the value of β (material constant) can be achieved to be 0.67 by the data in Figure 6. By integrating Equation (2) with Equation (3), the ε_c can be written as follows:

$$\varepsilon_c = 5.77 \times 10^{-5} Z^{0.39} \quad (4)$$

Table 1. The values of ε_p and ε_c under various hot-working conditions.

Temperature	ε_p				ε_c			
	1 s^{-1}	**0.1 s^{-1}**	**0.01 s^{-1}**	**0.001 s^{-1}**	**1 s^{-1}**	**0.1 s^{-1}**	**0.01 s^{-1}**	**0.001 s^{-1}**
850 °C	0.38	0.21	0.12	0.07	-	-	-	-
900 °C	0.34	0.14	0.11	0.055	-	-	0.07	0.038
950 °C	0.26	0.1	0.083	0.025	0.17	0.06	0.05	0.018
1000 °C	0.17	0.08	0.03	0.012	0.13	0.05	0.018	0.006
1050 °C	0.13	0.05	0.02	0.01	0.09	0.03	0.01	0.004

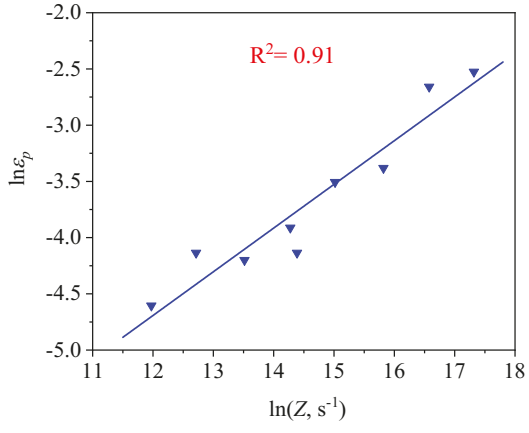

Figure 5. Relationship between the lnZ and lnε_p.

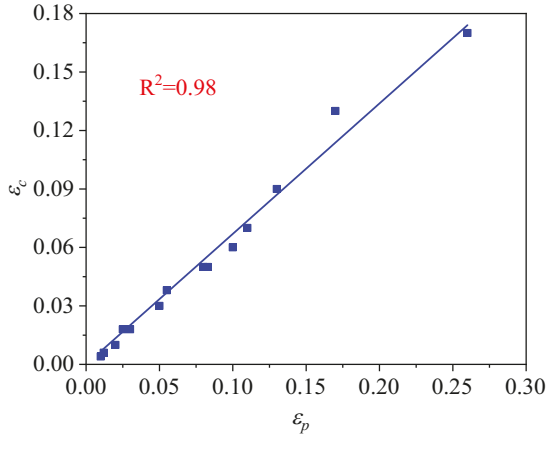

Figure 6. Relationship between the ε_c and ε_p.

3.3. Kinetics Model of DRX

The DRX behavior consisted of nucleation and growth during hot-working. For the discontinuous recrystallization mechanism, the nucleus of DRX grains generally formed in the grain boundaries, and then grew toward the interior of the grains with a high density nearby the grain boundaries. The X_{DRX} of DRX grains was significantly affected by the hot-working parameters, which is expressed by using the JMAK equation [32,33]:

$$X_{DRX} = 1 - \exp\left[-k \times \left(\frac{\varepsilon - \varepsilon_c}{\varepsilon_p}\right)^n\right] \quad (5)$$

where k and n represent the Avrami material constants. In previous work, the measuring of the X_{DRX} was usually obtained by OM and the Electron Backscatter Diffraction (EBSD) technique [33]; however, those methods require considerable calculations and are expensive to carry out. In order to solve the above problems, X_{DRX} is extensively computed based on the relationship between X_{DRX} and σ in the process of hot-working, which can be expressed as follows [34,35]:

$$X_{DRX} = \frac{\sigma_p - \sigma}{\sigma_p - \sigma_{ss}} \quad (6)$$

where σ_p and σ_{ss} are on behalf of the peak stress and the steady flow stress of the flow curve, respectively. To calculate the values of k and n in Equation (5), we take the natural logarithm on both sides of Equation (5), as written in Equation (7):

$$\ln[-\ln(1 - X_{DRX})] = \ln k + n \ln[(\varepsilon - \varepsilon_c)/\varepsilon_p] \quad (7)$$

The k and n (average values) can be calculated as 0.0021 and 1.88 by the data in Figure 7, respectively. Hence, the kinetic model of *DRX* was expressed as follows:

$$X_{DRX} = 1 - \exp\left[-0.0021 \times \left(\frac{\varepsilon - \varepsilon_c}{\varepsilon_p}\right)^{1.88}\right] \quad (8)$$

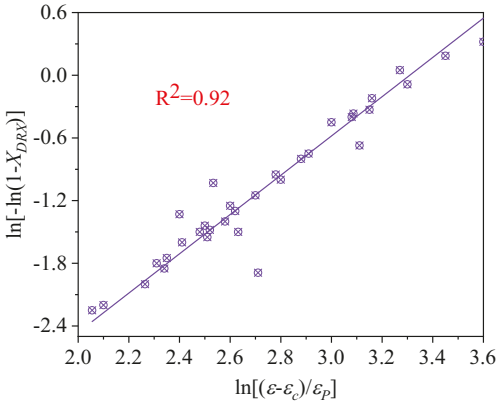

Figure 7. Relationship between $\ln[-\ln(1 - X_{DRX})]$ and $\mathrm{In}[(\varepsilon - \varepsilon_c)/\varepsilon_p]$.

The X_{DRX}-ε curves were obtained from the DRX kinetics model of 47Zr-45Ti-5Al-3V alloy at various deformation conditions, as shown in Figure 8. So, as to further analyze the growth behavior of DRX grains, the d_{DRX} as a function of Z parameter was characterized by the follow [35]:

$$d_{DRX} = CZ^{m_1} \quad (9)$$

where the C and m_1 are constants. The Equation (9) can be rewritten as the form of Equation (10):

$$\ln d_{DRX} = \ln C + m_1 \ln Z \tag{10}$$

The variation on the d_{DRX} with hot-working parameters was depicted in Figure 9. The material constants were calculated as C = 2565.73 and m_1 = −0.25, respectively. Therefore, the connection between the d_{DRX} and the Z parameter can be showed as follows:

$$d_{DRX} = 2565.73Z^{-0.25} \tag{11}$$

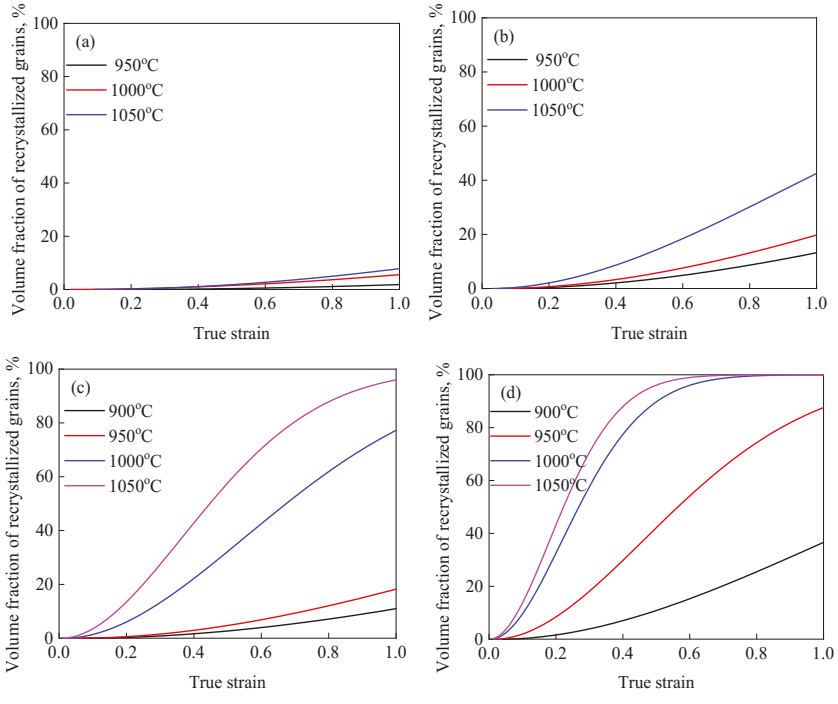

Figure 8. Variation in the X_{DRX} with true strain at different temperatures of (**a**) 1 s^{-1}, (**b**) 0.1 s^{-1}, (**c**) 0.01 s^{-1} and (**d**) 0.001 s^{-1}.

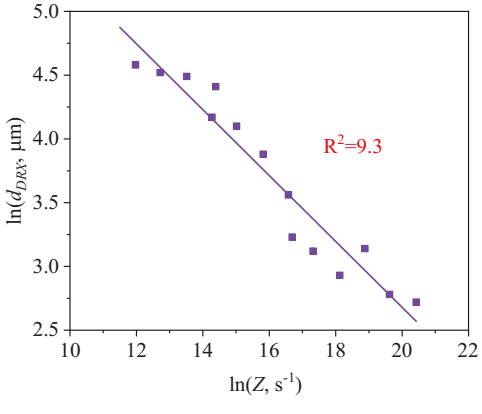

Figure 9. Relationship between lnd_{DRX} and lnZ.

3.4. FEM of DRX Behavior

Based on the DRX kinetic equation established above, the isothermal forging process was simulated by the DEFORM-3D software (Scientific Forming Technologies Corporation, Columbus, OH, USA) During the process of isothermal forging simulation, the elastic deformation can be usually ignored. Therefore, the workpiece was treated as an object with plasticity, while the tools were treated as an object with rigidity. For improving the efficiency of FEM calculation and increasing the accuracy of the simulation results, the FE model was established by symmetrical half cylinder. The sample for FEM was segmented in terms of tetrahedral meshes. The numbers of the meshes and the nodes were set to 26,538 and 4726, respectively. The top die was set as movable, while the bottom die was fixed. The coefficient of the friction was set to be 0.3 [33]. For the keeping consistency between experimental and the simulation results, the temperature of all items in the model was set to be consistent with the experimental temperature during the process of FEM. Figure 10 shows the sketch map of effective stress for FEM at the true strain of 0.7. It is seen that the deformation region is mainly divided into three different regions, according to the degree of the deformation, as marked in Figure 10. A heavy deformation took place in region *I*, while only a slight deformation was observed in region *II*. Usually, the region *II* is defined as the free deformation area. It is noted that non-deformation was presented in region *III*, namely "dead zone" [33,34]. This indicates that the plastic deformation of the samples is uneven.

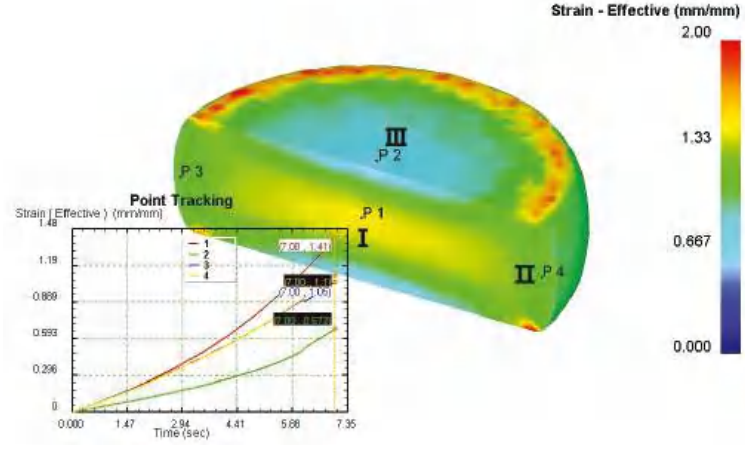

Figure 10. Diagram of deformation area.

Table 2 displays the distribution cloud maps of the d_{DRX} for 47Zr-45Ti-5Al-3V alloys. It is worth noting that the d_{DRX} distribution is uneven in different regions, due to the non-uniformity of deformation in the compression process. Under low T and high $\dot{\varepsilon}$ conditions, only a few DRX grains with small size formed in region *I*, while dynamic recrystallization cannot occur in region *III*, where the size of grains keeps the original grain size. With the augment of T and the drop of $\dot{\varepsilon}$, the size of DRX grains gradually increased. When the deformation condition is 1050 °C/0.001 s^{-1}, the size of DRX grains increased to approximately 128 μm. It is worth noting that the size of DRX grains in region *III* is higher than that in region *II*. Table 3 depicts the distribution cloud maps of the X_{DRX} deformed at the true strain of 0.7. It can be observed from Table 3 that the X_{DRX} is obviously low under low T and high $\dot{\varepsilon}$ conditions. With the augment of T and the drop of $\dot{\varepsilon}$, the X_{DRX} gradually increased. It is also important to note that the distribution of the X_{DRX} is also non-uniform in different regions during hot-working. Regions with a large degree of deformation have higher deformation storage energy, thereby promoting the nucleation of DRX [36–40]. The X_{DRX} in region *I* is higher than that in regions *II* and *III*.

Table 2. The distribution of d_{DRX} for 47Zr-45Ti-5Al-3V alloys deformed under various hot-working conditions at the true strain of 0.7.

Strain Rate/s^{-1}	Temperature/°C 900	950	1000	1050	d_{DRX}, μm
0.001					
0.01					
0.1	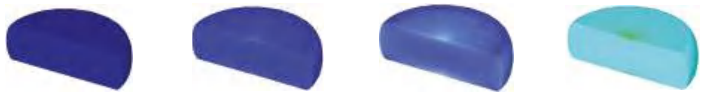				
1					

Table 3. The distribution of X_{DRX} for 47Zr-45Ti-5Al-3V alloys deformed under various hot-working conditions at the true strain of 0.7.

Strain Rate/s^{-1}	Temperature/°C 900	950	1000	1050	X_{DRX},%
0.001					
0.01					
0.1					
1					

Figures 11 and 12 illustrate a difference between the experimental and FEM results of d_{DRX} and X_{DRX}, respectively. A good consistency is observed between experimental and the simulation results. The change trends of d_{DRX} and X_{DRX} for the experimental and the simulation results are consistent. According to References [33,40], the correlation between the experimental and the simulation results was characterized by the correlation coefficient (R^2) and the average absolute relative error (Δ) value. It is seen from Figures 13 and 14 that the experimental results keep a linear relationship with the FEM results. The value of R^2 was 0.95 and 0.99 for the d_{DRX} and X_{DRX}, respectively. It is generally believed that DRX does not occur in the area where the X_{DRX} percentage is less than 5%; thus, the Δ value of the d_{DRX} and X_{DRX} for DRX grains was computed to be, respectively, 15.7% and 8.78%. This suggests that the DRX behavior of 47Zr-45Ti-5Al-3V alloy can be described well by the established kinetic equations that are embedded in the DEFORM-3D software.

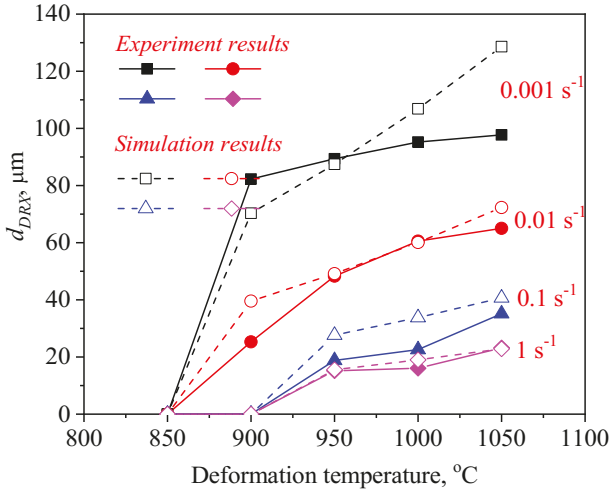

Figure 11. A comparison between the experimental and FE results of the grain size of recrystallized grains (d_{DRX}).

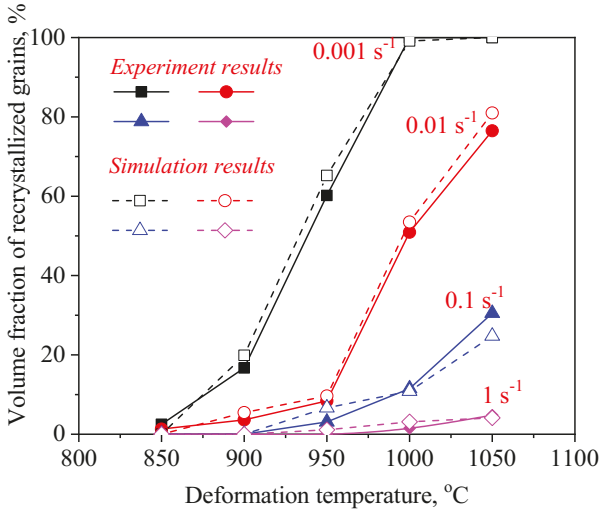

Figure 12. A comparison between the experimental and FE simulation results of the volume fraction of DRX (X_{DRX}).

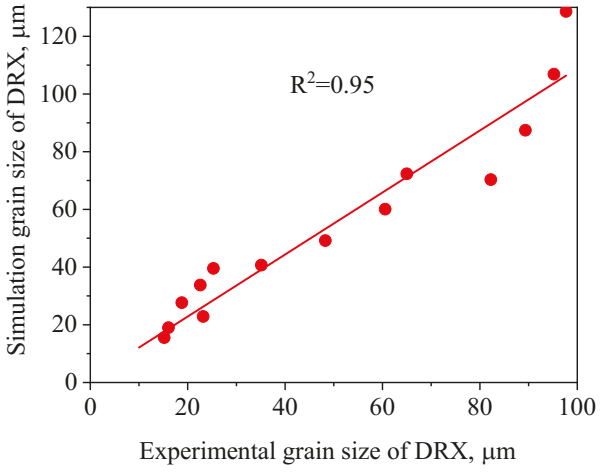

Figure 13. Correlation between the FEM and experimental grain size of DRX for 47Zr-45Ti-5Al-3V alloys after hot deformation.

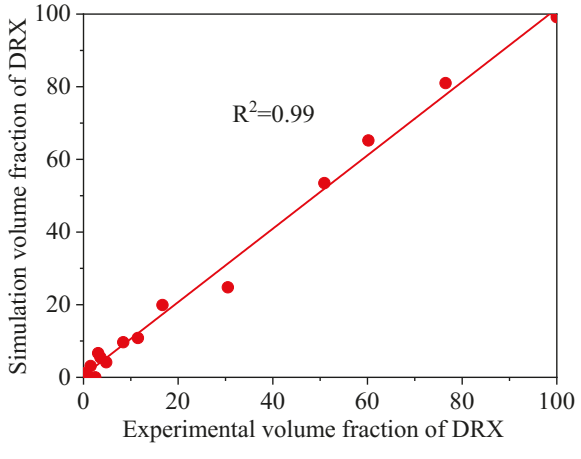

Figure 14. Correlation between the FEM and experimental volume fraction of DRX for 47Zr-45Ti-5Al-3V alloys after hot deformation.

3.5. CA of DRX Behavior

The CA method is a mathematical algorithm used to describe the evolution of a complex system in discrete space-time. Usually, the CA model consists of four basic elements: cell space, neighbor type, boundary conditions and cell state. The cell orientation is set to a random number from 1 to 180, and the cell transformation rule is "Moore neighbor". From the viewpoint of dislocation density, the plastic deformation of metals is attributed to dislocation slip and climbing. In the process of hot-working, the dislocation density in the matrix increases with the increase of strain, and the evolution of the microstructure during the hot deformation is always accompanied by the change of dislocation density. In the CA model, the dislocation model can be described as follows [22,41]:

$$\sigma = \alpha \mu b \sqrt{\rho} \quad (12)$$

$$\frac{d\rho}{d\varepsilon} = k_1\sqrt{\rho} - k_2\sqrt{\rho} \tag{13}$$

where the α is 0.5; ρ and $\overline{\rho}$ represent the dislocation density and average dislocation density respectively; b represents the Burger's vector; μ represents the shear modulus; and k_1 and k_2 represent work-hardening and dynamic-softening coefficients, respectively. There is no ρ gradient inside a single grain of alloy during the hot-working. The $\overline{\rho}$ during the CA simulation can be expressed as follows [42]:

$$\overline{\rho} = \frac{1}{N_0}\sum_{i,j}^{i=A,j=B}\rho_{i,j} \tag{14}$$

where A and B respectively represent the number of cells in the i and j directions; N_0 represents the total number of cells; and $\rho_{i,j}$ represents the dislocation density of the cell at coordinates (i, j). During the hot-working process, as the dislocation density reaches the critical dislocation density (ρ_c), the DRX grains begin to nucleate. In addition, the formation of DRX grains reduces the ρ of the alloy, and a new round of DRX occurs as the amount of deformation further increases. The nucleation rate ($\dot{n}$) is linearly related to the $\dot{\varepsilon}$ [22,42]:

$$\dot{n} = C\dot{\varepsilon}^{\alpha} \tag{15}$$

where C and α usually take 200 and 0.9, respectively.

Based on the initial microstructure of the solution-treated alloy, the initial solid solution structure was simulated by the CA simulation, as shown in Figure 1b. The experimental and predicted microstructures by CA after hot-working were displayed in Figure 15. The CA simulation results show that the evolution of DRX grains is strongly correlated with hot processing parameters. Figures 16 and 17 reveal that the experimental results keep a linear relationship with the CA results. The Δ value of the d_{DRX} and X_{DRX} for DRX grains was computed to be respectively 6.32% and 9.3%. In general, CA simulation has more accurate results than FEM simulation. However, FEM can more intuitively simulate the overall change of the alloy during the whole process of hot compression. The combination of FEM and CA simulation can more effectively predict the macro and micro evolution of DRX for 47Zr-45Ti-5Al-3V alloy.

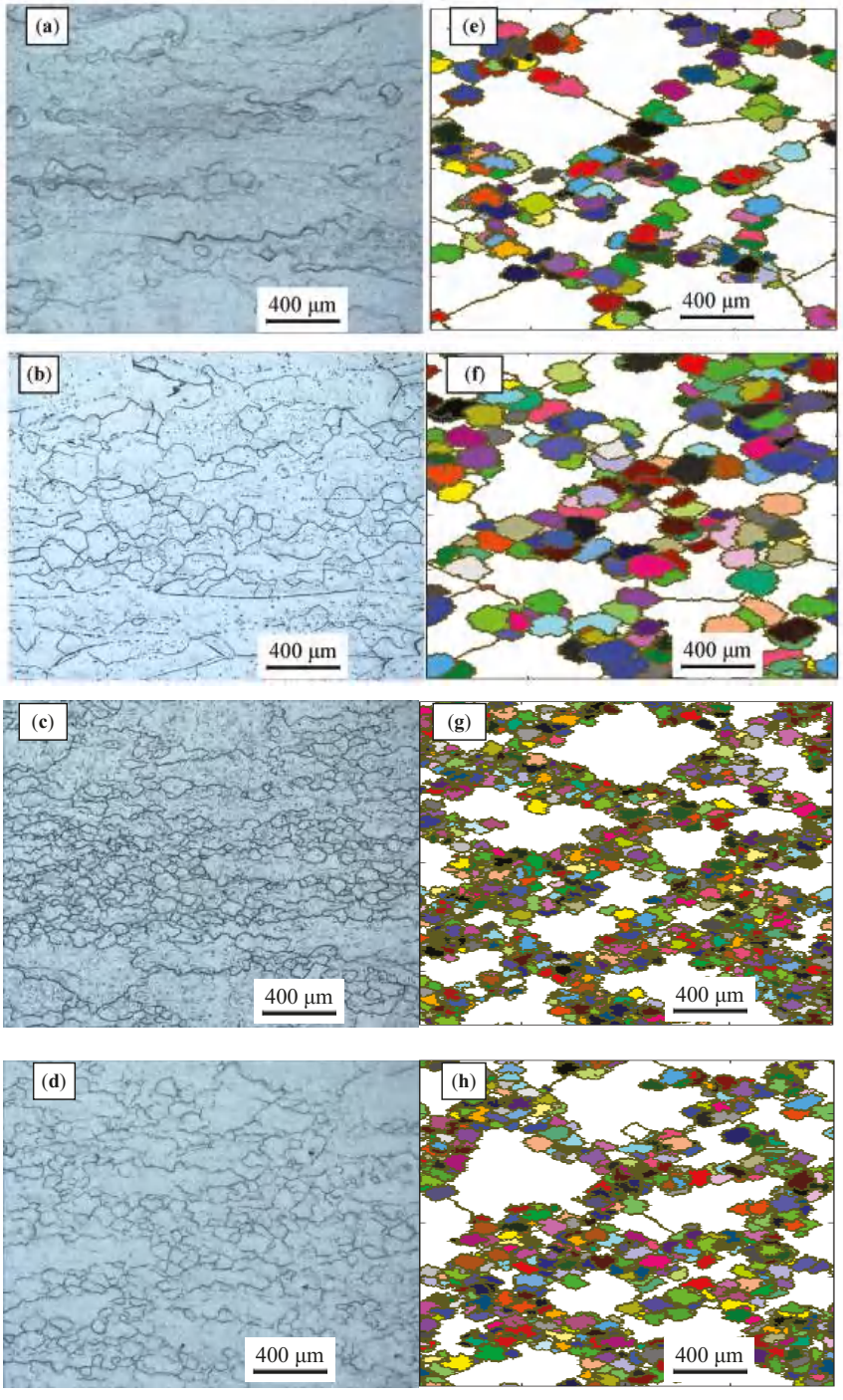

Figure 15. Microstructure of the 47Zr-45Ti-5Al-3V alloys after hot-working and CA simulation result: (**a**,**e**) 900 °C/10^{-3} s^{-1}, (**b**,**f**) 950 °C/10^{-3} s^{-1}, (**c**,**g**) 1000 °C/10^{-2} s^{-1} and (**d**,**h**) 1050 °C/10^{-2} s^{-1}.

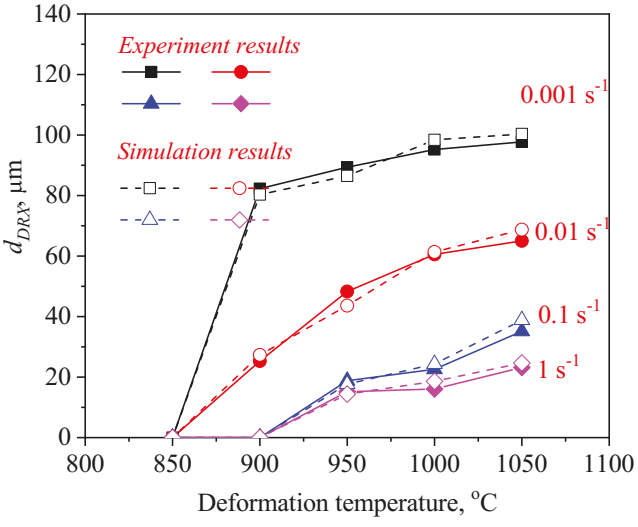

Figure 16. A comparison between the experimental and CA results of the d_{DRX}.

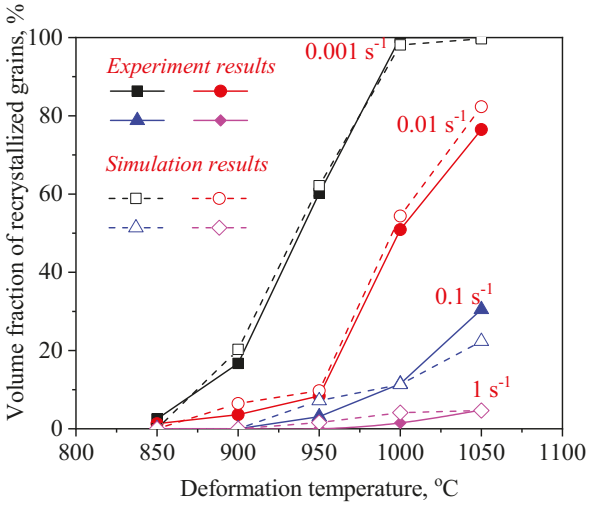

Figure 17. A comparison between the experimental and CA simulation results of the X_{DRX}.

4. Conclusions

The DRX behavior of the 47Zr-45Ti-5Al-3V alloy was investigated by using a CA–FE simulation. The main conclusion obtained can be drawn as follows:

(1) In this present study, the main softening mechanism of 47Zr-45Ti-5Al-3V alloy was regarded as DRX. The results revealed that the deformation T and $\dot{\varepsilon}$ have a strong effect on the DRX behavior of 47Zr-45Ti-5Al-3V alloy. The X_{DRX} and d_{DRX} of DRX grains increased with rising T and decreasing $\dot{\varepsilon}$.

(2) Based on the hot-working test, the X_{DRX} and d_{DRX} model of DRX were established, which can be written as the following formula:

$$\left\{ \begin{array}{c} X_{DRX} = 1 - exp\left[-0.0021 \times \left(\frac{\varepsilon - \varepsilon_c}{\varepsilon_p}\right)^{1.88}\right] \\ d_{DRX} = 2565.73Z^{-0.25} \end{array} \right\}$$

(3) The value of R^2 was, respectively, 0.95 and 0.99 for the d_{DRX} and X_{DRX} between the experimental and FEM results, while the average Δ value for the d_{DRX} and X_{DRX} was, respectively, 15.7% and 8.78%, which indicated that the FEM results of X_{DRX} and d_{DRX} are in great line with the experimental results.

(4) The Δ value of the d_{DRX} and X_{DRX} for DRX grains is respectively computed in the process of CA simulation. The Δ value of the d_{DRX} and X_{DRX} was, respectively, 6.32% and 9.3% for CA simulation, which indicated that CA simulation has more accurate results than FEM.

Author Contributions: Conceptualization, S.X. and Y.T.; methodology, Y.T., Y.Y. and W.Z.; software, F.Z. and Q.Y.; validation, Y.T.; formal analysis, W.Z.; investigation, W.Z. and Y.T.; resources, S.X. and Y.T.; data curation, W.Z.; writing—original draft preparation, W.Z.; writing—review and editing, Y.T.; visualization, Y.T. and W.Z.; supervision, S.X. and Y.T.; project administration, Y.T. and Q.Y.; funding acquisition, Y.T. and Y.Y. All authors have read and agreed to the published version of the manuscript.

Funding: This work was supported by the NSFC (Grant no. 51804087), Basic research program of Guizhou Province (Grant no. [2019]1091), Youth Science and Technology Talent Growth Project of Guizhou Education Bureau (No. [2018]107), Breeding programs of Guizhou University (Grant no. [2019]16) and Open program of Key Laboratory of Metastable Materials Science and Technology (Grant no. 202001).

Institutional Review Board Statement: Not applicable.

Informed Consent Statement: Not applicable.

Data Availability Statement: Data sharing is not applicable to this article.

Conflicts of Interest: The authors declare no conflict of interest.

References

1. Ma, B.; Qi, X.; Li, R.; Zhang, R.; Shang, H. The Zr alloying effect on microstructure evolution and mechanical properties of nanostructured Al-Zr alloyed films. *J. Alloys Compd.* **2020**, *858*, 157707.
2. Rodriguez, P. Irradiation effects in zirconium alloy core components of PHWRs. In Proceedings of the Symposium on Zirconium Alloys for Reactor Components, Bombay, India, 12–13 December 1991; Bhabha Atomic Research Centre: Bombay, India, 1992; pp. 46–95.
3. Tao, B.R.; Qiu, R.S.; Liu, Y.S.; Tan, X.N.; Liu, Q. FCC phase transformation of Zr alloy during air cooling and aging. *J. Nucl. Mater.* **2021**, *551*, 152989. [CrossRef]
4. Qu, L.; Yang, Z.N.; Zhang, F.C.; Zhang, M.; Zhang, X.Y.; Liu, R.P. Effect of deformation and heat treatment on the microstructure and mechanical properties of β-Zr40Ti5Al4V alloy. *J. Alloys Compd.* **2014**, *612*, 80–89. [CrossRef]
5. Tan, Y.B.; Ji, L.Y.; Liu, W.C.; Xiang, S.; Liang, Y.L. Effect of hot deformation on α→β phase transformation in 47Zr-45Ti-5Al-3V alloy. *Trans. Nonferrous Met. Soc.* **2018**, *28*, 1947–1957. [CrossRef]
6. Liang, S.X.; Yin, L.X.; Liu, X.Y.; Jing, R.; Zhou, Y.K.; Ma, M.Z.; Liu, R.P. Effects of annealing treatments on microstructure and mechanical properties of the Zr-45Ti-5Al-3V alloy. *Mater. Sci. Eng. A* **2013**, *582*, 374–378. [CrossRef]
7. Tan, Y.B.; Yang, L.H.; Duan, J.L.; Ji, L.Y.; Liu, W.C. Studies on the kinetics of β→α phase transformation in 47Zr-45Ti-5Al-3V alloy under isothermal conditions by X-ray diffraction. *Mater. Charact.* **2016**, *112*, 98–104. [CrossRef]
8. Tan, Y.B.; Yang, L.H.; Tian, C.; Liu, W.C.; Liu, R.P.; Zhang, X.Y. Processing maps for hot working of 47Zr-45Ti-5Al-3V alloy. *Mater. Sci. Eng. A* **2014**, *597*, 171–177. [CrossRef]
9. Tan, Y.B.; Yang, L.H.; Duan, J.L.; Liu, W.C.; Zhang, J.W.; Liu, R.P. Effect of initial grain size on the hot deformation behavior of 47Zr-45Ti-5Al-3V alloy. *J. Nucl. Mater.* **2014**, *454*, 413–420. [CrossRef]
10. Tan, Y.B.; Ji, L.Y.; Duan, J.L.; Liu, W.C.; Zhang, J.W.; Liu, R.P. A study on the hot deformation behavior of 47Zr-45Ti-5Al-3V alloy with initial lamellar α structure. *Metall. Mater. Trans. A* **2016**, *12*, 5974–5984. [CrossRef]

11. Tan, Y.B.; Yang, L.H.; Tian, C.; Liu, R.P.; Zhang, X.Y.; Liu, W.C. Hot deformation behavior of ZrTiAlV alloy with a coarse grain structure in the β phase field. *Mater. Sci. Eng. A* **2013**, *577*, 218–224. [CrossRef]
12. Sass, S.L. The Phase in a Zr-25 at.% Ti Alloy. *Acta Metall.* **1969**, *17*, 813–820. [CrossRef]
13. Chakravartty, J.K.; Dey, G.K.; Banerjee, S.; Prasad, Y.V.R.K. Characterization of Hot Deformation Behaviour of Zr-2.5Nb-0.5Cu Using Processing Maps. *J. Nucl. Mater.* **1995**, *218*, 247–255. [CrossRef]
14. Kutty, T.R.G.; Ravi, K.; Ganguly, C. Studies on Hot Hardness of Zr and Its Alloys for Nuclear Reactors. *J. Nucl. Mater.* **1999**, *265*, 91–99. [CrossRef]
15. Nikulina, A.V.; Markelov, V.A.; Peregud, M.M.; Voevodin, V.N.; Panchenko, V.L.; Kobylyansky, G.P. Irradiation-Induced Microstructural Changes in Zr-1%Sn-1%Nb-0.4%Fe. *J. Nucl. Mater.* **1996**, *238*, 205–210. [CrossRef]
16. Irani, M.; Joun, M. Determination of JMAK dynamic recrystallization parameters through FEM optimization techniques. *Comput. Mater. Sci.* **2018**, *142*, 178–184. [CrossRef]
17. Ji, H.C.; Cai, Z.M.; Pei, W.C.; Huang, X.M.; Lu, Y.H. DRX behavior and microstructure evolution of 33Cr23Ni8Mn3N: Experiment and finite element simulation. *J. Mater. Res. Technol.* **2020**, *9*, 4340–4355. [CrossRef]
18. Wu, H.; Xu, W.C.; Wang, S.B.; Yang, Z.Z.; Chen, Y.; Teng, B.G.; Shan, D.B.; Guo, B. A cellular automaton coupled FEA model for hot deformation behavior of AZ61 magnesium alloys. *J. Alloys Compd.* **2020**, *816*, 152562. [CrossRef]
19. Nithin, B.; Pandey, P.; Chattopadhyay, K.; Phanikumar, G. Influence of thermomechanical processing parameters on microstructural evolution of a gamma-prime strengthened cobalt based superalloy during high temperature deformation. *Mater. Sci. Eng. A* **2020**, *791*, 139498.
20. Geng, P.H.; Qin, G.L.; Zhou, J.; Li, T.Y.; Ma, N.S. Characterization of microstructures and hot-compressive behavior of GH4169 superalloy by kinetics analysis and simulation. *J. Mater. Process. Technol.* **2020**, *288*, 116879. [CrossRef]
21. Zhang, T.; Li, L.; Lu, S.H.; Gong, H.; Wu, Y.X. Comparisons of Different Models on Dynamic Recrystallization of Plate during Asymmetrical Shear Rolling. *Materials* **2018**, *11*, 151. [CrossRef]
22. Li, H.W.; Sun, X.X.; Yang, H. A three-dimensional cellular automata-crystal plasticity finite element model for predicting the multiscale interaction among heterogeneous deformation, DRX microstructural evolution and mechanical responses in titanium alloys. *Int. J. Plast.* **2016**, *87*, 154–180. [CrossRef]
23. Xie, B.C.; Zhang, B.Y.; Ning, Y.Q.; Fu, M.W. Mechanisms of DRX nucleation with grain boundary bulging and subgrain rotation during the hot working of nickel-based superalloys with columnar grains. *J. Alloys Compd.* **2019**, *786*, 636–647. [CrossRef]
24. Quan, G.Z.; Shi, R.J.; Zhao, J.; Liu, Q.; Xiong, W.; Qiu, H.M. Modeling of dynamic recrystallization volume fraction evolution for AlCu4SiMg alloy and its application in FEM. *Trans. Nonferr. Met. Soc.* **2019**, *29*, 1138–1151. [CrossRef]
25. Liu, J.; Cui, Z.; Ruan, L. A new kinetics model of dynamic recrystallization for magnesium alloy AZ31B. *Mater. Sci. Eng. A* **2011**, *529*, 300–310. [CrossRef]
26. Chen, L.; Zhang, Y.J.; Li, F.; Liu, X.G.; Guo, B.F.; Jin, M. Modeling of dynamic recrystallization behavior of 21Cr-11Ni-N-RE lean austenitic heat-resistant steel during hot deformation. *Mater. Sci. Eng. A* **2016**, *663*, 141–150. [CrossRef]
27. Zhou, S.S.; Deng, K.K.; Li, J.C.; Nie, K.B.; Xu, F.J.; Zhou, H.F.; Fan, J.F. Hot deformation behavior and workability characteristics of bimodal size SiCp/AZ91 magnesium matrix composite with processing map. *Mater. Des.* **2014**, *64*, 177–184. [CrossRef]
28. Wu, H.; Liu, M.X.; Wang, Y.; Huang, Z.Q.; Tan, G.; Yang, L. Experimental study and numerical simulation of dynamic recrystallization for a FGH96 superalloy during isothermal compression. *J. Mater. Res. Technol.* **2020**, *9*, 5090–5104. [CrossRef]
29. Li, X.C.; Duan, L.L.; Li, J.W.; Wu, X.C. Experimental study and numerical simulation of dynamic recrystallization behavior of a micro-alloyed plastic mold steel. *Mater. Des.* **2015**, *66*, 309–320. [CrossRef]
30. Buffa, G.; Ducato, A.; Fratini, L. FEM based prediction of phase transformations during friction stir welding of Ti6Al4V titanium alloy. *Mater. Sci. Eng. A* **2013**, *581*, 56–65. [CrossRef]
31. Liu, J.; Wang, X.H.; Liu, J.T.; Liu, Y.F.; Li, H.Y.; Wang, C. Hot deformation and dynamic recrystallization behavior of Cu-3Ti-3Ni-0.5Si alloy. *J. Alloys Compd.* **2019**, *782*, 224–234. [CrossRef]
32. Wan, Z.P.; Sun, Y.; Hu, L.X.; Yu, H. Experimental study and numerical simulation of dynamic recrystallization behavior of TiAl-based alloy. *Mater. Des.* **2017**, *122*, 11–20. [CrossRef]
33. Zhang, W.W.; Yang, Q.Y.; Tan, Y.B.; Ma, M.; Xiang, S.; Zhao, F. Simulation and Experimental Study of Dynamical Recrystallization Kinetics of TB8 Titanium Alloys. *Materials* **2020**, *13*, 4429. [CrossRef]
34. Ji, G.L.; Li, F.G.; Li, Q.H.; Li, H.Q.; Li, Z. Research on the dynamic recrystallization kinetics of Aermet100 steel. *Mater. Sci. Eng. A* **2010**, *527*, 2350–2355. [CrossRef]
35. Wang, S.L.; Zhang, M.X.; Wu, H.C.; Yang, B. Study on the Dynamic Recrystallization Model and Mechanism of Nuclear Grade 316LN Austenitic Stainless Steel. *Mater. Charact.* **2016**, *118*, 92–101. [CrossRef]
36. Zhang, C.S.; Wang, C.X.; Guo, R.; Zhao, G.Q.; Chen, L.; Sun, W.C.; Wang, X.B. Investigation of Dynamic Recrystallization and Modeling of Microstructure Evolution of an Al-Mg-Si Aluminum Alloy during High-Temperature Deformation. *J. Alloys Compd.* **2019**, *773*, 59–70. [CrossRef]
37. Wen, D.X.; Lin, Y.C.; Zhou, Y. A New Dynamic Recrystallization Kinetics Model for A Nb Containing Ni-Fe-Cr-Base Superalloy Considering Influences of Initial delta Phase. *Vacuum* **2017**, *141*, 316–327. [CrossRef]
38. Tan, K.; Li, J.; Guan, Z.J.; Yang, J.B.; Shu, J.X. The Identification of Dynamic Recrystallization and Constitutive Modeling during Hot Deformation of Ti55511 Titanium Alloy. *Mater. Des.* **2015**, *84*, 204–211. [CrossRef]

39. Zhao, Z.L.; Min, X.N.; Xu, W.X.; Cao, L.C.; Zang, G.; Song, X.Y.; Li, H. Dynamic Recrystallization Models of AerMet100 Ultrahighstrength Steel During Thermo-mechanical Processing. *Rare Met. Mater. Eng.* **2020**, *49*, 3285–3293.
40. Lin, Y.C.; Chen, M.S. Numerical Simulation and Experimental Verification of Microstructure Evolution in a Three-Dimensional Hot Upsetting Process. *J. Mater. Process. Technol.* **2009**, *209*, 4578–4583. [CrossRef]
41. Cao, Z.H.; Sun, Y.; Zhou, C.; Wan, Z.P.; Yang, W.H.; Ren, L.L.; Hu, L.X. Cellular Automaton Simulation of Dynamic Recrystallization Behavior in V-10Cr-5Ti Alloy under Hot Deformation Conditions. *Trans. Nonferrous Met. Soc. China* **2019**, *29*, 98–111. [CrossRef]
42. Cheng, F.; Cui, Z.S.; Liu, J.A.; Cheng, W.; Chen, S.J. Mesoscale Simulation of the Hightemperature Austenitizing and Dynamic Recrystallization by Coupling a Cellular Automaton with a Topology Deformation Technique. *Mater. Sci. Eng. A* **2010**, *527*, 5539–5549. [CrossRef]

materials

MDPI

Article

Correlation among the Power Dissipation Efficiency, Flow Stress Course, and Activation Energy Evolution in Cr-Mo Low-Alloyed Steel

Petr Opěla [1,*], Ivo Schindler [1], Petr Kawulok [1], Rostislav Kawulok [1], Stanislav Rusz [1], Horymír Navrátil [1] and Radek Jurča [2]

[1] Faculty of Materials Science and Technology, VSB–Technical University of Ostrava, 17. listopadu 2172/15, 70800 Ostrava–Poruba, Czech Republic; ivo.schindler@vsb.cz (I.S.); petr.kawulok@vsb.cz (P.K.); rostislav.kawulok@vsb.cz (R.K.); stanislav.rusz2@vsb.cz (S.R.); horymir.navratil@vsb.cz (H.N.)

[2] Třinecké železárny, a.s., Průmyslová 1000, 739 61 Třinec–Staré Město, Czech Republic; radek.jurca@trz.cz

* Correspondence: petr.opela@vsb.cz; Tel.: +420-597-324-349

Received: 1 July 2020; Accepted: 4 August 2020; Published: 7 August 2020

Abstract: In the presented research, conventional hot processing maps superimposed over the flow stress maps or activation energy maps are utilized to study a correlation among the efficiency of power dissipation, flow stress, and activation energy evolution in the case of Cr-Mo low-alloyed steel. All maps have been assembled on the basis of two flow curve datasets. The experimental one is the result of series of uniaxial hot compression tests. The predicted one has been calculated on the basis of the subsequent approximation procedure via a well-adapted artificial neural network. It was found that both flow stress and activation energy evolution are capable of expressing changes in the studied steel caused by the hot compression deformation. A direct association with the course of power dissipation efficiency is then evident in the case of both. The connection of the presence of instability districts to the activation energy evolution, flow stress course, and power dissipation efficiency was discussed further. Based on the obtained findings it can be stated that the activation energy processing maps represent another tool for the finding of appropriate forming conditions and can be utilized as a support feature for the conventionally-used processing maps to extend their informative ability.

Keywords: processing maps; activation energy maps; flow stress maps; artificial neural networks

1. Introduction

Since the end of the 2nd millennium, hot processing maps, introduced on the basis of the dynamic material model (DMM), have been being broadly used in the sense of the optimization of hot forming processes (forging, rolling, etc.) [1–28]. It is well known that the processing map displays the distribution of power dissipation efficiency and metallurgical instability in the strain rate–temperature coordinates under the specific value of strain. The thermomechanical conditions linked with the higher efficiency of power dissipation and in the same time with the absence of metallurgical instability are then usually considered as advantageous. In the case of a specific material, the results are usually presented as the series of processing maps assembled at various strains or as a volumetric chart, which allows these maps to be unified into one coherent unit [1,2].

The above approach has been employed to study the hot working behavior of various materials which were prepared and formed by different methods and subsequently used for different applications—for instance, steels: Fe-11Mn-10Al-0.9C duplex low-density steel susceptible to κ-carbides [3], as-extruded 42CrMo high-strength steel [4], 25Cr3Mo3NiNb steel [5], 10CrMo9-10 steel [6], 34CrNiMo medium carbon steel [7], medium carbon steel, microalloyed by B and Ti [8], medium-carbon

bainitic steel [9], 43CrNi steel [10], high-carbon/low-carbon steel composite [11], 347H austenitic heat-resistant stainless steel [12], high-titanium Nb-micro-alloyed steel [2]; nickel alloys: Ni-based superalloy [13], P/M nickel-based superalloy [14], IN-718 superalloy [15], NiTiNb shape memory alloy [16]; aluminum alloys: as-extruded 7075 [17], 5052 alloy [1], B_4C/6061Al nanocomposites fabricated by spark plasma sintering [18]; titanium alloys: Ti-15-3 [19], Ti-6242 [20], ATI425 [21], TC21 [22]; zirconium alloys: reactor-grade alpha-zirconium [23], Zr-2.5Nb [24]; and some other alloys: AZ31-1Ca-1.5 vol% nano-alumina composite [25], Cu–Cr–Zr–Nd alloy [26], Pb-Mg-10Al-0.5B alloy [27], Fe_3Al intermetallic alloy [28], etc.

Recently, some efforts have been made to improve the informative capability of the above-mentioned processing maps. In the case of a specific material, these maps are usually developed on the basis of an experimentally-achieved flow-curve dataset. Nevertheless, Quan et al. [17] have proposed to extend an experimental dataset by means of a prediction procedure since the limited number of experimental curves can lead to the inferior informative ability of compiled processing maps. This suggestion has been recently studied in the case of 10CrMo9-10 steel [6] when the additional (predicted) dataset revealed potentially inappropriate forming conditions. In connection with the above presented maps, Zhou et al. [1] utilized a term—conventional hot processing (CHP) maps. They pointed out the fact that, until now, employed processing maps do not take into account the difficulty of the course of material deformation. They demonstrated this assumption on the previously-published CHP maps—these maps indicated suitable forming conditions at thermomechanical circumstances in which the corresponding microstructure observations revealed notable shear bands [1]. Zhou et al. therefore introduced a so-called activation energy processing (AEP) maps. These maps combine the above discussed CHP maps and activation-energy (AE) maps. The activation energy characterizes the difficulty of a deformation course since embodies the capability of atoms to surmount energy barriers. Lower values of activation energy are then linked with the easier course of deformation. Thus, the potentially appropriate forming conditions are in the case of the AEP maps given by the high values of the efficiency of power dissipation in combination with the absence of instability regions and in the same time by the low values of activation energy [1,8,14,29]. In the case of the 5052-aluminum alloy, Zhou et al. [1] have confirmed that the introduced AEP maps display the suitable and aggravated forming conditions in comparison with the CHP maps more accurately.

The aim of the presented research is to find a correlation between the efficiency of power dissipation and the evolution of the activation energy for the case of Cr-Mo low-alloyed steel, and, in addition, also consider the relation of power dissipation efficiency to the flow stress course. This means the assembly of the above-mentioned AEP maps (i.e., the combination of CHP and AE maps) and creating the combination of the CHP maps with flow-stress (FS) maps will be realized. In addition, the relation of the presence of instability districts in the assembled CHP maps to the AEP maps and FS maps will be also taken into account.

2. Materials and Methods

2.1. Experimental Procedure

The chemical composition of the investigated Cr-Mo low-alloyed steel is displayed in Table 1. Cylindrical hot-compression-test samples with the diameter of 10 mm and the length of 15 mm (prepared by turning) were subjected to the series of uniaxial hot compression tests on the Gleeble 3800 in connection with the Hydrawedge II Mobile Conversion Unit (Dynamic Systems Inc., Poestenkill, NY, USA) [30].

Table 1. Chemical composition of the investigated Cr-Mo low-alloyed steel in wt%.

C	Cr	Mo	Mn	Si	Al	N
0.29	0.79	0.21	1.20	0.27	0.028	0.0093

Four strain rates (specifically: 0.02, 0.2, 2, and 20 s^{-1}) in combination with six deformation temperatures (1043, 1113, 1203, 1303, 1413, and 1553 K) have been tested in the frame of the current research, when the value of true strain reached to 1.0. Before the compression, each tested specimen was preheated to a deformation temperature by the heating rate of 5 $K{\cdot}s^{-1}$ (performed via direct electric resistance heating) with the following dwell time of 300 s. The temperature measurement was always realized on the sample surface in the middle length. This measurement was mediated via a pair of thermocouple wires (fixed by welding) of the K-type (i.e., Ni–Cr (+) and Ni–Al (−)) and R-type (Pt–13%Rh (+) and Pt (−)) as regards to the temperatures of 1043 K–1413 K and the temperature of 1553 K, respectively. The testing course was always performed under vacuum in order to prohibit oxidation processes. Tantalum foils in combination with a nickel-based high-temperature grease were chosen to protect the anvils and reduce the friction on the sample-anvils interface. The described experimental procedure resulted in a flow curve dataset expressing the evolution of true flow stress under the above-mentioned experimental values of true strain, strain rate and deformation temperature.

After the prime evaluation of subsequently assembled CHP-FS and AEP maps, additional compression tests were performed under various thermomechanical conditions in order to link these maps with a metallographic observation. The compressed specimens were immediately water-quenched to fix the structure, thereafter sectioned along the compression axis, mechanically polished, and then etched (solution of picric acid (50 g) and ferric chloride (5 g) in 100 mL of distilled water) to visualize the original grain boundaries. An optical microscopy (OM) observation has been subsequently realized by means of the Olympus GX51 inverted metallurgical microscope (Olympus Corporation, Tokyo, Japan).

2.2. Flow Curve Approximation and Prediction

Since the experimentally obtained flow curve dataset is intended to be used for the creation of CHP and AEP maps which is associated with the interpolation of the processed data, the approximation and subsequent prediction processes were applied to augment the input dataset and, thus, increase the interpolation accuracy.

Based on the previous experiences [6,31–33] and other various studies that have been done in recent decades (see, e.g., introduction in [31]), the artificial neural network (ANN) approach [34–36] was found to be appropriate to deal with the current approximation and prediction task. Specifically, a multi-layer perceptron (MLP) network type with the feed-forward course has been employed in order to create a functional relationship between the vectors of the independent variables (i.e., true strain, ε (-), strain rate $\dot{\varepsilon}$ (s^{-1}), and temperature, T (K)) and the vector of the dependent variable (i.e., true flow stress, σ (MPa). Generally, the functional relationship (MLP architecture) is given by the ad hoc established set of perceptrons (computational units) [35] which are arranged into one or more hidden layers and one summary layer, when the perceptrons of adjacent layers are connected via synaptic weights (material constants), see Figure 1. The detailed description of the ANN approximation background inclusive of MLP network type can be found, e.g., in [36].

Based on the adaptation procedure (analogical to that utilized in [6]), an ideal MLP-network architecture was found to be given by two hidden layers, each with eight perceptrons; these hidden perceptrons were activated via a hyperbolic-tangent sigmoid activation function [37].

Synaptic weights (material constants) were calculated on the basis of the minimization of the mean squared error [38] of MLP-output residuals (learning procedure). This minimization task has been solved by the use of the Levenberg–Marquardt algorithm [39–41] in a combination with the Bayesian regularization [42,43] and the back-propagation of error signal [44]. Note, 12 experimental flow curves were subjected to the minimization algorithm (training set), while six curves were used to evaluate the prediction ability during the training course (validation set) and other six curves then served for the subsequent final prediction evaluation of a trained MLP architecture (testing set)—see Table 2.

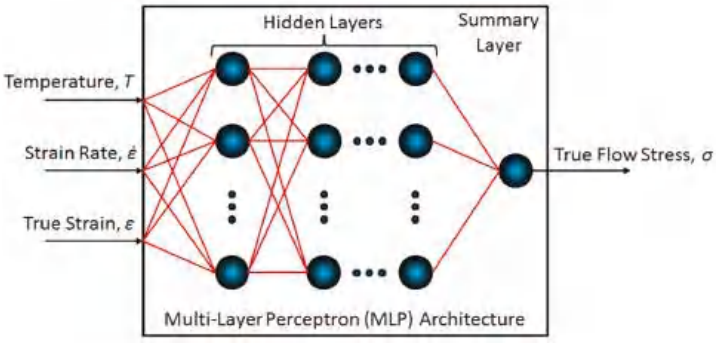

Figure 1. General architecture of the employed multi-layer perceptron (MLP) network.

It should be noted that the input vectors (ε, $\dot{\varepsilon}$, T) are introduced to the network in a normalized form (i.e., dimensionless and with the sample standard deviations equal to 1.0). The applied normalization procedure was analogical to that described previously in [6].

Table 2. Distribution of the temperature and strain rate combinations for the MLP learning purpose.

$\dot{\varepsilon}$ (s^{-1})/T (K)	1553	1413	1303	1203	1113	1043
0.02	train	test	valid	train	test	train
0.2	valid	train	train	test	valid	train
2	train	valid	test	train	train	test
20	test	train	train	valid	train	valid

Based on the assembled MLP network, flow curve prediction has been realized for five additional temperatures (1078, 1158, 1253, 1358, and 1483 K) under the experimentally tested strain rate levels.

The entire approximation and prediction procedures have been performed by means of MATLAB® 9.3 software [45] with the embedded Neural Network Toolbox™ 11.0 (MathWorks®, Natick, MA, USA) [46].

2.3. Conventional Hot Processing Maps

In the current research, CHP maps of the studied steel were compiled on the basis of the findings resulting from the Prasad's dynamic material model (DMM) [20,47,48]. With regard to the hot-formed workpiece, the DMM discloses a related energy-balance background. Specifically, it deals with the dissipation of power in the connection with a plastic deformation and associated metallurgical processes like, e.g., dynamic recovery (DRV) and recrystallization (DRX). On the foreground of the DMM theory, a dimensionless indicator is utilized to quantify the power dissipation in the wide range of thermomechanical circumstances, just with the relation to the microstructural changes—known as the efficiency of power dissipation, η (-, %) [20]:

$$\eta = \frac{2 \cdot m}{m+1}, \tag{1}$$

where the strain rate sensitivity, m (-), is given as [20]:

$$m = \left.\frac{\partial \ln \sigma}{\partial \ln \dot{\varepsilon}}\right|_{T,\varepsilon}, \tag{2}$$

Note that in order to perform this derivation, the relevant $\ln \sigma$—$\ln \dot{\varepsilon}$ data points were extracted from the combined experimental/predicted flow curve dataset.

The dependency of the efficiency of power dissipation with respect to the temperature and strain rate is under specific strains usually graphically expressed in the form of so-called power dissipation maps. These maps are usually combined with the so-called flow instability maps, when the superimposition of both map types resulting in the above introduced CHP maps. The presence of instability is conditioned by the continuum criterion [49,50]:

$$\xi\left(\dot{\varepsilon}\right) = \frac{\partial \ln\left(\frac{m}{m+1}\right)}{\partial \ln \dot{\varepsilon}} + m \leq 0, \tag{3}$$

where the value of $\xi(\dot{\varepsilon})$ (-) is known as the flow instability parameter.

2.4. Activation-Energy Maps

As it was mentioned in the introduction, the AEP maps, i.e., the combination of the CHP maps and the activation energy (AE) maps, can enhance the ability of CHP maps to reveal the potentially unstable forming conditions since the activation energy has the ability to reflect the difficulty of deformation course [1]. The creation of the AE maps requires the calculation of activation energy values under all thermomechanical conditions. In most cases, however, the activation energy is considered to be a material constant (so-called apparent activation energy) or, at most, strain dependent [21,26,51–54]. In order to deal with the activation energy as a strain, strain rate, and temperature dependent parameter, the method utilized, e.g., in [55,56] has been employed. Similarly, as in the case of the apparent activation energy, the calculation is based on the well-known Garofalo's relationship [57]. With the use of this relation, the values of the activation energy, Q (ε, $\dot{\varepsilon}$, T) (J·mol^{-1}), have been calculated as follows [55,56]:

$$Q\left(\varepsilon, \dot{\varepsilon}, T\right) = R \cdot n(\varepsilon, T) \cdot M\left(\varepsilon, \dot{\varepsilon}\right), \tag{4}$$

where the R (8.314 J·K^{-1}·mol^{-1}) is the universal gas constant, and the products of the $n(\varepsilon,T)$ (-) and $M(\varepsilon, \dot{\varepsilon})$ (K) parameters are given on the basis of the known values (experimental and predicted via MLP) of $\dot{\varepsilon}$, T and σ as follows [55,56]:

$$n(\varepsilon, T) \cdot M\left(\varepsilon, \dot{\varepsilon}\right) = \left.\frac{\partial \ln \dot{\varepsilon}}{\partial \ln\{\sinh[\alpha(\varepsilon, T) \cdot \sigma]\}}\right|_{\varepsilon,T} \cdot \left.\frac{\partial \ln\{\sinh[\alpha(\varepsilon) \cdot \sigma]\}}{\partial (1/T)}\right|_{\varepsilon,\dot{\varepsilon}}, \tag{5}$$

where the values of the stress multiplier $\alpha(\varepsilon,T)$ (MPa^{-1}) were estimated as [55,56]:

$$\alpha(\varepsilon, T) = \left.\frac{\partial \ln \dot{\varepsilon}}{\partial \sigma}\right|_{\varepsilon,T} \Big/ \left.\frac{\partial \ln \dot{\varepsilon}}{\partial \ln \sigma}\right|_{\varepsilon,T}. \tag{6}$$

Note that $\alpha(\varepsilon)$ is the arithmetic mean [58] of the $\alpha(\varepsilon,T)$ parameter under different temperatures. From the practical reasons, the above introduced parameters have been expressed in the form of the following multivariate polynomials:

$$M\left(\varepsilon, \dot{\varepsilon}\right) = \sum_{i=0}^{4}\sum_{j=0}^{4} a_{ij} \cdot \varepsilon^i \cdot \ln^j \dot{\varepsilon}, \tag{7}$$

$$n(\varepsilon, T) = \sum_{i=0}^{4}\sum_{j=0}^{4} b_{ij} \cdot \varepsilon^i \cdot T^j, \tag{8}$$

$$\alpha(\varepsilon, T) = \sum_{i=0}^{4}\sum_{j=0}^{4} c_{ij} \cdot \varepsilon^i \cdot T^j. \tag{9}$$

The material constants of the polynomials (7)–(9), i.e., a_{ij} (-), b_{ij} (-) and c_{ij} (-) (where i = [0, 4] $\subset$ $\mathbb{N}_0$ and j = [0, 4] $\subset$ $\mathbb{N}_0$), have been estimated on the basis of nonlinear least square method via the Levenberg–Marquardt iterative optimization algorithm [39–41].

3. Results and Discussion

3.1. Evaluation of the Performed Calculations

In order to evaluate the accuracy of the above performed MLP-approximation, the Pearson's correlation coefficient [59], R (-), and the average absolute relative error, $AARE$ (%), have been calculated—see Equations (10) and (11) [17]. In these equations, the T_i (MPa) and A_i (MPa) represent the flow stress values of the target (i.e., experimental) and approximated dataset, respectively. $i = [1, n] \subset \mathbb{N}$, where n is the number of elements in the flow stress vector. $\overline{T}$ (MPa) and $\overline{A}$ (MPa) then embody the mean values [58] of these vectors.

$$R = \frac{\sum_{i=1}^{n}\left(T_i - \overline{T}\right)\cdot\left(A_i - \overline{A}\right)}{\sqrt{\sum_{i=1}^{n}\left(T_i - \overline{T}\right)^2 \cdot \sum_{i=1}^{n}\left(A_i - \overline{A}\right)^2}}, \tag{10}$$

$$AARE = \frac{1}{n}\cdot\sum_{i=1}^{n}\left|\frac{T_i - A_i}{T_i}\right|\cdot 100. \tag{11}$$

As can be seen in Figure 2, both statistical indicators exhibit the favorable values. It is apparent, the approximated dataset, thanks to the utilized MLP approach, exhibits a good fit with the experimental one.

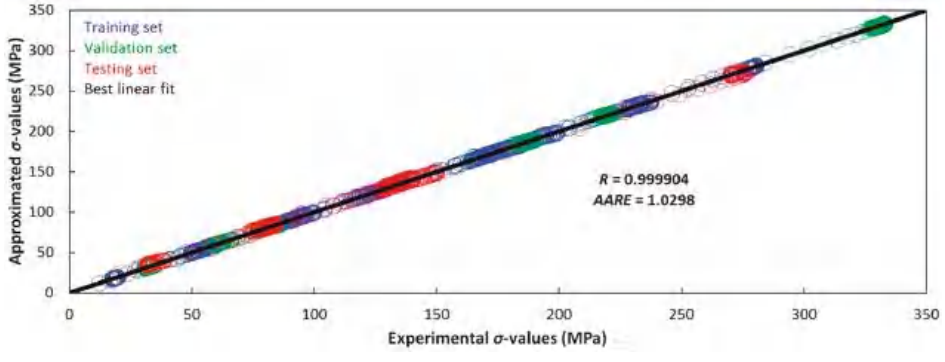

Figure 2. Correlation between the experimental and by-MLP approximated flow curve datasets.

The experimental and approximated flow curves are displayed in Figure 3 (see the color curves). In addition, the gray curves then represent the performed prediction. It can be seen, this graphical comparison confirms the above achieved statistical observation. It is also noticeable that the predicted curves fit into the presumed flow stress levels. The presented flow curves show the apparent manifestation of a DRX course and it is favorable that this characteristic flow stress course could be modeled via the assembled MLP network.

The calculated material constants of the above-introduced polynomials (7)–(9) are listed in Tables 3–5 together with the achieved values of the Pearson's correlation coefficient [59], R (-), Equation (10). In this equation, in association with the polynomials (7)–(9), T_i (K, -, MPa^{-1}) and A_i (K, -, MPa^{-1}) represent the target and approximated values of the studied parameters, i.e., $M(\varepsilon, \dot{\varepsilon})$, $n(\varepsilon, T)$, and $\alpha(\varepsilon,T)$. $i = [1, n] \subset \mathbb{N}$, where, n is the number of elements in the individual parameter vector. $\overline{T}$ (K, -, MPa^{-1}) and $\overline{A}$ (K, -, MPa^{-1}) then embody the mean values [58] of these vectors.

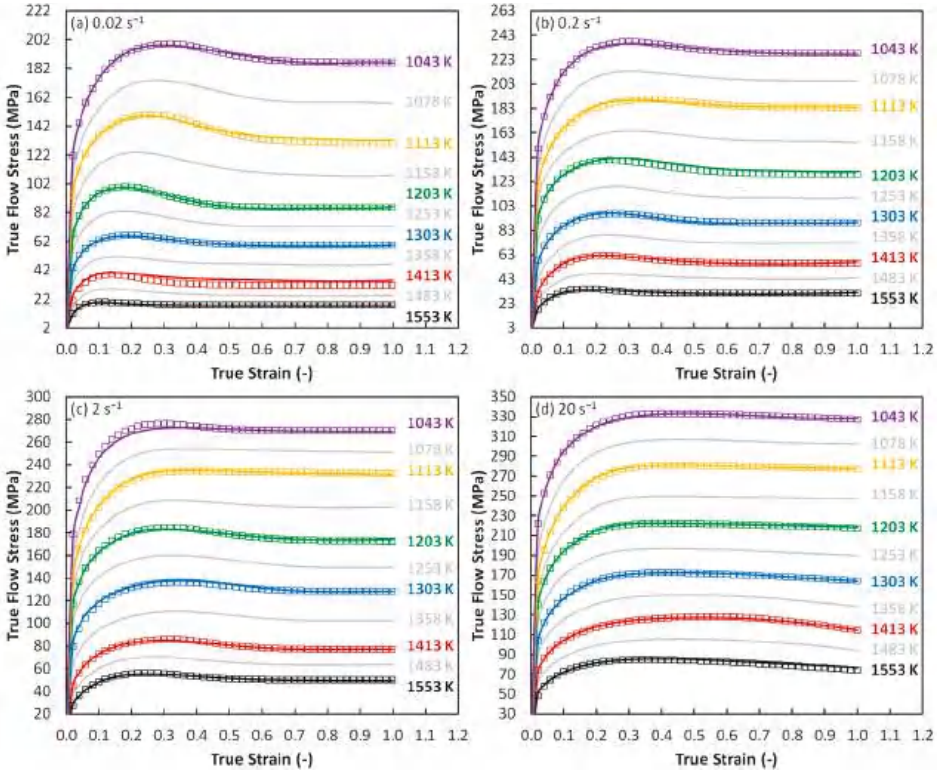

Figure 3. Experimental, approximated, and predicted flow curves of the examined Cr-Mo low-alloyed steel. (**a**) Strain rate of 0.02 s^{-1}; (**b**) strain rate of 0.2 s^{-1}; (**c**) strain rate of 2 s^{-1}; (**d**) strain rate of 20 s^{-1}. Boxes–experiment; color solid lines–approximation; gray solid lines–prediction.

Table 3. Material constants a_{ij} of the polynomial $M(\varepsilon, \dot{\varepsilon})$ (7).

a_{ij}	Value	a_{ij}	Value	a_{ij}	Value	a_{ij}	Value	a_{ij}	Value
$a_{0,0}$	8.95×10^{3}	$a_{1,0}$	4.73×10^{3}	$a_{2,0}$	-3.88×10^{3}	$a_{3,0}$	-8.05×10^{3}	$a_{4,0}$	1.02×10^{4}
$a_{0,1}$	-4.75×10^{2}	$a_{1,1}$	-7.10×10^{3}	$a_{2,1}$	1.50×10^{4}	$a_{3,1}$	-6.14×10^{3}	$a_{4,1}$	-3.86×10^{3}
$a_{0,2}$	-7.86×10^{2}	$a_{1,2}$	-4.11×10^{3}	$a_{2,2}$	7.21×10^{3}	$a_{3,2}$	1.28×10^{3}	$a_{4,2}$	-6.33×10^{3}
$a_{0,3}$	9.56×10^{1}	$a_{1,3}$	8.54×10^{2}	$a_{2,3}$	-1.73×10^{3}	$a_{3,3}$	4.16×10^{2}	$a_{4,3}$	7.78×10^{2}
$a_{0,4}$	5.94×10^{1}	$a_{1,4}$	4.24×10^{2}	$a_{2,4}$	-8.50×10^{2}	$a_{3,4}$	1.72×10^{2}	$a_{4,4}$	4.25×10^{2}
R	0.996611								

Table 4. Material constants b_{ij} of the polynomial $n(\varepsilon,T)$ (8).

b_{ij}	Value	b_{ij}	Value	b_{ij}	Value	b_{ij}	Value	b_{ij}	Value
$b_{0,0}$	5.67×10^{2}	$b_{1,0}$	6.53×10^{2}	$b_{2,0}$	-7.35×10^{2}	$b_{3,0}$	2.75×10^{2}	$b_{4,0}$	-6.53×10^{0}
$b_{0,1}$	-1.71×10^{0}	$b_{1,1}$	-1.33×10^{0}	$b_{2,1}$	1.30×10^{0}	$b_{3,1}$	-3.87×10^{-1}	$b_{4,1}$	0.00×10^{0}
$b_{0,2}$	1.97×10^{-3}	$b_{1,2}$	8.70×10^{-4}	$b_{2,2}$	-7.04×10^{-4}	$b_{3,2}$	1.40×10^{-4}	$b_{4,2}$	0.00×10^{0}
$b_{0,3}$	-1.01×10^{-6}	$b_{1,3}$	-1.85×10^{-7}	$b_{2,3}$	1.12×10^{-7}	$b_{3,3}$	0.00×10^{0}	$b_{4,3}$	0.00×10^{0}
$b_{0,4}$	1.93×10^{-10}	$b_{1,4}$	0.00×10^{0}	$b_{2,4}$	0.00×10^{0}	$b_{3,4}$	0.00×10^{0}	$b_{4,4}$	0.00×10^{0}
R	0.996660								

Table 5. Material constants c_{ij} of the polynomial $\alpha(\varepsilon,T)$ (9).

c_{ij}	Value	c_{ij}	Value	c_{ij}	Value	c_{ij}	Value	c_{ij}	Value
$c_{0,0}$	2.85×10^{-2}	$c_{1,0}$	-2.84×10^{-1}	$c_{2,0}$	2.86×10^{-1}	$c_{3,0}$	-1.06×10^{-1}	$c_{4,0}$	1.58×10^{-2}
$c_{0,1}$	-8.81×10^{-5}	$c_{1,1}$	5.65×10^{-4}	$c_{2,1}$	-4.64×10^{-4}	$c_{3,1}$	1.02×10^{-4}	$c_{4,1}$	0.00×10^{0}
$c_{0,2}$	1.32×10^{-7}	$c_{1,2}$	-3.74×10^{-7}	$c_{2,2}$	2.57×10^{-7}	$c_{3,2}$	-3.82×10^{-8}	$c_{4,2}$	0.00×10^{0}
$c_{0,3}$	-9.99×10^{-11}	$c_{1,3}$	7.75×10^{-11}	$c_{2,3}$	-3.76×10^{-11}	$c_{3,3}$	0.00×10^{0}	$c_{4,3}$	0.00×10^{0}
$c_{0,4}$	3.26×10^{-14}	$c_{1,4}$	0.00×10^{0}	$c_{2,4}$	0.00×10^{0}	$c_{3,4}$	0.00×10^{0}	$c_{4,4}$	0.00×10^{0}
R	0.999562								

3.2. Flow Stress Evolution

The experimental and predicted flow curve datasets are expressed together in the form of a volumetric chart (constructed using MATLAB® 9.3 software (MathWorks®, Natick, MA, USA) [45]), see Figure 4.

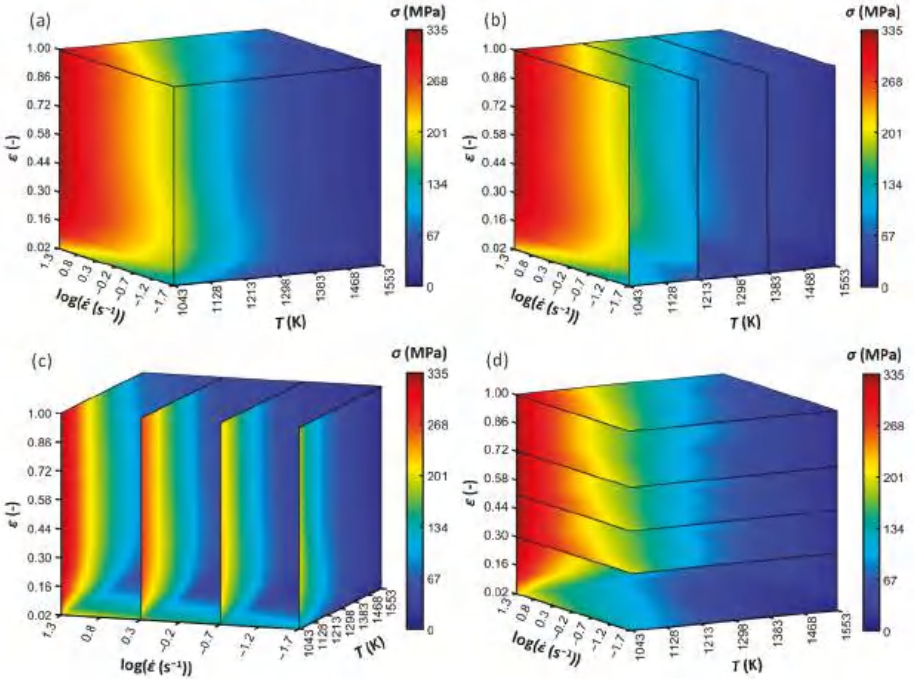

Figure 4. Volumetric expression of the experimental-predicted flow curve datasets of the Cr-Mo low-alloyed steel. Colors–flow-stress level. (**a**) Global overview; (**b**) sliced in the temperature axis; (**c**) sliced in the strain rate axis; (**d**) sliced in the strain axis.

The independent variables, i.e., deformation temperature, strain rate, and true strain are represented by the x, y, and z axes, respectively. The flow stress values are then embodied by the 3D-color-space matrix. For a better orientation, the volumetric chart is expressed also in the form of sliced panels along the x, y, and z exes. Predictably, the flow stress level declines with an increasing deformation temperature and decreasing strain rate. A DRX-like behavior can be observed—with the increase of strain, the flow stress increases up to a maximum level (strengthening phase) and then decreases to a steady-state flow (softening phase). In the case of the highest strain rate level (20 s^{-1}), however, the studied strain range is not enough to undergo through the entire DRX softening (i.e., reaching the steady-state).

3.3. Processing Maps

Based on the experimental and predicted flow curve datasets (see Figure 4), the calculations introduced in Section 2.3 enabled a gain in the η and ξ values of the investigated Cr-Mo steel under the wide range of thermomechanical conditions. These values have been subsequently expressed in the form of the above-mentioned CHP maps—see Figure 5a–c. The solid contours marked by the labels correspond to the percentage values of the power dissipation efficiency (i.e., η, Equation (1)). The dashed contours then delimit the areas of assumed flow instability (i.e., the ξ-values ≤ 0, Equation (3)).

Generally, higher η-values are connected with promising thermomechanical conditions. As it was implied above, the η-values reflect the progress of metallurgical processes (most often the DRV or DRX softening) under various thermomechanical conditions. The progress of these softening processes, of course, corresponds also with the changes in the flow-stress level. Since the η-values are calculated form the flow-stress values, their mutual ability to reflect the dynamic softening progress should, thus, be evident. In the case of this research, for the purpose of easier comparison, the assembled CHP maps have been combined with the flow-stress (FS) maps by their mutual superimposing—see the color background expressing the flow stress evolution (Figure 5a–c).

It is well-known that the purpose of the ξ-values is to reveal potentially aggravated forming conditions. Nevertheless, as presented in the introduction, the calculated ξ-values do not have to be sufficient for the revealing of all these unstable conditions. To deal with this issue, Zhou et al. [1] introduced the above-mentioned activation-energy processing (AEP) maps. The assumption is as follows: Since the activation energy expresses the difficulty of the deformation course, the Q-values can be utilized to reveal potentially aggravated forming conditions and thus encourage the results given by the ξ-values. The AEP maps of the investigated steel, i.e., superimposition of the CHP maps (Section 2.3) over the AE maps (Section 2.4), are offered in Figure 5d–f. The contours embody the CHP maps—the same as in the case of Figure 5a–c—however, in this case, the color background corresponds with the evolution of activation energy. All the above-mentioned maps have been assembled by means of the Gnuplot 5.2 graphing utility Patchlevel 7 [60].

Based on the gained η-range, the deformation course of the studied material can be associated with the specific metallurgical processes, e.g., η-range from 30 to 50% is usually attributed to the DRX course, lower values correspond with the DRV and the η-values above the ca. 60% can have connection to the superplastic behavior [6,23,24]. In the case of the studied steel, the η-values go beyond the 30% threshold (see Figure 5)—Thus, the softening course is probably mediated via DRX. This is in accordance with the observations in Figure 3.

It is clear, the η-values increase as the temperature level increases. The obvious η-increase is also observable with the decrease of strain rate under medium temperature levels. This phenomenon can be observed also under higher temperatures—however, local η-maximums can be visible at the highest strain rates (see, e.g., the parabolic η-course under the 1468 K in Figure 5b). The η-increase is then practically negligible under lower temperatures. Nevertheless, despite of the nuances in η-$\dot{\varepsilon}$ dependence, it can be said that the η-values generally increase with increasing temperature and decreasing strain rate. This behavior is closely linked with the softening course. It is understandable that the higher the temperature and the lower the strain rate, the earlier the DRX-start. In other words, the η-values represent the intensity of the DRX progress—higher η-values are coupled with a more progressed DRX course.

The relation between the η-values and DRX course can be observed in optical microscopy (OM) images (Figure 6). Based on the comparison of Figure 6a,b, it can be seen that microstructure under the higher temperature is fully recrystallized (see clearly non-elongated grains with distinctly equiaxed boundaries), which is linked with a higher η-level in Figure 5c,f. Further, Figure 6c,d demonstrates the growing of recrystallized grains with the decrease in strain rate as the consequence of longer grain-growth time, which is also linked with a higher η-level. Of course, the grain growth is also supported by higher temperature levels.

- Thus, it can be stated, the more progressed the DRX and the larger the grains, the higher the η-level.
- It is understandable that a larger grain size is not beneficial for the achievement of simultaneous high strength and high toughness [9,16]. Thus, it seems, too much high η-level does not have to be connected with the best thermomechanical conditions—at least as regards to the final material properties. The growing grain size with the increasing η-level has been also observed, e.g., in [1,9].

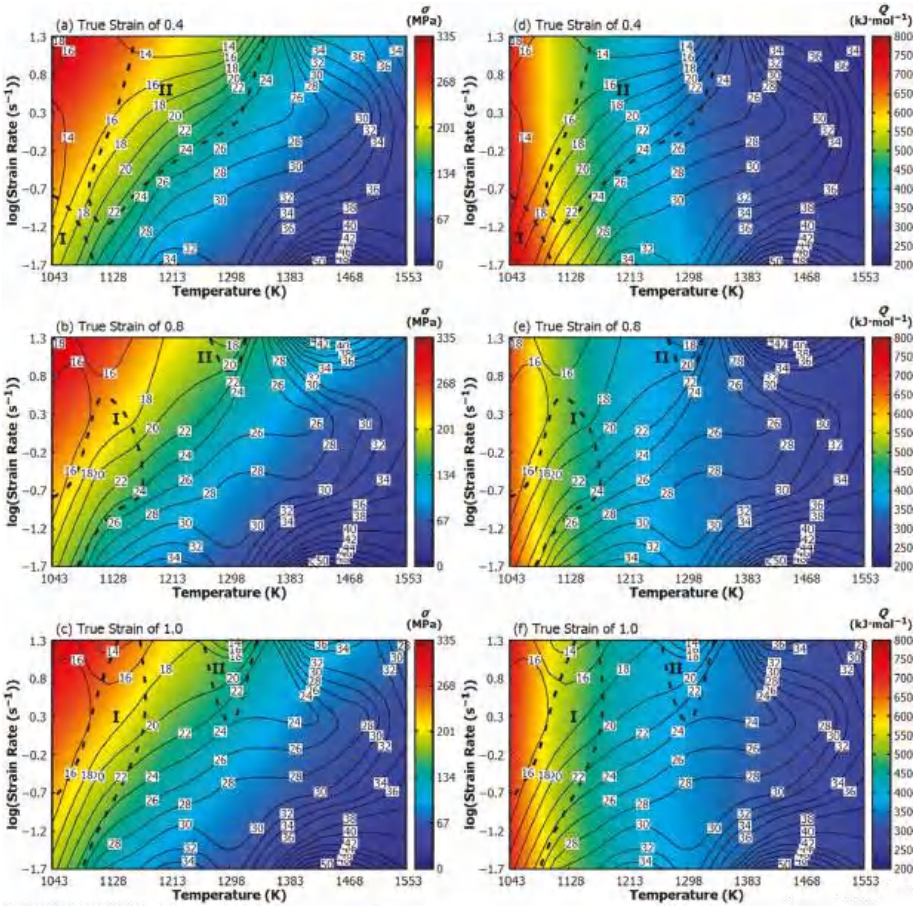

Figure 5. Processing maps of the investigated Cr-Mo low alloyed steel. (**a**–**c**) Conventional hot processing (CHP) maps superimposed by flow-stress (FS) maps; (**d**–**f**) activation-energy processing (AEP) maps. Solid contours with labels—power dissipation efficiency, dashed lines—districts of metallurgical instability, color background—flow stress evolution in (**a**–**c**) or activation energy evolution in (**d**–**f**).

The color background in Figure 5a–c distinctly illustrates the relation between the η-values and σ-values. It is observable, the η-values have practically an opposite evolution—they are rising as the σ-values are decreasing (i.e., inverse proportion). Thus, in connection to the flow stress course, higher η-values refer to deformation conditions which are beneficial form the point of view of lower forming forces and thus lower energetic consumption and also longer tool life.

The relation between the η-values and Q-values (see Figure 5d–f) is, however, quite different in comparison to the η-σ course. It is observable, if the temperature is rising, the η-values are increasing

and Q-values are decreasing (i.e., the inverse proportion). Nevertheless, if the strain rate is rising, the η-values and Q-values are both decreasing (i.e., direct proportion). Similar Q-evolution has also been observed in [56].

- Note, the decrease of the Q-values is coupled with the easier deformation course. Specifically, the decrease of the Q-values with the increasing temperature is linked with the higher kinetic energy of dislocation movement. The decrease of the Q-values with the increasing strain rate is then linked with the increasing shear stress, i.e., with the activation of dislocation movement. A more detailed explanation can be found in [55,56].

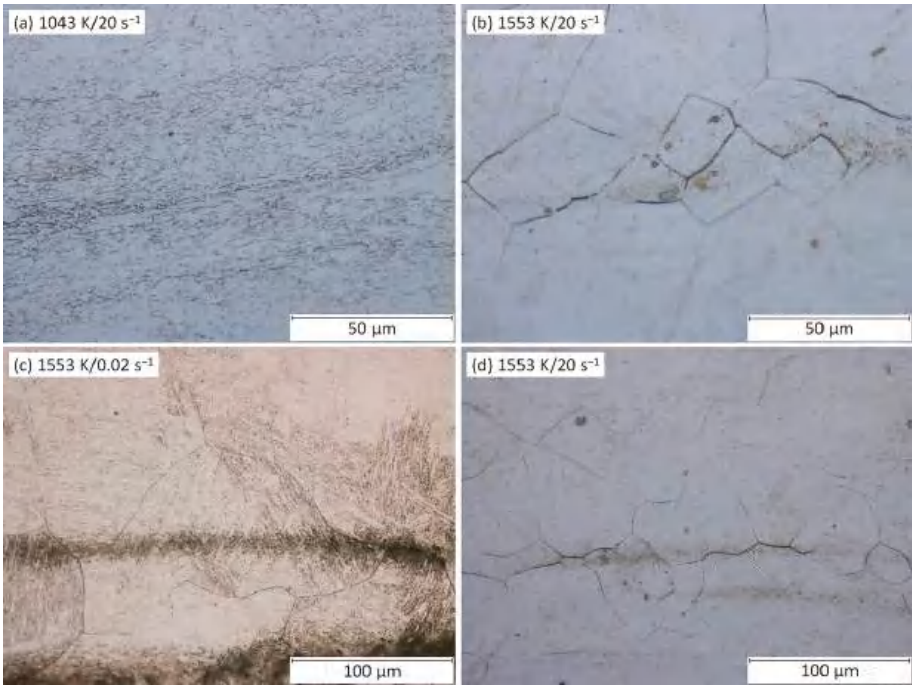

Figure 6. OM images of samples deformed under the true strain of 1.0. (**a**) 1043 K/20 s^{-1}, (**b**) 1553 K/20 s^{-1}, (**c**) 1553 K/0.02 s^{-1}, (**d**) 1553 K/20 s^{-1}.

It is discernable, the influence of the strain rate on the Q-values is rather less apparent—linked mainly with lower temperature levels. The strain rate influence is the most apparent under the temperature level of 1043 K at the true strain of 0.4 (Figure 5d). The Q-value decreased from 776 to 708 kJ·mol^{-1} when the strain rate increased from 0.02 to 20 s^{-1}. With respect to the highest temperature level, i.e., 1553 K, the Q-value decreased from 255 to 233 kJ·mol^{-1} as the strain rate increased from 0.02 to 20 s^{-1}.

- It is noticeable that this Q-decrease (representing a better deformation course) is in accordance with the decrease of the grain size due to the increasing strain rate as illustrated in Figure 6c,d.
- The raising of η-values and lowering of Q-values are commonly linked with the achieving of beneficial thermomechanical conditions. However, as stated above, the generally beneficial increase of η-values is in the same time coupled with the grain size growing (i.e., with the reaching of worse strength-toughness combination) because the η-increase is closely linked with an increasing temperature and decreasing strain rate. On the other hand, the generally beneficial decrease of Q-values is linked with a grain size growing only at the temperature increase.

- Nonetheless, the strain rate effect is quite opposite when the true strain achieves the highest level, i.e., 1.0 (Figure 5f). At the same temperature (specifically 1043 K), the Q-value increased from 699 to 725 kJ·mol^{-1} as the strain rate increased from 0.02 to 20 s^{-1}. At the highest temperature level (i.e., 1553 K), the Q-value increased from 263 to 273 kJ·mol^{-1} as the strain rate increased from 0.02 to 20 s^{-1}. Thus, it seems like that under the higher strains the Q-evolution and η-evolution become to be inverse proportional even in the case of the strain rate course.

Furthermore, Figure 7 offers a detailed view on the relationship between the calculated values of activation energy (solid lines) and strain level. This relation is in the same time compared with the flow stress course (boxes).

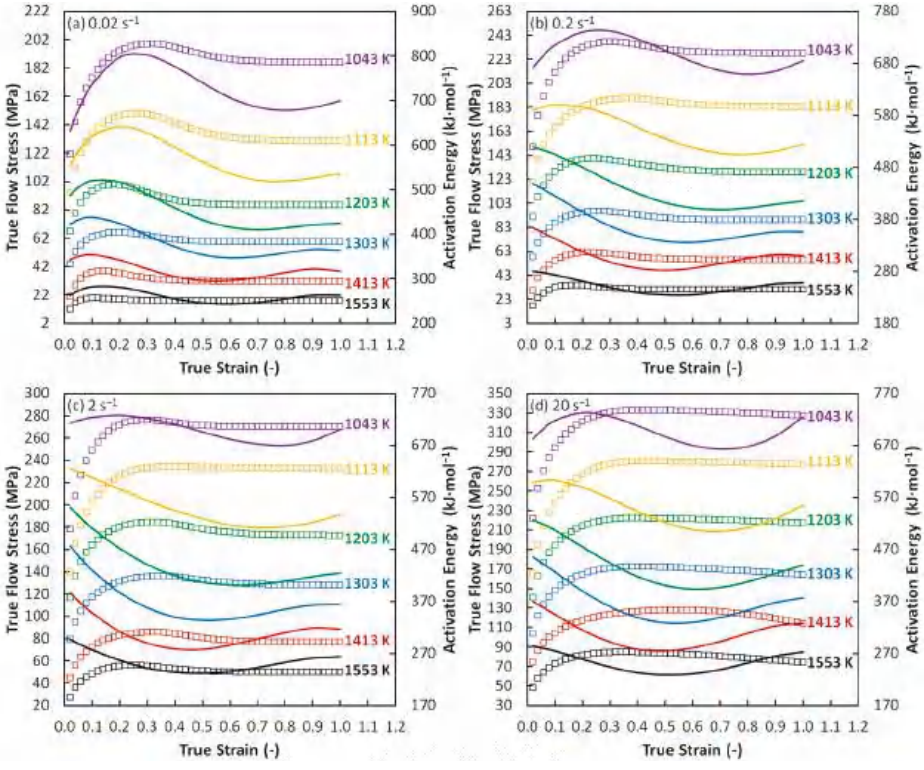

Figure 7. Correlation between the activation energy and flow stress course. (**a**) Strain rate of 0.02 s^{-1}; (**b**) strain rate of 0.2 s^{-1}; (**c**) strain rate of 2 s^{-1}; (**d**) strain rate of 20 s^{-1}. Boxes–experimental flow curves; solid lines–activation energy evolution.

It is visible that the stage of the σ-increase is under a strain rate of 0.02 s^{-1} coupled with the increase of Q (see e.g., 1043 K/0.02 s^{-1}). This Q-course seems to be related to the prevailing work hardening (i.e., aggravated deformation conditions). The observed Q-increase is then terminated by the achieving of maximum point with a following gradual decrease. This decrease can be then considered as the manifestation of the prevailing DRX course (also manifested by the σ-decrease) which is associated with better deformation conditions. Nevertheless, most of the Q-ε curves start immediately with a decrease phase regardless to the flow curve peak point. In addition, the decrease in Q-values is not associated with the following constant phase (equilibrium between the DRX and work hardening) as is typical for the σ-ε curves. Moreover, the following Q-increase with strain can be observed in the case of all Q-ε curves. This increase is under higher temperatures and lower strain

rates followed by another decrease. The observed increase signalizes other aggravation of deformation conditions although the corresponding σ-ε curves remain in constant phase. This fact can result in divergences in the prediction of unfavorable conditions via the above-discussed CHP and AEP maps.

In addition, Figure 8 shows the evolution of the parameters which were calculated as an intermediate step for the activation energy maps assembling.

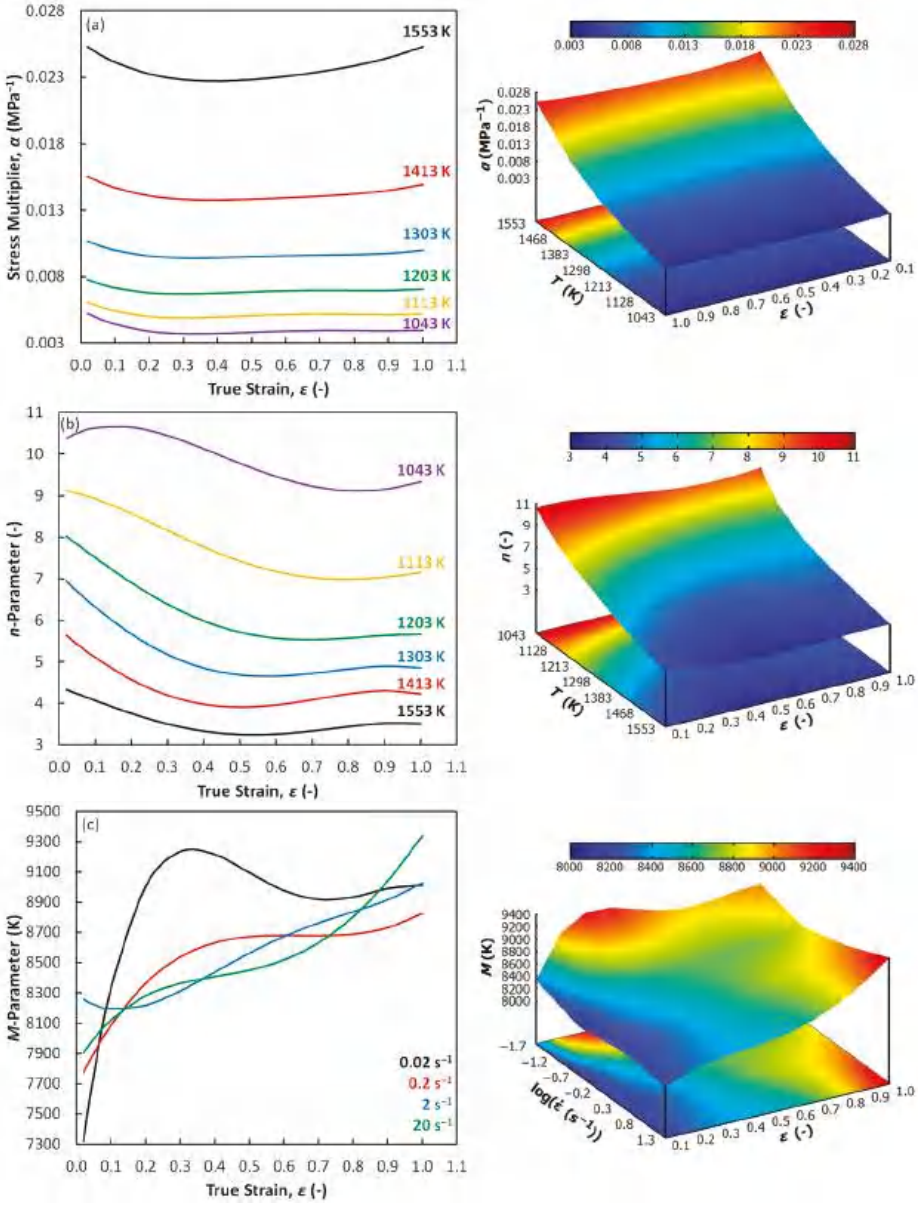

Figure 8. Evolution of the parameters for the activation energy calculation. (**a**) Stress multiplier α; (**b**) parameter n; (**c**) parameter M.

Figure 8a is aimed on the stress multiplier α. It is clear that this parameter is predominantly influenced by the temperature level and almost independent on the strain course. At first glance it is clear that the temperature dependence of the α-parameter is opposite in comparison to the temperature dependence of Q-values (Figure 7). However, the differences in the α-values between the highest and the lowest temperature levels are almost negligible. With respect to the n-parameter (see Figure 8b), the temperature and strain dependencies are very similar to those observed in Q-evolution (Figure 7). The course of the M-parameter (Figure 8c) is then more complicated. It can be seen that the strain dependency is, in the case of this parameter, strongly influenced by the strain rate level. Small strain rate values (0.02 and 0.2 s^{-1}) are associated with the most complicated course while the course under the higher rates seems to be simpler. It seems that this behavior can strongly influence the reaction of the Q-values on the changes in strain rate level (consider Equation (4)). As observed in Figure 5d, the Q-values are higher under the lower strain rates at the strain of 0.4, which corresponds with the observation under the strain of 0.4 in Figure 8c. The situation is opposite in the case of the strain of 1.0 (Figure 5f). This is also reflected by the M-course in Figure 8c—the M-values of the rates of 2 and 20 s^{-1} become to be higher. In addition, the complicated M-course is also manifested by the more complicated form of the polynomial description—compare the values in Table 3 (M-polynomial) with the values in Table 4 (n-polynomial) and Table 5 (α-polynomial). Table 3 does not contain zero values unlike the other tables, i.e., the full polynomial form had to be applied to properly describe the M-course. The complicated M-evolution is also apparent from the surface expression in Figure 8.

Furthermore, the flow instability areas (i.e., ξ-values ≤ 0) bring the information about the potential presence of metallurgical instabilities which can accompany the deformation course. Based on the formed material and thermomechanical circumstances, these instability areas can be appeared as the manifestation of e.g., flow localization, shear bands, Lüders' bands, kink bands, mechanical twinning, or cracks [1,6]. In the case of the above presented maps (Figure 5), two areas of metallurgical instability can be observed:

- As regards to the strain of 0.4, the first instability area (I) is situated in the very small temperature range of 1043–ca. 1128 K and the strain rate range of 0.02–ca. 0.2 s^{-1}. It is observable, this small area is growing with the increase of strain—especially towards to higher strain rates. Under the strain of 1.0, the district (I) covers the temperature range of 1043–ca. 1170 K and the strain rate range of 0.02–20 s^{-1}.
- Under the strain of 0.4, the second area (II) is located in the wide temperature range of ca. 1086–more than 1298 K and the wide strain rate range of ca. 0.06–20 s^{-1}. This area, however, is under the higher strains significantly reduced.
- It is observable, as the strain level increase the instability district (II) gives way to district (I). Practically, both districts are probably the part of the same instability domain.
- It is noticeable, the location of both districts is in the accordance with the thermomechanical conditions which are connected with the higher values of activation energy, higher flow stress values and lower values of power dissipation efficiency, i.e., with conditions potentially associated with an aggravated deformation course.
- Nevertheless, neither the microstructure observation (realized inside of the instability districts and in a surrounding area) (Figure 9) nor the flow curve course (Figure 3) proves the apparent manifestation of the typical above-mentioned instability features. Only inclusions and segregations can be visible as the consequence of the effort to visualize original grain boundaries via etching procedure (Figure 9). It should be noted that under the constant temperature the ξ-values are sensitive to the changes in σ-value with the strain rate level. Unfortunately, these changes can be negatively influenced in the stage of data-acquiring procedure. In addition, the final processing-map form is influenced by the subsequent data processing, e.g., utilized surface-interpolation methods. These facts can lead to the overestimation of results and microstructural observations then should confirm or refute these results.

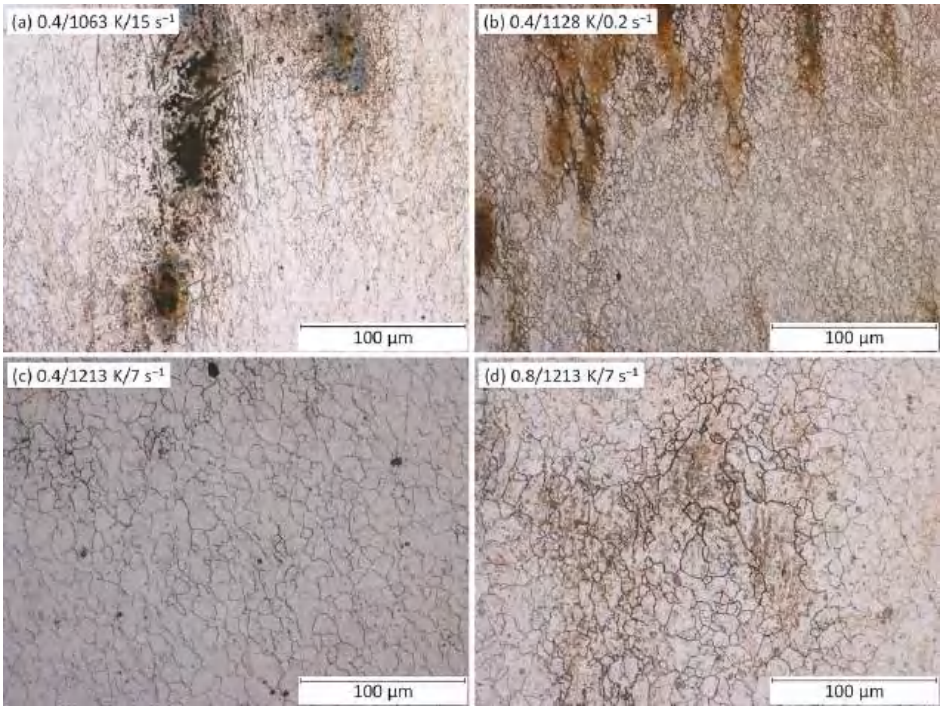

Figure 9. OM images of samples deformed under various strains. (**a**) 0.4/1063 K/15 s^{-1}; (**b**) 0.4/1128 K/0.2 s^{-1}; (**c**) 0.4/1213 K/7 s^{-1}; (**d**) 0.8/1213 K/7 s^{-1}.

The results have showed that the activation energy maps can be used as a support tool for the choice of appropriate forming conditions in cooperation with the conventional processing maps. As stated previously in [1] the main benefit of the AE maps is that they consider the difficulty of the deformation course. The above discussed correlation issue can enrich the overall awareness regarding the processing maps theory and can lead to the selecting of more useful forming conditions.

4. Conclusions

For the case of Cr-Mo low-alloyed steel, based on Prasad's dynamic material model, conventional hot processing maps, i.e., the maps of power dissipation efficiency (η) combined with the maps of metallurgical instability (ξ), have been assembled and subsequently superimposed over the maps of flow stress (σ) evolution and also over the maps of activation energy (Q) evolution.

Two flow curve datasets have been combined to assemble the mentioned maps. The experimental one has been acquired via a series of uniaxial hot compression tests realized up to the true strain of 1.0 in the temperature range of 1043–1553 K and the strain rate range of 0.02–20 s^{-1}. In order to gain a higher number of data points inside the experimental matrix, a multi-layer perceptron network has been assembled, trained, and subsequently utilized to predict the flow stress course under five additional temperature levels.

Based on the assembled maps, a correlation among the power dissipation efficiency, flow stress course, and activation energy evolution of the investigated steel has been studied. The basic presumption is: Higher η-values, lower Q-values, and lower σ-values should be connected with beneficial thermomechanical conditions. Correlation among these indicators should be natural since the relation between the flow stress and strain rate is utilized to calculate the η and Q values.

The η-evolution and σ-course are inversely proportional (the η-increase is connected with the σ-decrease). This indicates that η-increase is connected with the achieving of lower forming forces and energy consumption, and also with the progress of the softening course.

The η-evolution and Q-evolution are then proportional inversely with regard to the change in a temperature level (η-values increase as Q-values decrease). This indicates that Q-evolution and also η-evolution predict more beneficial conditions under the higher temperature levels. However, except of higher strains, they are non-unified with respect to the strain rate (both decrease as the strain rate increase). Thus, in contrast with the η-values, the Q-values predict better conditions under higher strain rates. Note, higher strain rates are beneficial with respect to the smaller grain size (providing a better strength-toughness combination).

Furthermore, the assembled processing maps reveal two instability districts. Both districts have been observed under the lower temperature levels, lower η-values, higher Q-values, and higher σ-values, i.e., under conditions linked with a harder deformation course.

The obtained findings can contribute to the enrichment of overall awareness about the processing maps theory, which can lead to the selecting of better forming conditions.

Author Contributions: Conceptualization: P.O.; data curation: P.O. and P.K.; formal analysis: P.O., R.K. and R.J.; investigation: P.O. and H.N.; methodology: P.O.; resources: R.J.; software: P.O.; supervision: P.O.; validation: P.O., I.S., P.K. and S.R.; visualization: P.O.; writing—original draft: P.O.; writing—review and editing: P.O., I.S., R.K., S.R. and H.N. All authors have read and agreed to the published version of the manuscript.

Funding: This research was funded by the project no. CZ.02.1.01/0.0/0.0/17_049/0008399 from the EU and CR financial funds provided by the Operational Programme "Research, Development and Education" and in within the frame of the Student Grant Competition SP2020/88 and SP2020/39 funded by Ministry of Education, Youth and Sports of the Czech Republic.

Acknowledgments: The authors wish to thank to Petr Vašíček (Department of Materials Forming, Faculty of Materials Science and Technology, VSB–Technical University of Ostrava) for the preparing of compression test samples and also to Ivana Malá (Department of Material Engineering, Faculty of Materials Science and Technology, VSB–Technical University of Ostrava) for the preparation of metallographic images.

Conflicts of Interest: The authors declare no conflict of interest. The funders had no role in the design of the study; in the collection, analyses, or interpretation of data; in the writing of the manuscript; or in the decision to publish the results.

References

1. Zhou, P.; Deng, L.; Zhang, M.; Gong, P.; Wang, X.-Y. Characterization of hot workability of 5052 aluminum alloy based on activation energy-processing map. *J. Mater. Eng. Perform.* **2019**, *28*, 6209–6218. [CrossRef]
2. Qian, P.; Tang, Z.; Wang, L.; Siyasiya, C.W. Hot Deformation characteristics and 3-D processing map of a high-titanium Nb-micro-alloyed steel. *Materials* **2020**, *13*, 1501. [CrossRef] [PubMed]
3. Liu, D.; Ding, H.; Cai, M.; Han, D. Hot Deformation behavior and processing map of a Fe-11Mn-10Al-0.9C duplex low-density steel susceptible to κ-carbides. *J. Mater. Eng. Perform.* **2019**, *28*, 5116–5126. [CrossRef]
4. Quan, G.Z.; Zhao, L.; Chen, T.; Wang, Y.; Mao, Y.P.; Lv, W.Q.; Zhou, J. Identification for the optimal working parameters of as-extruded 42CrMo high-strength steel from a large range of strain, strain rate and temperature. *Mater. Sci. Eng. A* **2012**, *538*, 364–373. [CrossRef]
5. Xu, L.; Chen, L.; Chen, G.; Wang, M. Hot deformation behavior and microstructure analysis of 25Cr3Mo3NiNb steel during hot compression tests. *Vacuum* **2018**, *147*, 8–17. [CrossRef]
6. Opěla, P.; Kawulok, P.; Kawulok, R.; Kotásek, O.; Buček, P.; Ondrejkovič, K. Extension of experimentally assembled processing maps of 10CrMo9-10 steel via a predicted dataset and the influence on overall informative possibilities. *Metals* **2019**, *9*, 1218. [CrossRef]
7. Zhang, C.; Zhang, L.; Shen, W.; Liu, C.; Xia, Y.; Li, R. Study on constitutive modeling and processing maps for hot deformation of medium carbon Cr–Ni–Mo alloyed steel. *Mater. Des.* **2016**, *90*, 804–814. [CrossRef]
8. Kliber, J.; Schindler, I.; Kawulok, P.; Sedláček, R. Energy dissipation and instability parameter at high temperature forming of middle carbon steel. In Proceedings of the 26th International Conference on Metallurgy and Materials, Brno, Czech Republic, 24–26 May 2017; Tanger Ltd.: Ostrava, Czech Republic, 2018; pp. 370–374, ISBN 978-80-87294-79-6.

9. Yang, Z.; Li, Y.; Li, Y.; Zhang, F.; Zhang, M. Constitutive modeling for flow behavior of medium-carbon bainitic steel and its processing maps. *J. Mater. Eng. Perform.* **2016**, *25*, 5030–5039. [CrossRef]
10. Kumar, N.; Kumar, S.; Rajput, S.K.; Nath, S.K. Modelling of flow stress and prediction of workability by processing map for hot compression of 43CrNi steel. *ISIJ Int.* **2017**, *57*, 497–505. [CrossRef]
11. Gao, X.J.; Jiang, Z.Y.; Wei, D.B.; Jiao, S.H.; Chen, D.F. Study on hot-working behavior of high carbon steel/low carbon steel composite material using processing map. *Key Eng. Mater.* **2014**, *622–623*, 330–339. [CrossRef]
12. Zhou, Y.; Liu, Y.; Zhou, X.; Liu, C. Processing maps and microstructural evolution of the type 347H austenitic heat-resistant stainless steel. *J. Mater. Res.* **2015**, *30*, 2090–2100. [CrossRef]
13. Zhang, P.; Hu, C.; Ding, C.-G.; Zhu, Q.; Qin, H.-Y. Plastic deformation behavior and processing maps of a Ni-based superalloy. *Mater. Des.* **2015**, *65*, 575–584. [CrossRef]
14. Mingjie, Z.; Fuguo, L.; Shuyun, W.; Chenyi, L. Characterization of hot deformation behavior of a P/M Nickel-base superalloy using processing map and activation energy. *Mater. Sci. Eng. A* **2010**, *527*, 6771–6779. [CrossRef]
15. Srinivasan, N.; Prasad, Y.V.R.K. Microstructural control in hot working of IN-718 superalloy using processing map. *Metall. Mater. Trans. A.* **1994**, *25*, 2275–2284. [CrossRef]
16. Wang, Y.; Jiang, S.; Zhang, Y. Processing map of NiTiNb shape memory alloy subjected to plastic deformation at high temperatures. *Metals* **2017**, *7*, 328. [CrossRef]
17. Quan, G.-Z.; Zou, Z.-Y.; Wang, T.; Liu, B.; Li, J.-C. Modeling the hot deformation behaviors of as-extruded 7075 aluminum alloy by an artificial neural network with back-propagation algorithm. *High. Temp. Mater. Process.* **2017**, *36*, 1–13. [CrossRef]
18. Liu, R.; Wang, W.; Chen, H.; Zhang, Y.; Wan, S. Hot deformation and processing maps of B_4C/6061Al nanocomposites fabricated by spark plasma sintering. *J. Mater. Eng. Perform.* **2019**, *28*, 6287–6297. [CrossRef]
19. Zhang, J.; Di, H.; Wang, H.; Mao, K.; Ma, T.; Cao, Y. Hot deformation behavior of Ti-15-3 titanium alloy: A study using processing maps, activation energy map, and Zener–Hollomon parameter map. *J. Mater. Sci.* **2012**, *47*, 4000–4011. [CrossRef]
20. Prasad, Y.V.R.K.; Gegel, H.L.; Doraivelu, S.M.; Malas, J.C.; Morgan, J.T.; Lark, K.A.; Barker, D.R. Modeling of dynamic materials behavior in hot deformation: Forging of Ti-6242. *Metall. Trans. A* **1984**, *15*, 1883–1892. [CrossRef]
21. Meng, Q.; Bai, C.; Xu, D. Flow behavior and processing map for hot deformation of ATI425 titanium alloy. *J. Mater. Sci. Technol.* **2018**, *34*, 679–688. [CrossRef]
22. Zhang, S.; Liang, Y.; Xia, Q.; Ou, M. Study on tensile deformation behavior of TC21 titanium alloy. *J. Mater. Eng. Perform.* **2019**, *28*, 1581–1590. [CrossRef]
23. Chakravartty, J.K.; Prasad, Y.V.R.K.; Asundi, M.K. Processing map for hot working of Alpha-Zirconium. *Metall. Trans. A* **1991**, *22A*, 829–836. [CrossRef]
24. Saxena, K.K.; Yadav, S.D.; Sonkar, S.; Pancholi, V.; Chaudhari, G.P.; Srivastava, D.; Dey, G.K.; Jha, S.K.; Saibaba, N. Effect of temperature and strain rate on deformation behavior of Zirconium alloy: Zr-2.5Nb. *Procedia Mater. Sci.* **2014**, *6*, 278–283. [CrossRef]
25. Suresh, K.; Dharmendra, C.; Rao, K.P.; Prasad, Y.V.R.K.; Gupta, M. Processing map of AZ31-1Ca-1.5 vol% nano-alumina composite for hot working. *Mater. Manuf. Process.* **2015**, *30*, 1–7. [CrossRef]
26. Zhang, Y.; Sun, H.; Volinsky, A.A.; Tian, B.; Song, K.; Chai, Z.; Liu, P.; Liu, Y. Dynamic recrystallization behavior and processing map of the Cu–Cr–Zr–Nd alloy. *Springer Plus* **2016**, *5*, 666. [CrossRef]
27. Duan, Y.; Ma, L.; Qi, H.; Li, R.; Li, P. Developed constitutive models, processing maps and microstructural evolution of Pb-Mg-10Al-0.5B alloy. *Mater. Charact.* **2017**, *129*, 353–366. [CrossRef]
28. Łyszkowski, R.; Bystrzycki, J. Hot deformation and processing maps of an Fe_3Al intermetallic alloy. *Intermetallics* **2006**, *14*, 1231–1237. [CrossRef]
29. Wang, S.; Luo, J.R.; Hou, L.G.; Zhang, J.S.; Zhuang, L.Z. Identification of the threshold stress and true activation energy for characterizing the deformation mechanisms during hot working. *Mater. Des.* **2017**, *113*, 27–36. [CrossRef]
30. GLEEBLE: Gleeble®Thermal-Mechanical Simulators. Available online: https://gleeble.com/ (accessed on 1 October 2019).
31. Opěla, P.; Schindler, I.; Kawulok, P.; Kawulok, R.; Rusz, S.; Rodak, K. Hot flow curve description of CuFe2 alloy via different artificial neural network approaches. *J. Mater. Eng. Perform.* **2019**, *28*, 4863–4870. [CrossRef]

32. Opěla, P.; Schindler, I.; Rusz, S.; Navrátil, H. A hot flow curve approximation via biology-inspired algorithms. In Proceedings of the 28th International Conference on Metallurgy and Materials, Brno, Czech Republic, 22–24 May 2019; Tanger Ltd.: Ostrava, Czech Republic, 2019; pp. 455–460, ISBN 978-80-87294-92-5.
33. Opěla, P.; Schindler, I.; Očenášek, V.; Kawulok, P.; Kawulok, R.; Rusz, S. Modelling the hot deformation behavior of AlSi1MgMn alloy via flow stress models utilizing intelligent algorithms. *Proced. Struct. Integr.* **2019**, *23*, 221–226. [CrossRef]
34. McCulloch, W.S.; Pitts, W.H. A logical calculus of ideas immanent in nervous activity. *Bull. Math. Biophys.* **1943**, *5*, 115–133. [CrossRef]
35. Rosenblatt, F. The perceptron: A probabilistic model for information storage and organization in the brain. *Psychol. Rev.* **1958**, *65*, 386–408. [CrossRef] [PubMed]
36. Krenker, A.; Bešter, J.; Kos, A. Introduction to the artificial neural networks. In *Artificial Neural Networks Methodological Advances and Biomedical Applications*; Suzuki, K., Ed.; InTech: Rijeka, Croatia, 2011; pp. 3–18.
37. Debes, K.; Koenig, A.; Gross, H.M. Transfer Functions in Artificial Neural Networks: A Simulation-based Tutorial. Available online: https://www.brains-minds-media.org/archive/151/ (accessed on 16 September 2019).
38. Gauss, J.C.F. *Theory of the Combination of Observations Least Subject to Errors*; Henricum Dieterich: Göttingen, Germany, 1823; pp. 53–57. (In Latin)
39. Levenberg, K. A method for the solution of certain non-linear problems in least squares. *Quart. Appl. Math.* **1944**, *2*, 164–168. [CrossRef]
40. Marquardt, D.W. An algorithm for least-squares estimation of nonlinear parameters. *J. Soc. Indust. Appl. Math.* **1963**, *11*, 431–441. [CrossRef]
41. Roweis, S. Levenberg-marquardt Optimization. Available online: https://cs.nyu.edu/~{}roweis/notes/lm.pdf (accessed on 1 October 2019).
42. Bayes, T.; Price, R. An essay towards solving a problem in the doctrine of chance. By the late Rev. Mr. Bayes, F.R.S. communicated by Mr. Price, in a letter to John Canton, A.M.F.R.S. *Phil. Trans.* **1763**, *53*, 370–418. [CrossRef]
43. MacKey, D.J.C. Bayesian interpolation. *Neural Comput.* **1992**, *4*, 415–447. [CrossRef]
44. Rumelhart, D.E.; Hinton, G.E.; Williams, R.J. Learning internal representations by error propagation. In *Parallel Distributed Processing: Explorations in the Microstructure of Cognition*; Feldman, J.A., Hayes, P.J., Rumelhart, D.E., Eds.; The MIT Press: Cambridge, MA, USA, 1986; Volume 1, pp. 318–362.
45. MathWorks. MATLAB® Math. Graphics. Programming. Available online: https://www.mathworks.com/products/matlab.html (accessed on 18 September 2019).
46. Beale, M.H.; Hagan, M.T.; Demuth, H.B. Neural Network Toolbox™ 7: User's Guide. Available online: https://www2.cs.siu.edu/~{}rahimi/cs437/slides/nnet.pdf (accessed on 18 September 2019).
47. Alexander, J.M. Mapping dynamic material behaviour. In *Modelling Hot Deformation of Steels*; Lenard, J.G., Ed.; Springer: Berlin Heidelberg, Germany, 1989; pp. 101–115.
48. Gegel, H.L.; Malas, J.C.; Doraivelu, S.M.; Shende, V.A. Modeling techniques used in forging process design: Dynamic material modeling. In *ASM Handbook*, 9th ed.; Semiatin, S.L., Ed.; ASM International: Geauga, OH, USA, 1996; pp. 918–924.
49. Kumar, A.K.S.K. Criteria for predicting metallurgical instabilities in processing. Master's Thesis, Institute of Science, Bangalore, India, 1987.
50. Prasad, Y.V.R.K. Recent Advances in the Science of Mechanical processing. *Indian J. Technol.* **1990**, *28*, 435–451.
51. Schindler, I.; Kawulok, P.; Kawulok, R.; Hadasik, E.; Kuc, D. Influence of calculation method on value of activation energy in hot forming. *High Temp. Mater. Process.* **2013**, *32*, 149–155. [CrossRef]
52. Schindler, I.; Kawulok, P.; Hadasik, E.; Kuc, D. Activation energy in hot forming and recrystallization models for magnesium alloy AZ31. *J. Mater. Eng. Perform.* **2013**, *22*, 890–897. [CrossRef]
53. Kawulok, P.; Schindler, I.; Kawulok, R.; Opěla, P.; Sedláček, R. Influence of heating parameters on flow stress curves of low-alloy Mn-Ti-B steel. *Arch. Metall. Mater.* **2018**, *63*, 1785–1792. [CrossRef]
54. Schindler, I.; Kawulok, P.; Očenášek, V.; Opěla, P.; Kawulok, R.; Rusz, S. Flow stress and hot deformation activation energy of 6082 aluminium alloy influenced by initial structural state. *Metals* **2019**, *9*, 1248. [CrossRef]

55. Mohamadizadeh, A.; Zarei-Hanzaki, A.; Abedi, H.R. Modified constitutive analysis and activation energy evolution of a low-density steel considering the effects of deformation parameters. *Mech. Mater.* **2016**, *95*, 60–70. [CrossRef]
56. Liu, L.; Wu, Y.X.; Gong, H.; Wang, K. Modification of constitutive model and evolution of activation energy on 2219 aluminum alloy during warm deformation process. *Trans. Nonferrous Met. Soc. China* **2019**, *29*, 448–459. [CrossRef]
57. Garofalo, F. An empirical relation defining the stress dependence of minimum creep rate in metals. *Trans. Metall. Soc AIME* **1963**, *227*, 351–356.
58. Simpson, T. A letter to the Right Honourable George Earl of Macclesfield, President of the Royal Society, On the Advantage of Taking the Mean of a Number of Observations in Practical Astronomy. *Philos. Trans.* **1755**, *49*, 82–93. [CrossRef]
59. Pearson, K. Note on regression and inheritance in the case of two parents. *Proc. R. Soc. Lond.* **1895**, *58*, 240–242.
60. Gnuplot: Portable Command-line Driven Graphing Utility. Available online: http://www.gnuplot.info/ (accessed on 18 September 2019).

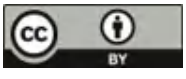

materials

MDPI

Article

Developments towards a Multiscale Meshless Rolling Simulation System

Umut Hanoglu [1,2,*] and Božidar Šarler [1,2]

[1] Institute of Metals and Technology, Lepi Pot 11, 1000 Ljubljana, Slovenia; bozidar.sarler@fs.uni-lj.si
[2] Faculty of Mechanical Engineering, University of Ljubljana, Aškerčeva 6, 1000 Ljubljana, Slovenia
* Correspondence: umut.hanoglu@imt.si; Tel.: +386-1-4701-906

Abstract: The purpose of the present paper is to predict the grain size of steel during the hot-rolling process. The basis represents a macroscopic simulation system that can cope with temperatures, stresses and strains of steel in a complete continuous rolling mill, including reversible pre-rolling and finishing rolling with several tenths of rolling passes. The grain size models, newly introduced in the present paper, are one-way coupled to the macro-scale calculations performed with the slice model assumption. Macroscale solution is based on a novel radial basis function collocation method. This numerical method is truly meshless by involving the space discretization in arbitrarily distributed nodes without meshing. A new efficient node generation algorithm is implemented in the present paper and demonstrated for irregular domains of the slice as they appear in different rolling passes. Multiple grain size prediction models are considered. Grain size prediction models are based on empirical relations. Austenite grain size at each rolling pass as well as the ferrite grain size at the end of rolling are predicted in this simulation. It is also shown that based on the rolling schedule, it is highly likely that recrystallization takes place at each pass throughout a continuous rolling mill. The simulation system is coded as a user-friendly computer application for industrial use based on programming language C# and an open source developer platform NET and runs on regular personal computers the computational time for a typical rolling simulation is usually less than one hour and can thus be straightforwardly used to optimize the rolling mill design in a reasonable time.

Keywords: meshless methods; radial basis functions; hot rolling; steel; recrystallization; austenite grain size; ferrite grain size

Citation: Hanoglu, U.; Šarler, B. Developments towards a Multiscale Meshless Rolling Simulation System. *Materials* **2021**, *14*, 4277. https://doi.org/10.3390/ma14154277

Academic Editor: Ivo Schindler

Received: 24 June 2021
Accepted: 26 July 2021
Published: 30 July 2021

1. Introduction

In the present paper, the macroscopic simulation system, coping with a complete continuous rolling mill, including reversible pre-rolling and finishing rolling with several tenths of rolling passes [1–5], is upgraded to deal with grain size prediction. The main aim is to calculate, in addition to the temperature and deformation fields, the austenite grain size at each rolling pass and ferrite grain size at the end. The microscopic grain-size prediction models are one-way coupled to the macroscopic thermo-mechanical simulation. A previously developed 2D numerical model [6], based on the slices that allow only plane strain deformation and are aligned perpendicular to the rolling direction, is used. The slices on which 2D stresses and temperature fields are computed are illustrated in Figure 1.

Shaping any metal, such as in the hot rolling process, requires consideration of large plastic deformation. An overview of related multiscale physics is given in the following paragraphs. The start of this plastic deformation process is triggered when the dislocations can move inside a grain. This threshold is the yield stress, and its value depends on the dislocation density. By applying deformation and heat treatment, dislocation density and the grain sizes face a significant variation.

If the strain rate and temperature are high enough, a different phenomenon, dynamic recrystallization, occurs. The dynamic recrystallization depends on the critical strain. As a

result, new grain sizes appear, either partially or fully. However, not all recrystallization takes place immediately after exceeding the critical strain. After a particular time, meta-dynamic crystallization may take place.

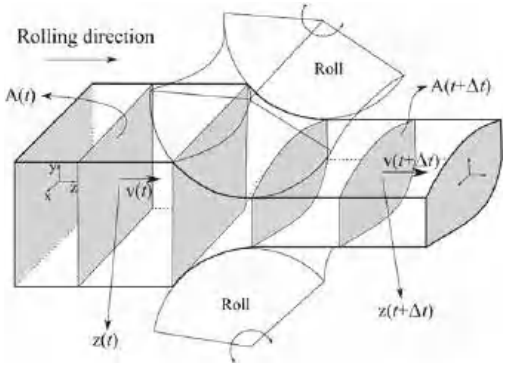

Figure 1. Scheme of slice model used in the macroscopic rolling simulations. $A(t)$ is area, $v(t)$ is velocity and $z(t)$ is position.

When the deformation is small, or there is no deformation, a softening process may occur due to sufficient time at high temperatures. The softening can again lead to partial or complete static recrystallization. Static recrystallization usually leads to larger grains with higher temperatures [7]. The stored energy in a material is proportional to the defect density. Therefore, an increase in grain size decreases the total grain boundary area and as a result, the stored energy is reduced.

The numerical prediction of grain size constitutes an essential aspect of microstructure studies [8]. Smaller grains may be desired since they lead to higher strength because it is harder for dislocations to pass over the grain boundaries during plastic deformation. Or the other way around for the ductility. The steel industry needs to predict the mechanical properties of their final product, which is only possible with the microstructure analysis [9].

In this paper, multiple grain size prediction models [10–17] were coupled with the macroscopic rolling simulation system. The basis of the micro-scale simulation used in the present paper is based on the model predicted by Hodgson and Gibbs [10] with minor adjustments. Multiple grain size prediction models for different types of steels were gathered. These models consist of empirical correlations to determine the critical strain and grain size after meta-dynamic, dynamic or static recrystallization. All the necessary input data for these models were obtained from the macroscopic 2D slice model results. Checking for possible recrystallization type and predicting the corresponding austenite grain size was performed immediately after obtaining the macroscopic results for each slice. After the hot rolling process was completed, the rolled steel was still hot and considered mainly in the austenite phase. Based on the models found in the literature, ferrite grain size prediction could be made as a function of the cooling process. Ferrite transformation temperature is calculated based on the material composition, and in the simulations, the steel is cooled down just below that transformation temperature. The discussion of how to implement the microscopic models can be found in textbooks [1,9]. Since it was not possible to obtain all the correlations for each steel grade separately for all the micro-scale simulation sections, a combination of those relations for various steel types were gathered and also applied. This was just to show that in this way, both macro and micro simulation results of hot rolling could be obtained easily by using a single meshless simulator. A specific model was used for each sub-section of micro simulation, but the necessary parameters were material dependent, and they could also be user-defined. In the results section, the first macro scale simulation results by using 16MnCrS steel were given. Later the same results were used as inputs for multiple micro-scale simulations. Comparison of different grain size prediction

models were shown to distinguish the behaviour of each model. Each collocation point in a computational domain represents a small area with a uniform grain structure.

Over the years, a comprehensive rolling simulation system has been developed for industrial use. The supporting steel factory provides rolling schedules in use, and macro-scale simulations have been up to now run by a successful macroscopic hot rolling simulation system [18]. The meshless solution of the macro-scale deformation was chosen here since it is very straightforward to distribute collation nodes over a computational domain. Therefore, it was easy to implement numerically and also did not require any background integration. Meshless methods were multiple times proven to solve thermal [19] and mechanical [20] problems efficiently and accurately. Recently, micro-scale simulation capabilities based on empirical relations found in the literature were added, and a one-way coupling between macro and micro-scale models was formed. The motivation for the present research was understanding and simulating the material behaviour in between the passes, which is usually ignored during a multi-pass rolling. In the majority of the simulations, the initial material definition was used throughout the simulation regardless of the number of deformation steps, time and temperature. This work clearly shows the possibility of recrystallization at each pass separately during hot rolling and how much the material properties may change, based on the change of the grain size.

In the present paper, the possibility of complete or partial recrystallization is modelled. This makes more realistic the assumption of complete recrystallization at each roll pass, as assumed in some publications [17]. Furthermore, the effects of the chemical composition of the steel billet on its macro response and grain structure are also investigated.

2. Materials and Methods

It is pointed out by Sellars [8] that the experimental tests or industrial trials are not enough to understand all the details of the hot rolling process since it is impossible to control or monitor all the parameters of rolling in industrial conditions and even in laboratory conditions. Therefore, the best solution suggested by Sellars [14] is combining the numerical simulations with empirical models based on experiments. A macro-scale numerical prediction of the deformation of steel with heat transfer during hot rolling has been previously developed [6,18]. To achieve the microstructure evolution just as described in Figure 2, we need to know the initial grain configuration and empirical models that depend on the involved steel grade.

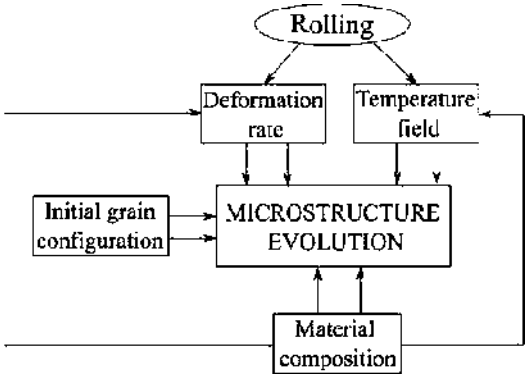

Figure 2. Picture of one-way macro-micro coupling.

2.1. Macro Scale Solution

Thermo-mechanical simulation of rolling is based on 2D slices aligned towards the rolling direction. The slices were simulated one after another, and both thermal and mechanical models were solved in a coupled way

$$\mathbf{L}^{\mathrm{T}}\boldsymbol{\sigma} + \mathbf{b} = 0, \tag{1}$$

$$\rho c_p \frac{\partial T}{\partial t} = \nabla \cdot (k \nabla T) + \dot{Q}, \tag{2}$$

where $\mathbf{L}, \boldsymbol{\sigma}, \mathbf{b}$ are derivative operator matrix, stress vector and body force vector, respectively. $\rho, c_p, T, k, \dot{Q}$ stand for the density, specific heat, temperature, thermal conductivity and internal heat generation, respectively. The meshless numerical procedure is based on the interpolation of an unknown field $\theta(\mathbf{p})$ at position $\mathbf{p} = p_x \mathbf{i}_x + p_y \mathbf{i}_y$, interpolated with radial basis shape functions $\psi(\mathbf{p})$ over seven neighbouring nodes (N) as shown in Figure 3,

$$\theta(\mathbf{p}) = \sum_{i=1}^{N} \psi_i(\mathbf{p}) \alpha_i, \tag{3}$$

where α_i are the collocation coefficients that need to be determined. The partial derivatives of the unknown field can be calculated as

$$\frac{\partial \theta(\mathbf{p})}{\partial x_j} = \sum_{i=1}^{N} \frac{\partial \psi_i(\mathbf{p})}{\partial x_j} \alpha_i. \tag{4}$$

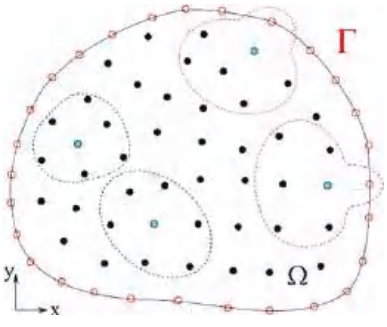

Figure 3. Scheme of the domain Ω and boundary Γ discretization with indicated local influence domains consisting of 7 node and for each central node in an influence domain is marked in blue.

The temperature in the thermal model and the mechanical model's displacement field are interpolated with the multi-quadric (MQ) radial basis functions (RBF). The details of the solution of these two models have been previously published in [21].

The boundary condition for the thermal model is of the Robin type,

$$-k \frac{\partial T}{\partial \mathbf{n}_\Gamma} = h\left(T - T^{ref}\right). \tag{5}$$

where k is thermal conductivity, $\mathbf{n}_\Gamma$ is unit normal vector on the surface, h is heat transfer coefficient, and T^{ref} is the reference temperature. The majority of complications during simulation usually appear at the contact boundaries between the strand and the groove. The heat flux there becomes very high in comparison with the non-contact boundaries. At the contact boundaries, T^{ref} is considered as the roll's surface temperature. The boundary conditions for the mechanical model are described both with the prescribed traction ($\overline{\tau}$) and the prescribed displacement ($\overline{u}$)

$$\overline{\tau} = -\mu p, \ \overline{u} = u, \tag{6}$$

where μ is the coefficient of friction, p is stress acting on the boundary, and u is the displacement. In some rare cases, when the groove surface has a unique geometry, prescribed

traction boundary condition may not be appropriately satisfied, and might lead to erroneous results. To overcome this issue, during the calculation step at first contact, an artificially sticking boundary condition was applied to some of the boundary points. This resulted in no relative motion between the roll surface and the boundary in one calculation step. Later all the boundary nodes received proper boundary conditions defined in Equation (6) as schematically seen in Figure 4.

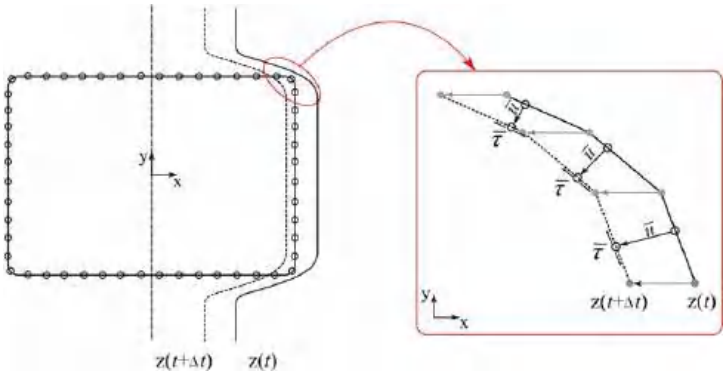

Figure 4. Boundary nodes during contact with groove surface and applied boundary conditions.

Interpolating an unknown field with regular node distribution over a rectangular domain works perfectly with meshless Local Radial basis Function Collocation Method (LRBFCM) and is also easy to implement numerically. However, severe deformation simulations, such as rolling or forging, require redistribution of the computational nodes. In other words, a solution with the regular node distribution becomes impossible in large deformations. An essential advantage of the LRBFCM is that it gives stable results also with scattered node distribution. A comparison of the results is shown later in this paper where a rectangular domain is interpolated with regular and scattered node distribution.

LRBFCM interpolates the temperature field in the thermal model, and the governing equation is solved through explicit time stepping. The time step is chosen as 1 ms. The nodes of the mechanical and thermal models coincide. The solution is obtained through local interpolation for each influence domain without creating a global matrix. In the mechanical model, interpolation of displacement filed over each local influence domain can be assembled into a global solution matrix (**A**) by replacing the local collocation coefficients with the inverse of the local interpolation matrix and the local displacement vector. Hence, the system of equations can be written in the following form

$$\mathbf{AU} = \mathbf{B}, \tag{7}$$

and solved for global column matrix of displacements $\mathbf{U} = \left[u_{x1}, u_{y1}, \ldots\ldots, u_{xN}, u_{yN}\right]^{\mathrm{T}}$ with the size of two times the number of collocation nodes ($2N$). The adjacent vector **B** includes the boundary values. As a result of the nonlinear material model of steel, the solution matrix **A** depends on the current state of displacements. The solution can only be achieved iteratively. In this paper, a direct iteration method was chosen due to its simplicity and to avoid assembling the Jacobian matrix. The local solution of the system of equations leads to a sparse matrix **A**, and with the help of the Intel math kernel library [22], it can be solved efficiently by direct iteration with iteration index j.

$$\mathbf{A}\left(\mathbf{U}^{j}\right)\mathbf{U}^{j+1} = \mathbf{B}, \tag{8}$$

2.2. Micro Scale Solution

In the present work, the critical strain, the time for dynamic, meta-dynamic or static recrystallization and the grain sizes after different types of recrystallization implemented through a sequence of different empirical models. It is assumed that each collocation point in a computational domain represents a small area with a uniform grain structure. Grain size prediction models were obtained for the austenite phase. Solution steps were adopted from Hodgson and Gibbs [10], as shown in Figure 5.

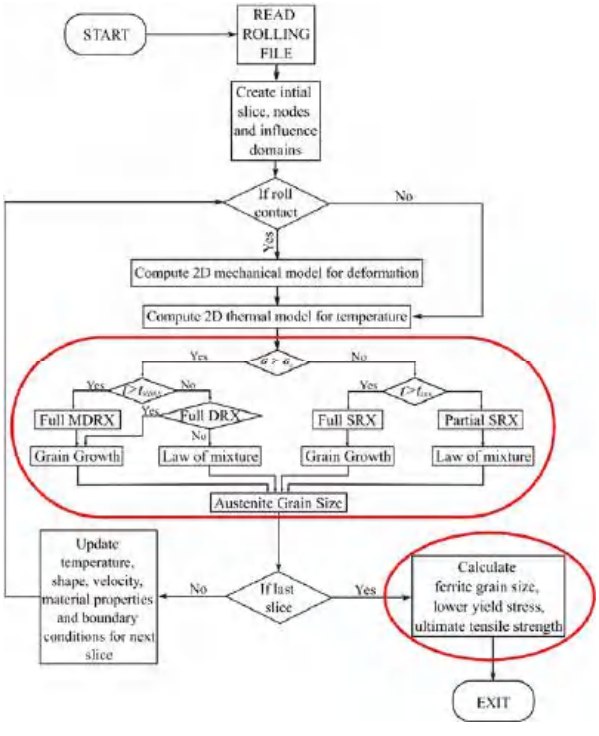

Figure 5. Scheme of the multiscale rolling simulation system. Micro-scale simulation steps are circled with red.

2.2.1. Critical Strain

The micro-scale modelling starts by checking first if the strain field in some of the points, some of the sub-areas or globally exceeds the critical strain value (ε_c)

$$\varepsilon_c = A_c \underbrace{\left(\dot{\varepsilon} \exp \frac{Q_d}{RT}\right)^p}_{Z} D^q, \tag{9}$$

where Z denotes the Zener–Hollomon parameter (s^{-1}), used in a multitude of empirical relations, $\dot{\varepsilon}$ is strain rate, Q_d is activation energy (J/mol K), R is ideal gas constant 8.314 J/mol K, T is temperature in Kelvin and D is the initial austenite grain size diameter. The coefficients in Equation (9) for different steel grades are listed in Table 1. The dynamic or meta-dynamic recrystallization is triggered at the points where the critical strain value is exceeded. This can occur locally or on the global scale of the domain.

Table 1. Parameters used in the critical strain definition for carbon–manganese steel in [11,12,14] and low carbon steel in [13].

Coefficients	[11]	[12]	[13]	[14]
A_c	6.82×10^{-4}	4.76×10^{-4}	4.9×10^{-4}	4.9×10^{-4}
Q_d	312,000	66,500	300,000	312,000
p	0.13	0	0.17	0.15
q	0	0	0.3	1

2.2.2. Dynamic Recrystallization

The dynamic recrystallization (*DRX*) occurs when the critical strain is reached, but time is not long enough for meta-dynamic recrystallization. The grain size is predicted from the following equation

$$D_{DRX} = A_d Z^r, \tag{10}$$

The coefficients of Equation (10) are defined in Table 2 below.

Table 2. Parameters used in the grain size equation for dynamic recrystallization of carbon–manganese steel.

Coefficients	[10]	[12]	[14]	[16]
A_d	16,000	22,600	1800	16,000
r	−0.23	−0.27	−0.15	−0.23
Q_d	312,000	267,100	312,000	300,000

2.2.3. Meta-Dynamic Recrystallization

The meta-dynamic crystallization is also called post dynamic recrystallization. Its effect on the grain size is similar to the dynamic recrystallization; however, there is a time-based criterion that includes strain rate. In this paper, the following definition is used [15],

$$t_{MDRX} = 1.166\varepsilon^{-0.8}, \tag{11}$$

as developed by Manohar et al. If the current time t at any deformation step exceeds the criterion ($t > t_{MDRX}$), it is considered that the meta-dynamic recrystallization (*MDRX*) occurs. If this is the case, the grain sizes must be recalculated from the following equation,

$$D_{MDRX} = A_m Z^r. \tag{12}$$

The grain size prediction model for the meta-dynamic and dynamic recrystallization is the same, but the coefficients are different. The constants of Equation (12) are defined in Table 3 below.

Table 3. Parameters used in the grain size equation for meta-dynamic recrystallization of carbon–manganese steel [10,14,16], and low carbon steel [10].

Coefficients	[10]	[13]	[14]	[16]
A_m	26,000	25,000	1600	26,000
r	−0.23	−0.23	−0.11	−0.23
Q_d	312,000	312,000	312,000	300,000

2.2.4. Static Recrystallization

There is a time criterion for static recrystallization (SRX) to occur, and in this paper, a model defined by Zhang et al. [16] for high carbon steel is used. It has the following form,

$$t_{SRX} = 1.944 \times 10^{-4} \varepsilon^{-1.0} D_0^{0.6} \left(\frac{3.6}{\dot{\varepsilon}}\right)^{0.28} \exp\left(\frac{6900}{RT}\right). \quad (13)$$

when the time during the simulation is larger than $(t > t_{SRX})$ then, static recrystallization may be expected. The grain size after the recrystallization is obtained from

$$D_{SRX} = A_s \varepsilon^m D_0^r \quad (14)$$

The coefficients for Equation (14) are defined in Table 4.

Table 4. Parameters used in the grain size prediction model when static recrystallization takes place. These parameters are obtained by Zhang [16] for high carbon steel and Sellars [8] for carbon manganese steel.

Coefficients	[13]	[7]
A_s	0.5	1
m	−0.67	−0.5
r	0.67	0.4

2.2.5. Grain Growth

After complete recrystallization, the grains will grow until the next partial or complete recrystallization. In the present paper, the following grain growth model to calculate the new grain size is considered for three types of steel.

$$D_{GG0} = D_0^n + k_s t \exp\left(\frac{Q_{GG}}{RT}\right). \quad (15)$$

The coefficients for Equation (15) are defined in Table 5.

Table 5. Parameters used in the grain growth calculation when complete recrystallization takes place. These parameters were obtained by Hodgson and Gibbs [10] for three types of steel.

Coefficients	C-Mn-V	C-Mn-Ti	C-Mn-Nb
n	7	10	4.5
k_s	1.45×10^{27}	2.6×10^{28}	4.1×10^{28}
Q_{GG}	−400	−437	−435

2.2.6. No-Recrystallization Temperature

It is known from the experiments that recrystallization may not occur every time, even though the conditions are met. This limitation comes from the temperature value. If it is below a certain value (T_{nr}), recrystallization will not take place. This temperature value is defined from the following equation given in [23]

$$T_{nr} = A_n \varepsilon^m \dot{\varepsilon}^n t^k, \quad (16)$$

where $A_n = 905$, $m = -0.045$, $n = -0.006$, $k = -0.024$ and t is the time in seconds. These values are for high strength low alloy steel, experimentally obtained in [24]. The time in Equation (16) is accounted for only during the deformation process.

2.2.7. Ferrite Grain Size Prediction

After the steel leaves the last rolling stand, it is cooled in a controlled way at the cooling bed. During the cooling process the austenite phase transforms into ferrite and perlite, especially for C-Mn steels. In this paper, only the ferrite transformation is considered, and the temperature at which the transformation occurs is called Ferrite Transformation Temperature (FTT). (FTT) for any type of steel in °C is calculated based on the following equation given in [25]:

$$T_{FTT} = 910 - 310[\%C] - 80[\%Mn] - 20[\%Cu] - 15[\%Cr] - 80[\%Mo] - [\%Ni]. \quad (17)$$

The steel has to cool down until the maximum temperature goes below the FTT, and with that specific cooling rate at that temperature, the ferrite grain size can be predicted based on the following equation.

$$D_F^0 = (\alpha_0 + \alpha_1 C_{eq}) + (\alpha_3 + \alpha_4 C_{eq})\dot{T}^{-0.5} + \alpha_4(1 - \exp(\alpha_5 D_A)). \quad (18)$$

The necessary coefficients are defined in Table 6. It is important here not to ignore the residual strain (ε_r) which has an impact on reducing the ferrite grain size. If complete recrystallization occurred at each roll pass, the residual strains were obtained only from the last rolling stand. The following model by Sellars and Beynon [26] is considered in the simulations to calculate the final ferrite grain size.

$$D_F = D_F^0(1 - 0.45\sqrt{\varepsilon_r}). \quad (19)$$

Table 6. Parameters used to calculate ferrite grain size for C-Mn steel.

Coefficients	[10] (%C) + (%Mn)/6 > 0.35	[10] (%C) + (%Mn)/6 < 0.35	[26] C-Mn-Ti
α_0	−0.4	22.6	1.4
α_1	6.37	−57	0
α_2	24.2	3	5
α_3	−59	0	0
α_4	22	22	22
α_5	0.015	0.015	0.015

2.3. Coupling of Micro and Macro Models

Macro-scale simulation is followed by micro-scale simulation for each slice at a time except for the final ferrite grain size, which is calculated at the end. The major steps of the macro and micro-simulation steps and the coupling between them can be seen in Figure 5. The results were visualized for each slice, in particular at the exit from each rolling stand. The temperature, strain and strain rate fields are the inputs of the micro-scale model and were obtained from the macro-scale simulation results. This solution procedure represents a one way coupled system. When the simulation is completed, switching between or rearranging the micro-scale models and recalculating them is possible. Each micro-scale simulation took a few seconds. It was unnecessary to rerun the macro-scale simulation, which is time-consuming, to make a sensitivity study with different micro-scale model parameters. It was also possible to add entirely new micro-scale correlations into the database. There are two different ways of visualization of the micro-scale results. First is the type of recrystallization to see if it is partial or complete and when it happens. The second outcome is the grain size at each slice position, scaled from the minimum to the maximum.

3. Node Positioning

After the continuous casting in a typical steel production line, the strand proceeds to a reheating furnace to remove the cast dendritic structures and homogenize most alloying elements [2]. The strand afterwards deforms in the reversing rolling mill to obtain the desired pre-shape for the continuous rolling mill. The initial rectangular shape for the finishing rolling was not a perfect rectangle, but it had curved corners. We obtained the proper initial shape for use in the finishing rolling by using the reversing rolling mill simulation results. The regular node distribution was straightforward to generate and effective for the perfect rectangular shape. However, the regularly distributed nodes did not correctly provide the appropriate results near the curved edges.

Most of the rolling schedules used in the simulations may be categorized into two groups when rolling the billets. In the first group, oval grooves were used to achieve more oval or round-shaped forms. In the second group, primarily flat rolls were used to get more slab-like shapes. Regular node distribution was adequate for most of the slab simulations; however, regular nodes faced stability issues for a schedule that turns a rectangular billet into a round bar. Previously we used an Elliptic Node Generation (ENG) algorithm [27,28] for positioning the nodes in the domains with curved boundaries. This algorithm successfully maps a rectangular shape to an arbitrary shape with four sides and ensures high orthogonality. The downside of this method represents a mapped corner. This corner is potentially most tricky during any interpolation, just like in a rectangular domain. However, if we use an irregular node arrangement, this corner complexity will be lost completely. This provides a much more extensive deformation range with stable results.

3.1. Regular vs. Irregular Node Positioning

A fast, irregular node generation algorithm [29] is numerically implemented in the rolling simulation system. Additionally, the first row of internal points, just next to the boundaries, is aligned in the opposite direction of the unit normal of the nearest boundary point.

3.2. Node Repelling Algorithm

Due to the different texture of internal points near the boundaries and the rest of the internal points, an iterative node adjustment algorithm was used. In this way, the neighbouring nodes have a more uniform distance to the central nodes. The adjustment is based on a node repelling algorithm. The vector component of displacement Δu_i, due to repelling, is defined as

$$\Delta u_i = C \sum_{j=1}^{N_{\max}} s \frac{p_i - p_i^j}{\left(\| p_i - p_i^j \| \right)^n}. \tag{20}$$

C is a smoothing factor usually taken between 0 and 1. The higher the node density, the smaller it should be. In this paper it is taken as $(1/6)$. s is also a similar factor taken as 1, and reduced to 0.8 when at least one neighbouring point is located at a boundary. N_{MAX} is a maximum number of the nearest nodes to consider without the boundary nodes. It was taken as 45 during the first iteration, and it was slowly reduced in each iteration until it reached seven nodes inside an influence domain.

4. Numerical Results

In this section, multiple numerical results from the represented multiscale rolling simulation system (Institute of metals and technology, version 7.6.4, Ljubljana, Slovenia) are illustrated. Macro-scale results are compared with regular and irregular collocation nodes and also compared with Finite Element Method (FEM) results. Later, an actual rolling schedule which consists of eight rolling stands, is applied. Micro-scale results are demonstrated in terms of grain size and recrystallization throughout the rolling schedule. The necessary values and definitions are given in Table 7.

Table 7. Parameters used in the rolling simulation.

General Data	
Initial size of the slab	60.48 × 60.48 mm
Initial temperature field of the slab	1100 °C
Entry velocity towards the rolling direction	760 mm/s
Coefficient of friction	0.15
Initial grain size	10 μm
Material Model	
$\overline{\sigma}\left(\overline{\varepsilon}, \dot{\overline{\varepsilon}}, T\right) = 589\overline{\varepsilon}^{0.214}\dot{\overline{\varepsilon}}^{0.2}\exp\left(\frac{38{,}000}{RT}\right)$ MPa, for 16MnCr5 alloyed steel	
Thermal Model	
Thermal conductivity	29 W/mmK
Specific heat	630 J/KgK
Density	7450 kg/m^3
Heat transfer coefficient to air	20 W/m^{2}K
Heat transfer coefficient to roll	10,000 W/m^{2}K
Roll surface temperature	600 °C
Groove and Roll Data	
Roll radii	230 mm
Roll gaps	34.5–26.5–118–22.5–112–20–107.4–18.2 (mm)
Groove geometries (H-horizontal, V-vertical)	flat (H)—flat (H)—oval box (V)—flat (H)—flat box (V)—flat (H)—flat box (V)—flat (H)
Distance between rolling stands	3 m (for the first five rolling stands), 4.5 m (after the fifth rolling stand).

4.1. Regular vs. Irregular Node Positioning—Slab

An initial slab with 217 × 45 mm^2 is flat-rolled into 34.5 mm height. The material is elastic with Young's modulus 10^6 Pa and Poisson's ratio 0.35. A regular node distribution with 546 nodes and irregular with 571 nodes are used, as shown in Figure 6. The deformation is calculated in 11 steps in both cases, and the coefficient of friction is taken as 0.1.

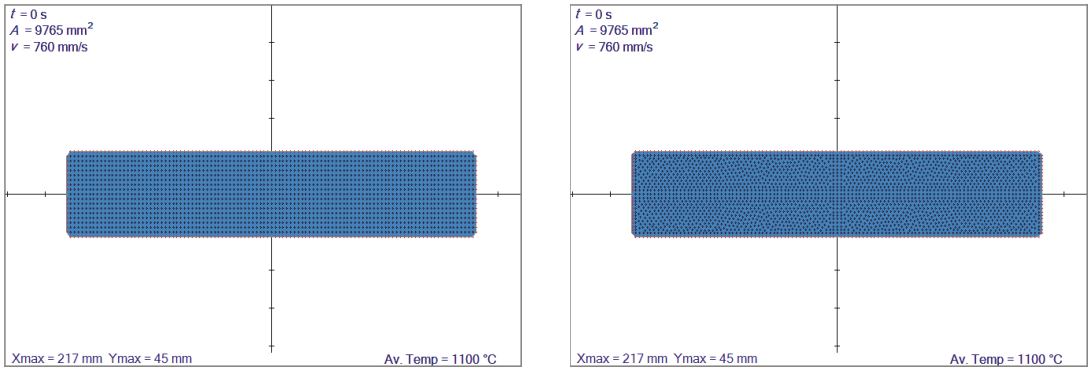

Figure 6. Comparison of different initial node arrangements. Regular node distribution (**left**), irregular node distribution (**right**). Av. Temp. stands for average temperature.

The results in terms of effective strain can be seen in Figure 7. The results are almost identical; therefore, for a slab that undergoes the flat rolling, irregular node generation has no distinct benefit.

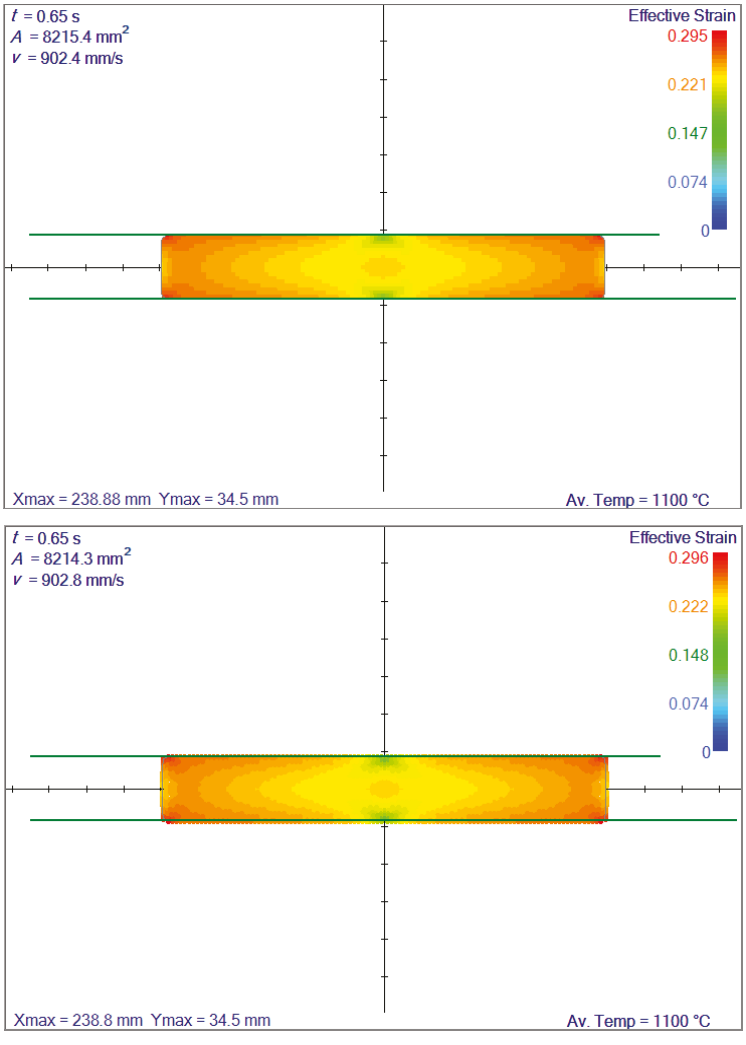

Figure 7. Comparison of effective strain fields after 10.5 mm of reduction. Av. Temp. stands for average temperature.

4.2. Regular vs. Irregular Node Distribution—Real Shape

More distinct differences occur when starting from an initial shape with curved corners, as obtained from the reversing rolling mill. The node arrangement is kept regular with ENG [28] and irregular with the algorithm [29], as shown in Figure 8. The regular and irregular node distributions involve 396 and 400 nodes, respectively.

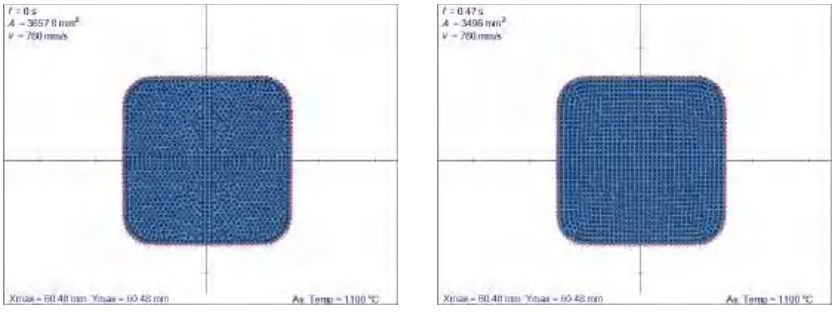

Figure 8. Irregular nodes (**left**) and regular nodes with mapping (**right**). Av. Temp. stands for average temperature.

The instability issue at the edge of the first contact is still carried out until the end of the simulation in the regular node arrangement. In Figure 9, it is shown that irregular node arrangement made a better interpolation when the boundary shape diverges from regular (rectangular) geometry. Smoothed corners created problems with regular node arrangement. Comparing with FEM results in Figure 9c, the overshoot near the corner in Figure 9b is very clear. However, this can be overcome by using an irregular node arrangement where the corner information is completely lost as shown in Figure 9a.

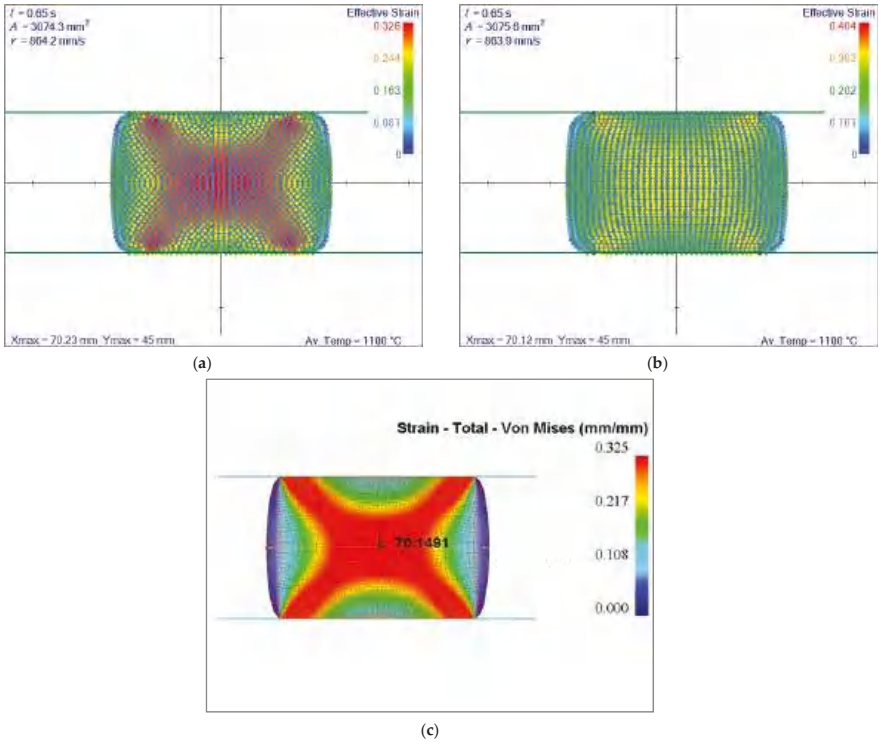

Figure 9. Comparison of simulated effective strain fields. Irregular nodes (**a**), regular nodes with mapping (**b**) and FEM results (**c**). The results of all three simulations are practically the same: (**a**) 70.23 mm, (**b**) 70.12 mm, (**c**) 70.15 mm. Av. Temp. stands for average temperature.

4.3. Irregular Meshless Node Distribution vs. FEM

The same flat rolling example as in Section 4.1 is chosen here with an ideal plastic material model. Effective stress–effective strain relation is $\overline{\sigma} = 589\overline{\varepsilon}^{0.2}$. A comparison is made with FEM code [30], and a good agreement is found. An example of a shear strain comparison is given in Figure 10 below. As expected, a good agreement has been found between the meshless results with irregular node arrangement and FEM.

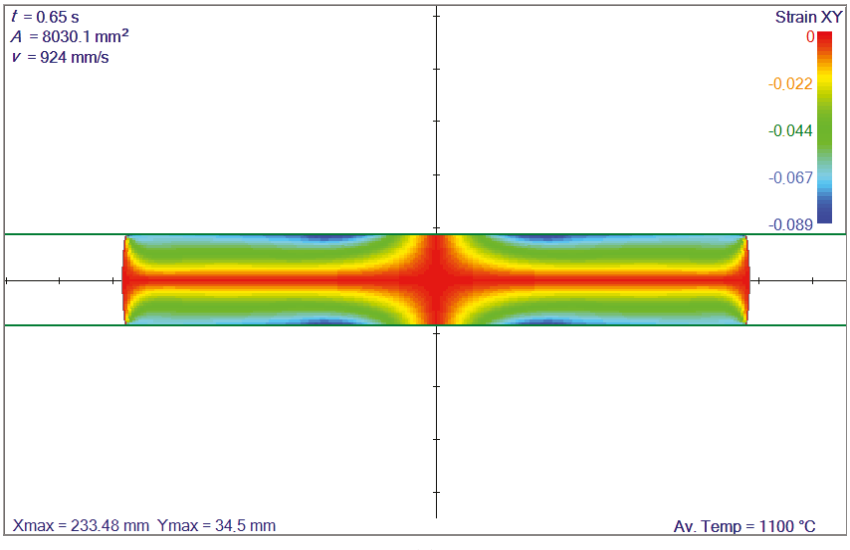

(**a**)

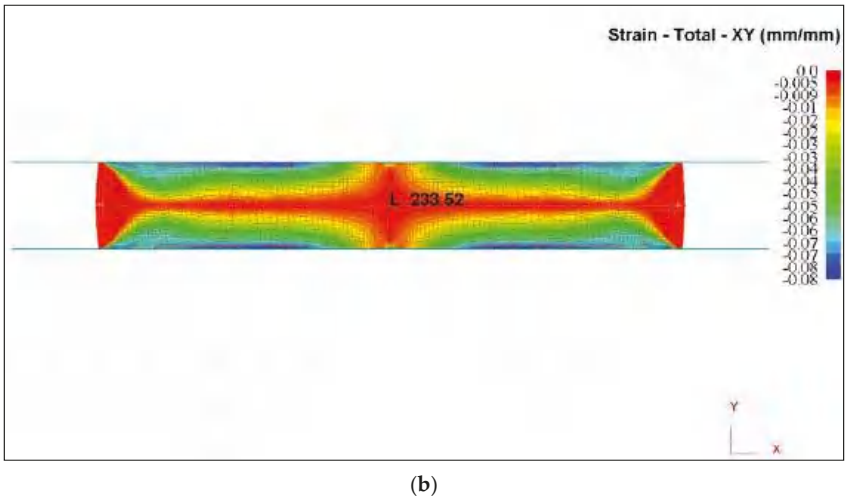

(**b**)

Figure 10. Comparison of strain fields. Meshless solution with irregular node arrangement is on top, FEM solution is shown at the bottom. The results of both calculations are almost the same: (**a**) 233.52 mm, (**b**) 233.48 mm. Av. Temp. stands for average temperature.

4.4. Rolling Schedule with Eight Rolling Stands

In this section, a rolling schedule from the industry with specific grooves are shown in Figure 11 The same was used in all subsequent simulations. The initial size of the billet was 60.48 by 60.48 mm, where the corners are rounded with a radius of 11 mm. An irregular node distribution, the same as demonstrated in Section 4.2, is used. This rolling schedule aimed to obtain a 45 × 30 mm^2 end shape within a half millimetre error range.

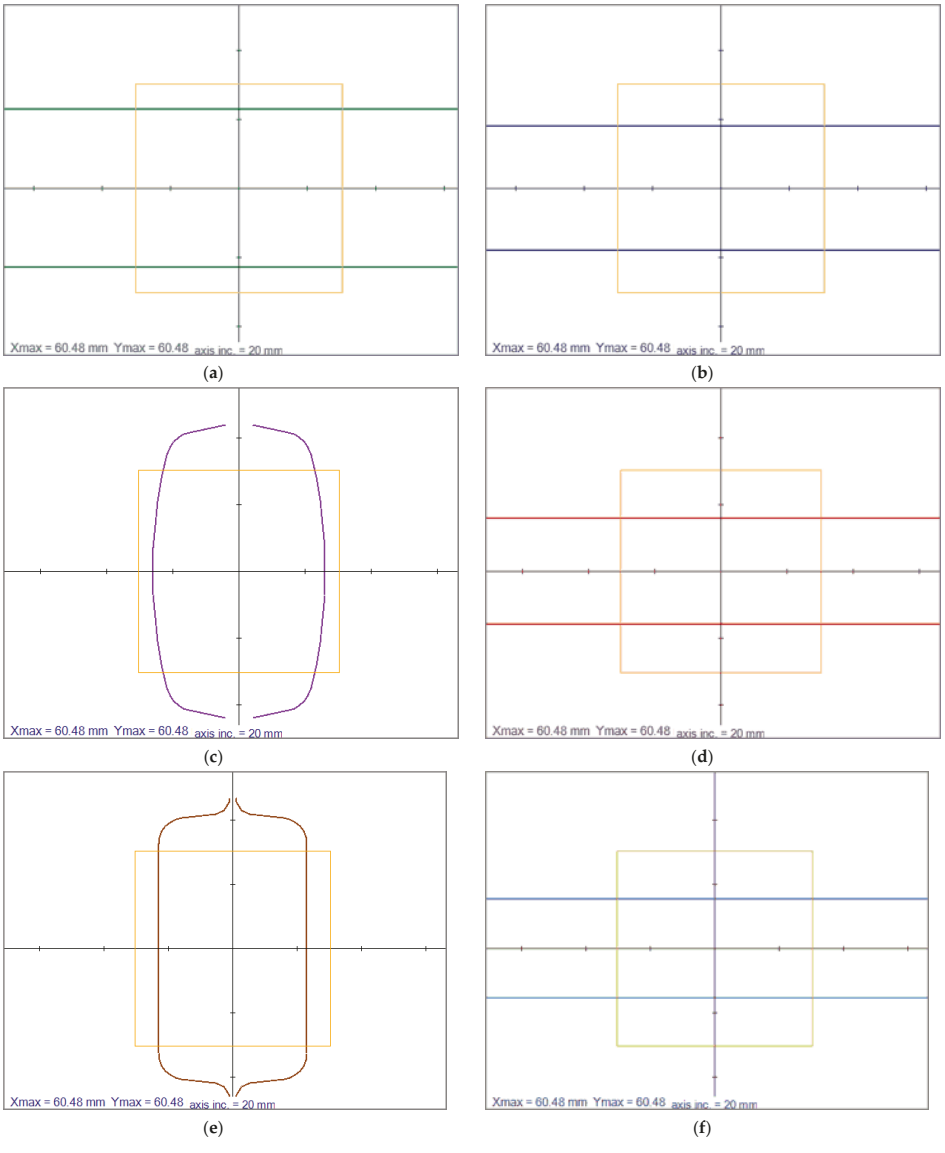

Figure 11. *Cont.*

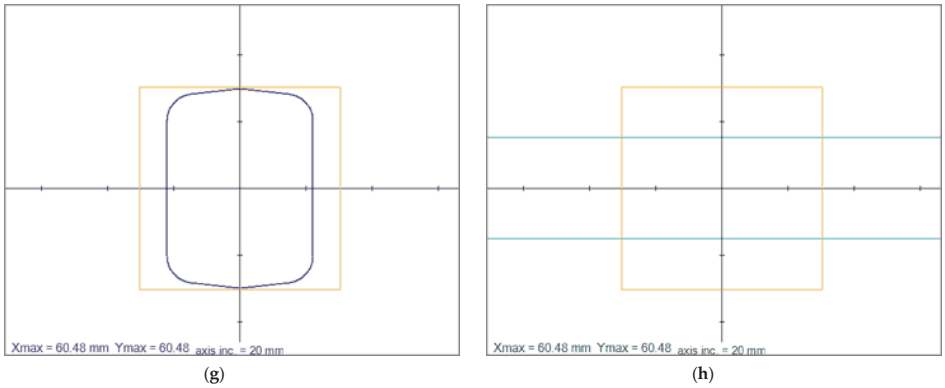

(**g**) (**h**)

Figure 11. Demonstration of the roll shapes of each of the roll passes of an 8-roll rolling schedule. (**a**) first roll pass, (**b**) second roll pass, (**c**) third roll pass, (**d**) forth roll pass, (**e**) fifth roll pass, (**f**) sixth roll pass, (**g**) seventh roll pass, (**h**) eighth roll pass. Axis inc. is the length of axis increments.

4.4.1. Effective Strain Results

Effective strain and temperature fields are the most critical inputs of the micro-scale models. The corresponding position and time of each slice have to be known throughout the simulation. Figure 12 represents the effective strain result of slices positioned at the exit of each roll pass. These results have shown the total effective strain through each of the rolling passes. Therefore these fields contain the highest possible values for each pass. These results are also crucial since they have a significant impact on the micro-scale simulation.

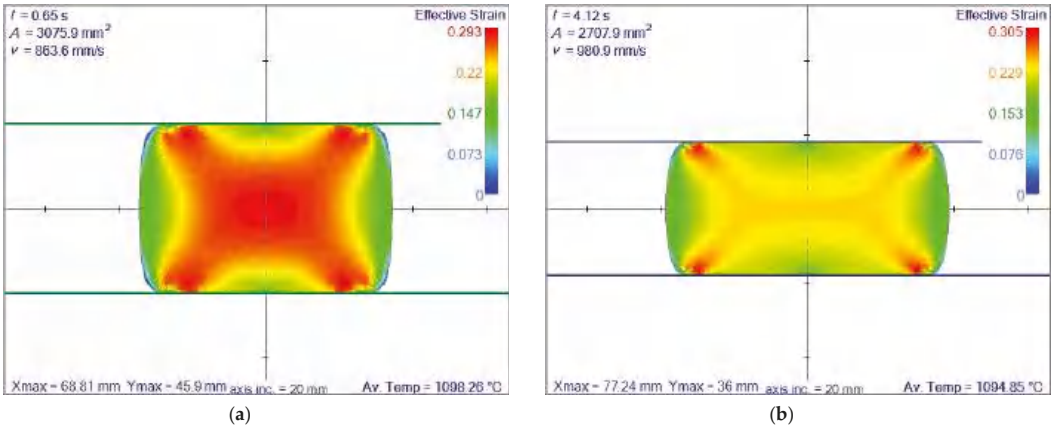

(**a**) (**b**)

Figure 12. *Cont.*

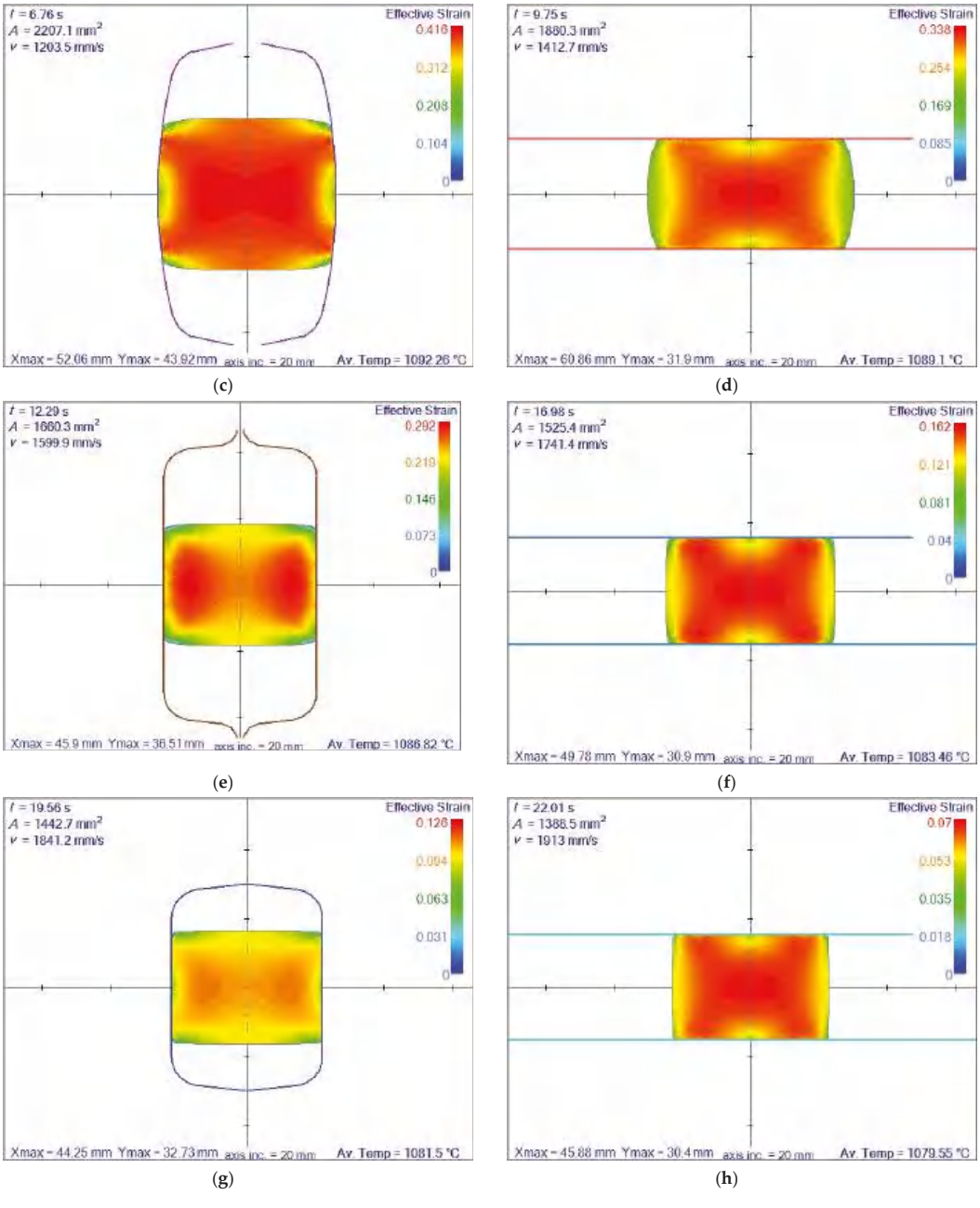

Figure 12. Simulation results of effective strain at the exit of each roll pass. (**a**) at first roll pass, (**b**) at second roll pass, (**c**) at third roll pass, (**d**) at forth roll pass, (**e**) at fifth roll pass, (**f**) at sixth roll pass, (**g**) at seventh roll pass, (**h**) at eighth roll pass. Axis inc. is the length of axis increments. Av. Temp. stands for average temperature.

4.4.2. Recrystallization Results at Each Pass

In the simulations, the deformation occurred so rapidly that the time for meta-dynamic or static recrystallization was never reached. However, at each pass, soon after the first contact, a complete dynamic recrystallization was always achieved except for the model developed by Yada [12]. In that model, the dynamic recrystallization was partial at each pass. To contrast, the results obtained by Yada's model are shown in Figure 13. In the three other models, there was always complete dynamic recrystallization.

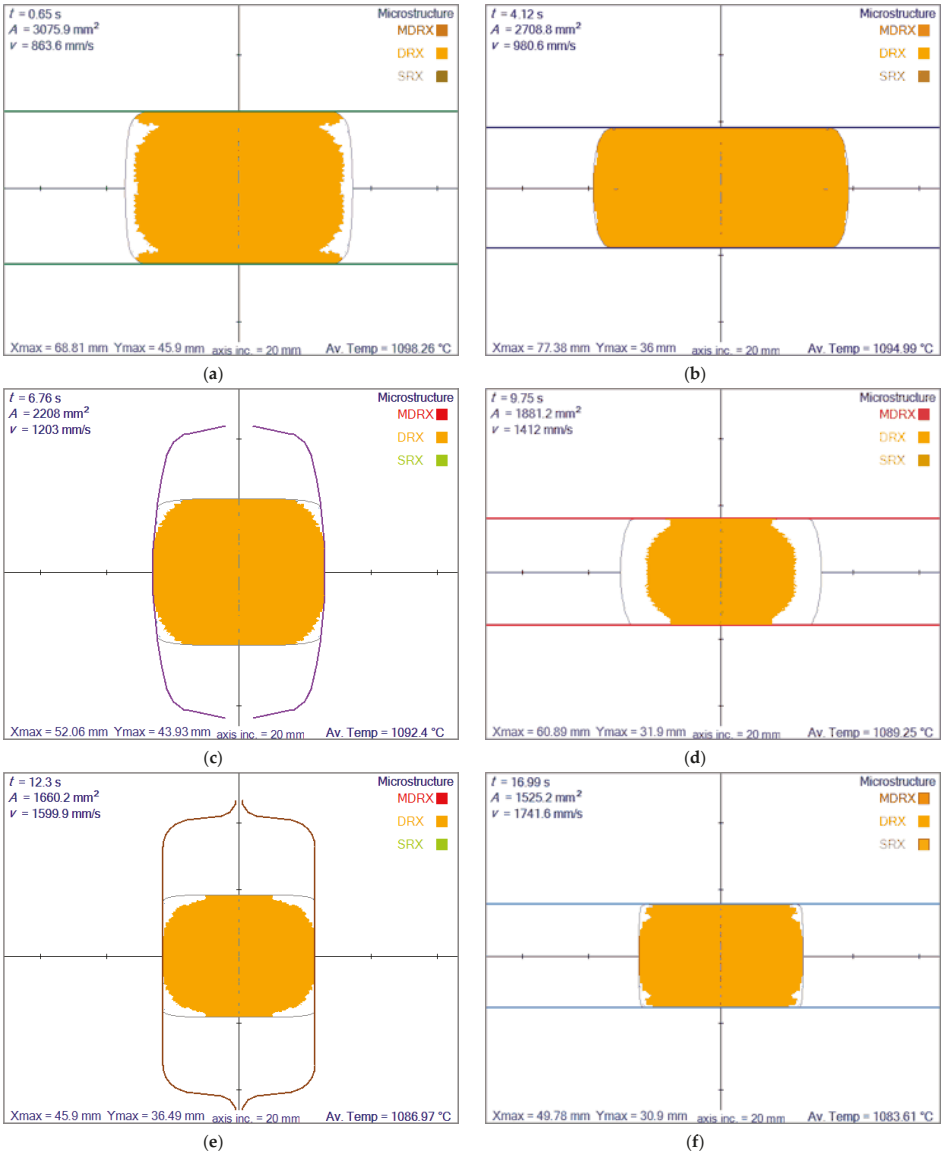

Figure 13. *Cont.*

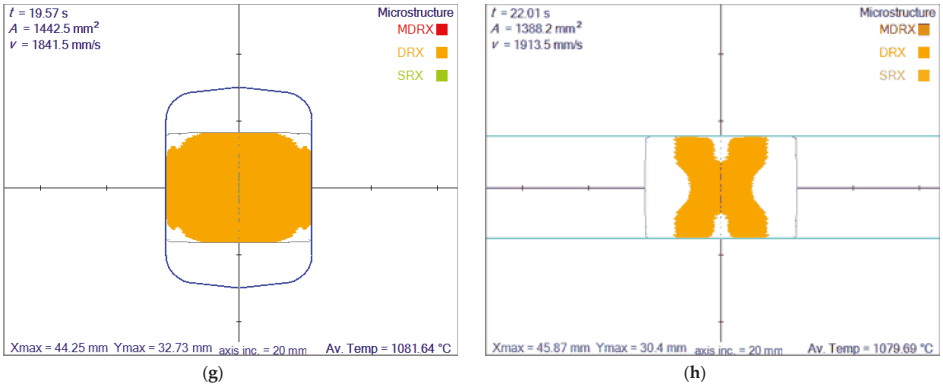

Figure 13. Recrystallization based on the model given by Yada [12] at the exit of each roll pass. (**a**) at first roll pass, (**b**) at second roll pass, (**c**) at third roll pass, (**d**) at forth roll pass, (**e**) at fifth roll pass, (**f**) at sixth roll pass, (**g**) at seventh roll pass, (**h**) at eighth roll pass. Possible recrystallization types are dynamic (DRX), meta-dynamic (MDRX) and static (SRX). Axis inc. is the length of axis increments and Av. Temps stands for average temperature.

4.4.3. Recrystallization Results at Each Pass with Yada Model

The results of partial dynamic recrystallization obtained by the rolling simulation system are shown in Figure 13 for slices at each roll pass's exit.

4.4.4. Grain Size Comparisons of Different Models

A rolling schedule is used as described in Section 4.4 and Figure 11. Grain size simulation results based on the model by Sellars and Whiteman [14] is shown in Figure 14.

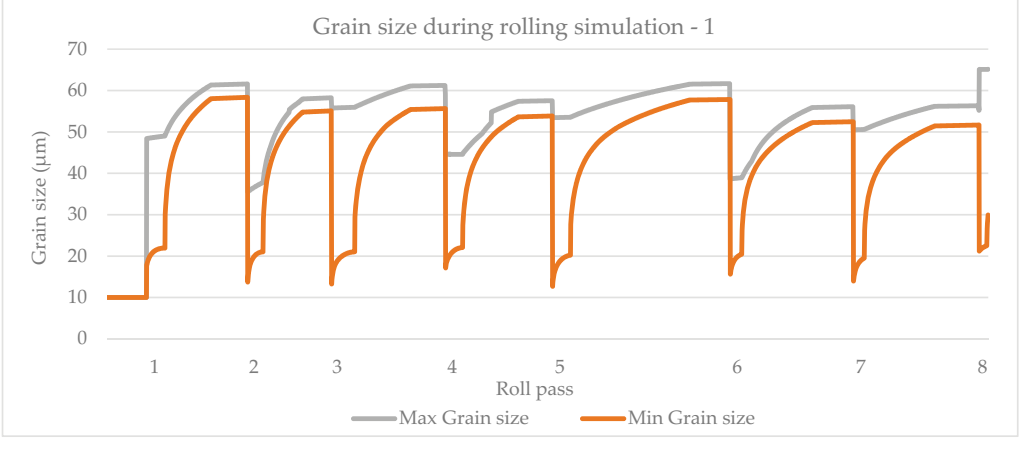

Figure 14. Simulation of maximum and minimum grain size based on the model by Sellars and Whiteman [14].

The model by Yada [12] is shown in Figure 15, the model by Manohar, et al. [15] is shown in Figure 16 and the model by Hodgson and Gibbs [10] is shown in Figure 17. The grain growth model is obtained in [10]. In micro-scale simulations, each collocation point in a computational domain represents a small area with a uniform grain structure.

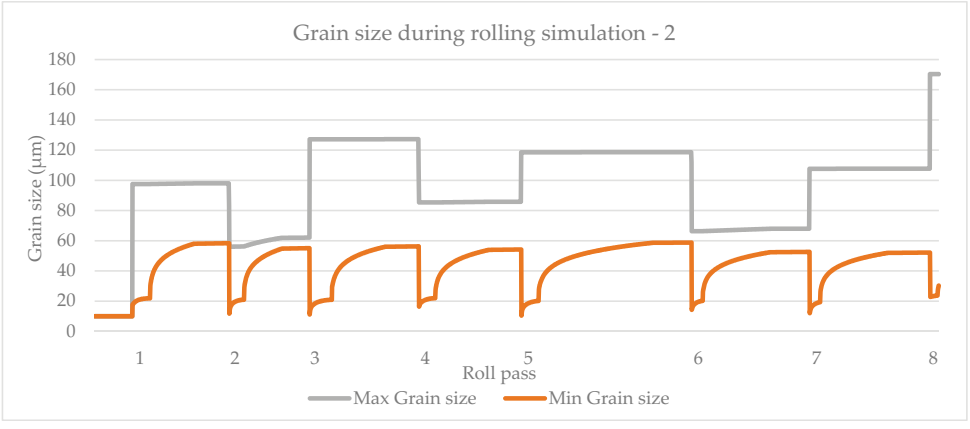

Figure 15. Simulation of maximum and minimum grain size based on the model by Yada [12].

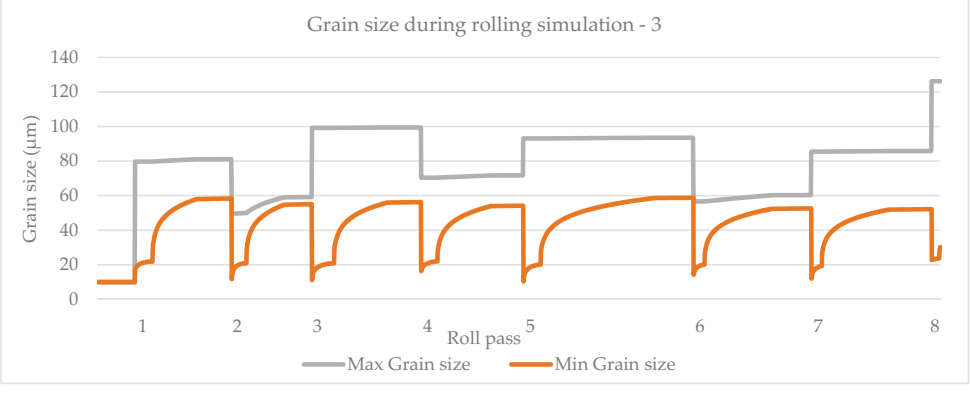

Figure 16. Simulation of maximum and minimum grain size based on the model by Manohar et al. [15].

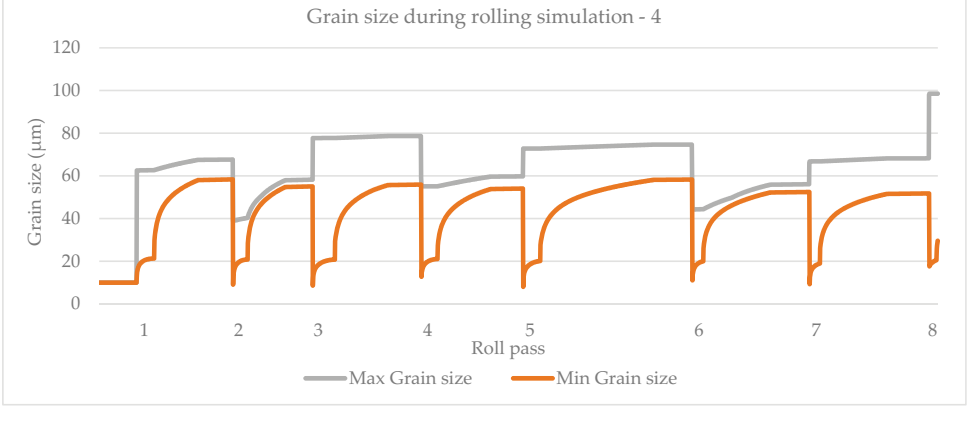

Figure 17. Simulation of maximum and minimum grain size based on the model by Hodgson and Gibbs [10].

4.4.5. Ferrite Grain Size for 16MnCr5

For the calculation of the final grain size in the ferrite phase, 16MnCr5 steel is considered. This steel grade has 0.16% carbon, 1.15% manganese and 0.95% chromium. The ferrite transformation temperature is based on the model given by Hodgson and Gibbs, calculated as 754.15 °C, and the user interface is displayed in Figure 18. The real-time cooling to below FTT took 14 min; however, the computational time took twice as long. The final ferrite grain size and comparison between the two models is shown in Figure 19. A strong dependence on residual strain on the ferrite grain size is observed.

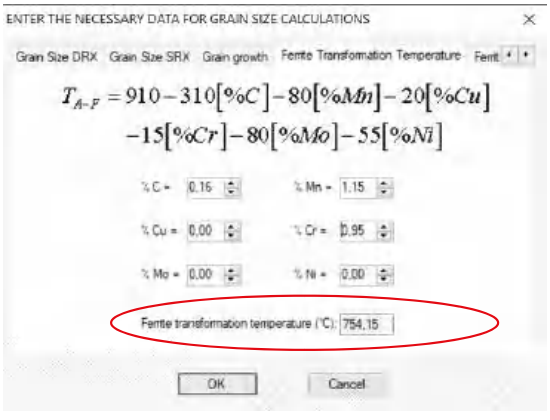

Figure 18. Ferrite transformation temperature used in the simulations based on the chemical composition of the steel.

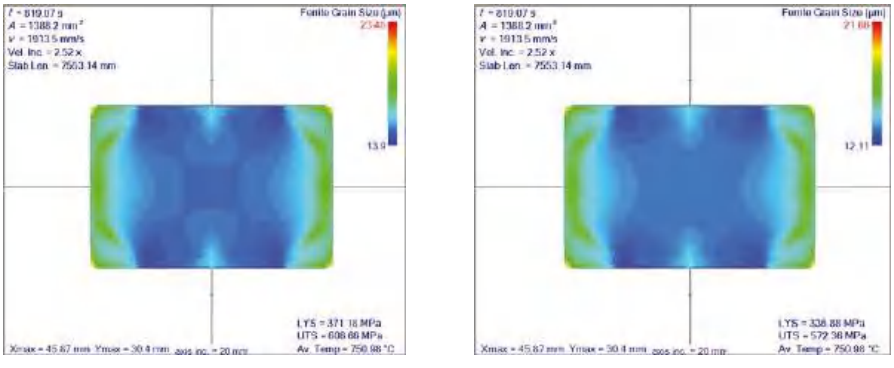

Figure 19. Comparison of final ferrite grain size based on the models given by Sellars and Whiteman (**left**) and Hodgson and Gibbs (**right**). Axis inc. is the length of the axis increments. Av. Temp. stands for average temperature. Vel. Inc. is the increase of the slab's velocity towards the rolling direction. Slab. Len. Is the length of the rolled slab. LYS is the lower yields stress and UTS is the ultimate tensile strength.

4.4.6. No Recrystallization Temperature

Based on the model expressed by Yang, et al. [24], no-recrystallization temperatures are calculated and compared with minimum and average temperature values for each slice position through the rolling simulation. The result is shown in Figure 20 below, and it is clear that for hot rolling at 1100 °C, the temperature of steel was always above the no-recrystallization temperature.

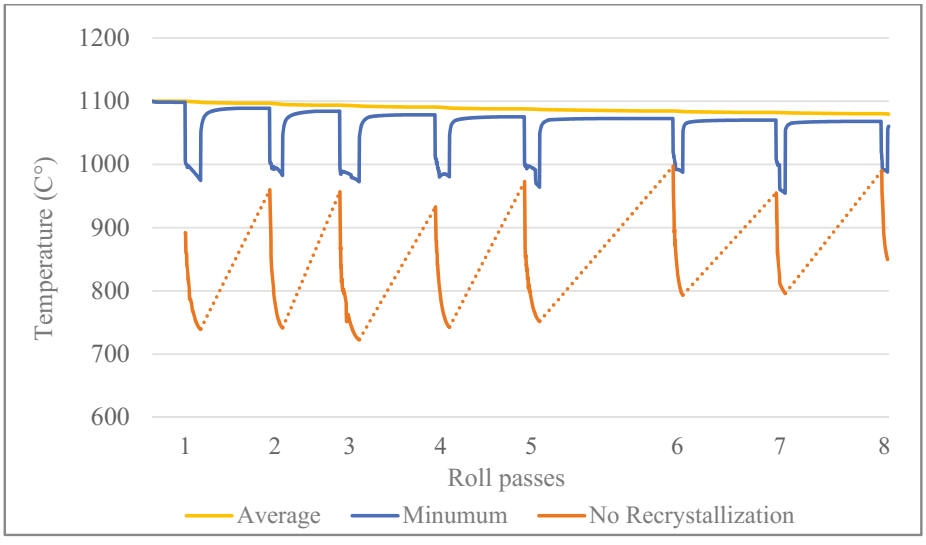

Figure 20. Comparison of estimated no-recrystallization temperature values at each rolling pass with the average and the minimum temperature values.

The positions of roll passes which are used in Figures 14–17 and 20 are given in Table 8 below. The origin of this coordinate ($z = 0$) is considered to be the initial slice's position.

Table 8. Positions of centres of each roll along the rolling direction with reference to the initial slice position.

Passes	**1**	**2**	**3**	**4**	**5**	**6**	**7**	**8**
Position on rolling direction (mm)	500	3500	6100	9700	13,300	20,800	25,300	29,800

5. Discussion

Micro-scale calculations are based on a multitude of empirical correlations obtained from the experiments in the last four decades. The simulation system is capable of checking for meta-dynamic, dynamic or static recrystallization. When recrystallization occurs, a new grain size is calculated. If there is a full recrystallization, grain growth will start. At the end of rolling, cooling is simulated with the thermal model until it reaches the ferrite transformation temperature. The simulation ends with ferrite grain size prediction. A comparison of different models based on maximum and minimum grain sizes is shown. The accuracy of those results are limited to the accuracy of the input data which is simulated by the macro-scale model and the accuracy of the empirical micro-scale models. It is known from the industrial user experience that the accuracy of the macro-scale results is highly satisfactory. Therefore, if the empirical models are based on enough experiments, the expected grain-related results should be between the maximum and minimum simulated values.

Another outcome of this research is to be able to come up with new grain size prediction models in the future. This is why all the definitions are implemented as user-defined functions. Numerous additional experimental results are needed to obtain this goal.

The simulation system is currently limited to austenite and ferrite grain size predictions and assumes only one phase at a time. This will be improved in the future with multiple initial phase definitions and phase transformation criteria. The micro-scale models are also limited to the adequacy of those coefficients used. All the necessary coefficients for each steel type may not be found. It is a long and complicated experimental process

to define all those parameters by analyzing numerous grain size data obtained by either using electron microscope [31] or ultrasound [32].

6. Conclusions

In the present paper, a rolling simulation system capable of predicting the grain structure is described. First, a macroscopic thermo-mechanical simulation is performed, based on a 2D solution over each cross-sectional slice. Displacement, strain, stress and temperature fields are calculated considering the defined process parameters (rolling schedule), heat transfer and material properties. The solution is achieved through a truly meshless radial basis function collocation method. A new irregular node generation algorithm is used, which is shown, by FEM comparison, to perform better on irregular domains. This method requires only the distribution of collocation nodes over a domain, without classical meshing. It is possible to represent the complex domain shapes more accurately with the irregular node distribution as with the regular node distribution. Due to the high possibility of recrystallization at each pass, strain filed during the last rolling stand leads to relatively smaller ferrite grain size. It was shown in the simulations that dynamic recrystallization always took place at each roll pass. Meta-dynamic and static recrystallizations did not occur due to time restrictions. It was also expressed that no-recrystallization temperatures most probably does not stop recrystallization during hot rolling of steel above 1100 °C. A list of all the correlations used in this paper may be found in Appendix A.

Author Contributions: Methodology, supervision and manuscript editing B.Š.; software, validation and writing U.H. All authors have read and agreed to the published version of the manuscript.

Funding: This research was funded by the Slovenian Grant Agency by grant numbers P2-0162 and L2-2609 and Štore-Steel Company (www.store-steel.si).

Data Availability Statement: Data sharing not applicable.

Conflicts of Interest: The authors declare no conflict of interest.

Appendix A

		C-Mn				Low C	High C	C-Mn-V	C-Mn-Ti	C-Mn-Nb	HSLA
Critical strain	A	6.82×10^{-4}	4.76×10^{-4}		4.9×10^{-4}	4.9×10^{-4}					
	Q_d	312,000	66,500		312,000	300,000					
	p	0.13	0		0.15	0.17					
	q	0	0		1	0.3					
Dynamic recrystallization	A	16,000	22,600	1800	16,000						
	r	−0.23	−0.27	−0.15	−0.23						
	Q_d	312,000	267,100	312,000	300,000						
Meta-dynamic recrystallization	A	26,000		1600	26,000	25,000					
	r	−0.23		−0.11	−0.23	−0.23					
	Q_d	312,000		312,000	300,000	312,000					
Static recrystallization	A	1					0.5				
	m	−0.5					−0.67				
	r	0.4					0.67				
Grain growth	m							7	10	4.5	
	k_s							1.45×10^{27}	2.6×10^{28}	4.1×10^{28}	
	Q_{GG}							−400	−437	−435	
No-recrystallization temperature	A										905
	m										−0.045
	n										−0.006
	k										0.024

			C-Mn	Low C	High C	C-Mn-V	C-Mn-Ti	C-Mn-Nb	HSLA
Ferrite grain size	α_0	−0.4	22.6				1.4		
	α_1	6.37	−57				0		
	α_2	24.2	3				5		
	α_3	−59	0				0		
	α_4	22	22				22		

References

1. Lenard, J.G.; Pietrzyk, M.; Cser, L. *Mathematical and Physical Simulation of the Properties of Hot Rolled Products*, 1st ed.; Elsevier: Oxford, UK, 1999.
2. Lenard, J.G. *Primer on Flat Rolling*, 1st ed.; Elsevier: Oxford, UK, 2007.
3. Roberts, W.L. *Hot Rolling of Steel*, 1st ed.; Marcel Dekker Inc.: New York, NY, USA, 1983.
4. Lee, Y.; Choi, S.; Kim, Y.H. Mathematical model and experimental validation of surface profile of a workpiece in round-oval-round pass sequence. *J. Mater. Process. Technol.* **2000**, *108*, 87–96. [CrossRef]
5. Solod, V.; Kulagin, R.; Beygelzimer, Y. A local approach to simulating bar forming in pass rolling. *J. Mater. Process. Technol.* **2007**, *190*, 23–25. [CrossRef]
6. Hanoglu, U.; Šarler, B. Multi-pass hot rolling simulation using a meshless method. *Comput. Struct.* **2018**, *194*, 1–14. [CrossRef]
7. Dong, X.; Cheng, J.; Hongyang, Z.; Dongying, J.; Miaoyong, Z. A new study on the growth behavior of austenite grains during heating processes. *Sci. Rep.* **2017**, *7*, 3968–3980.
8. Sellars, C.M. Modelling microstructural development during hot rolling. *Mater. Sci. Technol.* **1990**, *6*, 1072–1081. [CrossRef]
9. Goh, C.H.; Dachowicz, A.P.; Allen, J.K.; Mistree, F. *Integrated Computational Materials Engineering (ICME) for Metals Concept Case Studies*; John Willey and Sons: Hoboken, NJ, USA, 2018.
10. Hodgson, P.D.; Gibbs, R.K. A mathematical model to predict the mechanical properties of hot rolled C-Mn and microalloyed steels. *Iron Steel Inst. Jpn. Int.* **1992**, *32*, 1329–1338. [CrossRef]
11. Laasraoui, A.; Jonas, J.J. Prediction of temperature distribution, flow stress and microstructure during the multipass hot rolling of steel plate and strip. *Iron Steel Inst. Jpn. Int.* **1991**, *31*, 95–105. [CrossRef]
12. Yada, H. Prediction of microstructural changes and mechanical properties in hot strip rolling. In *Proceedings of the Metallurgical Society of the Canadian Institute of Mining and Metallurgy*, 1st ed.; Pergamon Press: Kidlington, UK, 1988; pp. 105–119. [CrossRef]
13. Kwon, H.C.; Lee, Y.; Kim, S.Y.; Woo, J.S. Numerical prediction of austenite grain size in round-oval-round bar rolling. *Iron Steel Inst. Jpn. Int.* **2003**, *43*, 676–683. [CrossRef]
14. Sellars, C.M.; Whiteman, J.A. Recrystallization and grain growth in hot rolling. *J. Met. Sci.* **1979**, *13*, 187–194. [CrossRef]
15. Manohar, P.A.; Lim, K.; Rollett, A.D.; Lee, Y. Computational exploration of microstructural evolution in a medium C-Mn steel and applications of rod mill. *Iron Steel Inst. Jpn. Int.* **2003**, *43*, 1421–1430. [CrossRef]
16. Zhang, Y.; Zhang, H.; Wang, G.; Hu, S. Application of mathematical model for microstructure and mathematical property of hot rolled wire rods. *Appl. Math. Model.* **2009**, *33*, 1259–1269. [CrossRef]
17. Biglou, J.; Lenard, J.G. A study of dynamic recrystallization during hot rolling of microalloyed steels. *CIRP Ann.* **1996**, *45*, 227–230. [CrossRef]
18. Hanoglu, U.; Šarler, B. Hot rolling simulation system for steel based on advanced meshless solution. *Metals* **2019**, *9*, 788. [CrossRef]
19. Zhou-Jia, F.; Li-Wen, Y.; Qiang, X.; Chein-Shan, L. A boundary collocation method for anomalous heat conduction analysis in functionally graded materials. *Comput. Math. Appl.* **2021**, *88*, 91–109.
20. Li, Y.; Li, J.; Wen, P.H. Finite and infinite block Petrov-Galerkin method for cracks in functionally graded materials. *Appl. Math. Model.* **2018**, *68*, 306–326. [CrossRef]
21. Vertnik, R.; Šarler, B. Meshfree local radial basis function collocation method for diffusion problems. *Comput. Math. Appl.* **2006**, *51*, 1269–1282.
22. *Intel Math Kernel Library (Intel MKL)*; Version 2018.0; Intel Corporation: Santa Clara, CA, USA, 2018; Available online: https://software.intel.com/oneapi/onemkl (accessed on 20 November 2019).
23. Bai, D.Q.; Yue, S.; Maccagno, T.; Jonas, J.J. Static recrystallization of Nb and Nb-B steels under continuous cooling conditions. *Iron Steel Inst. Jpn. Int.* **1996**, *36*, 1084–1093. [CrossRef]
24. Yang, H.; Zhou, X.; Liu, Z.; Wang, G. Determination of No-recrystallization temperature for NB-bearing Steel. *J. Wuhan Univ. Technol. Mater. Sci. Ed.* **2016**, *31*, 644–647. [CrossRef]
25. Fang, X.; Fan, Z.; Ralph, B.; Evans, P. Influence of accelerated cooling on microstructure and mechanical properties of C–Mn steels. *Mater. Sci. Technol.* **2002**, *18*, 47–53. [CrossRef]
26. Sellars, C.M.; Beynon, J. Microstructural development during hot rolling of titanium microalloyed steels. In *International Conference on High Strength Low Alloy Steels*; University of Wollongong: Wollongong, NSW, Australia, 1985; pp. 142–150.
27. Thompson, J.F.; Soni, B.K.; Weatherill, N.P. *Handbook of Grid Generation*, 1st ed.; Taylor & Francis Inc.: Abingdon, UK, 1998.
28. Hanoglu, U.; Šarler, B. Simulation of hot shape rolling of steel in continuous rolling mill by local radial basis function collocation method. *Comput. Model. Eng. Sci.* **2015**, *109*, 447–479.

29. Fornberg, B.; Flyer, N. Fast generation of 2-D node distributions for mesh-free PDE discretizations. *Comput. Math. Appl.* **2015**, *69*, 531–544. [CrossRef]
30. *DEFORM 2D*; Version 10.1; Scientific Forming Technologies Corporation: Columbus, OH, USA, 2009; Available online: http://www.deform.com (accessed on 25 May 2021).
31. Mingard, K.P.; Roebuck, B.; Bennett, E.G.; Gee, M.G.; Nordenstrom, H.; Sweetman, G.; Chan, P. Comparison of EBSD and conventional methods of grain size measurement of hardmetals. *Int. J. Refract. Met. Hard Mater.* **2009**, *27*, 213–223. [CrossRef]
32. Palanichamy, P.; Joseph, A.; Jayakumar, T.; Raj, B. Ultrasonic velocity measurements for estimation of grain size in austenitic stainless steel. *NDT E Int.* **1995**, *28*, 179–185. [CrossRef]

materials

MDPI

Article

Multi-Scale Modeling of Microstructure Evolution during Multi-Pass Hot-Rolling and Cooling Process

Xian Lin [1], Xinyi Zou [1], Dong An [1], Bruce W. Krakauer [2] and Mingfang Zhu [1,*]

[1] Jiangsu Key Laboratory for Advanced Metallic Materials, School of Materials Science and Engineering, Southeast University, Nanjing 211189, China; xianlin@seu.edu.cn (X.L.); 220181923@seu.edu.cn (X.Z.); dong.an@seu.edu.cn (D.A.)
[2] A. O. Smith Corporation, Milwaukee, WI 53224, USA; bkrakauer@aosmith.com
* Correspondence: zhumf@seu.edu.cn

Abstract: In this work, a 6-pass hot-rolling process followed by air cooling is studied by means of a coupled multi-scale simulation approach. The finite element method (FEM) is utilized to obtain macroscale thermomechanical parameters including temperature and strain rate. The microstructure evolution during the recrystallization and austenite (γ) to ferrite (α) transformation is simulated by a mesoscale cellular automaton (CA) model. The solute drag effect is included in the CA model to take into account the influence of manganese on the γ/α interface migration. The driving force for α-phase nucleation and growth also involves the contribution of the deformation stored energy inherited from hot-rolling. The simulation renders a clear visualization of the evolving grain structure during a multi-pass hot-rolling process. The variations of the nonuniform, deformation-stored energy field and carbon concentration field are also reproduced. A detailed analysis demonstrates how the parameters, including strain rate, grain size, temperature, and inter-pass time, influence the different mechanisms of recrystallization. Grain refinement induced by recrystallization and the $\gamma \rightarrow \alpha$ phase transformation is also quantified. The simulated final α-fraction and the average α-grain size agree reasonably well with the experimental microstructure.

Keywords: hot-rolling; recrystallization; austenite to ferrite transformation; cellular automaton; finite element method (FEM)

Citation: Lin, X.; Zou, X.; An, D.; Krakauer, B.W.; Zhu, M. Multi-Scale Modeling of Microstructure Evolution during Multi-Pass Hot-Rolling and Cooling Process. *Materials* **2021**, *14*, 2947. https://doi.org/10.3390/ma14112947

Academic Editor: Ivo Schindler

Received: 7 April 2021
Accepted: 26 May 2021
Published: 29 May 2021

Publisher's Note: MDPI stays neutral with regard to jurisdictional claims in published maps and institutional affiliations.

1. Introduction

Grain refinement is a critical objective of the thermomechanical processing of Advanced High Strength Steels (AHSS). During hot-rolling, grain refinement is achieved primarily by microstructure evolution during austenite (γ) recrystallization and following the austenite to ferrite ($\gamma \rightarrow \alpha$) transformation [1]. Therefore, the understanding of microstructure evolution during recrystallization and the $\gamma \rightarrow \alpha$ phase transformation is crucial for optimizing the rolling processes and enhancing the properties of products. Based on the time period that recrystallization takes place, there are three recrystallization mechanisms: (1) dynamic recrystallization (DRX)—nucleation and growth of recrystallized grains under deformation; (2) metadynamic recrystallization (MDRX)—growth of DRX grains during the inter-pass period; (3) static recrystallization (SRX)—nucleation and growth of recrystallized grain during the inter-pass period.

Extensive experiments have been carried out to study the microstructures and properties of AHSS under various rolling parameters, such as strain rate [2–4] and deformation temperature [5–7]. Those experimental studies provided important information concerning the relationship between process variables and grain structures after rolling. As a result of inherent experimental difficulties, these studies cannot fully elucidate the physical mechanisms contributing to grain refinement, because one needs to consider the temporal evolution of the multi-pass processes of recrystallization and the $\gamma \rightarrow \alpha$ transformation,

in order to analyze the contributions of recrystallization quantitatively, including DRX, MDRX, SRX, and the $\gamma \rightarrow \alpha$ phase transformation.

With the development of technologies in computer science, numerical simulation methods have popularized and become an important tool for understanding the mechanisms of microstructure formation during material processes due to their capabilities to present the visual, temporal evolution of microstructures. Among different numerical models, the cellular automata (CA) approach, combining both computational efficiency and simplicity [8], has been commonly applied to investigate various phenomena such as recrystallization [9–22], phase transformation [23–31], and grain coarsening [32,33].

Simulation studies on microstructure evolution during recrystallization for a single-pass process have been performed by utilizing a CA model [9–11] and combining the CA method with the finite element method (FEM) [12,13] or the crystal plasticity finite element method (CPFEM) [14–16]. Those studies investigated the mesoscale grain structural evolution as well as the macro- or meso-scale mechanical response. However, there are few simulation studies that focused on multi-pass hot deformation processes using a coupled FEM and CA approach. Barkóczy et al. [17] first simulated the 4-pass rolling process using a CA method, considering SRX and grain coarsening. Yet, the simulation was based on unrealistic material parameters and an unspecific deformation process. The mechanism of dislocation density evolution was also not reproduced. Zheng et al. [18] and Chen et al. [19] input actual material and technology parameters to simulate a 7-pass hot-rolling process and 4-stage hot compression process. The effect of hot deformation was coupled through the determination of deformation-stored energy variation and a topology deformation technique for reproducing the plastically deformed grain structure. Good agreement of average grain size was obtained among the results from the CA simulation, the in-house software of ROLLAN, and a Gleeble simulator. Nevertheless, the simplified assumptions of temperature variation and mechanical response in those studies were insufficient due to the multi-scale nature of hot deformation. Svyetlichnyy et al. [20,21] simulated multi-pass shape rolling processes using a coupled FEM and frontal cellular automata (FCA) method. The results can be used to predict the grain structure and kinetics of recrystallization. However, the above-mentioned studies only focused on recrystallization during multi-pass hot deformation. Svyetlichnyy et al. [22] used a combined FEM and FCA model to simulate recrystallization during 3-pass shape rolling and a subsequent phase transformation during cooling. Nevertheless, an arbitrary α/γ grain boundary migration rate was used for phase transformation. The simulated microstructure was not validated by an experiment.

For the $\gamma \rightarrow \alpha$ phase transformation in Fe-C-Mn alloys, the growth kinetics have been usually described by carbon diffusion and interface reaction based on the paraequilibrium condition, where only the interstitials are allowed to partition and reach the equality of chemical potentials between the α- and γ-phases, while the substitutional elements are not [34]. Several numerical simulation studies focused on the α-γ phase transformation during isothermal annealing [23,24], continuous cooling [25,26], continuous heating [27,28], and an entire anneal cycle [29–31] under the assumption of paraequilibrium. To account for the interaction of substitutional elements at the moving α/γ interface, Purdy et al. [35] proposed a solute drag model, where the Gibbs energy dissipation due to the trans-interface diffusion of the substitutional solute was introduced. An et al. [29] first coupled a solute drag model with a CA model to simulate the α-γ transformation in a dual-phase steel during different heat treatment processes. The simulation results agree well with those from phase field predictions, atom-probe tomography analyses, and SEM micrographs. However, a CA model incorporated with the solute drag effect for the simulation of the γ-α phase transformation has not been applied to the hot-rolling process.

As described above, at present, quantitative multi-scale simulation studies on both recrystallization and the $\gamma \rightarrow \alpha$ phase transformation during a multi-pass hot-rolling process are still limited. In this article, a coupled macroscopic FEM and mesoscopic CA model is proposed to investigate the recrystallization and $\gamma \rightarrow \alpha$ phase transformation during a 6-pass hot-rolling and continuous cooling process for an Fe-C-Mn steel. FEM is used to obtain

the macroscopic thermomechanical data for CA simulations. The solute drag model is embedded in the CA approach to take into account the effect arising from the redistribution of manganese atoms at the α/γ interface. The evolution of the microstructure, dislocation density, and carbon concentration field during a specific multi-pass hot-rolling process is displayed. The effects of thermomechanical parameters on the recrystallization are discussed in detail.

2. Experiments and FEM Simulation

The steel with the composition Fe-0.07C-1.2Mn-0.5Si-0.052P-0.01S (wt.%) was hot-rolled using a large-scale laboratory hot-rolling mill with 1500 mm diameter work rolls. Before hot-rolling, the slabs were reheated to 1150 °C for 2 h. Then, the slab was deformed by a 6-pass hot-rolling process following by air cooling at a cooling rate of ~4 °C s^{-1} to room temperature. The rolling temperature at the start of each deformation pass, i.e., the initial rolling temperature, and the temperature at the end of the sixth pass are measured using a high-temperature handheld infrared thermometer (Table 1). The accuracy of the thermometer is about 1% of reading, and the max resolution is about 1 °C. The finishing rolling temperature after the sixth pass measured in the experiment is ~880 °C. The rolling process parameters are also presented in Table 1. The true strain in Table 1 is the plastic strain along the loading direction.

Table 1. Strain and initial rolling temperature used for laboratory hot-rolling.

	Pass 1	Pass 2	Pass 3	Pass 4	Pass 5	Pass 6
Strain, ε	0.288	0.405	0.288	0.511	0.693	0.889
Initial rolling Temperature (°C)	1027 ± 10	1023 ± 10	1023 ± 10	1000 ± 10	950 ± 10	910 ± 10

The FEM simulation of the continuous rolling process is conducted using the commercial software DEFORM-3D (v11.0.2, Scientific Forming Technologies Corporation, Columbus, United States). Process parameters and geometric models used for FEM simulation are the same as those in experiments (Table 1). The material file selected for the slab is modified based on tensile tests and thermomechanical analysis experiments. The outset of each deformation, also the end of each previous inter-pass, is determined as the time when the simulated temperature at the center of the slab's upper surface is identical to the experimentally measured initial rolling temperature. The FEM simulation is finished when the simulated temperature at the center of slab upper surface equals the finishing rolling temperature of the sixth pass. Other thermophysical parameters are taken as follows. The convective heat transfer coefficient between the slab and air is 0.045 kW/m^2·°C. The heat transfer coefficient between the slab and rolls is 9.5 kW/m^2·°C. The coefficient of shear friction is 0.7.

3. Governing Equations and Numerical Methods of the CA Model

3.1. Model Description

A 2D mesoscopic CA model is proposed to simulate γ-recrystallization and the $\gamma \rightarrow \alpha$ transformation during a 6-pass hot-rolling and subsequent air-cooling process. Recrystallization occurs during the 6-pass hot-rolling and continues until the temperature cools down to the transformation start temperature. The $\gamma \rightarrow \alpha$ phase transformation takes place during the air-cooling process after 6-pass rolling.

The CA model of recrystallization simulation is divided into two parts. One part is for calculating the variation of dislocation density due to work hardening, recovery, and recrystallization. The other is for simulating the evolution of the plastically deformed microstructure under three recrystallization mechanisms, namely DRX, MDRX, and SRX, using the approach previously applied by Zheng et al. [18]. During the deformation period, the nucleation and growth of DRX grains occur. During the inter-pass interval, the growth of DRX grain, i.e., MDRX, as well as the nucleation and growth of SRX grains,

takes place. A uniform topology mapping technique [36] is utilized to simulate the grain deformation structure. The strain rate and temperature fields are taken as homogeneous in the CA calculation domain, since the whole CA domain is within one element of FEM. The distribution of deformation energy within a grain is considered to be nonuniform with respect to the distance of a cell from a grain boundary.

The CA simulation for the $\gamma \rightarrow \alpha$ phase transformation includes α-phase nucleation, α-grain growth and coarsening, and carbon diffusion, which is performed based on a quantitative CA model proposed by An et al. [29]. The multi-component steel used in the experiment is reduced to a ternary Fe-0.323C-1.231Mn (mol.%) alloy for simplicity. The assumption of paraequilibrium is adopted, where the partition of the substitutional element manganese at the γ/α interface is neglected. The solute drag effect of the element manganese is incorporated, which reproduces the decrease in grain boundary mobility due to manganese diffusion inside the α/γ interface. Moreover, the driving force for α-phase nucleation and growth also involves the contribution of the deformation-stored energy inherited from hot-rolling. Both the initial microstructure and deformation-stored energy field for phase transformation simulation are taken from those by the CA simulation at the end of the 6-pass hot-rolling. All thermodynamic data are obtained from Thermo-calc (TCFE9 database). The cooling rate is set as 4 °C/s as the rate measured in the experiment. The transformation temperature range is set from 832 °C to 650 °C based on thermal dilatometer measurements and kinetic factors.

In the CA model, space is discretized into a finite number of cells. Each cell is characterized by several state variables: (1) grain index, I; (2) dislocation density, $\rho_{i,j}$; (3) average carbon concentration, x_C; (4) α-phase volume fraction, φ ($\varphi = 1$ or 0 denotes the α- or γ-phase, respectively); (5) interface labels denote the recrystallized γ/unrecrystallized γ, γ/γ and α/α grain boundaries, and α/γ interfaces.

3.2. Austenite Recrystallization

3.2.1. Dislocation Density Evolution

During hot deformation, most of the energy (~99%) is released immediately as heat. The residual energy remains stored in the form of dislocations. This deformation-stored energy (per volume), E_{def}, can be calculated from the dislocation density, ρ, as follows [37]:

$$E_{\text{def}} = \beta \mu b^2 \rho, \tag{1}$$

where β is a constant of the order of 0.5; μ is the shear modulus of the γ-phase, 50×10^9 Pa [23]; b is the magnitude of the Burgers vector, 2.48×10^{-10} m [23]. The relationship between the flow stress, σ, and the average dislocation density of the material, ρ_{ave}, can be described as follows:

$$\sigma = \alpha_1 \mu b \sqrt{\rho_{\text{ave}}}, \tag{2}$$

where α_1 is a constant depending on the dislocation/dislocation interaction, and can be taken as 0.5. The Kocks–Mecking (KM) model [38] is applied to evaluate the variation in the dislocation density in each grain with respect to deformation strain using the following equation:

$$\frac{d\rho}{d\varepsilon} = k_1 \sqrt{\rho} - k_2 \rho, \tag{3}$$

where $k_1 = 2\theta_0/(\alpha_1 \mu b)$ is a constant representing work hardening; $k_2 = 2\theta_0/\sigma_s$ is the softening parameter representing dynamic recovery; θ_0 is the initial work hardening rate; σ_s is the saturated stress, and it can be determined by Hatta's model [39]:

$$\dot{\varepsilon} = A_0 [\sin \mathrm{h}(a\sigma_s)]^{n'} \exp\left(-\frac{Q_A}{RT}\right), \tag{4}$$

where $\dot{\varepsilon}$ is the strain rate; A_0, n', a, and Q_A are the material constants and can be obtained from flow stress-strain curve; R is the gas constant, 8.314 J mol^{-1} K^{-1}; T is the absolute

temperature. During the inter-pass intervals, static recovery occurs mainly via dislocation climbing. The decrease in the dislocation density due to static recovery can be expressed by [40]:

$$\frac{d\rho}{dt} = d \cdot (\rho - \rho_0), \tag{5}$$

where ρ_0 is the initial dislocation density and is set as the common dislocation density for annealed metals, 10^{10} m^{-2} [41]; d is a temperature-dependent coefficient representing the static recovery rate. It can be calculated by [40]

$$d = d_0 \overline{D}_\gamma^{md} \exp(-Q_{SRV}/RT), \tag{6}$$

where $\overline{D}_\gamma$ is the average γ-grain diameter; d_0, md, and Q_{SRV} are constants. In addition to recovery, recrystallization also accounts for dynamic and static softening. The dislocation density decreases in cell (i, j) caused by a recrystallized grain growing into a deformed grain can be expressed as

$$\Delta\rho_{i,j}^t = \Delta f(\overline{\rho_r} - \overline{\rho_{nr}}), \tag{7}$$

where $\overline{\rho_{nr}}$ is the average dislocation density of the deformed grain; $\overline{\rho_r}$ is the average dislocation density of the recrystallized grain; Δf is the recrystallization fraction in cell (i, j).

A simplified analytical model [42] is adopted to reproduce the heterogeneous distribution of deformation energy within grains. The stored energy in cell (i, j) belongs to grain S and can be expressed as

$$E_{S(i,j)} = f(L)H_{S,\,Max}\,,\frac{1}{n}\sum_{i,j} E_{S(i,j)} = \overline{E_S}, \tag{8}$$

where $H_{S,Max}$ is the maximum value of the stored energy in grain S; L is the distance of the cell (i, j) from the grain boundary; $f(L)$ is a factor decreasing from 1.0 to 0.2 in a length of 4.8 μm as L increases; n is the number of cells that belongs to grain S; $\overline{E_S}$ is the average deformation stored energy of grain S, which can be calculated from Equations (1) and (2).

3.2.2. Nucleation of Austenite Recrystallization

The nucleation of recrystallization is assumed only to occur at austenite grain boundaries once the accumulation of dislocations reaches the critical dislocation density. Moreover, it is assumed to be a continuous nucleation event. During deformation, the nucleation rate per potential nucleation area for DRX as a function of both temperature T and strain rate $\dot{\varepsilon}$ is calculated by [43]

$$\dot{n}_{DRX} = C\dot{\varepsilon}^{\eta} \exp\left(-\frac{Q_N}{RT}\right), \tag{9}$$

where C is the nucleation parameter, which can be estimated either by experiment or the inverse analysis method [44]. The value of C could be on the order of 10^{12}–10^{22} [10,11,45]. In the present study, it is set to 7.2×10^{15} by comparing the simulation results with experimental data; Q_N is the activation energy for nucleation, 170 KJ mol^{-1} [23]; the exponent η is set to be 1 in the present simulation. The critical dislocation density ρ_c for DRX nucleation on grain boundaries is evaluated by [46]

$$\rho_c = \left(\frac{20\gamma_b\dot{\varepsilon}}{3blM_b\tau^2}\right)^{\frac{1}{3}}, \tag{10}$$

where γ_b is high-angle grain boundary energy with a typical value of 0.56 $J{\cdot}m^{-2}$; $l = 10.5\,\mu b/\sigma$ is the dislocation mean free path [47]; $\tau = \mu b^2/2$ is the dislocation line energy; M_b is the high-angle grain boundary mobility, which can be expressed as [48]

$$M_b = \frac{D_0 b^2}{kT}\exp\left(-\frac{Q_b}{RT}\right), \tag{11}$$

where D_0 is the boundary self-diffusion coefficient, 1.13 × 10^{-6} m^2 s^{-1} [49]; Q_b is the activation energy for grain-boundary motion, 140 KJ mol^{-1} [18]; k is Boltzmann constant. During the inter-pass intervals, the nucleation rate of SRX per unit area in the deformed matrix is considered to be related to the distribution of deformation-stored energy E_{def} and temperature T. It is given by using a phenomenological model as follows [42]:

$$\dot{n}_{SRX} = Z(E_{def} - E_c)\exp\left(-\frac{Q_N}{RT}\right), \tag{12}$$

where Z is a nucleation parameter 1.389 × 10^{10}; E_c the critical stored energy for initiating SRX, which can be determined from the critical deformation strain as follows [50]:

$$E_c = \gamma_b \cdot 10^7 \left(\frac{\varepsilon_c}{2.2\varepsilon_c + 1.1}\right), \tag{13}$$

where the critical strain ϵ_c generally ranges from 0.05 to 0.1 for different materials, and it can be taken as 0.1 for C-Mn steel [51].

3.2.3. Grain Growth and Coarsening

The velocity of grain boundary movement, V, can be generally expressed as

$$V = M_b P, \tag{14}$$

where P is the driving pressure for the specific process. For the recrystallization front moving into the deformed matrix, P is determined by the stored energy difference between the recrystallized grains and deformed matrix. For grain coarsening occurring at all grain boundaries, the driving force P is derived from curvature and is expressed as

$$P = \gamma_b \kappa, \tag{15}$$

where κ is the grain boundary curvature and calculated by [52]

$$\kappa = \frac{A}{\Delta x}\frac{K_{ink} - N_S}{N+1}, \tag{16}$$

where Δx is the CA cell size; A = 1.28 is a coefficient; N = 24 is the number of the first- and second-nearest neighbors; N_S is the number of cells within the neighborhood belonging to the grain S; K_{ink} = 15 is the number of cells within the neighborhood belonging to grain S for a flat interface [52].

3.2.4. Uniform Topology Deformation

For the present 2D model, the 2 × 2 uniform deformation matrix $\boldsymbol{M}$ is utilized to represent deformation. The transformation matrix $\boldsymbol{M}$ alters the original vector $\boldsymbol{u}$ to a new vector $\boldsymbol{v}$. It can be written as $\boldsymbol{v} = \boldsymbol{M}\boldsymbol{u}$, or

$$\begin{bmatrix} v_x \\ v_y \end{bmatrix} = \begin{bmatrix} l_x & 0 \\ 0 & l_y \end{bmatrix}\begin{bmatrix} u_x \\ u_y \end{bmatrix}, \tag{17}$$

where u_i ($i = x, y$) and v_i ($i = x, y$) are the components of the original vector $\boldsymbol{u}$, and the new vector $\boldsymbol{v}$; l_i ($i = x, y$) is equal to the ratios of the final to initial lengths of vectors along two principal axes. The volume is assumed to be consistent during deformation, which means that $l_x l_y = 1$. Therefore, the true strain along the two principal axes of deformation can be written as

$$\varepsilon_i = \ln l_i (i = x, y) \tag{18}$$

3.3. Austenite to Ferrite Transformation

3.3.1. Ferrite Nucleation

During the cooling process after 6-pass hot-rolling, ferrite nucleates preferentially on the deformed γ-phase and γ-grain boundaries. The stored energy provides the additional driving force for ferrite nucleation. The classical nucleation theory is adopted to describe the nucleation rate of ferrite per unit in the potential nucleation area [53]:

$$J = \frac{K_1 D_C^{\gamma}}{\sqrt{kT}} \exp\left(-\frac{K_2}{kT\Delta G_V^2}\right), \tag{19}$$

where K_1 is a constant related to the density of nucleation sites, and is taken as 2.48×10^{10} $J^{1/2}$ m^{-4} in the present work; K_2 is a constant related to all the interfaces involved in nucleation, 2.5×10^{-18} J^3 mol^{-2} [54], which relates to the shape of the nucleus and interfacial energy; D_C^{γ} is the carbon diffusion coefficient in austenite; ΔG_V is the driving force for ferrite nucleation. It consists of both the chemical driving force, $\Delta G_{V,che}$, and the deformation stored energy, E_{def}:

$$\Delta G_V = \Delta G_{V,che} + E_{def} V_m, \tag{20}$$

where V_m is molar volume of austenite, 7.18×10^{-6} m^3 mol^{-1} [18]. $\Delta G_{V,che}$ is determined by the Gibbs chemical-free energy difference between the α- and γ-phases.

3.3.2. Ferrite Growth and Coarsening

A mixed-mode growth model is adopted to describe the γ→α transformation, where the kinetics of ferrite growth are controlled by both carbon diffusion and α/γ interface mobility. The migration velocity of the α/γ interface $V^{\alpha/\gamma}$ is calculated by

$$V^{\alpha/\gamma} = M^{\alpha/\gamma} P^{\alpha/\gamma}, \tag{21}$$

where $P^{\alpha/\gamma}$ is the effective driving pressure; $M^{\alpha/\gamma}$ is the interfacial mobility of the moving α/γ interface, which can be described as [55]

$$M^{\alpha/\gamma} = M_0^{\alpha/\gamma} \exp\left(-Q^{\alpha/\gamma}/RT\right), \tag{22}$$

where $M_0^{\alpha/\gamma}$ is the pre-exponential factor dependent on composition and processing history. It is adjustable and ranges from 1×10^{-4} to 0.5 mol m J^{-1} s^{-1} [29]. In the present study, $M_0^{\alpha/\gamma}$ is readjusted as 0.085 mol m J^{-1} s^{-1} based on the value estimated by Fazeli et al. [56] and by fitting the simulation results with the experimental micrograph; $Q^{\alpha/\gamma}$ is the activation energy for atom motion at the interface, 140 KJ mol^{-1}; The effective driving pressure, $P^{\alpha/\gamma}$, involving the chemical driving pressure of the γ→α transformation, ΔG_{che}, the solute drag pressure ΔG_{dis}, and the deformation stored energy E_{def}. $P^{\alpha/\gamma}$ is given by

$$P^{\alpha/\gamma} = \Delta G_{che} + E_{def} V_m - \Delta G_{dis}, \tag{23}$$

where ΔG_{dis} is the dissipated Gibbs energy due to the solute drag effect, Section 3.3.3. ΔG_{che} can be calculated from

$$\Delta G_{che} = \chi\left(x_C^{\gamma,\alpha/\gamma} - x_C^{\gamma,e}\right), \tag{24}$$

where χ is a proportionality factor; $x_C^{\gamma,e}$ is the equilibrium carbon concentration of the γ-phase, which can be obtained from thermodynamic calculation; $x_C^{\gamma,\alpha/\gamma}$ is the actual carbon concentration of the γ-phase at the α/γ interface, which is obtained from the solute transport calculation, Section 3.3.4. To eliminate the artificial anisotropy that originated

from the square CA cell, a geometrical factor g_{new} is introduced. It is related to the states of the neighboring cells and is defined by [29]

$$g_{\text{new}} = \min\left[1, \frac{1}{3}\left(\sum_{m=1}^{4} S_m^{\text{I}} + \frac{1}{\sqrt{2}}\sum_{m=1}^{4} S_m^{\text{II}}\right)\right], S^{\text{I}}, S^{\text{II}} = \begin{cases} 0\,(\varphi < 1) \\ 1(\varphi = 1) \end{cases}, \quad (25)$$

where S^{I} and S^{II} indicate the states of the nearest neighbor cells and the second-nearest neighbor cells, respectively; φ is the α-phase volume fraction of the neighboring cells. Thus, the increment of the α-phase fraction during $\gamma \rightarrow \alpha$ transformation is expressed as

$$\Delta\varphi = -g_{\text{new}} V^{\alpha/\gamma} \Delta t / \Delta x, \quad (26)$$

where Δt is the time step. To reflect the higher kinetics of phase transformation along grain boundaries, the interfacial velocity along the γ/γ grain boundaries is assumed to be 2.5 times faster than that in other directions during cooling.

The α-grain coarsening is driven by curvature and can be found in Section 3.2.3.

3.3.3. Solute Drag Model

The segregation of manganese at the α/γ interface would exert a solute drag pressure on the interface. A dissipated Gibbs energy, ΔG_{dis}, is introduced to consider the velocity reduction of the grain boundary resulting from the solute drag effect. ΔG_{dis} can be calculated from the redistribution of manganese in the interfacial region, which is evaluated by [35]

$$\Delta G_{\text{dis}} = -\int_{-\Lambda}^{+\Lambda} \left(x_{\text{Mn}}^{0} - x_{\text{Mn}}(y)\right) \frac{\mathrm{d}E(y)}{\mathrm{d}y} \mathrm{d}y\,, \quad (27)$$

where 2Λ is the physical interface thickness taken as 1 nm [57]; x_{Mn}^{0} is the manganese concentration in the bulk matrix; $x_{\text{Mn}}(y)$ is the manganese concentration profile across the interface; $E(y)$ is the interaction potential of manganese with the interface; y is the distance from the interface. $E(y)$ can be expressed as [35]

$$E(y) = \begin{cases} \mu_{\text{Mn}}^{\alpha} & y < -\Lambda \\ \mu_{\text{Mn}}^{\alpha} + \Delta E - E_0 + \frac{(\Delta E - E_0)}{\Lambda} y & -\Lambda \le y < 0 \\ \mu_{\text{Mn}}^{\alpha} + \Delta E - E_0 + \frac{(\Delta E + E_0)}{\Lambda} y & 0 \le y < +\Lambda \\ \mu_{Mn}^{\gamma} & y \ge +\Lambda \end{cases}, \quad (28)$$

where $2\Delta E$ is the potential difference in manganese between ferrite and austenite, which can be obtained from the thermodynamic calculation; E_0 is the binding energy, i.e., the minimum in potential profile. It can be taken as $1.4RT - 24{,}000$ J mol^{-1} [31]. $x_{\text{Mn}}(y)$ is given by [35]

$$D_{\text{Mn}}^{\text{int}} \frac{\partial x_{\text{Mn}}(y)}{\partial y} + \frac{D_{\text{Mn}}^{\text{int}} x_{\text{Mn}}(y)}{RT} \frac{\partial E(y)}{\partial y} + v^{\alpha/\gamma}\left(x_{\text{Mn}}(y) - x_{\text{Mn}}^{0}\right) = 0, \quad (29)$$

where $D_{\text{Mn}}^{\text{int}} = 1.42 \times 10^{-10} \exp(-132000/RT)$ m^2 s^{-1} is the diffusivity of solute manganese across the α/γ interface [56].

3.3.4. Carbon Diffusion

Carbon partition and diffusion are governed by

$$\partial x_{\text{C}}/\partial \text{t} = \nabla \cdot [D_{\text{C}}(\varphi) \cdot \nabla (x_{\text{C}}/p(\varphi))], \quad (30)$$

where $p(\varphi) = \varphi + k_{\text{e}}(1-\varphi)$; $k_{\text{e}} = x_{\text{C}}^{\gamma,\text{e}}/x_{\text{C}}^{\alpha,\text{e}}$ is the equilibrium partitioning coefficient; $D_{\text{C}}(\varphi) = \varphi D_{\text{C}}^{\alpha} + k_{\text{e}}(1-\varphi) D_{\text{C}}^{\gamma}$ is the carbon diffusion coefficient associated with the α-phase volume fraction, where D_{C}^{α}, D_{C}^{γ} are the temperature-dependent carbon diffusivities in the α- and γ-phases, respectively. They can be estimated by $D_{\text{C}}^{\alpha} = 2.2 \times 10^{-4} \exp(-122500/RT)$

$m^2\ s^{-1}$ and $D_C^{\gamma} = 1.5 \times 10^{-5} \exp(-142100/RT)\ m^2\ s^{-1}$ [58]. Equation (30) is solved using the explicit finite difference scheme. The time step is determined by $\Delta t = \Delta x^2 / (4.5 D_C^{\alpha})$. The zero-flux boundary condition is applied at the four walls of the calculation domain.

3.4. Coupling Scheme between CA and FEM Simulations

The initial grain structure for the CA simulation is generated through Voronoi tessellation according to the number and size of γ-grains measured from an experimental micrograph. The micrograph is obtained from a quenched sample after annealing at 1150 °C for 2 h. The initial microstructure for CA simulation, with an average grain size of ~174 μm, is generated based on the experimental microstructure (~179 μm), Figure 1. Similar grain sizes of the generated initial microstructure (~174 μm) and the experimental microstructure (~179 μm) are achieved, Figure 1. Macro-process parameters used in the CA simulation are obtained from the experiment and FEM simulations. The true strain for each pass in the CA simulation is identical to those in the hot-rolling experiment (Table 1). The temperature curve and the strain rate are obtained from the FEM simulation. The center element of the slab in the FEM calculation corresponds to the CA simulation domain. Moreover, the average effective strain rate of the center under deformation in FEM is taken for the CA simulation. Since the total reduction of the slab is extremely large (~94%), the calculation domain size reduces in each pass to improve the computational efficiency. Varying CA cell spacing is also required to accommodate the significantly changing average grain size in each pass. The domain size at the start of each deformation period and the CA cell spacing for each pass are listed in Table 2.

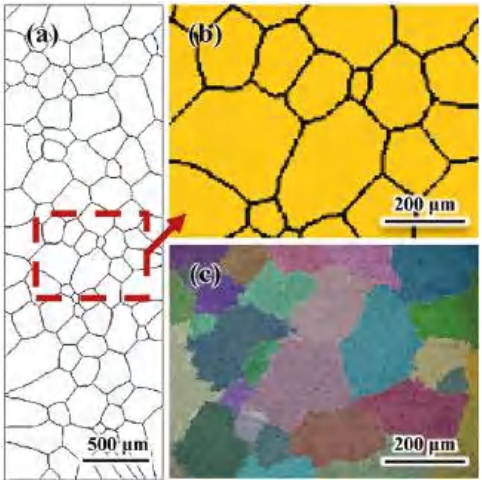

Figure 1. Initial grain structure before hot-rolling: (**a**) initial microstructure generated for the CA simulations; (**b**) enlarged microstructure in the region of the box in (**a**); (**c**) micrograph of the water-quenched sample cut from a slab after annealing at 1150 °C for 2 h before hot-rolling.

Table 2. CA simulation settings.

	Pass 1	Pass 2	Pass 3	Pass 4	Pass 5	Pass 6	Cooling
Initial simulation domain size (CA cells)	250 × 750	111 × 563	110 × 752	73 × 565	80 × 680	100 × 400	240 × 200
CA space step, Δ*x* (μm)	4.8	4.8	2.4	2.4	1.2	0.6	0.3

4. Results and Discussion

4.1. FEM Simulation of Hot-Rolling

First, FEM simulation using DEFORM-3D software is performed to obtain the average strain rate and the variations of the temperature field in the slab during the whole 6-pass hot-rolling process. Table 3 lists the simulated average effective strain rate, $\dot{\varepsilon}$, under each deformation period, which is in accordance with the variation of the true strain given in Table 1.

Table 3. Average effective strain rate obtained from the FEM simulation.

	Pass 1	Pass 2	Pass 3	Pass 4	Pass 5	Pass 6
Strain rate, $\dot{\varepsilon}$ (s^{-1})	3.724	4.770	3.964	5.632	10.000	12.024

Figure 2 displays the simulated temperature curves at the slab center and surface. In the curves, the sudden temperature changes imply the start of each pass. As shown, the simulated temperature at the surface is lower than that in the slab center by ~20–200 °C during the first to fourth pass, while the two temperature curves become nearly superposed in the last two passes, due to the fact that the rolled steel sheet becomes thin. During the hot-rolling process, the slab/sheet temperature is elevated by the heat generated under deformation. Simultaneously, at the slab surface, the temperature falls mostly by heat convection owing to the contact of slab/air and slab/rollers, while at the slab center, the temperature drops as a result of heat transfer from the center to surface. The surface temperatures measured in the experiment are also plotted with the simulated curve for comparison. However, the handheld pyrometer used in the experiments cannot determine the complete information on the slab temperature field. Therefore, it is necessary to perform FEM simulations to obtain the temperature field inside the slab.

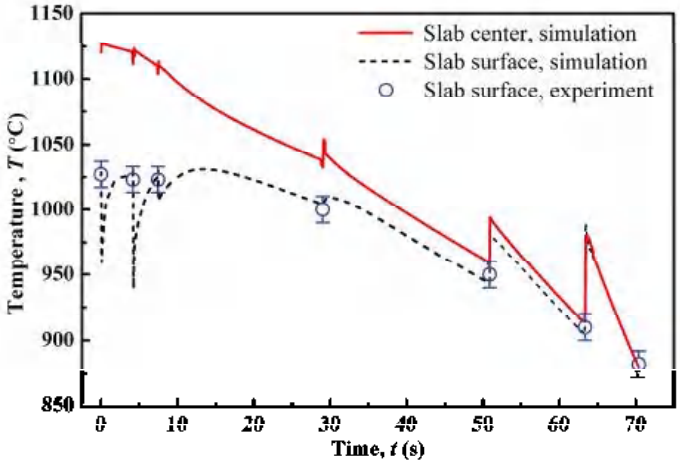

Figure 2. FEM-simulated temperatures of slab center (red line) and surface (black dash line) varying with time compared with the experimentally measured slab surface temperatures (blue circle).

4.2. CA Simulation of the Hot-Rolling Process

The CA model described in Sections 3.2 and 3.3 is applied to simulate the evolution of dislocation density and grain structure during the 6-pass hot-rolling process. The FEM-simulated temperature and strain rate are incorporated in the CA simulations. Figure 3 plots the simulated average dislocation density, ρ_{ave}, and the recrystallized nucleus density varying with time. Arrows in the curves indicate the end of each pass. As shown in

Figure 3a, the dislocation density increases rapidly under deformation and reaches a peak value in each pass. Then, it declines in the following inter-pass interval. For the whole process, the ρ_{ave} peak value shows an increasing trend with time except for the third pass. This corresponds to the strain rate with the pass number (Table 3), due to the fact that a higher strain rate enhances the dislocation density in the matrix. On the other hand, the ρ_{ave} valley value, representing the value of the remaining dislocation density in each pass, declines until the fourth interval. Especially at the end of the first and the second intervals, ρ_{ave} remains high (~1.5×10^{14} m^{-2}) in the matrix and is inherited by the next pass. ρ_{ave} is almost reduced to zero at the end of the fourth interval, and then rises slightly afterwards. In the end of sixth pass before cooling, ρ_{ave} is in the order of 10^{13} m^{-2}, which is in the range of typical values for hot-rolled C-Mn steels [59].

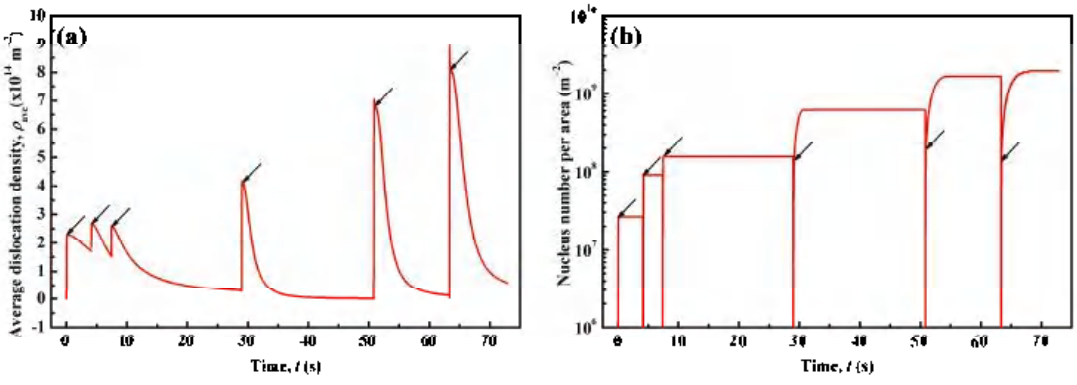

Figure 3. CA-simulated (**a**) average dislocation density and (**b**) recrystallized nucleus density varying with time. Arrows in the curves indicate the end of each pass.

In Figure 3b, the recrystallized nucleus density refers to the newly recrystallized nuclei in each pass, and thus it is zero at the start of each pass. As seen in each pass, the nucleus density increases rapidly. The steady value of the recrystallized nucleus density increases with the pass number. It is noted that there are almost no new nuclei appearing during the first to third inter-pass intervals, implying that the recrystallized nuclei are nearly produced by DRX during the former three passes. However, during the fourth to sixth inter-pass intervals, the nuclei number is increased, which is apparently generated by the SRX mechanism. The proportion of SRX to DRX nuclei also increases with the pass number. As shown in Figure 3a, the peak value of average dislocation density, ρ_{ave}, gradually increases during the fourth to sixth pass. Obviously, higher ρ_{ave} in the fourth to sixth pass exceeds the critical value for SRX nucleation and leads to a larger recrystallization nucleation rate, Equations (12) and (13). Thus, it is understandable that SRX could happen and produce more nuclei in the latter three intervals. On the other hand, it is interesting to note that there is an increase in the DRX nucleus density from the first to third pass, although the variation of ρ_{ave} is nearly the same in those passes. It is considered that the initial grain size could account for this phenomenon [60–62]. Finer primary grains could provide more grain boundary area as potential nucleation sites, leading to a higher nucleus density in the matrix.

Figure 4 presents the CA-simulated variation of average grain size and the grain structures at the end of each interval during the 6-pass hot-rolling process. The equivalent grain diameter is calculated using

$$D = \frac{1}{N_g} \sum_{i=1}^{N_g} \sqrt{\frac{4A_{Si}}{\pi}}, \quad (31)$$

where N_g is the number of grains in the calculation domain; A_{Si} is the area of grain S_i. It is seen in Figure 4 that for the first to third pass and interval, the average γ-grain size first reduces rapidly under deformation and then, as indicated by the arrows, rises immediately after finishing deformation. However, during the latter three intervals, the grain size is still reduced after deformation. As analyzed above, during the former three passes, the recrystallized nucleus is generated primarily by the DRX mechanism, while in the latter three passes and intervals, both DRX and SRX occur. Thus, in each pass, the dramatic reduction in average grain size results from the rapid nucleation of DRX. During the fourth to sixth intervals, the continuous decrease in average grain size after deformation results from SRX nucleation. The increase in grain size during the inter-pass period is due to the growth and coarsening of recrystallized grains.

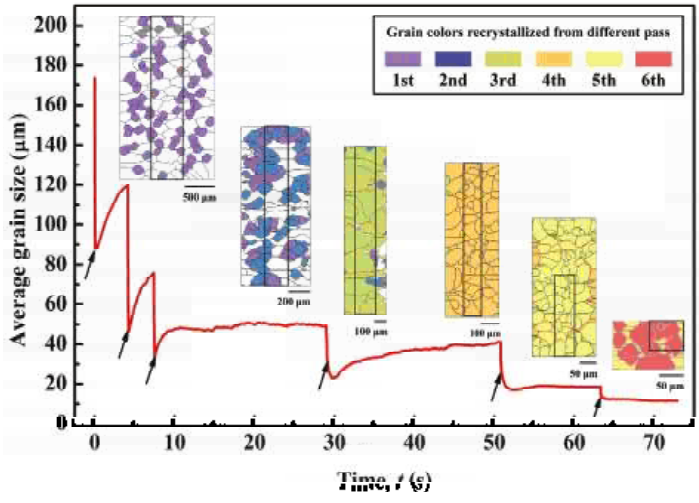

Figure 4. CA-simulated average grain size varying with time. Arrows indicate the end of each pass. Pictures from the left to right are the simulated grain structures at the end of each interval. The selected areas inside boxes shown in each picture are the input microstructures for the next pass. The sizes of each squared area are listed in Table 2. Recrystallized grains formed in different passes and intervals are shown in different colors; the initial matrix before the 1st pass is shown in white color.

Table 4 lists the average grain size of each type of grain at the end of each interval. The matrix grain refers to the grain structure inherited from the previous pass; DRX grain, formed by DRX and MDRX mechanisms, and SRX grain refer to the newly recrystallized grains in each pass. As shown, γ-grains are gradually refined from the initial ~174 μm to ~12 μm at the end of the sixth interval. At the end of each interval, the average matrix grain size ($\overline{D}_M$), average DRX grain size ($\overline{D}_{DRX}$), and average SRX grain size ($\overline{D}_{SRX}$) are smaller than the average γ-grain size ($\overline{D}_\gamma$) of the previous pass, which results in the refinement of the overall γ-grains. Each type of grain is also refined step by step except that $\overline{D}_{DRX}$ increases at the end of the third interval. At the end of the first and second intervals, the limited inter-pass time and relatively low strain rate constrain the growth of DRX grains, i.e., MDRX mechanism, which leads to a smaller $\overline{D}_{DRX}$ than $\overline{D}_M$. In the case of the third pass and interval, however, there is adequate inter-pass time for sufficient DRX grain structure development. Accordingly, the deformed matrix is greatly consumed. At the end of the third interval, $\overline{D}_{DRX}$ is much larger than $\overline{D}_M$ and $\overline{D}_\gamma$, leading to a weakening of grain refinement and grain size uniformity. In the fourth to sixth pass, the strain rate is high enough (Table 3), and high stored energy accumulates in the matrix, which drives SRX grain growth. SRX grain growth would consume both DRX and matrix grains. At the end of the fourth to the sixth intervals, the average SRX grain size is largest. It is noted

that, at the end of the sixth interval, no DRX grains remain, which means that DRX grain structure is totally replaced by SRX grains. The high strain rate in the sixth pass induces high stored energy remaining in the deformed matrix and DRX grains, and thus introduces a high difference in stored energy between SRX grains and other grain structures. The difference in stored energy provides a high driving force for SRX growing into matrix and DRX grains. Therefore, the SRX mechanism could take advantage of the high strain rate when competing with the MDRX mechanism.

Table 4. Average grain size at the end of each interval.

Pass Number	Initial	1	2	3	4	5	6
Average grain size, $\overline{D}_{\gamma}$ (μm)	174	120	76	49	41	19	12
Average matrix grain size, $\overline{D}_{M}$ (μm)	174	147	87	27	20	12	8
Average DRX grain size, $\overline{D}_{DRX}$ (μm)	–	93	63	72	33	15	–
Average SRX grain size, $\overline{D}_{SRX}$ (μm)	–	–	–	–	45	23	19

Figure 5 shows the recrystallization volume fraction, f_{RX}, varying with time. In Figure 5a, f_{RX} refers to the volume percentage of the newly recrystallized grains during each pass, and thus it is zero at the start of each pass. During the first to fourth intervals, f_{RX} increases gradually and approaches a nearly saturated value of ~1.0 at the end of fourth interval. Then, f_{RX} decreases in the fifth and sixth intervals. As indicated by the arrows, the f_{RX} increment is not evident during the deformation period. The obvious f_{RX} increase appears during the inter-pass period. This is because the deformation time is extremely short (~0.1 s), and thus the growth of DRX nuclei is quite limited during deformation. Rapid development of the recrystallized structure takes place during the inter-pass intervals. Therefore, MDRX and SRX are the controlling mechanisms for the recrystallized grain structure formation. As discussed, regarding Figures 3b and 4, there is no SRX occurring during the first to third interval. Therefore, MDRX provides the main contribution for recrystallization during the former three intervals. For the latter three intervals, MDRX and SRX dominate concurrently.

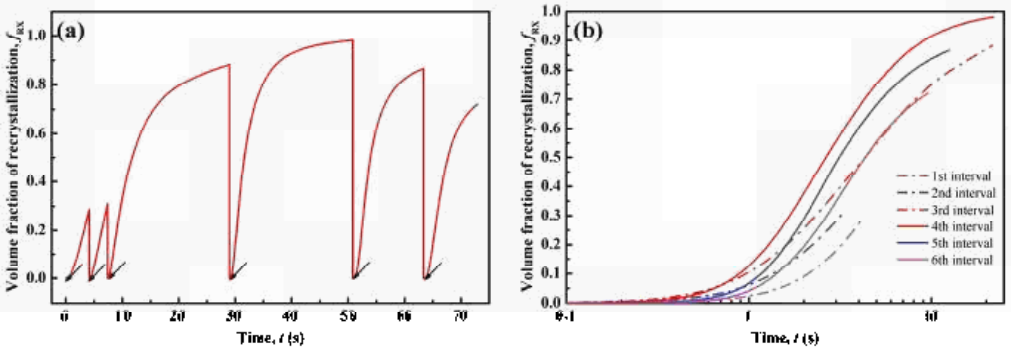

Figure 5. CA-simulated volume fraction of recrystallization varying with time: (**a**) an overview of the 6-pass hot-rolling process and (**b**) in each pass. Arrows in (**a**) indicate the end of each pass.

Figure 5b compares the recrystallization kinetics of each inter-pass interval. It is seen that the kinetics of recrystallization accelerate gradually from the first to fourth pass. The kinetics curve of the fourth interval becomes the highest. However, from the fifth to the sixth interval, the kinetics are reduced. Numerous experiments found that recrystallization kinetics are influenced by various factors, including strain rate [3,4], temperature [7], initial grain size [60–62], as well as inter-pass time. It is obvious that a higher strain rate enhances recrystallization by introducing more dislocations and thus provides a higher nucleation

rate and driving force for the growth of recrystallized grains. The increasing temperature also accelerates the kinetics by providing higher boundary mobility. The influence of initial grain size relates to the nucleation of both DRX and SRX. As shown in Figure 3b, the nuclei density increases gradually from the first to third pass, which is considered to result from gradually finer initial grain size. This leads to the acceleration in kinetics of MDRX in the former three passes. For the fourth interval, in addition to the effects of finer grains and increased strain rate, the SRX mechanism also contributes to the higher kinetics than in the third interval by generating more nuclei. Owing to the decreased temperature, the recrystallization kinetics of the last two intervals slow down, even though the strain rate is increased, and the grains are refined. Therefore, the recrystallization fraction in the fourth interval is the highest under the comprehensive effect of initial grain size, strain rate, temperature, as well as inter-pass time.

The first and the fourth passes are taken as examples to explain the variations in grain structure and the deformation-stored energy (E_{def}) field. Figure 6 presents the CA-simulated evolution of grain structure and the E_{def} field during the first pass and subsequent inter-pass period. As presented in Figure 6a, before hot-rolling, the initial grain structure is produced according to the experimental observation (see Figure 1). The initial E_{def} at grain boundaries is set to be somewhat higher than that within the grains, Equation (8). The deformed grain structures and nonuniform distribution of the E_{def} are achieved during deformation, Figure 6b,c. Figure 6c shows the grain structure and the E_{def} field at the end of deformation. It is seen that recrystallization does not occur evidently during the deformation period, reflecting the minor variation of f_{RX} in Figure 5a due to the limited deformation time. The E_{def} accumulates continuously under deformation, which corresponds to the increase in ρ_{ave} in the first pass (Figure 3a). During the inter-pass period, recrystallized grains appear at the γ/γ grain boundaries. As analyzed above, these recrystallized grains nucleate by the DRX mechanism. Then, as described by Equation (14), they grow into unrecrystallized grains by consuming the E_{def} during the inter-pass interval, Figure 6c–f. The E_{def} in some recrystallized grains is higher because they are generated prior to other recrystallized grains and thus accumulate more deformation-stored energy. It is also noted that the unrecrystallized grains surrounded by DRX grains have a relatively lower E_{def} than that far away from DRX grains, as the E_{def} in those grains is consumed by massive recrystallization, Equation (7).

Figure 7 presents the CA-simulated evolution of grain structure and the deformation-stored energy (E_{def}) field during the fourth pass and interval. As shown, the nucleation from DRX can hardly be observed in Figure 7a,b, which is the same as that in the first pass. The E_{def} of the matrix at the end of the fourth pass deformation is much higher compared to that of the first pass. The remaining E_{def} after the fourth pass still exceeds the critical value for SRX nucleation, leading to the occurrence of SRX, Equation (12). Thus, during the inter-pass period, some new grains nucleate at both the unrecrystallized and recrystallized grain boundaries, Figure 7c–e. When the recrystallized grains contact each other, grain coarsening driven by curvature takes place, Equations (14)–(16). It is seen from Figure 7e that at the end of the fourth pass, the matrix has been almost thoroughly occupied by the new recrystallized grains, and the E_{def} in the domain has been exhausted to relatively low values. As discussed for Figure 5b, the nearly completely recrystallized grain structure after the fourth pass interval is due to an integrating effect of high strain rate (5.632 s^{-1}), refined initial grain size (~40 μm), relatively long inter-pass time (~21 s), and moderate temperature (950–1050 °C).

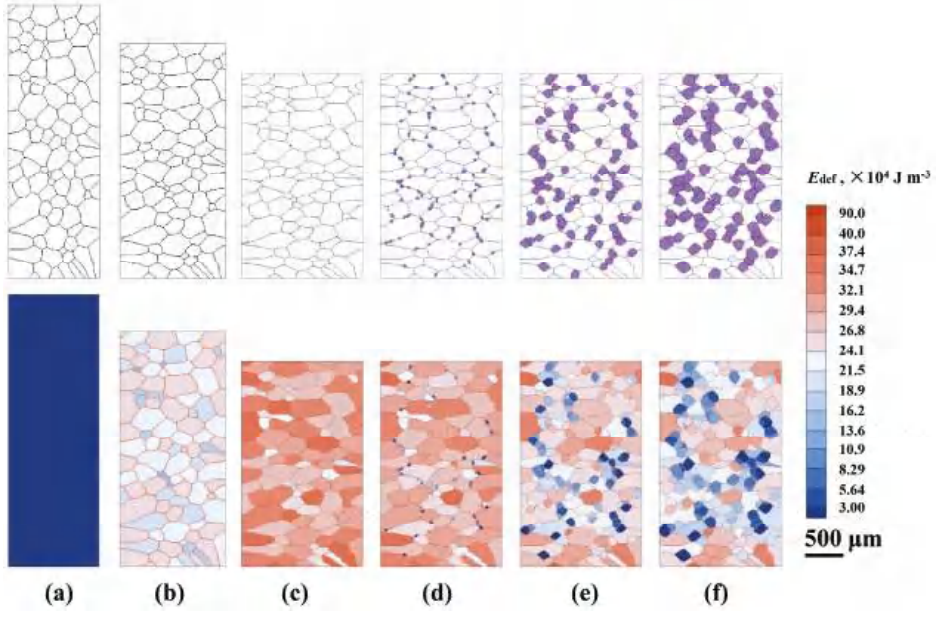

Figure 6. CA simulated evolution of the grain structure (upper row) and deformation-stored energy (lower row) during the 1st pass and interval: (**a**) t = 0.0 s; (**b**) t = 0.05 s; (**c**) t = 0.09 s, the end of deformation; (**d**) t = 1.0 s; (**e**) t = 3.0 s; (**f**) t = 4.1 s. In the upper row, the white and purple grains represent the initial and recrystallized grains generated in the 1st pass and interval, respectively. The horizontal and vertical directions are the rolling and compression directions, respectively.

4.3. CA Simulation of Cooling Process.

Finally, the CA model coupled with the solute drag effect as described in Section 3.3 is adopted to simulate the microstructure evolution during cooling after the sixth pass. The grain structure at the end of sixth pass (inside the box of the last grain structure picture in Figure 4) is taken as the initial microstructure (Figure 8a) for this simulation. According to the Calphad calculation and experimental measurement, the $\gamma \rightarrow \alpha$ transformation temperature range is set from 832 °C to 650 °C. Figure 8 displays the simulation results during cooling from 832 °C to 650 °C at a cooling rate of 4 °C s^{-1}. The SEM micrograph from the as-rolled sample is given in Figure 8d for comparison. As shown in Figure 8b, new α-grains nucleate primarily at γ/γ grain boundaries; some α-grains also appear inside the γ-grains. During cooling, the α-grains grow with the increasing carbon concentrations in both α- and γ-phases. The regions adjacent to the α/γ interfaces are more enriched in carbon due to the rejection of carbon atoms from the newly formed α-grains. When the simulation of phase transformation finishes, carbon enriches in the remaining γ-phase (light blue) in Figure 8c, which corresponds to the pearlite phase in Figure 8d. The final α volume fraction of the simulated microstructure presented in Figure 8c is ~0.92, which is nearly identical to the experimentally measured value, ~0.93. The simulated average α-grain size, ~9.4 μm, also agrees well with the experimental data, ~9.7 μm.

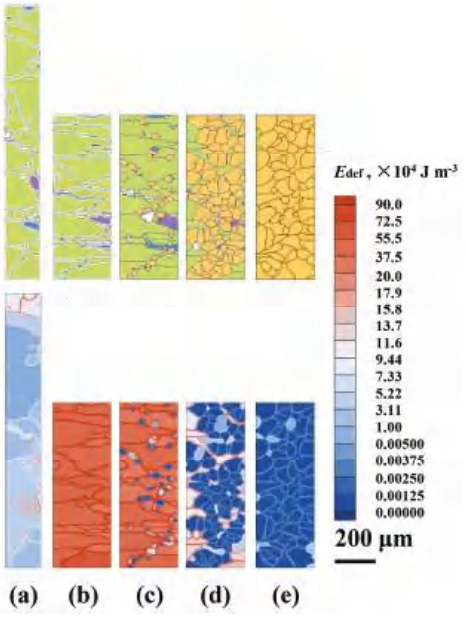

Figure 7. CA-simulated evolution of the grain structure (upper row) and deformation-stored energy (lower row) during the 4th pass and interval: (**a**) t = 0.0 s; (**b**) t = 0.1 s, the end of deformation; (**c**) t = 1.0 s; (**d**) t = 5.0 s; (**e**) t = 21.8 s. In the upper row, the purple, blue, green, yellow grains represent recrystallized grain generated in the 1st, 2nd, 3rd, 4th pass and interval, respectively. The horizontal and vertical directions are the rolling and compression directions, respectively.

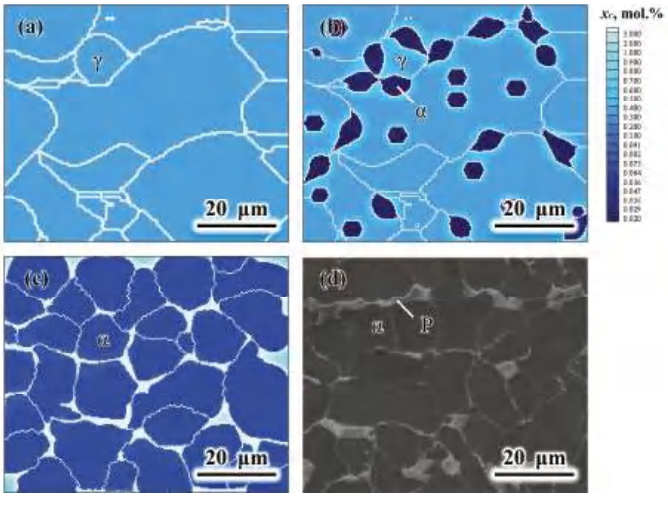

Figure 8. CA-simulated microstructures and carbon concentration fields during cooling from 832 °C to 650 °C at a cooling rate of 4 °C s^{-1}: (**a**) T = 832 °C; (**b**) T = 750 °C; (**c**) T = 650 °C (t = 45.5 s, f_α = ~0.92, D_α = ~9.4 μm); (**d**) SEM micrograph (f_α = ~0.93, D_α = ~9.7 μm) of the cooled sample at room temperature. f_α is the α volume fraction, and D_α is the average diameter of α-grains.

5. Conclusions

A coupled macroscale finite element method (FEM) and mesoscale cellular automaton (CA) model is proposed for the simulation of microstructural evolution during a 6-pass hot-rolling process. The FEM is adopted to calculate the deformation and temperature field. The CA approach is used to simulate the dislocation density and microstructure quantitatively, including recrystallization during hot-rolling, and the $\gamma \rightarrow \alpha$ phase transformation during cooling.

The calculation of the dislocation density field takes into account the effects of work hardening, dynamic recovery, static recovery, and recrystallization. For the simulation of the $\gamma \rightarrow \alpha$ phase transformation, the interaction between manganese atoms and α/γ interfaces is considered by incorporating a solute drag effect with the CA model; the contribution of deformation-stored energy to the driving forces is also involved.

The simulation results quantitively display the comprehensive effect of strain rate, grain size, temperature, and inter-pass time on the different mechanisms of recrystallization, including dynamic recrystallization (DRX), metadynamic recrystallization (MDRX), and static recrystallization (SRX). DRX is found to be mainly constrained to the nucleation of recrystallized grains due to the limited deformation time (~0.1 s) in the present rolling process. Under the relatively low strain rate of the first to third passes, MDRX dominates the grain structure evolution. For the high strain rates of the fourth to sixth passes, MDRX and SRX occur concurrently. High strain rate is found to be more beneficial to SRX than MDRX. A high temperature and fine initial grain size will enhance the kinetics of recrystallization. A sufficient inter-pass time is also necessary for MDRX and SRX to refine grain structure. However, too long of an inter-pass duration may lead to recrystallized grains coarsening.

The simulated average γ-grain size is reduced from ~174 μm to ~12 μm during the 6-pass hot rolling process. After the $\gamma \rightarrow \alpha$ phase transformation during subsequent cooling, the simulated final α volume fraction (0.92) and average α-grain size (~9.4 μm) agree reasonably with the experimental data (~0.93, ~9.7 μm). The simulation in the present work allows for quantification of the contributions of DRX, MDRX, SRX, and phase transformation on grain refinement, and thus provides insight into the mechanisms of microstructural evolution during a multi-pass hot-rolling process.

Author Contributions: Conceptualization, M.Z.; methodology, D.A. and M.Z.; software, D.A. and X.L.; validation, D.A. and X.Z.; formal analysis, X.L. and M.Z.; investigation, X.L. and M.Z.; resources, X.Z.; data curation, X.L. and X.Z.; writing—original draft preparation, X.L.; writing—review and editing, M.Z. and B.W.K.; visualization, X.L.; supervision, M.Z.; project administration, M.Z.; funding acquisition, M.Z. All authors have read and agreed to the published version of the manuscript.

Funding: This work was financially supported by A. O. Smith Corporation, USA, NSFC (Grant No. 51501091), and the Jiangsu Key Laboratory for Advanced Metallic Materials (BM2007204).

Institutional Review Board Statement: Not applicable.

Informed Consent Statement: Not applicable.

Data Availability Statement: The data presented in this study are available in this article.

Conflicts of Interest: The authors declare no conflict of interest.

Nomenclature

γ_b	high-angle grain boundary energy: J m^{-2}
ε	strain
ϵ_c	critical strain for SRX nucleation
$\dot{\varepsilon}$	strain rate, s^{-1}
θ_0	initial work hardening rate, MPa
κ	the grain boundary curvature, m^{-1}
Λ	half physical interface thickness, nm
μ	shear modulus of the γ-phase, Pa
ρ	dislocation density, m^{-2}
ρ_0	initial dislocation density, m^{-2}
ρ_c	critical dislocation density for DRX, m^{-2}
ρ_{ave}	average dislocation density of the material, m^{-2}
$\overline{\rho_{nr}}$	average dislocation density of the deformed grain, m^{-2}
$\overline{\rho_r}$	average dislocation density of the recrystallized grain, m^{-2}
σ	flow stress, Pa
σ_s	saturated stress, Pa
τ	dislocation line energy, J·m^{-1}
φ	α-phase volume fraction
χ	proportionality factor, J mol^{-1} mol.%$^{-1}$
α_1, β, η, a, n', A_0, Q_A	constants for calculating dislocation density evolution
A	coefficient for calculating curvature
A_{Si}	area of grain S_i
b	the magnitude of the Burgers vector, m
C	DRX nucleation parameter
d	coefficient representing static recovery rate
d_0, md Q_{SRV}	constants for calculating static recovery rate
$\overline{D}_\gamma$, $\overline{D}_M$, $\overline{D}_{DRX}$, $\overline{D}_{SRX}$, $\overline{D}_\alpha$	average diameters for γ-, matrix, DRX, SRX, α-grains, μm
D_C^α, D_C^γ	carbon diffusion coefficients in the α- and γ-phases, m^2 s^{-1}
D_0	boundary self-diffusion coefficient, m^2 s^{-1}
D_{Mn}^{int}	manganese diffusion coefficient across the α/γ interface, m^2 s^{-1}
E_{def}	deformation stored energy, J m^{-3}
E_c	critical deformation stored energy for SRX nucleation, J m^{-3}
$\overline{E_S}$	average deformation stored energy of grain S, J m^{-3}
E_0	binding energy of manganese, J mol^{-1}
ΔE	half potential difference of manganese between α- and γ-phases, J mol^{-1}
f_{RX}, f_α	volume fractions of recrystallized grains and α grains
ΔG_V	driving force of the ferrite nucleation, J mol^{-1}
$\Delta G_{V,che}$	Gibbs chemical free energy difference between the α- and γ-phases, J mol^{-1}
ΔG_{che}	chemical driving force of the γ→α transformation, J mol^{-1}
ΔG_{dis}	solute drag pressure, J mol^{-1}
g_{new}	geometrical factor
$H_{S,Max}$	maximum value of the stored energy in grain S, J m^{-3}
I	grain index
J	nucleation rate of ferrite, m^{-2} s^{-1}
k	Boltzmann constant, J K^{-1}
k_e	equilibrium partitioning coefficient
k_1, k_2	constants representing work hardening and dynamic recovery
K_1 K_2	constants for calculating the nucleation rate of ferrite
K_{ink}	number of cells within the neighborhood belonging to grain S for a flat interface
l	dislocation mean free path, m
l_i	ratio of the final to initial length of vector along corresponding axis
L	distance of the cell (i, j) from the grain boundary, μm
$f(L)$	factor for deformation stored energy distribution
$\boldsymbol{M}$	deformation matrix for topology mapping
M_b	high-angle grain boundary mobility, m^4 J^{-1} s^{-1}
$M^{\alpha/\gamma}$	interfacial mobility of the moving α/γ interface, mol m J^{-1} s^{-1}

$M_0^{\alpha/\gamma}$	pre-exponential factor, mol m J^{-1} s^{-1}
$\dot{n}_{DRX}$, $\dot{n}_{SRX}$	nucleation rates for DRX and SRX, m^{-2} s^{-1}
n	number of cells that belongs to grain S
N	number of the first and second nearest neighbors
N_S	number of cells within the neighborhood belonging to grain S
N_g	number of grains in the calculation domain
P	driving pressure, J m^{-3}
$p^{\alpha/\gamma}$	effective driving pressure for ferrite growth, J mol^{-1}
Q_N	activation energy for nucleation, KJ mol^{-1}
Q_b	activation energy for grain-boundary motion, KJ mol^{-1}
$Q^{\alpha/\gamma}$	activation energy for atom motion at the interface, KJ mol^{-1}
R	universal gas constant, J mol^{-1} K^{-1}
S^I, S^{II}	states of the nearest and the second-nearest neighbor cells
T	absolute temperature, K
$\boldsymbol{u}$, $\boldsymbol{v}$	original and the new vectors of the CA cell space
V	velocity of grain boundary movement, m s^{-1}
$V^{\alpha/\gamma}$	migration velocity of the α/γ interface, m s^{-1}
V_m	molar volume of austenite, m^3 mol^{-1}
$x_C^{\alpha,e}$	equilibrium carbon concentration of the α-phase, mol.%
$x_C^{\gamma,e}$	equilibrium carbon concentration of the γ-phase, mol.%
$x_C^{\gamma,\alpha/\gamma}$	actual carbon concentration of the γ-phase at the α/γ interface, mol.%
x_{Mn}^0	manganese concentration in the bulk matrix, mol.%
y	distance from the interface, μm
$x_{Mn}(y)$	the manganese concentration profile
$E(y)$	the interaction potential of manganese
Z	nucleation parameter for SRX, J^{-1} s^{-1}

References

1. Huang, K.; Logé, R.E. A Review of Dynamic Recrystallization Phenomena in Metallic Materials. *Mater. Des.* **2016**, *111*, 548–574. [CrossRef]
2. Zhao, L.; Park, N.; Tian, Y.; Shibata, A.; Tsuji, N. Mechanism of Dynamic Formation of Ultrafine Ferrite Grains during High Temperature Processing in Steel. *Adv. Eng. Mater.* **2017**, *19*, 1600778. [CrossRef]
3. Fang, Y.; Chen, X.; Madigan, B.; Cao, H.; Konovalov, S. Effects of Strain Rate on the Hot Deformation Behavior and Dynamic Recrystallization in China Low Activation Martensitic Steel. *Fusion Eng. Des.* **2016**, *103*, 21–30. [CrossRef]
4. Nicolaÿ, A.; Fiorucci, G.; Franchet, J.M.; Cormier, J.; Bozzolo, N. Influence of Strain Rate on Subsolvus Dynamic and Post-Dynamic Recrystallization Kinetics of Inconel 718. *Acta Mater.* **2019**, *174*, 406–417. [CrossRef]
5. Yu, S.; Du, L.X.; Hu, J.; Misra, R.D.K. Effect of Hot Rolling Temperature on the Microstructure and Mechanical Properties of Ultra-Low Carbon Medium Manganese Steel. *Mater. Sci. Eng. A* **2018**, *731*, 149–155. [CrossRef]
6. Ghosh, S.; Komi, J.; Mula, S. Flow Stress Characteristics and Design of Innovative 3-Steps Multiphase Control Thermomechanical Processing to Produce Ultrafine Grained Bulk Steels. *Mater. Des.* **2020**, *186*, 108297. [CrossRef]
7. Zhang, W.; Zhang, J.; Han, Y.; Liu, R.; Zou, D.; Qiao, G. Metadynamic Recrystallization Behavior of As-Cast 904L Superaustenitic Stainless Steel. *J. Iron Steel Res. Int.* **2016**, *23*, 151–159. [CrossRef]
8. Raabe, D. Cellular Automata in Materials Science with Particular Reference to Recrystallization Simulation. *Annu. Rev. Mater. Res.* **2002**, *32*, 53–76. [CrossRef]
9. Chen, F.; Zhu, H.; Zhang, H.; Cui, Z. Mesoscale Modeling of Dynamic Recrystallization: Multilevel Cellular Automaton Simulation Framework. *Metall. Mater. Trans. A* **2020**, *51*, 1286–1303. [CrossRef]
10. Zhang, F.; Liu, D.; Yang, Y.; Wang, J.; Liu, C.; Zhang, Z.; Wang, H. Modeling and Simulation of Dynamic Recrystallization for Inconel 718 in the Presence of Delta Phase Particles Using a Developed Cellular Automaton Model. *Model. Simul. Mater. Sci. Eng.* **2019**, *27*, 035002. [CrossRef]
11. Bararpour, S.M.; Jamshidi Aval, H.; Jamaati, R. Cellular Automaton Modeling of Dynamic Recrystallization in Al-Mg Alloy Coating Fabricated Using the Friction Surfacing Process. *Surf. Coat. Technol.* **2021**, *407*, 126784. [CrossRef]
12. Liu, H.; Zhang, J.; Xu, B.; Xu, X.; Zhao, W. Prediction of Microstructure Gradient Distribution in Machined Surface Induced by High Speed Machining through a Coupled FE and CA Approach. *Mater. Des.* **2020**, *196*, 109133. [CrossRef]
13. Madej, Ł.; Sitko, M.; Legwand, A.; Perzynski, K.; Michalik, K. Development and Evaluation of Data Transfer Protocols in the Fully Coupled Random Cellular Automata Finite Element Model of Dynamic Recrystallization. *J. Comput. Sci.* **2018**, *26*, 66–77. [CrossRef]
14. Kim, D.-K.; Woo, W.; Park, W.-W.; Im, Y.-T.; Rollett, A. Mesoscopic Coupled Modeling of Texture Formation during Recrystallization Considering Stored Energy Decomposition. *Comput. Mater. Sci.* **2017**, *129*, 55–65. [CrossRef]

15. Shen, G.; Hu, B.; Zheng, C.; Gu, J.; Li, D. Coupled Simulation of Ferrite Recrystallization in a Dual-Phase Steel Considering Deformation Heterogeneity at Mesoscale. *Comput. Mater. Sci.* **2018**, *149*, 191–201. [CrossRef]
16. Li, H.; Sun, X.; Yang, H. A Three-Dimensional Cellular Automata-Crystal Plasticity Finite Element Model for Predicting the Multiscale Interaction among Heterogeneous Deformation, DRX Microstructural Evolution and Mechanical Responses in Titanium Alloys. *Int. J. Plast.* **2016**, *87*, 154–180. [CrossRef]
17. Barkóczy, P.; Roósz, A.; Geiger, J. Simulation of Recrystallization by Cellular Automaton Method. *Mater. Sci. Forum* **2003**, *414–415*, 359–364. [CrossRef]
18. Zheng, C.; Xiao, N.; Li, D.; Li, Y. Microstructure Prediction of the Austenite Recrystallization during Multi-Pass Steel Strip Hot Rolling: A Cellular Automaton Modeling. *Comput. Mater. Sci.* **2008**, *44*, 507–514. [CrossRef]
19. Chen, F.; Cui, Z. Mesoscale Simulation of Microstructure Evolution during Multi-Stage Hot Forging Processes. *Model. Simul. Mater. Sci. Eng.* **2012**, *20*, 045008. [CrossRef]
20. Łach, Ł.; Svyetlichnyy, D. Multiscale Model of Shape Rolling Taking into Account the Microstructure Evolution—Frontal Cellular Automata. *Adv. Mater. Res.* **2014**, *998–999*, 545–548. [CrossRef]
21. Łach, Ł.; Svyetlichnyy, D. Frontal Cellular Automata Simulations of Microstructure Evolution during Shape Rolling. *Mater. Res. Innov.* **2014**, *18*, S6-295. [CrossRef]
22. Svyetlichnyy, D. Simulation of Microstructure Evolution during Shape Rolling with the Use of Frontal Cellular Automata. *ISIJ Int.* **2012**, *52*, 559–568. [CrossRef]
23. Zheng, C.; Xiao, N.; Hao, L.; Li, D.; Li, Y. Numerical Simulation of Dynamic Strain-Induced Austenite-Ferrite Transformation in a Low Carbon Steel. *Acta Mater.* **2009**, *57*, 2956–2968. [CrossRef]
24. Zheng, C.; Raabe, D. Interaction between Recrystallization and Phase Transformation during Intercritical Annealing in a Cold-Rolled Dual-Phase Steel: A Cellular Automaton Model. *Acta Mater.* **2013**, *61*, 5504–5517. [CrossRef]
25. Lan, Y.J.; Xiao, N.M.; Li, D.Z.; Li, Y.Y. Mesoscale Simulation of Deformed Austenite Decomposition into Ferrite by Coupling a Cellular Automaton Method with a Crystal Plasticity Finite Element Model. *Acta Mater.* **2005**, *53*, 991–1003. [CrossRef]
26. Su, B.; Ma, Q.; Han, Z. Modeling of Austenite Decomposition during Continuous Cooling Process in Heat Treatment of Hypoeutectoid Steel with Cellular Automaton Method. *Steel Res. Int.* **2017**, *88*, 1600490. [CrossRef]
27. Zhu, B.; Zhang, Y.; Wang, C.; Liu, P.X.; Liang, W.K.; Li, J. Modeling of the Austenitization of Ultra-High Strength Steel with Cellular Automation Method. *Metall. Mater. Trans. A* **2014**, *45*, 3161–3171. [CrossRef]
28. Su, B.; Han, Z.; Liu, B. Cellular Automaton Modeling of Austenite Nucleation and Growth in Hypoeutectoid Steel during Heating Process. *ISIJ Int.* **2013**, *53*, 527–534. [CrossRef]
29. An, D.; Baik, S.; Pan, S.; Zhu, M.; Isheim, D.; Krakauer, B.W.; Seidman, D.N. Evolution of Microstructure and Carbon Distribution During Heat Treatments of a Dual-Phase Steel: Modeling and Atom-Probe Tomography Experiments. *Metall. Mater. Trans. A* **2018**, *50*, 436–450. [CrossRef]
30. An, D.; Chen, S.; Sun, D.; Pan, S.; Krakauer, B.W.; Zhu, M. A Cellular Automaton Model Integrated with CALPHAD-Based Thermodynamic Calculations for Ferrite-Austenite Phase Transformations in Multicomponent Alloys. *Comput. Mater. Sci.* **2019**, *166*, 210–220. [CrossRef]
31. Bos, C.; Mecozzi, M.G.; Sietsma, J. A Microstructure Model for Recrystallisation and Phase Transformation during the Dual-Phase Steel Annealing Cycle. *Comput. Mater. Sci.* **2010**, *48*, 692–699. [CrossRef]
32. Vertyagina, Y.; Mahfouf, M.; Xu, X. 3D Modelling of Ferrite and Austenite Grain Coarsening Using Real-Valued Cellular Automata Based on Transition Function. *J. Mater. Sci.* **2013**, *48*, 5517–5527. [CrossRef]
33. Li, D.Z.; Xiao, N.M.; Lan, Y.J.; Zheng, C.W.; Li, Y.Y. Growth Modes of Individual Ferrite Grains in the Austenite to Ferrite Transformation of Low Carbon Steels. *Acta Mater.* **2007**, *55*, 6234–6249. [CrossRef]
34. Chen, H.; van der Zwaag, S. A General Mixed-Mode Model for the Austenite-to-Ferrite Transformation Kinetics in Fe–C–M Alloys. *Acta Mater.* **2014**, *72*, 1–12. [CrossRef]
35. Purdy, G.R.; Brechet, Y.J.M. A Solute Drag Treatment of the Effects of Alloying Elements on the Rate of the Proeutectoid Ferrite Transformation in Steels. *Acta Metall. Mater.* **1995**, *43*, 3763–3774. [CrossRef]
36. Chen, F.; Cui, Z.; Liu, J.; Chen, W.; Chen, S. Mesoscale Simulation of the High-Temperature Austenitizing and Dynamic Recrystallization by Coupling a Cellular Automaton with a Topology Deformation Technique. *Mater. Sci. Eng. A* **2010**, *527*, 5539–5549. [CrossRef]
37. Humphreys, J.; Rohrer, G.S.; Rollett, A. Chapter 7—Recrystallization of Single-Phase Alloys. In *Recrystallization and Related Annealing Phenomena*, 3rd ed.; Humphreys, J., Rohrer, G.S., Rollett, A., Eds.; Elsevier: Oxford, UK, 2017; pp. 245–304. ISBN 978-0-08-098235-9.
38. Mecking, H.; Kocks, U.F. Kinetics of Flow and Strain-Hardening. *Acta Metall.* **1981**, *29*, 1865–1875. [CrossRef]
39. Hatta, N.; Kokado, J.; Kikuchi, S.; Takuda, H. Modelling on Flow Stress of Plain Carbon Steel at Elevated Temperatures. *Steel Res.* **1985**, *56*, 575–582. [CrossRef]
40. Yoshie, A.; Fujita, T.; Fujioka, M.; Okamoto, K.; Morikawa, H. Formulation of the Decrease in Dislocation Density of Deformed Austenite Due to Static Recovery and Recrystallization. *ISIJ Int.* **1996**, *36*, 474–480. [CrossRef]
41. Barnoush, A.; Asgari, M.; Johnsen, R. Resolving the Hydrogen Effect on Dislocation Nucleation and Mobility by Electrochemical Nanoindentation. *Scr. Mater.* **2012**, *66*, 414–417. [CrossRef]

42. Ivasishin, O.M.; Shevchenko, S.V.; Vasiliev, N.L.; Semiatin, S.L. A 3-D Monte-Carlo (Potts) Model for Recrystallization and Grain Growth in Polycrystalline Materials. *Mater. Sci. Eng. A* **2006**, *433*, 216–232. [CrossRef]
43. Ding, R.; Guo, Z.X. Coupled Quantitative Simulation of Microstructural Evolution and Plastic Flow during Dynamic Recrystallization. *Acta Mater.* **2001**, *49*, 3163–3175. [CrossRef]
44. Chen, F.; Qi, K.; Cui, Z.; Lai, X. Modeling the Dynamic Recrystallization in Austenitic Stainless Steel Using Cellular Automaton Method. *Comput. Mater. Sci.* **2014**, *83*, 331–340. [CrossRef]
45. Fan, X.G.; Yang, H.; Sun, Z.C.; Zhang, D.W. Quantitative Analysis of Dynamic Recrystallization Behavior Using a Grain Boundary Evolution Based Kinetic Model. *Mater. Sci. Eng. A* **2010**, *527*, 5368–5377. [CrossRef]
46. Roberts, W.; Ahlblom, B. A Nucleation Criterion for Dynamic Recrystallization during Hot Working. *Acta Metall.* **1978**, *26*, 801–813. [CrossRef]
47. Takeuchi, S.; Argon, A.S. Steady-State Creep of Single-Phase Crystalline Matter at High Temperature. *J. Mater. Sci.* **1976**, *11*, 1542–1566. [CrossRef]
48. Davies, C.H.J. Growth of Nuclei in a Cellular Automaton Simulation of Recrystallisation. *Scr. Mater.* **1997**, *36*, 35–40. [CrossRef]
49. Kugler, G.; Turk, R. Modeling the Dynamic Recrystallization under Multi-Stage Hot Deformation. *Acta Mater.* **2004**, *52*, 4659–4668. [CrossRef]
50. Song, X.; Rettenmayr, M. Modelling Study on Recrystallization, Recovery and Their Temperature Dependence in Inhomogeneously Deformed Materials. *Mater. Sci. Eng. A* **2002**, *332*, 153–160. [CrossRef]
51. Zhang, J.; Zheng, C.-W.; Li, D.-Z. A Multi-Phase Field Model for Static Recrystallization of Hot Deformed Austenite in a C-Mn Steel. *Acta Metall. Sin. Engl. Lett.* **2018**, *31*, 208–215. [CrossRef]
52. Kremeyer, K. Cellular Automata Investigations of Binary Solidification. *J. Comput. Phys.* **1998**, *142*, 243–263. [CrossRef]
53. Umemoto, M.; Guo, Z.H.; Tamra, I. Effect of Cooling Rate on Grain Size of Ferrite in Carbon Steel. *Mater. Sci. Technol.* **1987**, *3*, 249–255. [CrossRef]
54. Offerman, S.E.; van Dijk, N.H.; Sietsma, J.; Grigull, S.; Lauridsen, E.M.; Margulies, L.; Poulsen, H.F.; Rekveldt, M.T.; van der Zwaag, S. Grain Nucleation and Growth During Phase Transformations. *Science* **2002**, *298*, 1003–1005. [CrossRef] [PubMed]
55. Krielaart, G.P.; Van Der Zwaag, S. Kinetics of $\gamma \rightarrow \alpha$ Phase Transformation in Fe-Mn Alloys Containing Low Manganese. *Mater. Sci. Technol.* **1998**, *14*, 10–18. [CrossRef]
56. Fazeli, F.; Militzer, M. Application of Solute Drag Theory to Model Ferrite Formation in Multiphase Steels. *Metall. Mater. Trans. A* **2005**, *36*, 1395–1405. [CrossRef]
57. Zhu, B.; Militzer, M. Phase-Field Modeling for Intercritical Annealing of a Dual-Phase Steel. *Metall. Mater. Trans. A* **2015**, *46*, 1073–1084. [CrossRef]
58. Militzer, M.; Mecozzi, M.; Sietsma, J.; Van Der Zwaag, S. Three-Dimensional Phase Field Modelling of the Austenite-to-Ferrite Transformation. *Acta Mater.* **2006**, *54*, 3961–3972. [CrossRef]
59. Li, Z.; Xu, Y.; Wu, D.; Zhao, X.; Wang, G. Investigation on recrystallization and dislocation densityin high temperature deformed of C-Mn steel. *Res. Iron Steel* **2004**, *32*, 35–38. [CrossRef]
60. Sun, W.P.; Hawbolt, E.B. Comparison between Static and Metadynamic Recrystallization—An Application to the Hot Rolling of Steels. *ISIJ Int.* **1997**, *37*, 1000–1009. [CrossRef]
61. Wang, Z.; Sun, S.; Wang, B.; Shi, Z.; Zhang, R.; Fu, W. Effect of Grain Size on Dynamic Recrystallization and Hot-Ductility Behaviors in High-Nitrogen CrMn Austenitic Stainless Steel. *Metall. Mater. Trans. A* **2014**, *45*, 3631–3639. [CrossRef]
62. Dehghan-Manshadi, A.; Hodgson, P.D. Dependency of Recrystallization Mechanism to the Initial Grain Size. *Metall. Mater. Trans. A* **2008**, *39*, 2830. [CrossRef]

materials

MDPI

Article

Shaping Microstructure and Mechanical Properties of High-Carbon Bainitic Steel in Hot-Rolling and Long-Term Low-Temperature Annealing

Tomasz Dembiczak [1,*] and Marcin Knapiński [2]

[1] Faculty of Science and Technology, Jan Dlugosz University in Czestochowa, 13/15 Armii Krajowej Street, 42-200 Czestochowa, Poland
[2] Faculty of Production Engineering and Materials Technology, Czestochowa University of Technology, 19 Armii Krajowej Street, 42-201 Czestochowa, Poland; marcin.knapinski@pcz.pl
* Correspondence: t.dembiczak@ujd.edu.pl

Abstract: Based on the research results, coefficients in constitutive equations, describing the kinetics of dynamic, meta-dynamic, and static recrystallization in high-carbon bainitic steel during hot deformation were determined. The developed mathematical model takes into account the dependence of the changing kinetics in the structural size of the preliminary austenite grains, the value of strain, strain rate, temperature, and time. Physical simulations were carried out on rectangular specimens. Compression tests with a flat state of deformation were carried out using a Gleeble 3800. Based on dilatometric studies, coefficients were determined in constitutive equations, describing the grain growth of the austenite of high-carbon bainite steel under isothermal annealing conditions. The aim of the research was to verify the developed mathematical models in semi-industrial conditions during the hot-rolling process of high-carbon bainite steel. Analysis of the semi-industrial studies of the hot-rolling and long-term annealing process confirmed the correctness of the predicted mathematical models describing the microstructure evolution.

Keywords: high-carbon bainitic steel; dynamic and post-dynamic softening; hot-rolling; final microstructure and mechanical properties

Citation: Dembiczak, T.; Knapiński, M. Shaping Microstructure and Mechanical Properties of High-Carbon Bainitic Steel in Hot-Rolling and Long-Term Low-Temperature Annealing. *Materials* **2021**, *14*, 384. https://doi.org/10.3390/ma14020384

Received: 3 December 2020
Accepted: 11 January 2021
Published: 14 January 2021

1. Introduction

The dynamic development of modern technologies of the plastic processing of metals is aimed at, in addition to giving the products the required shape, obtaining the most favorable material structure that has a significant impact on the mechanical properties of the product. Knowledge of the phenomena occurring during the plastic deformation of metal at high temperature, both in the deformation gap and outside it, allows the structural changes taking place in the processed material to be controlled. The modeling of thermoplastic processing processes is currently one of the most effective research methods used in the optimization of the technological parameters of these processes. The most important advantage of this method is that a quantitative description of the physical phenomena is obtained, the course of which, during plastic processing, shapes the final microstructure and mechanical properties of steel products. It also enables analysis of the influence of the evolution of austenite grains in the metal forming phase at high temperature on the dynamics of their decomposition during cooling and the obtained microstructure of the product after cooling to ambient temperature. Currently, the development and application of new materials and technologies requires a rapid transition from calculating the theoretical results and research on a laboratory scale to industrial implementation. Industrial research is the last, but usually very expensive, element of the implementation process. These costs can be reduced substantially, and the process itself can be significantly simplified and accelerated using modern methods of mathematical and physical modeling.

There are many works on mathematical and physical modeling available in the scientific literature, examples may be works [1–10].

The main objective of the research, the results of which are presented in the paper, was to comprehensively develop numerical models of dynamic, meta-dynamic, and static recrystallization phenomena occurring in alloy austenite during hot plastic working. High-carbon bainitic steel, for which the final mechanical properties are obtained by long-term low-temperature isothermal annealing, was tested. The product shaping process takes place at high temperatures, most often by rolling flat products. For the correct design of such a process, and in particular to determine the morphology of austenite after rolling, an important element is the knowledge of the kinetics of the recovery processes of the hot-deformed microstructure. The paper presents proprietary models of dynamic, meta-dynamic, and static recrystallization kinetics of alloy austenite under the conditions of hot plastic working. Changes in austenite grain size related to recrystallization processes as well as the kinetics of its isothermal growth were also determined. The numerical models developed on a laboratory scale using the Gleeble system were verified in rolling conditions with the use of a semi-industrial technological line for sheet rolling (LPS). The presented original research results are an added value to the current state of knowledge in publications on the numerical models of the kinetics of the alloy austenite recrystallization processes. The given numerical values of the equation coefficients enable other scientists or engineers to model the recrystallization processes of the tested steel. They supplement the database, which has been created for many years, on the quantitative assessment of recrystallization phenomena occurring during hot plastic working.

The final mechanical properties of high-carbon bainitic steel are obtained by long-term low-temperature isothermal annealing. During this process, carbide-free bainite is formed in the microstructure in the form of strips with a thickness of 20–100 nanometers, which, together with the residual austenite showing the TRIP effect, ensures very high strength with good plasticity of the product. Work on the understanding of the phenomena related to obtaining particularly high mechanical properties in steels of this type developed in the first decade of the 21st century [11–14], but the available literature does not contain much information on this subject, probably due to the potential use of this material for military purposes. The paper also presents the results of tests of selected mechanical properties of heavy plates from the analyzed steel rolled in various conditions after low-temperature annealing for 70 h.

2. Materials and Methods

2.1. Material Descriptions

The material used for the study was high-carbon bainitic steel developed in the Łukasiewicz Research Network—Institute of Iron Metallurgy in Gliwice [11], using the results of basic research on bainitic transformation and bainite structure [12–17]. The new generation bainitic steel is an alloy steel containing, depending on the intended use, 0.5 to 0.85% C, additions of Si, Mn, Co, Mo, Cr, and micro-additives of other elements. The use of this composition allows very high hardness in the range of 600–700 HV and high strength up to 2.5 GPa to be obtained, while maintaining good plastic properties. The special feature of this steel is its high impact resistance, which is why its main application may be ballistic shields. The use of ballistic shields made of high-carbon bainitic steel makes it possible to reduce the weight of the shields, leading to material and energy savings. Newly developed steel, in addition to applications in the defense industry, can also be used as a construction material, impact and abrasion resistant layers in coal and rock mining, as well as protection against explosion and rock impact. High-carbon bainitic steel is a new material, not yet produced in Poland on an industrial scale. In Great Britain, industrial trials with steels in this class have been successfully completed. The introduction of a new generation bainitic steel for industrial production in Poland is planned in the coming years. Table 1 presents the chemical composition of high-carbon bainitic steel (Łukasiewicz Research Network—Institute of Iron Metallurgy in Gliwice), which was the basic research material.

Table 1. Chemical composition of high-carbon bainitic steel used in tests, mass%.

C	Mn	Si	P	S	Cr	Ni	Mo
0.83	2.20	1.65	0.009	0.014	0.016	0.02	0.39
Co	V	Ti	Al max.	Al. metal.	Cu	N	O
1.58	0.092	0.002	0.039	0.038	0.018	0.0040	0.0009

2.2. Plastic Flow Curves

Plastic flow curves for the studied steel were determined for the following temperatures: 900, 950, 1000, 1050 and 1100 °C, strain rate: 0.1; 1 and 10 s^{-1} and true strain 0–1. To determine the plastic flow curves of the steel, plastometric tests were carried out using a Gleeble 3800 physical metallurgical processes simulator with a Hydrawedge II module. For the plastometric tests, rectangular samples with dimensions in millimeters of 10 × 15 × 20 were used. The plastic flow curves were determined in compression tests with a flat deformation state, reflecting the conditions of the hot-rolling process.

2.3. Methodology for Developing Constitutive Equations Describing Kinetics of Dynamic Recrystallization

The phenomenon of dynamic recrystallization occurring in the microstructure during the hot deformation of steel was analyzed in two stages in the temperature range of 900–1100 °C and at the strain rate of 0.1–10 s^{-1}. In the first stage, based on the developed plastic flow curves, considering the temperature correction and strain rate, the deformation parameters necessary to initiate the phenomenon of dynamic recrystallization were determined. The dependence of the coefficient strengthening intensity θ as a function of stress was determined, describing the behavior of the material during hot plastic deformation [18].

In the second stage of the mathematical modeling of dynamic recrystallization phenomena, the coefficients found in constitutive equations ε_p, ε_{kr}, $\varepsilon_{0.5}$ and d_{DRX} were determined, considering the influence of the temperature, strain rate described by the Zener–Hollomon (Z) parameter and the initial austenite grain size.

2.4. Methodology for Developing Constitutive Equations Describing Kinetics of Meta-Dynamic Recrystallization

The kinetics of meta-dynamic recrystallization were analyzed using the stress relaxation method. This method involves performing a single plastic deformation, after which the sample is held between anvils with the real-time recording of the decrease in force. After plastic deformation, during which dynamic recrystallization was initiated, the material undergoes a process of meta-dynamic recrystallization, as a result of which the value of internal stress decreases. The advantage of this method is that the full course of the recrystallization kinetics curve is obtained with only one compression test for selected plastic deformation conditions.

Experimental studies aimed at developing the constitutive equations of meta-dynamic recrystallization were carried out for a flat state of strain, using rectangular samples with dimensions in millimeters of 10 × 15 × 20, at temperatures of 900 °C, 1000 °C, 1100 °C, with a given plastic strain determined based on the model of dynamic recrystallization kinetics, and at strain rates of 0.1 s^{-1} and 10 s^{-1}. After deformation, the samples remained under load for 10 s, while recording a decrease in pressure force reflecting stress relaxation in high-carbon bainitic steel. The tests were carried out using the Gleeble 3800 physical simulator. The experimental research was divided into two stages.

In the second stage of mathematical modeling research, the coefficients were determined in the constitutive equation describing the time of meta-dynamic half-recrystallization $t_{0.5MDRX}$ as a function of the strain rate, temperature, and activation energy. The values of the coefficients appearing in the constitutive equation describing the time $t_{0.5MDRX}$ and the material constant were determined by logarithmizing both sides of the equation. Then,

depending on the relationship between ln $t_{0.5MDRX}$ and ln $\dot{\varepsilon}$ and ln $t_{0.5MDRX}$ and ln 1/T, the ascending coefficients were determined in the constitutive equation.

Based on metallographic tests, a constitutive equation of the mathematical model describing the size of meta-dynamically recrystallized grains d_{MDRX} was developed as a function of the Zener–Hollomon parameter. The coefficients appearing in this equation were determined from the relation between ln d_{MDRX} and ln Z.

2.5. Methodology for Developing Constitutive Equations Describing Kinetics of Static Recrystallization

The kinetics analysis of static recrystallization was carried out using the stress relaxation method. The experimental tests were performed for the temperatures of 950 °C and 1050 °C, with given strains of 0.05 and 0.10, and at strain rates of 0.1 s^{-1} and 10 s^{-1}. After deformation, the samples remained under load for 100 s. The tests were carried out using the Gleeble 3800 device and divided into two stages.

In the first stage, the analysis of the kinetics of static crystallization based on the Avrami equation makes it possible to determine the time $t_{0,5SRX}$ needed to recrystallize 50% of the material volume.

In the second stage of the tests coefficients were determined in the constitutive equation describing the time of half-static recrystallization $t_{0.5SRX}$ as a function of: strain, strain rate, initial austenite grain size, and activation energy. The values of the coefficients appearing in the constitutive equation describing time $t_{0.5SRX}$ and the material constant were determined after logarithmizing both sides of the equation. Then, depending on the relationships: ln $t_{0.5SRX}$ from ln ε, ln $t_{0.5SRX}$ from ln $\dot{\varepsilon}$, ln $t_{0.5SRX}$ from ln d_0 and ln $t_{0.5SRX}$ from ln 1/T, ascending coefficients were determined in the constitutive equation. Exponent n_3 appearing in the equation describing the kinetics of static recrystallization was determined from the relation between ln (ln $(1/1 - X)$) and ln t.

Based on metallographic examination, the constitutive equation of the model describing the size of statically recrystallized grains d_{SRX} as a function of the initial austenite grain size, strain, strain rate, and activation energy was developed. The coefficients appearing in this equation were determined from the relation: ln d_{SRX} from ln d_0, ln d_{SRX} from ln ε, ln d_{SRX} from ln $\dot{\varepsilon}$, ln d_{SRX} from ln 1/T.

2.6. Methodology for Developing Constitutive Equations Describing Growth of Alloy Austenite Grains

To develop a constitutive equation describing the growth of the alloy austenite grains, tests were conducted under isothermal heating conditions. The tests consisted of heating the samples to a given temperature, holding them for a specified period of time and rapid cooling leading to freezing of the structure. Then, metallographic tests were performed to determine the size of the austenite grains. The tests were carried out for temperatures of 900 °C, 1000 °C and 1100 °C. The samples were held for 0, 10, 30, 60, 90 min. The tests were carried out on cylindrical samples with dimensions in millimeters ϕ 5 × 10 using a DIL 805 A/D dilatometer. Based on the conducted tests, constitutive equations describing the grain growth of high-carbon bainitic steel under isothermal heating conditions were developed.

2.7. The Process of Rolling High-Carbon Bainitic Steel in Industrial Conditions

The aim of the research on a semi-industrial scale was to verify the mathematical models describing the evolution of the microstructure during the hot-rolling process of high-carbon bainite steel. The tests were carried out for three variants with the end temperatures of rolling: 950, 900 and 850 °C. After rolling, the end section of the strand, approximately 40 cm long, was quenched in a bath filled with water to freeze the structure. The strand at 250 °C was placed in an oven heated to 250 °C and annealed for 70 h for low-temperature heat treatment.

3. Results

Table 2 shows the results of the metallographic examinations under which the primary austenite grain size was defined.

Table 2. Preliminary austenite grain size.

Temperature (°C)	Grain Size (μm)
900	29.1
950	31.7
1000	32.1
1050	89.4
1100	92.8

During analysis of the plastic flow curves, a problem arises from the uncontrolled temperature increase of the sample resulting from strain occurring especially at strain rates higher than 5 s^{-1}. The mathematical description of the plastic flow curves using Equation (1) makes it possible to introduce a temperature correction [19–21]:

$$\sigma_p = f(\varepsilon, \dot{\varepsilon}) e^{\frac{Q}{RnT}} \quad (1)$$

where: ε—stres, $\dot{\varepsilon}$—strain rate Q—activation energy, R—gas constant, T—temperature, n—material constant.

By logarithmizing Equation (1) for the constant strain value and strain rate 0.1; 1 and 10 s^{-1}, a relationship was obtained between the logarithm of the metal flow stress and the reciprocal of the temperature. Based on the performed linear regression for the relationship ln (σ) − 1/T (Figure 1), the activation energy was determined for high-carbon bainitic steel.

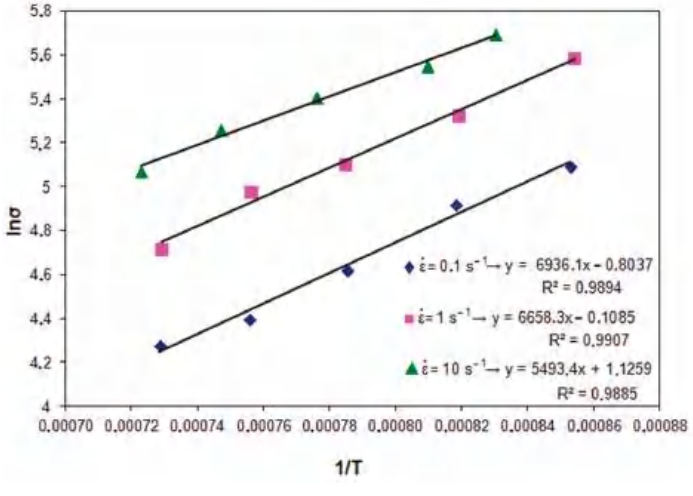

Figure 1. Relationship between yield stress and temperature for different strain rates.

Figure 2 shows the relationship between the activation energy and the strain rate. It was assumed that for the researched steel the dependence of the activation energy on the strain rate is logarithmic [22,23].

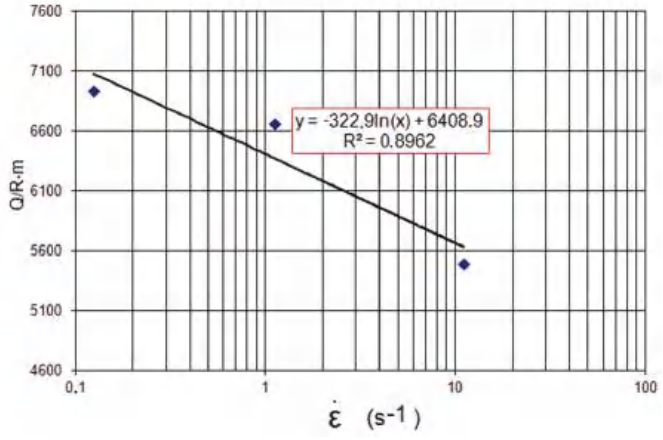

Figure 2. Change in activation energy as a function of strain rate from linear regression equation.

Finally, the following equation was used to describe the influence of the temperature and strain rate:

$$\sigma_p = f(\varepsilon, \dot{\varepsilon}) \dot{\varepsilon}^{\frac{c_1}{T}} e^{\frac{c_2}{T}} \quad (2)$$

where: c_1, c_2—coefficients dependent on the material, experimentally determined

The values of the coefficients ($c_1 = -322.89$, $c_2 = 6408.9$) and function f were determined from the regression equations and the measurement data provided in Figure 2. The coefficients developed in Equation (2) made it possible to correct the metal flow stress for the given deformation value, assumed temperature, and strain rate. An example of the course of an adjusted plastic flow curve of high-carbon bainitic steel is shown in Figure 3.

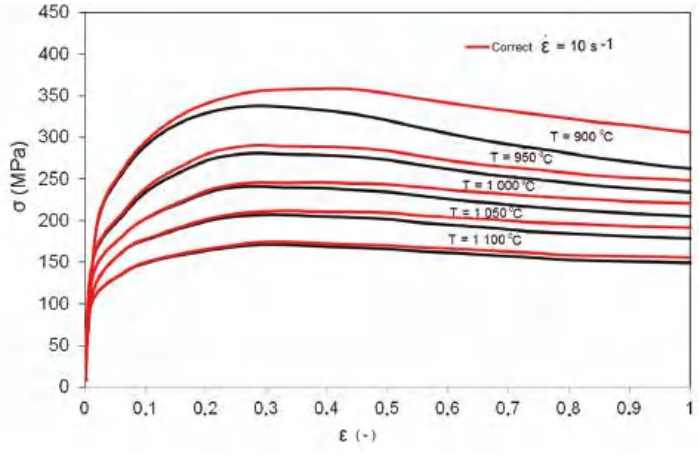

Figure 3. Plastic flow curves of high-carbon bainitic steel at strain rate of 10 s^{-1} at a temperature of 900–1100 °C.

By analyzing the obtained plastic flow curves, it can be concluded that in the examined temperature range and strain rate 10 s^{-1}, dynamic recrystallization in the steel takes place after exceeding the critical deformation value, and following this, the curves fall slightly in the directions of lower stress values, going into a steady state. This phenomenon is the dominant factor in the reconstruction of the structure.

3.1. Dynamic Recrystallization

The developed material coefficients in the mathematical models describing the phenomenon of dynamic recrystallization in high-carbon bainite steel are presented in detail in the authors' research [24].

The determined coefficients in the constitutive equation describing peak strain ε_p for the investigated steel are as follows [18,24–28]:

$$\varepsilon_p = 0.0656 d_0^{-0.2338} Z^{0.0634} \quad (3)$$

Critical strain ε_{kr} and peak strain ε_p are related by the material constant c, the experimental method of determination of which is shown in the work [24], and the mutual dependence of these strains is described by the following equation:

$$c = \frac{\varepsilon_{kr}}{\varepsilon_p} = 0.6220 \quad (4)$$

The value of constant c is an average value quotient of $\varepsilon_{kr}/\varepsilon_p$, determined for temperatures of 900–1100 °C and strain rates 0.1, 1 and 10 s^{-1}. The constitutive equation defining critical strain ε_{kr} was determined based on Equations (3) and (4) and finally has the following forms [24]:

$$\varepsilon_{kr} = 0.0408 d_0^{-0.2338} Z^{0.0634} \quad (5)$$

Finally, for the investigated steel, strain $\varepsilon_{0.5}$ was described by the equation [24]:

$$\varepsilon_{0.5} = 0.1333 d_0^{-0.2434} Z^{0.064} \quad (6)$$

The kinetics of dynamic recrystallization is described as follows [24]:

$$X_{DRX}(t) = 1 - \exp\left[-4.3802\left(\frac{\varepsilon - \varepsilon_{kr}}{\varepsilon_{0.5} - \varepsilon_{kr}}\right)^{2.2394}\right] \quad (7)$$

The equation describing the average size of dynamically recrystallized grains is described in the paper [24] as follows:

$$d_{DRX} = 11{,}111.1 Z^{-0.1535} \quad (8)$$

3.2. Meta-Dynamic Recrystallization

The value of plastic deformation in the experimental tests was selected based on the developed model describing the kinetics of dynamic recrystallization (Equation (7)) for two strain rates 0.1 and 10 s^{-1}. The development of a model describing the kinetics of this recrystallization in high-carbon bainite steel was carried out in two stages.

In the first stage, the change in the steel residual stresses as a function of time from the end of plastic deformation was analyzed using the stress relaxation method. Figure 4 shows examples of the curves of the steel residual stresses changes occurring during tests at temperatures of 900, 1000 and 1100 °C after plastic deformation of 0.28 set at the strain rates of 0.1 and 10 s^{-1}.

To evaluate the phase meta-dynamically recrystallized after time (t), the softening coefficient was used, defined as follows:

$$X_{m_{MDRX}}(t) = \left(\frac{\sigma_{rs} - \sigma_{rt}(t)}{\sigma_{rs} - \sigma_{rf}}\right) \quad (9)$$

where: σ_{rs}—initial stress value on the stress relaxation curve, σ_{rt} (t)—stress value during time relaxation (t), σ_{rf}—final stress value after completion of the relaxation process.

Table 3 shows examples of the calculated values of the softening coefficient of the investigated steel.

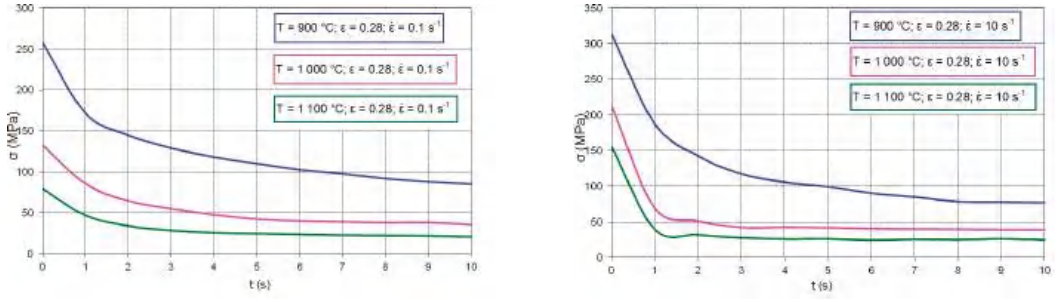

(**a**) (**b**)

Figure 4. Stress relaxation of high-carbon bainitic steel in temperature range 900–1100 °C and plastic deformation 0.28: (**a**) for strain rate 0.1 s^{-1}, (**b**) strain rate 10 s^{-1}.

Table 3. Values of softening coefficient under conditions of meta-dynamic recrystallization.

T (°C)	ε (-)	$\dot{\varepsilon}$ (s^{-1})	t (s)	$X_{m_{MDRX}}$
950	0.28	0.1	1	0.680
			5	0.839
			10	0.916
1000	0.28	0.1	1	0.686
			5	0.951
			10	0.986
1100	0.28	0.1	1	0.894
			5	0.974
			10	0.995

Based on the softening fraction, the kinetics of meta-dynamic recrystallization were developed according to the Avrami equation:

$$X = 1 - e^{(-kt^n)} \quad (10)$$

where: X—fraction of the recrystallized phase, t—time (s), k, n—coefficients for a given material grade determined experimentally

Figure 5 shows the dependencies based on which coefficients (k) and (n) were determined for the temperature of 900 °C, strain 0.28 and strain rate 0.1 s^{-1}.

The determined coefficients in the Avrami equation made it possible to describe the course of meta-dynamic recrystallization of the examined steel as a function of time for the deformation temperatures 900, 1000, 1100 °C and strain rates 0.1 and 10 s^{-1}. Based on the quantitative description of the kinetics of meta-dynamic recrystallization, the time needed for 50% of the material to recrystallize was determined. In the next stage of the research, the determined times of half-recrystallization were used to develop a constitutive equation describing $t_{0.5MDRX}$ as a function of the strain rate and activation energy. Table 4 shows the determined Avrami equation coefficients for the researched steel at temperatures 900, 1000, 1100 °C, strain 0.28 and strain rate 0.1 s^{-1}.

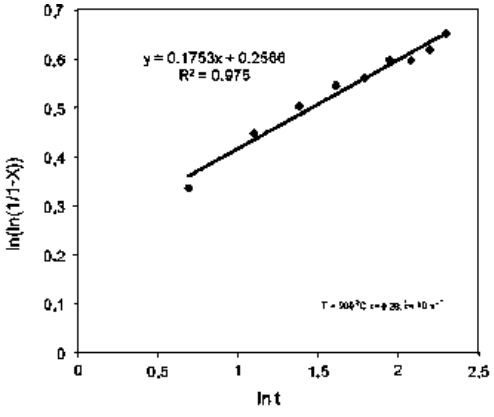

Figure 5. Dependence of ln (ln (1/1 − X)) on ln t for T = 900 °C; ε = 0.28; $\dot{\varepsilon}$ = 0.1 s^{-1}.

Table 4. Kinetics of meta-dynamic recrystallization based on Avrami equation.

T (°C)	ε (-)	$\dot{\varepsilon}$ (s^{-1})	Avrami Equation
900	0.28	0.1	$X = 1 - \exp(-0.2566t^{0.1753})$
1000	0.28	0.1	$X = 1 - \exp(-0.6850t^{0.803})$
1100	0.28	0.1	$X = 1 - \exp(-1.6706t^{0.4532})$

Figure 6 shows examples of meta-dynamic recrystallization determined based on the Avrami equation for T = 900, 1000, 1100 °C and $\dot{\varepsilon}$ = 0.1 s^{-1}.

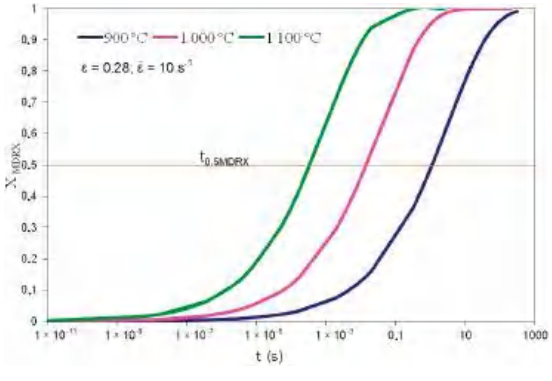

Figure 6. Kinetics of meta-dynamic recrystallization in high-carbon bainite steel based on Avrami equation.

In the second stage of the research, the material constants appearing in the constitutive equation describing the time of half meta-dynamic recrystallization $t_{0.5MDRX}$ in high-carbon bainite steel were determined. Figures 7 and 8 show the dependencies used to determine the coefficients in $t_{0.5MDRX}$.

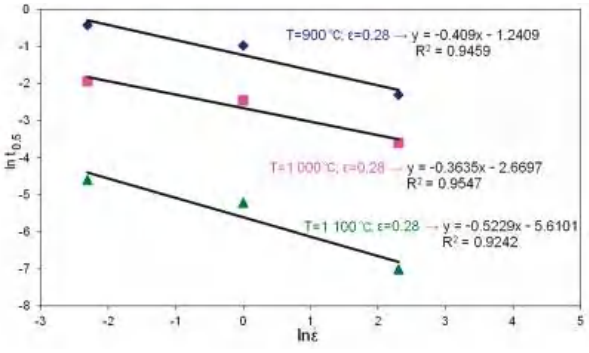

Figure 7. Dependence of half time of meta-dynamic recrystallization (ln $t_{0.5}$) on strain rate (ln $\dot{\varepsilon}$).

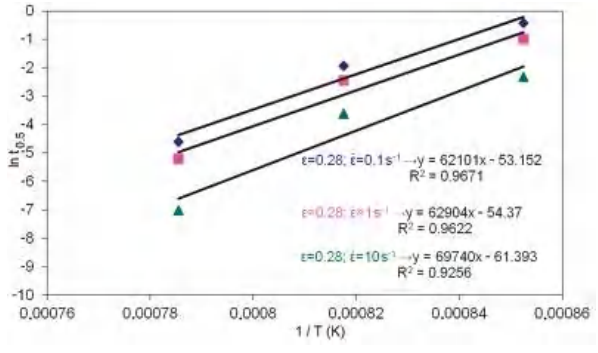

Figure 8. Dependence of half time of meta-dynamic recrystallization (ln $t_{0.5}$) on temperature (1/T).

The time needed to obtain 50% of the meta-dynamically recrystallized phase in high-carbon bainite steel is described as follows:

$$t_{0.5_{MDRX}} = 5.05 \times 10^{-24} \dot{\varepsilon}^{-0.4318} e^{\left(\frac{539703.3}{RT}\right)} \quad (11)$$

The exponent in the equation describing the kinetics of meta-dynamic recrystallization was determined based on the dependence presented in Figure 9.

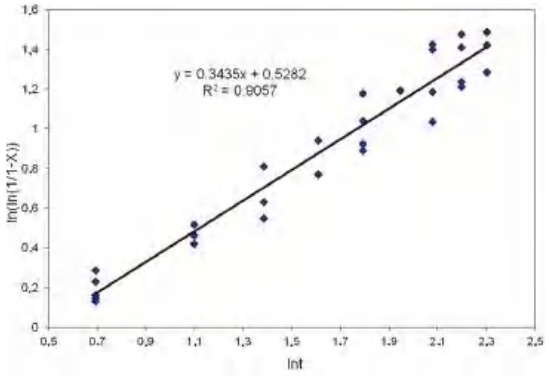

Figure 9. Relationship ln (ln (1/1 − X)) to ln t in range T = 900–1100 °C; ε = 0.28; $\dot{\varepsilon}$ = 0.1–10 s^{-1}.

The conducted research made it possible to determine all the coefficients of Equation (12) describing the amount of meta-dynamically recrystallized phase of material X_{MDRX} depending on the elapsed time (t) and considering the time $t_{0.5MDRX}$ needed to obtain 50% of the meta-dynamically recrystallized phase in material.

$$X_{MDRX} = 1 - \exp\left[-0.6931 \cdot \left(\frac{t}{t_{0.5_{MDRX}}}\right)^{0.3435}\right] \quad (12)$$

Figure 10 shows the kinetics of meta-dynamic recrystallization for high-carbon bainite steel according to the models described in Equations (11) and (12).

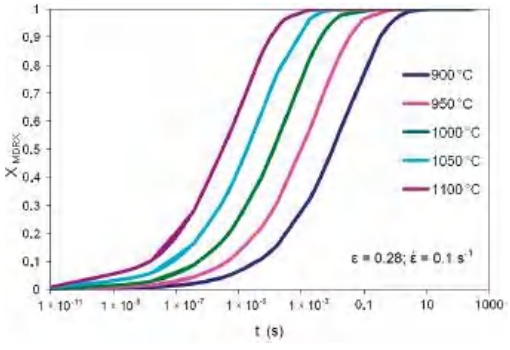

Figure 10. Kinetics of meta-dynamic recrystallization of high-carbon bainitic steel for T = 900–1100 °C, $\dot{\varepsilon} = 0.1\ s^{-1}$.

To determine the material coefficients of the model describing the grain size of meta-dynamically recrystallized austenite, metallographic tests were carried out after the performed experimental tests. Figure 11 shows an example of the microstructure of the meta-dynamically recrystallized alloy austenite grains obtained from the experimental tests carried out. 1.

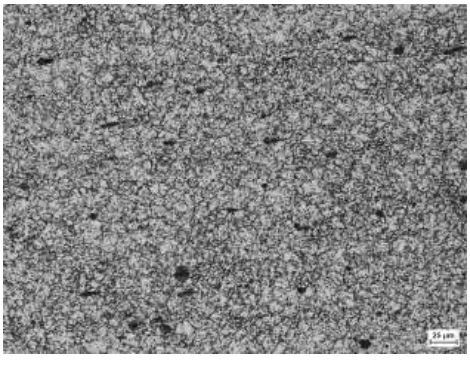

Figure 11. Microstructure of sample after experimental tests for T = 900 °C; $\varepsilon = 0.28$; $\dot{\varepsilon} = 0.1\ s^{-1}$ $d\gamma$ = 23.7 μm; area 200×; etched with picric acid ($C_6H_3N_3O_7$).

Figure 12 shows the dependence based on which the material constants were determined in the model describing the size of the meta-dynamically recrystallized grains in high-carbon bainite steel.

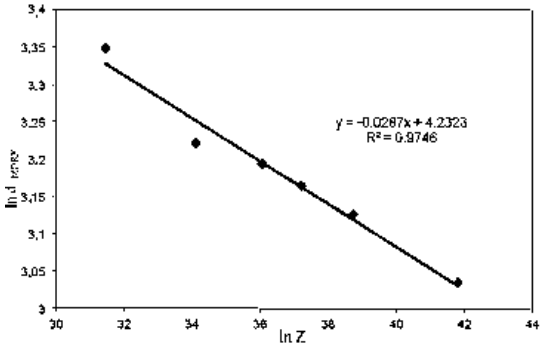

Figure 12. Dependence of meta-dynamically recrystallized austenite grains (ln d_{MDRX}) on Zener–Hollomon parameter (ln Z).

The model describing the size of the meta-dynamically crystallized grains for the studies steel is as follows:

$$d_{MDRX} = 68.875Z^{-0.0287}\ (\mu m) \quad (13)$$

3.3. Static Recrystallization

The value of plastic deformation in the experimental tests was selected based on analysis of the developed model describing the kinetics of the phenomenon of dynamic recrystallization and critical deformation described in the authors' work [24]. Based on these data, it was found that only static recrystallization occurs in the material if it is deformed to a plastic deformation value not greater than 0.1. The development of a model describing the kinetics of static recrystallization in high-carbon bainite steel was carried out in two stages.

In the first stage of the research, an analysis of the change in residual stress as a function of time from the moment of the end of plastic deformation was carried out using the stress relaxation method. Figure 13 show examples of the curves of the steel residual stress changes occurring during the tests at the temperatures of 950 and 1050 °C after plastic deformation of 0.05 and 0.1 at the strain rates of 0.1 and 10 s^{-1}.

To evaluate the amount of statically recrystallized phase after time (t), analysis of the softening degree of the material was used in accordance with Equation (9). Table 5 shows examples of the calculated softening degree of the examined steel for temperatures of 950 and 1050 °C, strain 0.1 and strain rate 10 s^{-1}.

To develop a model of static recrystallization kinetics for the investigated steel, the Avrami equation was used to describe the dependence of the softening fraction as a function of time for individual parameters of the deformation Equation (10). Figure 14 shows the relationship based on which the material coefficients were determined.

Table 5. Obtained results of static recrystallization using the stress relaxation method.

T (°C)	ε (-)	$\dot{\varepsilon}$ (s^{-1})	t (s)	$X_{m_{MDRX}}$
950	0.1	10	1	0.884
			10	0.948
			50	0.951
			100	0.979
1050	0.1	10	1	0.912
			10	0.966
			50	0.979
			100	0.994

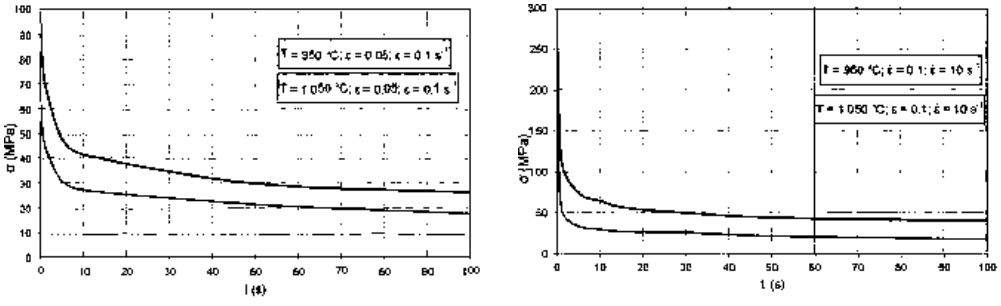

(**a**) (**b**)

Figure 13. Stress relaxation of high-carbon bainite steel for temperature 950 and 1050 °C: (**a**) $\varepsilon = 0.05$; $\dot{\varepsilon} = 0.1\ s^{-1}$, (**b**) $\varepsilon = 0.15$; $\dot{\varepsilon} = 10\ s^{-1}$.

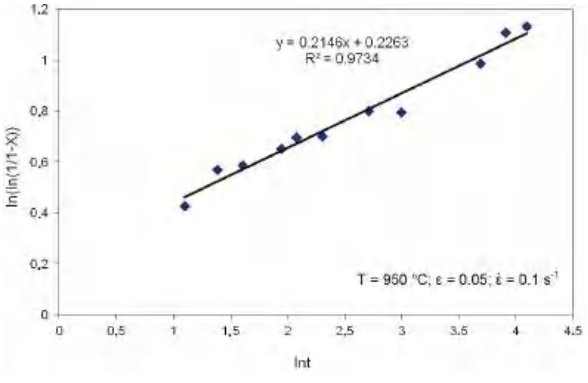

Figure 14. Dependence of ln (ln (1/1 − X)) on ln t for T = 950 °C; $\varepsilon = 0.05$; $\dot{\varepsilon} = 0.1 s^{-1}$.

For all the deformation values, strain rates and temperatures analyzed at this stage, the values of the coefficients of Equation (10) were determined in accordance with the methodology shown in Figure 14. Table 6 presents exemplary equations with the determined coefficients that describe the change in the proportion of the statically recrystallized phase X in the material with the passage of time (t).

Table 6. Kinetics of static recrystallization based on Avrami equation.

T (°C)	ε (-)	$\dot{\varepsilon}$ (s^{-1})	Avrami Equation
950	0.1	10	$X = 1 - \exp(-2.0456t^{0.1451})$
1050	0.1	10	$X = 1 - \exp(-2.4133t^{0.2138})$

Figure 15 shows the course of static recrystallization based on the Avrami equation for the temperature of 950 °C, strain 0.05 and strain rate 0.1 s^{-1}.

The description of the relationship between the amount of statically recrystallized phase and time by means of equations made it possible to precisely determine the half times of static recrystallization for the given parameters of plastic deformation.

In the second step, the coefficients were determined in the model describing $t_{0.5SRX}$ as a function of the strain, strain rate, temperature, and initial grain size. Figure 16 shows the dependencies used to determine the coefficients in the model describing $t_{0.5SRX}$ in high-carbon bainite steel.

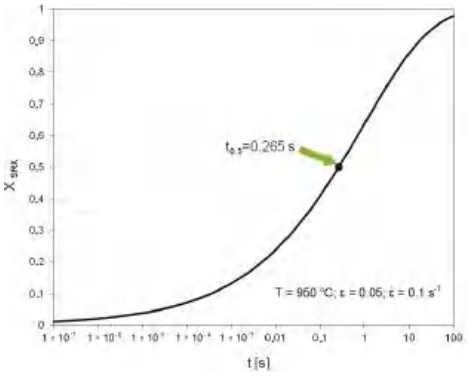

Figure 15. Kinetics of static recrystallization in high-carbon bainitic steel based on Avrami equation.

The time needed to obtain 50% of the static recrystallized phase in high-carbon bainite steel is described as follows:

for $T \leq 1000$ °C

$$t_{0.5_{SRX}} = 6.2828 \times 10^{-25} \varepsilon^{-1.9188} \dot{\varepsilon}^{-0.7344} d_0^{1.9256} e^{\left(\frac{419690.7}{RT}\right)} \quad (14)$$

for $T > 1000$ °C

$$t_{0.5_{SRX}} = 3.0514 \times 10^{-21} \varepsilon^{-1.6558} \dot{\varepsilon}^{-0.62355} d_0^{1.9256} e^{\left(\frac{318023}{RT}\right)} \quad (15)$$

The exponent in the model describing the kinetics of static recrystallization was determined from the relationship presented in Figure 17.

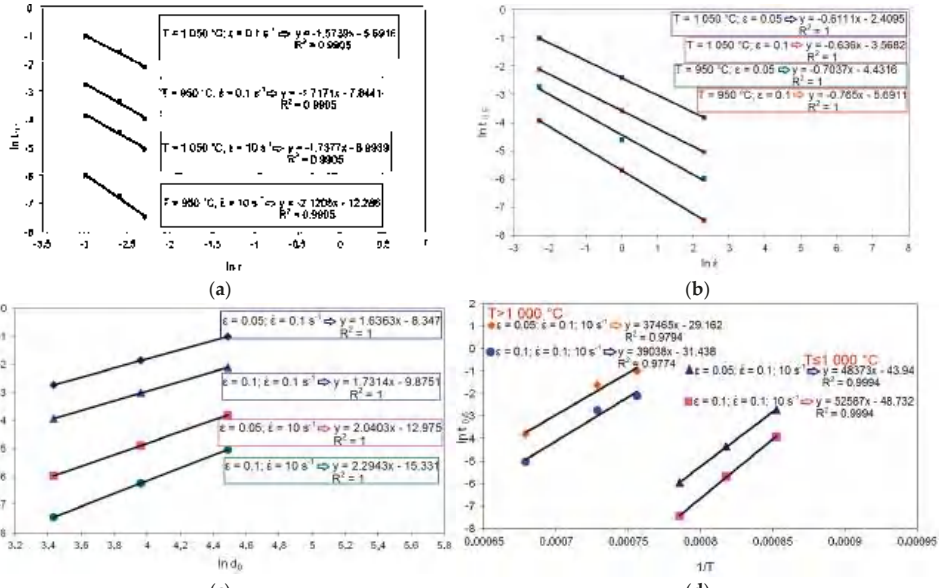

Figure 16. Dependence of half time of static recrystallization (ln $t_{0.5}$) on: (**a**) ln ε, (**b**) ln $\dot{\varepsilon}$, (**c**) ln d_0, (**d**) 1/T.

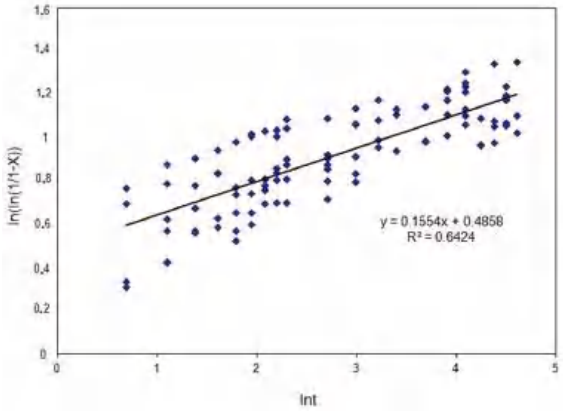

Figure 17. Dependence of ln (ln1/1 − X)) on time (ln t) in range T = 950–1050 °C; ε = 0.05 and 0.1; $\dot{\varepsilon}$ = 0.1 and 10 s^{-1}, according to which exponent in model describing kinetics of static recrystallization was determined.

The mathematical model describing the kinetics of static recrystallization in high-carbon bainite steel is as follows:

$$X_{SRX} = 1 - \exp\left[-0.6931 \cdot \left(\frac{t}{t_{0.5_{SRX}}}\right)^{0.1554}\right] \quad (16)$$

Figure 18 shows an example of the kinetics of static recrystallization based on the developed model for high-carbon bainitic steel for the temperature range 900–100 °C, strain rate 10 s^{-1} and strain 0.1.

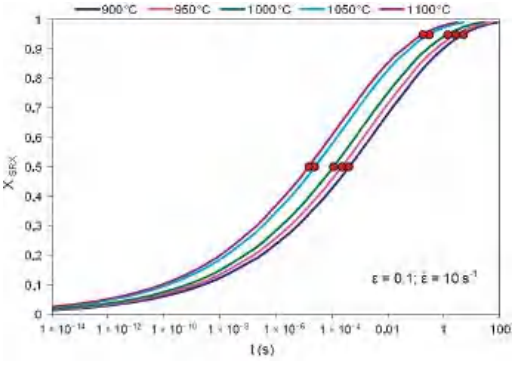

Figure 18. Example of kinetics of static recrystallization in high-carbon bainitic steel based on the developed coefficients in mathematical model.

To determine the material coefficients of the model describing the grain size of static recrystallized austenite, metallographic tests were carried out after the performed experimental tests. Figure 19 shows an example of the microstructure of static recrystallized alloy austenite grains obtained from the conducted experimental tests.

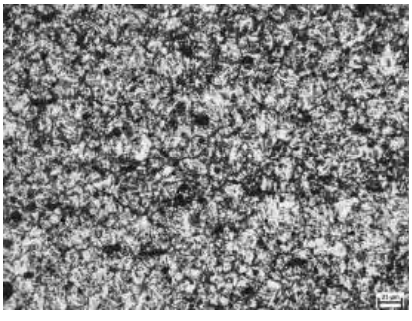

Figure 19. Microstructure of samples after experimental testing for T = 950 °C; ε = 0.1; $\dot{\varepsilon}$ = 10 s^{-1}; dγ = 27.2 μm; area 75×; etched with picric acid ($C_6H_3N_3O_7$).

The mathematical model describing the size of the statically recrystallized grains was developed based on the relationships shown in Figure 20.

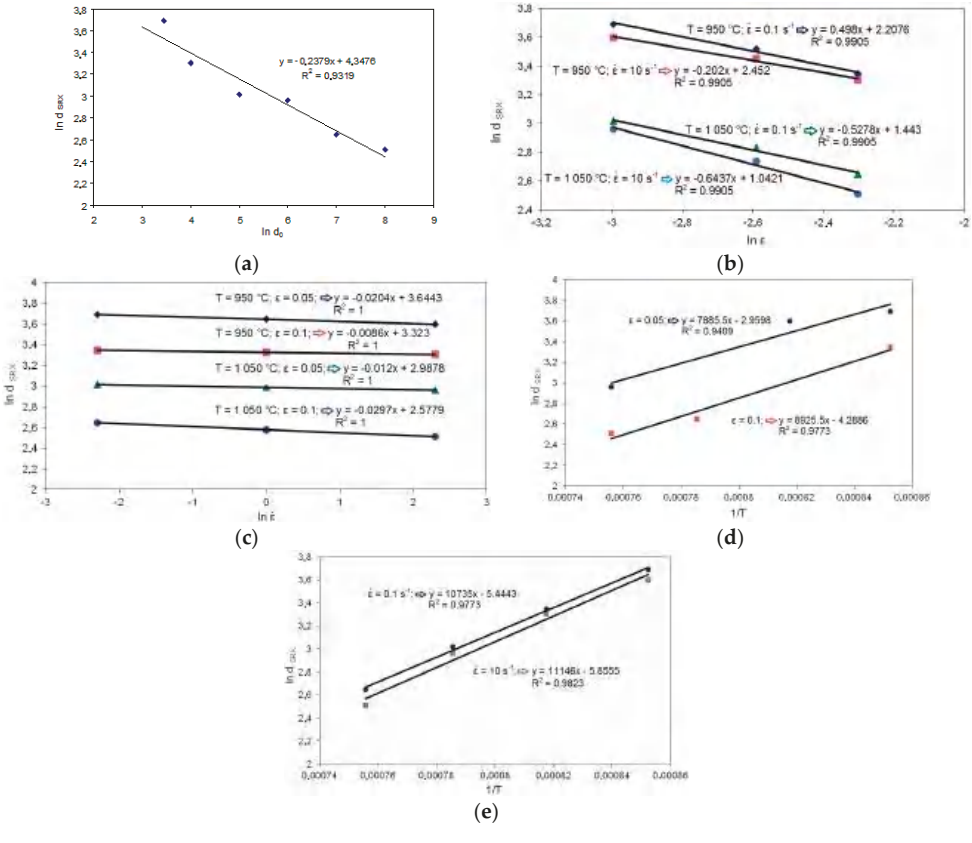

Figure 20. Dependence of statically recrystallized austenite grains ($\ln_{dSRX}$) on: (**a**) $\ln d_0$; (**b**) $\ln \varepsilon$; (**c**) $\ln \dot{\varepsilon}$; (**d**) 1/T for different values of strain, (**e**) 1/T for different values of strain rate.

Based on the relations presented in Figure 20, the coefficients of the model describing the size of the statically recrystallized grains were determined. The model for high-carbon bainite steel is as follows:

$$d_{SRX} = 7.362 \times 10^{-3} d_0^{-0.2379} \varepsilon^{-0.5224} \dot{\varepsilon}^{-0.0177} e^{\left(\frac{80421.32}{RT}\right)} \ (\mu m) \quad (17)$$

3.4. Isothermal Growth of Alloy Austenite Grains

During the rolling process, deformed and recrystallized austenite grains grow in the gaps between deformations. The research was carried out to develop a model describing grain growth during isothermal annealing. Figure 21 shows sample metallographic photos of samples from the conducted experimental tests.

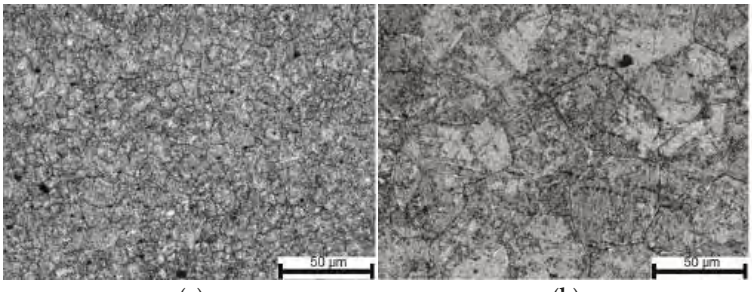

(**a**) (**b**)

Figure 21. Size of austenite grains after growing at T = 1100 °C: (**a**) after 0 s, d_0 = 59.7 µm; (**b**) after 3600 s, d_0 = 98.1 µm; area 100×; etched with picric acid ($C_6H_3N_3O_7$).

Based on the measured austenite grain sizes, the growth kinetics are described by the following equation:

$$d(t)^{14.66} = d_{rx}^{14.66} + \left(7.79 \times 10^{17}\right) \cdot t \cdot e^{\left(\frac{45279.96}{RT}\right)} \ (\mu m) \quad (18)$$

3.5. The Process of Rolling High-Carbon Bainitic Steel in Industrial Conditions

The hot-rolling process on a semi-industrial scale was carried out in the LPS rolling line located in the laboratory of the Department of Manufacturing Technology and Application of Products in the Łukasiewicz Research Network—Institute of Iron Metallurgy in Gliwice [10,29]. The rolling process was carried out for three variants: variant A with the finish rolling temperature of 950 °C to obtain full recrystallization in the rolled strip, variant B with the finish rolling temperature of 900 °C in order to obtain partial recrystallization in the rolled strip, variant C with the finish rolling temperature of 850 °C in order to achieve no recrystallization in the rolled strip. Figure 22 presents metallographic photos showing the disclosed size of the alloy austenite grains in the samples from the rolling process according to variants A, B, and C.

Figure 23 displays the course of changes in the average austenite grain size on the time axis during the experimental tests. To analyze the evolution of the alloy austenite, the average values of plastic strain, strain rate, and temperatures were used in the calculations. The course of changes in the austenite grain size was obtained from the implemented models of dynamic, meta-dynamic, and isothermal recrystallization of the grains. Due to the small amount of material intended for actual rolling, it was only possible to compare the amount of recrystallized phase in the steel and the austenite grain size after freezing the structure for 8 s after the completion of rolling. The grain size of the alloy austenite present in the ingot discharged from the rolling furnace was calculated based on earlier research on grain growth and the isothermal grain growth model. It was calculated that after about 50 min. of heating, the grain size is about 102 µm. Moreover, during transport from the furnace to the rolling stand, it undergoes very slight growth, reaching a value

of about 104 μm. The deformation set at the temperature of 1040 °C activates dynamic and then meta-dynamic recrystallization of the steel. The effect of these phenomena is a reduction in the average austenite grain size to about 25 μm.

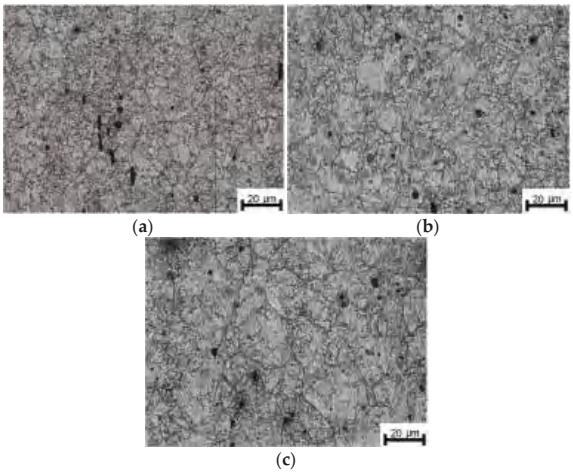

(**a**) (**b**)

(**c**)

Figure 22. Average grain size: (**a**) variant A: T = 950 °C; dγ. = 26.3 μm, (**b**) variant B: T = 900 °C; dγ. = 28.2 μm; (**c**) variant C: T = 850 °C; dγ. = 29.8 μm. Area 200×; etched with picric acid ($C_6H_3N_3O_7$).

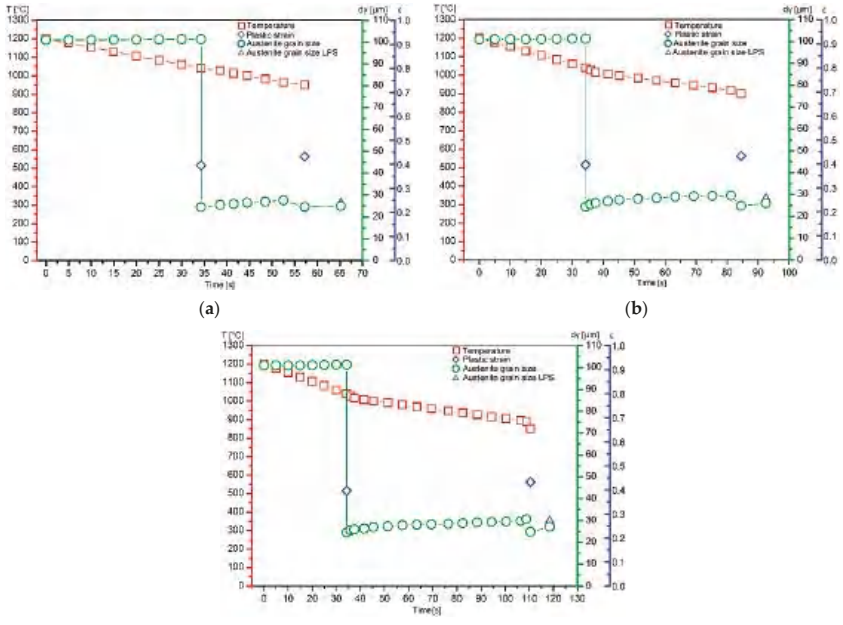

(**a**) (**b**)

(**c**)

Figure 23. Course of changes in grain size of alloy austenite under conditions of two plastic strains: (**a**) finish rolling temperature of 950 °C, (**b**) finish rolling temperature of 900 °C, (**c**) finish rolling temperature of 850 °C.

In the break between the deformations, which for individual rolling variants is from 18 to 71 s, the grain size increases slightly in the steel. On the other hand, the task of the second deformation causes the activation of recrystallization processes of varying intensity, which in turn leads to obtaining structures of various grain sizes in the steel (Figure 22), while the average austenite grain size in all the studied rolling conditions is similar and amounts to about 28 μm. The grain sizes measured based on the analysis of the metallographic specimens reveal very small differences for the individual variants. It should also be added that considering the difficulties in defining the boundaries of the primary austenite grain and the accuracy of the adopted methods of quantitative analysis of the microstructure, the measurement error should be at the level of about 10%. Comparing the results of measurements of the austenite grain size obtained based on experimental tests and mathematical modeling, it can be concluded that the coefficients appearing in the models describing the size of dynamically and meta-dynamically recrystallized grains were correctly developed. Figure 24 shows the verification of the developed model describing the kinetics of meta-dynamic recrystallization with the results obtained based on experimental tests. Based on quantitative metallography, the percentage of the recrystallized phase of the research samples was determined.

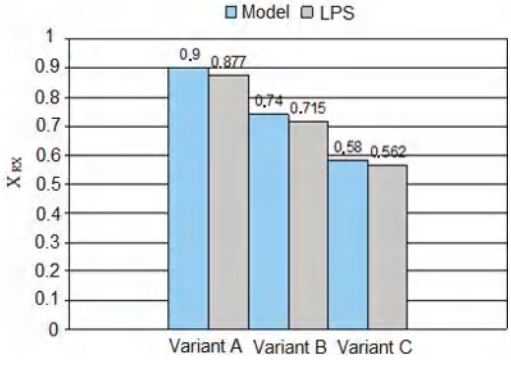

Figure 24. Verification of developed model of microstructure evolution of high-carbon bainitic steel based on experimental tests carried out on semi-industrial LPS rolling line.

The performed quantitative metallographic analysis of the samples taken from the rolled strands after freezing the structure showed that in the considered variants of the rolling process, different austenite recrystallization occurred. This is the effect of the temperature values adopted in the third pass, at which the plastic deformations were applied. For full verification of the results obtained from numerical models, it would be advisable to conduct more experiments using the LPS line. Unfortunately, it turned out to be impossible due to the lack of rolling material and the high costs of re-melting the rolled sheets and subsequent rolling trials. Nonetheless, for the assumed experimental conditions, the compliance of the amount of recrystallized phase in the steel predicted by the developed numerical models and the final austenite grain size were confirmed.

3.6. Study of Mechanical Properties after Heat Treatment

Tests of the mechanical properties were carried out after the rolling process to determine whether the refinement of the alloy austenite obtained by recrystallization during hot-rolling has an impact on the mechanical properties of the sheets after heat treatment. Figure 25 presents metallographic photos, based on which the structure of the material was identified after low-temperature heat treatment.

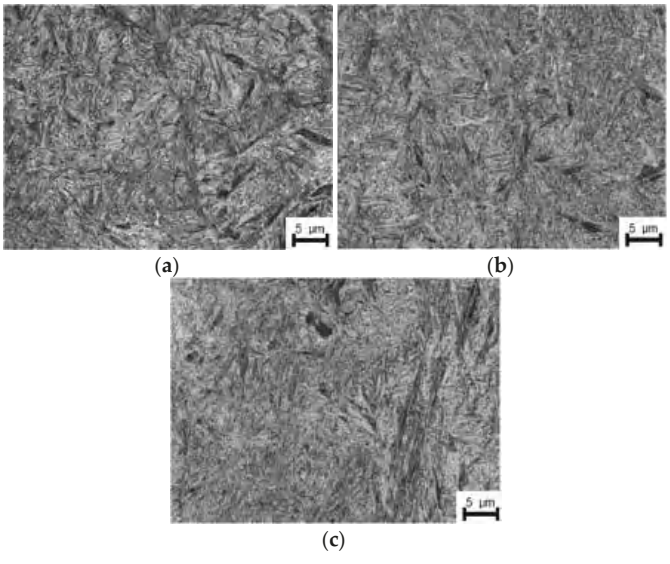

Figure 25. Martensitic-bainitic structure after low-temperature heat treatment at 250 °C for 70 h, area 750×: (**a**) variant A, (**b**) variant B, (**c**) variant C.

Tables 7 and 8 show the results of the measurements of Vickers hardness (HV) and tensile strength (TS) after the heat treatment of high-carbon bainitic steel.

Table 7. Average values of Vickers hardness.

Variant	Average Measurement Results	Standard Deviation
A	681 HV10	27.6
B	680 HV10	17.2
C	706 HV10	16.8

Table 8. The mean values of the tensile strength.

Variant	Average Measurement Results	
	TS (MPa)	A_5 (%)
A	1892	1.7
B	1752	2.6
C	1668	2.2

The research results presented above indicate that the mechanical properties of the sheets after heat treatment that most depend on the applied rolling scheme, and thus the level of the austenite structure refinement, are the TS and elongation. The maximum TS values were obtained for the sheets at the end of the rolling process at the temperature of 950 °C. The smallest elongation was also noted for these conditions. Nevertheless, taking into account the results of plasticity tests, it can be concluded that 900 °C is the most favorable end temperature of rolling among the one studied. For the sheet rolled in this way, the most favorable plastic parameters were obtained.

4. Conclusions

The following conclusions were drawn from the conducted research.

Based on the results of the conducted experimental studies, the coefficients and material constants appearing in the constitutive equations describing the phenomena occurring

during hot plastic deformation were developed. Thus, a mathematical description of the kinetics of the dynamic, meta-dynamic, static, and isothermal growth of austenite grains was made. The coefficients and material constants appearing in the equations describing the size of the dynamically, meta-dynamically, and statically recrystallized grains were developed.

The investigated steel undergoes dynamic recrystallization quite quickly with the increase in plastic strain. The value of the critical deformation ε_{kr} at the deformation speed of 0.1 s^{-1} ranges from 0.11 to 0.20 at temperatures from 1100 to 900 °C.

In the examined steel, it was observed that at the temperatures of 950, 1000, 1050, and 1100 °C in the deformation rate range of $0.1 \div 10$ s^{-1}, full meta-dynamic recrystallization takes place after times shorter than 10 s. However, for temperatures above 1000 °C, the time after which the full volume of the material recrystallizes can only be estimated based on the model forecast.

Static recrystallization processes are slower than meta-dynamic recrystallization. The times of half-static recrystallization after deformation in the range of 0.05–0.10 at the rate of deformation of 1 s^{-1} are: 1.38×10^{-4}–0.63 s for temperatures in the range of 1100–900 °C. Due to the relatively low values of critical deformations initiating dynamic recrystallization, the share of static recrystallization in actual plastic working processes is relatively small.

The test rolling carried out in the LPS line provided a relatively small amount of data that could be used to verify the developed models, which was associated with a very limited amount of material for rolling. Notwithstanding, the analysis of the obtained results, especially in the field of quantitative metallography, confirmed the correctness of the forecasting of the developed mathematical models.

The presented results of mechanical tests of sheets after heat treatment show that the TS is dependent on the applied rolling scheme, and thus the level of the austenite structure refinement. The maximum value of TS = 1892 MPa was obtained for variant A with the finish rolling temperature of 950 °C with full recrystallization in the rolled plate. The influence on the final mechanical properties depends on the long-term low-temperature heat treatment resulting in the formation of carbide-free bainite. It is a very long process, and 70 hours of annealing may be not enough to reach full mechanical parameters. Probably therefore we did not obtain the assumed level of TS up to the 2.5 GPa.

Author Contributions: T.D. coordinated the experimental activities, processed the results, and wrote the first draft of the manuscript, performed a literary analysis and experiments; M.K. performed the experiments and analyzed the stress–strain curves; T.D. and M.K. evaluated the results of structural analysis; T.D and M.K. contributed to the processing and comparison of results the hot-rolling process on a semi-industrial scale; all authors revised and approved the final version of the manuscript. All authors have read and agreed to the published version of the manuscript.

Funding: This research received no external funding.

Data Availability Statement: Data sharing is not applicable to this article.

Conflicts of Interest: The authors declare no conflict of interest.

References

1. Gawad, J.; Niznik, B.; Kuziak, R.; Pietrzyk, M. Validation of multi-scale model describing microstructure evolution in steels. *Steel Res. Int.* **2008**, *79*, 652–659. [CrossRef]
2. Madej, L.; Gawad, J.; Hodgson, P.D.; Pietrzyk, M. Contribution to Digital Representation of Materials Subjected to Thermomechanical Processing. In *Materials Science and Technology Conference and Exhibition, MS and T'07—Exploring Structure, Processing, and Applications Across Multiple Materials Systems*; Materials Science and Technology: London, UK, 2007; Volume 3, pp. 1677–1688.
3. Llanos, L.; Pereda, B.; Lopez, B.; Rodriguez-Ibabe, J.M. Modelling of static recrystallization behavior of high manganese austenitic steels with different alloying contents. *ISIJ Int.* **2016**, *56*, 1038–1047. [CrossRef]
4. Yang, Z.; Li, Y.; Li, Y.; Zhang, F.; Zhang, M. Constitutive Modeling for Flow Behavior of Medium-Carbon Bainitic Steel and Its Processing Maps. *J. Mater. Eng. Perform.* **2016**, *25*, 5030–5039. [CrossRef]
5. Ferdowsi, M.R.G.; Nakhaie, D.; Benhangi, P.H.; Ebrahimi, G.R. Modeling the high temperature flow behavior and dynamic recrystallization kinetics of a medium carbon microalloyed steel. *J. Mater. Eng. Perform.* **2014**, *23*, 1077–1087. [CrossRef]

6. Zhang, X.L.; Li, H.; Xu, S.X.; Li, Z.C.; Mi, Z.L. Dynamic recrystallization behavior of high carbon chromium bearing steel. In *Applied Mechanics and Materials*; Trans Tech Publications Ltd: Zurich, Switzerland, 2014; Volume 584–586, pp. 1011–1016.
7. Bianchi, J.H.; Karjalainen, L.P. Modelling of dynamic and metadynamic recrystallisation during bar rolling of a medium carbon spring steel. *J. Mater. Process. Technol.* **2005**, *160*, 267–277. [CrossRef]
8. Banaszek, G.; Berski, S.; Dyja, H. Theoretical Modelling of Metallurgical Defect Closing-Up Processes during Forming a Forging. *J. Iron Steel Res. Int.* **2013**, *20*, 111–116. [CrossRef]
9. Pater, Z.; Tofil, A.; Tomczak, J. Steel balls forming by cross rolling with upsetting. *Metalurgija* **2013**, *52*, 103–106.
10. Kuziak, R.; Pidvysots'kyy, V.; Zalecki, W.; Molenda, R.; Łapczyński, Z. Symulacja numeryczna i symulacja fizyczna w skali laboratoryjnej zmian mikrostrukturalnych austenitu w procesie walcowania blach ze stali konstrukcyjnej wielofazowej. *Pr. Inst. Metal. Żelaza* **2012**, *64*, 17–23.
11. Institute for Ferrous Metallurgy. Bainitic—Austenitic Steel and Method of Plates Production of the Concerned Steel. No. of Submission P.394037 [WIPO ST 10/C PL394037], 25 February 2011. Available online: https://www.imz.pl/en/news/NanoStal/Results/[44,357,,,,] (accessed on 14 January 2021).
12. Caballero, F.G.; Bhadeshia, H.K.D.H. Very strong bainite. *Curr. Opin. Solid State Mater. Sci.* **2004**, *8*, 251–257. [CrossRef]
13. Garcia-Mateo, C.; Caballero, F.G.; Bhadeshia, H.K.D.H. Acceleration of Low-temperature Bainite. *ISIJ Int.* **2003**, *11*, 1821–1825. [CrossRef]
14. Garcia-Mateo, C.; Caballero, F.G.; Bhadeshia, H.K.D.H. Development of Hard Bainite. *ISIJ Int.* **2003**, *8*, 1238–1243. [CrossRef]
15. Edwards, H.R.; Kennon, N.F. The Morphology and Mechanical Properties of Bainite from Deformed Austenite. *Metall. Trans. A* **1978**, *9*, 1801–1809. [CrossRef]
16. Gao, J.; Thompson, R.G. Real time temperature models for Monte Carlo simulation of normal grain growth. *Acta Mater.* **1996**, *44*, 4565–4570. [CrossRef]
17. Garbarz, B.; Bołd, T. Influence of austenite substructure on structure and properties of low alloy steels quenched directly from hot deformation temperature. *Met. Sci.* **1984**, *18*, 357–361. [CrossRef]
18. Shaban, M.; Eghbali, B. Determination of critical conditions for dynamic recrystallization of a microalloyed stell. *Mater. Sci. Eng. A* **2010**, *527*, 4320–4325. [CrossRef]
19. Knapiński, M.; Kawałek, A.; Dyja, H.; Kwapisz, M. Krzywe umocnienia stali mikrostopowej przeznaczonej do produkcji blach grubych w kategorii wytrzymałościowej X80. *Hut. Wiadomości Hut.* **2011**, *9*, 818–821.
20. Knapinski, M.; Dyja, H.; Kawalek, A.; Fraczek, T.; Laber, K. Analysis of the microstructure evolution during thermo-mechanical treatment of the steel plates in grade X80-X100. *Metalurgija* **2013**, *52*, 239–242.
21. Knapinski, M.; Dyja, H.; Kawalek, A.; Kwapisz, M.; Koczurkiewicz, B. Physical Simulations of the Controlled Rolling Process of Plate X100 with Accelerated Cooling. In *Mechatronic Systems and Materials V, Solid State Phenomena*; Trans Tech Publications Ltd.: Zurich, Switzerland, 2013; Volume 199, pp. 484–489.
22. Gray, V.; Whittaker, M.A. Discussion of Non-Constant Creep Activation Energy. *J. Mater. Sci. Eng.* **2017**, *6*, 372.
23. Yadav, B.N.; Muchhala, D.; Sriram, S.; Mondal, D.P. Study on activation energy and strain rate sensitivity of closed-cell aluminium hybrid composite foam. *J. Alloy. Compd.* **2020**, *832*, 154860. [CrossRef]
24. Dembiczak, T.; Knapiński, M.; Garbarz, B. Mathematical modeling of phenomena of dynamic recrystallization during hot plastic deformation in high-carbon bainitic steel. *Metalurgija* **2017**, *56*, 107–110.
25. Liu, J.; Cui, Z.; Ruan, L. A new kinetics model of dynamic recrystallization for magnesium alloy AZ31B. *Mater. Sci. Eng. A* **2011**, *529*, 300–310. [CrossRef]
26. John, J.J.; Xavier, Q.; Lan, J.; Etienne, M. The Avrami kinetics of dynamic recrystallization. *Acta Mater.* **2009**, *57*, 2748–2756.
27. Mirzadeh, H.; Najafizadeh, A. Prediction of the critical conditions for initiation of dynamic recrystallization. *Mater. Des.* **2010**, *31*, 1174–1179. [CrossRef]
28. Chen, F.; Cui, Z.; Chen, S. Recrystallization of 30Cr2Ni4MoV ultra-super-critical rotor steel during hot deformation. Part I: Dynamic recrystallization. Mater. Sci. Eng. A 2011, 528, 5073–5080. **2011**, *528*, 5073–5080.
29. Beynon, J.H.; Sellars, C.M. Modelling microstructure and its effects during multipass hot rolling. *ISIJ Int.* **1992**, *32*, 359–367. [CrossRef]

materials

MDPI

Article

Analysis of the Microstructure Development of Nb-Microalloyed Steel during Rolling on a Heavy-Section Mill

Michal Sauer [1,2,*], Richard Fabík [1], Ivo Schindler [2], Petr Kawulok [2], Petr Opěla [2], Rostislav Kawulok [2], Vlastimil Vodárek [2] and Stanislav Rusz [2]

[1] Liberty Ostrava, a.s., Vratimovská 689/117, 71900 Ostrava, Czech Republic
[2] Faculty of Materials Science and Technology, VŠB-Technical University of Ostrava, 17., 70800 Ostrava, Czech Republic
* Correspondence: michal.sauer@libertysteelgroup.com

Abstract: It is not realistic to optimize the roll pass design of profile rolling mills, which typically roll hundreds of profiles, using physical modelling or operational rolling. The use of reliable models of microstructure evolution is preferable here. Based on the mathematical equations describing the microstructure evolution during hot rolling, a modified microstructure evolution model was presented that better accounts for the influence of strain-induced precipitation (SIP) on the kinetics of static recrystallization. The time required for half of the structure to soften, $t_{0.5}$, by static recrystallization was calculated separately for both situations in which strain-induced precipitation occurred or did not occur. On this basis, the resulting model was more sensitive to the description of grain coarsening in the high-rolling-temperature region, which is a consequence of the rapid progress of static recrystallization and the larger interpass times during rolling on cross-country and continuous mills. The modified model was verified using a plain strain compression test (PSCT) simulation of rolling a 100-mm-diameter round bar performed on the Hydrawedge II hot deformation simulator (HDS-20). Four variants of simulations were performed, differing in the rolling temperature in the last four passes. For comparison with the outputs of the modified model, an analysis of the austenite grain size after rolling was performed using optical metallography. For indirect comparison with the model outputs, the SIP initiation time was determined based on the NbX precipitate size distribution obtained by TEM. Using the PSCT and the outputs from the modified microstructure evolution model, it was found that during conventional rolling, strain-induced precipitation occurs after the last pass and thus does not affect the austenite grain size. By lowering the rolling temperature, it was possible to reduce the grain size by up to 56 μm, while increasing the mean flow stress by a maximum of 74%. The resulting grain size for all four modes was consistent with the operating results.

Keywords: static recrystallization; strain-induced precipitation; microstructure evolution; PSCT

Citation: Sauer, M.; Fabík, R.; Schindler, I.; Kawulok, P.; Opěla, P.; Kawulok, R.; Vodárek, V.; Rusz, S. Analysis of the Microstructure Development of Nb-Microalloyed Steel during Rolling on a Heavy-Section Mill. *Materials* **2023**, *16*, 288. https://doi.org/10.3390/ma16010288

Academic Editors: Alexander Yu Churyumov and Thomas Niendorf

Received: 7 November 2022
Revised: 21 December 2022
Accepted: 22 December 2022
Published: 28 December 2022

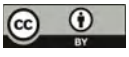

1. Introduction

Thermomechanical steel processing, also referred to in the literature as controlled forming, aims to achieve the desired microstructure, i.e., the desired mechanical and physical properties, of the final product. This is primarily achieved by refining the final ferritic grain, which is transformed from deformed austenite. Controlled forming is, therefore, possible in order to achieve the desired properties of the product, with a significant reduction in the alloying content elements and heat treatment costs compared to conventionally rolled material [1,2]. Controlled forming has been extensively described in the literature [2–5]. Therefore, the following text briefly describes three selected types of controlled forming using mainly retarding austenite recrystallization due to a combination of microalloying elements in solid solution and interactions between recrystallization and strain-induced precipitation (SIP).

Recrystallization-controlled rolling is commonly used for rolling thick plates and thin-walled seamless tubes, where the rolling forces are close to the limit value of rolling

mills [6]. The forming process is carried out at high temperatures (above 950 °C), and complete static recrystallization (SRX) can occur during the interpass times. For this purpose, steel microalloying elements, i.e., Ti and V, are added to the steel to allow complete static recrystallization (SRX) between passes and simultaneously prevent grain growth after recrystallization before the following pass. The addition of Ti leads to the precipitation (SIP) of TiN during the continuous casting of the billets, which then prevents extensive grain growth after recrystallization. The addition of V leads to the precipitation of VN in the ferritic region, which leads to hardening of the steel. The recrystallization-controlled forming process should be associated with high cooling rates to achieve a fine ferritic grain after transformation from austenite. This method can achieve a ferritic grain size of about 7 to 10 μm [2–7].

Conventional controlled rolling aims to produce flattened austenitic grains due to plastic deformation without any softening process, leading to increased nucleation sites for transforming from austenite to ferrite. This process then leads to the formation of fine ferritic grains approximately 5 to 8 μm in size. Conventional controlled rolling generally involves high heating temperatures to achieve the complete transition of the microalloying elements, i.e., Nb and V, into a solid solution. During the rolling process, which takes place below zero recrystallization temperature, strain-induced precipitation of Nb(C, N) occurs, causing complete suppression of recrystallization between each pass [2–7].

Dynamic recrystallization-controlled rolling involves the initiation of dynamic recrystallization in one or more passes during the rolling process. It is characteristic for rolling wires and bars on continuous rolling lines but also rolling strips and seamless tubes [7]. This can be achieved by applying a large amount of deformation in one pass or accumulating strain in several individual passes. In the case of both methods, a critical strain is required to initiate dynamic recrystallization. The final ferrite grain size can reach 1 to 2 μm [2–7].

Many authors [8–11] have used microstructure evolution models to design controlled forming regimes. Usually, however, these are models created for strip rolling on the final sequence of (semi)continuous mills at low rolling temperatures, where the SIP effect has already caused, or will soon cause, a slowing down (in the case of continuous mills with short interpass times, a practical stop) of recrystallization. Our experience shows that such models do not give reliable results when simulating rolling of long products at higher temperatures. This is due to the use of a single equation to calculate $t_{0.5}$ for both situations in which SIP did or did not take place.

The purpose of this study is to propose and verify a new model for microstructure evolution that will be more accurate in both situations.

2. Microstructure Evolution Model

In recent decades, considerable attention has been paid to developing mathematical models that predict the microstructure evolution of hot-rolled products [1–23]. A significant advantage of these models is the possibility to optimize the rolling conditions and thus obtain a good combination of thermomechanical parameters to achieve optimal mechanical properties of the final product. A weakness of most mathematical models described in the literature is the weak connection between the processes of precipitation and recrystallization. This, then, especially in the case of a cross-country rolling mill (higher interpass time) at higher temperatures, leads to unrealistically fast static recrystallization (SRX) and thus to enormous coarsening of the austenitic grain. Therefore, this work aims to modify the mathematical models predicting austenitic grain evolution during hot rolling to better account for the relationship between recrystallization and precipitation.

Description of the Microstructure Development Model Modification

In the literature [24–30], one can encounter two-step curves describing the growth of the fraction of the softened structure as a function of the thermodynamic conditions of the forming process, i.e., temperature, strain, strain rate and grain size, during the interpass time. The most complete data set represents the work of authors around Medina [27–37].

The data of these authors were used in the modification of our model. Figure 1 is an example of the two-stage softening curves [37] for steel, with the chemical composition listed in Table 1 for N8 steel.

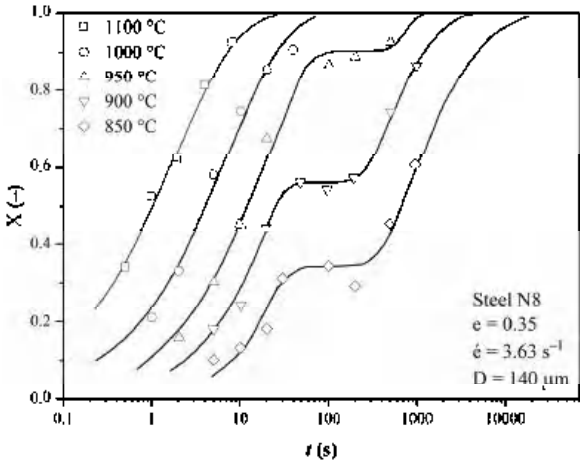

Figure 1. Variation in the recrystallized fraction (X_a) with time (t), Reprinted from Ref. [14].

Table 1. Chemical composition of steels used for model modification in wt.%.

Steel	C	Si	Mn	P	S	Al	N	Nb
N3	0.21	0.18	1.08	0.023	0.014	0.007	0.0058	0.024
N4	0.21	0.19	1.14	0.023	0.015	0.008	0.0061	0.058
N8	0.2	0.2	1.0	0.024	0.013	0.006	0.0056	0.007

These curves generally determine the time to soften half of the structure, $t_{0.5}$, that occurs in the JMAK equation. This is the imaginary intersection of the value of $X = 0.5$ with these curves. In the case of simple S-curves, this is their inflection point. In the case of two-degree curves, this rule no longer applies. The values of $t_{0.5}$ thus obtained are used to develop an equation that respects the effect of precipitation on the kinetics of recrystallization. The disadvantage, however, is that the equation thus developed leads to a shift of $t_{0.5}$ to high times in cases where the conditions for initiating strain-induced precipitation (SIP) have not yet been fulfilled during the previous rolling. Moreover, in the temperature region of the nose of the curve of the onset of precipitation, the values of $t_{0.5}$ in the equations thus developed are biased because they do not consider the step effect of the precipitation on the kinetics of recrystallization. We attempted to use published data for steels N3, N4 and N8 to develop new equations to calculate $t_{0.5}$ separately for the situation in which SIP takes place and separately for the situation in which SIP does not occur at all.

The experimental data were fitted with Avrami S-curves so that the sum of the squares of the deviations of the measured values from these curves was minimal. In the case of two-degree curves, two S-curves were used separately for the two degrees of the curves. Data occurring in the region of a constant proportion of the softened structure were not counted (see Figure 2).

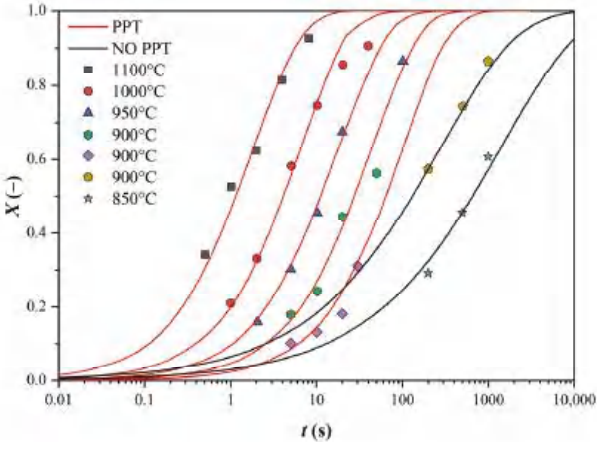

Figure 2. Plotting the experimental data with S-curves of the original data (see Figure 1).

In this way, we first obtained the values of the coefficient *n* in the Avrami equation (see Table 2). First, we needed to check whether the coefficient *n* is a function of temperature, as some authors state, or whether it is affected by other influences.

Table 2. Values of the coefficient *n* in the Avrami equation.

	n (-)					No SIP						SIP			
Steel	**Strain (-)**	**1200**	**1150**	**1100**	**1050**	**1025**	**1000**	**950**	**900**	**850**	**1025**	**1000**	**950**	**900**	**850**
N3	0.2		0.68		0.86		0.71	0.71				0.34	0.42		
	0.35	0.60	0.62	0.82	0.87		0.90	0.83				0.21	0.50		
N4	0.2	1.01		1.23	1.05	1.06	1.12				0.65	0.71			
	0.35	0.86	0.91	0.93	0.89	0.85	0.90				0.21	0.60			
N8	0.2			0.85			0.83	0.67	0.70				0.42	0.59	
	0.35			0.65			0.65	0.64	0.66	0.65				0.53	0.62
	Mean	0.82	0.74	0.90	0.92	0.96	0.85	0,71	0.68	0.65	0.43	0.46	0.45	0.56	0.62
	Median	0.86	0.68	0.85	0.88	0.96	0.86	0,69	0.68	0.65	0.43	0.47	0.42	0.56	0.62
	Mean					0.82							0.48		
	Median					0.84							0.52		

The negligible effect of temperature on the coefficient *n* is illustrated in Figure 3. The effect of the Nb content and strain size was similar.

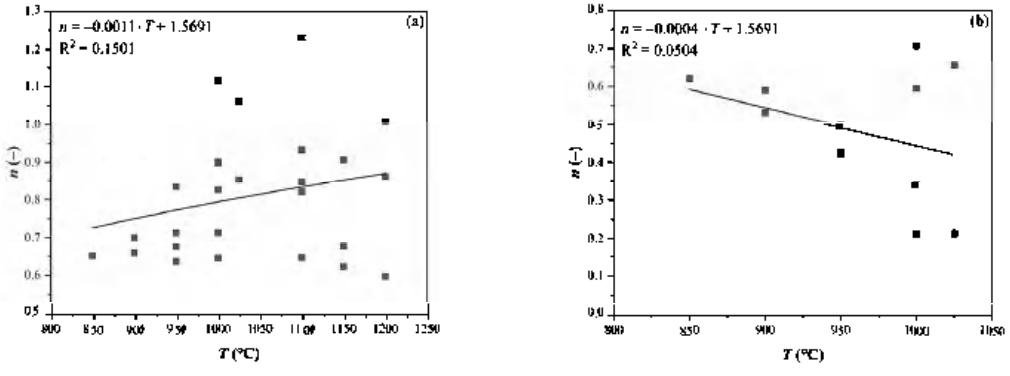

Figure 3. Effect of temperature on the *n* value: (**a**) without SIP and (**b**) with SIP.

Finally, the value of n was determined as the average for the curves without SIP (n = 0.823) and with SIP (n = 0.484). These values were used to correct the S-curves in the plots similar to Figure 2 (separately for each of the 3 steels and for the 2 strain values of 0.2 and 0.35). By varying the value of the n coefficient in each curve, the curves were shifted towards the optimum based on the least squares method. Therefore, the position of the curves was changed again so that the minimum sum of the squares of the deviations of the measured points from the S-curves was again achieved. From the curves thus generated, a $t_{0.5}$ value was determined for each curve separately (see Table 3).

Table 3. Values of $t_{0.5}$ in the JMAK equation.

Steel	$t_{0.5}$ (s) D (μm)	e (-)	No SIP 1200	1150	1100	1050	1025	1000	950	900	850	SIP 1025	1000	950	900	850
N3	210	0.2		1.91		7.26		24.45	57.25				111.09	970.42		
		0.35	0.77	1.33	2.44	4.49		13.34	35.29				92.56	644.69		
N4	190	0.2	1.33		4.47	10.46	27.66	50.76				183.03	593.68			
		0.35	0.72	1.33	2.75	6.84	12.60	26.01				136.56	384.77			
N8	140	0.2			3.73			14.17	42.33	126.00				123.68	671.66	
		−0.3			1.18			4.21	11.12	27.63	64.85				131.37	656.52

The data from Table 3 were plotted against the reciprocal thermodynamic temperature (see Figure 4). The activation energy values (exponent multiplied by the molar gas constant; see Table 4) and the value of the K constant were determined using exponential regression.

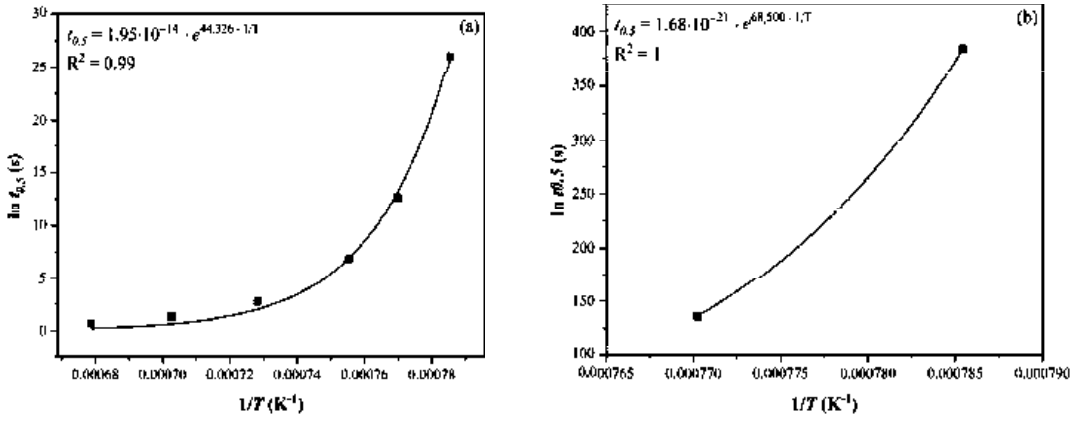

Figure 4. Dependence of $t_{0.5}$ on the reciprocal thermodynamic temperature: (**a**) without SIP and (**b**) with SIP (steel N4, e = 0.35).

Table 4. Values of Q and K in the equation to describe $t_{0.5}$.

Steel	Strain (-)	No SIP Q (J·mol^{-1})	No SIP K (-)	SIP Q (J·mol^{-1})	SIP K (-)
N3	0.2	251 048	1.08×10^{-9}	561 218	1.05×10^{-21}
N4		281 684	1.11×10^{-10}	646 761	1.73×10^{-24}
N8		236 541	3.37×10^{-9}	403 719	7.09×10^{-26}
N3	0.35	229 855	4.76×10^{-9}	502 583	2.22×10^{-19}
N4		275 192	1.09×10^{-10}	569 336	1.68×10^{-21}
N8		209 681	1.19×10^{-8}	352 517	2.64×10^{-14}

The graph in Figure 5 shows the activation energy of the studied steels as a function of the Nb content and strain value in both the non-SIP and SIP conditions. In both cases, there seemed to be a statistically significant dependence, so the activation energy values were determined by multilinear regression as a function of the Nb content and strain in the form:

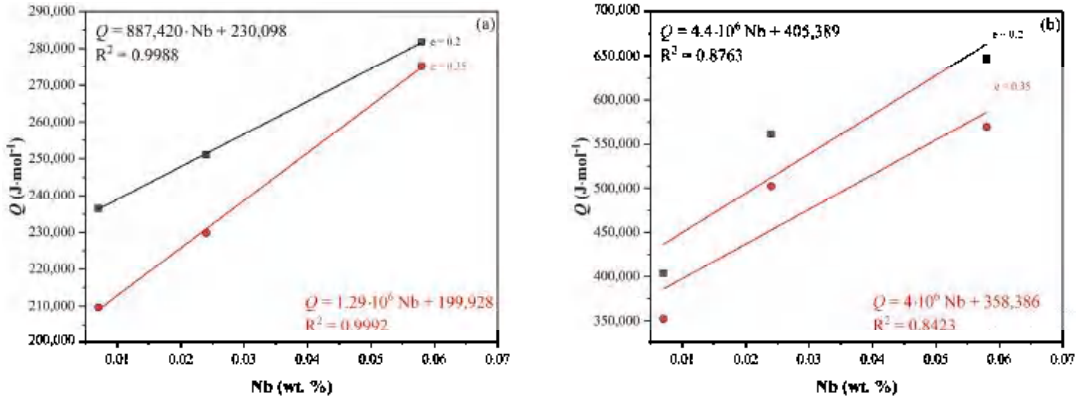

Figure 5. Dependence of Q on the strain and Nb content (without SIP): (**a**) without SIP and (**b**) with SIP.

Without SIP:

$$Q = 1089469 \cdot \%Nb - 121212 \cdot e + 248346 \quad (1)$$

With SIP:

$$Q = 418324 \cdot \%Nb - 416137 \cdot e + 496325 \quad (2)$$

A comparison of the measured and calculated values according to Equations (1) and (2) is made in Figure 6.

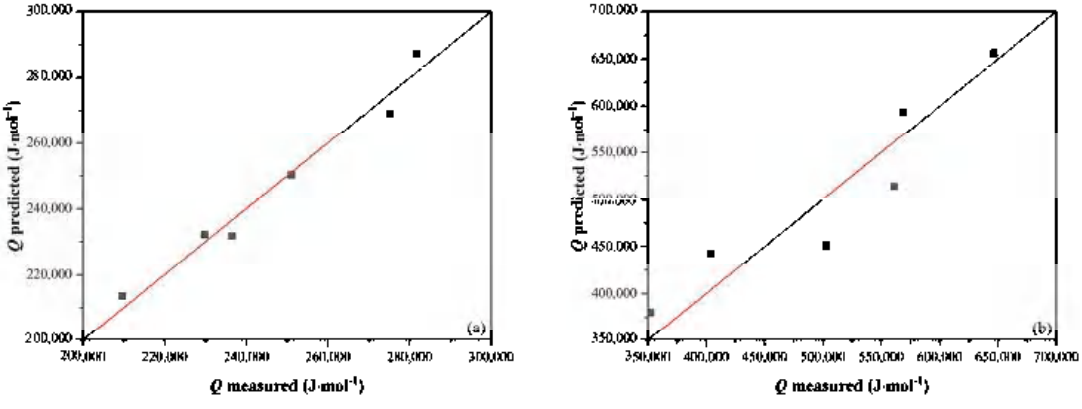

Figure 6. Comparison of measured and calculated values: (**a**) without SIP according to Equation (1) and (**b**) with SIP according to Equation (2).

The equations obtained to describe $t_{0.5}$ had the following form:
Without SIP:

$$t_{0.5} = \exp(6.036 \cdot e - 80.87 \cdot \%Nb - 19.83) \cdot \exp\left(\frac{1089469 \cdot \%Nb - 121212 \cdot e + 248346}{R \cdot T}\right) \quad (3)$$

With SIP:

$$t_{0.5} = \exp(32.235 \cdot e - 329.6 \cdot \%Nb - 43.24) \cdot \exp\left(\frac{4184324 \cdot \%Nb - 416137 \cdot e + 496325}{R \cdot T}\right) \quad (4)$$

The comparison of the measured values according to Equations (3) and (4) is shown in the plot in Figure 7. The conformity between the measured and calculated values for $t_{0.5}$ without SIP is good, but in the case of $t_{0.5}$ with SIP, the scatter of the data around the mean line is visibly worse. The arrangement of the data into layers by steel number can be seen here (data labels in the plot in Figure 7b). All $t_{0.5}$ values are below the mean line for N3 steel, while the opposite is true for N8 steel. Apart from the Nb content, the steels used differ mainly in the Mn and Si content ratio, significantly affecting Nb precipitation. This effect is more pronounced in steels with a higher Nb content because the solubility of Nb in steel decreases with an increasing Mn/Si ratio. Therefore, Equation (4) was modified to the following form:

$$t_{0.5} = \exp\left[1.37 \cdot 10^{-4} \cdot \left(\frac{\%Mn}{\%Si}\right)^{5.1282}\right] \cdot \exp(32.235 \cdot e - 329.6 \cdot \%Nb - 43.24) \cdot \exp\left(\frac{4184324 \cdot \%Nb - 436137 \cdot e + 496325}{R \cdot T}\right) \quad (5)$$

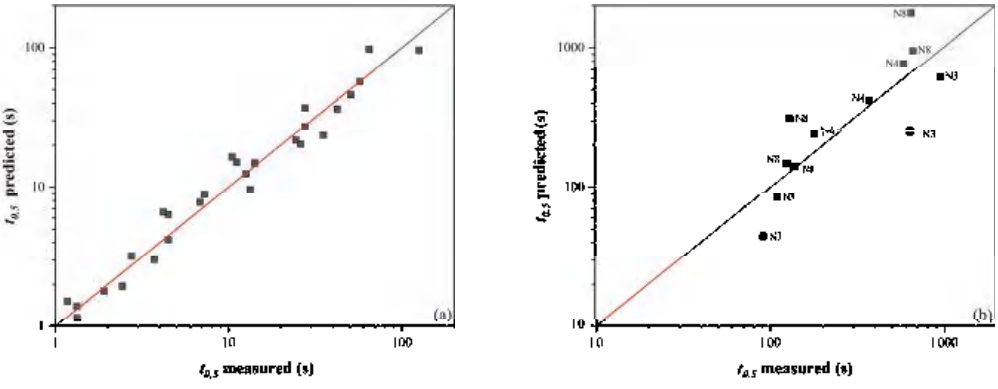

Figure 7. Comparison of measured and calculated $t_{0.5}$ values: (**a**) without SIP according to Equation (3), and (**b**) with SIP according to Equation (4) (data labels here represent steel designations.)

Using this correction factor, the scatter of values around the mean line was minimized (Figure 8). If the data were further refined, more measured softening curves' data would be required for the variant with SIP.

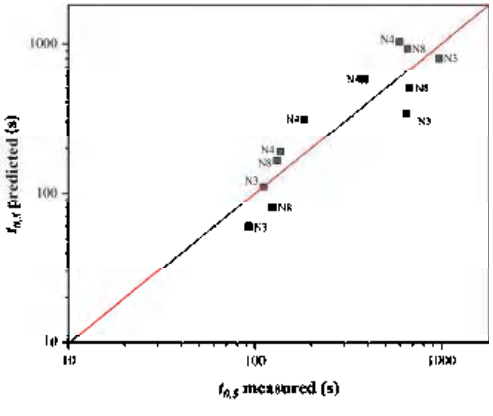

Figure 8. Comparison of measured and calculated $t_{0.5}$ values with SIP according to Equation (5) (data labels here represent steel designations).

Since in the experiment from which our data were taken, the grain size ranged from 140 to 210 μm, it was necessary to add a term to the equations to describe $t_{0.5}$ to account for the change in grain size during actual rolling. The effect of grain size D was included in previous equations in the following form:

$$t_{0.5(D)} = \frac{t_{0.5(D)}}{D'} \tag{6}$$

where D' is the average value of the grain size used in the experiment (180 μm).

To use the equations obtained to describe $t_{0.5}$ in the microstructure evolution model, it is necessary to solve the determination of $t_{0.5}$ in the pass in which the SIP occurs. In this pass, it is assumed that $t_{ip} > t_{ps}$. The following two situations can occur (see Figure 9). The fraction of the softened structure at time t_{ip} for a curve with SIP is

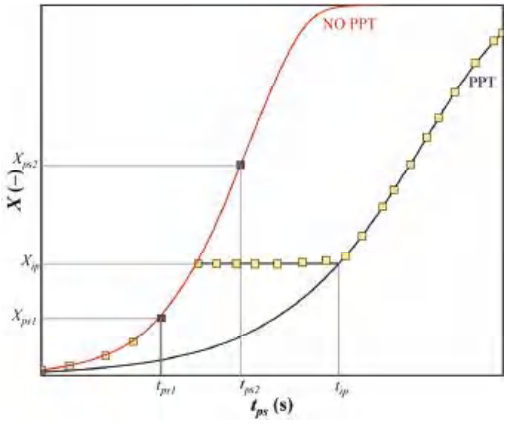

Figure 9. Possible situations that may occur in the collection in which the conditions for the start of SIP are met.

- greater than the proportion of the softened structure at time t_{ps} for the curve without SIP (t_{ps1} and X_{tps1} in Figure 9);
- less than the proportion of the softened structure at time t_{ps} for the curve without SIP (t_{ps2} and X_{tps2} in Figure 9).

In the first case, the model will calculate the X values from the SIP curve and vice versa in the second case.

The last point of the model modification is the modification of the parameters of the Hodgson equation [37] for the grain size calculation after static recrystallization. The data obtained from the PSCT (see the next section) showed that our HSLA steel has a significantly coarser grain. The modified equation has the following form:

$$d_{SRX} = 450 \cdot d_0^{0.4} \cdot e^{-0.5} \cdot exp\left(\frac{-45000}{R \cdot T}\right) \tag{7}$$

3. Plain Strain Compression Test (PSCT)

3.1. Experiment Description

HSLA steel (S355J2), whose chemical composition is shown in Table 5, was selected to verify the modified microstructure evolution model. A total of 5 cubic specimens of 20 × 20 × 20 mm were prepared from the 180 × 180 mm continuously cast block specimen for the laboratory experiments to determine the carbonitride dissolution temperature during heating and 4 specimens of 10 × 15 × 20 mm for the plain strain compression test (PSCT).

Table 5. Chemical composition of the selected HSLA steel in wt.%.

C	Mn	Si	P	S	Al	Nb	N	Ti
0.161	1.38	0.178	0.019	0.011	0.035	0.033	0.0044	0.001

The aim of the laboratory simulations was:

(1) to determine the temperature for complete dissolution of carbonitrides during heating;

(2) PSCT simulation of rolling a round bar of 100 mm diameter on a cross-country rolling mill at Liberty Ostrava a.s.

(3) analysis of the microstructure of samples after PSCT by transmission electron microscopy (TEM).

To determine the amount of Nb in the solid solution γ after heating, a simple quenching and tempering experiment was performed on samples heated to different heating temperatures. A total of 5 samples were individually heated in an electric resistance furnace to a temperature of 1100–1150–1200–1220–1240 °C for 30 min. After the hold time, the samples were quenched in water with ice and then tempered at 575 °C for 60 min. After the specimens were cut, ground and polished, an average hardness of HBW 30 was determined in the central region of the specimens, based on 5 imprints each time. Based on the results shown in Figure 10, the heating temperature required for complete dissolution of the precipitates was determined to be 1200 °C.

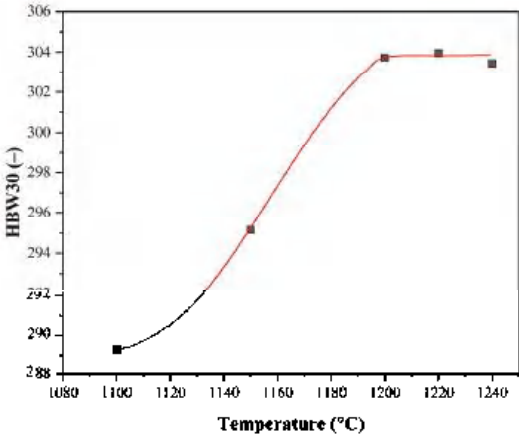

Figure 10. Average hardness of samples after quenching and tempering as a function of heating temperature.

In the plane strain compression tests performed on the Hydrawedge II hot deformation simulator HDS-20, anvils with a working width of 5 mm were pressed into the test specimens with dimensions of 10 × 15 × 20 mm. A total of 4 simulations were performed with a uniform heating temperature of 1200 °C with a 15 min hold at this temperature. The true strain, calculated based on the elongation factor, was converted using the control program with a conversion factor of 1.155 to strain intensity values that respected the law of volume conservation, along with dimensional changes in all 3 directions. In total, 7 passes were simulated in each variant at deformation temperature T, strain rate $\dot{e}$ and interpass times t_{ip}. A simplified schematic representation of the PSCTs is shown in Figure 11.

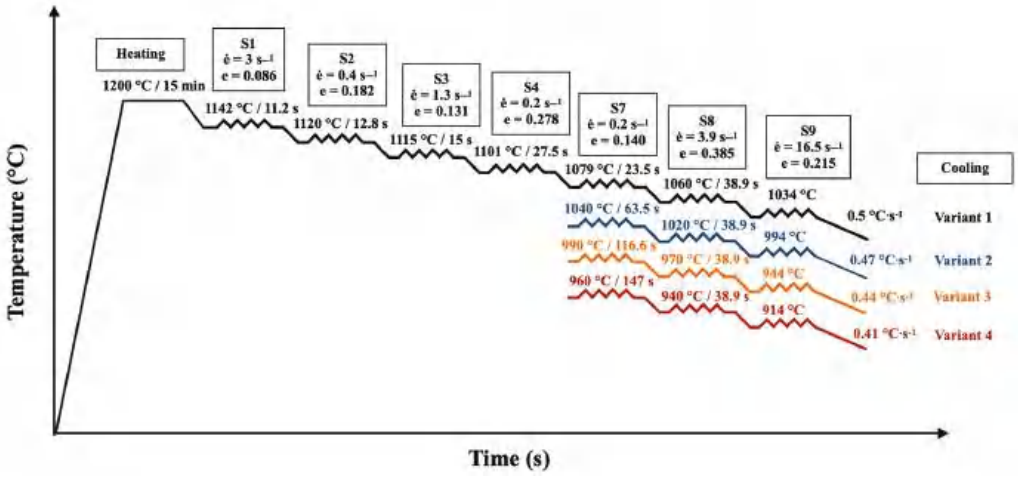

Figure 11. Schematic illustration of PSCTs (represents an individual pass).

3.2. Microstructural Analysis

The microstructure of samples V1–V4 (corresponding to PSCT simulation variants 1–4) was preferentially examined in the centre of the deformed region in terms of its width and height.

Figure 12 documents the microstructure in the deformed part of sample V1, along with the marked areas of detailed microstructural analysis.

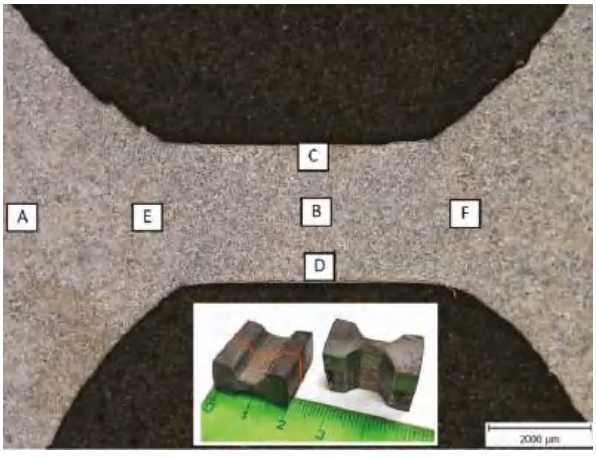

Figure 12. Marking of microstructure documentation sites (sample: variant 1). V1–V4 represent the areas of detailed microstructural analysis.

In general, the microstructure in the undeformed part of all samples was comparable: allotriomorphic ferrite along the boundaries of the original austenitic grains. The remaining microstructure was predominantly a mixture of Widmanstätten ferrite and a minor perlitic phase. The presence of a small proportion of bainite could not be dismissed (see Figure 13). Due to allotriomorphic ferrite, which nucleates at the original austenitic grain boundaries and continues to grow preferentially at these boundaries, we can estimate the austenitic grain size after heating (see the red original austenite boundary in Figure 13). Using image

analysis in ImageJ software, the size of the largest original austenitic grains was determined (the position of the cutting plane strongly influences the measured size, we can assume that the structure is homogeneous in terms of grain size and the largest grains are those that are split by the cutting plane close to their centre). The results of the measurements are summarized in Table 6.

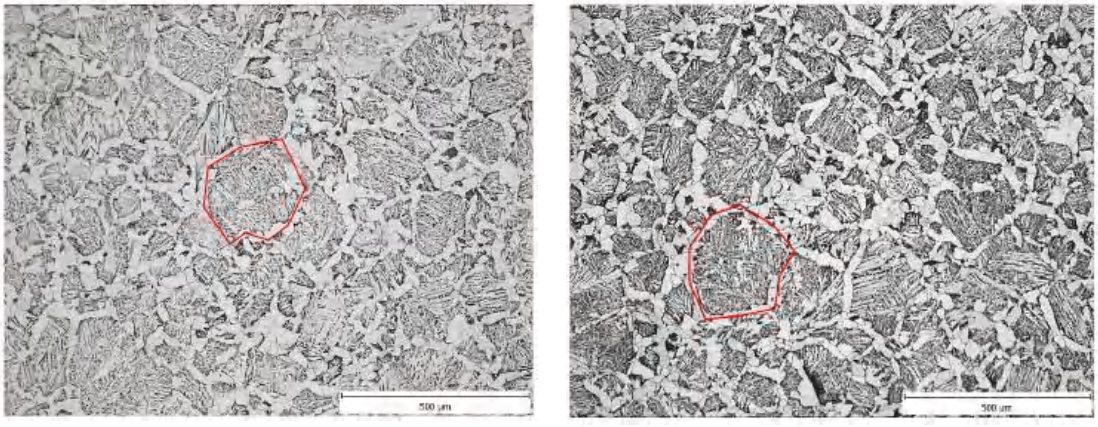

Figure 13. Microstructure consisting of allotriomorphic ferrite, pearlite and acicular ferrite in the undeformed region A: (**left**) sample V1 and (**right**) sample V3. The original austenitic grain boundary is marked in red.

Table 6. Average austenitic grain size values at heating temperature.

Variant	*D* (μm)
1	229
2	258
3	240
4	241

The so-called forging cross was clearly visible in samples V3 and V4. In the centre of the forging cross, the microstructure of these samples was a fine-grained mixture of ferrite and pearlite—Figures 14 and 16. In samples V1 and V2, without a distinct forging cross, the microstructure in the centre of the cross-section of the samples was a mixture of allotriomorphic ferrite, Widmanstätten ferrite and pearlite—Figures 15 and 16. Due to the presence of allotriomorphic ferrite, it is again possible to estimate the austenitic grain size before the onset of phase transformation using image analysis. The results of the measurements are summarized in Table 7, in which the average microhardness values are also given for comparison.

Table 7. Average austenitic grain size values before phase transformation and average microhardness values.

Variant	*D* (μm)	HV 0.3 (-)
1	96	168
2	72	183
3	50	169
4	46	162

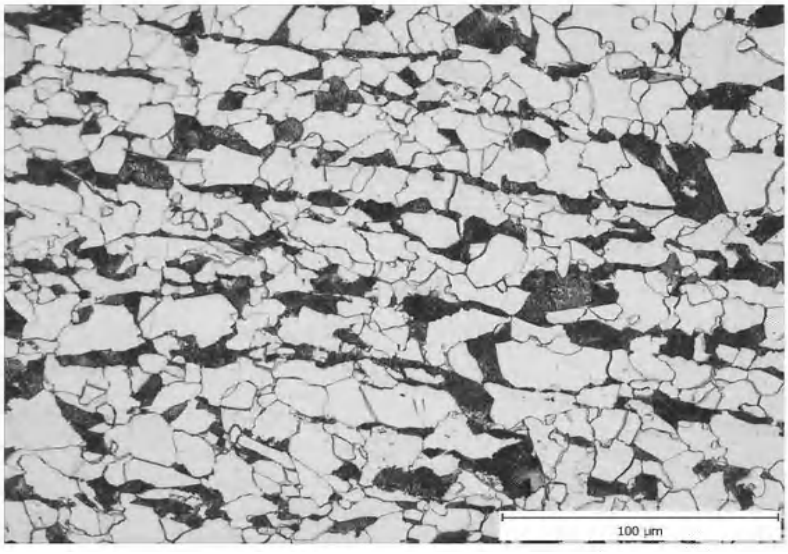

Figure 14. Ferritic–perlitic linear microstructure in the centre (sample V4).

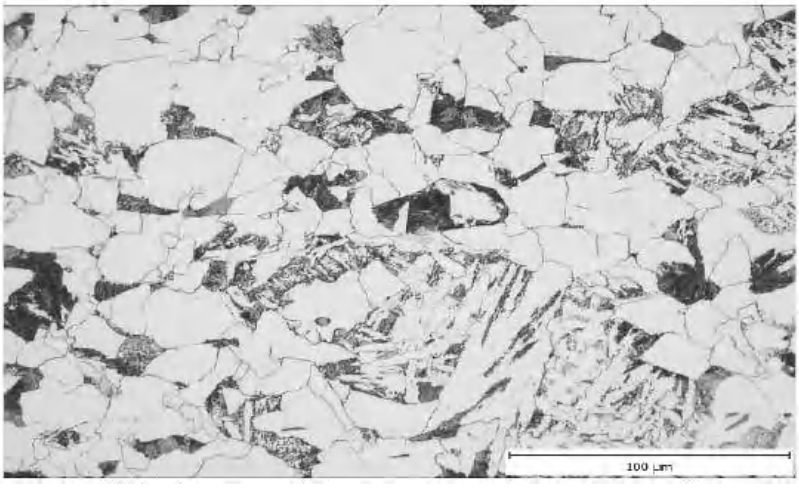

Figure 15. Microstructure consisting of allotriomorphic ferrite, pearlite and acicular ferrite in the centre (sample V1).

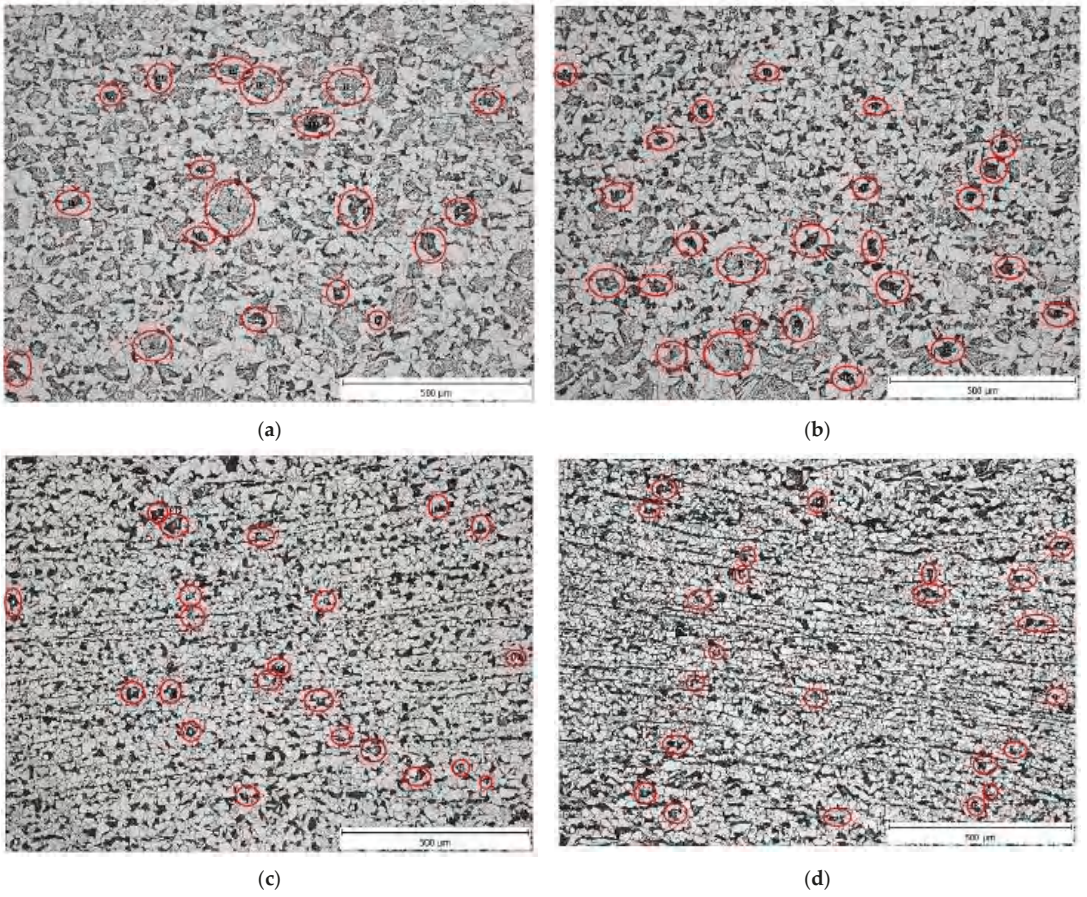

Figure 16. Comparison of the resulting microstructure in the centre of the samples for all variants. V1 and V2—a mixture of allotriomorphic ferrite, acicular ferrite and pearlite; V3 and V4—a mixture of allotriomorphic ferrite and pearlite. The red ellipses indicate the maximum size of the original austenitic grain. (**a**) Variant 1, region B, deformed part; (**b**) variant 2, region B, deformed part; (**c**) variant 3, region B, deformed part; and (**d**) variant 4, region B, deformed part.

3.3. Precipitate Analysis

TEM studies were performed using carbon extraction replicas. Sample masking was used in the preparation of the replicas in order to obtain slides only from the centre of the deformed part of the samples. When studying the replicas in TEM, areas where the microstructure was mainly ferrite and pearlite were preferred. Documentation of precipitate particles was performed only in ferritic grains. Minority phases on the replicas were identified using energy-dispersive X-ray spectroscopy (EDX). In all samples, only cementite particles (part of the pearlitic component, possibly bainite, whose presence cannot be excluded, although most of the austenite decay products morphologically corresponded to Widmanstätten ferrite) and NbX phase particles were detected. EDX showed that small amounts of titanium, chromium and niobium were present in the NbX particles (Table 8). The presence of small amounts of iron in the EDX spectra probably represents an artefact associated with the preparation of the slides. No clear differences were found between the chemical composition of coarser and fine NbX particles. Given the chemical composition of HSLA steel, it can be assumed that the particles are carbides rather than carbonitrides.

In the studied samples, we could identify a total of three different sizes of NbX particles. In the variants, samples V1 and V2, only coarse particles with a size above 80 nm were present (see Figure 17. In samples V3 and V4, besides coarse particles, there were also fine particles with a size of around 60 nm and even fine particles below 20 nm (see Figure 17). In samples V3 and V4, it could be seen that the fine particles were arranged in rows, suggesting that they are precipitates formed during deformation when slip bands became the sites for the formation of the nuclei. If no further deformation occurs, the precipitates coarsen. If further deformation occurs, new slip bands and thus new sites for NbX nuclei appear, as the solid solution is depleted of Nb and C around the original slip bands. This would then cause the appearance of 2 peaks on the histogram in the region corresponding to the strain-induced precipitates. A detailed analysis of the occurrence of particles is made in the following section.

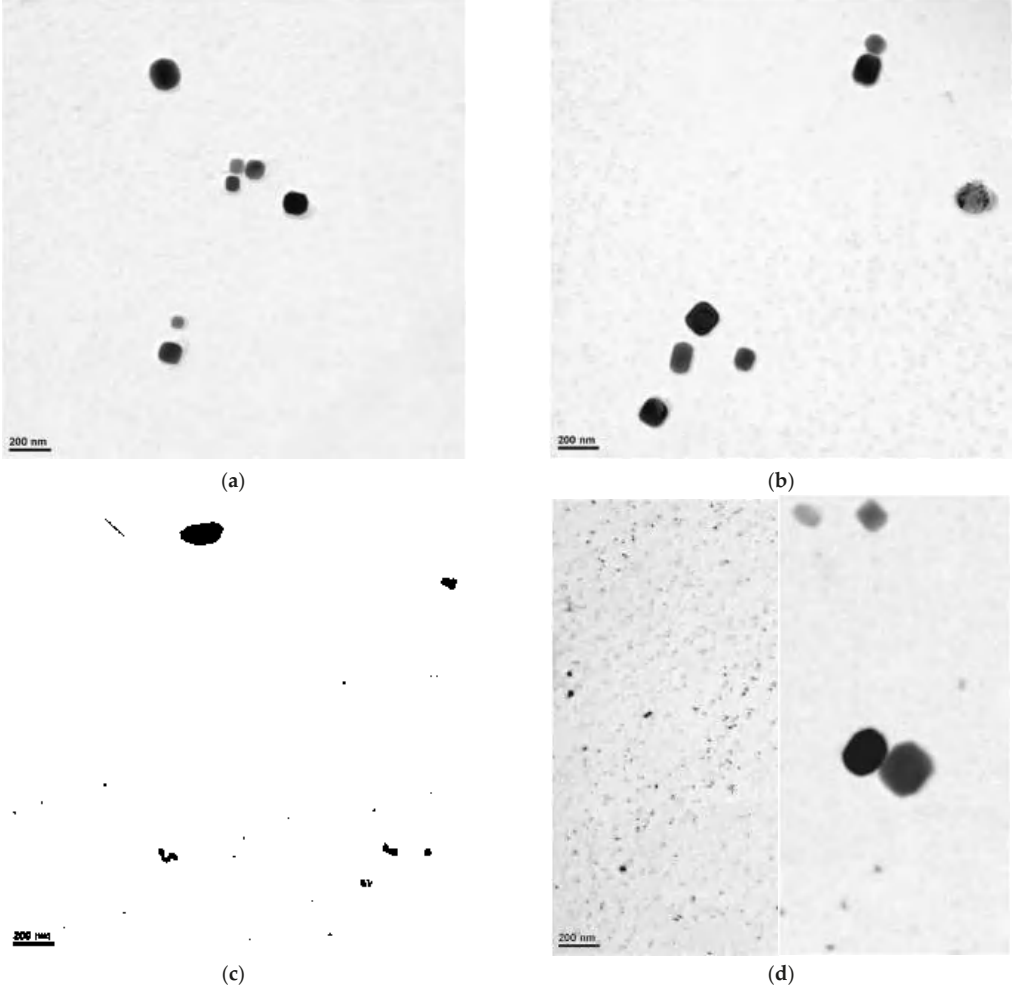

(**a**) (**b**) (**c**) (**d**)

Figure 17. Summary of all precipitate images for each variant V1 to V4. Images were selected that showed examples of precipitates of all observed sizes. For sample V4, it was not possible to capture different-size precipitates in one image; therefore, two images with the same scale are presented. (**a**) V1, (**b**) V2, (**c**) V3, and (**d**) V4.

Table 8. Results of semi-quantitative EDX analysis of the NbX phase (wt.%).

No. of Analysis	Ti	Cr	Fe	Nb
1	0.9	1.6	1.8	96.6
2	0.6	1.6	2.4	96.0
3	0.8	1.4	1.9	96.4
Mean	0.77	1.53	2.03	96.33
Std. deviation	0.153	0.115	0.321	0.306

3.4. Simulation of PSCTs Using a Modified Microstructure Evolution Model

Using a modified microstructure evolution model, microstructure evolution was simulated for all 4 variants of PSCT rolling simulation. The grain size evolution for all PSCT variants is shown in Figure 18. For variant 1, which represents conventional rolling, the gradual grain refinement was due to fully completed static recrystallization after almost every pass. Figure 18 shows undesirable grain coarsening occurred after the 5th and 7th passes. During cooling after rolling, at 1009 °C and a time of $t_{ip,7}$ = 49.44 s, SIP occurred. The time available for recrystallization or grain coarsening after the last pass of $t_{ip,7}$, which represents the x-intercept of the length of the cooling curve before its intersection with the precipitation onset curve (see Figure 19a), was calculated using the following Equation (8):

$$t_{ip,7} = t_{PPT} - t_{ps,7} \cdot \sum_{i=1}^{8} \frac{t_{ip}}{t_{ps}} \quad (8)$$

where t_{SIP} is the time of onset of precipitation during cooling (intersection of curves in Figure 19a).

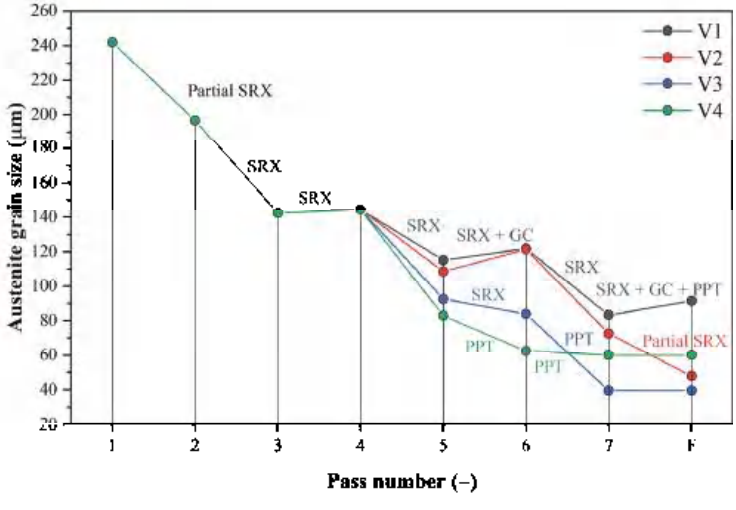

Figure 18. Grain size evolution for all PSCT variants calculated using the modified model.

Thus, the onset of precipitation in the case of variant 1 stops the grain coarsening process, and the resulting grain size before phase transformation was around 96 μm, which fit exactly the measured grain size from PSCT (96 μm).

The grain size evolution for variant 2 was almost identical to variant 1 until the last pass. Due to the faster onset of precipitation after rolling ($t_{ip,7}$ = 10.0 s; see the x-projection of the length of the cooling curve before it intersects with the curve of the onset of precipitation in Figure 19b), there was no termination of static recrystallization (X = 0.42). Thus, the structure contained original unrecrystallized grains about 73 μm in size (58% of

them) elongated in the direction of deformation before the phase transformation, which corresponds well to the measured grain size from the PSCT (72 μm) and recrystallized equal grains 48 μm in size. The residual strain before phase transformation of the austenite was about 0.13.

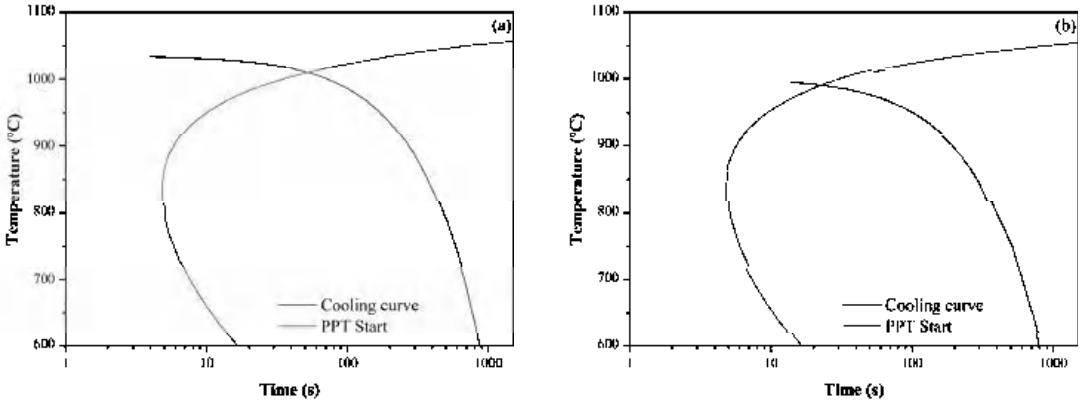

Figure 19. Interaction of cooling curves and precipitation onset curve: (**a**) variant 1 and (**b**) variant 2.

For variant 3, there was a noticeable decrease in grain size due to the reduced temperature before the last three passes. In the 6th pass, strain-induced precipitation (SIP) stopped the ongoing static recrystallization ($X = 0.61$), thus reducing the grain size to 40 μm, which corresponds fairly well to the measured grain size from the PSCT. In the last pass, no static recrystallization occurred despite the accumulated strain from the previous pass; thus, the grain size did not change. Thus, a relatively large, elongated grain (residual strain 0.6) with an area corresponding to an equal grain of 40 μm diameter was present in the structure before phase transformation.

In variant 4, compared to variant 3, SIP already occurred in the 5th pass. The SIP stopped the ongoing static recrystallization ($X = 0.85$), and the grain size after this pass dropped to 63 μm (the smallest of all variants at this rolling stage). However, in the subsequent passes, static recrystallization did not occur, so the grain size did not change. Only the rate of elongation due to the accumulated strain of 0.76 increased.

The mean flow stress (MFS) values predicted by the model were compared with the MFS values calculated from the measured forming forces during the PSCT according to the Formula (9).

$$\sigma = 0.866 \cdot \frac{F}{l_s \cdot b_0} \tag{9}$$

where F (N) is the measured force, l_s (mm) is the length of the contact area between the sample and the anvil (in our case $l_s = 5$ mm) and b_0 (mm) is the width of the tested sample (in our case $b_0 = 20$ mm).

According to the modified Misaka equation, the MFS values were 25 to 100 Mpa lower than the MFS values calculated from the measured forces. Therefore, we built our model in the following form for further simulation:

$$MFS = 6 \cdot e^{0.179} \cdot \dot{e}^{0.081} \cdot \exp\left(\frac{4263}{T}\right) \tag{10}$$

A comparison of all the MFS values calculated from the measured forces according to Equation (10) is plotted in Figure 20. The dependence of MFS on the temperature and strain rate calculated according to Equation (10) is shown in Figure 21.

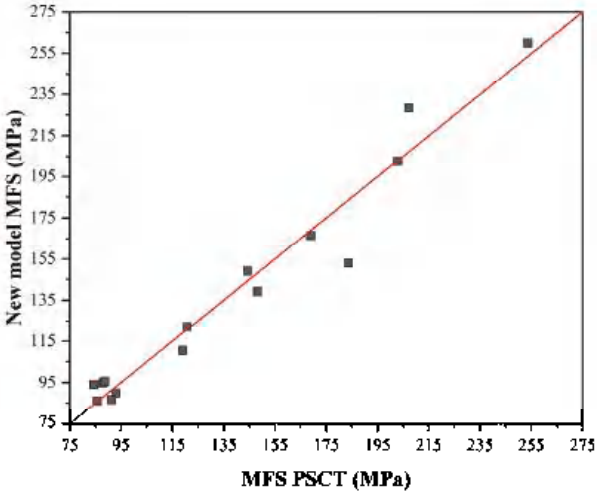

Figure 20. Comparison of measured and calculated MFS values according to Equation (10).

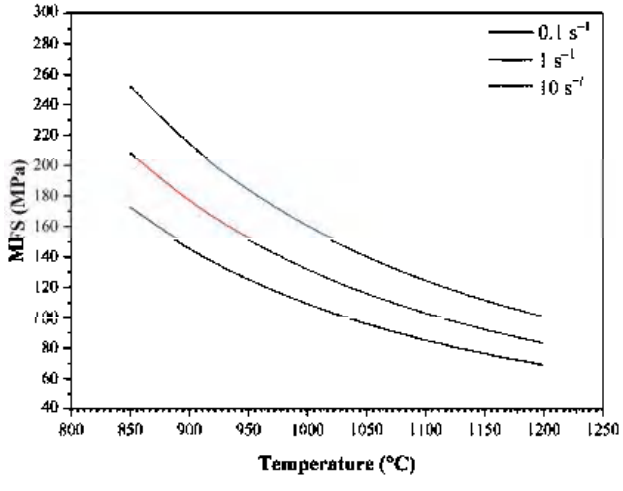

Figure 21. Dependence of MFS on the temperature and strain rate calculated according to Equation (10).

The dependence of the MFS on the reciprocal temperature for all 4 rolling variations is shown in Figure 22. From the 5th pass onwards, we saw an MFS increase due to a rolling temperature decrease. The high MFS value in the 6th pass was due to the largest partial strain increase due to the cumulative strain from the previous passes (for variants 1 to 3, we had a cumulative strain in the 6th pass of about 0.4; for variant 4, it was already 0.56 due to the SIP started in the 5th pass). For variants 1 and 2, the increase in the MFS in the last pass was relatively small compared to the increase for variants V3 and V4, where static recrystallization did not occur due to the ongoing SIP, and we had cumulative strain values of 0.6 and 0.76 in the last pass for variants 3 and 4, respectively. Using a rolling mode that induces SIP while rolling is still in progress, we estimated an MFS increase of at least 50%. In our simulation, this was 53 and 74% for variants 3 and 4, respectively. Similar percentage increases can be expected for roll-separating forces and torques during real rolling.

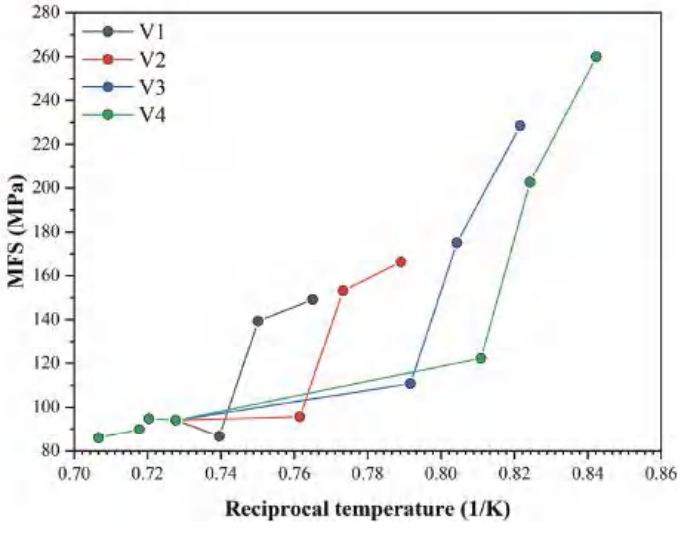

Figure 22. MFS dependencies on reciprocal temperature for each simulation variant.

3.5. Analysis of Precipitate Size Distribution

Simulations of each variant using the modified model were now used to clarify the occurrence of precipitates of different sizes in the PSCT samples for all variants (see Figure 17). All available images from the previous section were subjected to image analysis in ImageJ software. The results of this analysis are presented for all variants using histograms for particle diameter values (calculated from the particle area). Using a single histogram to represent the frequency of occurrence of precipitates of different sizes over the whole observed range from 1 nm to 250 nm is misleading, as fine precipitates are much more abundant than coarse ones. Therefore, we divided the data into two groups (group 1: 1 nm to 40 nm; group 2: 40 nm to 250 nm) using the absolute frequency for fine precipitates and the relative area of coarse precipitates in the structure (area of all precipitates in a given class divided by the total area of all precipitates). Histograms depicting the size distribution of fine precipitates are shown in Figure 23.

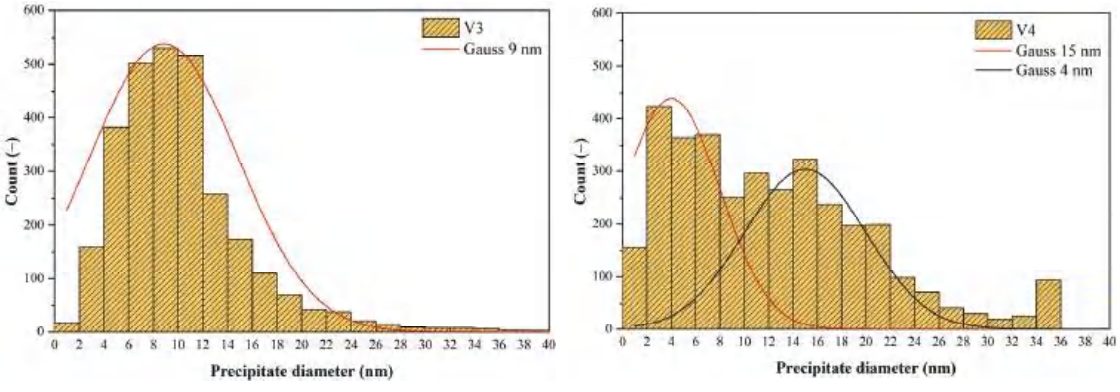

Figure 23. Histograms showing the distribution of precipitates below 40 nm in the samples for V3 (**left**) and V4 (**right**).

For variants 1 and 2, there were practically no precipitates with a size below 40 nm in the structure, so we did not show histograms here. For variant 3, the histogram had a regular bell shape, with a mean value of 9 nm and a standard deviation of 5 nm. For variant 4, we saw a classical two-peaked histogram, which indicates that the data came from two independent sets. The first had a mean value of 4 nm and a standard deviation of 3 nm, while the second had a mean value of 15 nm and a standard deviation of 4 nm.

The histograms in Figure 24 were influenced by the significantly lower frequency of measured data (precipitates below 40 nm were measured in total for variants 3 and 4 over 6300, but those above 40 nm were only 295 for all variants). Here, we also considered two peaks for all variants. One (represented in all graphs by a Gaussian curve with a mean value of 172 nm) corresponded to precipitates not dissolved when heated to the forming temperature. The mean values were calculated from all the variants together because, according to the results of other authors (Vervynckt et al. [25]), it can be assumed that the actual forming regime does not influence the size of the undissolved precipitates. The second peak of the histogram was then at a different mean value of precipitate size for each variant, with the mean value shifting towards smaller values as the number of variants increased.

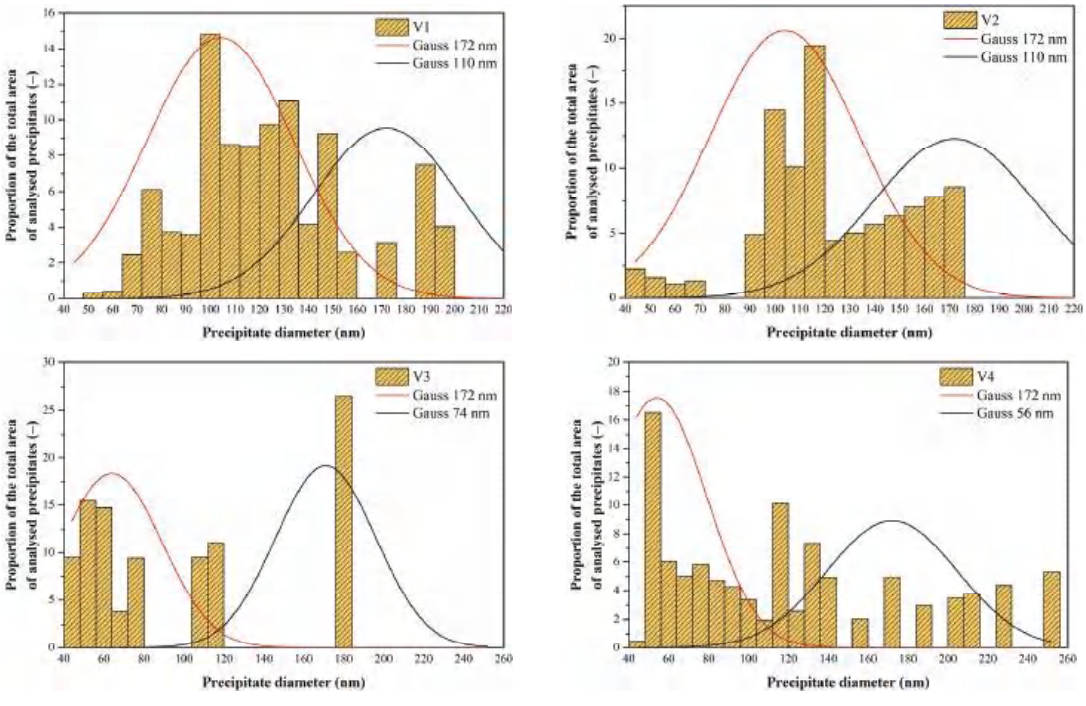

Figure 24. Modified histograms showing the distribution of precipitates above 40 nm in the samples for all variants.

Now that we know the precipitation history by simulating all the modified microstructure evolution model variants, we can analyze the precipitate size distribution in HSLA steel in detail.

For variants 1 and 2, we had two groups of precipitates:

– undissolved precipitates with a mean value of 172 nm;

- precipitates formed during cooling after rolling with mean values for V1 and V2 of 110 and 105 nm, respectively. The lower value for V2 is due to the lower precipitation temperature (1009 °C for V1 vs. 989 °C for V2).

In variant V3, we had 3 groups of precipitates:

- undissolved precipitates with a mean value of 172 nm;
- precipitates formed during cooling after rolling with a mean value of 64 nm (precipitation temperature 944 °C, solid solution partially depleted of Nb due to previous precipitation);
- precipitates formed during precipitation in the pause between the 6th and 7th passes; these have a mean size of only 9 nm due to the limited time for precipitation (24 s).

For variant V4, we had even 4 groups of precipitates:

- undissolved precipitates with a mean value of 172 nm;
- precipitates formed during cooling after rolling with a mean value of 56 nm (precipitation temperature 914 °C, solid solution partially depleted of Nb due to previous precipitation);
- precipitates formed during precipitation in the pause between the 6th and 7th passes; these have a mean size of 15 nm due to the limited time for precipitation (32 s);
- precipitates formed during precipitation in the pause between the 5th and 6th passes; these have an average size of only 4 nm due to the limited time for precipitation (19 s).

Based on these values of precipitation parameters and the corresponding values of precipitate size, it was possible to develop Equation (11) describing the effect of temperature and precipitation time on the size of NbX precipitates:

$$D_{PPT} = 616.9 \cdot t^{0.742} \cdot \exp\left(\frac{-8195.8}{T}\right) \quad (11)$$

The graph in Figure 25 documents the accuracy of Equation (11). The dependence of precipitate size on time and precipitation temperature calculated by Equation (11) is shown in Figure 26. This equation can now be included in the modified microstructure evolution model.

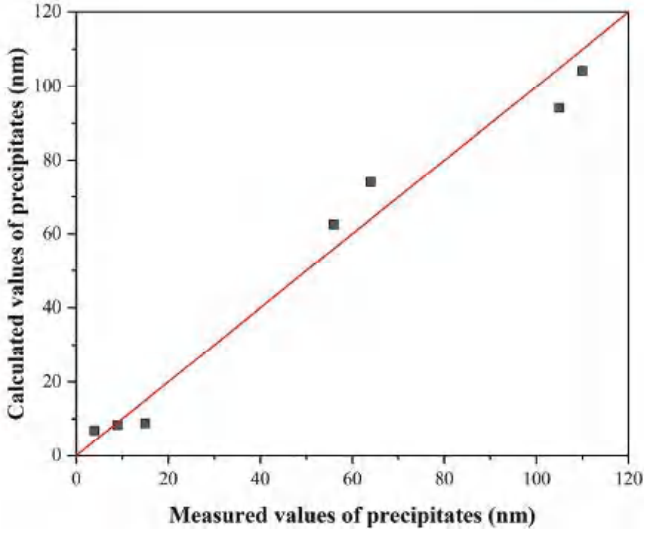

Figure 25. Comparison of measured and calculated values of precipitate size according to Equation (11).

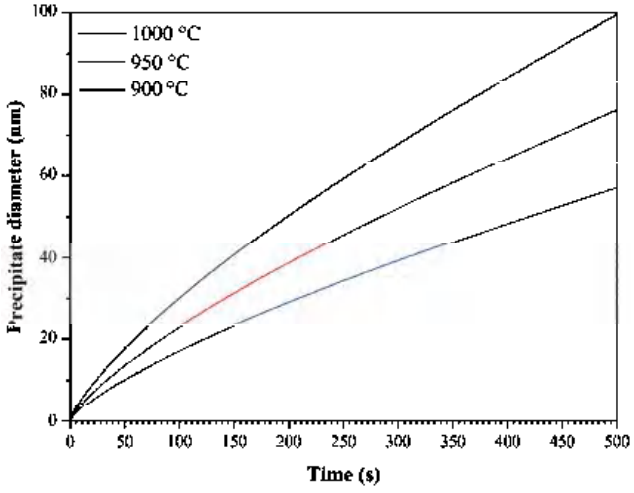

Figure 26. Dependence of precipitate size on the time and temperature of precipitation calculated according to Equation (11).

4. Discussion

Based on the modification of the mathematical model, simulations of the microstructure evolution during the rolling of a round bar from HSLA steel with a diameter of 100 mm were performed, including a comparison with the operational results from a heavy-section mill.

Four situations corresponding to the plain strain compression test were modelled. In the case of the first scenario corresponding to conventional rolling, SIP occurs only after the last pass, which does not affect grain size. The predicted grain size is around 96 μm, which corresponds well to the operational results. The evolution of austenitic grain size is almost identical for variants 1 and 2. Due to the more rapid onset of SIP after rolling, SRX after the last pass is not terminated, and the structure contains original recrystallized grains with a size of about 73 μm elongated in the deformation direction and recrystallized equiaxed of about 48 μm before phase transformation. In the third variant, a noticeable decrease in austenitic grain size can be observed due to the reduced temperature before the last three passes. In the sixth pass, SIP occurs, which stops the ongoing SRX, and thus, the grain size reduces to about 40 μm. In the last pass, despite the accumulated strain from the previous pass, no SRX occurs; therefore, the grain size does not change. Thus, in the structure before phase transformation, a relatively large amount of elongated austenitic grain with a residual strain of 0.6 is present with an area corresponding to an equiaxed grain of 40 μm diameter. Compared to variant 4, there is a suspension of SRX due to SIP in the fifth pass. The grain size in this pass drops to 63 μm, which is the smallest of all simulated variants at this rolling stage. In the following passes, static recrystallization does not occur anymore, so the resulting austenitic grain size does not change. Only the elongation rate due to the accumulated strain of 0.76 increases. All simulation results thus correspond well with the operational results. From the MFS point of view, we can observe an increase in the values from the fifth pass onwards due to the decreasing rolling temperature. The accumulated strain due to the largest partial strain increases the high MFS value in the sixth pass from the previous. For variants 1 and 2, the increase in the last pass is relatively small compared to the increase in variants 3 and 4. Using a rolling mode that induces SIP while rolling, we estimate an increase in the MFS of at least 50%. In the case of our simulations, this was 53% for variant 3 and even 74% for variant 4. Similar percentage increases can be expected for roll-separating forces and torques during real rolling.

Simulations of the different variants were used to clarify the occurrence of precipitates of different sizes, which showed that up to four types of precipitates are present in the investigated samples. These are precipitates that do not dissolve during heating and precipitates that form during rolling between passes, or precipitates that form during cooling.

5. Conclusions

This paper showed a modification of the mathematical model of microstructure evolution that reflects the effect of SIP on SRX kinetics in comparison with existing models. The model showed good agreement with the PSCT simulation results of rolling a 100-mm-diameter round bar of HSLA steel.

Currently, the model is used at Liberty Ostrava to optimize rolling temperatures when rolling round and flat bars and I, V and L profiles on a heavy-section mill (continuous cross-country-type mill). Its verification in rolling bars and profiles on medium- and fine-section mills (continuous mill) is under preparation.

Author Contributions: M.S. processed the results and wrote the first draft of the manuscript, R.F. coordinated the experimental activities and developed a new model for microstructure evolution, I.S. contributed to the data processing, P.K. performed the experiments, P.O. contributed to editing and literary analysis, R.K. analyzed the curves from the PSCT, V.V. evaluated the results of structural analysis and S.R. contributed to the comparison of the results. All authors have read and agreed to the published version of the manuscript.

Funding: The article was created thanks to project no. CZ.02.1.01/0.0/0.0/17_049/0008399 from the EU and CR financial funds provided by the Operational Programme Research, Development and Education, Call 02_17_049 Long-Term Intersectoral Cooperation for ITI, Managing Authority: Czech Republic–Ministry of Education, Youth and Sports, and as part of the students' grant projects SP2022/68 and SP2022/73 supported at the VŠB—TU Ostrava by the Ministry of Education, Youth and Sports of the Czech Republic.

Institutional Review Board Statement: Not applicable.

Informed Consent Statement: Not applicable.

Data Availability Statement: Not applicable.

Acknowledgments: I would like to thank the metallographic laboratories of Liberty Ostrava a.s. for the preparation and analysis of the samples.

Conflicts of Interest: The authors declare no conflict of interest.

References

1. Bhadeshia, H.K.D.H.; Honeycombe, R.W.K. *Steels: Microstructure and Properties*, 4th ed.; Butterworth-Heinemann: Amsterdam, The Netherlands, 2017; ISBN 978-0-08-100270-4.
2. *Mathematical and Physical Simulation of the Properties of Hot Rolled Products*; Elsevier: Amsterdam, The Netherlands, 1999; ISBN 978-0-08-042701-0.
3. *Thermomechanical Processing of High-Strength Low-Alloy Steels*; Elsevier: Amsterdam, The Netherlands, 1988; ISBN 978-0-408-11034-1.
4. Verlinden, B.; Cahn, R.W. *Thermo-Mechanical Processing of Metallic Materials*, 1st ed.; Verlinden, B., Cahn, R.W., Eds.; Pergamon materials series; Pergamon/Elsevier: Amsterdam, The Netherlands; Boston, MA, USA, 2007; ISBN 978-0-08-044497-0.
5. Lin, J.; Balint, D.S.; Pietrzyk, M. *Microstructure Evolution in Metal Forming Processes*; Lin, J., Balint, D.S., Pietrzyk, M., Eds.; Woodhead publishing in materials; Woodhead Publishing: Oxford, UK; Philadelphia, PE, USA, 2012; ISBN 978-0-85709-074-4.
6. Siciliano, F.; Rodrigues, S.F.; Aranas, C.; Jonas, J.J. The Dynamic Transformation of Ferrite Above Ae3 and the Consequences on Hot Rolling of Steels. *TMM* **2020**, *17*, 90–95. [CrossRef]
7. Siciliano, F. Mathematical Modelling of the Hot Strip Rolling of Niobium Microalloyed Steels. Ph.D. Thesis, McGill University, Montreal, QC, Canada, 1999.
8. Phaniraj, M.P.; Behera, B.B.; Lahiri, A.K. Thermo-Mechanical Modeling of Two Phase Rolling and Microstructure Evolution in the Hot Strip Mill. *J. Mater. Process. Technol.* **2006**, *178*, 388–394. [CrossRef]
9. Zhang, Y.; Zhang, H.; Wang, G.; Hu, S. Application of Mathematical Model for Microstructure and Mechanical Property of Hot Rolled Wire Rods. *Appl. Math. Model.* **2009**, *33*, 1259–1269. [CrossRef]
10. Shkatov, V.V.; Mazur, I.P.; Shkatov, V.V. Forecasting the Mean Flow Stress of Carbon and Low-Alloy Steels in Hot Rolling on a Strip Mill. IOP Conf. *Ser. Mater. Sci. Eng.* **2018**, *461*, 012051. [CrossRef]

11. Shkatov, V.; Mazur, I. Modeling the Dynamic Recrystallization and Flow Curves Using the Kinetics of Static Recrystallization. *Materials* **2019**, *12*, 3024. [CrossRef] [PubMed]
12. Sellars, C.M. Modelling Microstructural Development during Hot Rolling. *Mater. Sci. Technol.* **1990**, *6*, 1072–1081. [CrossRef]
13. Dutta, B.; Sellars, C.M. Effect of Composition and Process Variables on Nb (C, N) Precipitation in Niobium Microalloyed Austenite. *Mater. Sci. Technol.* **1987**, *3*, 197–206. [CrossRef]
14. Pereda, B.; Rodriguez-Ibabe, J.M.; López, B. Improved Model of Kinetics of Strain Induced Precipitation and Microstructure Evolution of Nb Microalloyed Steels during Multipass Rolling. *ISIJ Int.* **2008**, *48*, 1457–1466. [CrossRef]
15. Irvine, K.J.; Pickering, F.B.; Gladman, T. Grain-refined C-Mn steels. *Iron. Steel. Inst. J.* **1967**, *205*, 161–182.
16. Siciliano, F.; Maccagno, T.M.; Jonas, J.J.; Nelson, B.D. Modeling of Softening and Precipitation during the Hot Strip Rolling of Niobium Steels. In *THERMEC 97: International Conference on Thermomechanical Processing of Steels and other Materials*; TMS: Warrendale, PA, USA, 1997.
17. Siciliano, F.; Jonas, J.J. Mathematical Modeling of the Hot Strip Rolling of Microalloyed Nb, Multiply-Alloyed Cr-Mo, and Plain C-Mn Steels. *Met. Mat. Trans. A* **2000**, *31*, 511–530. [CrossRef]
18. Minami, K.; Siciliano, F., Jr.; Maccagno, T.M.; Jonas, J.J. Mathematical Modeling of Mean Flow Stress during the Hot Strip Rolling of Nb Steels. *ISIJ Int.* **1996**, *36*, 1507–1515. [CrossRef]
19. Pereda, B.; Fernández, A.I.; López, B.; Rodriguez-Ibabe, J.M. Effect of Mo on Dynamic Recrystallization Behavior of Nb-Mo Microalloyed Steels. *ISIJ Int.* **2007**, *47*, 860–868. [CrossRef]
20. Solhjoo, S.; Ebrahimi, R. Prediction of No-Recrystallization Temperature by Simulation of Multi-Pass Flow Stress Curves from Single-Pass Curves. *J. Mater. Sci.* **2010**, *45*, 5960–5966. [CrossRef]
21. Poliak, E.I.; Jonas, J.J. Prediction of Interpass Softening from the Strain Hardening Rate Prior to Unloading. *ISIJ Int.* **2004**, *44*, 1874–1881. [CrossRef]
22. Radionova, L.V.; Perevozchikov, D.V.; Makoveckii, A.N.; Eremin, V.N.; Akhmedyanov, A.M.; Rushchits, S.V. Study on the Hot Deformation Behavior of Stainless Steel AISI 321. *Materials* **2022**, *15*, 4057. [CrossRef] [PubMed]
23. Yin, L.; Wu, Y. Comparison of Constitutive Models and Microstructure Evolution of GW103K Magnesium Alloy during Hot Deformation. *Materials* **2022**, *15*, 4116. [CrossRef]
24. Wang, Z.; Sun, X.; Yang, Z.; Yong, Q.; Zhang, C.; Li, Z.; Weng, Y. Effect of Mn Concentration on the Kinetics of Strain Induced Precipitation in Ti Microalloyed Steels. *Mater. Sci. Eng. A* **2013**, *561*, 212–219. [CrossRef]
25. Vervynckt, S.; Verbeken, K.; Thibaux, P.; Houbaert, Y. Recrystallization–Precipitation Interaction during Austenite Hot Deformation of a Nb Microalloyed Steel. *Mater. Sci. Eng. A* **2011**, *528*, 5519–5528. [CrossRef]
26. Vervynckt, S.; Verbeken, K.; Thibaux, P.; Liebeherr, M.; Houbaert, Y. Austenite Recrystallization–Precipitation Interaction in Niobium Microalloyed Steels. *ISIJ Int.* **2009**, *49*, 911–920. [CrossRef]
27. Hong, S.G.; Kang, K.B.; Park, C.G. Strain-Induced Precipitation of NbC in Nb and Nb–Ti Microalloyed HSLA Steels. *Scr. Mater.* **2002**, *46*, 163–168. [CrossRef]
28. Maccagno, T.M.; Jonas, J.J.; Yue, S.; McCrady, B.J.; Slobodian, R.; Deeks, D. Determination of Recrystallization Stop Temperature from Rolling Mill Logs and Comparison with Laboratory Simulation Results. *ISIJ Int.* **1994**, *34*, 917–922. [CrossRef]
29. Jorge-Badiola, D.; Gutiérrez, I. Study of the Strain Reversal Effect on the Recrystallization and Strain-Induced Precipitation in a Nb-Microalloyed Steel. *Acta Mater.* **2004**, *52*, 333–341. [CrossRef]
30. Zhong, L.; Wang, B.; Hu, C.; Zhang, J.; Yao, Y. Hot Deformation Behavior and Dynamic Recrystallization of Ultra High Strength Steel. *Met.* **2021**, *11*, 1239. [CrossRef]
31. Medina, S.F. The Influence of Niobium on the Static Recrystallization of Hot Deformed Austenite and on Strain Induced Precipitation Kinetics. *Scr. Metall. Mater.* **1995**, *32*, 43–48. [CrossRef]
32. Medina, S.F.; Mancilla, J.E. Influence of Alloying Elements in Solution on Static Recrystallization Kinetics of Hot Deformed Steels. *ISIJ Int.* **1996**, *36*, 1063–1069. [CrossRef]
33. Medina, S.F.; Quispe, A. Influence of Strain on Induced Precipitation Kinetics in Microalloyed Steels. *ISIJ Int.* **1996**, *36*, 1295–1300. [CrossRef]
34. Medina, S.F.; Quispe, A.; Valles, P.; Baños, J.L. Recrystallization-Precipitation Interaction Study of Two Medium Carbon Niobium Microalloyed Steels. *ISIJ Int.* **1999**, *39*, 913–922. [CrossRef]
35. Medina, S.F.; Quispe, A.; Gomez, M. Model for Strain-Induced Precipitation Kinetics in Microalloyed Steels. *Met. Mat. Trans. A* **2014**, *45*, 1524–1539. [CrossRef]
36. Gómez, M.; Medina, S.F.; Quispe, A.; Valles, P. Static Recrystallization and Induced Precipitation in a Low Nb Microalloyed Steel. *ISIJ Int.* **2002**, *42*, 423–431. [CrossRef]
37. Hodgson, P.D.; Gibbs, R.K. A Mathematical Model to Predict the Mechanical Properties of Hot Rolled C-Mn and Microalloyed Steels. *ISIJ Int.* **1992**, *32*, 1329–1338. [CrossRef]

materials

MDPI

Article

Effects of Austenitization Temperature and Pre-Deformation on CCT Diagrams of 23MnNiCrMo5-3 Steel

Ivo Schindler [1,*], Rostislav Kawulok [1], Petr Opěla [1], Petr Kawulok [1], Stanislav Rusz [1], Jaroslav Sojka [1], Michal Sauer [1], Horymír Navrátil [1] and Lukáš Pindor [2]

[1] Faculty of Materials Science and Technology, VŠB—Technical University of Ostrava, 17. listopadu 2172/15, 70800 Ostrava, Czech Republic; rostislav.kawulok@vsb.cz (R.K.); petr.opela@vsb.cz (P.O.); petr.kawulok@vsb.cz (P.K.); stanislav.rusz2@vsb.cz (S.R.); jaroslav.sojka@vsb.cz (J.S.); michal.sauer@vsb.cz (M.S.); horymir.navratil@vsb.cz (H.N.)

[2] Technology and Research, TŘINECKÉ ŽELEZÁRNY, a. s., Průmyslová 1000, 73961 Třinec, Czech Republic; lukas.pindor@trz.cz

* Correspondence: ivo.schindler@vsb.cz

Received: 15 October 2020; Accepted: 11 November 2020; Published: 13 November 2020

Abstract: The combined effect of deformation temperature and strain value on the continuous cooling transformation (CCT) diagram of low-alloy steel with 0.23% C, 1.17% Mn, 0.79% Ni, 0.44% Cr, and 0.22% Mo was studied. The deformation temperature (identical to the austenitization temperature) was in the range suitable for the wire rolling mill. The applied compressive deformation corresponded to the true strain values in an unusually wide range. Based on the dilatometric tests and metallographic analyses, a total of five different CCT diagrams were constructed. Pre-deformation corresponding to the true strain of 0.35 or even 1.0 had no clear effect on the austenite decomposition kinetics at the austenitization temperature of 880 °C. During the long-lasting cooling, recrystallization and probably coarsening of the new austenitic grains occurred, which almost eliminated the influence of pre-deformation on the temperatures of the diffusion-controlled phase transformations. Decreasing the deformation temperature to 830 °C led to the significant acceleration of the austenite → ferrite and austenite → pearlite transformations due to the applied strain of 1.0 only in the region of the cooling rate between 3 and 35 °C·s^{-1}. The kinetics of the bainitic or martensitic transformation remained practically unaffected by the pre-deformation. The acceleration of the diffusion-controlled phase transformations resulted from the formation of an austenitic microstructure with a mean grain size of about 4 μm. As the analysis of the stress–strain curves showed, the grain refinement was carried out by dynamic and metadynamic recrystallization. At low cooling rates, the effect of plastic deformation on the kinetics of phase transformations was indistinct.

Keywords: low-alloy steel; austenitization temperature; plastic deformation; phase transformations; CCT diagram; dynamic recrystallization

1. Introduction

The individual phase transformations can be effectively controlled by the cooling rate of the rolled or forged steel products. This significantly contributes to achieving the desired combinations of mechanical properties of the material. The kinetics of austenite decomposition is not only fundamentally influenced by the chemical composition of the steel but also by the parameters of the structure entering the given phase transformation. The prior microstructure depends on the austenitization conditions, the parameters of the pre-deformation, and the cooling time [1–6]. The continuous cooling transformation (CCT) diagrams show the temperatures of the phase transformations, and the individual decomposition

products of austenite depend on the cooling at different rates. They are always constructed for the specific austenitization parameters and initial microstructure. The deformation continuous cooling transformation (DCCT) diagrams include the effect of pre-deformation, characterized mainly by the strain value [7–11].

The very complex influence of chemical composition on the kinetics of austenite decomposition has been studied in detail in many works. For example, the combined effect of manganese, silicon, nickel and vanadium [12], niobium, copper, silicon and molybdenum [13], carbon, manganese, silicon, chromium, molybdenum and vanadium [14], or niobium alone as the microalloying element content has been investigated in different steels [15,16].

From the point of view of the influence of the prior structure, the size of austenitic grains is a crucial parameter (both the initial and secondary grain size, which can also be influenced by the austenitization conditions) [17,18]. The cause of the coarsening of the prior structure is a high heating temperature, a long stay at the austenitization temperature, or a long time interval between austenitization (or deformation at this temperature) and the phase transformation itself; this applies in particular to the very low cooling rates. On the contrary, dynamic recrystallization induced by deformation at a suitable combination of temperature and strain rate can be used to refine the austenitic grains [19–21]. The influence of the austenitic grain size is significant, especially where transformations take place with a diffusion mechanism, which preferably uses the boundaries of the original grains for the nucleation of the new phase components. In the case of smaller austenitic grains, the matrix contains a higher density of grain boundaries and thus more nucleation sites, which mainly accelerates the ferritic transformation [18–24]. The fine-grained austenitic microstructure also leads to a reduction in the critical deformation for a ferrite formation by dynamic strain-induced transformation (DSIT) and to a relatively homogeneous size distribution of ferritic grains. Conversely, in the case of a coarse-grained prior structure, the newly formed ferritic grains are primarily located along the boundaries of the austenitic grains [25–28]. However, this conclusion is only valid in the case of allotriomorphic ferrite. With the increasing size of the prior austenitic grains, intragranular nucleation of ferrite indirectly favors (e.g., at inclusions located inside the austenitic grains), leading to the formation of idiomorphic ferrite instead of allotriomorphic ferrite [29]. The austenitic grain size also plays an important role in the kinetics of pearlitic transformation, as the most favorable conditions for a pearlite nucleation are in the high-energy locations. These places in the homogeneous austenite are mainly the grain boundaries, where the greatest accumulation of crystal lattice defects is. In the case of coarse-grained steels, the rate of austenite → ferrite transformation is lower, because the density of sites favorable to nucleation is low [22,30–32].

The coarse austenitic grains support the martensitic transformation by increasing the temperature of its start and finish. The austenitic grain size also impacts the morphology of martensite, because the coarse-grained structure affects the size of martensitic plates or needles [20,33,34].

The major effect of the previous plastic deformation should be the displacement of the phase transformations to higher temperatures and shorter times. This is caused by the increased diffusivity of elements in the deformed austenite and a higher density of the favored nucleation places for the diffusional transformation products. Such places are found particularly in the shear bands and grain boundaries with high density of dislocations [35–37].

The accelerating effect of plastic deformation on ferritic or pearlitic transformation has been confirmed by many researchers—see, e.g., [14,22,38–41]. This phenomenon is used in practice, for example, in achieving ultrafine-grained structures through strain-induced ferrite transformation (DSIT) of austenite to ferrite [42]. The strain-induced ferrite transformation (DIFT) has been identified as a very effective mechanism contributing to the grain refinement of the transformation-induced plasticity (TRIP) steel at just below the austenite → ferrite transformation temperature [43].

The impact of plastic deformation on the bainitic transformation varies depending on the strain value and especially on the chemical composition of the steel. There are two opposing phenomena in deformed austenite. The nucleation of the new phase component is accelerated, because the nuclei

first form in the deformation bands as narrow ferritic particles lined with carbides. At the same time, however, the growth of nuclei by the shear mechanism is delayed. The growth rate of nuclei can also be affected by the deformation-induced precipitation of carbides, which act as barriers to the movement of the phase interface. However, if the plastic deformation takes place even during the bainitic transformation itself, this structure-forming process is significantly accelerated [44–48].

As for the martensitic transformation, the previous plastic deformation usually has a slight decelerating effect. During the deformation of austenite, a dense dislocation network is formed, which slows down the phase interface movement. Despite the large number of nuclei, the portion of the new phase component tends to be smaller than in the case of the transformation of undeformed austenite, especially at higher cooling rates. Sometimes, however, the opposite phenomenon occurs when the accumulated lattice defects initiate the formation of martensite, and it begins to form at relatively higher temperatures [49–51].

The influence of the strain value on the kinetics of phase transformations is ambiguous. Varying the strain value from 5 to 25% had no influence on the phase transformations in manganese–nickel and manganese low-alloy steels but modified the microstructure after cooling due to the formation of coarser austenite grains under deformation of the "critical" strain value [52]. It depends considerably on the deformation temperature and thus on whether the already recrystallized austenitic or deformed grains enter the phase transformation. This is evidenced by the comparison of the CCT and DCCT diagrams constructed for the 34CrMo4, 42CrMo4, 52CrMo4, 51CrV4, and 34NiMo6 steels at a strain value of 0, 30, and 60% [22]. Due to the high temperature of plastic deformation (i.e., 1200 °C), the individual phase transformations were not affected directly by the deformation strengthening but only indirectly by the size of the recrystallized austenitic grain. Therefore, due to the pre-deformation, only slight changes in the curves corresponding to the start and finish of the phase transformations were observed.

2. Experimental Material and Methods

The aim of the experimental work was to investigate the combined effect of the deformation temperature and strain value on the continuous cooling transformation diagram of steel low-alloyed with manganese, nickel, chromium, and molybdenum. The deformation temperature (identical to the austenitization temperature) should be in the range suitable for the particular continuous wire rolling mill. The applied plastic deformation intentionally corresponded to the true strain values in an unusually wide range (from 0 to 1.0) to reflect the intensive accumulation of strengthening during multi-pass wire rolling in the finishing blocks.

The 23MnNiCrMo5-3 steel is currently one of the most required materials for the production of chains, in terms of price–quality ratio. After cooling from the finish-rolling temperature, it is suitable to achieve the highest possible bainite content in its microstructure. According to operational experience, bainite appears to be the most suitable structural component for annealing, which precedes the actual production of chains. This steel can be used for the welded round link chains and various components for chain hoists, chain conveyors in the mining industry, etc. The final properties of these products are then affected by quenching and tempering. The chemical composition of this low-alloy steel, tested in the hot rolled state, is presented in Table 1. The steel was melted and cast in TŘINECKÉ ŽELEZÁRNY a. s. (Třinec, Czech Republic).

Table 1. Chemical composition of the investigated steel in wt.%.

C	Mn	Si	P	S	Ni	Cr	Mo	Al	N
0.23	1.17	0.16	0.015	0.006	0.79	0.44	0.22	0.034	0.0056

For the purpose of the experiment, the simple cylindrical samples with a diameter of 6 mm and length of 86 mm were prepared from the wire with a diameter of 10 mm. The dilatometric tests

were performed with the use of the Model 39,112 Scanning Non-Contact Optical Dilatometer and Extensometer System with Green LED Technology of the Gleeble 3800 Hot Deformation Simulator (Dynamic Systems Inc., Poestenkill, NY, USA). Radial components of the strain of the sample can be measured with a repeatability of ±0.3 µm by a frequency of up to 2400 Hz.

The first step was to determine the transformation temperature A_{c3} (i.e., the temperature at which the ferrite is completely transformed into austenite by the heating process). The sample was heated with a rate of 5 °C·s^{-1} to a temperature of 500 °C; then, the heating rate was slowed down to 0.167 °C·s^{-1} to reach the maximum temperature of 1000 °C. Evaluation of the measured data was carried out using the semi-automatic CCT software (Dynamic Systems Inc., Poestenkill, NY, USA), which applies the tangential method in combination with the derivative of the dilatation curve to determine the transformation temperatures. The result of this test is presented in Figure 1.

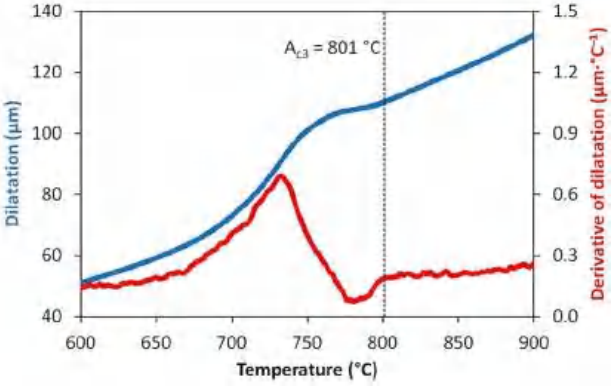

Figure 1. Determination of the transformation temperature A_{c3} for the tested steel.

Based on the experimentally obtained value A_{c3} = 801 °C and the finish-rolling temperature commonly used on the continuous wire mill in TŘINECKÉ ŽELEZÁRNY a. s., the austenitization temperature T_A = 880 °C was used in the first stage of the dilatometric experiments. This value corresponds to the requirements of DIN 17115 German standard for the quenching temperature of the studied steel, which is 870 to 890 °C. The samples were resistively heated at a rate of 10 °C·s^{-1} in the measured zone to the austenitization temperature and after a duration of 600 s, they were deformed by uniaxial compression at a strain rate of 1 s^{-1} to the value of the true strain e = 0.35 or 1.0 (for construction of the DCCT diagrams), or no deformation was applied (i.e., e = 0; for construction of the CCT diagram) before the controlled cooling to almost room temperature. Constant nominal cooling rates in the range of 0.2–50 °C·s^{-1} were achievable using the samples described above. To achieve cooling rates of 100 or 200 °C·s^{-1}, the samples had to have a special hollow-head shape for high-speed cooling realized by air nozzles. Unfortunately, such a sample does not allow any deformation in principle before dilatometric measurement in the course of cooling. Figure 2 shows the shape of the central parts of the simple dilatometric samples after various deformations.

The dilatometric results were verified by metallographic analyses and HV30 hardness measurement; these tests were performed on a cross section, taken in the middle of the length of the heated part of the samples. Samples intended for the light-microscopy analysis were prepared by using mechanical grinding and polishing. The microstructure was revealed via etching with the 4% Nital solution (a mixture of nitric acid and ethanol) and observed on the Olympus GX51 inverted metallurgical microscope (Olympus Corporation, Tokyo, Japan). In the case of visualization of the prior austenitic grain boundaries in the selected quenched samples, a solution of 50 g of picric acid and 5 g of ferric chloride in 100 mL of distilled water was used as an etchant. The quenched samples were pre-heated to 40 °C, and the etching time was chosen differently based on the partial results. A linear

intercept technique for measuring the average size of austenitic grains by software QuickPHOTO Industrial 3.2 (PROMICRA, s.r.o., Prague, Czech Republic) was used, and only the grains with clearly drawn boundaries were taken into account. At least 217 grains were thus measured for each sample.

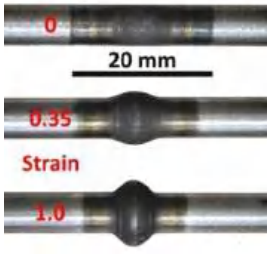

Figure 2. The shape of the samples after dilatometric testing—details of the heated central part.

After evaluating the results of the first stage of the dilatometric tests, the experiments were repeated in the second stage for a lower austenitization temperature of 830 °C. This value is based on the operating limits of the relevant rolling mill and is particularly interesting in terms of the possible refinement of the prior austenitic grains. In this case, only strains $e = 0$ or $e = 1.0$ were used. In total, two CCT diagrams and three DCCT diagrams were compiled for the investigated steel.

Stress–strain curves were experimentally determined for the strain rate of 1 s^{-1} and deformation temperatures of 880 °C and 830 °C. Uniaxial compression tests were performed on a Gleeble 3800 simulator. Cylindrical specimens with a diameter of 8 mm and a height of 12 mm were heated in the same mode as in the case of dilatometric tests. The critical strain values of e_c required to initiate dynamic recrystallization were calculated from the obtained flow curves according to the procedure described and applied, e.g., in [53–56]. In the beginning, the first derivative of the stress- strain curve in its up-to-peak region with respect to the true strain has to be gained. Secondly, the obtained derivative (specifically the dependency of the logarithm of strain-hardening rate ln θ versus true strain e) is described by means of the third-degree polynomial. The inflection point, i.e., the result of the second derivative of this polynomial with respect to the true strain put into the equality with zero, then corresponds with the required value of strain e_c—see Figure 3 for an example. The analysis of the flow curves was performed using data smoothing and numerical derivative in the OriginPro 9 software (OriginLab Corporation, Northampton, MA, USA).

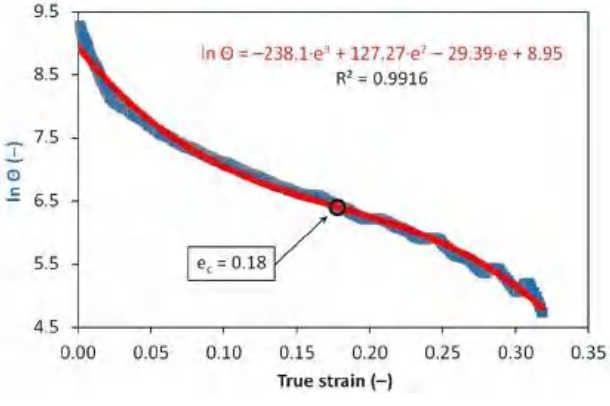

Figure 3. Determination of strain e_c for deformation temperature of 880 °C.

3. Results and Discussion

3.1. CCT and DCCT Diagrams

The graphs in Figures 4–8 show the temperatures of the individual phase transformations (black points) for different experimental conditions; these values were determined based on the analysis of dilatometric curves. The manually interpolated curves form the boundaries of areas characterized by the existence of a particular phase component—ferrite (F), pearlite (P), bainite (B), and martensite (M).

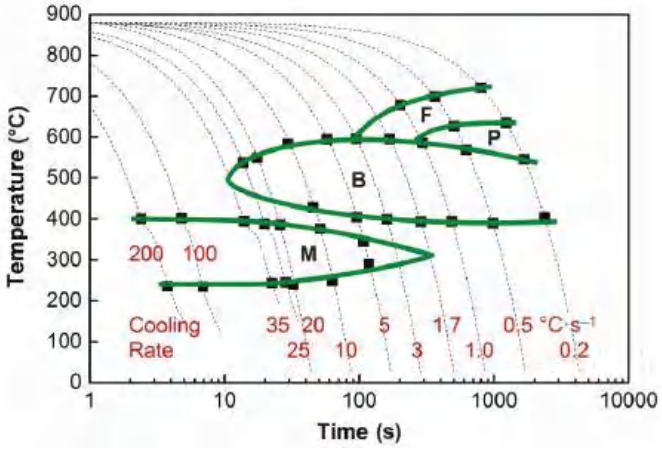

Figure 4. Continuous cooling transformation (CCT) diagram (e = 0) for the austenitization temperature of 880 °C.

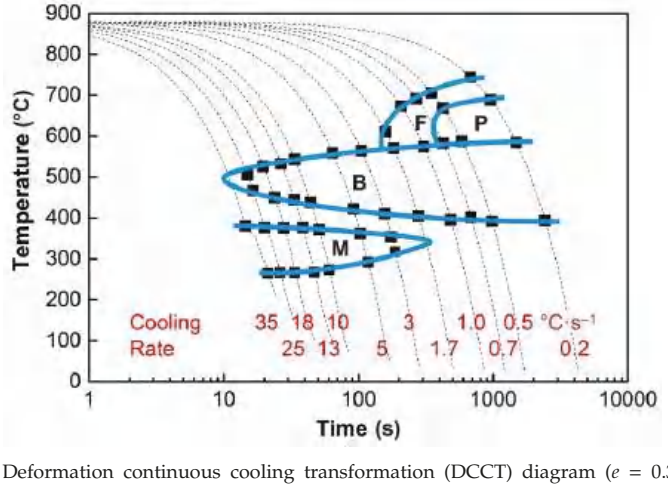

Figure 5. Deformation continuous cooling transformation (DCCT) diagram (e = 0.35) for the austenitization temperature of 880 °C.

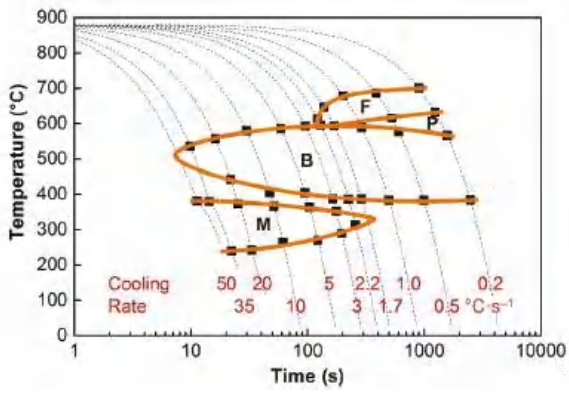

Figure 6. DCCT diagram (e = 1.0) for the austenitization temperature of 880 °C.

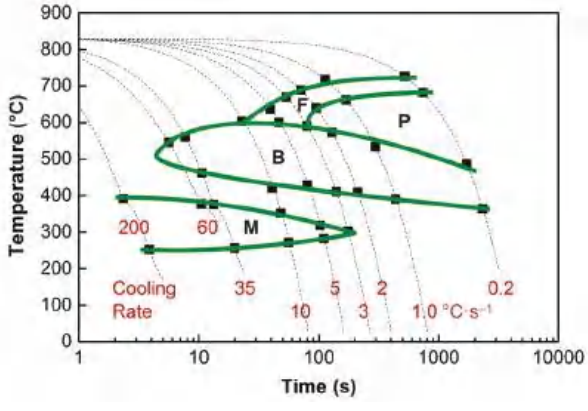

Figure 7. CCT diagram (e = 0) for the austenitization temperature of 830 °C.

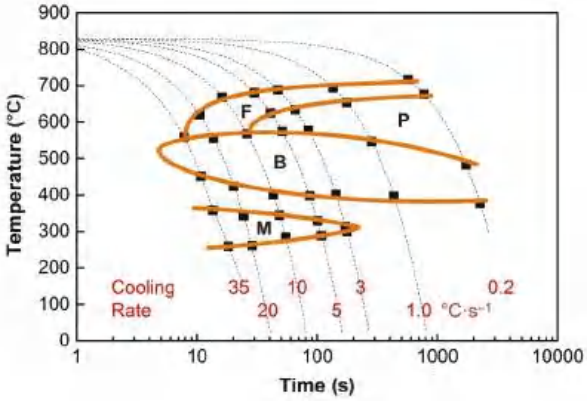

Figure 8. DCCT diagram (e = 1.0) for the austenitization temperature of 830 °C.

The chemical composition of the investigated steel ensures the presence of bainite in the structure already after cooling at a rate of 0.2 °C·s^{-1}. To induce a martensitic transformation, cooling at a rate of approx. 2–3 °C·s^{-1} is always sufficient. The decomposition of austenite to ferrite and pearlite is significantly affected only by deformation at low austenitization temperature.

3.2. Phase Composition of Samples after Dilatometry

The results of metallographic analyses are summarized in Table 2. The fractions of the structural components are arranged from the largest (left) to the smallest (right). The meaning of the parentheses is as follows: (very small amount), [rare, trace amount]. The data in Table 2 are documented by the microstructure of selected samples after dilatometry (see Figures 9–13).

Table 2. Phase composition of the selected samples after dilatometry.

Cooling	Austenitization Temperature/True Strain				
Rate	T_A = 880 °C			T_A = 830 °C	
(°C·s^{-1})	e = 0	e = 0.35	e = 1.0	e = 0	e = 1.0
0.2	F + P + B	F + P + B	F + B + P	F + P + B	F + B + P
0.5	–	B + F + (P)	–	–	–
0.7	–	B + F + (P)	–	–	–
1.0	F + B + (P)	–	F + B + (P)	F + B + (P)	F + B + (P)
1.7	B + M + (F)	B + M + [F]	B + M + (F) + [P]	–	–
2.2	–	–	B + M + [F]	–	–
3.0	B + M + [F]	B + M	B + M	B + M + F + [P]	B + M + F + (P)
5.0	M + B	–	–	B + M + [F]	M + B + F + [P]
10	–	M + B	–	B + M + [F]	M + B + (F)
20	–	–	–	–	M + B + [F]
25	M + (B)	M + (B)	–	–	–
35	M + (B)	M + (B)	M + (B)	M + (B)	M + (B) + [F]
50	–	–	M + [B]	–	–
100	M	–	–	–	–
200	–	–	–	M	–

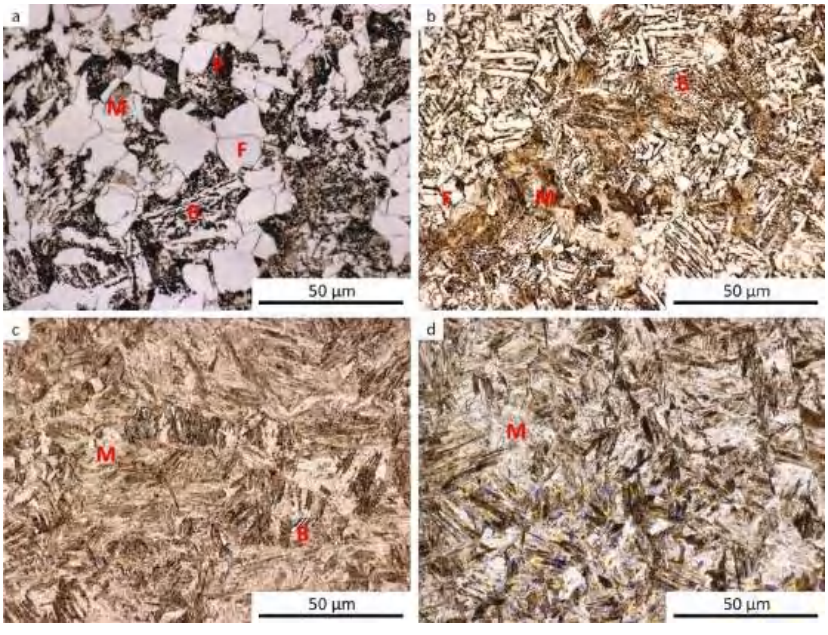

Figure 9. Microstructure of the samples after dilatometry—austenitization at 880 °C, undeformed. (**a**) Cooling rate of 0.2 °C·s^{-1}; (**b**) cooling rate of 3 °C·s^{-1}; (**c**) cooling rate of 35 °C·s^{-1}; (**d**) cooling rate of 100 °C·s^{-1}.

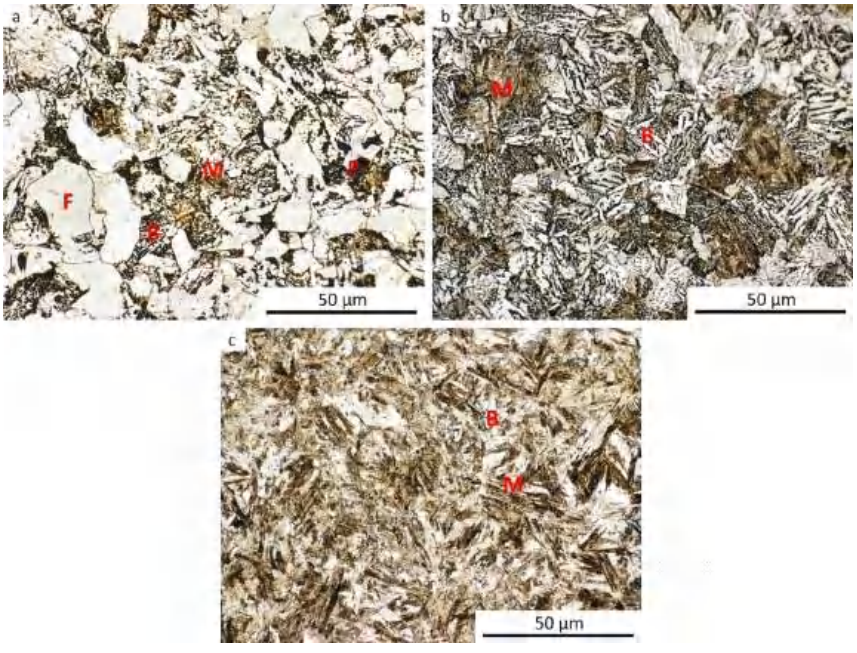

Figure 10. Microstructure of the samples after dilatometry—austenitization at 880 °C, strain $e = 0.35$. (**a**) Cooling rate of 0.2 °C·s^{-1}; (**b**) cooling rate of 3 °C·s^{-1}; (**c**) cooling rate of 35 °C·s^{-1}.

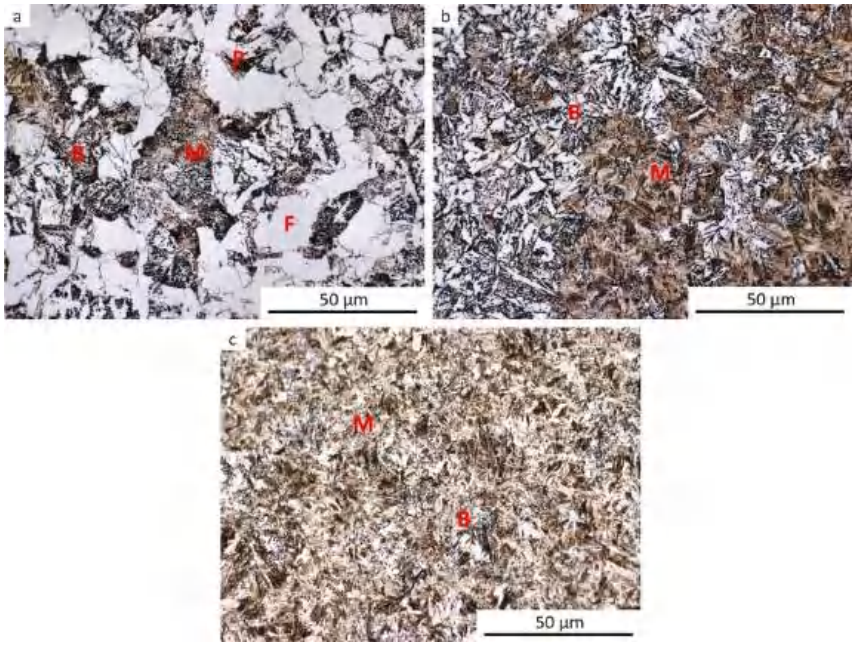

Figure 11. Microstructure of the samples after dilatometry—austenitization at 880 °C, strain $e = 1.0$. (**a**) Cooling rate of 0.2 °C·s^{-1}; (**b**) cooling rate of 3 °C·s^{-1}; (**c**) cooling rate of 35 °C·s^{-1}.

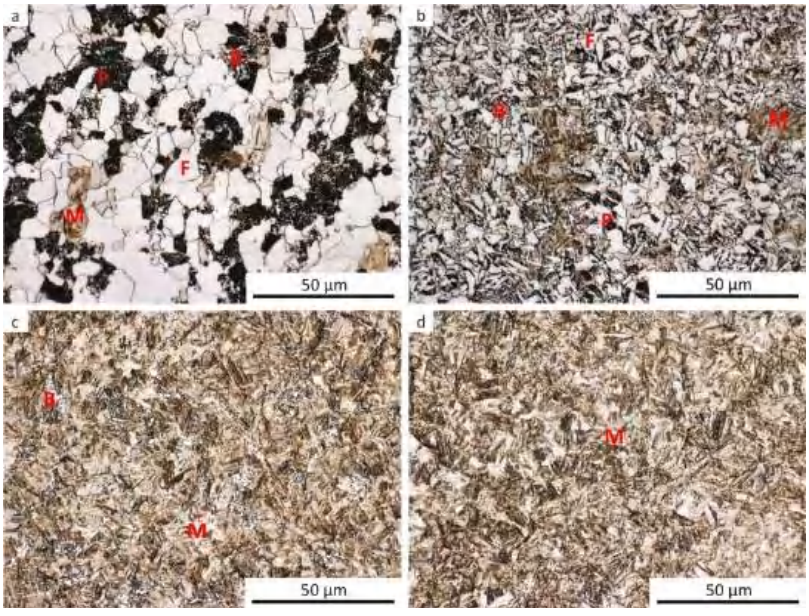

Figure 12. Microstructure of the samples after dilatometry—austenitization at 830 °C, undeformed. (**a**) Cooling rate of 0.2 °C·s^{-1}; (**b**) cooling rate of 3 °C·s^{-1}; (**c**) cooling rate of 35 °C·s^{-1}; (**d**) cooling rate of 100 °C·s^{-1}.

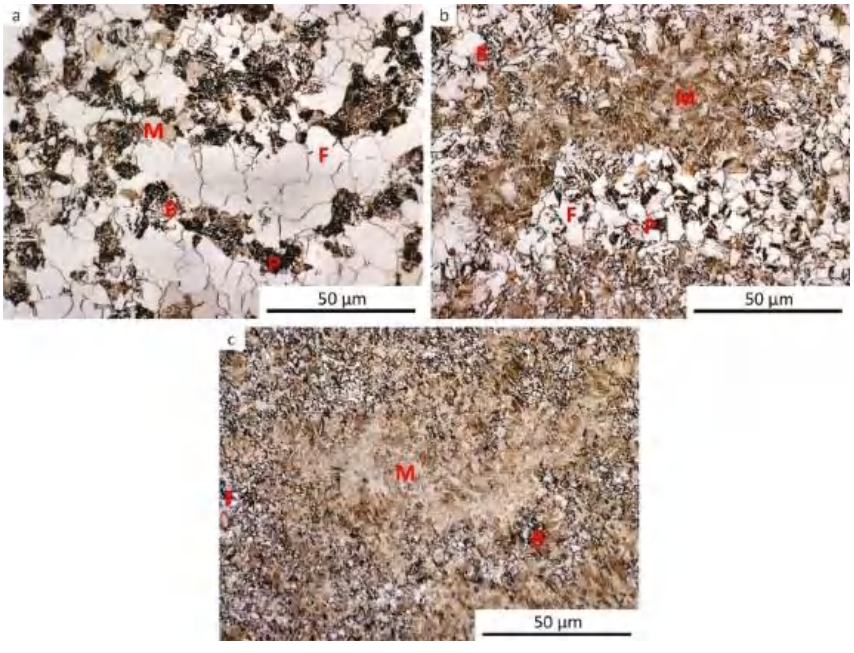

Figure 13. Microstructure of the samples after dilatometry—austenitization at 830 °C, strain e = 1.0. (**a**) Cooling rate of 0.2 °C·s^{-1}; (**b**) cooling rate of 3 °C·s^{-1}; (**c**) cooling rate of 35 °C·s^{-1}.

It should be noted that martensite was found in all samples, at least in trace amounts, even after cooling at the lowest rate. This occurrence of martensite was so small that it could not be manifested in the analysis of the dilatation curves. The minor local occurrence of martensite in microsegregations (probably of manganese and chromium [57]) was documented in the photographs (see Figure 9a for an example) but was not included in Table 2. In case of the cooling rate minimization and quasi-equilibrium conditions' achievement in the dilatometry of the investigated steel, the fraction of ferrite and perlite would further increase at the expense of the bainite and martensite content. However, due to the existence of microsegregations, some trace occurrence of martensite cannot be excluded even under these conditions.

For comparison, a metallographic analysis of the initial hot-rolled structure of the investigated steel was also performed (see Figure 14). Due to its phase composition, this microstructure is close to structures obtained after dilatometric testing from the lower austenitization temperature and using the cooling rate of about 3 °C·s^{-1}. The hot-rolled microstructure appears to be somewhat coarser.

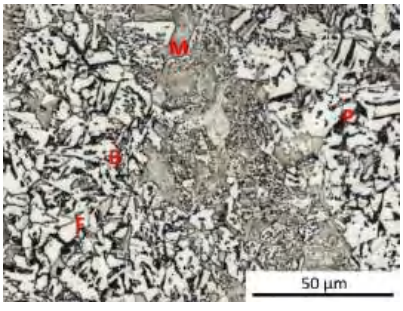

Figure 14. Structure components in the initial hot-rolled state.

3.3. Hardness Influenced by the Cooling Rate

Table 3 presents the hardness values measured for selected samples after dilatometry. The HV30 hardness in the range of about 225 to 495 was achieved. As the cooling rate increases, the total fracture of bainite and martensite in the structure increases, leading to steady growth in hardness. After cooling at a rate of 50 °C·s^{-1} and higher, the structure consists almost exclusively of martensite and the hardness remains practically stable.

Table 3. Hardness HV30 of the selected samples after dilatometry.

Cooling	Austenitization Temperature/True Strain				
Rate	T_A = 880 °C			T_A = 830 °C	
(°C·s^{-1})	e = 0	e = 0.35	e = 1.0	e = 0	e = 1.0
0.2	223	228	243	229	223
0.5	–	255	–	–	–
0.7	–	263	–	–	–
1.0	258	–	266	260	268
1.7	267	283	277	–	–
2.2	–	–	303	–	–
3.0	294	309	328	293	300
5.0	347	–	–	308	319
10	–	400	–	355	358
20	–	–	–	–	387
25	472	443	–	–	–
35	478	475	487	462	428
50	–	–	497	–	–
100	500	–	–	–	–
200	–	–	–	494	–

3.4. Comparison of the Results

The comparative graph in Figure 15 shows that, for 23MnNiCrMo5-3 steel, it is not possible to unambiguously determine the effect of deformation on the kinetics of phase transformations after high-temperature austenitization. Both the bainitic and martensitic regions remain almost intact by the pre-deformation. The only significant deviation is the course of the perlite-start curve after deformation $e = 0.35$.

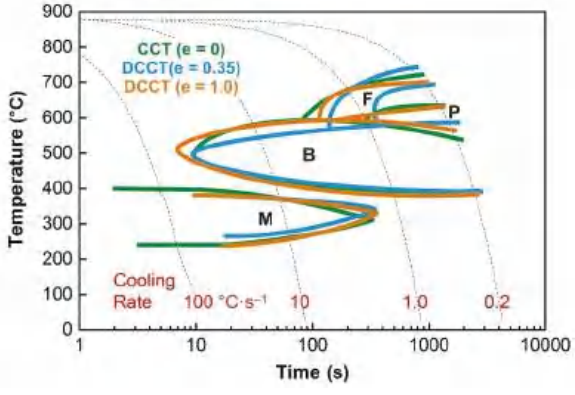

Figure 15. Comparison of the transformation diagrams for the austenitization temperature of 880 °C.

Such behavior is surprising and inconsistent with the results of many other studies on the effect of plastic deformation on the continuous cooling transformation diagrams [1–3,5,6,10,14,22,38–41,58]. However, less unambiguous data can be found comparing the CCT and DCCT diagrams for some steels. The effect of austenitization temperature (940 °C or 1000 °C) as well as the pre-deformation (true strain of 0 or 0.35) was quite insignificant in the case of high-carbon steel with 0.73% C [37]. Relatively low strain values of up to 25% had almost no effect in manganese–nickel and manganese low-alloy steels [52]. For the HSLA steel microalloyed with niobium and vanadium, the CCT and DCCT (strain $e = 0.35$) diagrams differed only slightly after austenitization at 900 °C [7]. At cooling rates below about 4 °C·s^{-1}, the ferrite-start temperatures were even lower in the case of pre-deformation. This deceleration of austenite → ferrite transformation at the slow cooling rates could have been caused by the static recrystallization of deformed austenite, followed by a certain grain growth. A similar result was presented in article [1] for steel containing 0.28% C, 1.41% Mn, 0.26% Cr, 0.22% Mo, 0.027% Nb, 0.028% Ti, 0.019% V, and 0.003% B; the austenitizatin temperature was 885 °C and true strain $e = 0.69$. The pre-strain $e = 0.2$ after austenitization at 900 °C did not influence the ferrite-start transformation temperatures at all, and the ferrite-finish transformation temperatures increased only at cooling rates above 5 °C·s^{-1} [8].

In the case of low-temperature austenitization, the results for the 23MnNiCrMo5-3 steel already correspond to the theoretical assumptions—see Figure 16. The plastic deformation almost does not affect the austenite → bainite or austenite → martensite transformation, but it fundamentally expands the ferrite and pearlite regions towards the higher cooling rates. At low cooling rates (approx. below 2 °C·s^{-1}), the effect of deformation on the ferrite-start or pearlite-start temperature is more or less not manifested.

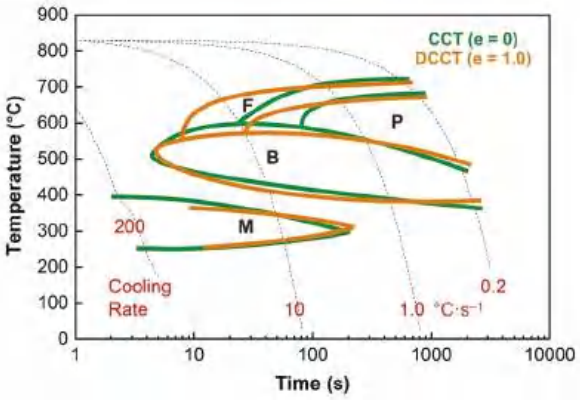

Figure 16. Comparison of the transformation diagrams for the austenitization temperature of 830 °C.

Qualitatively similar results were obtained when testing bainitic steel containing 0.04% C, 1.0% Mn, 1.0% Cr, and 0.065% Nb after austenitization at 880 °C [59]. The pre-deformation with a total strain of 0.6 and a strain rate of 1 s^{-1} had a great effect on the structural constituents. In the case of the CCT diagram, the microstructure was a mixture of bainitic ferrite and granular bainite over a wide range of the cooling rates. Plastic deformation of austenite changed the microstructure to fully polygonal ferrite at all the investigated cooling rates, apart from the appearance of a very small fraction of pearlite at cooling rates ranging from 2 to 20 °C·s^{-1}. The acceleration of the phase transformation austenite → ferrite due to plastic deformation was very effective in this case.

The graph in Figure 17 also corresponds well to the comparative Figures 15 and 16. Considering the common scatter of the measured values, it can be stated that after high-temperature austenitization, the hardness is not affected by the previous strain value—see the trend indicated by the solid curve. In the medium cooling rate range, the hardness of the samples austenitized at 830 °C is relatively lower. This is particularly evident in the case of the pre-deformation e = 1, primarily due to the increased content of soft ferrite (see the dashed line).

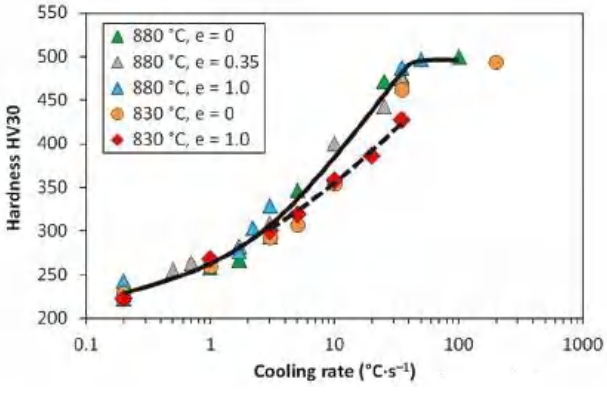

Figure 17. Hardness as a function of experimental conditions and cooling rate.

A definite explanation of the causes of these phenomena is not easy, because we do not always have evidence of the nature of the austenitic structure entering the relevant phase transformation. This mainly concerns the low cooling rates, leading to the decomposition of austenite into ferrite and pearlite. Conversely, after higher cooling rates, it is relatively easier to obtain information about the

prior austenitic grains by etching the as-quenched material. The visualization of such grain boundaries is documented by examples in Figure 18.

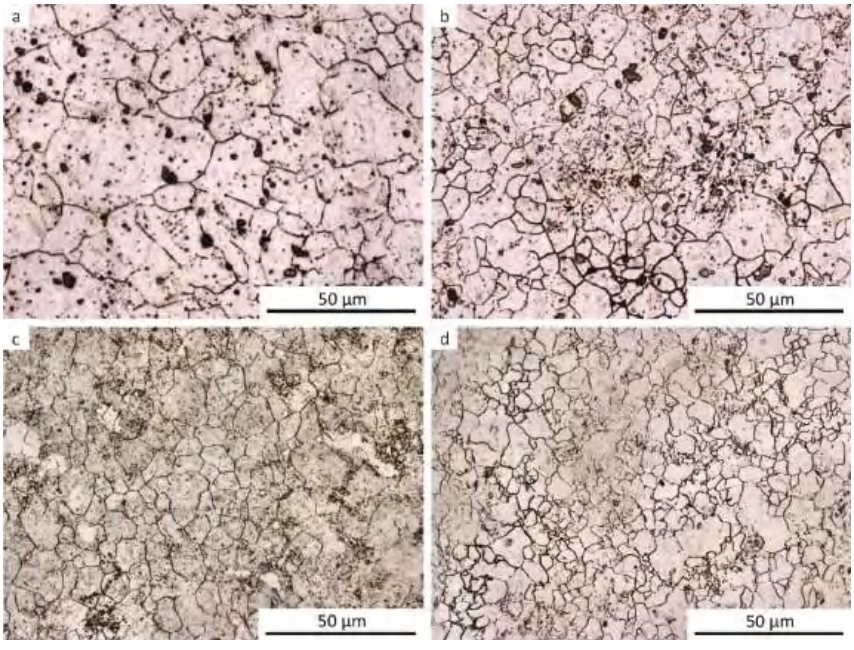

Figure 18. Prior austenitic grain boundaries in the samples cooled at a rate of 10 °C·s^{-1}. (**a**) T_A = 880 °C, undeformed; (**b**) T_A = 880 °C, strain e = 1.0; (**c**) T_A = 830 °C, undeformed; (**d**) T_A = 830 °C, strain e = 1.0.

After deformation and cooling, the austenitic grains were always more or less equiaxed but with considerably different sizes. This indicates an uneven course of recrystallization and probably also the growth of some recrystallized grains.

The prior austenitic grain data for samples cooled at a rate 10 °C·s^{-1} are compared in Figure 19. Confidence intervals (see the red vertical line segments) were estimated for the significance level α = 0.05.

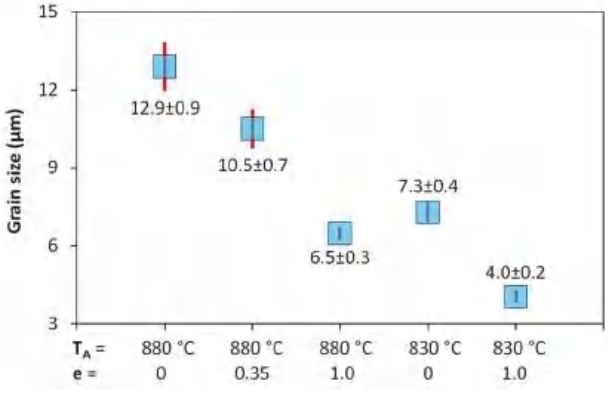

Figure 19. Influence of the austenitization and deformation parameters on the size of prior austenitic grains.

Reducing the austenitization temperature by 50 °C decreased the austenitic grain size after heating by almost half. The plastic deformation of $e = 1.0$ resulted in grain refinement of about 50% at an austenitization temperature of 880 °C and 45% at an austenitization temperature of 830 °C, respectively. However, these changes in the prior structure significantly affected the kinetics of phase transformations only in the case of low-temperature austenitization. Thus, it is not only the absolute grain size that could be decisive but probably also the type of softening processes taking place during the cooling of the deformed austenite. The graph in Figure 20 plots parts of the hot flow curves around the stress peak corresponding to both austenitization temperatures and strain rate of 1 s^{-1}. From the calculated values of e_c, it is clear that at both used deformation temperatures the strain $e = 0.35$ is sufficient to start the dynamic recrystallization. Consequently, a combination of metadynamic and static recrystallization can be expected during cooling in this case. The strain $e = 1.0$ corresponds to a steady state for both temperatures, and only metadynamic recrystallization should occur during cooling. Thus, the post-dynamic softening mechanisms did not differ significantly after the intense plastic deformation performed at a temperature of 830 °C or 880 °C. The key will be the role of cooling time, of course longer in the case of the higher austenitization and deformation temperature. At low cooling rates, these times are prolonged, which allows the more perfect softening of the deformed structure and possibly also coarsening of the austenitic grains before the actual phase transformation. The decomposition of austenite is markedly different only in the case of a single combination of experimental conditions (T_A = 830 °C and $e = 1.0$), when there is a significant shift of the ferrite-start and pearlite-start curves towards the shorter times (see Figures 15 and 16). In this case, the austenitic grain size of 4.0 μm is almost 40% smaller than in the test performed at T_A = 880 °C and $e = 1.0$ (i.e., 4.0 μm vs. 6.5 μm—see Figure 19). This is true for the area of medium cooling rates (close to 10 °C·s^{-1}), where the differences between the CCT and DCCT diagrams in Figure 16 are most pronounced. During slow cooling (about below 2 °C·s^{-1}), the differences in austenitic grain size are probably blurred, as evidenced by the agreement of the ferrite-start and pearlite-start temperatures in the transformation diagrams corresponding to the low austenitization temperature.

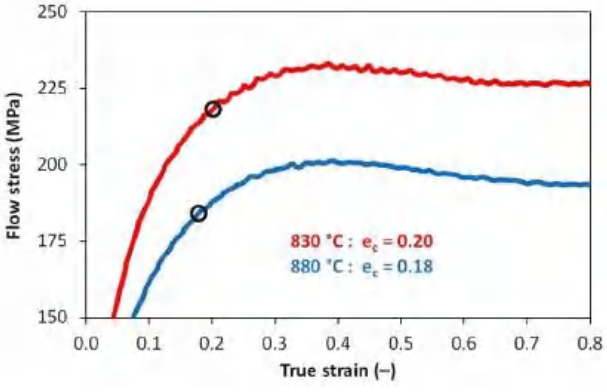

Figure 20. Experimentally determined stress–strain curves and strain e_c values necessary to initiate dynamic recrystallization—detail of the peak stress area.

Generally, the austenitization temperature can have a major effect on the kinetics of phase transformations during the cooling of the deformed structure. The prior grain size and the state of precipitates in HSLA steel are important [7], leading to a significant acceleration of the austenite → ferrite transformation at cooling rates above about 4 °C·s^{-1} after austenitization at 900 °C compared to preheating at 1280 °C. The effect of the very high temperature of austenitization (e.g., 1200 °C vs. 885 °C in [1]) is strong and results in the shift of the C-curves for diffusion controlled transformations towards the longer times. Experiments performed on 34CrMo4 steel showed a minor effect of a high

austenitization and deformation temperature of 1200 °C on the DCCT diagram in comparison with the CCT diagram [22]. A compressive deformation of 30 or 60% only slightly changed the transformation behavior except for a rise in the martensite-start temperature.

It should be emphasized that the results obtained for 23MnNiCrMo5-3 steel are valid to true strain rate $\dot{e} = 1\ s^{-1}$. Changing the parameters of dilatometric tests could lead to rather different results. The problem is probably not the direct influence of the strain rate on the kinetics of phase transformations [19,27] but rather influencing the type of the interconnected softening processes during plastic deformation and during subsequent cooling. It may be important whether dynamic and thus metadynamic recrystallization can be induced, or whether static recrystallization will dominate [60–62]. The critical strain values of e_c required to initiate dynamic recrystallization in various alloys is a function of the temperature-compensated strain rate (i.e., the Zener–Hollomon parameter Z (s^{-1})) according to the Sellars model [63–69]:

$$e_c = A \cdot Z^B, \tag{1}$$

$$Z = \dot{e} \cdot \exp\left(\frac{Q}{R \cdot T}\right) \tag{2}$$

where T (K) is temperature, $R = 8.314\ J \cdot mol^{-1} \cdot K^{-1}$ is the gas constant, and A and B are the material constants. As the strain rate increases, the critical strain e_c will grow, and the probability of at least partial metadynamic recrystallization during cooling will decrease. In addition, the dependence according to Equation (2) can be complicated by varying the size of prior austenitic grains [70].

4. Conclusions

Using dilatometric tests and metallographic analyses, a total of five different continuous cooling transformation diagrams were made for 23MnNiCrMo5-3 steel. Pre-deformation corresponding to the compressive true strain of 0.35 or even 1.0 had no clear effect on the austenite decomposition kinetics at the austenitization temperature of 880 °C. The reason is too great a difference between this high deformation temperature and the A_{c3} temperature determined to be 801 °C. During the long-lasting cooling, recrystallization and probably coarsening of the new austenitic grains occurred, which practically eliminated the influence of plastic deformation on the temperatures of the diffusion-controlled phase transformations.

Decreasing the austenitization and deformation temperature to 830 °C has already led to the expected results regarding the effect of plastic deformation on the individual phase transformations in steels. In the region of the cooling rate approximately between 3 $°C \cdot s^{-1}$ and 35 $°C \cdot s^{-1}$, there was a significant acceleration of the austenite → ferrite and austenite → pearlite transformations due to the applied strain of 1.0. A shift of the curves of ferrite-start and pearlite-start towards the shorter times is evident. On the contrary, the kinetics of the bainitic or martensitic transformation remained almost unaffected by the pre-deformation. The acceleration of the diffusion-controlled phase transformations results from the formation of a fine-grained austenitic microstructure with a mean grain size of about 4 μm. As the analysis of the stress–strain curves showed, the grain refinement was performed by dynamic and metadynamic recrystallization in this case. At low cooling rates, the effect of plastic deformation on the kinetics of phase transformations was more or less blurred again.

The obtained results showed the key importance of the austenitization or finish-rolling temperature in combination with the cooling rate for the structure-forming processes taking place in the investigated steel. The DCCT diagrams enable us to optimize the cooling rate of the continuously rolled wire and thus obtain a suitable microstructure with a sufficient fraction of bainite. The CCT diagram corresponding to the austenitization temperature of 880 °C is important for determining the cooling rate, which ensures a fully martensitic microstructure after the final hardening of the high-strength chains.

Author Contributions: I.S. coordinated the experimental activities, processed the results, and wrote the first draft of the manuscript; R.K. performed a literary analysis and experiments; P.O. performed the experiments and analyzed the stress–strain curves; P.K. analyzed the dilatometric curves; S.R. performed the experiments; J.S. evaluated the results of structural analysis; M.S. contributed to the processing and comparison of results; H.N.

contributed to a literary analysis and editing; L.P. provided the material and its characterization, and contributed to the processing of results; all authors revised and approved the final version of the manuscript. All authors have read and agreed to the published version of the manuscript.

Funding: The article was created thanks to the project No. CZ.02.1.01/0.0/0.0/17_049/0008399 from the EU and CR financial funds provided by the Operational Programme Research, Development and Education, Call 02_17_049 Long-Term Intersectoral Cooperation for ITI, Managing Authority: Czech Republic—Ministry of Education, Youth and Sports; and as part of the internal grant project SP2020/88 supported at VŠB—TU Ostrava by the Ministry of Education, Youth and Sports of the Czech Republic.

Acknowledgments: The authors would like to thank Ivana Malá (VŠB—TU Ostrava) for performing the light optical microscopy and metallographic analyses.

Conflicts of Interest: The authors declare no conflict of interest.

References

1. Opiela, M.; Zalecki, W.; Grajcar, A. Influence of plastic deformation on CCT-diagrams of new-developed microalloyed steel. *J. Achiev. Mater. Manuf. Eng.* **2012**, *51*, 78–89.
2. Mun, D.J.; Shin, E.J.; Choi, Y.W.; Lee, S.J.; Koo, Y.M. Effects of cooling rate, austenitizing temperature and austenite deformation on the transformation behavior of high-strength boron steel. *Mater. Sci. Eng. A* **2012**, *545*, 214–224. [CrossRef]
3. Kawulok, R.; Schindler, I.; Sojka, J.; Kawulok, P.; Opěla, P.; Pindor, L.; Grycz, E.; Rusz, S.; Ševčák, V. Effect of strain on transformation diagrams of 100Cr6 steel. *Crystals* **2020**, *10*, 326. [CrossRef]
4. Rusz, S.; Schindler, I.; Kawulok, P.; Kawulok, R.; Opěla, P.; Kliber, J.; Solowski, Z. Phase transformation and cooling curves of the mild steel influenced by previous hot rolling. *Metalurgija* **2016**, *55*, 655–658.
5. Kawulok, P.; Schindler, I.; Mizera, J.; Kawulok, R.; Rusz, S.; Opěla, P.; Olszar, M.; Čmiel, K.M. The influence of a cooling rate on the evolution of microstructure and hardness of the steel 27MnCrB5. *Arch. Metall. Mater.* **2018**, *63*, 907–914. [CrossRef]
6. Timoshenkov, A.; Warczok, P.; Albu, M.; Klarner, J.; Kozeschnik, E.; Gruber, G.; Sommitsch, C. Influence of deformation on phase transformation and precipitation of steels for oil country tubular goods. *Steel Res. Int.* **2014**, *85*, 954–967. [CrossRef]
7. Schindler, I.; Kawulok, R.; Seillier, Y.; Kawulok, P.; Opěla, P.; Rusz, S.; Vodarek, V.; Turoň, R. Continuous cooling transformation diagrams of HSLA steel for seamless tubes production. *J. Min. Metall. Sect. B-Metall.* **2019**, *55*, 413–426. [CrossRef]
8. Yogo, Y.; Kurato, N.; Iwata, N. Investigation of hardness change for spot welded tailored blank in hot stamping using CCT and deformation-CCT diagrams. *Metall. Mater. Trans. A* **2018**, *49*, 2293–2301. [CrossRef]
9. Chen, Z.; Nash, P.; Zhang, Y. Correlation of cooling rate, microstructure and hardness of S34MnV steel. *Metall. Mater. Trans. B* **2019**, *50*, 1718–1728. [CrossRef]
10. Kawulok, R.; Kawulok, P.; Schindler, I.; Opěla, P.; Rusz, S.; Ševčák, V.; Solowski, Z. Study of the effect of deformation on transformation diagrams of two low-alloy manganese-chromium steels. *Arch. Metall. Mater.* **2018**, *63*, 1735–1741. [CrossRef]
11. Grajcar, A.; Kuziak, R.; Zalecki, W. Designing of cooling conditions for Si-Al microalloyed TRIP steel on the basis of DCCT diagrams. *J. Achiev. Mater. Manuf. Eng.* **2011**, *45*, 115–124.
12. Liu, S.K.; Yang, L.; Zhu, D.G.; Zhang, J. The influence of the alloying elements upon the transformation kinetics and morphologies of ferrite plates in alloy steels. *Metall. Mater. Trans. A* **1994**, *25*, 1991–2000. [CrossRef]
13. Calvo, J.; Jung, I.H.; Elwazri, A.M.; Bai, D.; Yue, S. Influence of the chemical composition on transformation behaviour of low carbon microalloyed steels. *J. Mater. Sci. Eng. A* **2009**, *520*, 90–96. [CrossRef]
14. Xie, H.J.; Wu, X.C.; Min, Y.A. Influence of Chemical Composition on Phase Transformation Temperature and Thermal Expansion Coefficient of Hot Work Die Steel. *J. Iron Steel Res. Int.* **2008**, *15*, 56–61. [CrossRef]
15. Javaheri, V.; Khodaie, N.; Kaijalainen, A.; Porter, D. Effect of niobium and phase transformation temperature on the microstructure and texture of a novel 0.40% C thermomechanically processed steel. *Mater. Charact.* **2018**, *142*, 295–308. [CrossRef]
16. Cota, A.B.; Lacerda, C.A.M.; Oliveira, F.L.G.; Machado, F.A.; da Silva Araújo, F.G. Effect of the austenitizing temperature on the kinetics of ferritic grain growth under continuous cooling of a Nb microalloyed steel. *Scr. Mater.* **2004**, *51*, 721–725. [CrossRef]

17. Białobrzeska, B.; Konat, Ł.; Jasiński, R. The Influence of Austenite Grain Size on the Mechanical Properties of Low-Alloy Steel with Boron. *Metals* **2017**, *7*, 26. [CrossRef]
18. Khlestov, V.M.; Konopleva, E.V.; McQueen, H.J. Effects of deformation and heating temperature on the austenite transformation to pearlite in high alloy tool steels. *Mater. Sci. Technol.* **2002**, *18*, 54–60. [CrossRef]
19. Feng, Y.; Zhang, D.; Zhang, M.; Li, J.; Ning, J. Effects of initial austenite grain size on microstructure evolution of medium carbon steel. In Proceedings of the 2016 International Conference on Materials Science, Resource and Environmental Engineering, Xi'an, China, 10–11 December 2016. [CrossRef]
20. Andersson, M.; VanHumbeeck, J.; Ågren, J. Effect of Recrystallization and Grain Size on the Martensitic Transformation in Fe-31%Mn-5%Si Alloy. *Mater. Trans.* **1996**, *37*, 1363–1370. [CrossRef]
21. Aranda, M.M.; Kim, B.; Rementeria, R.; Capdevila, C.; García de Andres, C. Effect of prior austenite grain size on pearlite transformation in a hypo-eutectoid Fe-C-Mn steel. *Metall. Mater. Trans. A* **2014**, *45*, 1778–1786. [CrossRef]
22. Nürnberger, F.; Grydin, O.; Schaper, M.; Bach, F.W.; Koczurkiewicz, B.; Milenin, A. Microstructure transformations in tempering steels during continuous cooling from hot forging temperatures. *Steel Res. Int.* **2010**, *81*, 224–233. [CrossRef]
23. Karmakar, A.; Mandal, M.; Mandal, A.; Basiruddin, M.S.; Mukherjee, S.; Chakrabarti, D. Effect of starting microstructure on the grain refinement in cold-rolled low-carbon steel during annealing at two different heating rates. *Metall. Mater. Trans. A* **2016**, *47*, 268–281. [CrossRef]
24. Han, J.; Silva, A.K.; Ponge, D.; Raabe, D.; Lee, S.M.; Lee, Y.K.; Hwang, B. The effects of prior austenite grain boundaries and microstructural morphology on the impact toughness of intercritically annealed medium Mn steel. *Acta Mater.* **2017**, *122*, 199–206. [CrossRef]
25. Choo, W.Y.; Um, K.K.; Lee, J.S.; Seo, D.H.; Choi, J.K. Enhancement of fine formation by strain induced dynamic transformation and mechanical properties of fine grained steel. In Proceedings of the International Symposium on Ultrafine Grained Steels, Fukuoka, Japan, 20–22 September 2001; Iron and Steel Institute of Japan: Tokyo, Japan, 2001; pp. 2–9.
26. Beladi, H.; Kelly, G.L.; Shokouhi, A.; Hodgson, P.D. The evolution of ultrafine ferrite formation through dynamic strain-induced transformation. *Mater. Sci. Eng. A* **2004**, *371*, 343–352. [CrossRef]
27. Ghosh, C.; Aranas, C.J.; Jonas, J.J. Dynamic transformation of deformed austenite at temperatures above the Ae3. *Prog. Mater. Sci.* **2016**, *82*, 151–233. [CrossRef]
28. Park, N.; Zhao, L.; Shibata, A.; Tsuji, N. Dynamic Ferrite Transformation Behaviors in 6Ni-0.1C Steel. *JOM* **2014**, *66*, 765–773. [CrossRef]
29. Capdevila, C.; Caballero, F.G.; García-Mateo, C.; de Andres, C.G. The role of inclusions and austenite grain size on intragranular nucleation of ferrite in medium carbon microalloyed steels. *Mater. Trans.* **2004**, *45*, 2678–2685. [CrossRef]
30. Kawulok, R.; Schindler, I.; Mizera, J.; Kawulok, P.; Rusz, S.; Opěla, P.; Podolinský, P.; Čmiel, K.M. Transformation diagrams of selected steel grades with consideration of deformation effect. *Arch. Metall. Mater.* **2018**, *63*, 55–60. [CrossRef]
31. Zheng, C.; Raabe, D.; Li, D. Prediction of post-dynamic austenite-to-ferrite transformation and reverse transformation in a low-carbon steel by cellular automaton modeling. *Acta Mater.* **2012**, *60*, 4768–4779. [CrossRef]
32. Wang, C.; Wang, X.; Kang, J.; Yuan, G.; Wang, G. Effect of Austenitization Conditions on the Transformation Behavior of Low Carbon Steel Containing Ti–Ca Oxide Particles. *Materials* **2017**, *12*, 1070. [CrossRef]
33. Karmakar, A.; Ghosh, M.; Chakrabarti, D. Cold-rolling and inter-critical annealing of low-carbon steel: Effect of initial microstructure and heating-rate. *Mater. Sci. Eng. A* **2013**, *564*, 389–399. [CrossRef]
34. Zhao, H.; Wynne, B.P.; Palmiere, E.J. Effect of austenite grain size on the bainitic ferrite morphology and grain refinement of a pipeline steel after continuous cooling. *Mater. Charact.* **2017**, *123*, 128–136. [CrossRef]
35. Tsukatani, I.; Hashimoto, S.; Inoue, T. Effects of silicon and manganese addition on mechanical properties of high-strength hot-rolled sheet steel containing retained austenite. *ISIJ Int.* **1991**, *31*, 992–1000. [CrossRef]
36. Adamczyk, J.; Grajcar, A. Structure and mechanical properties of DP-type and TRIP-type sheets obtained after the thermomechanical processing. *J. Mater. Process. Technol.* **2005**, *162–163*, 267–274. [CrossRef]
37. Grajcar, A.; Morawiec, M.; Zalecki, W. Austenite Decomposition and Precipitation Behavior of Plastically Deformed Low-Si Microalloyed Steel. *Metals* **2018**, *8*, 1028. [CrossRef]

38. Kawulok, R.; Schindler, I.; Kawulok, P.; Rusz, S.; Opěla, P.; Solowski, Z.; Čmiel, K.M. Effect of deformation on the CCT diagram of steel 32CrB4. *Metalurgija* **2015**, *54*, 473–476.
39. Yin, S.B.; Sun, X.J.; Liu, Q.Y.; Zhang, Z.B. Influence of Deformation on Transformation of Low-Carbon and High Nb-Containing Steel during Continuous Cooling. *J. Iron Steel Res. Int.* **2010**, *17*, 43–47. [CrossRef]
40. Domański, T.; Piekarska, W.; Kubiak, M.; Saternus, Z. Determination of the final microstructure during processing carbon steel hardening. *Procedia Eng.* **2016**, *136*, 77–81. [CrossRef]
41. Kawulok, R.; Schindler, I.; Kawulok, P.; Rusz, S.; Opela, P.; Kliber, J.; Solowski, Z.; Čmiel, K.M.; Podolinsky, P.; Mališ, M.; et al. Transformation kinetics of selected steel grades after plastic deformation. *Metalurgija* **2016**, *55*, 357–360.
42. Cai, M.H.; Ding, H.; Lee, Y.K. Dynamic strain-induced ferrite transformation during hot compression of low carbon Si-Mn steels. *Mater. Trans.* **2011**, *52*, 1722–1727. [CrossRef]
43. Mohamadizadeh, A.; Zarei-Hanzaki, A.; Heshmati-Manesh, S.; Imandoust, A. The effect of strain induced ferrite transformation on the microstructural evolutions and mechanical properties of a TRIP-assisted steel. *Mater. Sci. Eng. A* **2014**, *607*, 621–629. [CrossRef]
44. Du, L.X.; Yi, H.L.; Ding, H.; Liu, X.H.; Wang, G.D. Effects of Deformation on Bainite Transformation During Continuous Cooling of Low Carbon Steels. *J. Iron Steel Res. Int.* **2006**, *13*, 37–39. [CrossRef]
45. Grajcar, A.; Zalecki, W.; Skrzypczyk, P.; Kilarski, A.; Kowalski, A.; Kołodziej, S. Dilatometric study of phase transformations in advanced high-strength bainitic steel. *J. Therm. Anal. Calorim.* **2014**, *118*, 739–748. [CrossRef]
46. Liu, Z.; Yao, K.F.; Liu, Z. Quantitative research on effects of stresses and strains on bainitic transformation kinetics and transformation plasticity. *Mater. Sci. Technol.* **2000**, *16*, 643–647. [CrossRef]
47. Xu, Y.; Xu, G.; Mao, X.; Zhao, G.; Bao, S. Method to evaluate the kinetics of bainite transformation in low-temperature nanobainitic steel using thermal dilatation curve analysis. *Metals* **2017**, *7*, 330. [CrossRef]
48. Kawata, H.; Fujiwara, K.; Takahashi, M. Effect of carbon content on bainite transformation start temperature in low carbon Fe–9Ni–C alloys. *ISIJ Int.* **2017**, *57*, 1866–1873. [CrossRef]
49. He, B.B.; Xu, W.; Huang, M.X. Increase of martensite start temperature after small deformation of austenite. *Mater. Sci. Eng. A* **2014**, *609*, 141–146. [CrossRef]
50. Nikravesh, M.; Nadeiri, M.; Akbari, G. Influence of Hot Plastic Deformation and Cooling Rate on Martensite and Bainite Start Temperatures in 22MnB5 steel. *Mater. Sci. Eng. A* **2012**, *540*, 24–29. [CrossRef]
51. Wang, H.Z.; Yang, P.; Mao, W.M.; Lu, F.Y. Effect of hot deformation of austenite on martensitic transformation in high manganese steel. *J. Alloys Compd.* **2013**, *558*, 26–33. [CrossRef]
52. Kruglova, A.A.; Orlov, V.V.; Khlusova, E.I. Effect of hot plastic deformation in the austenite interval on structure formation in low-alloyed low-carbon steels. *Met. Sci. Heat Treat.* **2007**, *49*, 556–560. [CrossRef]
53. Ryan, N.D.; McQueen, H.J. Flow Stress, Flow stress, dynamic restoration, strain hardening and ductility in hot working of 316 steel. *J. Mater. Process. Technol.* **1990**, *21*, 177–199. [CrossRef]
54. Poliak, E.I.; Jonas, J.J. A one-parameter approach to determining the critical conditions for the initiation of dynamic recrystallization. *Acta Mater.* **1996**, *44*, 127–136. [CrossRef]
55. Pilehva, F.; Zarei-Hanzaki, A.; Fatemi-Varzaneh, S.M.; Khalesian, A.R. Hot Deformation and Dynamic Recrystallization of Ti-6Al-7Nb Biomedical Alloy in Single-Phase β Region. *J. Mater. Eng. Perform.* **2015**, *24*, 1799–1808. [CrossRef]
56. Luo, R.; Zheng, Q.; Zhu, J.J.; Guo, S.; Li, D.S.; Xu, G.F.; Cheng, X.N. Dynamic recrystallization behavior of Fe–20Cr–30Ni–0.6Nb–2Al–Mo alloy. *Rare Met.* **2019**, *38*, 181–188. [CrossRef]
57. Schindler, I.; Opěla, P.; Kawulok, P.; Sojka, J.; Konečná, K.; Rusz, S.; Kawulok, R.; Sauer, M.; Turoňová, P. Hot deformation behaviour of Mn–Cr–Mo low-alloy steel in various phase regions. *Metals* **2020**, *10*, 1225. [CrossRef]
58. Adamczyk, J.; Opiela, M. Influence of the thermo-mechanical treatment parameters on the inhomogeneity of the austenite structure and mechanical properties of the Cr-Mo steel with Nb, Ti, and B microadditions. *J. Mater. Process. Technol.* **2004**, *157*, 456–461. [CrossRef]
59. Ali, M.; Nyo, T.; Kaijalainen, A.; Hannula, J.; Porter, D.; Kömi, J. Influence of chromium content on the microstructure and mechanical properties of thermomechanically hot-rolled low-carbon bainitic steels containing niobium. *Appl. Sci.* **2020**, *10*, 344. [CrossRef]
60. Sun, W.P.; Hawbolt, E.B. Comparison between static and metadynamic recrystallization an application to the hot rolling of steels. *ISIJ Int.* **1997**, *37*, 1000–1009. [CrossRef]

61. Zahiri, S.H.; Hodgson, P.D. The static, dynamic and metadynamic recrystallisation of a medium carbon steel. *Mater. Sci. Technol.* **2004**, *20*, 458–464. [CrossRef]
62. Li, L.; Zheng, L.; Ye, B.; Tong, Z. Metadynamic and static recrystallization softening behavior of a bainite steel. *Met. Mater. Int.* **2018**, *24*, 60–66. [CrossRef]
63. Zener, C.; Hollomon, J.H. Effect of Strain Rate Upon Plastic Flow of Steel. *J. Appl. Phys.* **1944**, *15*, 22–32. [CrossRef]
64. Sellars, C.M.; Whiteman, J.A. Recrystallization and grain growth in hot rolling. *Met. Sci.* **1979**, *13*, 187–194. [CrossRef]
65. Najafizadeh, A.; Jonas, J.J. Predicting the Critical Stress for Initiation of Dynamic Recrystallization. *ISIJ Int.* **2006**, *46*, 1679–1684. [CrossRef]
66. Liu, X.G.; Zhang, L.G.; Qi, R.S.; Chen, L.; Jin, M.; Guo, B.F. Prediction of Critical Conditions for Dynamic Recrystallization in 316LN Austenitic Steel. *J. Iron Steel Res. Int.* **2016**, *23*, 238–243. [CrossRef]
67. Ma, Z.; Hu, F.; Wang, Z.; Fu, K.; Wei, Z.; Wang, J.; Li, W. Constitutive Equation and Hot Processing Map of Mg-16Al Magnesium Alloy Bars. *Materials* **2020**, *13*, 3107. [CrossRef] [PubMed]
68. Vajinder, S.; Mondal, C.; Sarkar, R.; Bhattacharjee, P.P.; Ghosal, P. Dynamic recrystallization of a β(B2)-stabilized γ-TiAl based Ti–45Al–8Nb–2Cr-0.2B alloy: The contributions of constituent phases and Zener-Hollomon parameter modulated recrystallization mechanisms. *J. Alloys Compd.* **2020**, *828*, 154386. [CrossRef]
69. Kumar, S.; Karmakar, A.; Nath, S.K. Comparative Assessment on the Hot Deformation Behaviour of 9Cr–1Mo Steel with 1Cr–1Mo Steel. *Met. Mater. Int.* **2020**, *26*, 1–16. [CrossRef]
70. Varela-Castro, G.; Cabrera, J.M.; Prado, J.M. Critical strain for dynamic recrystallisation. The particular case of steels. *Metals* **2020**, *10*, 135. [CrossRef]

materials

MDPI

Article

Effect of Dynamic Recrystallization on Microstructural Evolution in B Steels Microalloyed with Nb and/or Mo

Irati Zurutuza [1,2], Nerea Isasti [1,2], Eric Detemple [3], Volker Schwinn [3], Hardy Mohrbacher [4,5] and Pello Uranga [1,2,*]

[1] Materials and Manufacturing Division, CEIT-Basque Research and Technology Alliance (BRTA), 20018 Donostia-Saint Sebastian, Basque Country, Spain; izurutuza@ceit.es (I.Z.); nisasti@ceit.es (N.I.)
[2] Mechanical and Materials Engineering Department, Universidad de Navarra, Tecnun, 20018 Donostia-Saint Sebastian, Basque Country, Spain
[3] Aktien-Gesellschaft der Dillinger Hüttenwerke, 66763 Dillingen/Saar, Germany; Eric.Detemple@dillinger.biz (E.D.); Volker.Schwinn@dillinger.biz (V.S.)
[4] NiobelCon BV, 2970 Schilde, Belgium; hm@niobelcon.net
[5] Department of Materials Engineering (MTM), KU Leuven, 3001 Leuven, Belgium
* Correspondence: puranga@ceit.es; Tel.: +34-943-212-800

Abstract: The dynamic recrystallization behavior of ultra-high strength boron-microalloyed steels optionally alloyed with niobium and molybdenum is analyzed in this paper. Multipass torsion tests were performed to simulate plate rolling conditions followed by direct quenching. The influence of alloy composition on the transformed microstructure was evaluated by means of EBSD, thereby characterizing the morphology of the austenite grain morphology after roughing and finishing passes. The results indicated that for Nb-microalloyed steel, partial dynamic recrystallization occurred and resulted in local clusters of fine-sized equiaxed grains dispersed within the pancaked austenitic structure. A recrystallized austenite fraction appeared and transformed into softer phase constituents after direct quenching. The addition of Mo was shown to be an effective means of suppressing dynamic recrystallization. This effect of molybdenum in addition to its established hardenability effects hence safeguards the formation of fully martensitic microstructures, particularly in direct quenching processes. Additionally, the circumstances initiating dynamic recrystallization were studied in more detail, and the interference of the various alloying elements with the observed phenomena and the potential consequences of dynamic recrystallization before quenching are discussed.

Keywords: austenite conditioning; multipass torsion tests; dynamic recrystallization; Nb–Mo-microalloyed steels

Citation: Zurutuza, I.; Isasti, N.; Detemple, E.; Schwinn, V.; Mohrbacher, H.; Uranga, P. Effect of Dynamic Recrystallization on Microstructural Evolution in B Steels Microalloyed with Nb and/or Mo. *Materials* **2022**, *15*, 1424. https://doi.org/10.3390/ma15041424

Academic Editor: Ivo Schindler

Received: 26 January 2022
Accepted: 10 February 2022
Published: 15 February 2022

1. Introduction

Ultra-high strength steel with a martensitic microstructure is the preferred material for structural applications requiring an extreme load-bearing capacity or superior wear resistance. Martensitic steels are traditionally produced by conventional quenching (CQ), where the steel is reheated from ambient temperature back into austenite before quenching. Direct quenching (DQ) is an increasingly often practiced variant for processing ultra-high strength steel that enables cost and capacity optimization in steel mills [1]. The DQ method typically applies fast cooling to conditioned austenite, while the CQ method acts on a normalized (equiaxed) austenite microstructure. Accordingly, the martensite substructure originating from the DQ process develops within a pancaked austenite microstructure [2].

The microstructural homogeneity of austenite before quenching is related to recrystallization phenomena occurring along the entire austenite hot working process. An inhomogeneous prior austenite microstructure is detrimental for the toughness and (particularly) ductile-to-brittle transition temperature of the quenched steel [2,3]. Microstructural heterogeneity in austenite can be generated at different stages during the hot working

process. Alloy additions of boron, niobium, and molybdenum induce strong solute drag on austenite boundaries, thus delaying austenite recrystallization at temperatures between 1000 and 1100 °C [4]. If the austenite temperature during the last passes of recrystallizing rolling (roughing) drops into that range, the recrystallization of austenite, especially in the plate center, may not completely occur and individual non-recrystallized grains may not be as refined as the recrystallized ones. This heterogeneity cannot be removed by subsequent austenite conditioning (pancaking), resulting in pancaked grains of different thicknesses. Only a complete normalization, as occurs under CQ conditions, results in a homogeneous austenite microstructure.

On the other hand, strong austenite conditioning, which is typically connoted with high reduction ratio and low finishing temperatures, can trigger dynamic recrystallization in part of a microstructure. This event produces a fraction of very fine equiaxed austenite grains. It has been shown that the application of large deformation strain at low austenite temperature and the presence of dynamically recrystallized austenite compromises the hardenability effect related to boron microalloying [2,5–8]. The hardenability related to molybdenum alloying, however, appears to be much more robust under the same processing conditions. Although the impacts of Nb and Mo in dynamic recrystallization kinetics have been already analyzed, the synergetic effect of Nb, Mo and B for higher Mo contents needs to be further explored. Therefore, the authors of the current study investigates the circumstances initiating dynamic recrystallization in more detail. The interference of the various alloying elements (Mo, Nb, and B) with the observed phenomena and potential consequences of dynamic recrystallization before quenching are discussed.

2. Materials and Methods

The chemical composition of the boron-microalloyed steel designs using individual or combined Nb and Mo additions is listed in Table 1. Boron was stopped from forming boron nitride with an appropriate microalloy addition of titanium. The CMnB steel was used as a reference and for comparison based on previous papers.

Table 1. Chemical composition of the steels investigated in this work (in weight percent).

Steel	C	Si	Mn	Mo	Nb	B
CMnB	0.15	0.32	1.05	-	-	0.0022
CMnNbB	0.16	0.29	1.05	-	0.026	0.0019
CMnMoB	0.16	0.28	1.07	0.5	-	0.0022
CMnNbMoB	0.16	0.31	1.07	0.5	0..026	0.0018

Multipass torsion tests were performed to carry out hot rolling simulations followed by direct quenching. The torsion samples comprised a reduced central gauge section of 17 mm in length with a diameter of 7.5 mm. The torsion specimens were subjected to the thermomechanical deformation schedule shown in Figure 1. After soaking at 1200 °C for 10 min, allowing for the nearly complete dissolution of the microalloying elements B and Nb, five deformation passes with the austenite temperature gradually decreasing from 1170 to 1150 °C were executed in order to re-produce the roughing stage. In the roughing passes, a deformation strain of 0.2 at a strain rate of 2 s^{-1} and an interpass time of 6 s was applied. Between roughing and finishing, the material was held for 360 s, allowing for cooling to a finishing–start temperature of 880 °C. Eight finish deformation passes, each applying a strain of 0.2, were applied with a strain rate of 5 s^{-1}. The finish deformation sequence ended at 830 °C. Subsequent slow cooling (1 °C/s) until 790 °C was followed by accelerated cooling at a rate of approximately 30 °C/s down to ambient temperature.

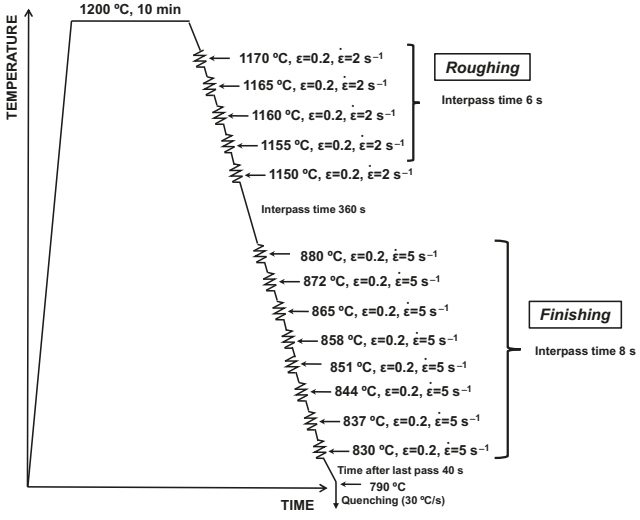

Figure 1. Schematics of multipass thermomechanical cycle employed with the torsion testing machine for simulating plate hot rolling.

Two specific hot torsion schedules (Figure 2) were designed to evaluate the influence of the alloying elements Nb and Mo on the occurrence of dynamic recrystallization and to verify under which conditions this mechanism was triggered during finishing deformation passes. Both thermomechanical cycles started from reheating at 1200 °C for 10 min, followed by five roughing passes, similar to the ones defined for the hot rolling simulation (Figure 1). In one schedule (Figure 2a), the samples were cooled down to 850 °C after the last roughing pass, when 8 finish deformation passes were isothermally applied with a strain of 0.2, a strain rate of 5 s^{-1} and an interpass time of 1 s. The other schedule (Figure 2b) consisted of one large deformation cycle at 850 °C, with a strain of 4 and a strain rate of 5 s^{-1}. Both schedules were followed by quenching to room temperature with a rate of approximately 30 °C/s.

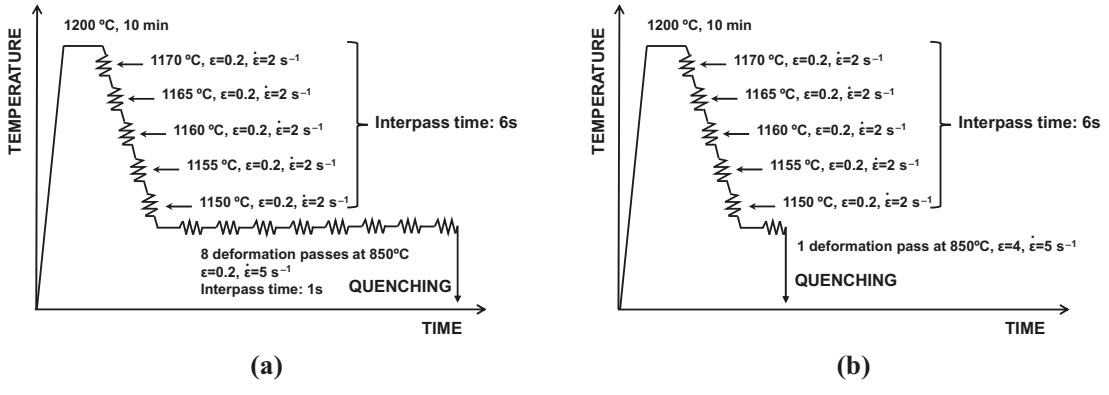

Figure 2. Thermomechanical schedules employed at the torsion testing machine for analyzing dynamic recrystallization phenomena: (**a**) roughing simulation followed by 8 deformation passes at 850 °C (ε = 0.2 and $\dot{\varepsilon}$ = 5 s^{-1}) and (**b**) roughing simulation followed by a deformation pass at 850 °C (ε = 4 and $\dot{\varepsilon}$ = 5 s^{-1}).

The quenched martensitic microstructures were metallographically characterized in the sub-surface longitudinal section, corresponding to 0.9 of the outer radius of the torsion specimen. The analysis of the austenite structure was performed after etching in 2% Nital by optical microscopy (OM, LEICA DM1500 M, Leica microsystems, Wetzlar, Germany), and the quantification of microstructural features was performed via electron backscattered diffraction (EBSD). The EBSD samples were polished down to 1 μm, and the final polishing was performed with colloidal silica. EBSD was performed on the equipment with a camera NORDLYS II (Oxford Instruments, Abingdon, UK), a well as an acquisition program and data analysis, OXFORD HKL CHANNEL 5 PREMIUM coupled to the JEOL JSM-7100 F FEG-SEM (JEOL Ltd., Tokyo, Japan). A scan step size of 0.2 μm was used, and a total scanned area of 140 × 140 μm^2 was defined for characterization of martensitic microstructure. The EBSD scans were analyzed by means of TSL OIM™ Analysis 5.31 software (EDAX, Mahwah, NJ, USA).

Besides analyzing the direct quenched martensite, the austenitic structures prior to martensite transformation were also characterized after etching in a solution of saturated picric acid HCl. Due to the highly deformed austenitic microstructure, the reconstruction of austenite was carried out by means of EBSD. For reconstructing the austenite prior to transformation, a scan step size of 1 μm and a total scanned area of 500 × 500 μm^2 were defined. The analysis of strain-induced precipitation was also performed in the sub-surface longitudinal section of the torsion specimen using a transmission electron microscope (TEM, JEOL 2100, JEOL Ltd., Tokyo, Japan) with a voltage of 200 kV and LaB6 thermionic filament. This analysis was done using carbon extraction replicas.

3. Results

3.1. Characterization of the Direct Quenched Martensitic Microstructure after Plate Hot Rolling Simulation

The microstructures of the direct quenched steels following the hot deformation illustrated in Figure 1 are shown in Figure 3a–c. While the Mo and NbMo added steels exhibited fully martensitic microstructures, the CMnNbB steel comprised clusters consisting of non-polygonal ferrite within the martensitic microstructure. The presence of the ferrite phase resulted in a rather low hardness of 290 HV. The Mo- and NbMo-alloyed steels had much higher hardness values of 394 and 422 HV, respectively.

EBSD analysis was performed in the same specific locations corresponding to the optical images. Figure 3d–f shows grain boundary maps, in which low angle (between 2° and 15°) and high angle boundaries (>15°) are represented by red and black colors, respectively. Grain boundary maps corresponding to the three steel grades confirm the formation of a very fine-sized and complex microstructure. The presence of a substructure is reflected in a high density of low angle boundaries. However, in the CMnNbB steel (Figure 3d), some areas are clearly lacking this substructure, thus indicating that a softer phase was formed within the otherwise martensitic matrix. The mean unit sizes considering both tolerance angles (D2° and D15°) are indicated in the grain boundary maps. The CMnMoB and CMnNbMoB steels showed similar mean unit sizes, D2° and D15°, of about 0.9 and 1.3 μm, respectively. However, for CMnNbB grades, slightly coarser mean unit sizes of 1.1 and 1.5 μm were found for D2° and D15°, respectively. The kernel average misorientation (KAM) maps shown in Figure 3g–i reflect the presence of highly dislocated microstructures such as martensite and bainite (red- and yellow-colored areas, respectively). Yet in the CMnNbB steel, larger islands with lower dislocation density (blue and green colored areas) can be seen; these represent softer ferritic phases. The KAM value increased from 1.38° in CMnNb steel to 1.57° in the CMnMoB and CMnNbMo steels. In Figure 3j–l, the unit size distributions considering low and high angle misorientation criteria (boundaries between 2° and 15° and boundaries higher than 15°, respectively) are plotted for the three steels. For both misorientation criteria, a finer unit size distribution can be observed in the CMnNbMoB steel compared to the CMnNbB steel.

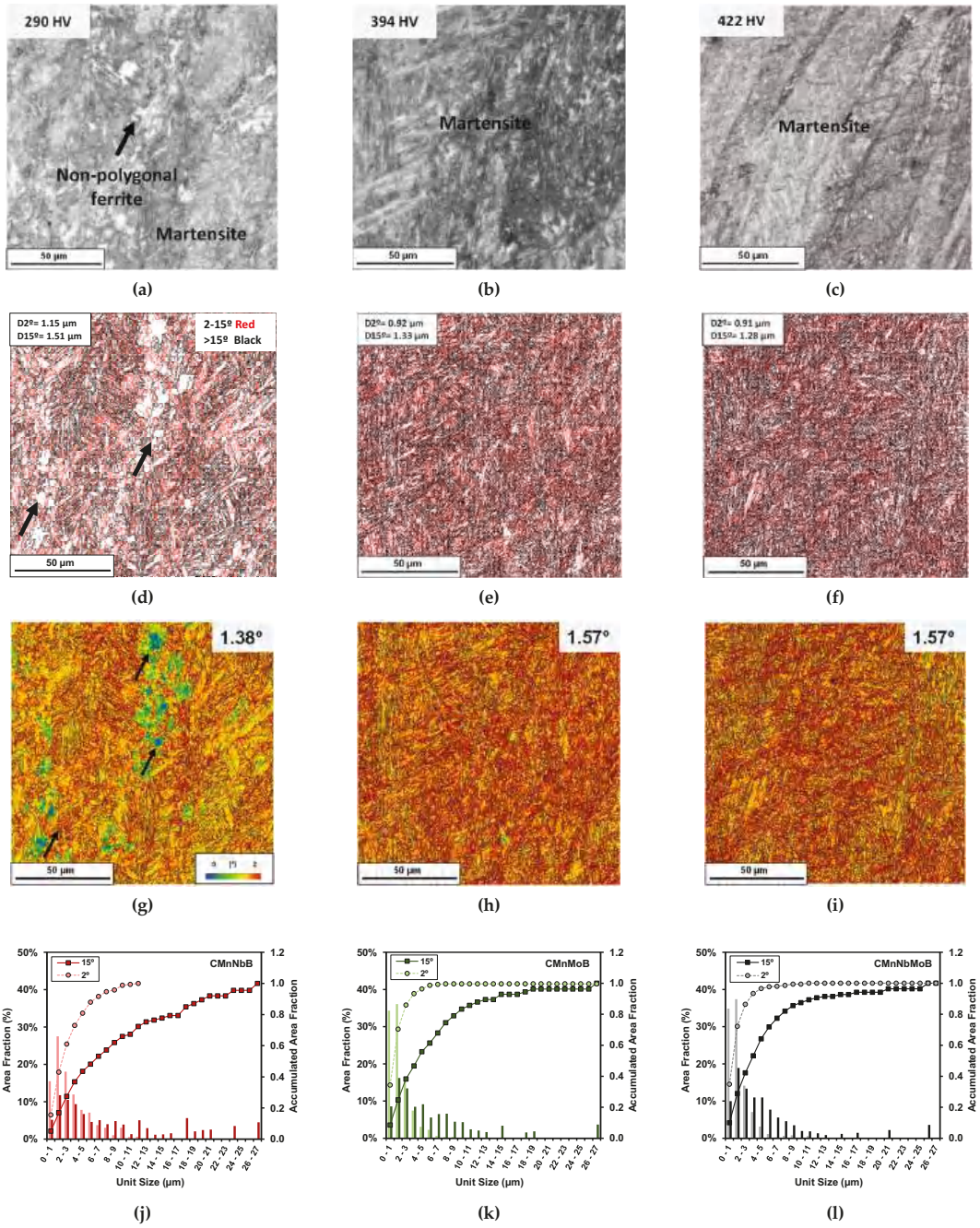

Figure 3. (**a**–**c**) Optical images, (**d**–**f**) grain boundary maps, and (**g**–**i**) kernel maps obtained for (**a**,**d**,**g**) CMnNbB, (**b**,**e**,**h**) CMnMoB, and (**c**,**f**,**i**) CMnNbMoB steels. (**j**–**l**) Unit size distributions measured for Nb, Mo, and NbMo grades, respectively (low and high angle misorientation criteria are considered).

3.2. Impact of Adding Nb and Mo on Austenite Conditioning

As the final martensitic features are strongly influenced by the austenite morphology prior to phase transformation, the characterization of the prior austenitic structure was analyzed (Figure 4). However, hot rolling simulations generating extremely deformed austenite hinder quantitative characterization. In all steel alloys, the microstructure comprised highly elongated austenite grains (Figure 4a,c,e). The accumulation of deformation was most pronounced for the combined addition of Nb and Mo (Figure 4e,f). Analyzing the optical images obtained at higher magnifications (Figure 4b,d,f) revealed a fraction of fine equiaxed grains in the CMnNbB grade, as indicated with red arrows in Figure 4b. These must have resulted from localized dynamic recrystallization occurring during final deformation. In the Mo-bearing steel grades, such equiaxed grains were not observed (see Figure 4d,f).

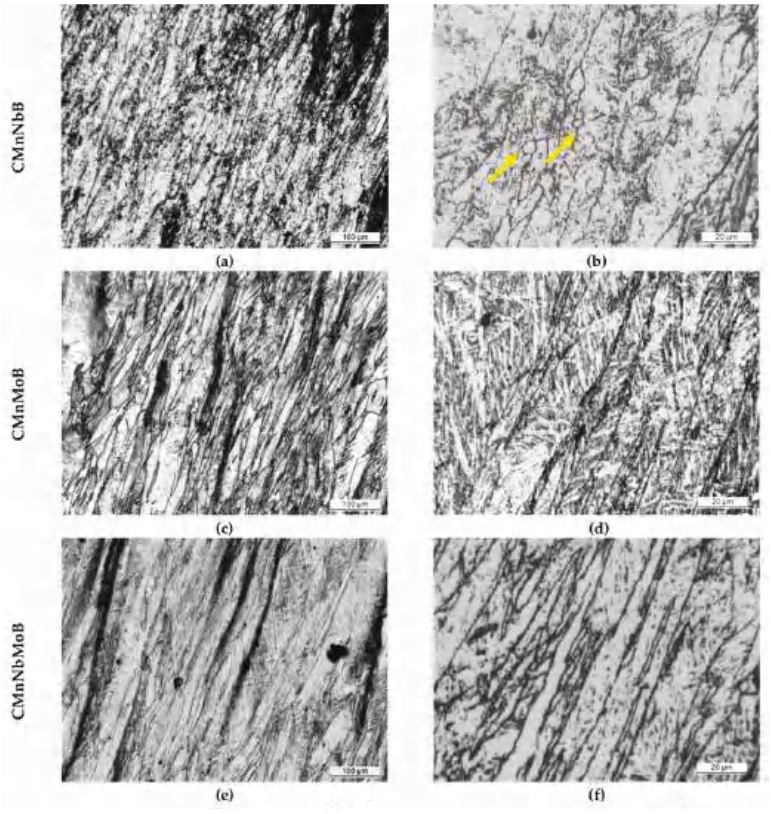

Figure 4. Optical micrographs at different magnifications ((**a**,**c**,**e**) and (**b**,**d**,**f**), at low and high magnifications, respectively) corresponding to all steel grades after the multipass torsion test (etched by Picric acid).

EBSD inverse pole figure (IPF) maps obtained on the martensitic microstructures (Figure 5a–c) allowed for the reconstruction of the prior austenite grain structure (Figure 5d–f) according to a procedure defined in [9,10]. The reconstruction confirmed the presence of elongated austenite grains in all steels. In agreement with the optical microscopy analysis, the reconstructed austenite structure of the CMnNbB steel demonstrated a fraction of very fine equiaxed grains.

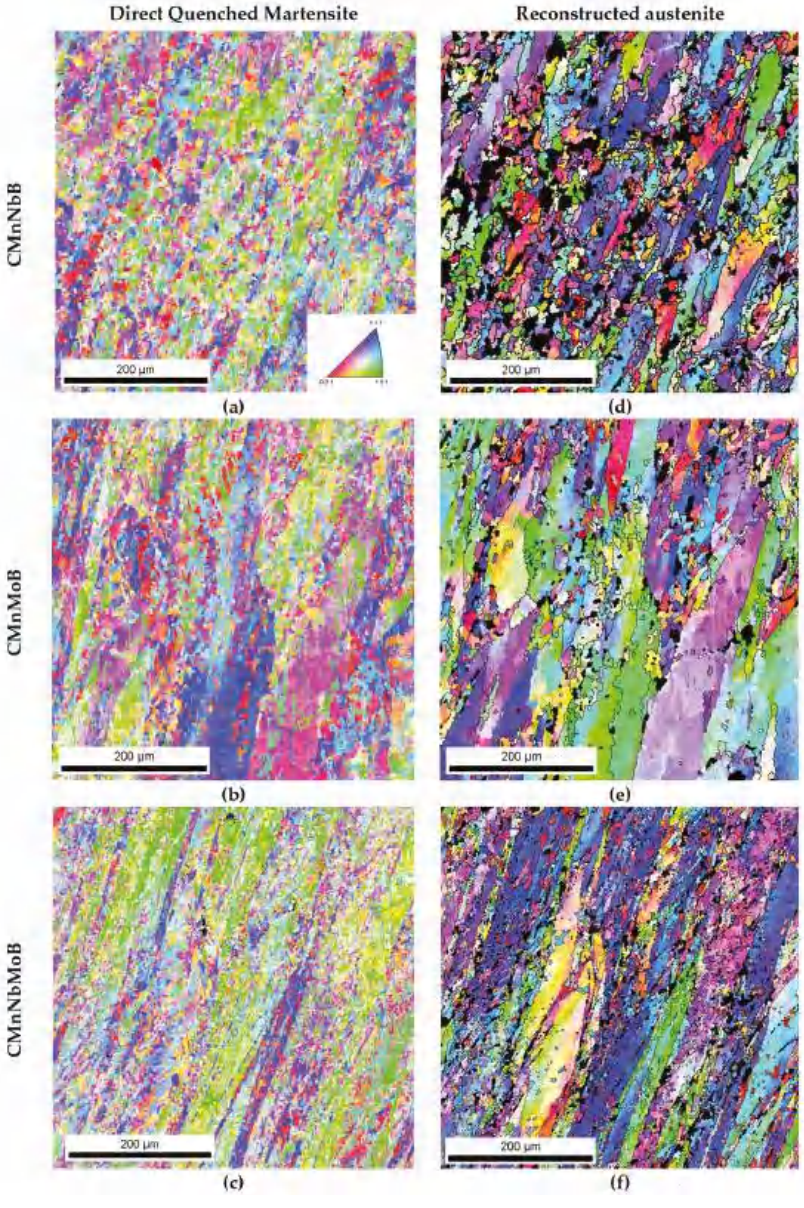

Figure 5. (**a**–**c**) IPF maps corresponding to the martensitic microstructure and (**d**–**f**) Reconstructed austenite microstructures for different steel grades.

When deforming Nb-microalloyed steels at austenite temperatures below T_{nr}, strain-induced precipitates can be formed, delaying static recrystallization and promoting strain accumulation prior to transformation. Usually, the pinning effect of these strain-induced particles is assumed to be strong enough to block any further static recrystallization during conventional hot deformation sequences. Carbon extraction replicas of the CMnNbB steel were analyzed with TEM, as shown in Figure 6, where different precipitate populations can be identified. Precipitates composed of Nb and Ti of relatively larger size (Figure 6a) were

likely undissolved particles existing prior to the soaking treatment. Additionally, strain-induced precipitates in the size range between 10 and 30 nm were observed (Figure 6b–d). The microanalysis shown in Figure 6e shows that Nb and Ti comprised these carbide particles. These strain-induced precipitates efficiently blocked static recrystallization during the finishing passes.

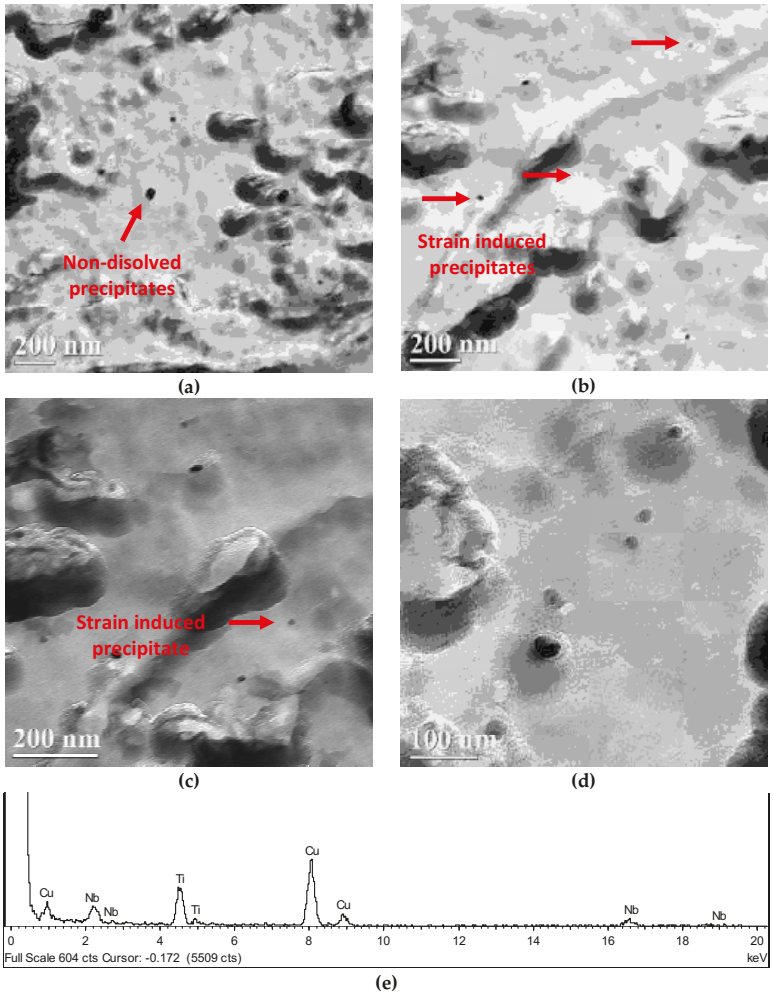

Figure 6. (**a**–**d**) Presence of non-dissolved Nb–Ti precipitates and strain-induced fine precipitates (NbTi-rich) in CMnNbB steel after plate hot rolling simulation and DQ. (**e**) Microanalysis of the strain-induced precipitate marked in (**c**) with a red arrow (the presence of Cu in the spectrum is associated with the grid holding of the carbon replica).

Molybdenum, on the other hand, does not precipitate in austenite due to its high solubility even for the current addition of 0.5 mass% [11]. Hence, the observed austenite pancaking in the CMnMoB steel must have primarily been caused by a strong solute drag effect acting on the grain boundaries. The absence of fine-sized equiaxed austenite grains in the microstructure of that steel suggests that the presence of strain-induced precipitates is not decisive for the avoidance of dynamic recrystallization.

3.3. Analysis of Dynamic Recrystallization Onset

The deformation schedule specified in Figure 2a was designed to provoke dynamic recrystallization in the investigated steels. The resulting stress–strain curves in Figure 7a–c indicate that the peak stress was reached during the fifth deformation pass for the Nb-microalloyed steels and during the seventh deformation pass for the CMnMoB steel. The molybdenum-alloyed steels reached a higher peak stress than the CMnNbB steel. The stress–strain curve reveals a transition from continuous yielding to pronounced yielding in the second pass for the Nb-microalloyed steels. This could have been related to the strain-induced precipitation of Nb. The Nb-free steel only showed this yielding phenomenon during later passes. Potentially, Ti or B formed precipitates in that steel since molybdenum does not form carbides in austenite due to its good solubility. Analyzing the austenite grain structure after eight deformation passes (Figure 8a–c) revealed a fraction of extremely fine-sized equiaxed austenite grains within the pancaked austenite matrix of all steels, as indicated with red arrows in Figure 8a. The recrystallized austenite grains were clustered in areas where austenite pancakes were particularly thin. Apparently, molybdenum alloying could not completely prevent the initiation of dynamic recrystallization. However, molybdenum significantly suppressed the volume fraction of recrystallized austenite grains during the simulated plate rolling schedule (Figure 5).

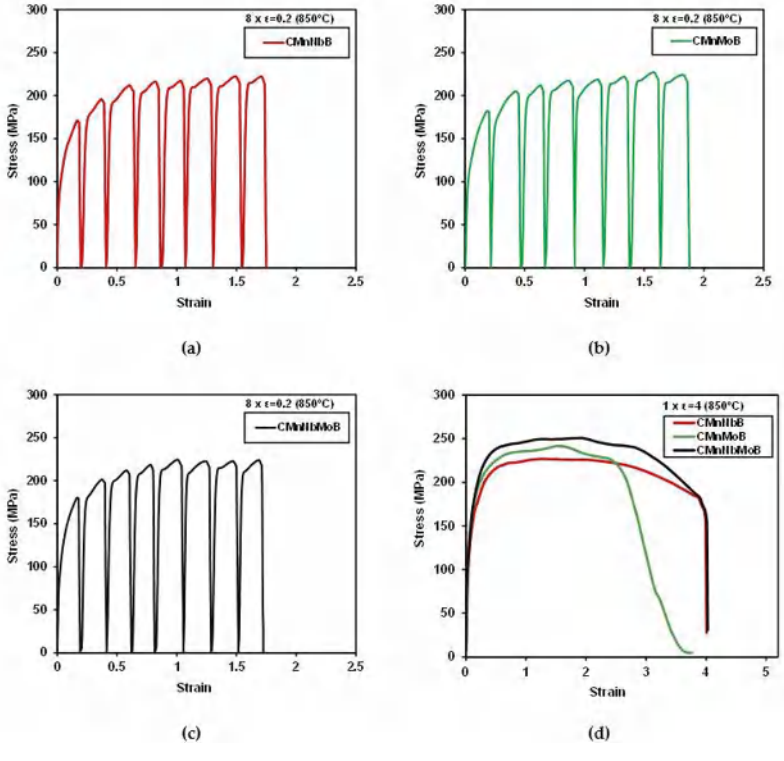

Figure 7. (**a**–**c**) Stress–strain curves for 8 deformation passes of $\varepsilon = 0.2$ (CMnNbB, CMnMoB, and CMnNbMoB grades, respectively) and (**d**) one deformation pass of $\varepsilon = 4$ at 850 °C.

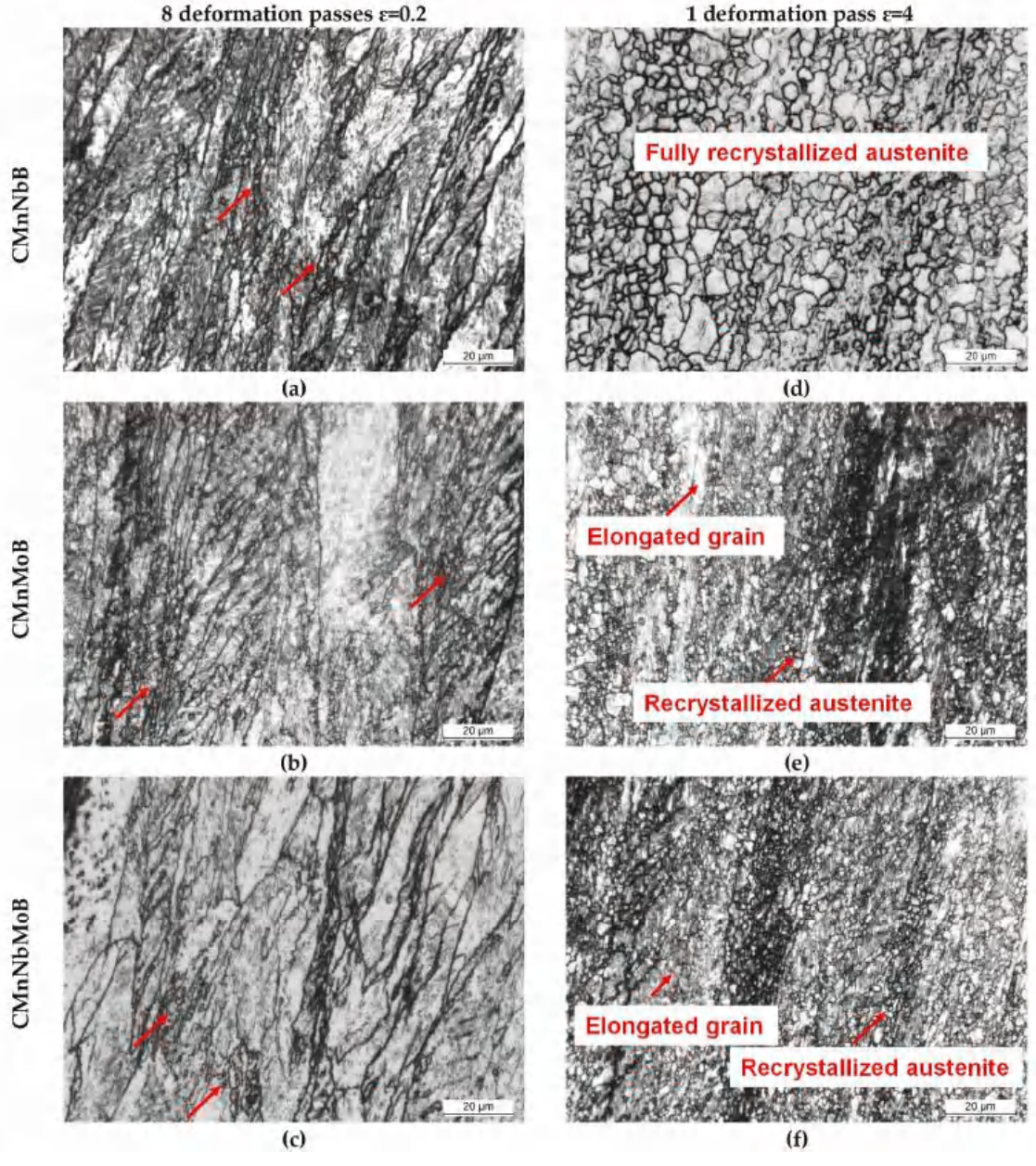

Figure 8. Optical images corresponding to the austenitic structure obtained after the thermomechanical cycle shown in Figure 2: (**a**–**c**) Roughing simulation and 8 deformation passes of 0.2 at 850 °C (see Figure 2a); (**d**–**f**) roughing simulation and 1 deformation pass of 4 at 850 °C (see Figure 2b). Dynamically recrystallized grains are indicated with red arrows.

This effect was further elucidated after applying a large strain during a single deformation pass according to Figure 2b. The stress–strain curves of all three steels reveal continuous yielding (Figure 7d). The mean flow stress increased in the order of CMnNbB,

CMnMoB, and CMnMoNbB steels. The austenite grain structure after the large deformation cycle (Figure 8d–f) reflected the nearly complete recrystallization in the CMnNbB steel, which showed fine-sized equiaxed grains with sizes of up to around 10 μm. The molybdenum-alloyed steels, however, presented a mixed microstructure consisting of elongated grains and recrystallized grains. The recrystallized grains were extremely fine-sized, typically smaller than 3 μm. This observation again indicates that molybdenum alloying did not completely prevent the initiation of dynamic recrystallization. For analyzing the critical strain triggering dynamic recrystallization, single pass deformation cycles were interrupted at lower strain values. Dynamically recrystallized grains were not found for a strain of $\varepsilon = 1$ (Figure 9a,b). At the strain of peak stress, ε_p (being 1.26 and 1.30 for the CMnNbB and CMnNbMoB steels, respectively), dynamic recrystallization did occur (Figure 9c,d). The critical strain, εc, triggering dynamic recrystallization was determined to be 1.08 and 1.1 for the CMnNbB and CMnNbMoB steels, respectively. The ratio of critical strain to peak strain was around 0.85 for both steels; this ratio is in the range of those reported in the literature for C–Mn and microalloyed steels [12]. Thus, the critical strain was obviously not significantly influenced by molybdenum alloying. However, molybdenum appeared to strongly obstruct the nucleation and growth of austenite grains under dynamic recrystallization conditions.

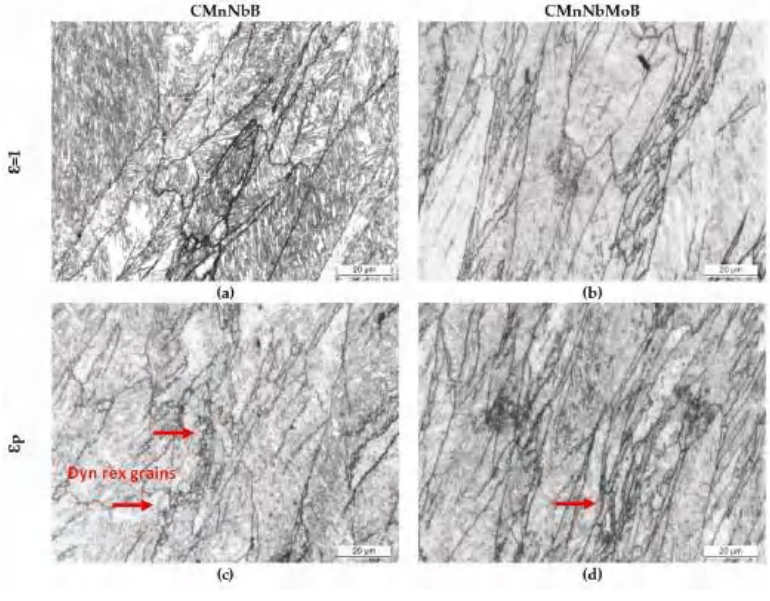

Figure 9. Optical micrographs after (**a**,**b**) $\varepsilon = 1$ and (**c**,**d**) ε_p deformation passes for: (**a**,**c**) CMnNbB and (**b**,**d**) CMnNbMoB steel grades (dynamically recrystallized grains are indicated with red arrows).

4. Discussion

The kinetics of dynamic recrystallization is influenced by the initial austenite grain size and the Zener–Hollomon parameter defined as $Z = \dot{\varepsilon}\exp(Q_{def}/RT)$, where Q_{def} is the activation energy, R is the gas constant, $\dot{\varepsilon}$ is the strain rate, and T is the absolute temperature [13]. For coarse grain sizes, DRX kinetics is delayed due to the reduction of the amount of available nucleation sites as the grain boundary area per unit volume is decreased. No significant difference regarding the initial average austenite grain size after roughing simulation was observed in the studied steels. The measured values were approximately 50 μm in all steels. Therefore, the main influencing factor in the kinetics of DRX in the present experiments must have been the Zener–Hollomon parameter. Since the

strain rate and deformation temperature were equal in all experiments, the activation energy was the main criterion accounting for the observed differences. The solutes having variable influence on the activation energy were Nb and Mo. Most of the Ti was bound in TiN, and a residual fraction participated in strain-induced NbC particles, so the residual solute amount of Ti was negligibly small. Solute Mo is known to impede the movement of high angle grain boundaries due to solute drag [14]. Schambron et al. [15] experimentally demonstrated that the activation energy for DRX correlates with Mo content (in mass percent) by a factor of 323 kJ/mol. Hence, the studied Mo content of 0.5 mass% increased the activation energy by 160 kJ/mol. Niobium is considered the most potent element in retarding DRX by solute drag [13]. However, under the applied hot deformation conditions, Nb partially precipitated and thereby lowered its solute content. From previous experiments on the same steels, it was concluded that the amount of soluble Nb after quenching hot worked steel is below 0.01 mass%. Strain-induced precipitates, on the other hand, are not very effective in suppressing DRX. Accordingly, DRX is expected to more likely occur in the CMnNbB steel, in agreement with the present experimental observations. Boron has been claimed to facilitate a softening effect due to its non-equilibrium grain boundary segregation [16,17]. A similar effect must have occurred in all investigated steels because the boron content was nominally identical.

The T_{nr} temperatures for the current steels were previously determined as 955, 980, 1010, and 1024 °C for the CMnB, CMnNbB, CMnMoB, and CMnNbMoB steels, respectively [4]. Accordingly, all finishing temperatures shown in the current experiments were below T_{nr}. Though the Nb- and/or Mo-alloyed steels presented a pronouncedly pancaked austenite structure (Figure 5), the CMnB base steel comprised a completely equiaxed austenite microstructure with a generally fine average grain size (Figure 10). Due to this refinement, the total austenite grain boundary area per material volume was significantly increased. It was shown by de Rosa et al. [18] that boron segregation to austenite grain boundaries occurs extremely quickly and even during the quenching cycle. Several studies using atom probe tomography [19,20] have indicated a high concentration of boron in the immediate vicinity of austenite grain boundaries while the grain interior away from the boundaries becomes nearly depleted of boron. When boron segregation proceeds during austenite conditioning, additionally supported by a strong flux of vacancies towards the austenite boundaries, it is possible that no diffusible boron is left for covering the new austenite grain boundaries generated by dynamic recrystallization. Earlier investigations on the current and other boron-alloyed steels [2,6–8] revealed that the hardenability effect related to boron is weakened when applying substantial strain immediately before quenching. In CCT diagrams reported in the previous works, the ferrite and bainite phase fields are then shifted towards shorter times and higher transformation temperatures under direct quenching conditions.

In the CMnNbB steel, DRX fully occurred only when large strain (ε = 4) was applied. Thus, under conditions representing a TMCP rolling schedule, pancaked grains with accumulated strain could coexist with fine-sized recrystallized grains. The strain accumulation increased the driving force for transformation while the recrystallized grain fraction was exposed to insufficient boron protection, as described before. The presence of ferrite colonies (Figure 3) in the former partially recrystallized austenite area indicated an early transformation, probably due to insufficient boron protection. The combination of both effects further extended the ferrite phase field under direct quenching conditions compared to completely recrystallized CMnB steel [6].

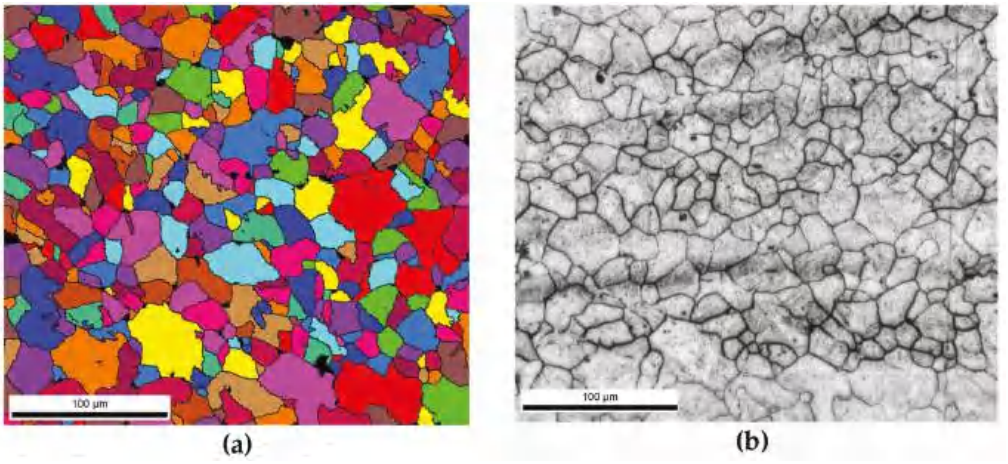

Figure 10. (**a**) Reconstructed austenite by EBSD and (**b**) optical image corresponding to austenite obtained after picric acid for CMnB steel grade.

The molybdenum-alloyed steels showed high strain accumulation without causing obvious dynamic recrystallization for the simulated rolling schedule (Figure 4). Their hardenability is much better than that of the Mo-free variants [6]. Ferrite formation was substantially retarded to a similar extent for direct quenching and conventional quenching conditions. That means the ferrite-suppressing effect of molybdenum was not measurably influenced by the presence of accumulated strain. This behavior is in good agreement with the results of Hannula et al. [7] who investigated the hardenability of very similar DQ steel alloys. Their results indicated the formation very fine-grained equiaxed austenite decorating the boundaries of much larger pancaked austenite grains when finish rolling at 800 °C. Such necklace structures gradually disappeared when molybdenum was added to the CMnB steel in amounts of 0.25 and 0.5 mass%. They were generally absent when applying less severe austenite pancaking and using a higher finish rolling temperature of 900 °C. However, despite severe pancaking and strain accumulation at the low finishing temperature, full hardenability was achieved in the molybdenum-alloyed steels in contrast to the CMnB steel. Like boron, molybdenum is strongly segregating at austenite grain boundaries [19,20]. Yet, a sufficiently high concentration level remained in the grain interior due to the comparably high molybdenum alloy addition. Accordingly, the Zener–Hollomon parameter had to have been significantly increased in the region near the grain boundary.

The micrographs of Figure 4 indicate that the austenite microstructure was not homogeneously deformed after the simulated rolling schedule but comprised a considerable range of austenite pancake thicknesses. Dynamic recrystallization was found to primarily initiate in the zones of most narrow pancakes. This was similar in all investigated steels (Figure 8a–c). The stress–strain curve for large deformation (Figure 7d) reveals that the stress initially increased to a relatively broad peak stress and then slowly declined to a steady state at large strain. In the steady state, the recrystallized grains generally grew in the CMnNbB steel, while they remained much finer in the molybdenum-alloyed steels (Figure 8 d–f). The observed features suggest geometric dynamic recrystallization (GDRX) as the acting mechanism [21]. In this mechanism, the impingement of serrated austenite pancake boundaries occurred when the pancake thickness approached 1–2 sub-grain size dimensions. Furthermore, the micrographs in Figure 9 indicate that GDRX did not instantaneously occur upon reaching the critical stress. The narrow ends of pancakes show the first appearance of ultrafine equiaxed grains in agreement with the model of de Pari and Misiolek [22], suggesting the gradual progress of GDRX with increasing strain. The steady state sub-grain size decreased with the increasing Zener–Hollomon parameter in

the molybdenum-alloyed steels compared to the CMnNbB steel. In areas where extremely thin pancakes were clustered prior to GDRX, the molybdenum concentration must have been increased due to the close proximity of boundary segregation profiles. Therefore, the recrystallized grain size remained smaller in these areas, while it was larger in areas of formerly thicker pancakes. Petterson et al. [23], using hot torsion tests, showed that the critical strain for GDRX is directly related to the initial grain size and inversely related to the sub-grain size. Both features were similar in the currently discussed steels, as were the observed critical strains regardless of the Zener–Hollomon parameter. The critical strain triggering GDRX under deformation in compression was indicated to become smaller than that in torsion [23], which is of relevance when considering industrial rolling.

The occurrence of partial GDRX before quenching has additional implications for martensitic transformation behavior. Experimental and theoretical studies [24–26] have indicated that the martensite-start temperature rapidly decreases for prior austenite grain sizes below 10 µm. Equiaxed grains originating from GDRX have sizes in the order of 1 µm and hence transform at lower temperature than surrounding austenite pancakes. The delayed transformation of the ultrafine austenite grains during quenching can thus lead to the buildup of residual stress because the dilatation caused by the martensitic transformation cannot be accommodated by plastic deformation in the previously transformed martensitic matrix. Such residual stresses typically result in unwanted quench distortion [27] and can have a negative impact regarding hydrogen-induced delayed cracking [28].

5. Conclusions

The current study has confirmed that dynamic recrystallization (DRX) can occur in direct quenching steels during austenite conditioning at low temperatures. After applying a typical TMCP deformation-temperature schedule to standard CMnB steel, DRX resulted in a fully equiaxed microstructure. The microalloying of niobium (0.026%) to such steel produced pancaked austenite with the localized appearance of very fine equiaxed austenite grains originating from DRX. The addition of molybdenum (0.5%) completely suppressed DRX under the same TMCP conditions. This effect of molybdenum was related to a significant increase of the Zener–Hollomon parameter.

Specific austenite conditioning, applying larger strain at low austenite temperature, demonstrated that the molybdenum-alloyed steel could experience DRX, resulting in ultrafine austenite grains. The progress of DRX and the austenite grain size was evidently smaller than in the niobium-microalloyed steel without molybdenum addition.

The initiation of DRX in the niobium- and molybdenum-added steels was related to the mechanism of geometrical DRX (GDRX). GDRX appeared to occur when the thickness of individual austenite pancakes was approaching the dimension of 1–2 sub-grains and proceeded gradually. Under a large single-pass strain ($\varepsilon = 4$), DRX was completed in the Nb-microalloyed steel but not in the molybdenum-alloyed steels. The larger Zener–Hollomon parameter in the latter steels resulted in a smaller size of the recrystallized grains.

The presence of fine-grained austenite generated by DRX was shown to produce soft phases upon quenching under an industrial cooling rate of 30 °C/s. It was argued that the sudden and late increase of the austenite grain boundary area caused by DRX could weaken the hardenability effect related to boron.

Molybdenum alloying acts twofold—by its high inherent hardenability effect and by avoiding DRX.

The presence of fine-grained austenite originating from DRX within a partially coarser microstructure is expected to cause non-synchronous martensite transformation, with the fine grains transforming at lower temperature. This phenomenon can induce residual stresses that lead to quench distortion and should be investigated in a dedicated study.

Author Contributions: I.Z. carried out the experiments and wrote the manuscript; N.I. supervised the results, analyzed the data and wrote the manuscript; E.D., V.S. and H.M. contributed to the interpretation of the data and edited the manuscript; P.U. managed the project and edited the manuscript. All authors have read and agreed to the published version of the manuscript.

Funding: This research received funding by the International Molybdenum Association (IMOA).

Institutional Review Board Statement: Not applicable.

Informed Consent Statement: Not applicable.

Data Availability Statement: The data presented in this study are available on request from the corresponding author. The data are not publicly available due to project confidentiality.

Acknowledgments: The authors would like to acknowledge the International Molybdenum Association (IMOA) for funding this project.

Conflicts of Interest: The authors declare no conflict of interest.

References

1. Uranga, P.; Shang, C.-J.; Senuma, T.; Yang, J.-R.; Guo, A.-M.; Mohrbacher, H. Molybdenum alloying in high-performance flat-rolled steel grades. *Adv. Manuf.* **2020**, *8*, 15–34. [CrossRef]
2. Hannula, J.; Kömi, J.; Porter, D.A.; Somani, M.C.; Kaijalainen, A.; Suikkanen, P.; Yang, J.R.; Tsai, S.P. Effect of Boron on the Strength and Toughness of Direct-Quenched Low-Carbon Niobium Bearing Ultra-High-Strength Martensitic Steel. *Metall. Mater. Trans. A* **2017**, *48*, 5344. [CrossRef]
3. Zurutuza, I.; Isasti, N.; Detemple, E.; Schwinn, V.; Mohrbacher, H.; Uranga, P. Toughness Property Control by Nb and Mo Additions in High-Strength Quenched and Tempered Boron Steels. *Metals* **2021**, *11*, 95. [CrossRef]
4. Zurutuza, I.; Isasti, N.; Detemple, E.; Schwinn, V.; Mohrbacher, H.; Uranga, P. Effect of Nb and Mo on austenite microstructural evolution during hot deformation in Boron high strength steels. *Metall. Mater. Trans. A* **2022**, *accepted*. [CrossRef]
5. Bai, D.Q.; Yue, S.; Maccagno, T.M.; Jonas, J.J. Effect of Deformation and Cooling Rate on the Microstructures of Low Carbon Nb–B Steels. *ISIJ Int.* **1998**, *38*, 371–379. [CrossRef]
6. Zurutuza, I.; Isasti, N.; Detemple, E.; Schwinn, V.; Mohrbacher, H.; Uranga, P. Effect of Quenching Strategy and Nb-Mo Additions on Phase Transformations and Quenchability of High-Strength Boron Steels. *JOM* **2021**, *73*, 3158–3168. [CrossRef]
7. Hannula, J.; Porter, D.A.; Kaijalainen, A.; Kömi, J. Evaluation of Mechanical Properties and Microstructures of Molybdenum and Niobium Microalloyed Thermomechanically Rolled High-Strength Press Hardening Steel. *JOM* **2019**, *71*, 2405–2412. [CrossRef]
8. Ali, M.; Nyo, T.; Kaijalainen, A.; Javaheri, V.; Tervo, H.; Hannula, J.; Kömi, J. Incompatible effects of B and B+Nb additions and inclusions characteristics on the microstructures and mechanical properties of low-carbon steels. *Mater. Sci. Eng. A* **2021**, *819*, 141453. [CrossRef]
9. Sanz, L.; López, B.; Pereda, B. Characterization of Austenite Microstructure from Quenched Martensite Using Conventional Metallographic Techniques and a Crystallographic Reconstruction Procedure. *Metals* **2018**, *8*, 294. [CrossRef]
10. Sanz, L.; Pereda, B.; López, B. Validation and Analysis of the Parameters for Reconstructing the Austenite Phase from Martensite Electron Backscatter Diffraction Data. *Metall. Mater. Trans. A* **2017**, *48*, 5258–5272. [CrossRef]
11. Pavlina, E.J.; Speer, J.G.; Van Tyne, C.J. Equilibrium solubility products of molybdenum carbide and tungsten carbide in iron. *Scr. Mater.* **2012**, *66*, 243–246. [CrossRef]
12. Bellavoine, M.; Dumont, M.; Drillet, J.; Hébert, V.; Maugis, P. Combined Effect of Heating Rate and Microalloying Elements on Recrystallization During Annealing of Dual-Phase Steels. *Metall. Mater. Trans. A* **2018**, *49*, 2865–2875. [CrossRef]
13. Fernandez, A.I.; Uranga, P.; López, B. Dynamic Recrystallization behaviour covering a wide austenite grain size range in Nb and Nb-Ti microalloyed steels. *Mater. Sci. Eng. A* **2003**, *361*, 367–376. [CrossRef]
14. Pereda, B.; Fernández, A.I.; López, B.; Rodriguez-Ibabe, J.M. Effect of Mo on Dynamic recrystallization behavior of Nb-Mo microalloyed steels. *ISIJ Int.* **2007**, *47*, 860–868. [CrossRef]
15. Schambron, T.; Dehghan-Manshadi, A.; Chen, L.; Gooch, T.; Killmore, C.; Pereloma, E. Effect of Mo on Dynamic Recrystallization and Microstructure Development of Microalloyed Steels. *Met. Mater. Int.* **2017**, *23*, 778–787. [CrossRef]
16. López-Chipres, E.; Mejía, I.; Maldonado, C.; Bedolla-Jacuinde, A.; El-Wahabi, M.; Cabrera, J.M. Hot flow behavior of boron microalloyed steels. *Mater. Sci. Eng. A* **2008**, *480*, 49–55. [CrossRef]
17. Gao, Y.L.; Xue, X.X.; Yang, H. Effect of boron concentration on dynamic recrystallization behavior of low-carbon steel. *Acta Metall. Sin. Engl. Lett.* **2015**, *28*, 931–939. [CrossRef]
18. Da Rosa, G.; Maugis, P.; Portavoce, A.; Drillet, J.; Valle, N.; Lentzen, E.; Hoummada, K. Grain-boundary segregation of boron in high-strength steel studied by nano-SIMS and atom probe tomography. *Acta Mater.* **2020**, *182*, 226–234. [CrossRef]
19. Li, Y.J.; Ponge, D.; Choi, P.; Raabe, D. Segregation of boron at prior austenite grain boundaries in a quenched martensitic steel studied by atom probe tomography. *Scr. Mater.* **2015**, *96*, 13–16. [CrossRef]
20. Mohrbacher, H.; Senuma, T. Alloy optimization for reducing delayed fracture sensitivity of 2000 MPa press hardening steel. *Metals* **2020**, *10*, 853. [CrossRef]
21. Huang, K.; Logé, R.E. A review of dynamic recrystallization phenomena in metallic materials. *Mater. Des.* **2016**, *111*, 548–574. [CrossRef]
22. De Pari, L., Jr.; Misiolek, W.Z. Theoretical predictions and experimental verification of surface grain structure evolution for AA6061 during hot rolling. *Acta Mater.* **2008**, *56*, 6174–6185. [CrossRef]

23. Pettersen, T.; Holmedal, B.; Nes, E. Microstructure development during hot deformation of aluminum to large strains. *Metall. Mater. Trans. A* **2003**, *34*, 2737–2744. [CrossRef]
24. García-Junceda, A.; Capdevila, C.; Caballero, F.G.; De Andres, C.G. Dependence of martensite start temperature on fine austenite grain size. *Scr. Mater.* **2018**, *58*, 134–137. [CrossRef]
25. Yang, H.S.; Bhadeshia, H.K.D.H. Austenite grain size and the martensite-start temperature. *Scr. Mater.* **2009**, *60*, 493–495. [CrossRef]
26. Guimarães, J.R.C.; Rios, P.R. Martensite start temperature and the austenite grain-size. *J. Mater. Sci.* **2010**, *45*, 1074–1077. [CrossRef]
27. Tobie, T.; Hippenstiel, F.; Mohrbacher, H. Optimizing gear performance by alloy modification of carburizing steels. *Metals* **2017**, *7*, 415. [CrossRef]
28. Eliaz, N.; Shachar, A.; Tal, B.; Eliezer, D. Characteristics of hydrogen embrittlement, stress corrosion cracking and tempered martensite embrittlement in high-strength steels. *Eng. Fail. Anal.* **2002**, *9*, 167–184. [CrossRef]

materials

MDPI

Article

Microstructure Evolution during Hot Deformation of UNS S32750 Super-Duplex Stainless Steel Alloy

Elisabeta Mirela Cojocaru [1], Anna Nocivin [2], Doina Răducanu [1], Mariana Lucia Angelescu [1], Ion Cinca [1], Irina Varvara Balkan [1], Nicolae Șerban [1] and Vasile Dănuț Cojocaru [1,*]

[1] Materials Science and Engineering Faculty, University POLITEHNICA of Bucharest, 060042 Bucharest, Romania; mirela.cojocaru@mdef.pub.ro (E.M.C.); doina.raducanu@upb.ro (D.R.); lucia.angelescu@mdef.pub.ro (M.L.A.); ion.cinca@upb.ro (I.C.); irina.balkan@mdef.pub.ro (I.V.B.); nicolae.serban@upb.ro (N.Ș.)

[2] Faculty of Mechanical, Industrial and Maritime Engineering, Ovidius University of Constanța, 900527 Constanța, Romania; anocivin@univ-ovidius.ro

* Correspondence: dan.cojocaru@upb.ro; Tel.: +40-21-402-9531; Fax: +40-21-316-9562

Abstract: The present paper analyzes UNS S32750 Super-Duplex Stainless Steel hot deformation behavior during processing by upsetting. The objective of this paper is to determine the optimum range of deformation temperatures, considering that both austenite and ferrite have different deformation behaviors due to their different morphology, physical, and mechanical properties. Because the capability of plastic deformation accommodation of ferrite is reduced when compared to austenite, side cracks and fissures can form during the hot deformation process. Consequently, it is important to find the optimum conditions of deformation of this type of stainless steel to establish the best processing parameters without deteriorating the material. The experimental program involved the application of hot deformation by the upsetting method on a series of samples between 1000 °C and 1275 °C, with a total degree of deformation of 30%. The resultant samples were examined by SEM-EBSD to establish and analyze the evolution of the phases present in the structure from several points of view: nature, distribution, morphology (size and shape), and their structural homogeneity. The GROD (Grain Reference Orientation Deviation) distribution map was also determined while taking into account the possible precipitation of the secondary austenite phase (γ_2-phase) and the analysis of the dynamic recrystallization process according to the applied deformation temperature. The main conclusion was that UNS S32750 SDSS steel can be safely deformed by upsetting between 1050–1275 °C, with an experimented total degree of deformation of 30%.

Keywords: super-duplex stainless steel (SDSS); SEM-EBSD microstructural analysis

Citation: Cojocaru, E.M.; Nocivin, A.; Răducanu, D.; Angelescu, M.L.; Cinca, I.; Balkan, I.V.; Șerban, N.; Cojocaru, V.D. Microstructure Evolution during Hot Deformation of UNS S32750 Super-Duplex Stainless Steel Alloy. *Materials* **2021**, *14*, 3916. https://doi.org/10.3390/ma14143916

Academic Editor: Ivo Schindler

Received: 16 June 2021
Accepted: 11 July 2021
Published: 14 July 2021

1. Introduction

The material considered in this experimental research is Super-Duplex Stainless Steel (SDSS), which shows a bi-phasic microstructure, composed of proportionally equal phases of, δ ferrite, and γ austenite, with a sufficient content of Cr, Mo, and N to deliver high corrosion resistance to pitting and to stress corrosion cracking [1,2]. In addition to these important characteristics, SDSS displays an industrially recognized combination of high mechanical strength and toughness [3,4]. However, this stainless steel represents only approximately 1% of the total production of stainless steels manufactured, including other two important types, austenitic stainless steels (ASSs), and ferritic stainless steels (FSSs) [5,6]; compared to these two types of steel, one problem arises for SDSS due to the distinct mechanical behavior of the two contenting phases that can lead to non-uniform deformation in the case of thermomechanical processing of this material. It is known that the main thermomechanical processing parameters (deformation temperature and applied deformation degree) play a crucial role in all the hot-deformation processes of metallic materials. This is because the correct selection and control of these parameters

can prevent the unwanted generation of defects in the final products [7–10]. A suitable hot-deformation regime must be established according to the distinct properties of the contenting phases of the metallic material, such as: phase morphology, flow stress, strain hardening coefficient, etc. In the case of SDSS, both stresses and strains from the applied hot working regime are unevenly distributed in ferrite δ and austenite γ due to the lower capability of plastic deformation accommodation of ferrite than that of austenite. This triggers different deformation behavior for degrees of deformation [11–15]. It has been reported that, in the case of applied recrystallization treatments prior to hot deformation processing, the initial grains of γ austenite are smaller than the grains of δ ferrite, with a direct repercussion on the microstructure of the alloy that was obtained after hot deformation, resulting in a more homogenous deformed γ austenite phase compared to the δ ferrite phase [16,17]. In addition, several reports indicate that micro-cracks may appear in the δ phase, which expand towards phase boundaries, leading to sample failure [15,18–22]. It stands to reason that finding and establishing the hot deformation temperature and the applied deformation degree are important goals for the optimal thermomechanical processing of SDSS alloys. Consequently, the main objectives of this research were the determination of the optimum hot deformation temperatures range of the UNS S32750 SDSS alloy, and the study of the main microstructural changes occurring during hot deformation. The optimal degree of deformation for the UNS S32750 SDSS alloy, was analyzed in a previous paper [23]. The current paper represents a continuation of these earlier experiments, with the aim of establishing a whole package of optimal, useful, and necessary hot deformation processing parameters.

2. Materials and Methods

2.1. Thermomechanical Processing Route

From the as-received (AR) UNS S32750 SDSS alloy (Sverdrup Steel, Stavanger, Norway), cylindrical-shaped samples with an h/d ratio of 1.5 (height h = 27 mm, and diameter d = 18 mm) were machined. The inspection with penetrant liquid was used to verify, porosity, presence of microcracks, laps (pre-existing defects), etc., on the lateral surface of all samples. Hot deformation of samples was conducted by upsetting, in axial compression, up to 30% total deformation degrees, by applying a 0.37 s^{-1} strain rate (a crosshead speed of 10 mm/s, consistently maintained). The deformation temperature range was selected between 1000 °C and 1275 °C, in 25 °C steps. For "freezing" the internal microstructure after the hot deformation processing, all samples were cooled in water. The inspection with penetrant liquid was used after cooling to again investigate the samples for fissures/microcracks. A detailed presentation of the thermomechanical processing equipment used is presented in an earlier paper [23].

2.2. Microstructural Characterization

The reference system of the samples is shown schematically in Figure 1. Considering this system, the samples were investigated in the LD-TD plane, in a/the selected area, situated two thirds (2/3) from the sample center. For cutting the samples, a precision Metkon MICRACUT 200 (Metkon Instruments Inc., Bursa, Turkey) diamond cutting equipment was used. All samples were hot mounted in conductive phenolic resin (NX-MET, Echirolles, France) at 138 °C and 10 min holding time. The mounted samples were further polished, using a Metkon Digiprep ACCURA (Metkon Instruments Inc., Bursa, Turkey) machine. An additional super-polishing phase was conducted on a Buehler VibroMet™ 2 machine (Buehler, Lake Bluff, IL, USA) for improving the sample surface quality. The polishing and super-polishing phases of sample preparation are presented in detail in a previous paper [23].

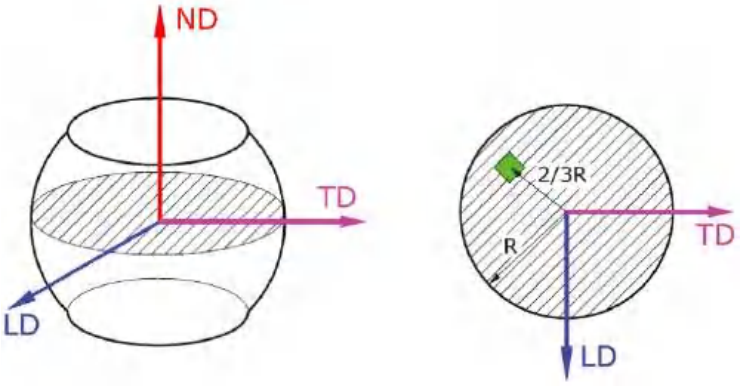

Figure 1. The reference system for the investigated samples: the initial deformed sample (**left**); the LD-TD section at middle-height of sample (**right**); the area investigated by SEM-EBSD analysis (green square); longitudinal direction (LD); transverse direction (TD); normal direction (ND).

A TESCAN VEGA II—XMU (TESCAN, Brno, Czech Republic) scanning electron microscope (SEM) was used for the microstructural analysis using the SEM-EBSD technique. This microscope is equipped with an EBSD detector—BRUKER Quantax eFlash (Bruker Corporation, Billerica, MA, USA). According to Figure 1, the analysis was conducted on the LD-TD plane, at middle height, and a distance from the sample axis equal to 2R/3 (R is the radius of the sample in the LD-TD plane). The phases considered for identifying the microstructural constituents the of investigated UNS S32750 SDSS alloy, were as follows: austenite phase (γ) and ferrite phase (δ). Both phases were indexed in the cubic system (γ-225 and δ-229), the space group Fm3m for γ and Im3m for δ, and the lattice parameter a = 3.66 Å for γ and a = 2.86 Å for δ, respectively. The parameters applied for the SEM-EBSD analysis were as follows: a magnification of $\times$ 300, a resolution of 320 pixels $\times$ 240 pixels, an acquisition time per pixel of 10 ms, a binning size of 1 $\times$ 1, and zero solutions below 3%.

For the constituent phases, the weight fraction (proportion), the nature, morphology, distribution, grain size, structural homogeneity, and dynamic recrystallization, were analyzed in correlation with the considered hot upsetting temperature.

3. Results and Discussion

3.1. The As-Received (AR) UNS S32750 Super-Duplex Stainless Steel

The SEM-EDS technique was used to investigate the chemical composition of as-received (AR) UNS S32750 Super-Duplex Stainless Steel. Figure 2a shows a representative SEM-BSE image for the investigated SDSS alloy in the AR state. Figure 2b–g show the maps for the dispersion of the main alloying elements within the SDSS structure (chromium, nickel, molybdenum, manganese, silicon, and copper). Two main constituent phases are observed after analyzing the distribution maps: a first one rich in Cr (Figure 2b), Mo (Figure 2d), Mn (Figure 2e), and Si (Figure 2f); and a second one enriched in Ni (Figure 2c) and Cu (Figure 2g). Table 1 shows the computed global chemical composition. It can be observed that the weight percentage of alloying elements are consistent with the intervals stated in the main standards (UNS S32750, ASTM A479 F53, AISI F53, WS 1.4410: Cr 24–26%wt; Ni 6–8%wt; Mo 3–5%wt; Mn max. 1.2%wt; Si max. 0.8%wt; Cu max. 0.5%wt; N 0.2–0.3%wt; S max. 0.01%wt; P max. 0.035%wt; C max. 0.03%wt). The presence of oxygen, nitrogen, carbon, and some other elements with a low Z (atomic number) were not quantified, considering the limitations of the SEM-EDS technique.

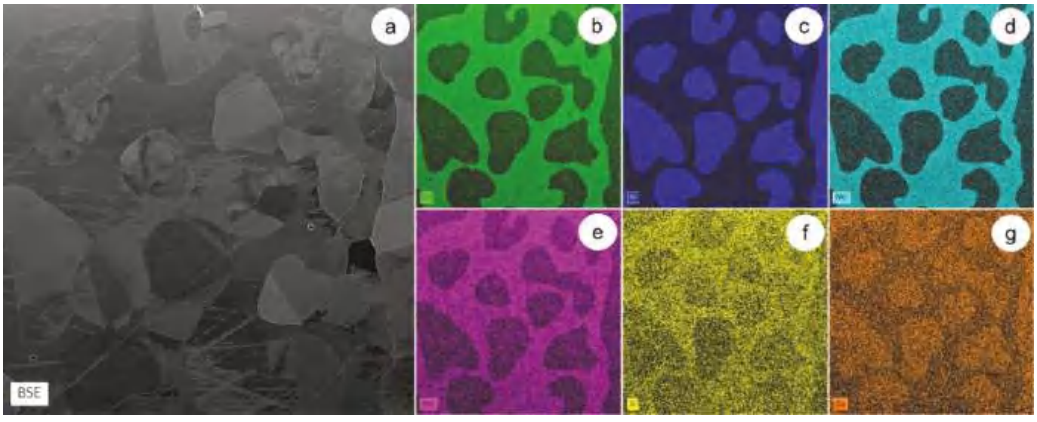

Figure 2. SEM-EDS colorized maps showing the main alloying elements distribution in the AR UNS S32750 Super-Duplex Stainless Steel: SEM-BSE image of the microstructure (**a**); distribution map of Cr (**b**); Ni (**c**); Mo (**d**); Mn (**e**); Si (**f**); Cu (**g**).

Table 1. The average chemical composition of the AR UNS S32750 Super-Duplex Stainless Steel.

Constituent Phase	Chemical Composition, [%, wt]						
	Cr	**Ni**	**Mo**	**Mn**	**Si**	**Cu**	**Fe**
global	25.85 ± 0.10	6.62 ± 0.12	3.05 ± 0.11	0.46 ± 0.09	0.38 ± 0.05	0.19 ± 0.03	balance
δ-phase	28.42 ± 0.09	5.17 ± 0.04	3.73 ± 0.12	0.48 ± 0.01	0.39 ± 0.01	0.15 ± 0.01	balance
γ-phase	25.28 ± 0.04	8.06 ± 0.04	2.31 ± 0.01	0.42 ± 0.02	0.37 ± 0.01	0.23 ± 0.01	balance

Figure 3a illustrates typical SEM-EBSD microstructural images of the AR UNS S32750 Super-Duplex Stainless Steel. Microstructural analysis showed that the UNS S32750 microstructure in the initial state, is homogeneous, with just two phases being identified (see Figure 3b): (1) austenite-γ, colorized in red, with elongated irregular grains dispersed within the ferrite phase; (2) ferrite-δ colorized in blue, which acts as a metallic matrix. The average grain size of austenite γ is higher than that of ferrite δ, around 95 μm compared to 75 μm—see the grain size distribution from Figure 4. The proportion of constituent phases is approximately 50–52% for δ ferrite and 50–48% for γ austenite. Other secondary phases were not detected. The average chemical composition of both phases (γ and δ) is presented in Table 1.

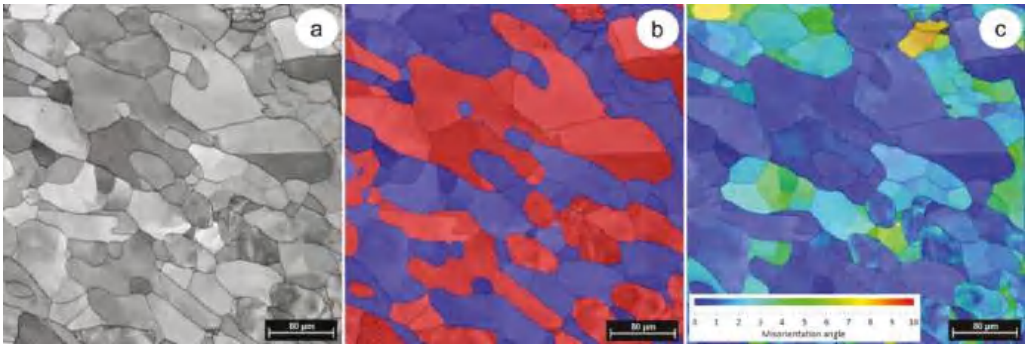

Figure 3. Typical SEM-EBSD microstructure images of AR UNS S32750 Super-Duplex Stainless Steel (**a**); distribution map of constituent phases (γ-phase—red colorized and δ-phase—blue colorized) (**b**); GROD distribution map for both γ-phase and δ-phase (**c**).

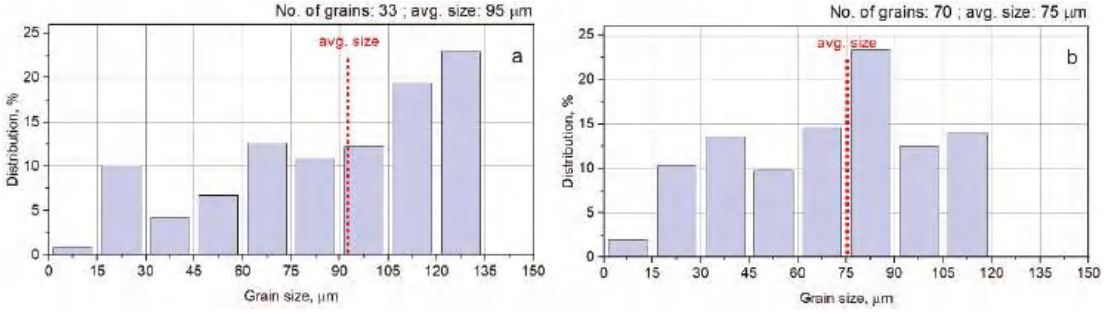

Figure 4. Grain size distribution of γ-phase in AR UNS S32750 Super-Duplex Stainless Steel (**a**); grain size distribution of δ-phase (**b**).

Grain Reference Orientation Deviation (GROD) distribution map for both γ-phase and δ-phase, in the investigated field, is shown in Figure 3c. The GROD map serves as a tool used for assessing the accumulated deformation or strain at a microstructural level [24,25]; the MO (misorientation) between a reference point and some other points of the considered grain is the basis of GROD. The average orientation of the considered grain was established as a reference point [26,27]. The GROD distribution map of the as-received (AR) UNS S32750 SDSS (Figure 3c) shows that both γ-phase and δ-phase present low stressed grains, with a maximum GROD of 9° recorded for the δ-phase. It can also be observed that the γ-phase shows a lower and more uniform distribution of GROD compared to the δ-phase (Figure 3c). Due to the low GROD, one can assume that the AR UNS S32750 Super-Duplex Stainless Steel shows a low susceptibility to the generation of microcracks.

3.2. SEM-EBSD Microstructural Analysis of the Hot-Deformed Alloy

Figure 5 shows a series of representative SEM-EBSD images for the samples processed by hot upsetting, from 1000 °C to 1275 °C, with a total deformation degree of 30%. For characterizing the microstructural evolution during hot deformation, the following characteristics were analyzed: distribution of constituent phases; the shape and size of grains; GROD distribution map for constituent phases; the occurrence of recrystallization (RX) in δ-phase grains, as well as the secondary austenite phase (γ_2-phase) precipitation.

The analysis of microstructure evolution, from 1000 °C to 1275 °C, showed the presence of the following constituent phases: ferrite (δ-phase)—blue colorized, primary austenite (γ-phase), and secondary austenite (γ_2-phase)—red color, and σ-phase—yellow color. At temperatures below 1050 °C, the presence of deleterious σ-phase can be observed, mainly at the δ/γ interface, the decreased quantity of σ-phase fraction, indicating that the dissolution of σ-phase is completed at 1050 °C. Another important observation can be made for temperatures above 1175 °C, where one can observe the presence of a secondary austenite phase (γ_2-phase), mainly within the δ-phase at the δ/δ interface. This secondary austenite (γ_2-phase) is generated during heating within an intensely deformed δ-phase matrix by heterogeneous nucleation, in sections where the supersaturation in N of the δ-phase is supporting the precipitation phenomenon. Furthermore, the microstructure inclusions are working as preferential nucleation sites for the γ_2-phase, which can easily nucleate next to these inclusions [28,29].

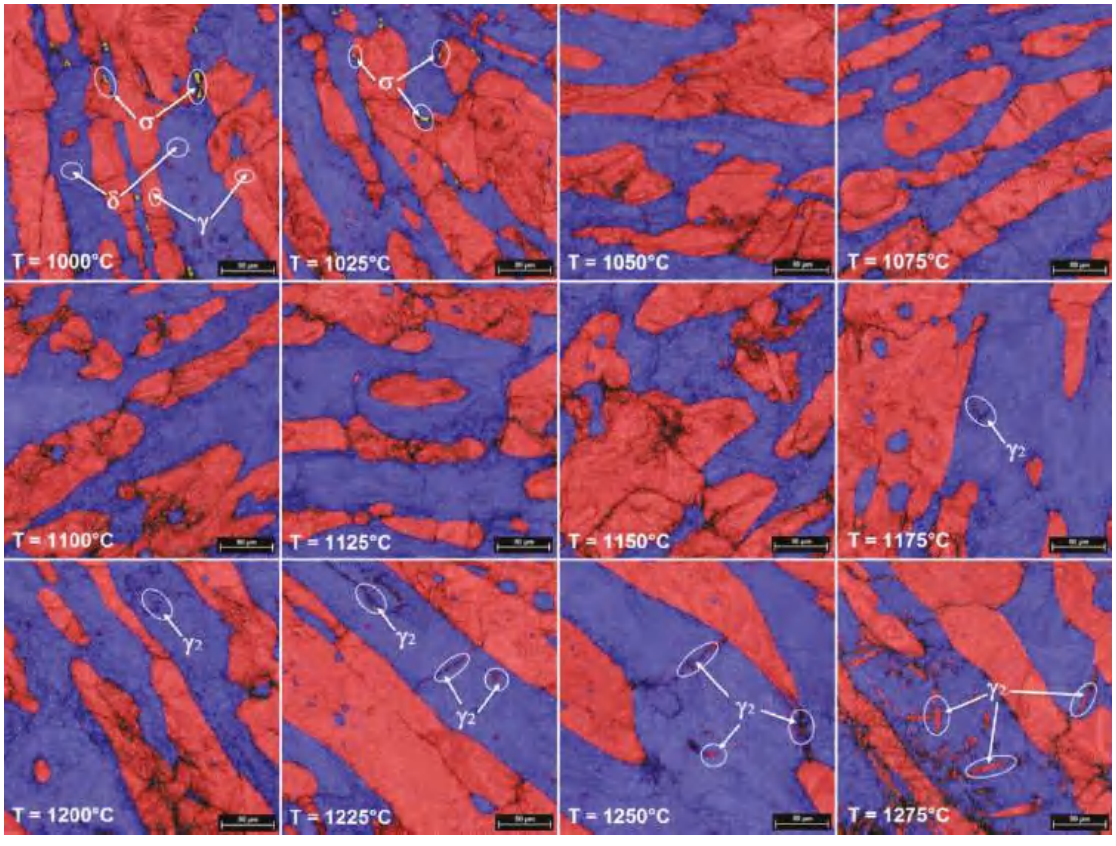

Figure 5. SEM-EBSD images showing typical constituent phase distribution maps in hot-deformed UNS S32750 SDSS alloy (from 1000 °C to 1275 °C).

Figure 6 shows a series of representative GROD distribution maps of samples processed by upsetting, from 1000 °C to 1275 °C, with a total deformation degree of 30%. Analyzing the GROD evolution, one can identify the following: for temperatures between 1000 °C to 1175 °C, the maximum GROD is registered for the δ-phase; while for temperatures between 1200 °C to 1275 °C the maximum GROD is registered for the γ-phase. Analyzing the GROD evolution in the case of δ-phase, it was observed that the GROD increases from 38° (at 1000 °C) to 49° (at 1100 °C), when maximum GROD is recorded, followed by a continuous decreasing to 21° (until 1275 °C). Analyzing the GROD evolution in the case of the γ-phase it was observed that the GROD increases from 26° (at 1000 °C) to 44° (at 1200 °C), followed by a continuous decreasing to 32° (until 1275 °C). It can also be observed that within the δ-phase areas, where GROD shows low-values (marked with white circles); this indicates the recrystallization (RX) occurrence in δ-phase grains.

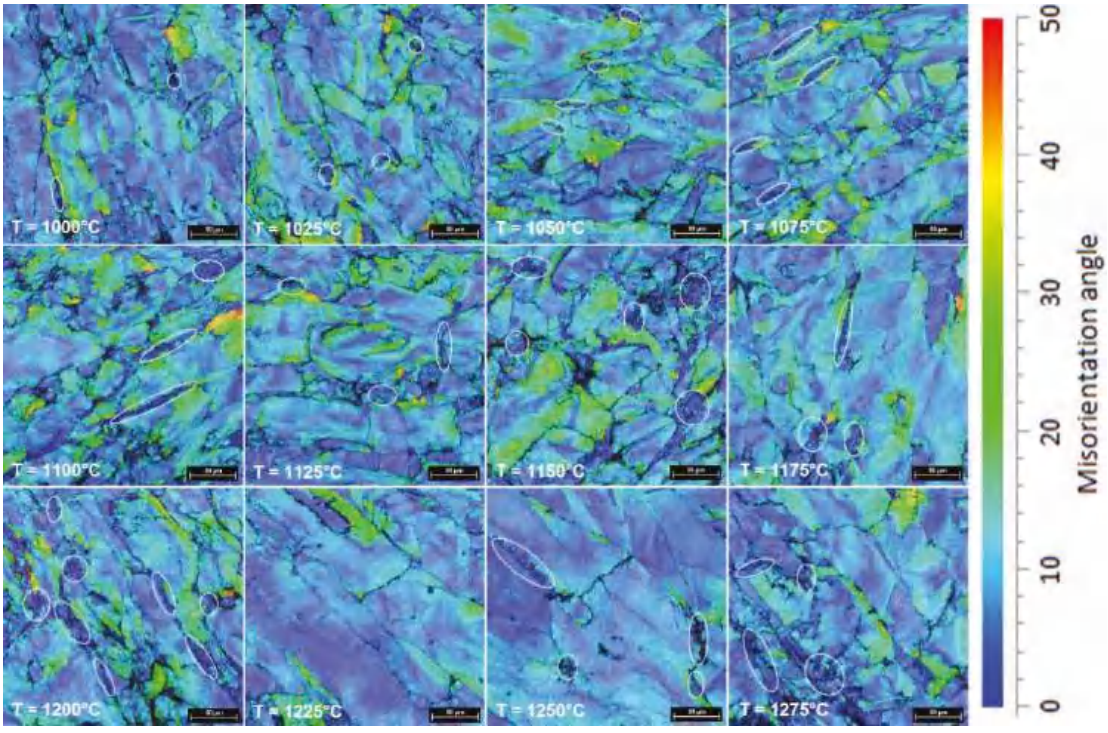

Figure 6. Typical GROD distribution maps, for both γ-phase and δ-phase, in hot-deformed UNS S32750 SDSS alloy (from 1000 °C to 1275 °C).

During deformation of the alloy, the microstructure suffers an increase in defect density, mainly in dislocation density with some new dislocations that are nucleating continuously, from the primary Frank–Read sources. These are blocked at grain level, thus resulting in an increased defect density. Moreover, during hot deformation, the grains suffer rotations to accommodate the increased strain–stress fields. All those effects result in large elastic strains and residual stress fields, visualized as high GROD areas (see Figure 6). The observed behavior, in terms of GROD evolution, suggests that both the stress relieving phenomena and the dynamic recrystallization of new grains phenomena must be considered. The stress relieving phenomena, which occurs during heating, induces important changes within the deformed microstructure of the alloy, decreasing the imperfections density and lowering the residual stress fields and the elastic strains [30–33]. One must also consider the influence of the dynamic recrystallization of new grains, which can also decrease the elastic strains and residual stress fields [30].

By analyzing all the microstructural images, one can observe that in all cases both δ and γ phases show some representative morphologies of strain-hardened microstructures. It is only in the case of δ-phase that some new RX grains are noticed (see Figures 6 and 7). The small size of new RX grains is due to short duration of the hot upsetting process at temperatures ranging from 1000 °C to 1275 °C. By analyzing the influence of the deformation temperature on microstructural evolution, one can observe that the increase in deformation temperature is leading to increased fragmentation in both γ and δ phases, which results in a continuously decreasing average grain size for both phases (see Figures 7 and 8). At 1000 °C, one can observe the presence of some small new ferrite grains, with a low GROD, which shows the occurrence of the RX phenomenon in δ phase (the sectors indicated by white circles from Figures 6 and 7). For deformation temperatures up to 1200 °C, one can

observe that the RX mechanism intensifies with the increasing of deformation temperature, which considerably increases the weight fraction of the new recrystallized grains of δ phase (see the sectors pointed by white circles from Figure 7). For the γ phase, no RX phenomena was observed. Moreover, for upsetting temperatures above 1200 °C, the presence of a secondary austenite phase (γ_2-phase) can be noticed, mainly within the δ-phase at the δ/δ interface, due to the $\delta \rightarrow \gamma$ phase transition, showing an increased weight fraction with the increase in deformation temperature (Figure 8).

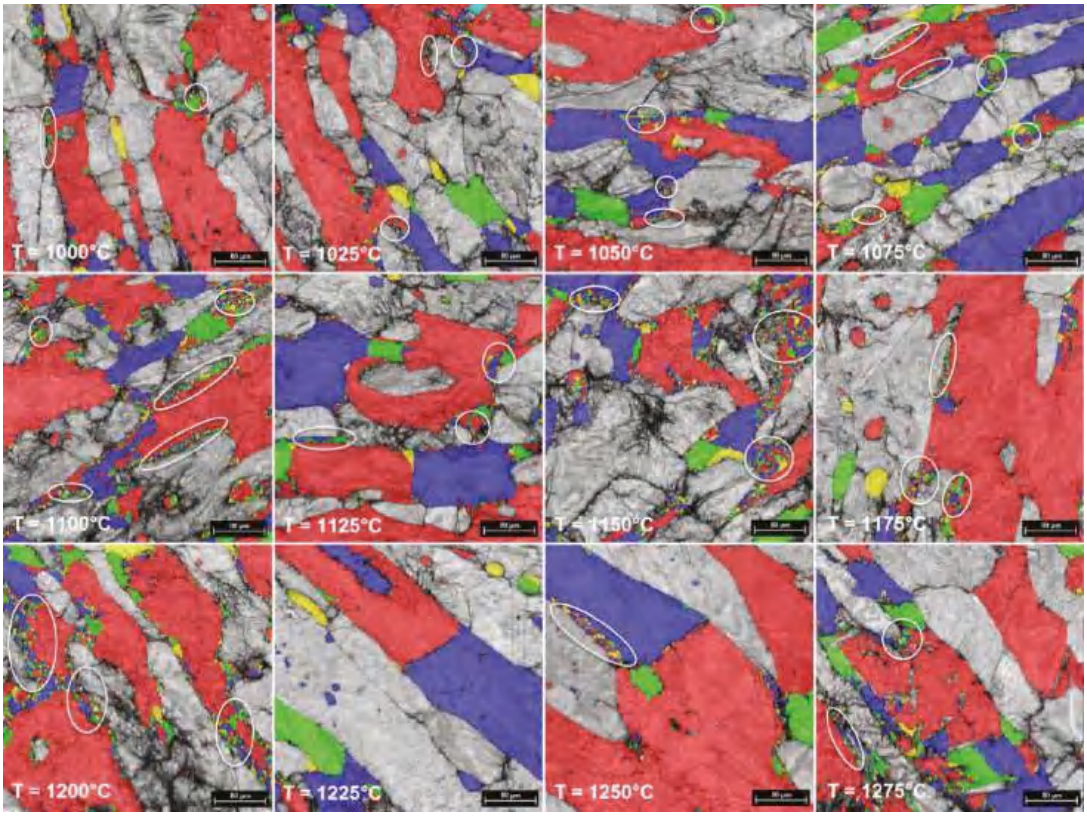

Figure 7. Typical random-colorized δ-phase grain size distribution maps in hot-deformed UNS S32750 SDSS alloy (from 1000 °C to 1275 °C).

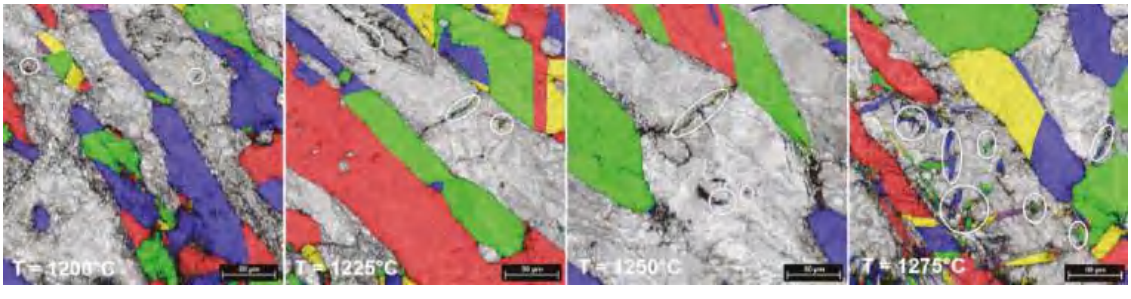

Figure 8. Typical random-colorized γ-phase grain size distribution maps in hot-deformed UNS S32750 SDSS alloy (from 1200 °C to 1275 °C).

If one considers that all new recrystallized grains show a grain size below 5 μm, then the weight fraction of the recrystallized grains belonging to both the δ-phase and γ_2-phase can be computed for each deformation temperature. Figure 9 shows the computed weight fraction of the recrystallized δ-phase (a) and precipitated γ_2-phase (b) grains as a function of deformation temperature. One can observe that, in the case of δ-phase, the weight fraction of recrystallized grains is continuously increasing from 1000 °C (when the recorded weight fraction was close to 5.8%), up to 1175 °C (when the weight fraction is reaching the maximum value, close to 14.6%). Further increasing the upsetting temperature above 1200 °C leads to a decrease in the weight fraction of the δ-phase, with a value close to 4.4% being recorded at 1275 °C. Considering the case of γ_2-phase, it can be observed that the weight fraction of newly precipitated γ_2-phase grains is continuously increasing in the 1200–1275 °C range, from 1.8% to 4.9%, due to the $\delta \rightarrow \gamma$ phase transition, which occurs mainly within the δ-phase at the δ/δ interface (Figure 8).

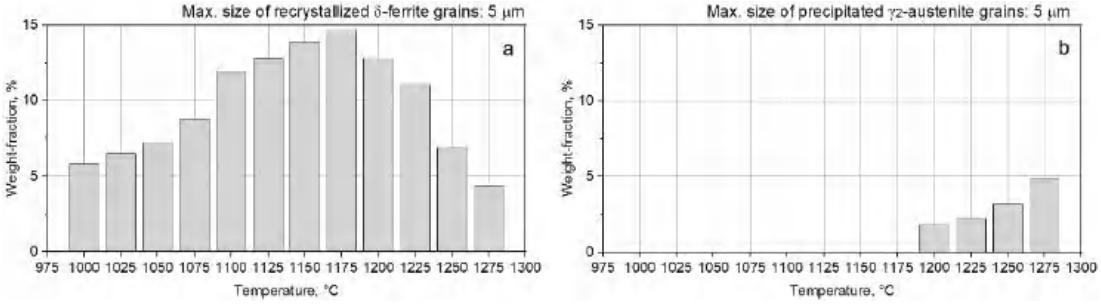

Figure 9. Weight fraction of recrystallized δ-phase (**a**) and precipitated γ_2-phase (**b**) grains as a function of deformation temperature.

All the above analysis concerning the microstructural modifications during hot deformation of the experimented material should be correlated with the mechanisms of deformation that govern thermomechanical processing. Since the material contains two phases with different deformation behaviors, the descriptions should be initiated separately on each phase, and then correlated with each other.

When considering the austenite-γ phase, it must be highlighted that it is more ductile than ferrite δ, due to the fcc crystalline structure of γ, as opposed to the bcc crystalline structure of δ. The reason is that the atomic density is nearly double for the fcc crystal structure when compared to the bcc crystal structure [34,35]; this leads to a lower critical energy necessary for activating the slip/twinning processes that assure easier deformation behavior. Consequently, it results that the δ phase (ferrite) manifests a higher strength and resistance to plastic deformation compared to austenite, due to a lower potential to accommodate plastic deformation and a higher critical energy for activating the slip/twinning systems [24–27].

Taking into account the criteria of minimum activation energy, the easiest slip system to activate for the fcc crystals is the {111} <110> primary system, while for bcc crystals it is the {110} <111> system; as for the easiest to activate twinning system, for the fcc crystals it is the {111} <112> primary system, while for the bcc crystals it is the {112} <111> system [24–27,35]. Therefore, the double atomic density mentioned above for austenite-γ is manifested in the fcc {111} atomic twinning/slip planes compared to {110} and {112} twinning/slip planes corresponding to the bcc system. As a result, it is understandable why fcc crystalline phases adapt faster to deformation processes than the bcc crystalline phases for the same processing conditions or for the same level of external stress. Additionally, it can be mentioned that, if the deformations of the material are more intense, secondary twinning/slip systems can be activated alongside primary twinning/slip systems, with lower atomic density and higher Miller indices than primary ones [26,27].

4. Conclusions

The main results of this research can be summarized as follows:

(a) For the experimented temperature range (1000–1025 °C) applied for hot deforming the UNS S32750 Super-Duplex Stainless Steel by upsetting with a total degree of deformation of 30%, the microstructure of the studied material is composed of approximately equal ratios of γ-phase and δ-phase before and after the hot deforming process.

(b) After all the applied variants of hot deforming, both δ and γ phases showed typical morphologies of strain-hardened structures. During all experimented variants, lateral fissures or cracks were not observed on the surface of UNS S32750 SDSS samples.

(c) The microstructural analysis via SEM-EBSD showed the presence of σ-phase between 1000–1025 °C, at the δ/γ interface; at temperatures above 1050 °C, this deleterious phase was not present due to its complete dissolution.

(d) For the temperature range 1200–1275 °C, the SEM-EBDS analysis indicated the increasingly intense formation of the secondary phase-γ_2 at the δ/δ interface, as the temperature increased up to 1275 °C. This signaled precipitation process can be correlated with GROD analysis, which indicated a decrease in values for δ in this temperature range, from 49° to 21° i.e., a decreasing stress for δ grains to values that favor the precipitation of γ_2 as well as intensifying dynamic recrystallization. The small size of the new δ recrystallized grains occurs due to the short duration of the hot deformation process. For the γ phase, no RX mechanism was observed.

(e) Considering the experimented temperatures for hot deforming (1000–1275 °C) and the signalized presence of the deleterious σ-phase between 1000–1025 °C, it can be concluded that the UNS S32750 Super-Duplex Stainless Steel can be safely deformed by upsetting between 1050–1275 °C with an experimented total degree of deformation of 30%.

Author Contributions: Conceptualization, E.M.C., A.N., D.R. and V.D.C.; Data Curation, E.M.C., A.N. and D.R.; Formal Analysis, E.M.C., A.N., D.R., M.L.A., I.C., I.V.B., N.Ș. and V.D.C.; Investigation, E.M.C., A.N., D.R., M.L.A., I.C., I.V.B., N.Ș. and V.D.C.; Methodology, E.M.C., A.N., D.R., I.C., I.V.B., N.Ș. and V.D.C.; Validation, E.M.C., A.N., M.L.A. and V.D.C.; Visualization, D.R.; Writing—Original Draft, E.M.C., A.N. and V.D.C. All authors have read and agreed to the published version of the manuscript.

Funding: This research received no funding.

Institutional Review Board Statement: Not applicable.

Informed Consent Statement: Not applicable.

Data Availability Statement: The data presented in this study are available on request from the corresponding author.

Conflicts of Interest: The authors declare no conflict of interest. The funders had no role in the design of the study; in the collection, analyses, or interpretation of data; in the writing of the manuscript, or in the decision to publish the results.

References

1. Xiong, J.; Tan, M.Y.; Forsyth, M. The corrosion behaviors of stainless steel weldments in sodium chloride solution observed using a novel electrochemical measurement approach. *Desalination* **2013**, *327*, 39–45. [CrossRef]
2. Zanotto, F.; Grassi, V.; Balbo, A.; Zucchi, F.; Monticelli, C. Investigation on the Corrosion Behavior of Lean Duplex Stainless Steel 2404 after Aging within the 650–850 °C Temperature Range. *Metals* **2019**, *9*, 529. [CrossRef]
3. Zanotto, F.; Grassi, V.; Balbo, A.; Monticelli, C.; Zucchi, F. Stress corrosion cracking of LDX 2101® duplex stainless steel in chloride solutions in the presence of thiosulphate. *Corros. Sci.* **2014**, *80*, 205–212. [CrossRef]
4. Tavares, S.S.M.; Silva, V.G.; Pardal, J.M.; Corte, J.S. Investigation of stress corrosion cracks in a UNS S32750 superduplex stainless steel. *Eng. Fail. Anal.* **2013**, *35*, 88–94. [CrossRef]
5. Nilsson, J.O. Super Duplex Stainless Steels. *J. Mater. Sci. Technol.* **1992**, *8*, 685–700. [CrossRef]
6. Hoseinpoor, M.; Momeni, M.; Moayed, M.H.; Davoodi, A. EIS assessment of critical pitting temperature of 2205 duplex stainless steel in acidified ferric chloride solution. *Corros. Sci.* **2014**, *80*, 197–204. [CrossRef]

7. Fargas, G.; Anglada, M.; Mateo, A. Effect of the annealing temperature on the mechanical properties, formability and corrosion resistance of hot-rolled duplex stainless steels. *J. Mater. Process. Technol.* **2009**, *209*, 1770–1782. [CrossRef]
8. Maki, T.; Furuhara, T.; Tsuzaki, K. Microstructure Development by Thermomechanical Processing in Duplex Stainless Steel. *ISIJ Int.* **2001**, *41*, 571–579. [CrossRef]
9. Moverare, J.J.; Odén, M. Deformation behaviour of a prestrained duplex stainless steel. *Mater. Sci. Eng. A* **2002**, *337*, 25–38. [CrossRef]
10. Kleber, S.; Hafok, M. Multiaxial Forging of Super Duplex Steel. *Mat. Sci. Forum* **2010**, *638–642*, 2998–3003. [CrossRef]
11. Rys, J.; Cempura, G. Microstructure and deformation behavior of metastable duplex stainless steel at high rolling reductions. *Mater. Sci. Eng. A* **2017**, *700*, 656–666. [CrossRef]
12. Primig, S.; Ragger, K.S.; Buchmayr, B. EBSD Study of the Microstructural Evolution during Hot Compression Testing of a Superduplex Steel. *Mat. Sci. Forum.* **2013**, *783-786*, 973–979. [CrossRef]
13. Kim, S.K.; Kang, K.Y.; Kim, M.S.; Lee, J.M. Low-Temperature Mechanical Behavior of Super Duplex Stainless Steel with Sigma Precipitation. *Metals* **2015**, *5*, 1732–1745. [CrossRef]
14. Pettersson, N.; Wessman, S.; Thuvander, M.; Hedström, P.; Odqvist, J.; Pettersson, R.F.A.; Hertzman, S. Nanostructure evolution and mechanical property changes during aging of a super duplex stainless steel at 300 °C. *Mater. Sci. Eng. A* **2015**, *647*, 241–248. [CrossRef]
15. Liu, G.; Wang, Y.; Li, S.; Du, K.; Wang, X. Deformation behavior of thermal aged duplex stainless steels studied by nanoindentation, EBSD and TEM. *Mater. High. Temp.* **2016**, *33*, 15–23. [CrossRef]
16. Wroński, S.; Tarasiuk, J.; Bacroix, B.; Baczmański, A.; Braham, C. Investigation of plastic deformation heterogeneities in duplexsteel by EBSD. *Mater. Charact.* **2012**, *73*, 52–60. [CrossRef]
17. Dakhlaoui, R.; Baczmański, A.; Braham, C.; Wroński, S.; Wierzbanowski, K.; Oliver, E.C. Effect of residual stresses onindividual phase mechanical properties of austeno-ferriticduplex stainless steel. *Acta Mater.* **2006**, *54*, 5027–5039. [CrossRef]
18. Kang, J.H.; Heo, S.J.; Yoo, J.; Kwon, Y.C. Hot working characteristics of S32760 super duplex stainless steel. *J. Mech. Sci. Technol.* **2019**, *33*, 2633–2640. [CrossRef]
19. Cojocaru, V.D.; Serban, N.; Angelescu, M.L.; Cotrut, M.C.; Cojocaru, E.M.; Vintila, A.N. Influence of Solution Treatment Temperature on Microstructural Properties of an Industrially Forged UNS S32750/1.4410/F53 Super Duplex Stainless Steel (SDSS) Alloy. *Metals* **2017**, *7*, 210. [CrossRef]
20. Cojocaru, V.D.; Raducanu, D.; Angelescu, M.L.; Vintila, A.N.; Serban, N.; Dan, I.; Cojocaru, E.M.; Cinca, I. Influence of Solution Treatment Duration on Microstructural Features of an Industrial Forged UNS S32750/1.4410/F53 Super Duplex Stainless Steel (SDSS) Alloy. *JOM* **2017**, *69*, 1439–1445. [CrossRef]
21. Örnek, C.; Engelberg, D.L. Towards understanding the effect of deformation mode on stress corrosion cracking susceptibility of grade 2205 duplex stainless steel. *Mater. Sci. Eng. A* **2016**, *666*, 269–279. [CrossRef]
22. Serban, N.; Cojocaru, V.D.; Angelescu, M.L.; Raducanu, D.; Cinca, I.; Vintila, A.N.; Cojocaru, E.M. High temperature deformation behaviour of an industrial S32760/1.4501/F55 super duplex stainless steel (SDSS) alloy. *Metall. Ital.* **2019**, *111*, 41–48.
23. Angelescu, M.L.; Cojocaru, V.D.; Serban, N.; Cojocaru, E.M. Evaluation of Optimal Forging Temperature Range for an Industrial UNS S32750 SDSS Alloy Using SEM-EBSD Analysis. *Metals* **2018**, *8*, 496. [CrossRef]
24. Schayes, C.; Bouquerel, J.; Vogt, J.B.; Palleschi, F.; Zaefferer, S. A comparison of EBSD based strain indicators for the study of Fe-3Si steel subjected to cyclic loading. *Mater. Charact.* **2016**, *115*, 61–70. [CrossRef]
25. Kamaya, M. Characterization of microstructural damage due to low-cycle-fatigue by EBSD observation. *Mater. Charact.* **2009**, *160*, 1454–1462. [CrossRef]
26. Wright, S.I.; Nowell, M.M.; Field, D.P. A review of strain analysis using electron backscatter diffraction. *Microsc. Microanal.* **2011**, *17*, 316–329. [CrossRef] [PubMed]
27. Kamaya, M. Assessment of local deformation using EBSD: Quantification of local damage at grain boundaries. *Mater. Charact.* **2012**, *66*, 56–67. [CrossRef]
28. Magalhaes, C.H.X.M.; Faria, G.L.; Lagoeiro, L.E.; Silva, J.D. Characterization of the austenite reformation mechanisms as a function of the Initial ferritic state in a UNS S32304 duplex stainless steel. *Mater. Res.* **2017**, *20*, 1470–1479. [CrossRef]
29. Muthupandi, V.; Srinivasan, P.B.; Shankar, V.; Seshadri, S.K.; Sundaresan, S. Effect of nickel and nitrogen addition on the microstructure and mechanical properties of power beam processed duplex stainless steel (UNS 31803) weld metals. *Mater. Lett.* **2005**, *59*, 2305–2309. [CrossRef]
30. Sun, Z.Q.; Yang, W.Y.; Qi, J.J.; Hu, A.M. Deformation enhanced transformation and dynamic recrystallization of ferrite in a low carbon steel during multipass hot deformation. *Mater. Sci. Eng. A* **2002**, *334*, 201–206. [CrossRef]
31. Ciuffini, A.F.; Barella, S.; Peral Martínez, L.B.; Mapelli, C.; Fernández Pariente, I. Influence of Microstructure and Shot Peening Treatment on Corrosion Resistance of AISI F55-UNS S32760 Super Duplex Stainless Steel. *Materials* **2018**, *11*, 1038. [CrossRef] [PubMed]
32. Mészáros, I.; Bögre, B. Complex Study of Eutectoidal Phase Transformation of 2507-Type Super-Duplex Stainless Steel. *Materials* **2019**, *12*, 2205. [CrossRef]

33. Biserova-Tahchieva, A.; Cabrera, J.M.; Llorca-Isern, N. Study of the Thermochemical Surface Treatment Effect on the Phase Precipitation and Degradation Behaviour of DSS and SDSS. *Materials* **2020**, *13*, 165. [CrossRef] [PubMed]
34. Liang, Z.Y.; Huang, M.X. Deformation twinning in small-sizedface-centred cubic single crystals: Experiments and modelling. *J. Mech. Phys. Solids* **2015**, *85*, 128–142. [CrossRef]
35. Chen, Z.; Cai, H.; Li, S.; Zhang, X.; Wang, F.; Tan, C. Analysis ofcrystallographic twinning and slip in fcc crystals underplane strain compression. *Mater. Sci. Eng. A* **2007**, *464*, 101–109. [CrossRef]

materials

MDPI

Article

Microstructure and Texture Evolution in Low Carbon and Low Alloy Steel during Warm Deformation

Sheng Xu [1,2], Haijie Xu [1], Xuedao Shu [1,*], Shuxin Li [1] and Zhongliang Shen [2]

[1] College of Mechanical Engineering and Mechanics, Ningbo University, Ningbo 315211, China; xs@zbti.edu.cn (S.X.); xuhaijie@nbu.edu.cn (H.X.); lishuxin@nbu.edu.cn (S.L.)
[2] Department of Mechanical Engineering, Zhejiang Business and Technology Institute, Ningbo 315012, China; szl@zbti.edu.cn
* Correspondence: shuxuedao@nbu.edu.cn

Abstract: Warm compression tests were carried out on low carbon and low alloy steel at temperatures of 600–850 °C and stain rates of 0.01–10 s^{-1}. The evolution of microstructure and texture was studied using a scanning electron microscope and electron backscattered diffraction. The results indicated that cementite spheroidization occurred and greatly reduced at 750 °C due to a phase transformation. Dynamic recrystallization led to a transition from {112}<110> texture to {111}<112> texture. Below 800 °C, the intensity and variation of texture with deformation temperature is more significant than that above 800 °C. The contents of the {111}<110> texture and {111}<112> texture were equivalent above 800 °C, resulting in the better uniformity of γ-fiber texture. Nucleation of <110>//ND-oriented grains increased, leading to the strengthening of <110>//ND texture. Microstructure analysis revealed that the uniform and refined grains can be obtained after deformation at 800 °C and 850 °C. The texture variation reflected the fact that 800 °C was the critical value for temperature sensitivity of warm deformation. At a large strain rate, the lowest dislocation density appeared after deformation at 800 °C. Therefore, 800 °C is a suitable temperature for the warm forming application, where the investigated material is easy to deform and evolves into a uniform and refined microstructure.

Keywords: low carbon and low alloy steel; warm deformation; texture; recrystallization

Citation: Xu, S.; Xu, H.; Shu, X.; Li, S.; Shen, Z. Microstructure and Texture Evolution in Low Carbon and Low Alloy Steel during Warm Deformation. *Materials* **2022**, *15*, 2702. https://doi.org/10.3390/ma15072702

Academic Editor: Ivo Schindler

Received: 14 March 2022
Accepted: 4 April 2022
Published: 6 April 2022

1. Introduction

In industrial conditions, more than 80% of energy is consumed in heating and the rest in rolling [1]. Taking the advantages of cold forming and hot forming, warm forming at a temperature of 650–850 °C was applied in industry as an energy-saving technology. The behavior and microstructure evolution of warm deformation have been studied on various carbon steels. Typically, recovery and recrystallization occurred simultaneously and interacted with each other during deformation, and their speed and share in microstructural variation depended on the chemical composition, initial microstructure and process parameters [2]. At low deformation temperature and high strain rate, the work softening rate increased significantly [3], and the increase in carbon content led to a decrease in deformation activation energy [4].

Grain refinement occurred in both medium carbon and low carbon alloy steels during warm deformation [5–7]. Ultra-fine grain microstructure also can be obtained by warm deformation of ultra-low carbon steel [8,9]. Continuous dynamic recrystallization (CDRX) can lead to the formation of new fine ferrite grains [7,10]. The cementite precipitated at the ferrite boundaries, due to intragranular nucleation activation, then caused ferrite to nucleate over the α/γ interface [11]. The elongated ferrite grains continuously dynamically recrystallize to form the equiaxed fine ferrite grains [12]. Eghbali [13,14] conducted extensive research on the warm deformation of low carbon steels and discovered that strain rate had an important effect on grain refinement in the CDRX process.

Grain refinement was also directly related to the spheroidization of cementite during warm deformation [15,16]. Warm deformation at 650–750 °C promoted the spheroidization of carbides, leading to flow softening [17,18]. In addition, the spheroidization of pearlite was accelerated due to the heavy warm deformation of ferritic-pearlitic carbon steel, resulting in the formation of completely spheroidized cementite, and the deformation at 670–700 °C led to homogeneous distribution of cementite particles [19].

It is well recognized that texture is one of the key factors affecting the properties of BCC metals and alloys [20], and texture might have negative effects on material characteristics [20,21], such as ridging, earring, etc. A large number of scholars paid attention to the grain orientation for different annealing processing parameters of steel sheets [22], so as to obtain large plastic strain ratios. In general, {111}// ND has a larger Taylor factor than {100}//ND in BCC metals, which means that many slip systems are activated and grain fragmentation is easily promoted in {111}//ND [23]. The texture of {001}<110> and {111}<110> developed significantly, and the fraction of the high angle boundary increased with the equivalent strain in an ultra-low carbon steel compression [24]. The {111} orientations were the first to recrystallize while the α-fiber was present until the end of recrystallization [25].

At present, there have been a large number of studies on warm deformation of carbon steel. In most previous studies, steel sheets were investigated to obtain blank material with better plasticity for further cold processing [26], such as drawing or stamping. In fact, the warm rolling or warm cross wedge rolling (WCWR) of shaft parts and warm extrusion of auto parts are also widely applied in industry [27–29]. Bulzak [1] suggested that WCWR consumed less energy to heat the workpiece than hot rolling. In contrast, Huang [29] proposed that the warm rolling torque was three times that of the hot rolling torque and, although the heating energy consumption was reduced, the spheroidization of cementite and the recrystallization of ferrite had remarkable effects on the tensile strength and yield strength. In addition, most of the experimental materials in previous studies were heated to complete austenitization then cooled to the ferrite-austenite region and ferrite region for compression testing [30]. In fact, the material is directly heated to the forming temperature in the industrial applications. Even if the final temperature is the same, the microstructure evolution from ferrite to austenite (heating process) is significantly different to the evolution from austenite to ferrite (cooling process). Thus, an appropriate forming temperature is provided by warm rolling, especially in heavy deformation, and determines the energy consumption, formability and microstructure that influences the mechanical properties of products. Moreover, investigating the temperature sensitivity of the material, the influence of process parameters on microstructure evolution, and the homogeneity of plastic deformation, is helpful and essential to optimize the technical parameters (temperature, strain rate, area reduction, etc.) to accomplish the more effective forming qualities with fewer resources [31].

In this study of warm deformation, low carbon and low alloy steel (20CrMoA) with high quenching ability, good machinability, cold strain plasticity, and which is widely used in shafts and gears [32], was investigated as an experimental material. The evolution of microstructure and texture during warm deformation under different parameters was studied. Meanwhile, it is considered that the warm forming process in industrial applications mostly involves heavy deformation at high strain rate. The microstructure at high strain rate is thoroughly analyzed to determine the proper deformation temperature and provide a reference for process application.

2. Material and Experimental Procedure

The chemical composition of the studied low carbon and low alloy structural steel was 0.2%C, 0.24%Si, 0.52%Mn, 0.92%Cr, 0.16%Mo (in wt%). The initial microstructure of the low carbon steel was lamellar with alternate formations of ferrite and pearlite. The cylindrical specimens, with a diameter of 8 mm and a height of 12 mm sampled from a homogenized bar, were compressed on a Gleeble-3500 thermal simulator. In this experiment, the deformation temperature was 600, 650, 700, 750, 800 and 850 °C. Each

specimen was heated to the specified deformation temperature at a rate of 10 °C/s and held for 3 min under isothermal conditions for heat balance. The specimen was compressed along the axial direction (ND) at strain rates of 0.01, 0.1, 1, and 10 s^{-1} with the deformation ratio of 70% as shown in Figure 1. The specimens were immediately quenched in water to maintain the microstructure after compression. After that, the compressed specimens were sectioned, polished, and etched to obtain the microstructures under different compression conditions. Micro-textures were examined by electron backscattered diffraction (EBSD), and microstructures were observed using a scanning electron microscope (SEM). The percentages of high-angle grain boundaries (HAGBs) with the misorientation angles higher than 15° and low-angle grain boundaries (LAGBs) with the misorientation angles between 2° and 15° were calculated [33,34].

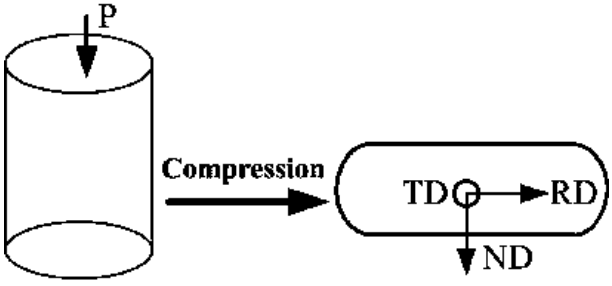

Figure 1. Compression process and the orientations of the specimen.

The EBSD map of initial microstructure was shown in Figure 2. The uniform microstructure consisting of equiaxed grains can be observed with the average size of the grains of 10.74 μm. The transformation temperature was calculated by JmatPro software (Version 7.0, Sente Software Ltd., Guildford, Surrey, UK) based on the chemical composition of the experimental steel.

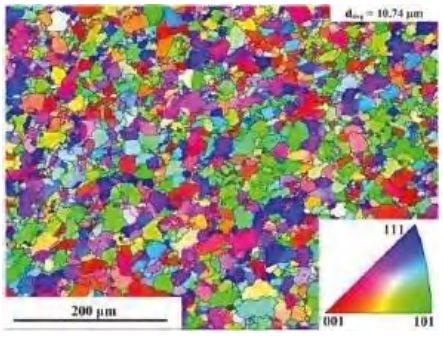

Figure 2. EBSD map of non-deformed microstructure.

3. Results and Discussion

3.1. Microstructures Evolution

According to the results calculated by JmatPro software, the start equilibrium transformation temperature AC1 and finish equilibrium transformation temperature Ac3 from ferrite to austenite are determined to be 731.5 °C and 824.7 °C, respectively. Figure 3 shows the low magnification SEM images of different deformation conditions. At 700 °C and 0.01 s^{-1}, the microstructure of steel comprises pearlite and ferrite, even though the deformation time is longer (Figure 3a). At 750 °C, apparent transformation occurred and the steel showed the α + γ double-phase region. In this region, recrystallized ferrite and

the amount of martensite formed after cooling of austenite were observed as shown in Figure 3b. In addition, a few FeC_3 particles appeared. With the increasing deformation temperature, the fraction volume of martensite increases, while FeC_3 particles were not observed in the microstructure (Figure 3c). Moreover, the ferrite grains are smaller. In the case that the deformation temperature exceeds the AC3 temperature, the steel is completely austenitized (Figure 3d).

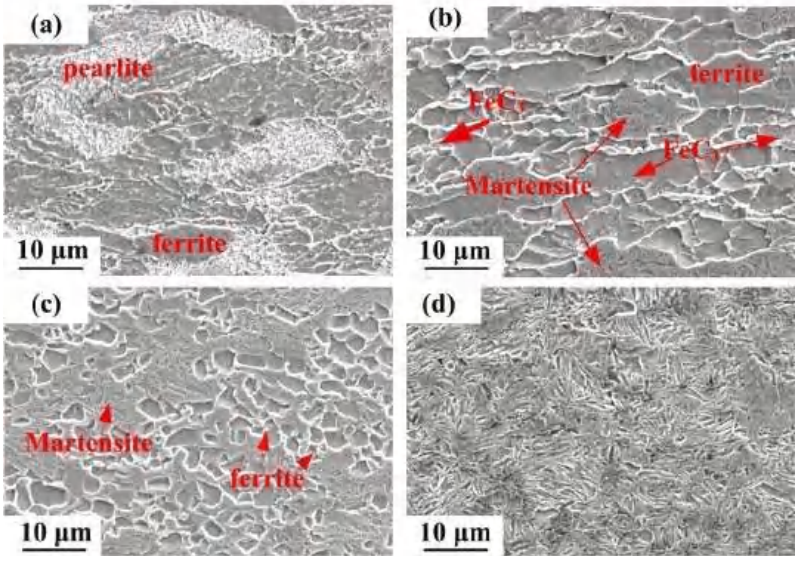

Figure 3. Low magnification SEM images of (**a**) 700 °C, 0.01 s^{-1} (**b**) 750 °C, 0.01 s^{-1} (**c**) 800 °C, 1 s^{-1} (**d**) 850 °C, 1 s^{-1}.

To distinguish details in the microstructures, higher-magnification SEM images in different deformation conditions are provided in Figure 4. Significant fragments and particles are observed as a result of the rupture and spheroidization of cementite. At 650 °C and 0.1 s^{-1} as shown in Figure 4a, cementites are dominated by broken fragments, which is related to the deformation temperature. In the process of warm deformation, the ferrite and cementite in pearlite can deform co-ordinately at small strain. During heavy deformation, the co-ordinative deformation state will be broken due to significant differences in the mechanical properties between ferrite and cementite. The cementite with a poor plastic property is prone to bending, melting and spheroidization. When heavy deformation compression is carried out at low temperature, the cementite is fractured under a strong plastic deformation force, and the fragments are in heterogeneous nucleation. At high deformation temperature, the lamellar cementite gradually dissolves and shrinks to short rods, driven by interface energy. Therefore, more pieces of short rod cementite appeared after the compression at 700 °C, as shown in Figure 4b. The main mechanism is that a large number of dislocations are produced in the ferrite during warm deformation, providing a channel for the rapid diffusion of carbon atoms. Subsequently, the increase of deformation temperature further intensifies the diffusion, causing the concentration gradient of carbon. The lamellar cementites dissolved in the ferrite, under the action of deformation force and thermal effect. When carbon was supersaturated in ferrite, the fine cementite particles precipitated.

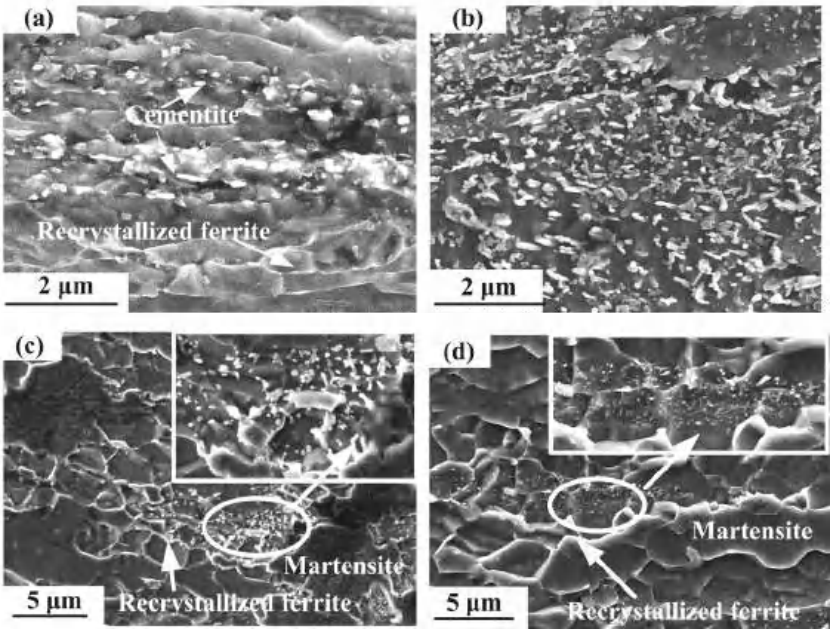

Figure 4. High magnification SEM images of (**a**) 650 °C, 0.1 s^{-1}; (**b**) 700 °C, 10 s^{-1}; (**c**) 750 °C, 0.1 s^{-1}; (**d**) 750 °C, 10 s^{-1}.

As shown in Figure 4c,d, the cementite spheroidized at the boundary between the recrystallized ferrite grain and martenties. In addition, the spheroidization of cementite is greatly reduced in the process of deformation at 750 °C, whether the strain rate is low or high. This is related to the phase transformation in the steel, i.e., the ferrite transferred into austenite at 750 °C. In general, austenite nucleates at the interface of ferrite and cementite. Because a lot of cementites were dissolved by the diffusion of austenite, the spheroidized cementite particles decrease greatly during the deformation. While the undissolved cementite particles remain at the junction of ferrite and austenite which is transformed into martentie after cooling.

3.2. Recrystallization Behavior

The EBSD maps of substructure, recrystallized and deformed grains after deformation at 600, 650, and 700 °C (ferrite region) are shown in Figure 5. The blue regions represent recrystallized grains, and the red regions indicate that the grains have undergone plastic deformation and stored distortion energy. The yellow regions refer to the substructures that were not completely recrystallized, and the energy stored in those regions is lower than that in the red regions. In the ferrite region, the EBSD maps of the microstructures were basically the same, and mostly contained deformed grains. Dynamic recrystallization (DRX) of ferrite did not readily occur and dynamic recovery (DRV) was the main softening mechanism, due to the high stacking fault energy (SFE) of the BCC structure, which was susceptible to dislocation climb and cross slip [35]. According to the previous study [36], the width of extended dislocation is small in high SFE materials, which commonly leads to the clustered imperfect dislocations. During heat deformation, dislocation climb and cross slip easily proceeded, resulting in sufficient dynamic recovery. However, the remaining stored energy is insufficient to facilitate the dynamic recrystallization.

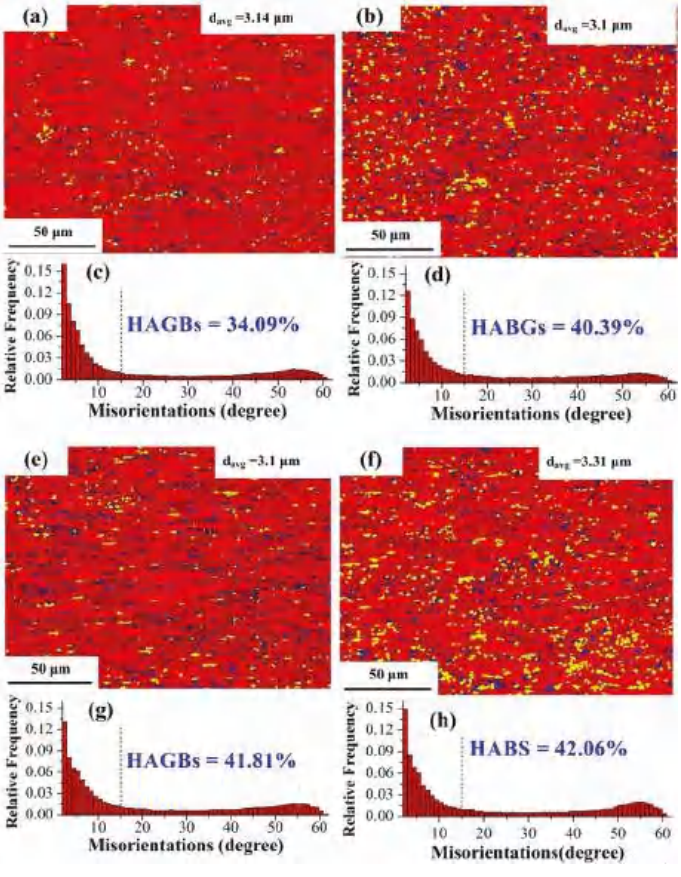

Figure 5. EBSD maps of recrystallized, substructure, and deformed grains; misorientation angle distributions (**a**,**c**) 600 °C, 0.01 s^{-1} (**b**,**d**) 650 °C, 0.1 s^{-1} (**e**,**g**) 700 °C, 0.1 s^{-1} (**f**,**h**) 700 °C, 1 s^{-1}.

The fractions of recrystallized grains, substructure, and deformed grains are shown in Figure 6a, and the fraction of formed grains exceeds 84% under all deformation conditions. Therefore, LAGBs dominate in the misorientation angle, accounting for more than 58% as shown in Figure 5c,d,g,h. The higher proportion of HAGBs can be attributed to the higher volume fraction of DRX [37]. In addition, a low proportion of HAGBs and recrystallized grains indicates that only partial dynamic recrystallization occurs and the main soft mechanism is DRV.

There is no significant difference in grain size under different deformation conditions, with an average grain size of around 3.1 μm. Figure 6b shows the grain size distribution under different deformation conditions. The proportion of size 0–5 μm exceeds 83%, with grains in the size of 0–2 μm being around 40%, indicating that grains are refined due to the local dynamic recrystallization of ferrite.

Figure 7 shows the EBSD maps of recrystallized, substructure, and deformed grains after deformation at 750, 800, and 850 °C. Figure 8a shows the fraction of recrystallized grains, substructure and deformed grains under different deformation conditions, and Figure 8b presents the distribution of grain sizes. As shown in Figure 8a, at a strain rate of 10 s^{-1}, the proportion of recrystallized grain after deformation at 850 °C is only 3.73%, which is much less than 32.08% at 800 °C and 5.56% at 650 °C with the strain rate of 0.1 s^{-1}. This phenomenon is mainly attributed to phase transformation. Complete austenitizing

occurs during deformation at 850 °C due to the fact that the deformation temperature is higher than the AC3 temperature. Consequently, the recrystallized grains at 850 °C are all austenite. However, 850 °C is lower than the complete recrystallization temperature of austenite grains, so only a small amount of dynamic recrystallization occurs in the microstructure.

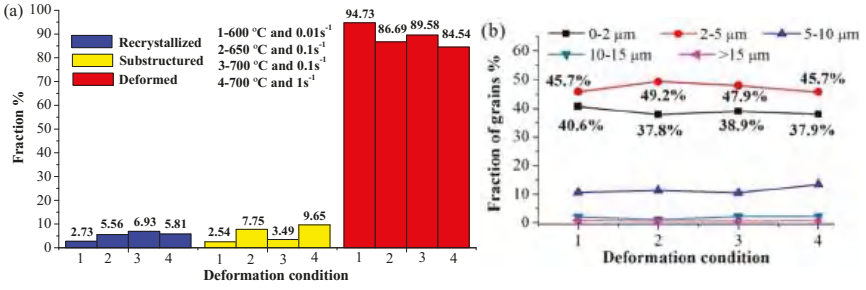

Figure 6. (**a**) The fraction of recrystallized, substructure and deformed grains under different deformation conditions (**b**) Distribution of grain size under different deformation conditions.

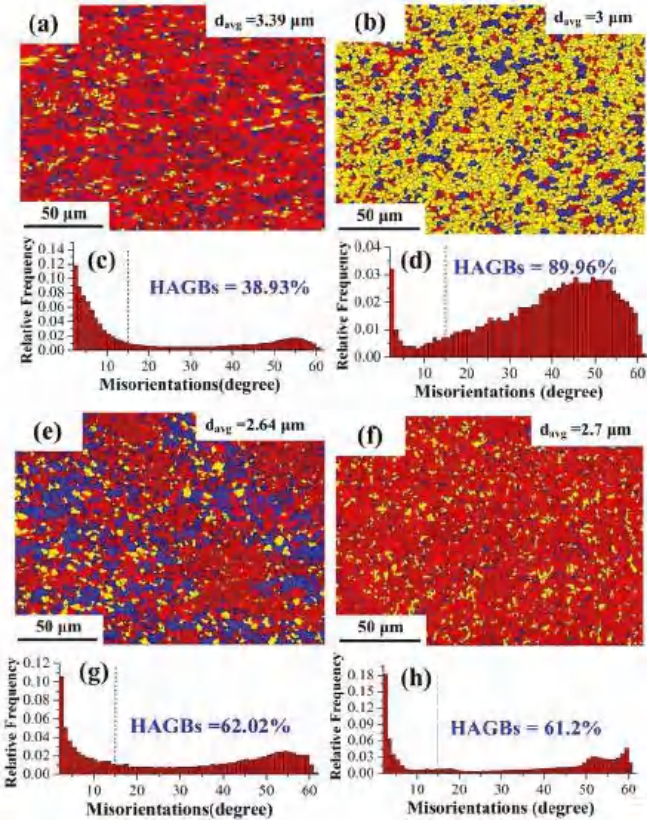

Figure 7. EBSD maps of recrystallized, substructure, and deformed grains, and misorientation angle distributions (**a**,**c**) 750 °C, 1 s^{-1}; (**b**,**d**) 800 °C, 1 s^{-1}; (**e**,**g**) 800 °C, 10 s^{-1}; (**f**,**h**) 850 °C, 10 s^{-1}.

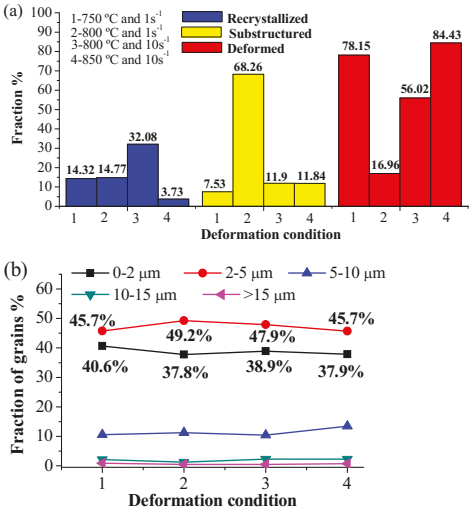

Figure 8. (**a**) The fraction of recrystallized grains, substructure and deformed grains under different deformation conditions, (**b**) Distribution of grain size under different deformation conditions.

The volume fraction of recrystallized grain is 32.08% at 800 °C and 10 s^{-1}, which is much higher than 14.77% at 800 °C and 1 s^{-1}, but the area fraction of substructure is apparently low. There are three main reasons for this phenomenon [38,39]: (i) The deformation time is longer at a low strain rate and the continuous deformation results in the substructures consisting of entangled dislocations in dynamically recrystallized grains. (ii) More severe shear deformation at a large strain rate intensifies dynamic recrystallization to a certain extent. (iii) At large strain rates, most of the deformation heat cannot be dissipated, and is instead stored as heat energy, leading to the temperature rise of the specimen. The higher temperature rise due to a larger strain rate is more favorable for dynamic recrystallization during heavy deformation.

The distributions of misorientation angle and the percentages of HABs reveal the recrystallization behavior shown in Figure 7c,d,g,h. It is worth noting that the proportion of HAGBs is close to 90% at 800 °C and 1 s^{-1}, even at a lower percentage of recrystallized grains, indicating that the substructures were not composed of subgrains with LAGBs. DRV excessively consumed the distortion energy at a higher temperature [35,37], so there was a high proportion of both substructures and HAGBs.

Figure 8b illustrates the grain size distribution under different deformation conditions. The proportion of size 0–5 μm also exceeded 82%, In addition, the percentage of grains with the diameter of 0–2 μm decreased, while that in the diameter of 2–5 μm increased, compared with the grains' size in the ferrite region. Low strain rate provides a longer deformation time, and the recrystallized grains have the opportunity to grow into large sizes. As a result, the average size of grains at 1 s^{-1} is larger than that at 10 s^{-1}.

To analyze the dispersion degree of grain distribution, the standard deviation of grain size under each deformation condition was calculated as shown in Figure 9. It can be found clearly that the standard deviation of grain size distribution is smaller when the deformation temperature is higher than 800 °C and the minimum value is 1.08 at 800 °C and 1 s^{-1}, indicating that the microstructure with a more uniform grain distribution can be obtained at 800 °C or 850 °C.

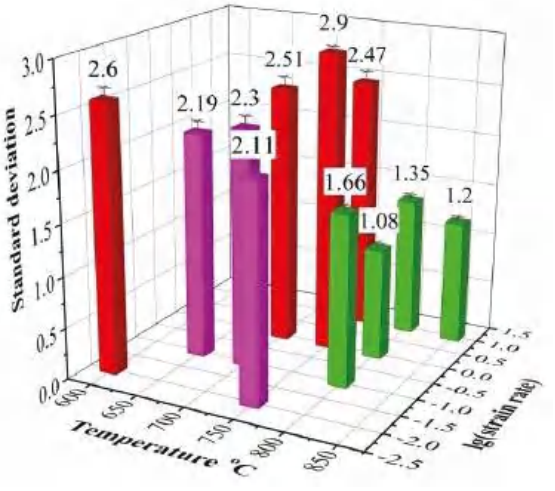

Figure 9. Standard deviation of grain size.

3.3. Texture Evolution

Figure 10 shows the main texture components and fibers of BCC steels in the $\varphi_2 = 45°$ section of the Euler space [40]. Figure 11 shows the orientation maps and micro-texture after deformation at 650 and 700 °C. The grains having blue, red, and green colors are <111>//ND, <001>//ND, <101>//ND orientation, respectively. Under each deformation condition, the microstructure was characterized by elongated grains and mainly consisted of <111>//ND and <001>//ND textures. The intensity of <111>//ND texture is significantly higher than <001>//ND texture. Barnett [41] revealed that {111}<112> grains were nucleated in situ and {111}<110> grains were nucleated at the grain boundaries of deformed {111}<112> grains during recrystallization. In addition, {112}<110> texture transformed to {111}<112>, and {001}<110> transformed to {111}<112> or {111}<110>. Thus, the formation of strong {111}<112> and {111}<110> are attributed to nucleation rate and growth rate [42,43].

As shown in Figure 11, {112}<110> was weak at 650 °C and 0.1 s^{-1} and disappeared at 700 °C and 0.1 s^{-1}, indicating that {112}<110> was completely consumed during the recrystallization process, even if the recrystallization proportion was very low. With the increasing temperature or decreasing strain rate, the intensity of <111>//ND texture and {001}<110> (R-Cube) decreased. Meanwhile, the intensity of {001}<110> (Cube) increased under conditions favorable for recrystallization, which indicated that the Cube is recrystallized texture.

Figure 12 shows the orientation maps and micro-texture after deformation at 750, 800 and 850 °C. The microstructures were mainly characterized by elongated grains at 750 °C. After deformation at 800 °C and 850 °C, the equiaxed grains with an average size of 3 μm dynamically recrystallized in the dual-phase deformed microstructures. As in the ferrite region, the texture mainly consisted of <111>//ND and <001>//ND fibers. However, the intensity of each texture component at 750 °C was much stronger than that above 800 °C.

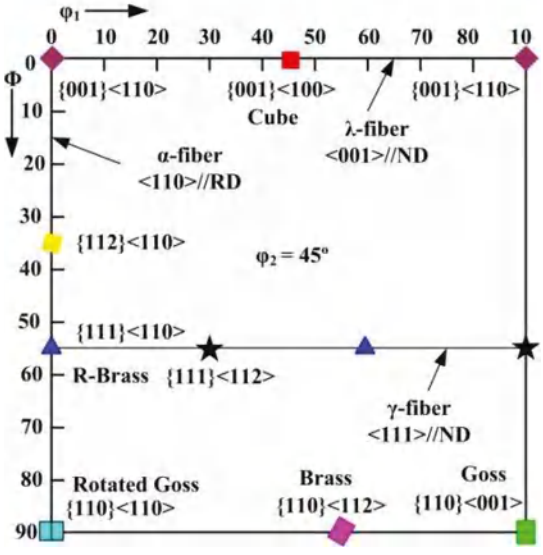

Figure 10. Main texture components and fibers of BCC steels of the Euler space: $\varphi_2 = 45^{\circ}$ section.

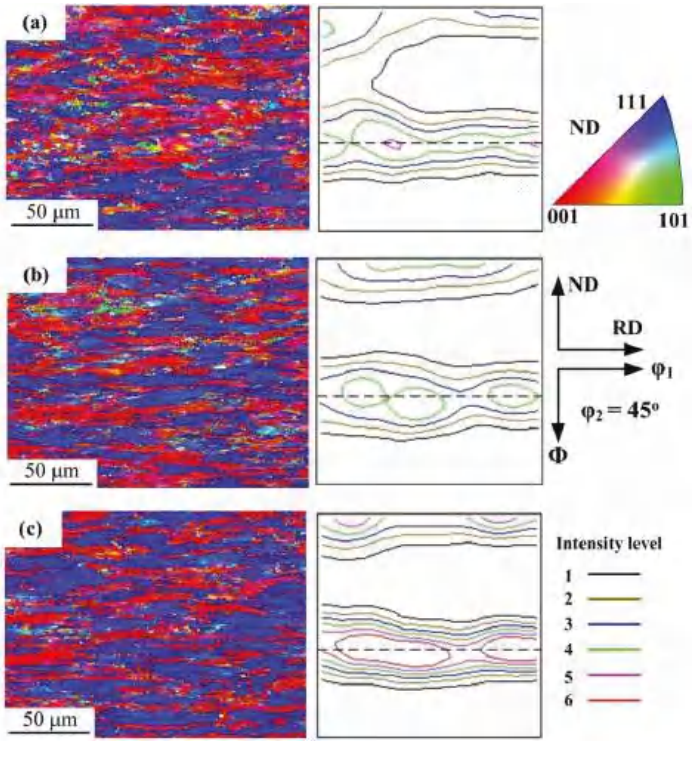

Figure 11. Grain orientation map of (**a**) 650 °C, 0.1 s^{-1} (**b**) 700 °C, 0.1 s^{-1} (**c**) 700 °C, 1 s^{-1}.

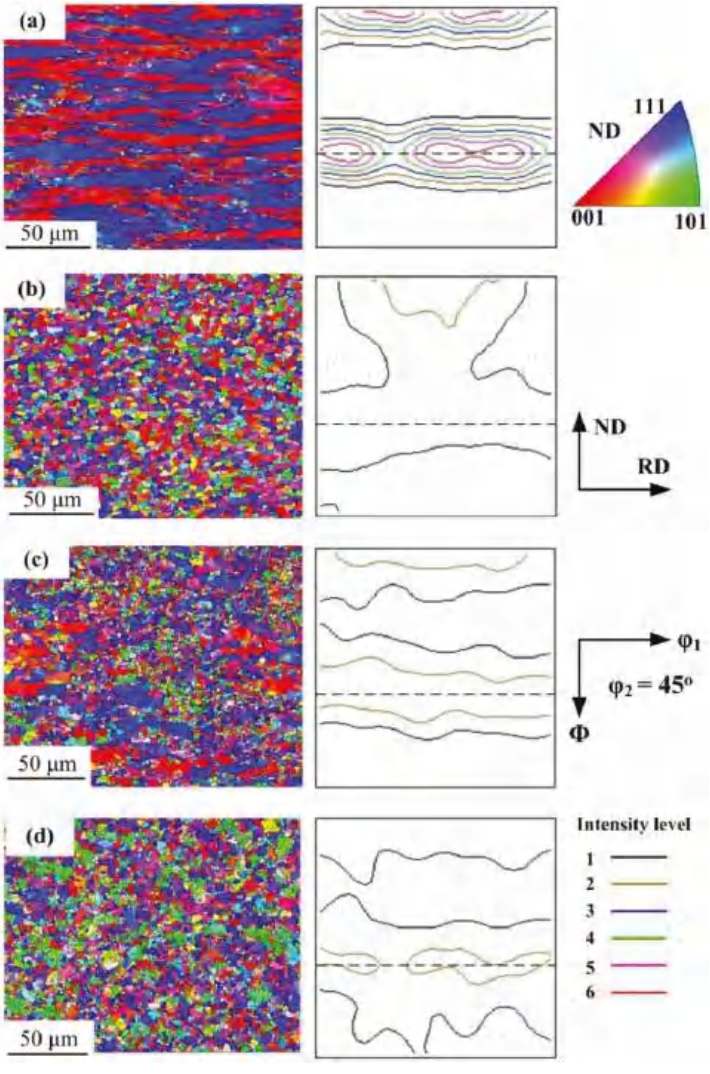

Figure 12. Grain orientation map of (**a**) 750 °C, 1 s^{-1} (**b**) 800 °C, 1 s^{-1} (**c**) 800 °C, 10 s^{-1} (**d**) 850 °C, 10 s^{-1}.

At the fixed strain rate of 1 s^{-1}, the intensity of {111}<110> and {001}<100> at 750 °C was higher than that at 700 °C and 800 °C. It indicated that a small amount of austenite has a significant effect on {111}<110> and {001}<100> in the initial stage of phase transformation.

In addition, when the deformation temperature rose from 750 °C to 800 °C, the reduction of texture intensity was much larger than that at the same temperature interval (from 800 °C to 850 °C) and a larger strain rate of 10 s^{-1}. It is inferred that there was a critical temperature range between 750 °C and 800 °C, where the texture intensity decreased rapidly with the phase transformation due to rising temperature, and the deformation behavior was more sensitive to the temperature below 800 °C. The steel was in the end stage of phase transformation and austenite was dominant at 800 °C where texture type and intensity variation were similar to austenite, thus the texture intensity was higher than that at 850 °C. It is worth noting that above 800 °C the nucleation of <110>//ND oriented grains increased, leading to the strengthening of <110>//ND texture.

3.4. Effect of Warm Deformation Parameters on Texture Uniformity

Table 1 shows the percentage of the texture component under different deformation conditions. When the deformation temperature reached 800 °C, the content of <111>//ND texture and <001>//ND texture decreased greatly, but there is no significant difference in content between {111}<110> and {111}<112>. Since the stored energy of {111}<112> is higher than that of {111}<110>, {111}<112> preferentially nucleates in the recrystallization process [44], and the content of the components is usually higher than that of {111}<110>. In addition, the transformation rate of {111}<112> oriented grains to {111}<110> orientation is far greater than that of {111}<110> to others [45]. Due to the higher recrystallization proportion above 800 °C, the transformation between {111}<112> and {111}<110> is sufficient, and the intensity of the two components is equivalent. Thus, the uniformity of γ-fiber texture is better above 800 °C. The percentage of <110>//ND texture increased greatly above 800 °C, which shows that the austenite influenced the evolution of <110>//ND texture during warm deformation. At the strain rate of 10 s^{-1} and above 800 °C, the texture of λ-fiber has better uniformity.

Table 1. The percentage of the texture component (divergence angle = 20°).

	{111}	{111}<110>	{111}<112>	{001}	{001}<110>	{001}<100>	{110}
	Texture, %	**Component, %**	**Component, %**	**Texture, %**	**Component, %**	**Component, %**	**Texture, %**
650 °C 0.1 s^{-1}	46.1	24.2	26.3	35.1	15.5	9.17	4.96
700 °C 0.1 s^{-1}	48.6	24.6	30.2	36.9	10.9	15	5.21
700 °C 1 s^{-1}	58.2	32.4	36.7	34.8	15.6	10.2	1.79
750 °C 1 s^{-1}	51.1	33.7	27.7	40.4	13.5	17.1	2.64
750 °C 10 s^{-1}	49.2	25.5	31.6	40.9	12.6	18.1	3.77
800 °C 1 s^{-1}	29.4	14.5	14.3	26.2	4.7	11	21.4
800 °C 10 s^{-1}	37.1	18.3	19	26.5	8.48	8.77	18.4
850 °C 10 s^{-1}	31.6	15.4	15.6	16.8	6.58	6.68	31.7

3.5. Kernel Average Misorientation Distribution

Kernel Average Misorientation (KAM) distribution can reflect the degree of deformation. The blue region possesses the dislocation with the lowest density, while the red region possesses the dislocation with the highest density [44,46]. The grains with low KAM values exhibit a uniform strain distribution, and high values indicate a greater degree of plastic deformation or a higher defect density. From the experience of engineering applications, warm forming such as warm rolling or warm extrusion is heavy deformation under a large strain rate. The KAM maps at large strain rates of 1 s^{-1} and 10 s^{-1} are shown in Figure 13. At strain rate of 1 s^{-1}, the dislocation density decreases with the increase of deformation temperature. The sample after deformation at 800 °C has the lowest dislocation density and most homogenous strain distribution. At a fixed strain rate of 10 s^{-1}, the dislocation density in the sample deformed at 850 °C looks more uniform, but apparently higher than the others. The sample deformed at 800 °C has a lower dislocation density than the sample with 750 °C, which will show relative stable properties in subsequent processing.

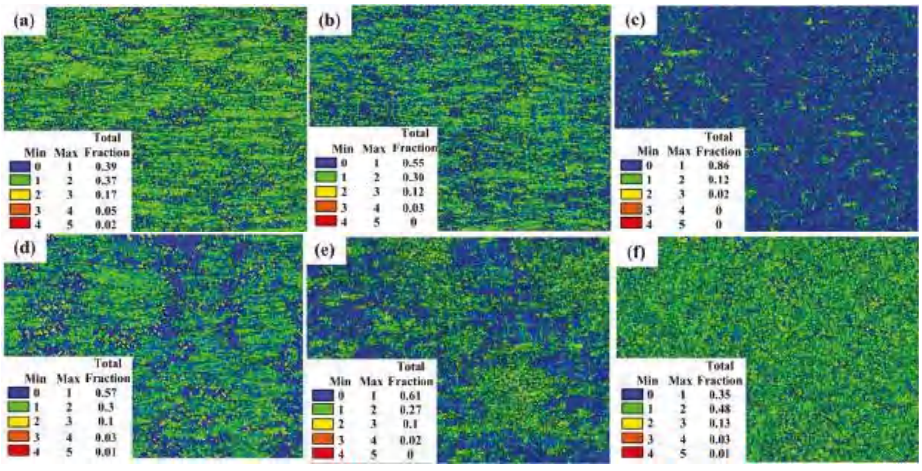

Figure 13. KAM map. (**a**) 700 °C, 1 s^{-1} (**b**) 750 °C, 1 s^{-1} (**c**) 800 °C, 1 s^{-1} (**d**) 750 °C, 10 $s>^{-1}$; (**e**) 800 °C, 10 s^{-1}; (**f**) 850 °C, 10 s^{-1}.

4. Conclusions

(1) The spheroidization of cementite is related to deformation temperature. At low temperature, the broken fragments are dominant, while the cementite spheroidizes into small particles and short rods at 700 °C. In the dual-phase region, the cementite is dissolved due to the austenitizing, and the spheroidizing particles decrease rapidly. After deformation at 800 °C, equiaxed grains with the size of 3 μm were observed, which is caused by the dynamic recrystallization of ferrite.

(2) In the ferrite region, the texture mainly consists of <111>//ND, <001>//ND fibers. With the increasing temperature or/and the decreasing strain rate, the intensity of {001}<100> (Cube) texture decreases and the {112}<110> texture transforms to {111}<112> texture.

(3) 800 °C is the critical value for temperature sensitivity of warm deformation. At temperatures below 800 °C, the texture mainly consisted of strong γ-fiber and λ-fiber texture, and the variation of texture strength with deformation temperature is significant. Above 800 °C, the γ-fiber texture shows relatively uniform distribution. The <110>//ND oriented grains appears, leading to the strengthening of <110>//ND texture.

(4) Equiaxed grains with smaller average grain size and uniform distribution can be obtained at 800 °C. Under a large strain rate, the fraction of KAM values indicating lower dislocation at 800 °C is much higher than at other deformation temperatures. For this reason, 800 °C is a suitable temperature for warm forming applications.

Author Contributions: Conceptualization, X.S.; methodology, S.L.; software, S.X. and H.X.; validation, S.L.; formal analysis, S.X. and H.X.; investigation, S.X.; resources, Z.S.; data curation, S.X.; writing—original draft preparation, S.X.; writing—review and editing, H.X.; visualization, S.X.; supervision, S.L.; project administration, X.S.; funding acquisition, X.S. and Z.S. All authors have read and agreed to the published version of the manuscript.

Funding: This research was funded by the National Natural Science Foundation of China (Grant no, 51975301) and Public Welfare Technology Application Research Project of Zhejiang Province of China (Grant no, LGG20E050001).

Institutional Review Board Statement: Not applicable.

Informed Consent Statement: Not applicable.

Data Availability Statement: The data presented in this study are available on request from the corresponding author.

Conflicts of Interest: The authors declare no conflict of interest.

References

1. Bulzak, T.; Pater, Z.; Tomczak, J.; Majerski, K. Hot and warm cross-wedge rolling of ball pins-Comparative analysis. *J. Manuf. Process.* **2020**, *50*, 90–101. [CrossRef]
2. Niechajowicz, A.; Tobota, A. Warm deformation of carbon steel. *J. Mater. Process. Tech.* **2000**, *106*, 123–130. [CrossRef]
3. Li, Q.; Wang, T.; Jing, T.; Gao, Y.; Zhou, J.; Yu, J.; Li, H. Warm deformation behavior of quenched medium carbon steel and its effect on microstructure and mechanical properties. *Mat. Sci. Eng. A* **2010**, *515*, 38–42. [CrossRef]
4. Li, Q.; Wang, T.-S.; Li, H.-B.; Gao, Y.-W.; Li, N.; Jing, T.-F. Warm deformation behavior of steels containing carbon of 0.45% to 1.26% with martensite starting structure. *J. Iron Steel Res. Int.* **2010**, *17*, 34–37. [CrossRef]
5. Kimura, Y.; Inoue, T. Influence of warm tempforming on microstructure and mechanical properties in an ultrahigh-strength medium-carbon low-alloy steel. *Met. Mat. Trans. A* **2013**, *44*, 560–576. [CrossRef]
6. Eghbali, B.; Shaban, M. Warm deformation of low carbon steel using forward extrusion-equal channel angular pressing technique. *J. Iron Steel Res. Int.* **2013**, *20*, 68–71. [CrossRef]
7. Eghbali, B. EBSD study on the formation of fine ferrite grains in plain carbon steel during warm deformation. *Mater. Lett.* **2007**, *61*, 4006–4010. [CrossRef]
8. Barbosa, J.V.; Melo, T. Santos DB. Dynamic and static softening behavior of a titanium added ultra-low carbon steel during hot and warm deformation. *J. Mater. Res. Technol.* **2020**, *9*, 2810–2817. [CrossRef]
9. Kang, J.H.; Inoue, T.; Torizuka, S. Effect of strain on microstructural evolution under warm deformation in an ultra-low carbon steel. *Mater. Trans.* **2008**, *50*, 34–39. [CrossRef]
10. Zhao, X.; Yang, X.L.; Jing, T.F. Effect of initial microstructure on warm deformation behavior of 45 steel. *J. Iron Steel Res. Int.* **2012**, *19*, 75–781. [CrossRef]
11. Arruabarrena, J.; López, B.; Rodriguez-Ibabe, J.M. Influence of DIT parameters on the cementite spheroidization in a low-alloy medium carbon steel. *Metall. Mater. Trans. A* **2015**, *47*, 412–423. [CrossRef]
12. Eghbali, B.; Shaban, M. Warm deformation microstructure of a plain carbon steel. *J. Iron Steel Res. Int.* **2011**, *18*, 41–46. [CrossRef]
13. Eghbali, B.; Abdollah-Zadeh, A.; Beladi, H.; Hodgson, P. Characterization on ferrite microstructure evolution during large strain warm torsion testing of plain low carbon steel. *Mat. Sci. Eng. A* **2006**, *435*, 499–503. [CrossRef]
14. Eghbali, B.; Abdollah-zadeh, A.; Hodgsonc, P.D. Dynamic softening of ferrite during large strain warm deformation of a plain-carbon steel. *Mat. Sci. Eng. A* **2007**, *462*, 259–263. [CrossRef]
15. Wu, T.; Wang, M.Z.; Gao, Y.W. Effects of plastic warm deformation on cementite spheroidization of a eutectoid steel. *J. Iron Steel Res. Int.* **2012**, *19*, 60–66. [CrossRef]
16. Arruabarrena, J.; López, B.; Rodriguez-Ibabe, J.M. Influence of prior warm deformation on cementite spheroidization process in a low-alloy medium carbon steel. *Met. Mater. Trans. A* **2014**, *45*, 1470–1484. [CrossRef]
17. Huo, Y.; He, T.; Chen, S.; Wu, R. Mechanical behavior and microstructure evolution of bearing steel 52100 during warm compression. *JOM.* **2018**, *70*, 1112–1117. [CrossRef]
18. He, T.; Huo, Y.; Shi, X.; Chen, S. Modeling of carbide spheroidization mechanism of 52100 bearing steel under warm forming conditions. *Met. Mater. Trans. A* **2018**, *50*, 936–946. [CrossRef]
19. Storojeva, L.; Ponge, D.; Kaspar, R.; Raabe, D. Development of microstructure and texture of medium carbon steel during heavy warm deformation. *Acta Mater.* **2004**, *52*, 2209–2220. [CrossRef]
20. Onuki, Y.; Okayasu, K.; Fukutomi, H. Texture development in ferritic steels during high temperature uniaxial compression deformation. *Trans. Tech. Publ.* **2012**, *702–703*, 810–813. [CrossRef]
21. Hyung, J.S.; Joon, K.A.; Soo, H.P.; Dong, N.L. The effect of texture on ridging of ferritic stainless steel. *Acta Mater.* **2003**, *51*, 4693–4706.
22. Zhuang, D.-D.; Wang, L.-G.; Huang, Y.; Li, X.-M.; Zhang, H.-Y.; Ren, D.-W. Microstructure and texture evolution during recrystallization of low-carbon steel sheets. *J. Iron Steel Res. Int.* **2017**, *24*, 84–90. [CrossRef]
23. Chin, G.Y.; Mammel, W.L. Computer solutions of the Taylor analysis for axisymmetric flow. *Trans. AIME* **1967**, *239*, 1400–1405.
24. Kang, J.H.; Inoue, T.; Torizuka, S. Effect of shear strain on the microstructural evolution of a low carbon steel during warm deformation. *Mater. Trans.* **2010**, *51*, 27–35. [CrossRef]
25. Sánchez-Araiza, M.; Godet, S.; Jacques, P.; Jonas, J. Texture evolution during the recrystallization of a warm-rolled low-carbon steel. *Acta Mater.* **2006**, *54*, 3085–3093. [CrossRef]
26. Zebarjadi Sar, M.; Barella, S.; Gruttadauria, A.; Mombelli, D.; Mapelli, C. Impact of warm rolling process parameters on crystallographic textures, microstructure and mechanical properties of low-carbon boron-bearing steels. *Metals* **2018**, *8*, 927. [CrossRef]
27. Xiong, Y.; Sun, S.; Li, Y.; Zhao, J.; Lv, Z.; Zhao, D.; Zheng, Y.; Fu, W. Effect of warm cross-wedge rolling on microstructure and mechanical property of high carbon steel rods. *Mater. Sci. Eng. A* **2006**, *431*, 152–157. [CrossRef]

28. Sun, S.H.; Xiong, Y.; Zhao, J. Microstructure characteristics in high carbon steel rod after warm cross-wedge rolling. *Scripta Mater.* **2005**, *53*, 137–140. [CrossRef]
29. Huang, X.; Wang, B.; Zhou, J.; Ji, H.; Mu, Y.; Li, J. Comparative study of warm and hot cross-wedge rolling: Numerical simulation and experimental trial. *Int. J. Adv. Manuf. Technol.* **2017**, *92*, 3541–3551. [CrossRef]
30. Huang, Y.D.; Yang, W.Y.; Sun, Z.Q. Formation of ultrafine grained ferrite in low carbon steel by heavy deformation in ferrite or dual phase region. *J. Mater. Process Tech.* **2003**, *134*, 19–25. [CrossRef]
31. Alhazaa, A.; Haneklaus, N. Diffusion bonding and transient liquid phase (TLP) bonding of type 304 and 316 austenitic stainless steel-a review of similar and dissimilar material joints. *Metals* **2020**, *10*, 613. [CrossRef]
32. He, A.; Chen, L.; Wang, S.; Huangfu, L.X. Research on dynamic recrystallization behavior of 20crmo alloy steel during hot deformation. *Adv. Mater. Res.* **2013**, *683*, 488–491. [CrossRef]
33. Moshtaghi, M.; Safyari, M.; Kuramoto, S.; Hojo, T. Unraveling the effect of dislocations and deformation-induced boundaries on environmental hydrogen embrittlement behavior of a cold-rolled Al-Zn-Mg-Cu alloy. *Int. J. Hydrogen. Energ.* **2021**, *46*, 8285–8299. [CrossRef]
34. Kobayashi, M.; Takayama, Y.; Kato, H. Preferential growth of cube-oriented grains in partially annealed and additionally rolled aluminum foils for capacitors. *Mater. Trans.* **2005**, *45*, 3247–3255. [CrossRef]
35. He, G.; Peng, T.; Jiang, B.; Hu, X.; Liu, Y.; Wu, C. Recrystallization behavior and texture evolution in low carbon steel during hot deformation in austenite/ferrite region. *Steel Res. Int.* **2021**, *92*, 2100047. [CrossRef]
36. Yun, X.B. *Mechanisms of Metal Plastic Forming*; Metallurgical Industry Press: Beijing, China, 2012; pp. 5–25.
37. Zhao, H.T.; Palmiere, E.J. Influence of cooling rate on the grain-refining effect of austenite deformation in a HSLA steel. *Mater. Charact.* **2019**, *158*, 109990. [CrossRef]
38. Fang, Y.; Chen, X.; Madigan, B.; Cao, H.; Konovalov, S. Effects of strain rate on the hot deformation behavior and dynamic recrystallization in China low activation martensitic steel. *Fusion Eng Des.* **2016**, *103*, 21–30. [CrossRef]
39. Li, Z.Z.; Nai, Q.L.; Wang, B.S.; Su, C.; Dong, J.X. Effect of high strain rate on hot deformation behavior and extrusion feasibility of 690 alloy. *Rare Metal. Mmat. Eeng.* **2018**, *47*, 3372–3380.
40. Xu, H.; Xu, Y.; Jiao, H.; Cheng, S.; Misra, R.; Li, J. Influence of grain size and texture prior to warm rolling on microstructure, texture and magnetic properties of Fe-6.5 wt% Si steel. *J Magn. Magn. Mater.* **2018**, *453*, 236–245. [CrossRef]
41. Barnett, M.R.; Kestens, L. Formation of {111}<110> and {111}<112> textures in cold rolled and annealed if sheet steel. *ISIJ Int.* **1999**, *9*, 923–929. [CrossRef]
42. Nagataki, Y.; Hosoya, Y. Origin of the recrystllization texture formation in an interstitial free steel. *ISIJ Int.* **1996**, *36*, 451–460. [CrossRef]
43. Toshiaki, U.; Jonas, J.J. Modeling texture change during the recrystallization of an IF steel. *ISIJ Int.* **1994**, *34*, 435–442.
44. Jia, J.; Dai, L.B.; Yuan, S.L.; Song, X.; Yuan, Z.; Chai, X. Effects of P and Ti on {111} plane texture in high strengthIF steels. *J. Mater. Res. Chin.* **2011**, *25*, 656–660.
45. Cao, S.Q. Grain Boundaries and the Evolution of Texture in Interstitial-Free (IF) Steels. Ph.D. Thesis, Shanghai Jiao Tong University, Shanghai, China, 2005.
46. Wu, Y.; Kou, H.; Wu, Z.; Tang, B.; Li, J. Dynamic recrystallization and texture evolution of Ti-22Al-25Nb alloy during plane-strain compression. *J. Alloy. Compd.* **2018**, *749*, 844–852. [CrossRef]

materials

MDPI

Article

The Influence of Ce, La, and SiC Particles Addition on the Formability of an Al-Si-Cu-Mg-Fe SiCp-MMC

Andong Du [1,2], Lucia Lattanzi [3], Anders E. W. Jarfors [2,3,*], Jie Zhou [4], Jinchuan Zheng [2], Kaikun Wang [1,*] and Gegang Yu [2]

[1] Department of Materials Processing and Control Engineering, School of Materials Science and Engineering, University of Science and Technology Beijing, Xueyuan Road 30, Haidian District, Beijing 100083, China; b20170186@xs.ustb.edu.cn
[2] Institute of Semi-Solid Metal Technology, China Academy of Machinery Sciences and Technology (Jiangle), Huancheng East Road 22, Jiangle County, Sanming 353300, China; zhengjc@cam.com.cn (J.Z.); yugg@cam.com.cn (G.Y.)
[3] School of Engineering, Materials and Manufacturing, Jönköping University, P.O. Box 1026, 551 11 Jönköping, Sweden; lucia.lattanzi@ju.se
[4] Jiangsu University of Technology, Zhongwu Road 1801, Changzhou 213001, China; zhou_j09@163.com
* Correspondence: anders.jarfors@ju.se (A.E.W.J.); kkwang@mater.ustb.edu.cn (K.W.); Tel.: +46-3610-1651 (A.E.W.J.)

Abstract: Road transport and the associated fuel consumption plays a primary role in emissions. Weight reduction is critical to reaching the targeted reduction of 34% in 2025. Weight reduction in moving parts, such as pistons and brake disc rotors, provide a high-impact route to achieve this goal. The current study aims to investigate the formability of Al–Si alloys reinforced with different fractions and different sizes of SiCp to create an efficient and lightweight Al-MMC brake disk. Lanthanum (La) and cerium (Ce) were added to strengthen the aluminium matrix alloy and to improve the capability of the Al-MMC brake discs to withstand elevated temperature conditions, such as more extended braking periods. La and Ce formed intermetallic phases that further strengthened the composite. The analysis showed the processability and thermal stability of the different material's combinations: increased particle sizes and broader size range mixture supported the formation of the SiCp particle interactions, acting as an internal scaffolding. In conclusion, the additions of Ce and La strengthened the softer matrix regions and resulted in a doubled compression peak strength of the material without affecting the formability, as demonstrated by the processing maps.

Keywords: aluminium; metal matrix composite; brake disk; thermal stability; forming; processing map

Citation: Du, A.; Lattanzi, L.; Jarfors, A.E.W.; Zhou, J.; Zheng, J.; Wang, K.; Yu, G. The Influence of Ce, La, and SiC Particles Addition on the Formability of an Al-Si-Cu-Mg-Fe SiCp-MMC. *Materials* **2022**, *15*, 3789. https://doi.org/10.3390/ma15113789

Academic Editor: Ivo Schindler

Received: 27 April 2022
Accepted: 23 May 2022
Published: 26 May 2022

1. Introduction

The International Energy Agency declared transport responsible for 25% of fuel consumption, and road transport plays a primary role in emissions. By 2025, transport emissions should be reduced by 34% to reach the goal that the global temperature will not increase by 2 °C [1]. Considering the electricity generation and materials production emissions, the weight reduction in automotive components has an immediate effect on emissions saving. Weight reduction is critical for moving parts, which have the most significant influence on energy consumption, and it could improve the vehicle's driveability during acceleration and deceleration [2]. Al-based metal matrix composites (Al-MMCs) are valid candidates to substitute cast iron in the lightweight automotive application as pistons and brake discs [3,4].

After an initial interest in the 1990s [5,6], Al-based matrix composites have attracted attention again in recent years [7–9] due to their high specific modulus and specific strength, excellent wear resistance, and good stiffness. Typical components, such as pistons and brake discs, demand high strength even at high temperatures, which is the weak point of

Al alloys. Several Al-based MMCs with different ceramic reinforcements find extensive application in the automotive industry, as summarised in Table 1.

Table 1. List of automotive application of Al-based MMCs with different reinforcements.

Matrix	Reinforcement	Applications	References
Al and Al alloys	Al_2O_3	Piston rings, connecting rods	[10,11]
	Al_2O_3-Cf	Engine blocks	[12,13]
	MoS_2p	Drive shafts	[14]
	B_2O_3w	Piston rings	[12,13]
	SiCp	Brake rotors, pistons, propeller shafts	[15]
	SiCw	Connecting rods	[16]
	TiCp	Pistons, connecting rods	[17]

f: fibre; p: particle; w: whisker.

The addition of transition metals [18–20] and rare earth elements [21,22] to the matrix alloy helps to improve the maximum operating temperature of the composite material. Several methods produce metal matrix composites [23], such as powder metallurgy, pressure infiltration, spray deposition, and stir casting. The least expensive method is stir-casting, and the stirring force improves the wettability between the particles and the molten metal [24]. Workability is another critical drawback of Al-based composite materials. The challenge lies in the difficulty of machining composite materials with high SiCp fractions due to the hardness of SiC [25]. Yamagata et al. [3] studied a new approach to manufacturing pistons and concluded that casting and forging offer an efficient route to near-net-shape processing, saving time, and improving production efficiency.

The Arrhenius equation has been widely used to describe the relationship between strain rate, flow stress, and temperature. The effects of temperature and strain rate on the deformation behaviour are represented by the Zener–Hollomon parameter (Z) in an exponent type equation [26]. Other work on Al-based composites with Zener–Hollomon includes Hao et al. [27] who studied the 35% SiCp/2024Al metal matrix composites and indicated that the flow stress behaviour of composite during hot compression deformation can be represented by a Zener–Hollomon parameter in the hyperbolic sine form. Lattanzi et al. [20] did research on the relationship between the Z parameter and temperatures and strain rates, and it indicated that peak stress at high temperatures and low strain rates was reduced because of dynamic recovery and recrystallisation, and Z values decreased. Conversely, the Z values increased at low temperatures and high strain rates, indicating dislocation generation. This phenomenon led to work hardening and higher peak stress. Patel et al. [28] studied the AA2014–10 wt.% SiCp composites; the Z parameter described the flow behaviour of the samples. The Z value decreased with increasing temperature, and it is essentially due to extensive dynamic softening.

The processing maps are an additional tool to analyse the hot compression response of the material and guide the choice of the hot working parameters as they show safe and unsafe ranges of temperatures and strain rates to avoid operational regions in which damage occurs. The extreme damage mechanisms were identified as cavity formation at hard particles in a soft matrix, occurring at low temperatures and high strain rates, and wedge cracking at grain boundaries, occurring at high temperatures and low strain rates [29]. Several works in the literature defined the processing map for Al-based composites, mainly Al–Cu systems. Huang et al. [30] investigated the hot deformation of an Al–Cu–Mg alloy reinforced with 14 vol.% of SiCp. The temperature range was 355–495 °C, and the strain rate range was 0.001–1 s^{-1}. The authors assigned different deformation mechanisms to different temperature ranges and concluded that temperature had a more significant influence than strain rate on the material response. Hao et al. [27] investigated the deformation behaviour of an Al–Cu–Mg alloy reinforced with 35 vol.% of SiCp; according to the processing map and the micrograph, the authors concluded that the optimal workability temperature and strain rate were 500 °C and 0.1 s^{-1}, respectively. Xiao et al. [31] investigated an Al–Cu alloy reinforced with 15 vol.% of SiCp produced by powder metallurgy. The highest effi-

ciency value was at 500 °C and 0.001 s^{-1}, a lower value than the results by Hao et al. [27]. Patel et al. [28] investigated the hot deformation behaviour of an Al–Cu system reinforced with 10 wt.% of SiCp. The authors reported that the failure mechanisms mainly involved interfacial cracking between particles/matrix and intermetallic/matrix. Decohesion was severe at low strain rates. Ramanathan et al. [32] studied the workability of an Al–Cu alloy reinforced with 15 vol.% of SiC particles. They reported that the optimum domain for dynamic recrystallisation occurred in the temperature and strain rate range of 360–460 °C and 0.1–0.7 s^{-1}. Wedge cracking was observed in the temperature range 460–500 °C under a lower strain rate.

The current research gap is on the role of different fractions and sizes of the reinforcement, and the role played by the matrix alloy in the overall response of the composite material. In light of this literature analysis, the present study investigates the formability of Al–Si alloys reinforced with different fractions and different sizes of SiCp. Besides, to improve the high-temperature performance of the composite, lanthanum (La) and cerium (Ce) were added to the matrix alloy in one case. Previous works on La and Ce added to Al alloys demonstrated that, from a sustainability standpoint and business perspective, these elements support efficient strength, save money, and are environment-friendly [33]. The processing maps of the materials shed light on their formability and the role played by the size and fraction of the reinforcement [33].

2. Materials and Methods

This section describes the experimental procedure of the presented work and Figure A1 in Appendix A summarises it in a schematic representation.

2.1. Material Production

Five different SiCp reinforced Al-based composites were produced with different matrixes and sizes of carbide particles, and the composition is listed in Table 1. An amount of 20 wt.% of SiCp were added into the matrix, and the materials were processed by a proprietary stir-casting method to keep porosity at a minimum level. The carbides were heat-treated at 1000 °C for one hour to develop a layer of silicon oxide (SiO_2) on the surface of particles. This treatment enables evenly dispersed SiC particles in the molten material because the wetting angle between SiO_2 and molten Al will be below 68.8 degrees [34]. The C0 matrix alloy is the base alloy; the C1 alloy was obtained by adding the master alloys Al–30% Ce, Al–30% La, Al–50% copper (Cu), Al–10% nickel (Ni), and Al–20% manganese (Mn) to the C0 alloy. The 23 μm, 50 μm, 10 μm and, mix size SiCp were used in this research, and the dimension is the cut-off limit for the batch of particles. The compositions of the alloys were measured using direct current plasma emission spectroscopy (DCPMS) (ATI Wah Chang, Albany, OR, USA). Please note that due to analysis limitations Ce and La could not be assessed using DCPMS, and Ce and La are given as nominal values. The detailed information is shown in Table 2. Five different SiCp-reinforced Al-based composites were produced with different matrixes and sizes of carbide particles, and the composition is listed in Table 2.

Table 2. Chemical composition [wt.%] of the composite materials and the weight fraction of SiCp.

Matrix Alloy	Si	Cu	Ni	Fe	Mn	Ti	Mg	Ce	La	Al	Code Name	SiC Size [μm]
C0	10	0.2	-	0.1	-	0.1	0.8	-	-	bal.	C0_23	23
											C0_50	50
											C0_10	10
											C0_mix	23 + 50 + 10 [1]
C1	10	1.9	1.9	0.1	0.8	0.3	0.8	1	1	bal.	C1_23	23

[1] Different sizes were added at the same mass ratio in material C0_mix.

2.2. Metallography

Metallographic observations were performed by Olympus DSX1000 (Olympus Corporation, Shinjuku, Japan) optical microscope (OM). Quantitative image analysis was performed with ImageJ software (version 1.51j8, National Institutes of Health, Bethesda, MD, USA) on at least 20 micrographs for each material to evaluate the SiCp fraction. Assuming that the area percentage of SiCp in the image is equal to the volume percentage, then the weight percentage of SiCp in the matrix could be calculated by the volume percentage value. The ImageJ software was used for quantitative image analysis of SiC particles. The centre of mass of the SiC particles were then used as input data to calculate the first-, second-, and third-nearest neighbour distances (1NND, 2NND, and 3NND) using the MATLAB function 'knnsearch'. A schematic representation of the 'knnsearch' function is depicted in Figure A2.

2.3. Mechanical Testing

Thermal compression tests were used to review the formability of composite materials in this research. Compression tests were carried out with a Zwick Roell Z100 (Zwick Roell, Ulm, Germany) testing unit at different strain rates: 0.001/s, 0.01/s, 0.1/s, and 1/s; and different temperatures: 25 °C, 350 °C, 420 °C, 470 °C. The current maximum operating temperature is 420 °C and the aim is to increase it to 470 °C. For this reason, the 350–470 °C temperature range was selected. The room temperature data are used as a reference for comparison. Before each test, the sample was heated for 10 min at the desired temperature. A compliance curve was registered to consider the stiffness of the machine in data analysis. The compliance curve was fitted with a linear function, and the related strain was removed from the curves.

3. Results

3.1. Microstructural Analysis

Figure 1 shows the microstructure of the five materials. The weight fraction of SiCp is listed in Table 2. The targeted quantity of 20 wt.% of particles was added to all the materials, but the transfer efficiency was not constant and resulted in different incorporated fractions depending on the size of the particles.

For the C0 matrix alloy, the transfer efficiency varied with the size of the SiC particles and the actual fractions were: 14% in the material C0_23 with 23 μm sized particles (Figure 1a), 19% for the 50 μm sized particles in material C0_50 (Figure 1b), only 4% in the material C0_10 with 10 μm sized particles (Figure 1c), and 10% for the mixture of 10, 23, and 50 μm sized particles, added at the same mass ratio, in the material C0_mix (Figure 1d). The material C1_23 also resulted in 14% of the 23 μm sized particles (Figure 1e). These results suggest that the particle size is the dominant parameter for transfer efficiency, almost 100% for the largest size of 50 μm and decreased to 20% for the smallest size of 10 μm.

Figure 1a shows the material reinforced with 23 μm sized SiCp, the phases are primary α-Al, and the binary Al–Si eutectic; the dispersion of SiCp particles is uniform, with almost no clusters observed. Figure 1b shows the material reinforced with 50 μm sized particles, the largest size in all materials, and Figure 1c shows the material reinforced with 10 μm sized particles. Due to the small size of the particles, a significant number of clusters were observed, and homogenous dispersion of particles was not achieved. This is visible in the significant standard deviation of the higher-order measures 2NND and 3NND listed in Table 3. Several particle-free areas confirm that the transfer efficiency was lower than other materials. Figure 1d shows the material reinforced with the mixed-sizes particles. The dispersion is better than in Figure 1c, and the addition of 50 μm size particles was limited, while most of the particles were 23 μm and 10 μm sized. There are several small clusters made of mixed-size SiC particles.

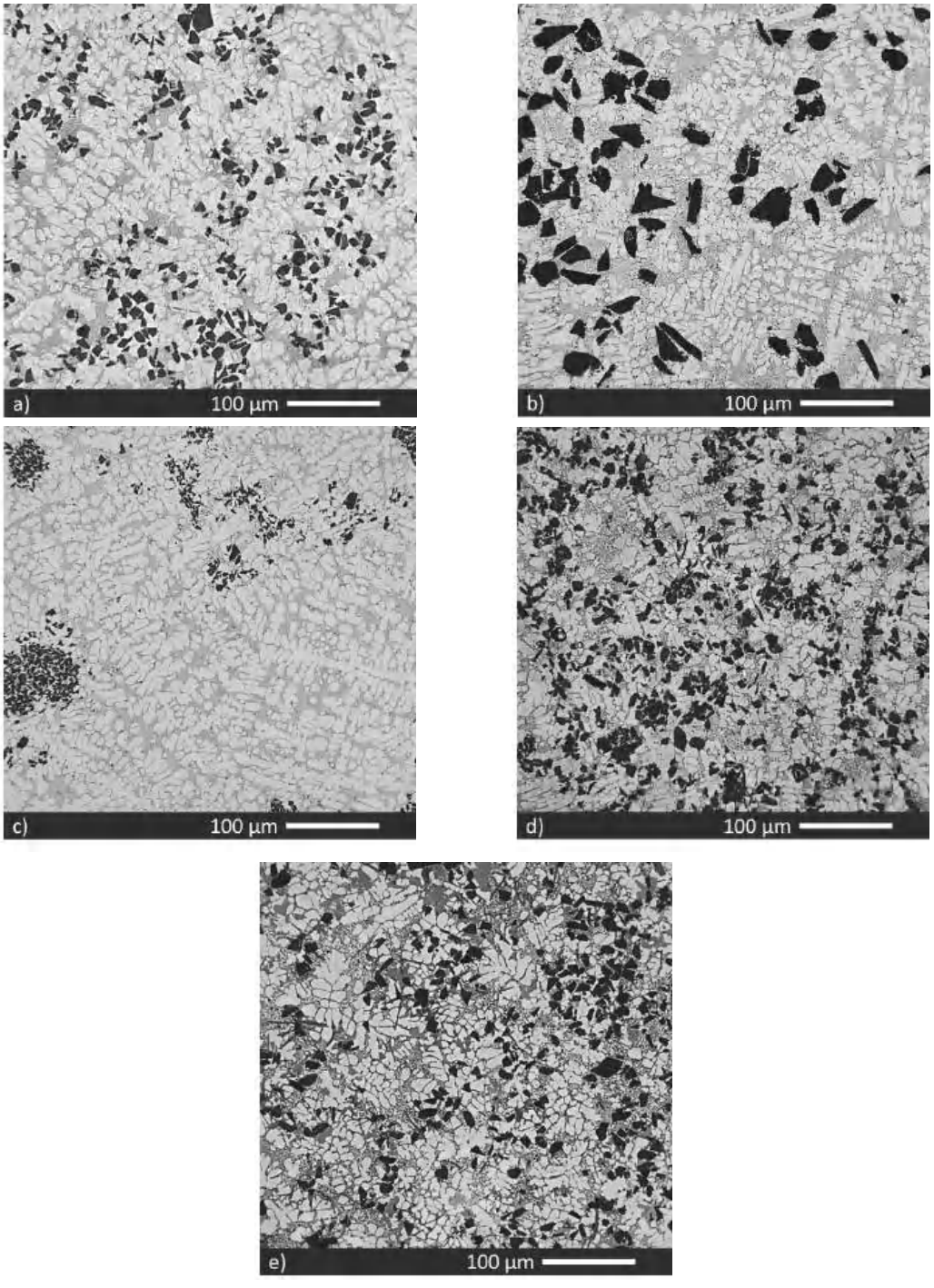

Figure 1. Micrographs: (**a**) material C0_23; (**b**) material C0_50; (**c**) material C0_10; (**d**) material C0_mix; (**e**) material C1_23.

Table 3. Results of the quantitative image analysis performed using the ImageJ and MATLAB software. SD = standard deviation.

Material	SiC Fraction ± SD [wt.%]	SiC Size ± SD [μm]	1NND ± SD [μm]	2NND ± SD [μm]	3NND ± SD [μm]
C0_23	14 ± 2.7%	14 ± 0.9	14 ± 0.7	19 ± 1.1	24 ± 1.5
C0_50	19 ± 2.1%	32 ± 1.4	30 ± 2.5	41 ± 3.1	52 ± 3.3
C1_23	14 ± 1.9%	15 ± 1.1	16 ± 0.8	22 ± 1.2	28 ± 1.6
C0_10	4 ± 1.6%	12 ± 1.8	19 ± 4.7	32 ± 14.8	41 ± 17.1
C0_mix	12 ± 3.3%	19 ± 1.5	18 ± 1.8	26 ± 2.7	33 ± 3.6

Figure 1e shows the 23 μm size SiCp reinforced Al matrix composite with RE addition. The particle dispersion was uniform, and the addition of La and Ce to the matrix alloy did not change the transfer efficiency of SiC particles; hence the SiC fraction of the C0_23 and C1_23 alloy was similar. The generation of new phases in the C1_23 material, previously identified as α-$Al_{15}(Fe,Mn)_3Si_2$, $Al_{20}(La,Ce)_3Ti_2$ and $Al_{11}(La,Ce)_3$ [22], did not alter particle addition and distribution.

3.2. Mechanical Testing

Flow stress is described as a function of composition SiCp addition, temperature, strain, and strain rate. The true stress–true strain plots are given in Figure 2.

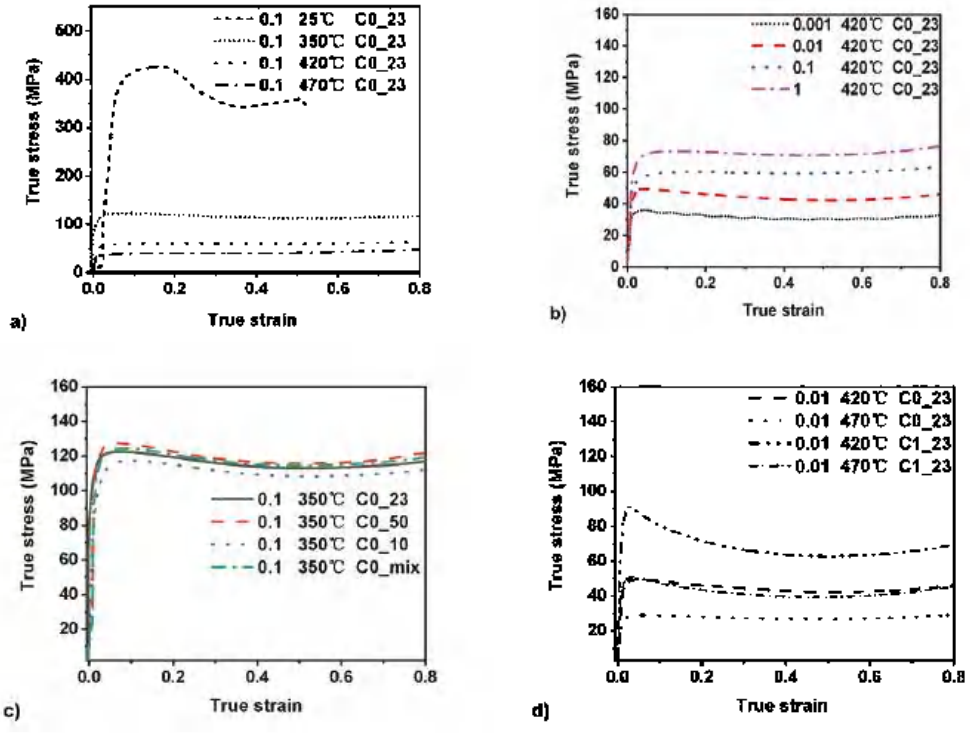

Figure 2. Compression curves: (**a**) material C0_23, the effect of the temperature at same strain rate; (**b**) material C0_23, the effect of strain rate at the same temperature; (**c**) constant temperature and strain rate, the effect of varying fraction; (**d**) materials C0_23 and C1_23 at constant strain rate, comparison at two temperatures.

Figure 2a shows the temperature effect on the flow stress of material C0_23. The stress decreased as the compression temperature increased. The peak flow stress at room temperature reached a value of 426 MPa and was more than three times higher than the 350 °C peak stress value of 121 MPa. The 470 °C peak stress value of only 37 Mpa suggests that the softening mechanism is more powerful than the work-hardening mechanism at room temperature.

Figure 2b shows the strain rate effect on the flow stress of the C0_23 material at 420 °C and different strain rates. With the increase in strain rate, the peak flow stress of the curve increased. At the strain rates of 0.01 s^{-1}, 0.1 s^{-1} and 1 s^{-1}, the flow curve appeared smooth, while at the strain rate of 0.001 s^{-1}, the curve appeared corrugated due to internal friction in the materials.

Figure 2c shows the true stress–true strain curve with different particle sizes and weight fractions at a constant temperature of 350 °C and a strain rate of 0.1 s^{-1} and C0 matrix. The peak value is at the range of 117–128 MPa, and the weight fraction is at the range of 4–19%. Even though the material C0_50 possesses 19 wt.% SiCp particle addition and 50 μm size particles reinforced, the peak stress is only 3 MPa higher than the C0_mix material. The lowest peak stress curve is the material C0_10, which displayed a peak stress of 117 MPa, 5 MPa lower than the material C0_23 and 11 MPa lower than the material C0_50. This result indicates that weight percentage and particle size slightly influence the flow stress during deformation.

Figure 2d shows the true stress–true strain curve of materials C0_23 and C1_23 at temperatures 420 °C and 470 °C. The materials C0_23 and C1_23 have the same particle volume fraction, 14 wt.% and the same particle size, 23 μm. At the temperature of 420 °C, the peak stress values of materials C1_23 and C0_23 were 90 MPa and 49 MPa, respectively. The peak stress value of material C1_23 at 470 °C is slightly higher than the material C0_23 at 420 °C. The difference between material C0_23 and material C1_23 is shown in Table 1. The addition of RE and transition elements almost doubled the strength compared to the C0_23 material. Figure 2d clarifies that the matrix alloy was more critical than the particle size and particle weight fraction on the effect of SiCp reinforced composite material deformation.

3.3. Zener−Hollomon Analysis

Equation (1) collects the constitutive equations used to calculate the material constants in the softening segment after peak stress:

$$\dot{\varepsilon} = \begin{cases} A \cdot \sigma^{n1} \cdot e^{-Q_A/RT} & \alpha\sigma < 0.8 \\ A \cdot e^{\beta\,\sigma} \cdot e^{-Q_A/RT} & \alpha\sigma > 1.2 \\ A \cdot [\sinh(\alpha\sigma)]^{n2} \cdot e^{-Q_A/RT} & \text{for all } \sigma \end{cases} \quad (1)$$

Here n1, n2, $\alpha = \beta/n1$ [1/MPa], β [1/MPa], and A [1/s] are material constants independent of temperature. α was described by Jonas et al. [35] as the reciprocal stress at which the strain rate changes from power to exponential dependence on stress. σ [MPa] is the flow stress, $\dot{\varepsilon}$ [1/s] is the strain rate, and R = 8.314 J/K·mol is the universal gas constant. Q_A [kJ/mol] is the activation energy of deformation and comes from Equation (2):

$$Q_A = R \cdot \left[\frac{\partial \ln \dot{\varepsilon}}{\partial \ln[\sinh(\alpha\sigma)]}\right]_T \cdot \left[\frac{\partial \ln[\sinh(\alpha\sigma)]}{\partial(1/T)}\right]_{\dot{\varepsilon}} \quad (2)$$

In simpler words, the activation energy indicates the energy barriers to plastic deformation during the hot deformation of metallic materials. If flow stress increases with the increasing Q_A value at the same deformation temperature and strain rate, it is suggested that the materials with lower Q_A value can be deformed more easily with a lower force. Figure 3 depicts the graphical solution of the Zener−Hollomon model in Equations (1) and (2). The parameter n1 is the slope in the graph $\ln\dot{\varepsilon}$ v. σ (Figure 3a), and the parameter β is the slope in the graph $\ln\dot{\varepsilon}$ v. $\ln\sigma$ (Figure 3b). The parameter n2 is the slope in the graph $\ln\dot{\varepsilon}$ v.

ln[sinh(ασ)] in Figure 3c and corresponds to the first term in Equation (2). The second term in Equation (2) is the slope in the graph ln[sinh(ασ)] v. 1000/T, in Figure 3d.

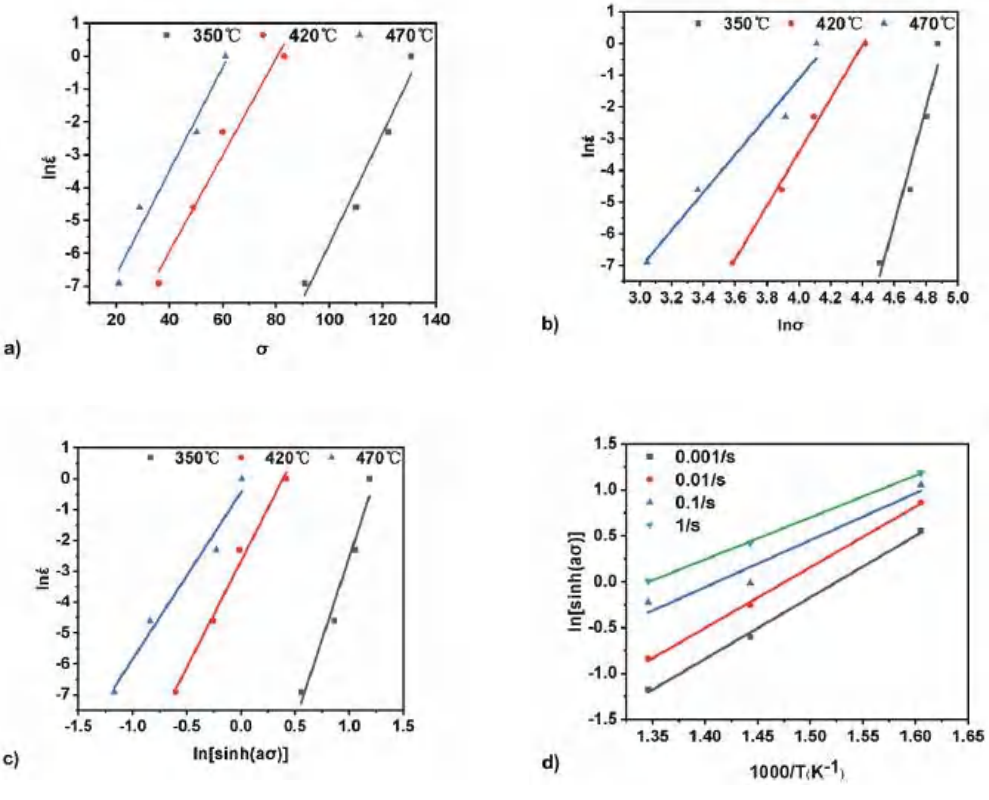

Figure 3. Graphical solutions for the Zener−Hollomon model: (**a**) the parameter n1 is the slope in the graph lnε̇ v. σ; (**b**) the parameter β is the slope in the graph lnε̇ v. lnσ; (**c**) the parameter n2 is the slope in the graph lnε̇ v. ln[sinh(ασ)]; (**d**) the second term in Equation (3) is the slope in the graph ln[sinh(ασ)] v. 1000/T.

The material constants A and n2 were determined from the ln(Z) v. ln[sinh(ασ)] plot. Table 4 lists the material constants and the activation energy calculated for the investigated materials. The activation energy for the hot deformation of composite ranges 301–584 kJ/mol, which is higher than the bulk self-diffusion of pure Al 142 kJ/mol.

Table 4. Material constants and activation energy of the hot compressed composites, evaluated from the constitutive relations in Equation (2).

Material	n1	β [1/MPa]	α [1/MPa]	Q_A [kJ/mol]	n2
C0_23	10.9	0.158	0.0145	365	7.63
C0_50	12.2	0.224	0.0184	498	8.45
C1_23	11.8	0.126	0.0107	452	8.10
C0_10	8.62	0.146	0.0170	301	6.00
C0_mix	13.6	0.254	0.0187	584	9.07

The Origin software was used to model the relationship between the activation energy Q_A (kJ/mol), the RE addition to the matrix alloy, and the SiC particles' microstructural parameters. The multiple linear regression resulted in Equations (3) and (4):

$$Y = 395 \times f_{SiC} + 6 \times d_{SiC} + 1871 \times [\text{RE wt.\%}] + 265,\ R^2 = 0.38 \quad (3)$$

$$Y = 23 \times d_{SiC} + 1166 \times [\text{RE wt.\%}] - 21 \times 1\text{NND} + 420,\ R^2 = 0.619 \quad (4)$$

where Y is the activation energy Q_A [kJ/mol], f_SiC represents the SiCp fraction, d_SiC represents the average Feret diameter [μm] of the carbides, [RE wt.%] is the RE content in the matrix alloy, 1NND [μm] is the first-nearest neighbour distance between SiC particles. These results suggest that particle size and the interparticle spacings are better factors than the fractions of particles added, as indicated by the R^2-factor.

The particle fraction, particle size, and nearest neighbour distance are independent parameters, depending on each other. Equation (3) uses the SiCp fraction (f_SiC), SiCp particle size (d_SiC), and RE addition ([RE wt.%]). The parameters in Equation (3) show that an increase in any of the factors causes an increase in the activation energy. The value R^2 = 0.38 illustrated that the fit is poor and does not describe the effect well. In Equation (4), the SiCp fraction was replaced by the nearest neighbour distance (1NND). An increasing 1NND represents a reduced clustering behaviour of the particles to some extent. Replacing the fraction SiCp with the 1NND increased the fit value to R^2 = 0.62. The fact that R^2 increased suggests that it is not the mass fraction of particles that matters but rather their arrangement. The main conclusion is that bringing particles closer, increasing their size, and adding RE to form intermetallic phases to lock the matrix from moving increase the activation energy and stabilise the materials at elevated temperatures.

3.4. Processing Maps

The processing map consists of the superimposed map of power dissipation and an instability map. These are developed based on the Dynamic Materials Model [36]. The objective is to manufacture components with controlled microstructure and properties without macro or microstructure defects. Power dissipation is the percentage of energy converted into thermal and microstructure change. The factor that partitions power into these two forms is the strain rate sensitivity exponent. The strain rate sensitivity exponent, m value, was estimated from Equation (5). The processing map consists of the superimposed map of power dissipation and an instability map. These are developed based on the Dynamic Materials Model [36]. The objective is to manufacture components with controlled microstructure and properties without macro or microstructure defects. Power dissipation is the percentage of energy converted into thermal and microstructure change. The factor that partitions power into these two forms is the strain rate sensitivity exponent. The strain rate sensitivity exponent, m value, was estimated from Equation (5):

$$m = \left.\frac{\partial(\ln(\sigma))}{\partial(\ln(\dot{\varepsilon}))}\right|_{\varepsilon} \quad (5)$$

where m denotes the strain rate sensitivity of the flow stress at a constant strain of ε. A dimensionless parameter called efficiency of power dissipation η was defined in Equation (6):

$$\eta = \frac{2m}{m+1} \quad (6)$$

A dimensionless parameter called instability criterion ξ is used to obtain the instability map, and it was defined according to Equation (7):

$$\xi(\dot{\varepsilon}) = \frac{\partial \ln\left(\frac{m}{m+1}\right)}{\partial \ln \dot{\varepsilon}} + m > 0 \quad (7)$$

Figure 4a–e show the processing map of all five materials. The contour numbers represent power dissipation efficiency, and the shaded domains indicate the regions of flow instability, with $\xi < 0$. The purpose of the hot-processing map is to guide the choice of the metal-forming parameters to avoid macro and microstructural defects in a repeatable manufacturing environment [29].

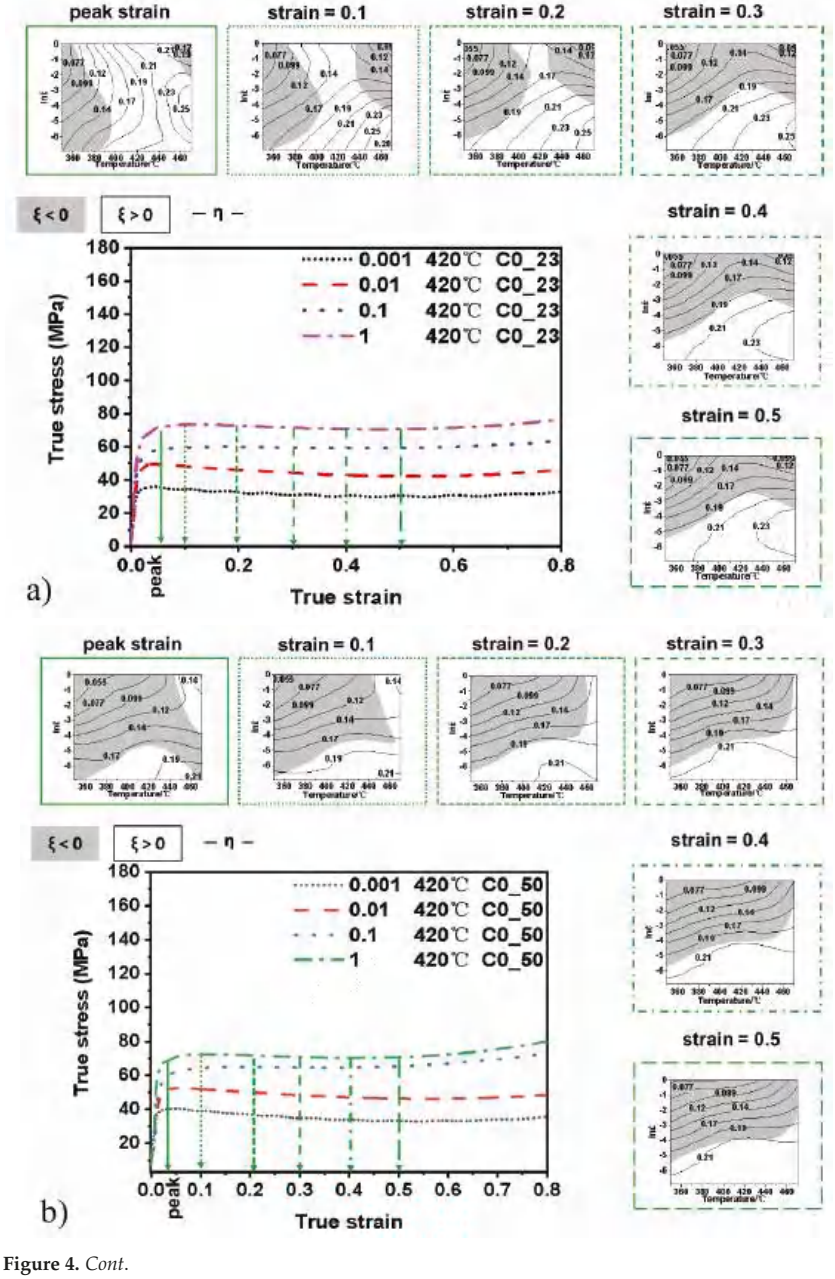

Figure 4. *Cont.*

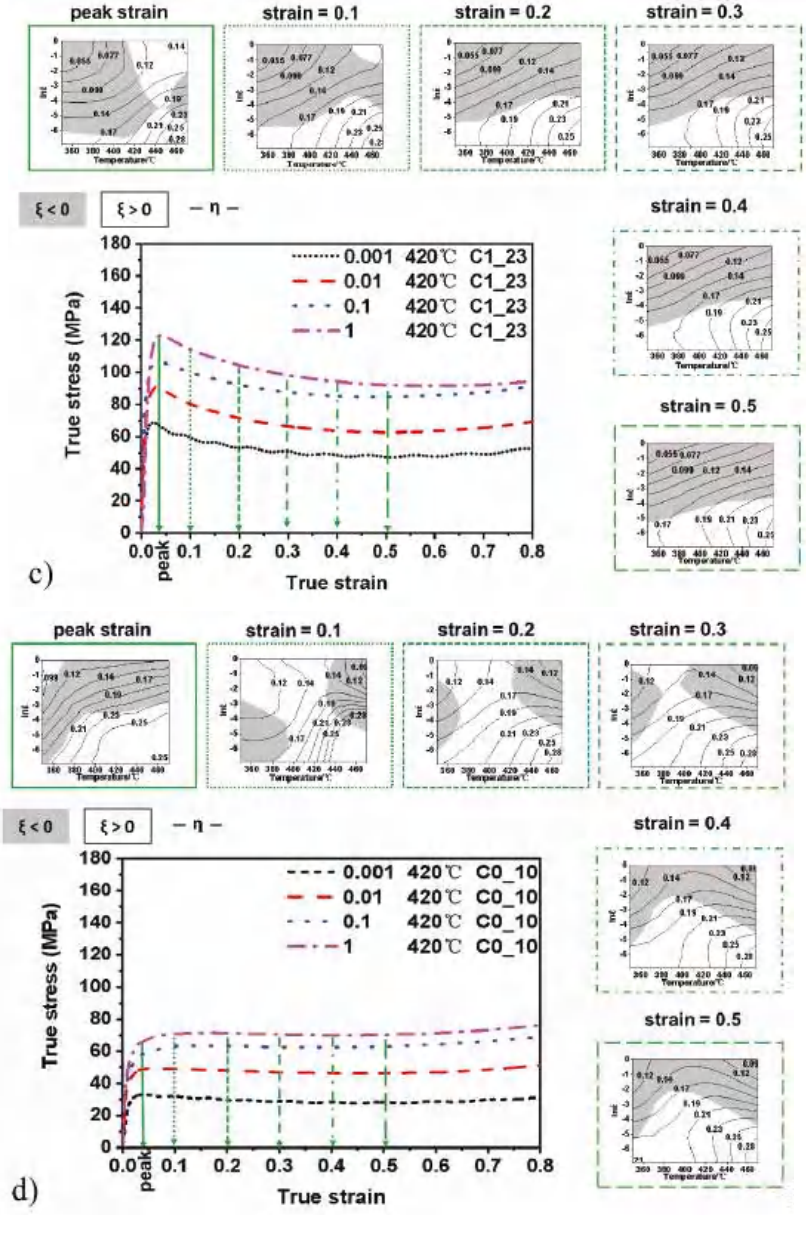

Figure 4. *Cont.*

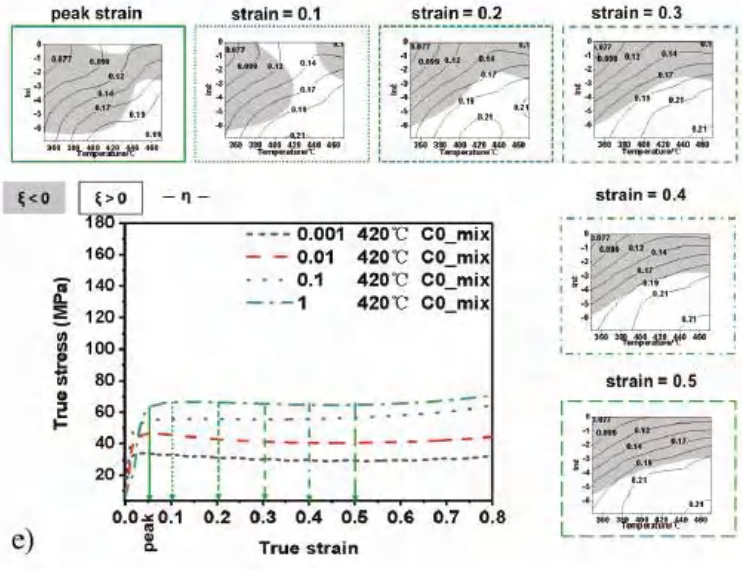

Figure 4. Processing maps of the investigated materials at different strain levels and related compression curves at 420 °C and different strain rates: (**a**) material C0_23; (**b**) material C0_50; (**c**) material C1_23; (**d**) material C0_10; (**e**) material C0_mix.

The material C0_23 represents a baseline in this study as the standard 23 μm size SiCp reinforced composite without RE-additions. The processing map for the material C0_23 is shown in Figure 4a, where the contour numbers represent power dissipation efficiency, and the shaded domains represent the regions of flow instability. The processing map at different strain levels is shown together with the associated stress–strain curves at some preselected levels of strains from the strain at peak stress up to a strain of 0.5. During the whole process, the processing map could guide the choice of the hot working parameters for the composites. At the peak strain processing map, the highest power dissipation efficiency value is 0.25, and the stable region separates two regions of instability. Instability is generated by a lower temperature or high temperature and high strain rates. Increasing the strain in the materials closes that gap between the instability regions, forcing the stable region towards lower strain rates and higher temperatures. At strains equal to 0.3 and above, the process map appears to stop changing and stabilise, and the highest efficiency is 0.23. This behaviour approximately coincides with reaching a planar portion of the stress–strain curves, where there is a weak tendency towards softening after the peak stress (Figure 4a).

The material C0_50 is similar to the material C0_23 but has an increased SiCp particle size. Figure 4b), where there is a large and dominant unstable region and efficient deformation is only possible at low strain rates, or high strain rates and high temperature. The processing maps appear to stabilise already at strain above 0.2. It should be noted that there is a tendency to tolerate higher strain rates at the highest temperatures. A broad zone also allows deformation at an energy dissipation efficiency above 0.21.

In Figure 4c, the effect of RE elements in the material C1_23 shows similarities to both material C0_23 and C0_50. Firstly, there is a separation between the two unstable regions at peak strain. These two regions join, and just as in the material C0_23, the pattern stabilises the stable deformation is pushed towards lower strain rates. It should be noted that the peak stress is significantly higher than for both material C0_23 and C0_50 and is followed by a significant softening. The SiCp particles do not deform during the deformation process, and the matrix material absorbs all deformation. The RE-additions significantly increase

the strength of the matrix, as seen in the peak strength in Figure 2d. The difference to the C0_50 material that would have a softer matrix is that at the highest temperature, the stable region is pushed further down towards low strain rates and that the energy dissipation goes above 0.25 compared to 0.21 for the C0_50 material. This outcome suggests increased formability at the highest temperatures.

The material C0_10 has a soft matrix with a lower fraction of smaller SiCp particles that seemed more clustered. As expected, the peak stress is lower, and the processing map is similar to the C0_23 material (Figure 4a,d). The processing map for the material C0_10 shows a relatively wide gap between the unstable regions. The degree of softening after the peak strength exists but it is weak, just as for the material C0_23. The change in the processing maps is similar, and the two instability regions join and forces the stable regions towards lower strain rates at strains from 0.3 and up. There is no significant breakdown at the maximum strain investigated. The low fraction and small size of the SiCp particles suggest that the matrix deformation dominates this type of processing map.

The material C0_mix is a mixture of large and small SiCp particles targeted to better lock the movement of the material flow, and Figure 4e shows a similar effect to the one seen with the RE-addition in Figure 4c. The two instability regions are joined at peak stress but separated at 0.1 to join again at 0.2. Strains from 0.2 and up appear to be stable, coinciding with a steady-state behaviour in the stress–strain curve. It should also be noted that for all the materials with the C0 matrix base materials (Figure 4a,d,e), except for C0_50 (Figure 4b), the stable regions tolerate a higher strain rate at temperatures around 420–440 °C. Strengthening the matrix with RE-addition shows the same behaviour, but the stable region was forced to lower strain rates.

4. Discussion

4.1. Strengthening Mechanisms

In Al-based composite materials, the strengthening can be classified as (i) load bearing, (ii) Hall–Petch mechanism, (iii) Orowan strengthening, and (iv) the modulus mismatch [37]. In Al-based composite materials, the strengthening can be classified as (i) load bearing, (ii) Hall–Petch mechanism, (iii) Orowan strengthening, and (iv) the modulus mismatch [37]. In the present study, the load bearing and the modulus mismatch significantly improve composite strength. The SiC particles used in this research are micro-scales, and only the nano-scale particles contribute to the Orowan strengthening. Figure 1 shows that the secondary dendrite arm spacing does not change significantly, so the Hall–Petch mechanism does not vary significantly and may be lumped into the σ_0-term, Equation (8). Equation (8) shows the relation used to calculate the total flow stress with the different strengthening contributions listed in Table 5:

$$\sigma_{tot} = \sigma_0 + \Delta\sigma_{LB} + \Delta\sigma_{MM} + \Delta\sigma_{os} \quad (8)$$

Table 5. Equations used for the contribution of the different strengthening mechanisms.

Strengthening Mechanism	Relation	Values
Matrix alloy	Equation (9)	C_{MM} = 1.47 MPa·$\sqrt{}$m [21]
Load bearing [37]	Equation (10)	
Modulus mismatch [37]	Equation (11)	C_{MM} = 1.47 MPa·$\sqrt{}$m [21]
Orowan [38]	Equation (12)	G = 41 GPa [22] b = 0.286 nm

Equation (9) was used to calculate the material C0 matrix strength σ_0 without the reinforcing SiC particles. Equation (10) describes the contribution from load bearing,

and Equation (11) describes the strengthening contribution from the modulus mismatch effect [37]. Equation (12) describes the contribution of the Orowan strengthening [38].

$$\sigma_0 = \frac{\left(\sigma_{C0\_10} - C_{MM} \times \sqrt{\frac{f_{SiC}}{d_{SiC}}}\right)}{(1 + 0.5 \times f_{SiC})} \quad (9)$$

$$\sigma_0 = \frac{\left(\sigma_{C0\_10} - C_{MM} \times \sqrt{\frac{f_{SiC}}{d_{SiC}}}\right)}{(1 + 0.5 \times f_{SiC})} \quad (10)$$

$$\Delta\sigma_{MM} \approx C_{MM} \times \left(\sqrt{\frac{f_{SiC}}{d_{SiC}} \times \varepsilon} + \sqrt{\frac{f_{int}}{d_{int}} \times \varepsilon}\right) \quad (11)$$

$$\Delta\sigma_{OS} = \left(0.538 \times \frac{G \times b \times \sqrt{f_\theta}}{d_\theta}\right) \times \ln\left(\frac{d_\theta}{2 \times b}\right) \quad (12)$$

In Table 5, G is the shear modulus [GPa], b is Burger's vector, d [m] is the actual diameter of the precipitates, f_SiC and f_int are the volume fractions of SiC particles and intermetallic phases, d_SiC and d_int are the characteristic dimension of the particles and σ_0 [MPa] is the strength of the matrix alloy. The results of materials C0_50 and C1_23 are representative and presented in Figure 5a. The average error value between the experimental data and the calculated data in the material C0_50 is 7.65%, considered acceptable. Whereas the error value in the material C1_23 is large enough for reconsideration.

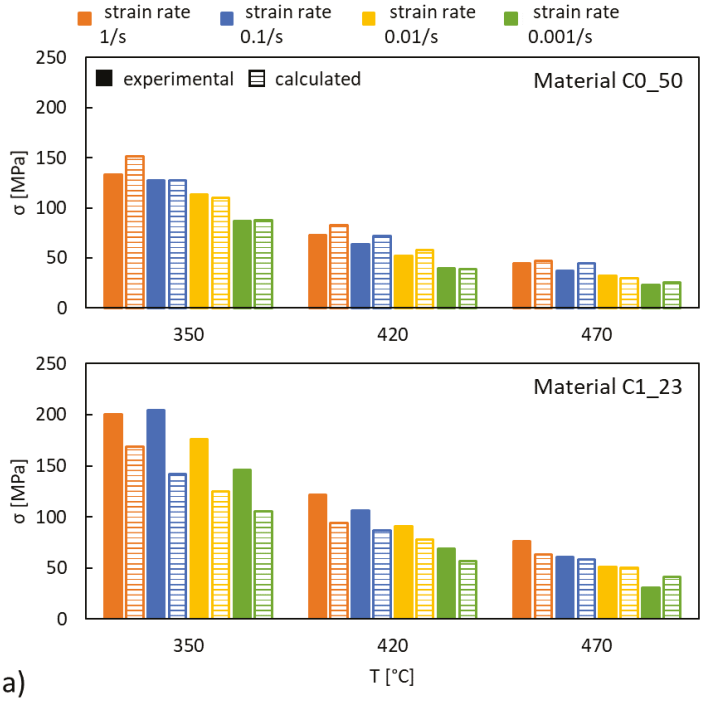

Figure 5. *Cont.*

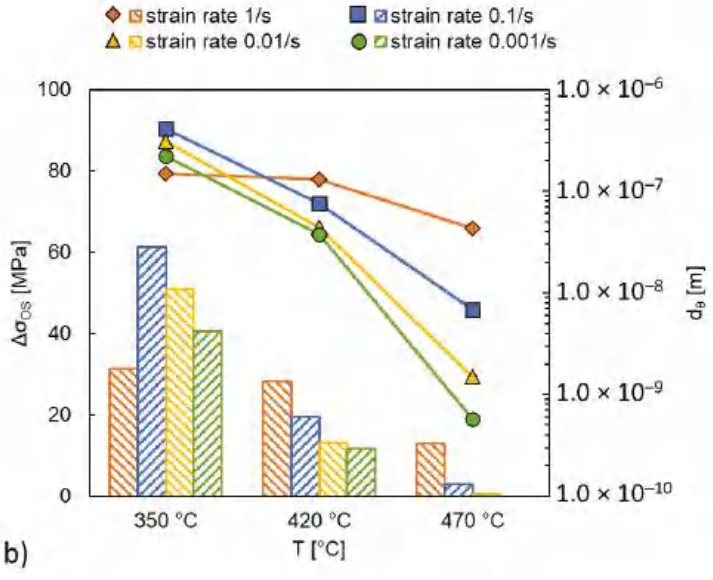

Figure 5. (**a**) The comparison between experimental data and calculated values with $\Delta\sigma_{LB}$ and $\Delta\sigma_{MM}$ for materials C0_50 and C1_23; (**b**) fitted Feret diameter d_θ of θ-Al_2Cu particles and the resulting Orowan strength contribution $\Delta\sigma_{OS}$.

The Thermo-Calc software was used to calculate the volume fraction of precipitates formed in the material C1_23 at test temperature, θ-Al_2Cu phases were predicted. The peak fraction of θ-Al_2Cu was predicted to be 1.08% at 170 °C. This value was used to calibrate the Orowan contribution at 350 °C at $\dot{\varepsilon} = 1/s$. The Orowan contribution at all other conditions was expressed as a function of particle size only. Figure 5b shows that the Feret diameter of θ-Al_2Cu particle tends towards smaller sizes, as the deformation temperature increases, and test duration increases (i.e., reduced strain rate). Equation (12) was used in the material C1_23 to calculate strength contribution from precipitated θ-Al_2Cu phases. The Orowan strengthening was fitted to match the gap between experimental data and calculated data for the material C1_23. The comparison of experimental data and calculated data confirmed that in the C0 matrix alloys, the strengthening mechanism was load bearing and modulus mismatch. In the C1_23 material, in addition to the above strengthening mechanisms, the Orowan strengthening should be included. The numerical results are presented in Tables A1 and A2, Appendix B.

4.2. The Activation Energy

Equations (3) and (4) illustrate the relationship between the activation energy Q_A (kJ/mol), the RE addition ([RE wt.%]), and the main microstructural features of the SiC particles: the fraction (f_SiC), the average size (d_SiC), and the first-nearest neighbour distance (1NND). Figure 5 illustrates that the SiCp fraction on the *x*-axis is not sufficient to describe the evolution of the activation energy: the maximum value of Q_A does not correspond to the highest fraction of SiCp. The SiCp size and level of clustering determine the characteristic interaction distance to activate the material flow.

The Stoke–Einstein Equation (13) relates diffusion to viscosity [39,40]:

$$D = \frac{kT}{6\pi r \times \mu} \quad (13)$$

where D [m^2/s] is the diffusion coefficient, k = 1.381 × 10^{-23} J/K is the Boltzmann's constant, T [K] is the temperature, r [m] is the radius of the particle, and μ [Pa*s] is the viscosity. Inserting the Arrhenius equations for D and μ in Equation (13) results in Equation (14):

$$D_0 \exp\left(-\frac{Q_D}{RT}\right) = \frac{kT}{6\pi r \times \mu_0 \exp\left(-\frac{Q_A}{RT}\right)} \quad (14)$$

where Q_D [J/mol] is the activation energy for self-diffusion and Q_A [J/mol] is the activation energy for the material flow. D_0 = 3.5 × 10^{-6} m^2/s for aluminium. Rearranging and applying the natural logarithm results in Equation (15):

$$\frac{Q_D + Q_A}{RT} = \ln\left(\frac{6\pi r \times \mu_0 D_0}{kT}\right) \quad (15)$$

Taking the ratio between two materials i and j and assuming a value for μ_0, it is possible to solve for r_i in Equation (16) with the constant C in Equation (17) under the assumption of an initial size r_j:

$$r_i = \exp\left(\left(\ln(r_j) + C\right)\frac{(Q_D + Q_A)_i}{(Q_D + Q_A)_j} - C\right) \quad (16)$$

$$C = \ln\left(\frac{6\pi \times \mu_0 D_0}{kT}\right) \quad (17)$$

In the C0_10 material, characterised by the smallest SiC size, the presence of clustering (Figure 1d) and the lowest SiC fraction, the characteristic size was assumed in the order of the atomic radius, 1.43 × 10^{-10} m or 1.43 Å, because the material flow mainly involved the matrix alloy. This material was taken as the reference one (material j in Equation (16)) for the other materials having higher SiC fractions, larger SiC sizes, and less frequent clustering. The μ_0 value in Equation (16) was assumed, as in Equation (18), based on the von Mises flow stress criterion:

$$\mu_0 = \frac{\sigma_{470\ ^\circ C}}{\sqrt{3} \times \dot{\varepsilon}_{max}} = \frac{38270000\ Pa}{\sqrt{3} \times 1\ s^{-1}} = 2.210\ Pa \times s \quad (18)$$

In the C0_23 material, the characteristic interaction distance increased to 10 nanometres and even more to 100 microns for the C0_50 material. This outcome aligns with the increasing SiC fraction and size through materials C0_23 and C0_50 in Figure 6. The interaction changes from the atomic level to the level of the secondary phase and finally to the SiC particles' order of magnitude.

The size mixture in the C0_mix material led to a complex interconnection between particles with different sizes and more frequent clustering events. This outcome determines the characteristic distance in the order of 1 cm to activate the material flow, which is the dimension of the sample. The entire structure is involved in the deformation, and thus the energy required to activate the material flow is 20 to 90% higher than the materials reinforced with one-sized SiC particles.

The role of RE-based phases can be observed by comparing the materials C0_23 and C1_23. The presence of $Al_{11}(Ce,La)_3$ and $Al_{20}(Ce,La)Ti_2$ phases and the Al matrix strengthened by Cu in solid solution constitute an additional obstacle to hot deformation, and this contributes to higher values of activation energy compared to the C0_23 material having the same fraction and size of SiC particles. The entity to be moved in the C1_23 material is in the micrometre range, two orders larger than the one in the C0_23 material.

The interaction distance affects the activation energy and not the SiCp fraction itself, and this result agrees with Equations (3) and (4) results with an improved R^2-value for size and distance and not for fraction SiCp.

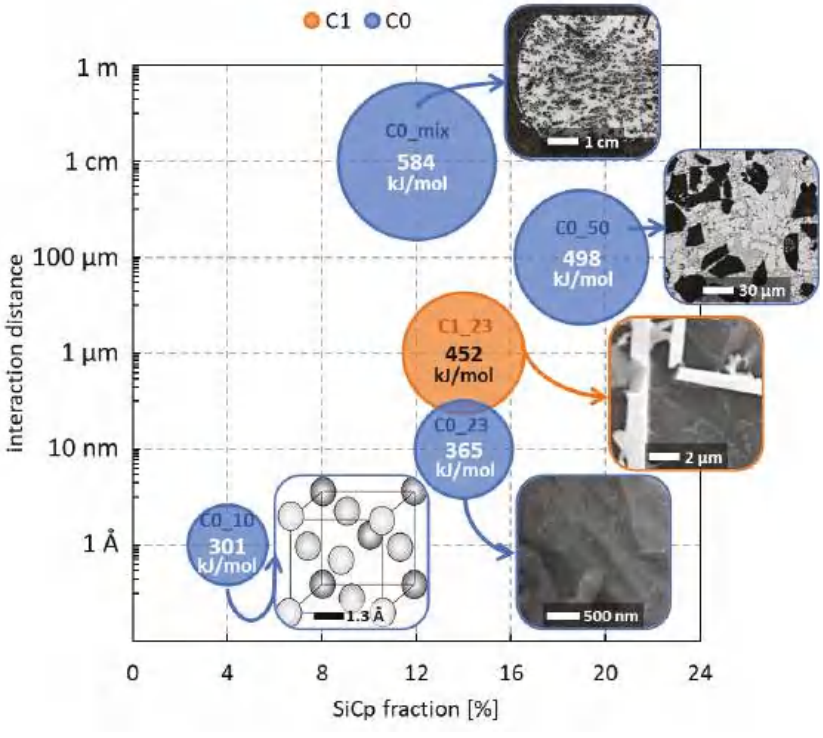

Figure 6. Relation between the activation energy Q_A, the SiCp fraction and the interaction distance. The size of the bubble is proportional to the Q_A value.

4.3. The Processing Maps

The processing maps provided the forming parameters to avoid defects during deformation. According to the processing maps, at strains above 0.3, the stable and unstable regions tended to stabilise and did not change significantly with additional straining. The highest dissipation efficiency values and the stable region were located at low strain rates, in the range 0.01–0.001/s. Below a strain of 0.3, the highest dissipation efficiency values and the stable region resulted in a high temperature range, 380–470 °C and 0.001/s strain rate. The previous studies on processing maps of Al-based composites did not compare the result at different strain levels. Hao et al. [27] investigated an Al-Cu/SiCp35 material and reported the processing map at the strain of 0.5, and it had a wide safe region, from 350 to 500 °C and 0.1–10/s strain rates. This result is very different from what was observed in the present study for the different materials: low strain rates, in the range 0.001–0.01/s, facilitate a stable forming operation of the composites. A similar result was reported by Xiao et al. [31], who investigated an Al-Cu/SiCp15 composite. Going from 0.3 to 0.5 strain, the unstable area expanded in the 1–10/s strain rate range at all temperatures. A comparison with the results from Huang et al. [30] and Ramanathan et al. [32] is not directly possible because the authors used the decimal logarithm of the strain rate instead of the natural logarithm to build the processing maps.

The processing map of the material C1_23 shows the safe region during whole strain located at a narrow area in the temperature range 420–470 °C and at 0.001 strain rate. This feature highlights that the RE addition limited the forming performance. The formation of stable phases and the reduced interaction distance of particles increased the activation energy and the difficulty of formability; this phenomenon locked the soft matrix, hindering the deformation of the material. On the other hand, the addition of La and Ce to the

matrix alloy determines a doubled peak stress, and this is due to the presence of hard phases dispersed in the matrix. As previously reported [21,22], the $Al_{11}(Ce,La)_3$ and $Al_{20}(Ce,La)Ti_2$ phases strengthen the matrix alloy significantly, giving 15% higher elastic modulus and 55% higher strength at 300 °C. The material can be considered a two-level composite: both the (La,Ce)-based phases and the SiC particles act as reinforcement. A similar phenomenon occurs also in the C0_mix material. The large-sized and the small-sized particles size combined in an inter-locking structure that hindered the flow of the soft matrix and thus increased activation energy. This behaviour resulted in a limited stable domain, at 440–470 °C and a strain rate of 0.01–0.001/s.

5. Conclusions

The present study focuses on the effect of the addition of RE and different sizes and amounts of SiC particles on activation energy, processing map, and strengthening mechanism. Thermal compression tests were used to review the formability of composite materials and combined with microstructural analysis.

The dominant contribution to peak strength was the soft alloy matrix. The addition of RE and transition elements significantly impacted the peak strength through an interaction between the SiC particle and the RE-containing intermetallic compounds. The main reinforcing effects in the C0 materials were the load bearing and modulus mismatch strengthening, while the Orowan strengthening also played an essential role in the C1 composite due to the Cu addition. The safe-forming region in the RE-added composite was stable from peak stress to 0.5 strain in the temperature range 420–470 °C and at 0.001/s strain rate. The power dissipation was 0.23–0.28. For the C0 materials, the processing map tended to stabilise after 0.2 strain, with no further changes in the stable and unstable regions. The particle–particle interaction distance plays a central role in thermal stability. The diffusion–viscosity simile revealed that the scale of particle–particle interaction distance impacted the thermal stability. The impact revealed itself as a difference between activation energies, from the one of self-diffusion to the Zener–Hollomon one assessed from the visco–plastic deformation. The SiC particle size, the presence of thermal stable phases, and the SiC particle distance—all these parameters influence the interaction distance.

The use of Al-MMCs brake discs is one way to tackle emissions reduction, both weight-related and material-related emissions. Awe [8] highlighted that the automotive vehicle exhaust emissions reduced drastically from 2000 to 2014. The Al–Si/SiCp composite brake disk reduces exhaust emissions by being 50% lighter than the cast iron equivalent, and it also has higher wear resistance, uniform friction, light weight, and reduced light distance braking ability.

Author Contributions: Conceptualisation, A.E.W.J. and J.Z. (Jinchuan Zheng); methodology, A.D., L.L., J.Z. (Jie Zhou) and A.E.W.J.; investigation, A.D. and L.L.; resources, A.E.W.J. and J.Z. (Jinchuan Zheng); writing—original draft preparation, A.D. and L.L.; writing—review and editing, all authors together; supervision, A.E.W.J., J.Z. (Jinchuan Zheng), J.Z. (Jie Zhou), G.Y. and K.W.; project administration, A.E.W.J. and J.Z. (Jinchuan Zheng); funding acquisition, A.E.W.J., J.Z. (Jinchuan Zheng) and L.L. All authors have read and agreed to the published version of the manuscript.

Funding: This research was funded by the Short-term Recruitment Program of Foreign Expert (China), grant 20181215, and the Stiftelsen för Kunskaps-och Kompetensutveckling (Sweden), ProSpekt grant ProForAl-20201702. The APC was funded by the Stiftelsen för Kunskaps-och Kompetensutveckling (Sweden), ProSpekt grant ProForAl-20201702.

Institutional Review Board Statement: Not applicable.

Informed Consent Statement: Not applicable.

Data Availability Statement: Data available in a publicly accessible repository.

Acknowledgments: The authors acknowledge the staff at Jönköping University and CAM Science and Technology (Jiangle) Institute of Semi-Solid Metal Technology.

Conflicts of Interest: The authors declare no conflict of interest.

Nomenclature

Letters and acronyms	
A [1/s]	material constant in the Zener–Hollomon model
b [m]	Burger's vector
D [m^2/s]	diffusion coefficient
d [m]	diameter
k = 1.381 × 10^{-23} J/K	Boltzmann's constant
f	fraction
G [GPa]	shear modulus
m	strain rate sensitivity exponent
n1	material constant in the Zener–Hollomon model
n2	material constant in the Zener–Hollomon model
Q_A [kJ/mol]	activation energy of plastic deformation
Q_D [kJ/mol]	activation energy of self-diffusion
r [m]	radius
R = 8.314 J/K·mol	the universal gas constant
T [K]	temperature
Greek letters	
α = β/n1 [1/MPa]	material constant in the Zener–Hollomon model
β [1/MPa]	material constant in the Zener–Hollomon model
ε	strain
$\dot{\varepsilon}$ [1/s]	strain rate
η	the efficiency of power dissipation
μ [Pa*s]	dynamic viscosity
ξ	instability criterion
σ [MPa]	stress
Δσ	strengthening contribution
Subscripts	
0	reference material
f	fibres
i, j	two arbitrary materials
int	intermetallic
θ	Al_2Cu phase
LB	load bearing
MM	modulus mismatch
OS	Orowan strengthening
p	particles
SiC	silicon carbide
w	whiskers

Appendix A. Experimental Procedure

The appendix collects schematic representations of the experimental procedure (Figure A1) and the 'knnsearch' Matlab function (Figure A2).

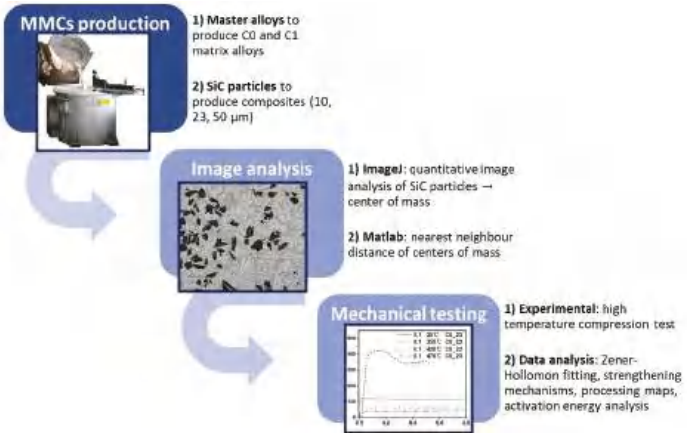

Figure A1. Schematic description of the experimental procedure described in Section 2.

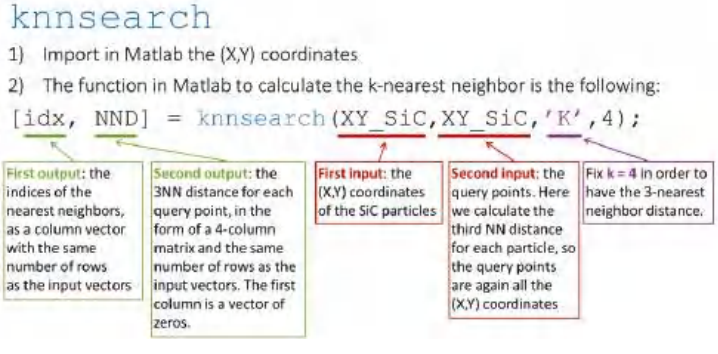

Figure A2. Description of the 'knnsearch' Matlab function used to evaluate the third nearest-neighbour (NN) distance.

Appendix B. Strengthening Mechanisms

The results of material C0_50 and C1_23, depicted in Figure 5a, are representative and listed in Table A1.

Table A1. The comparison between experimental data and calculated values with $\Delta\sigma_{LB}$ and $\Delta\sigma_{MM}$.

Strength [MPa]	$\dot{\varepsilon}$ [1/s]	1		0.1		0.01		0.001	
Material	**Temperature [°C]**	**Exp.**	**Calc.**	**Exp.**	**Calc.**	**Exp.**	**Calc.**	**Exp.**	**Calc.**
C0_50	350	133	151	127	127	113	110	87	88
	420	73	83	64	72	52	58	40	39
	470	45	47	37	45	32	30	23	26
C1_23	350	200	169	204	142	176	125	146	105
	420	122	94	106	87	91	78	69	57
	470	76	63	61	58	51	50	31	41

Table A2 shows the numerical data depicted in Figure 5b. Equation (12) was used in material C1_23 to calculate strength contribution from precipitated θ-Al_2Cu phases.

Table A2. Fitted Feret diameter of θ-Al_2Cu particles and the resulting Orowan strength contribution $\Delta\sigma_{OS}$.

$\dot{\varepsilon}$ [1/s]	1		0.1		0.01		0.001	
	d_θ [m]	$\Delta\sigma_{OS}$ [MPa]	d_θ [m]	$\Delta\sigma_{OS}$ [MPa]	d_θ [m]	$\Delta\sigma_{OS}$ [MPa]	d_θ [m]	$\Delta\sigma_{OS}$ [MPa]
350 °C	1.5×10^{-7}	31.26	4.1×10^{-7}	61.32	3.1×10^{-7}	50.81	2.2×10^{-7}	40.40
420 °C	1.3×10^{-7}	28.18	7.6×10^{-8}	19.38	4.4×10^{-8}	13.14	3.8×10^{-8}	11.67
470 °C	4.3×10^{-8}	12.90	6.9×10^{-9}	2.96	1.5×10^{-9}	0.54	5.7×10^{-10}	0.00

References

1. International Energy Agency. *Energy Technology Perspectives 2015*, 2015th ed.; IEA Publications: Paris, France, 2015; ISBN 9789264233416.
2. Serrenho, A.C.; Norman, J.B.; Allwood, J.M. The impact of reducing car weight on global emissions: The future fleet in Great Britain. *Philos. Trans. R. Soc. A Math. Phys. Eng. Sci.* **2017**, *375*, 20160364. [CrossRef] [PubMed]
3. Yamagata, H.; Kurita, H.; Aniolek, M.; Kasprzak, W.; Sokolowski, J.H. Thermal and metallographic characteristics of the Al–20% Si high-pressure die-casting alloy for monolithic cylinder blocks. *J. Mater. Process. Technol.* **2008**, *199*, 84–90. [CrossRef]
4. Das, D.K.; Mishra, P.C.; Singh, S.; Pattanaik, S. Fabrication and heat treatment of ceramic-reinforced aluminium matrix composites—A review. *Int. J. Mech. Mater. Eng.* **2014**, *9*, 6. [CrossRef]
5. Mortensen, A.; Jin, I. Solidification processing of metal matrix composites. *Int. Mater. Rev.* **1992**, *37*, 101–128. [CrossRef]
6. Ibrahim, I.A.; Mohamed, F.A.; Lavernia, E.J. Particulate reinforced metal matrix composites—A review. *J. Mater. Sci.* **1991**, *26*, 1137–1156. [CrossRef]
7. Thomas, A.; Zervos, N.; Ekelund, A.; Awe, S.A. Simulation Study on the Thermomechanical Behaviour of Al-MMC Automotive Brake Discs. In Proceedings of the Eurobrake 2019, Dresden, Germany, 21–23 May 2019; pp. 1–12.
8. Awe, S.A. Developing Material Requirements for Automotive Brake Disc. *Mod. Concepts Mater. Sci.* **2019**, *2*, 1–4. [CrossRef]
9. D'Errico, F.; Casari, D.; Alemani, M.; Perricone, G.; Tosto, M. Industrial semisolid casting process for secondary aluminium alloys for decarbonising lightweight parts in automotive sector. *MATEC Web Conf.* **2020**, *326*, 06007. [CrossRef]
10. Radha Krishnan, B.; Ramesh, M. Experimental Evaluation of Al-Zn-Al2O3 Composite on Piston Analysis by CAE Tools. *Mech. Mech. Eng.* **2019**, *23*, 212–217. [CrossRef]
11. Stojanović, B. Application of aluminium hybrid composites in automotive industry. *Teh. Vjesn.* **2015**, *22*, 247–251. [CrossRef]
12. Baisane, V.; Sable, Y.; Dhobe, M.; Sonawane, P. Recent development and challenges in processing of ceramics reinforced Al matrix composite through stir casting process: A Review. *Int. J. Eng. Appl. Sci. IJEAS* **2015**, *2*, 11–16.
13. Mavhungu, S.T.; Akinlabi, E.T.; Onitiri, M.A.; Varachia, F.M. Aluminum Matrix Composites for Industrial Use: Advances and Trends. *Procedia Manuf.* **2017**, *7*, 178–182. [CrossRef]
14. Rebba, B.; Ramanaiah, N. Evaluation of Mechanical Properties of Aluminium Alloy (Al-2024) Reinforced with Molybdenum Disulphide (MOS 2) Metal Matrix Composites. *Procedia Mater. Sci.* **2014**, *6*, 1161–1169. [CrossRef]
15. Awe, S.A.; Thomas, A. The Prospects of Lightweight SICAlight Discs in the Emerging Disc Brake Requirements. In Proceedings of the Eurobrake 2021, Online, 17–21 May 2021; pp. 1–6.
16. Peng, L.M.; Zhu, S.J.; Wang, F.G.; Chen, H.R. Creep behavior in an Al-Fe-V-Si alloy and SiC whisker-reinforced Al-Fe-V-Si composite. *J. Mater. Sci.* **1998**, *3*, 5643–5652. [CrossRef]
17. Agrawal, E.; Tungikar, V. Wear performance of Al-TiC composite at elevated temperature. *World J. Eng.* **2022**, *19*, 346–351. [CrossRef]
18. Xia, F.; Gao, X.S.; Liang, M.X.; Guo, Y.C.; Li, J.P.; Yang, Z.; Wang, J.L.; Zhang, L.L. Effect of thermal exposure on microstructure and high-temperature fatigue life of Al-Si piston alloys. *J. Mater. Res. Technol.* **2020**, *9*, 12926–12935. [CrossRef]
19. Zhang, J.Y.; Zuo, L.J.; Feng, J.; Ye, B.; Kong, X.Y.; Jiang, H.Y.; Ding, W.J. Effect of thermal exposure on microstructure and mechanical properties of Al-Si-Cu-Ni-Mg alloy produced by different casting technologies. *Trans. Nonferrous Met. Soc. China* **2020**, *30*, 1717–1730. [CrossRef]
20. Lattanzi, L.; Etienne, A.; Li, Z.; Manjunath, T.; Nixon, N.; Jarfors, A.E.W.; Awe, S.A. The influence of Ni and Zr additions on the hot compression properties of Al-SiCp composites. *J. Alloys Compd.* **2022**, *905*, 164160. [CrossRef]
21. Du, A.; Jarfors, A.E.W.; Zheng, J.; Wang, K.; Yu, G. The influence of La and Ce on microstructure and mechanical properties of an Al-Si-Cu-Mg-Fe alloy at high temperature. *Metals* **2021**, *11*, 384. [CrossRef]
22. Du, A.; Lattanzi, L.; Jarfors, A.W.E.; Zheng, J.; Wang, K.; Yu, G. On the hardness and elastic modulus of phases in sic-reinforced al composite: Role of la and ce addition. *Materials* **2021**, *14*, 6287. [CrossRef]
23. Seetharaman, S.; Gupta, M. Fundamentals of Metal Matrix Composites. In *Encyclopedia of Materials: Composites*; Elsevier: Amsterdam, The Netherlands, 2021; pp. 11–29. ISBN 9780128197240.
24. Rohatgi, P. Cast aluminum-matrix composites for automotive applications. *JOM* **1991**, *43*, 10–15. [CrossRef]
25. Sun, W.; Duan, C.; Yin, W. Chip formation mechanism in machining of Al/SiCp composites based on analysis of particle damage. *J. Manuf. Process.* **2021**, *64*, 861–877. [CrossRef]

26. Rezaei Ashtiani, H.R.; Parsa, M.H.; Bisadi, H. Constitutive equations for elevated temperature flow behavior of commercial purity aluminum. *Mater. Sci. Eng. A* **2012**, *545*, 61–67. [CrossRef]
27. Hao, S.; Xie, J.; Wang, A.; Wang, W.; Li, J.; Sun, H. Hot deformation behaviors of 35%SiCp/2024Al metal matrix composites. *Trans. Nonferrous Met. Soc. China* **2014**, *24*, 2468–2474. [CrossRef]
28. Patel, A.; Das, S.; Prasad, B.K. Compressive deformation behaviour of Al alloy (2014)-10wt.% SiCp composite: Effects of strain rates and temperatures. *Mater. Sci. Eng. A* **2011**, *530*, 225–232. [CrossRef]
29. Prasad, Y.V.R.K.; Rao, K.P.; Sasidhara, S. *Hot Working Guide*, 2nd ed.; Prasad, Y.V.R.K., Rao, K.P., Sasidhara, S., Eds.; ASM International: Materials Park, OH, USA, 2015; ISBN 978-1-62708-091-0.
30. Huang, Z.; Zhang, X.; Xiao, B.; Ma, Z. Hot deformation mechanisms and microstructure evolution of SiCp/2014Al composite. *J. Alloys Compd.* **2017**, *722*, 145–157. [CrossRef]
31. Xiao, B.L.; Fan, J.Z.; Tian, X.F.; Zhang, W.Y.; Shi, L.K. Hot deformation and processing map of 15%SiCp/2009 Al composite. *J. Mater. Sci.* **2005**, *40*, 5757–5762. [CrossRef]
32. Ramanathan, S.; Karthikeyan, R.; Ganasen, G. Development of processing maps for 2124Al/SiCp composites. *Mater. Sci. Eng. A* **2006**, *441*, 321–325. [CrossRef]
33. Jarfors, A.E.W.; Du, A.; Yu, G.; Zheng, J.; Wang, K. On the sustainable choice of alloying elements for strength of aluminum-based alloys. *Sustainability* **2020**, *12*, 1059. [CrossRef]
34. Laurent, V.; Chatain, D.; Eustathopoulos, N. Wettability of SiO2 and oxidized SiC by aluminium. *Mater. Sci. Eng. A* **1991**, *135*, 89–94. [CrossRef]
35. Jonas, J.J.; Sellars, C.M.; Tegart, W.J.M.M. Strength and structure under hot-working conditions. *Metall. Rev.* **1969**, *14*, 1–24. [CrossRef]
36. Prasad, Y.V.R.K.; Gegel, H.L.; Doraivelu, S.M.; Malas, J.C.; Morgan, J.T.; Lark, K.A.; Barker, D.R. Modeling of dynamic material behavior in hot deformation: Forging of Ti-6242. *Metall. Trans. A* **1984**, *15*, 1883–1892. [CrossRef]
37. Ceschini, L.; Dahle, A.; Gupta, M.; Jarfors, A.E.W.; Jayalakshmi, S.; Morri, A.; Rotundo, F.; Toschi, S.; Singh, R.A. *Aluminum and Magnesium Metal Matrix Nanocomposites*; Engineering Materials; Springer: Singapore, 2017; ISBN 978-981-10-2680-5.
38. Gladman, T. Precipitation hardening in metals. *Mater. Sci. Technol.* **1999**, *15*, 30–36. [CrossRef]
39. Einstein, A. Über die von der molekularkinetischen Theorie der Wärme geforderte Bewegung von in ruhenden Flüssigkeiten suspendierten Teilchen. *Ann. Phys.* **1905**, *322*, 549–560. [CrossRef]
40. Sutherland, W. LXXV. A dynamical theory of diffusion for non-electrolytes and the molecular mass of albumin. *London Edinburgh Dublin Philos. Mag. J. Sci.* **1905**, *9*, 781–785. [CrossRef]

materials

MDPI

Article

Superplastic Deformation of Al–Cu Alloys after Grain Refinement by Extrusion Combined with Reversible Torsion

Kinga Rodak *, Dariusz Kuc and Tomasz Mikuszewski

Faculty of Materials Engineering, Silesian University of Technology, Krasińskiego 8, 40-019 Katowice, Poland; dariusz.kuc@polsl.pl (D.K.); tomasz.mikuszewski@polsl.pl (T.M.)
* Correspondence: kinga.rodak@polsl.pl; Tel.: +48-32-603-4408

Received: 16 November 2020; Accepted: 15 December 2020; Published: 18 December 2020

Abstract: The binary as-cast Al–Cu alloys Al-5%Cu, Al-25%Cu, and Al-33%Cu (in wt %), composed of the intermetallic θ-Al_2Cu and α-Al phases, were prepared from pure components and were subsequently severely plastically deformed by extrusion combined with reversible torsion (KoBo) to refinement of α-Al and Al_2Cu phases. The extrusion combined with reversible torsion was carried out using extrusion coefficients of λ = 30 and λ = 98. KoBo applied to the Al–Cu alloys with different initial structures (differences in fraction and phase size) allowed us to obtain for alloys (Al-25%Cu and Al-33%Cu), with higher value of intermetallic phase, large elongations in the range of 830–1100% after tensile tests at the temperature of 400 °C with the strain rate of 10^{-4} s^{-1}. The value of elongation depended on extrusion coefficient and increase, with λ increasing as a result of α-Al and Al_2Cu phase refinement to about 200–400 nm. Deformation at the temperature of 300 °C, independently of the extrusion coefficient (λ), did not ensure superplastic properties of the analyzed alloys. A microstructural study showed that the mechanism of grain boundary sliding was responsible for superplastic deformation.

Keywords: KoBo extrusion; mechanical properties; Al–Cu alloys; microstructure and superplastic deformation

1. Introduction

Superplasticity is a diffusion-controlled process that refers to the ability of a metallic material to demonstrate elongation by more than several hundred percent without visible necking under tensile tests at relatively high temperature (0.5–0.7) Tm (where Tm is the absolute melting temperature) and low strain rate [1–3]. Superplastic deformation is mainly controlled by three mechanisms that operate during high temperature deformation: grain boundary sliding, dislocation slip/creep, and diffusion creep or directional diffusion flow [2,4]. From this, superplastic deformation may be accompanied by various processes, for instance, grain boundaries migration; static/dynamic grain growth; and grain rotation, recovery, and recrystallization [1,3]. Moreover, superplasticity is a characteristic feature of materials with stable, equiaxed, and fine (less than 10 μm) grains. Suerplasticity process covers various metallic materials, one of which is Al alloys due to their low density and high specific strength. For this reason, they are widely utilized in the aerospace and automobile industries. In practice, these alloys have particles of secondary intermetallic phases that restrict resistance to deformation. The superplastic properties may improve formability of alloys with reduced deformation resistance [3,5].

Some superplastic alloys are already industrially produced and used in practice. Among the most known and useful alloys are the Al–Cu–Mg alloys, with elongation of more than 600% [6], and Al–3Li–0.5Zr alloy, with elongation to failure of 1035% at 370 °C [7]. Highashi et al. [8] experienced exceptional superplastic elongation of 5500% in aluminum bronze at 800 °C and 6.3×10^{-3} s^{-1} strain

rate. Much research has been reported in superplasticity of metals such as in magnesium-, iron-, titanium-, and nickel-based alloys [1,3,9].

Alloys with superplastic properties have eutectoidal or eutectic composition, although they have not been applied in practice due to unsuitable mechanical properties, although they possess good plasticity. In these alloys, the plasticity of one phase is different from the other due to the difference in crystal structure and/or chemical composition, i.e., the two phases are not equally easy to deform [10–12]. According to the literature, plastic deformation starts in the soft phase while the hard phase could still be in the elastic state [4,12]. As the plastic deformation proceeds further, the soft phase is strain hardened and internal stresses at interfaces drastically build up via dislocation accumulation and pile up [10,13,14]. Thus, there is a stress gradient and a strain gradient, which lead to the build-up of back stress [13,14]. Eventually, co-deformation of the two phases begins. Temperature increase causes a change in deformation mechanisms not only in grain interior but also, mainly, in interfaces. This factor primarily allows deformation of such materials. The second factor is connected with the applied technique of deformation. The high shear strain imposed by severe plastic deformation (SPD) can refine the grains in materials down below the ultra-fine-grained (UFG) regime. The phases in alloys can also be significantly and uniformly distributed, unlike the unprocessed samples. The SPD processing very often may be connected with temperature increase during deformation. This phenomenon of SPD may simplify superplastic deformation. Valiev et al. [15] utilized high-pressure torsion (HPT) to process Al–Cu–Zr alloy and obtained elongation of 250% at a low temperature of 220 °C. This confirmed that the SPD process is an important way to increase plasticity of alloy.

The strengthened Al–Cu alloys are commonly used for structural engineering applications, and in civil engineering [13,16]. In practice, these alloys are used in heat treatment state after supersaturation and aging. As-cast alloys with a higher fraction of intermetallic phases can also be useful in engineering applications due to some interesting properties. The intermetallic phases are particularly responsible for formability, mechanical properties, and fracture behavior of as-cast Al–Cu alloys. Fracture toughness and formability decrease with increased fraction of intermetallic phases [3,14]. Intermetallic phases are responsible for increased mechanical properties, and as a result, the application of these alloys at higher temperatures is possible [11,16].

Extrusion combined with reversible torsion (KoBo) is one of the SPD methods [17]. The complex state of stress and deformation enables deformation of practically non-deformable materials. Under conditions induced by KoBo, when the process is realized with higher deformation intensity, it is possible to obtain higher strength properties. Additionally, temperature of deformed material can rise enough to generate some structural changes, indicating the occurrence of dynamic recovery and recrystallization [17,18], and as a consequence, the observed structure becomes composed very often of equiaxed grains, which are typical for increase of plastically properties.

Thus, in this article, the structural and mechanical properties of grain refinement of Al–Cu alloy with a high-volume fraction of Al_2Cu phase using the KoBo method is presented. For this reason, alloys that nearly cross the eutectic line, have hypoeutectic composition, and have eutectic composition were analyzed. Method samples refined by KoBo were tensile tested at high temperature to obtain superplastic properties.

2. Materials and Methods

The binary Al–Cu alloys with 5 wt % of Cu (Al_5Cu), with 25 wt % of Cu ($Al_{25}Cu$), and with 33 wt % of Cu ($Al_{33}Cu$), were prepared from pure Cu (99.99 wt %) and Al (99.99 wt %). The alloys were obtained by melting in the Leybold–Heraues furnace. The alloy components were melted using high frequency generator under purified argon atmosphere and cast into a steel mold of cylindrical shape of 50 mm diameter. After cooling, the ingots were removed from the molds, and next were machined to 49.5 mm in diameter and were cut to the length of 100 mm. Then the alloys were extruded using KoBo technique to form rods with diameters of 9 and 6 mm that corresponded to reduction

coefficients of λ = 30 and λ = 98, respectively. The coefficient was expressed as follows: $\lambda = [do]^2/[dk]^2$, where do—initial diameter of ingot, dk—diameter of rod after KoBo.

The severe plastic deformation tests were carried out with the modernized KoBo 2.5 MN horizontal hydraulic press. The recipient temperature was about 130 °C. All deformation tests were carried out at constant angle of die reverse-rotation +/−8°. The die oscillation frequency was 5 Hz. The tensile tests were performed on a Zwick/Roell 100 machine (Zwick Roell AG, Ulm, Germany) at room temperature, 300 °C, and 400 °C, with a rate of 10^{-4} s^{-1}. The dimensions of the samples were diameter (d) = 4 mm, length (lo) = 50 mm. The microstructure was analyzed by the optical microscope Olympus GX71 (Olympus, Glasgow, UK) and the scanning electron microscope (SEM) LEO GEMINI 1525 (Leo Inc., NY, USA) operated at 30 kV. Additionally, a scanning transmission electron microscope (STEM) Hitachi HD-2300 A (Hitachi-Science&Technology, Tokyo, Japan) equipped with a Field Emission Gun (FEG) operated at 200 kV was used for microstructure characterization on longitudinal sections of the extruded billet. For microstructure examination, we used transmitted electron (TE) and Z contrast (ZC) imaging. The metallographic specimens were mechanically grinded and polished, and then were treated by electropolishing in 80% ethanol and 20% perchloric acid solution combined with anodic oxidation in Barker's reagent. For STEM investigations, foils with a diameter of 3.0 mm after electrolytic thinning were used.

The X-ray phase analysis was performed on an X'Pert3 Powder diffractometer (Malvern Panalytical, Chester, UK) using a copper anode lamp (λCuK-1.5406 Å) supplied with a current of 30 mA at a voltage of 40 kV. The recording was made in 0.02° steps in the angular range from 10° to 90°2. The tests were carried out on solid samples. The identification of the crystalline phases was performed using the International Centre for Diffraction Data (ICDD PDF-4+) database.

3. Results and Discussion

The microstructures of Al_5Cu, $Al_{25}Cu$, and $Al_{33}Cu$ alloys at as-cast state are presented in Figure 1. The mass weight of Cu in Al_5Cu alloy was on the limit of maximum Cu solubility in Al. Therefore, the particles of Al_2Cu phase were visible in dendrites of α phase in a wide range of sizes (large particles with eutectic composition and dispersoids) (Figure 1a). Increase of Cu content led to increase of interdentritic regions in $Al_{25}Cu$ alloy. The interdentritic regions consisted of massive eutectoid composition (α + Al_2Cu phase) and dendrites of α-Al matrix (Figure 1b). Micrometric lamellar structure of the θ-Al_2Cu and α-Al phase was characteristic for $Al_{33}Cu$ alloy (Figure 1c).

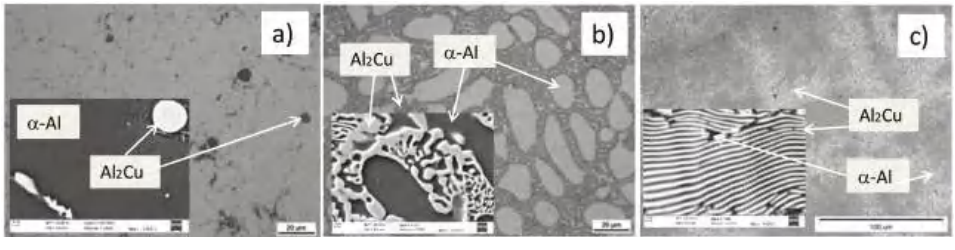

Figure 1. Microstructure of (**a**) Al–Cu alloy with 5 wt % of Cu (Al_5Cu), (**b**) with 25 wt % of Cu ($Al_{25}Cu$), and (**c**) with 33 wt % of Cu ($Al_{33}Cu$) in initial state.

The X-ray analysis showed the presence of an aluminum-based solid solution α-Al (face-centered cubic lattice) phase and an intermetallic Al_2Cu (C16, tetragonal lattice) phase (Figure 2).

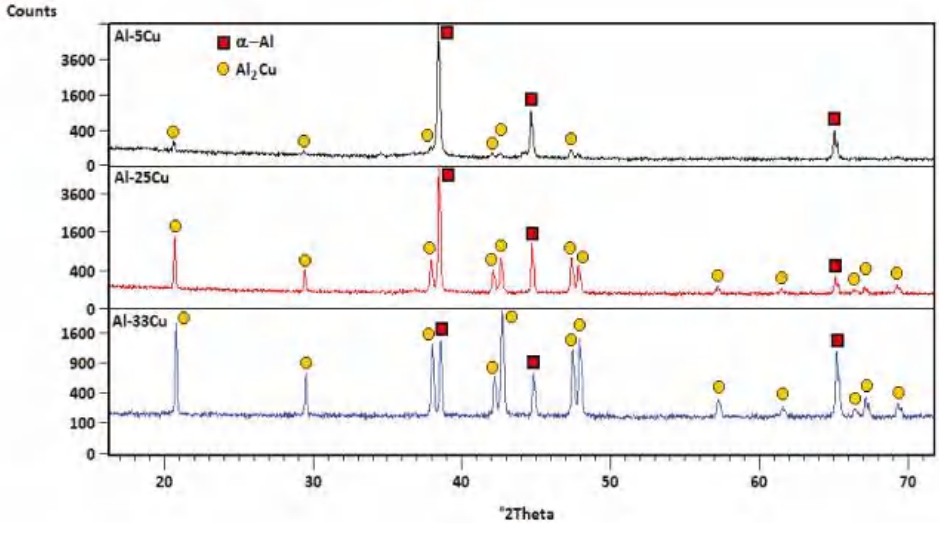

Figure 2. X-ray diffraction patterns of Al–Cu alloys.

During KoBo tests, we recorded temperature for samples that left the device using the ThermaCam SC640 (Flir Systems Inc., Portland, OR, USA) mobile thermal imaging system equipped with software for thermographic analysis. Examples of thermograms for the Al_5Cu and $Al_{25}Cu$ alloys after using the KoBo method are shown in Figure 3. The temperature was recorded in the range from approximately 37° to 132° for the Al_5Cu alloy deformed with $\lambda = 98$, and in a range from approximately 63° to 247° for the $Al_{25}Cu$ alloy deformed with $\lambda = 98$. Similar changes in temperature recorded as those for $Al_{25}Cu$ alloy were observed for the $Al_{33}Cu$ alloy. Differences in recorded temperatures between Al_5Cu and $Al_{25}Cu$ alloys followed from thermal conductivity coefficient of the tested materials. Thermal imaging revealed an increase in temperature on the surface of the material. However, we cannot exclude the potential of a higher increase in temperature inside the sample, where material was intensively deformed.

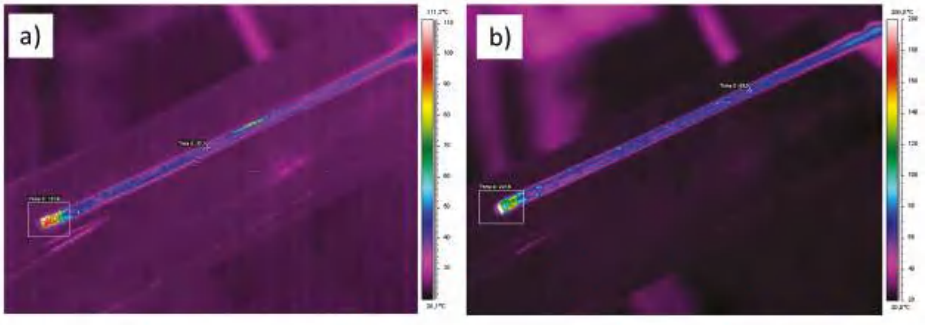

Figure 3. Thermographical pictures of surface samples of Al–Cu alloys after extrusion combined with reversible torsion (KoBo) processing with $\lambda = 98$: (**a**) Al_5Cu alloy, (**b**) $Al_{25}Cu$ alloy.

After KoBo deformation, the microstructures visible in the longitudinal section showed characteristic fibrous structure as a result of the extrusion process (Figure 4). Increase in deformation did not introduce noticeable changes in microstructure. Massive regions of eutectoid composition occasionally observed in $A_{l5}Cu$ alloy were shown to not be deformed. It was evident that α-Al phase

underwent recovery as a result of temperature increase. Visible in Figure 4a are grains of α-Al phase with different grain sizes. The difference in grain sizes may have been the result the localization of fine Al_2Cu phases that were not uniformly distributed during KoBo. In Figure 4b, the grains of α-Al phase are not visible, meaning that the grains were very small and essentially invisible when using light microscopy (LM) imaging. In $Al_{25}Cu$ alloy, the refinement process occurred for θ-Al_2Cu and α-Al phases (Figure 4c,d). SPD process was connected with distribution of Al_2Cu phase, which assured a more equiaxial structure compared with sample in as-cast state. Independently of deformation value, heterogeneity in microstructure was visible (Figure 4c,d). The Al_2Cu phase areas were clearly separated from the α-Al phase areas. Refined Al_2Cu phase was elongated in the extrusion direction. Although the KoBo process did not introduce homogeneity in the arrangement of the individual θ-Al_2Cu and α-Al phases for $Al_{25}Cu$ alloy, lamellar structure observed for $Al_{33}Cu$ alloy promoted homogeneity in microstructure and made the microstructure consist of near equiaxed intermetallic Al_2Cu and α-Al phases (Figure 4e,f). This was a consequence of eutectic structure, which is the most susceptible to fragmentation and formation of equiaxed grains.

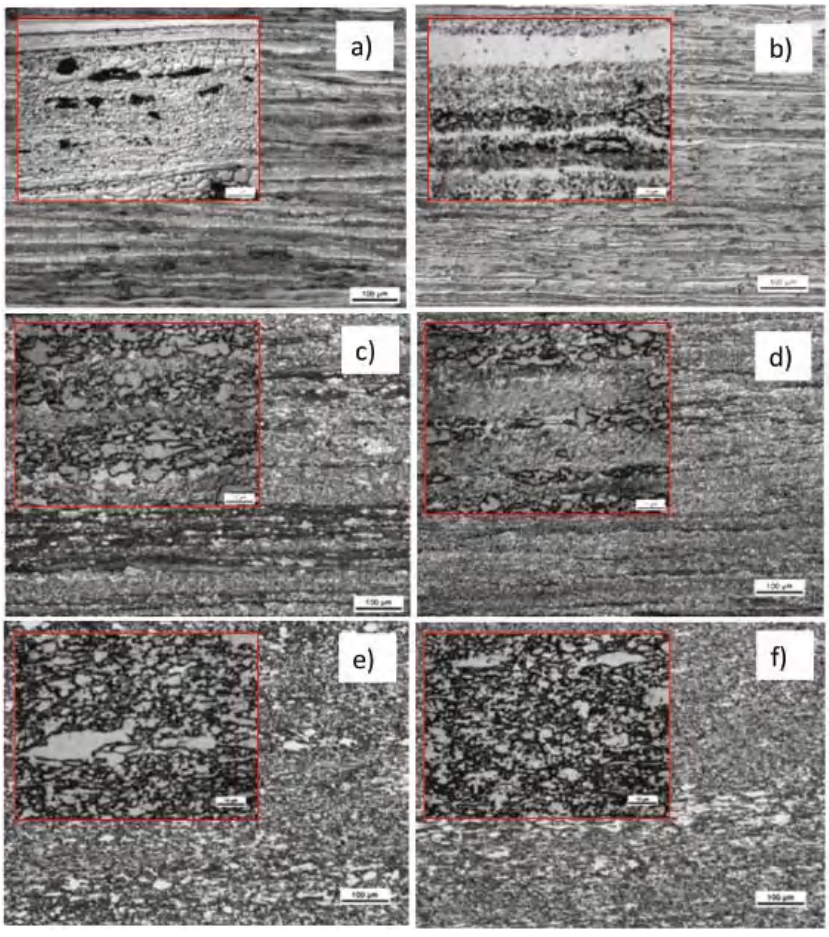

Figure 4. Microstructure of Al–Cu alloys after KoBo deformation: (**a**,**b**) Al_5Cu alloy, (**c**,**d**) $Al_{25}Cu$ alloy, (**e**,**f**) $Al_{33}Cu$ alloy, (**a**,**c**,**e**) λ = 30, (**b**,**d**,**f**) λ = 98.

Since there were no significant microstructural changes observed using LM, we selected samples after λ = 98 deformation for further STEM investigations in order to focus our attention mainly on the processes accompanying the fragmentation and rearrangement of individual phases. The choice of the deformation with λ = 98 suggested that the structure was more refined and more homogeneous. To show differences between θ-Al_2Cu and α-Al matrix phases and to show dislocation structure of individual phases, we recorded the microstructures by using ZC imaging (left side of Figure 5) and TE imaging (right side of Figure 5). The bright phases in the left side represent θ-Al_2Cu phase, which in figures in right sides is shown as dark phases.

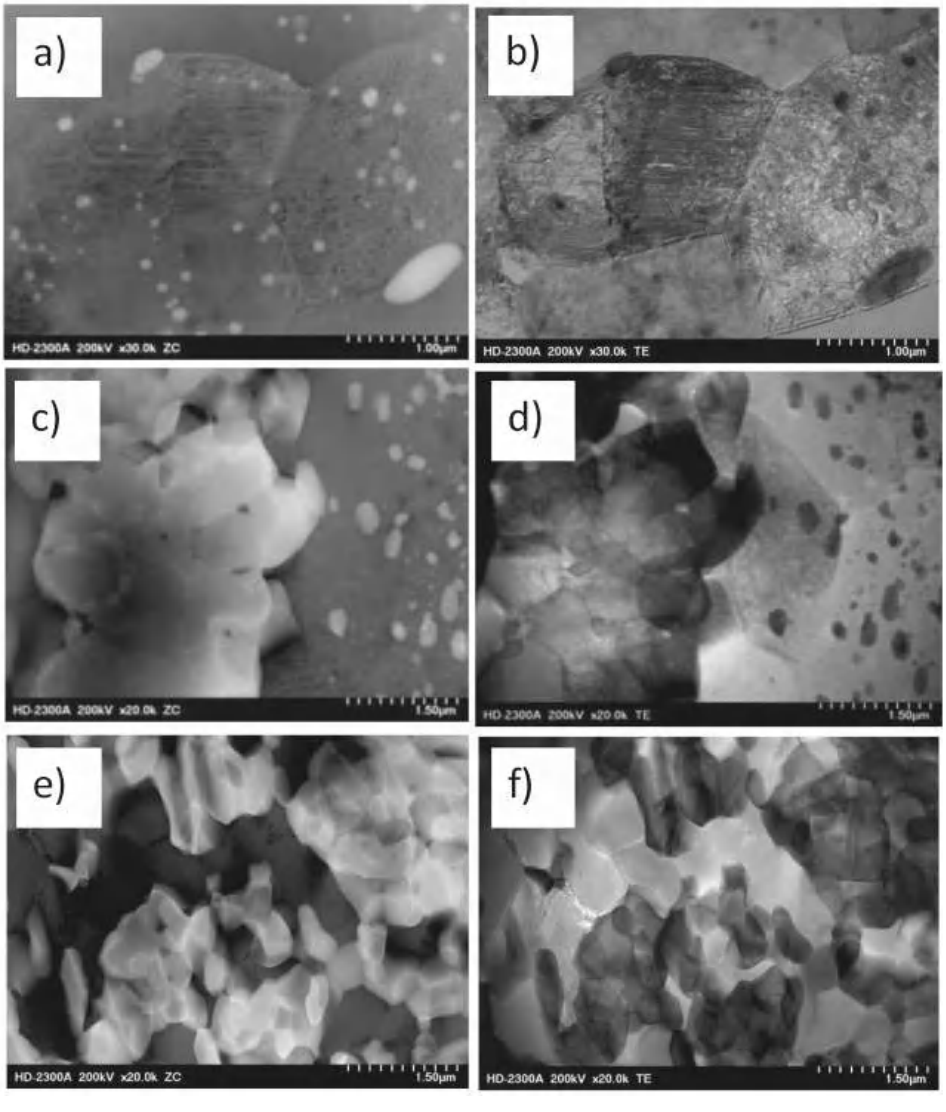

Figure 5. TEM images showing the characteristic microstructures of Al–Cu alloys after KoBo processing at λ = 98. The microstructures on the left side represent Z contrast (ZC) images, while the microstructures visible on the right side represent transmitted electron (TE) images. (**a**,**b**) Al_5Cu alloy, (**c**,**d**) $Al_{25}Cu$ alloy, (**e**,**f**) $Al_{33}Cu$ alloy.

In Al_5Cu alloys, small Al_2Cu particles acted as effective barriers of dislocation movement and were responsible for blocking of grain/subgrain boundaries (Figure 5a). The grains of α-Al matrix were visible as equiaxed structures with high dislocation density inside. The diffraction contrast of individual grains means that misorientation between grains was high (Figure 5b). In $Al_{25}Cu$ alloy, the role of small and very small particles of Al_2Cu phase was the same as in Al_5Cu alloy (Figure 5c,d). Observed massive microareas of Al_2Cu phase were refined with the characteristic effect connected with creation of grain/subgrain boundaries as a result of dislocation accumulation and their rearrangement (Figure 5d). Even through the microstructure of Al_2Cu phase was not completely fragmented (Figure 5c), there were observed microvoids pointing to the initiated process of grain refinement (Figure 5c). The microcracks were formed at the boundaries of new grains/grains or at the contact point of three grains. The observed phenomenon proved that first the fragmentation of the structure occurred, as the process of dislocation generation and rearrangement, and then the phase fragmentation process occurred. This process was especially visible when the TE and ZC images were combined, as shown in Figure 5c,d. The generation and rearrangement of dislocations proved the deformability of the intermetallic phase. The examples of generated voids shown in the Figure 5c,d may indicate the initiated process of grain boundary sliding. Temperature increase during KoBo deformation may enable this process. Similar phenomena of creating dislocation boundaries and then phase fragmentation through mutual separation of individual blocks and their mutual rotations were observed in the $Al_{33}Cu$ alloy (Figure 5e,f). In this case, the grain refinement process was facilitated by the lamellar structure of the eutectic alloy.

Mechanical properties extruded by KoBo samples are shown in Table 1.

Table 1. Measured mechanical parameters: yield strength (YS), ultimate tensile strength (UTS), and elongation to fracture (Ac) of deformed Al–Cu alloys with KoBo processing.

Alloys	Reduction Coefficient	UTS (MPa)	YS (MPa)	Ac (%)
Al_5Cu	λ = 30	208	75	46
	λ = 98	191	104	55
$Al_{25}Cu$	λ = 30	328	92	12
	λ = 98	280	126	13
$Al_{33}Cu$	λ = 30	446	438	9
	λ = 98	483	398	7

High fraction of α-Al phase in microstructure was characterized by high plasticity. For sample Al_5Cu, elongation to fracture (Ac) was over 45%, while for $Al_{33}Cu$ alloy (Ac), it was about 7%. Ultimate tensile strength (UTS) of Al_5Cu alloy after the KoBo extrusion reached 160 MPa. Increase of Cu content in alloys ($Al_{25}Cu$ and $Al_{33}Cu$ alloys) resulted in the increase of strength. $Al_{25}Cu$ alloys in terms of UTS were in the range of 280–330 MPa. For $Al_{33}Cu$ alloys, the UTS was in range of 450–480 MPa. Strengthening by the intermetallic particles in $Al_{25}Cu$ alloy and $Al_{33}Cu$ alloy was accompanied by a drastic drop of ductility. For $Al_{25}Cu$ alloy, the elongation to fracture (Ac) was about 12%; this value decreased to 7% for $Al_{33}Cu$ alloys. Interesting tensile test results were obtained for the alloys deformed with increasing value of deformation. An increase in the λ value caused a slight decrease in UTS with simultaneous increase in elongation. This indicated a favorable phenomenon related to an increase in both strength and plastic properties. The observed high strength properties were a combination of various strengthening mechanisms, i.e., precipitation strengthening, deformation strengthening by generating high dislocation density, and strengthening by grain boundaries (refinement process). Improvement of plastic properties may be attributable to the more homogeneous microstructure with ultra-fine-grained equiaxed grains with high misorientation angles.

The superplastic tensile stress–strain curves at 300 °C and 400 °C are shown in Figure 4. Additionally, the results of mechanical measurement are displayed in Table 2.

Table 2. Measured mechanical parameters: stress peak (σ_{max}), elongation to failure (ε_{max}) of deformed Al–Cu alloys.

Alloys	Mechanical Properties	300 °C		400 °C	
		λ = 30	λ = 98	λ = 30	λ = 98
Al_5Cu	σ_{max} (MPa)	46	15	18	14
	ε_{max} (%)	29	60	57	63
$Al_{25}Cu$	σ_{max} (MPa)	46	30	13	14
	ε_{max} (%)	192	114	787	827
$Al_{33}Cu$	σ_{max} (MPa)	49	21	11	10
	ε_{max} (%)	140	345	987	1085

From Figures 6–8, we see that the flow stress and elongation depended on the deformation temperature and value of λ. As shown in Figure 6, the flow stress curves of Al_5Cu alloy for 300 °C and λ = 30 were raised sharply to the peak values of about 46MPa and then decreased quite rapidly, with a strain failure of about 30%. As the sample was deformed at λ = 98, the value of peak stress decreased and was about 15MPa. It should be noted that the deformation value was also responsible for the strain increase. The elongation was about 60%. For samples deformed at 400 °C with λ = 30 and λ = 98, the value of peak stress was in range from 14 MPa to 18 MPa. Simultaneously, the samples reached failure in the range from −57% to 63%. It should be noted that samples deformed at 300 °C with λ = 98 were characterized by a similar level of elongation and stress as samples deformed at 400 °C. It was found that the Al_5Cu alloys had maximal elongation at a temperature of 400 °C. The typical characteristic of flow curves (approaching a steady state) indicated the occurrence of softening effect, which began to be dominated by the acceleration of dynamic recovery during deformation.

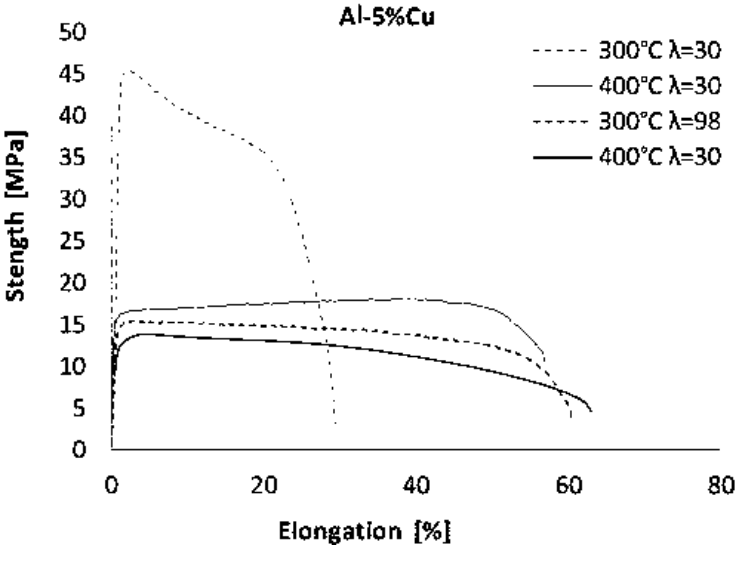

Figure 6. The superplastic tensile stress–strain curves for Al_5Cu alloy.

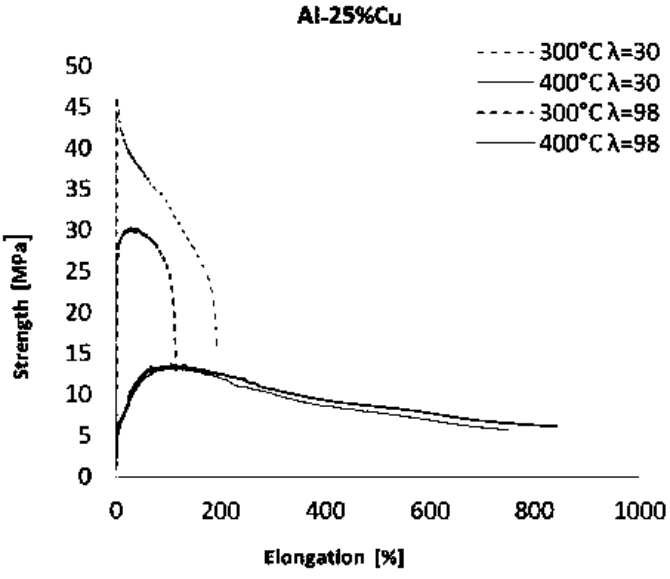

Figure 7. The superplastic tensile stress–strain curves for $Al_{25}Cu$ alloy.

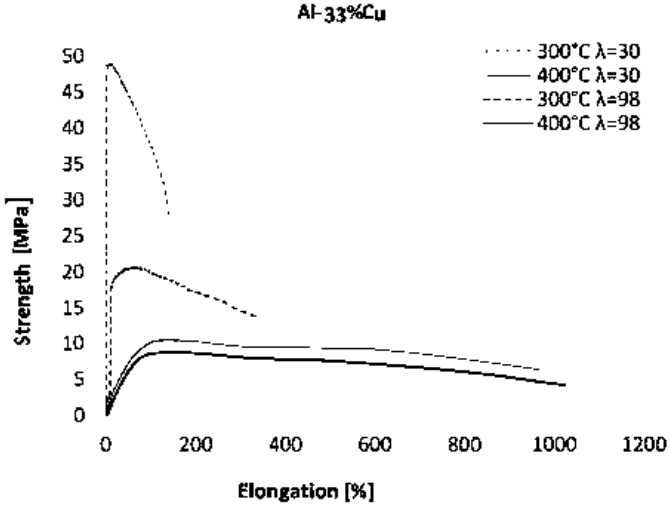

Figure 8. The superplastic tensile stress–strain curves for $Al_{33}Cu$ alloy.

The influence of the deformation temperature on the superplasticity effect in the case of the $Al_{25}Cu$ alloy was significant (Figure 7). The superplastic properties of the alloy were evidently demonstrated at the higher deformation temperature. For samples deformed at 400 °C with λ = 30 and λ = 98, the flow peaks were comparable and amounted to approximately 13–14 MPa. Simultaneously, the samples reached failure in the range from 787% to 827%. Generally, the increase in the deformation value in the case of samples deformed at the temperature of 400 °C led only to an increase in elongation. As the samples were deformed at 300 °C, the increase of λ value influence on flow peaks decreased and increased in elongation. However, in this temperature, the alloys did not show evident superplastic properties.

Similar deformation characteristics as those of the previously described $Al_{25}Cu$ alloy were observed for the $Al_{33}Cu$ alloy (Figure 8). In this case, an increase in the elongation (about 987% and 1085% for the deformation of $\lambda = 30$ and $\lambda = 98$, respectively) were noted during deformation at a temperature of 400 °C, with a lowering value of the stress of approximately 10–11 MPa. The samples of $Al_{33}Cu$ alloy deformed at 300 °C maintained quite a high level of peak stress equal to 49 MPa and 21 MPa for $\lambda = 30$ and $\lambda = 98$, respectively. The elongation value did not exceed 350% for samples deformed with $\lambda = 98$. On the basis of performed experiments, we must note that the experimental alloys had maximal superplasticity at a temperature of 400 °C. The minimum value of the stress peak and maximum elongation to failure were obtained for $Al_{33}Cu$ alloy with the equiaxed ultrafine-scale structure.

The microstructures presented in Figure 9 show selected examples of high-temperature deformation of alloys at the temperature of 400 °C for $\lambda = 98$. First of all, the microstructural changes visible near the fracture site were taken into account in order to visualize the material fracture mechanism. From Figure 9a–c, it was visible that many of the large- and intermediate-sized particles cracked or detached from the matrix because of their random orientation. Since there were relatively few precipitates in the alloys of high and medium size, the nature of the cracking depended mainly on the matrix, which was plastic and well deformable. Discontinuities visible in interfaces as a result of the mismatch of the crystallographic lattices were much more common than in the process of material decohesion as a result of intermetallic phase cracking. Very small precipitates presented in the matrix (Figure 9a,c) did not support the material cracking process. Small particles rarely fractured, hence reducing crack formation. The fraction of precipitation did not change with deformation increase. The important role of ultra-fine precipitates of Al_2Cu phase reduced the grain size with deformation. This was important in the process of superplasticity and may have affected increase in elongation.

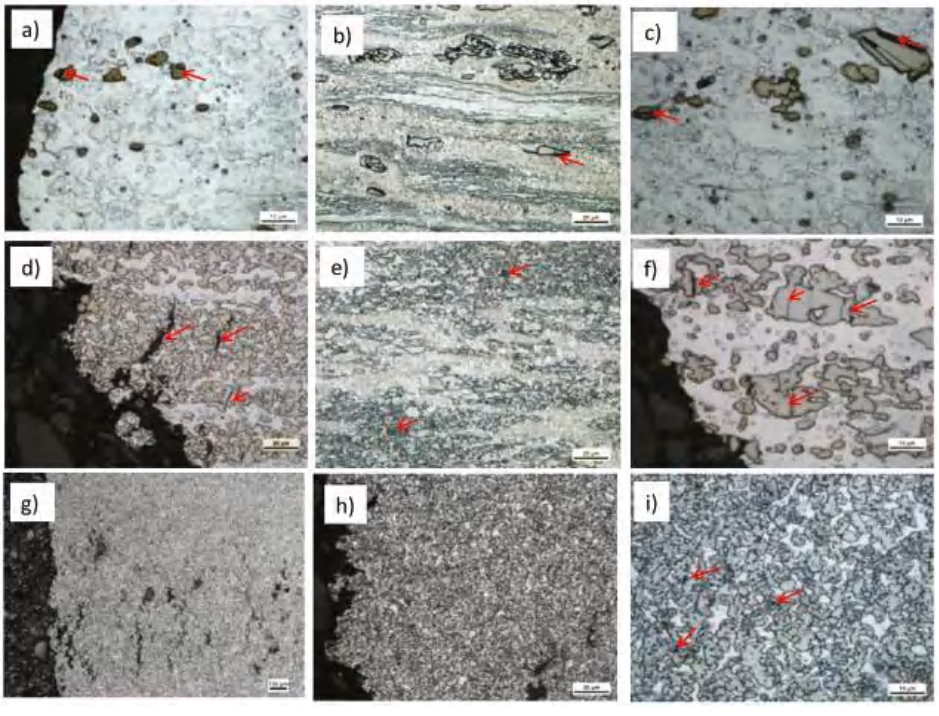

Figure 9. Microstructure of Al–Cu alloys after tensile test at 400 °C: (**a–c**) Al_5Cu alloy, (**d–f**) $Al_{25}Cu$ alloy, (**g–i**) $Al_{33}Cu$ alloy.

In the $Al_{25}Cu$ samples, cracks were generated in Al_2Cu phase and spread in this phase in the direction perpendicular to the tensile direction, as shown in Figure 9d. Moreover, the formation of large discontinuities was favored by numerous cracks present in the massive, non-separated areas of intermetallic phases (Figure 9f). Very often, the span of the crack was determined by the size of the phase. During the next deformation, the cracks merged and a distinct fracture was formed, which was not stopped by the plastic phase. The crack propagated through one intermetallic particle into another, likely due to their proximity (Figure 9e). The fracture was stopped only in the area of the plastic matrix (Figure 9d).

In the case of the $Al_{33}Cu$ alloy, where the distances between the individual phases were much smaller, the developed fracture was retained or absorbed by the α-Al phase. In this case, many cracks were formed (Figure 9g–i). The course of cracks was not as pronounced as in the case of the $Al_{25}Cu$ alloy, which was characterized by a heterogeneous structure with an irregular distribution of α-Al and Al_2Cu phases. The bond between the particle and matrix appeared to be exceptionally strong. Meanwhile, the fine grain structure often increases a material's ability to tolerate plastic deformation without fracture.

According to the literature [3] and performed mechanical investigations of superplasticity properties, it should be noted that the effect of deformation temperature on superplasticity is closely related to the microstructure. Due to the rise in plastic deformation temperature, the atomic energy of the alloy is increased, and the activity of atoms is higher [1,2]. Therefore, the binding force of the atoms decreases, resulting in a significant reduction of the dislocation barrier, and thereby reducing the flow stress. On the basis of the obtained data, for microstructural analysis using STEM, we chose samples deformed at the temperatures of 300 °C and 400 °C with $\lambda = 98$. This selection was made on the basis of the obtained superplasticity characteristics presented in Figures 6–8. Moreover, we considered the fact that a high value of deformation results in a much greater homogeneity of microstructure and in grain refinement [19–21]. Therefore, one should expect an increase in superplasticity.

STEM observations (Figure 10) showed the presence of clearly visible α-Al phase grains with high angle boundaries as a result of deformation (Figure 10a,b). In the new grains, a great number of dislocations occurred as a result of deformation at 300 °C. High density of dislocations inside the grains was the result of the presence of a large number of Al_2Cu phase precipitates. For samples deformed at 400 °C, the dislocation amount was much less (Figure 11a,b). Equiaxial and elongated grains (in the tensile direction) with different sizes were also observed. Figure 10a evidently demonstrates that dislocations were formed in grains during deformation at 300 °C and eventually transforming into subgrains/grains (Figure 10b) with increased temperature. Therefore, the strengthening stage was found to be related to the continuous accumulation of defects and formation and growth of the grains. From these findings, we considered the contribution of intragranular deformation. The structural changes reflect the character of the curves shown in Figure 6. The high density of dislocation in the Al_5Cu alloy in particular resulted in a greater value of stress peak.

In the $Al_{25}Cu$ alloy deformed at the temperature of 300 °C, the dislocations were presented both in the massive phase of Al_2Cu and α-Al phase (Figure 10c,d). Dislocations present in the Al_2Cu phase as a result of deformation created numerous dislocation tangles without signs in creation of low- or high-angle boundaries, as were visible for the α-Al phase. This phenomenon indicates differences in the deformation process of both phases. The existence of subgrains and dislocation tangles contributed in a minor way to slide and rotation of Al_2Cu phase. STEM observations performed for $Al_{25}Cu$ alloy deformed at 400 °C showed the presence of well-defined grains/subgrains inside massive Al_2Cu phase. The microvoids observed in Al_2Cu phase accelerated the process of grain boundary slipping (Figure 11c). Dislocations accumulated in α-Al phase as a result of deformation generated the new boundaries and multiplication of new grains as a process of continuous recovery (Figure 11d). A probable mechanism of superplasticity is the high angle grain boundary sliding [1,22]. This situation is evidently characteristic for $Al_{33}Cu$ alloys. Although the STEM microstructure of the specimens after deformation at 300 °C in some areas was visible as lamellar structure with dislocation density inside

Al_2Cu phase and α-Al phase (Figure 10e,f), we nevertheless found visible examples of equiaxial phases that were fragmented. The evident example of samples with occurrence of grain boundary sliding is shown in Figure 11e, where grains gradually twisted and moved along the tensile direction. When the stress reached its critical value, the alloy was fractured. As presented in Figure 11e, grain boundary sliding occurred more readily for superfine grains with high grain boundaries, an example of which was the eutectic $Al_{33}Cu$ alloy. Maximal elongation shown in 400 °C tensile process was the result of the high mobility of grain boundaries (Figure 11e).

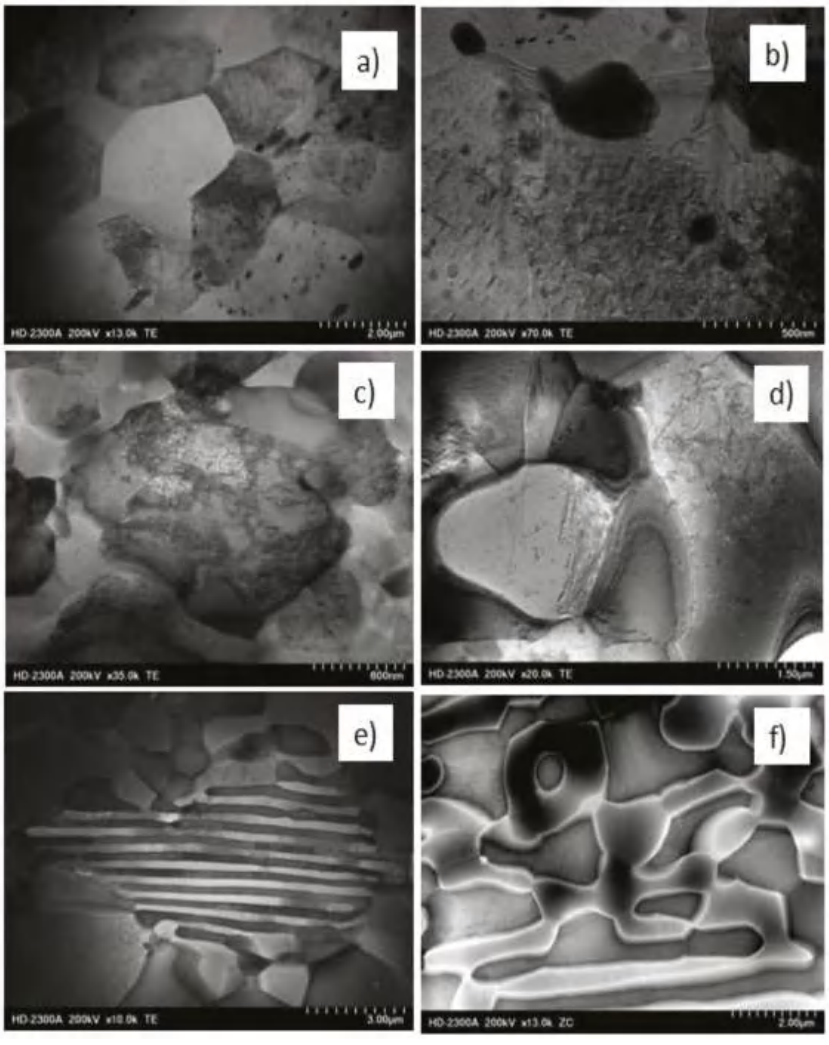

Figure 10. Scanning transmission electron microscope (STEM) images showing the characteristic microstructures of Al–Cu alloys after tensile test at 400 °C. The microstructures on the left side represent ZC images, while the microstructures visible on the right side represent TE images. (**a**,**b**) Al_5Cu alloy, (**c**,**d**) $Al_{25}Cu$ alloy, (**e**,**f**) $Al_{33}Cu$ alloy.

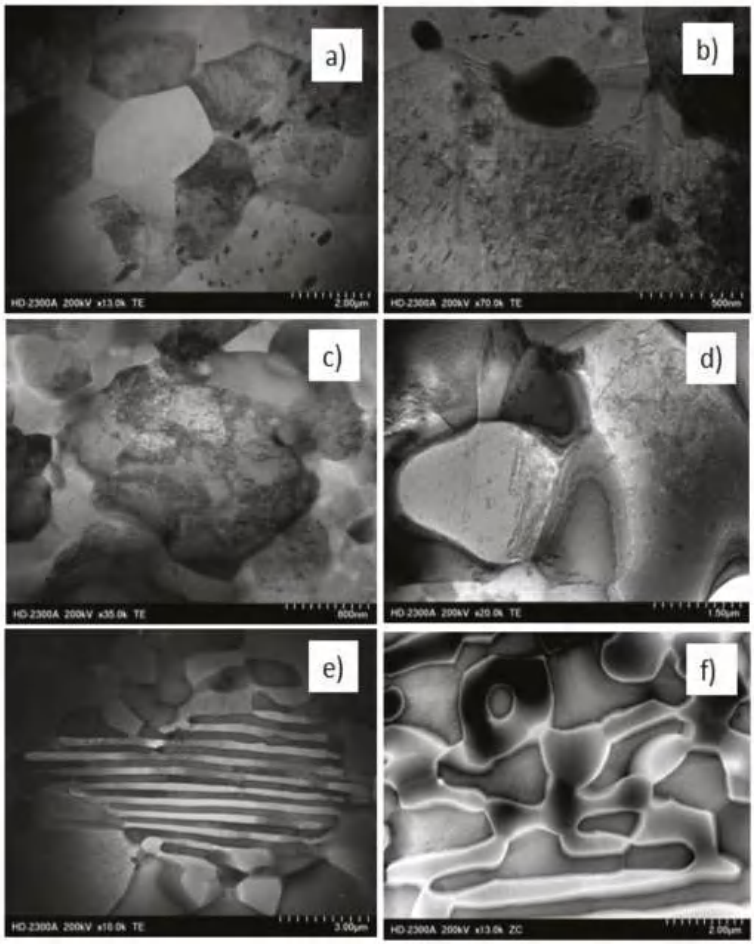

Figure 11. STEM images showing the characteristic microstructures of Al–Cu alloys after tensile test at 400 °C. The microstructures on the left side represent ZC images, while the microstructures visible on the right side represent TE images. (**a**,**b**) Al_5Cu alloy, (**c**,**d**) $Al_{25}Cu$ alloy, (**e**,**f**) $Al_{33}Cu$ alloy.

There is only limited information in the literature in terms of the theme connected with understanding of the deformation process of the two-phase microstructure of Al–Cu alloy with a high volume fraction of secondary phase on mechanical properties. For example, in a study by [23], Equal Channel Angular Pressing (ECAP) was successfully applied on a lamellae eutectic alloy of $Al_{33}Cu$ at 400 °C, up to an equivalent strain of ≈8. After deformation, a homogeneous fine equiaxed duplex microstructure with an average size of 1.1 mm was obtained. Obtained by using KoBo deformation, microstructures of AlCu alloys are connected with ultrafine near-equiaxed grains of α-Al and Al_2Cu phase. The obtained grain size and somewhat homogeneous microstructure are capable of achieving superplastic properties. The refinement in the microstructure means that the fraction of grain boundaries, which are responsible for superplastic properties, is increasing, because in the area of grain boundary, the main processes related to superplastic flow take place. After high temperature (400 °C) deformation with $\lambda = 98$, the microstructure remained more equiaxed and the microstructure was still fine grained; for this reason, the elongation was higher. The thermally stable and equiaxed grains provided evidence of GBS occurrence. Detailed investigations using scanning transmission electron

microscopy showed that grains of the α-Al phase had a higher density of dislocations than Al_2Cu phase during deformation at 400 °C (Figure 11d,f). This situation was connected with the fact that for Al_2Cu phase, the processes of recovery can proceed easier than for the α-Al phase. The obtained results are in accordance with the literature [24,25]. During deformation in Al_2Cu phase, we observed a mechanism connected with non-conservative motion of glide dislocation. This mechanism provided rapid diffusion channels during plastic deformation and indicated structural instability. The high population of vacancies observed in Al_2Cu alloys facilitated the diffusion of the alloying elements; thus, it may have accelerated de-alloying of Al from Al_2Cu. In addition, it is conjectured that the easy climb of dislocations driven by dislocation interaction will reduce the glide ability of a dislocation, limiting plastic shear under mechanical loading [25].

On the basis of the obtained results, we found that the intermetallic phase can inhibit the GBS. The nanoscale particles could effectively make the microstructure stable and prevent grain growth so that superior plasticity could be achieved. It is also worth noting that the nanoscale/ultrafine precipitates were of high melting point so as to inhibit the grain growth effectively, with this situation being especially typical for Al_5Cu and $Al_{25}Cu$ alloys.

These mechanical characteristics demonstrated that Al–Cu alloys with high fraction of intermetallic phase are characterized by the typical fine-grained superplasticity.

4. Conclusions

1. The KoBo method allowed grain refinement of the AlCu alloys to the micrometric level.
2. Recipient heating and additionally severe plastic deformations contributed to temperature increase; as a result, the processes related to the formation of equiaxial grains with a large fraction of high-angle boundaries were observed. This microstructure is helpful in achieving superplastic properties.
3. The applied value of deformation (λ) played a significant role in the deformation of KoBo. If the samples were deformed with λ = 98, then the grains were refined and the structure was more homogeneous. Deformation increase resulted in an increase of plastic properties with a decrease in strength properties.
4. The samples deformed at 400 °C showed superplastic properties. This problem mainly concerned the $Al_{25}Cu$ and $Al_{33}Cu$ alloys. Both the phase composition (a large fraction of the intermetallic phase and a large fraction of high angle boundaries) guaranteed superplastic properties of the analyzed alloys.
5. The eutectic $Al_{33}Cu$ alloy, due to its specific structure and considerable grain refinement, had the highest elongation during tensile test at high temperature. The $Al_{25}Cu$ alloy did not provide comparable value in an elongation to the $Al_{33}Cu$ alloy due to the high heterogeneity in the microstructure.
6. The grain boundary sliding mechanism was already initiated during KoBo deformation. During KoBo deformation, microcracks formed, which were observed in the Al_2Cu phase and in interfaces areas. This microstructural elements in the conditions of superplastic deformation facilitated deformation using the GBS mechanism.

Author Contributions: Conceptualization, K.R.; methodology, K.R., D.K., T.M.; software, K.R., D.K., T.M.; validation, K.R., D.K., T.M.; formal analysis, K.R.; investigation, K.R., D.K., T.M.; resources, K.R., D.K., T.M.; data curation, K.R.; writing—original draft preparation, K.R.; writing—review and editing, K.R.; visualization, K.R.; project administration, K.R.; funding acquisition, K.R. All authors have read and agreed to the published version of the manuscript.

Funding: This research was funded by Ministry of Science and Higher Education within the statutory research, grant number 11/030/BK_20/0285.

Conflicts of Interest: The authors declare no conflict of interest.

References

1. Islamgaliev, R.K.; Yunusova, N.F.; Nikitina, M.A.; Nesterov, K.M. The effect of alloying elements on superplasticity in an ultrafine-grained aluminum alloy. *Rev. Adv. Mater. Sci.* **2010**, *25*, 241–248.
2. Bhatta, L.; Pesin, A.; Zhilyaev, A.P.; Tandon, P.; Kong, C.; Yu, H. Recent development of superplasticity in aluminum alloys: A review. *Metals* **2020**, *10*, 77. [CrossRef]
3. Wang, X.; Li, Q.; Wu, R.; Zhang, X.; Ma, L. A review on superplastic formation behaviour of Al alloys. *Adv. Mater. Sci. Eng.* **2018**, *2018*, 7606140. [CrossRef]
4. Alabort, E.; Kontis, P.; Barba, D.; Dragnevski, K.; Reed, R.C. On the mechanism of superplasticity in Ti-6Al-4V. *Acta Mater.* **2016**, *105*, 449–463. [CrossRef]
5. Moguchevaa, A.; Yuzbekovab, D.; Kaibyshev, R. Superplasticity in a 5024 aluminium alloy subjected to ECAP and subsequent cold rolling. *Mater. Sci. Forum* **2016**, *838*, 428–433. [CrossRef]
6. Higashi, K.; Ohnishi, T.; Nakatani, Y. Superplastic behavior of commercial aluminum bronze. *Scr. Metall.* **1985**, *19*, 821–823. [CrossRef]
7. Wadsworth, J.; Palmer, I.G.; Crooks, D.D. Superplasticity in Al-Li based alloys. *Scr. Metall.* **1983**, *17*, 347–352. [CrossRef]
8. Horiuchi, R.; El-Sebai, A.B.; Otsuka, M. Superplasticity in the ternary eutectic alloys, Al-33% Cu-7% Mg and Al-25% Cu-11% Mg. *Scr. Metall.* **1973**, *7*, 1101–1104. [CrossRef]
9. Valle, J.A.D.; Ruano, O.A. Influence of grain size fluctuations on ductility of superplastic magnesium alloys processed by severe plastic deformation. *Mater. Sci. Technol.* **2008**, *24*, 1238–1244. [CrossRef]
10. Ma, A.; Saito, N.; Takagi, M.; Nishida, Y.; Iwata, H.; Suzuki, K.; Shigematsu, I.; Watazu, A. Effect of severe plastic deformation on tensile properties of a cast Al-11 mass % Si alloy. *Mater. Sci. Eng. A* **2005**, *395*, 70–76. [CrossRef]
11. Zhuo, L.; Wang, H.; Zhang, T. Hierarchical ultrafine-grained network mediated high strength and large plasticity in an Al-based alloy. *Mater. Lett.* **2014**, *24*, 28–31. [CrossRef]
12. Heim, F.M.; Zhang, Y.; Li, X. Uniting strength and toughness of Al matrix composites with coordinated Al_3Ni and Al_3Ti reinforcements. *Adv. Eng. Mater.* **2017**, *20*, 1700605. [CrossRef]
13. Zhang, B.; Zhang, L.; Wang, Z.; Gao, A. Achievement of high strength and ductility in Al-Si-Cu-Mg alloys by intermediate phase optimization in as-cast heat treatment conditions. *Materials* **2020**, *13*, 647. [CrossRef] [PubMed]
14. Haghshenas, M.; Jamali, J. Assessment of circumferential crack in hypereutectic Al-Si clutch housings. *Case Stud. Reengineering Fail. Anal.* **2017**, *8*, 11–20. [CrossRef]
15. Valiev, R.Z.; Kuznetsov, R.I.; Kaibyshev, O.A.; Musalimov, R.S.; Tsenev, N.K. Low-temperature superplasticity of metallic materials. *Sov. Phys. Dokl.* **1988**, *33*, 626.
16. He, H.; Yi, Y.; Huang, S.; Zhang, Y. Effects of deformation temperature on second-phase particles and mechanical properties of 2219 Al-Cu alloy. *Mater. Sci. Eng. A* **2018**, *712*, 414–423. [CrossRef]
17. Korbel, A.; Bochniak, W. Refinement and control of the structure elements by plastic deformation. *Scr. Mater.* **2004**, *51*, 755–759. [CrossRef]
18. Korbel, A.; Bochniak, W. Liquid- like behaviour of solid metals. *Manuf. Lett.* **2017**, *11*, 5–7. [CrossRef]
19. Kawasaki, M.; Lee, H.J.; Jang, J.; Langdon, T.G. Strengthening of materials through severe plastic deformation. *Rev. Adv. Mater. Sci.* **2017**, *48*, 13–24.
20. Orlov, D.; Todaka, Y.; Umemoto, M.; Beygelzimer, Y.; Horita, Z.; Tsuji, N. Plastic flow and grain refinement under simple shear-based severe plastic deformation processing. *Mater. Sci. Forum* **2009**, *604–605*, 171–179. [CrossRef]
21. Cao, Y.; Ni, S.; Liao, X.; Song, M.; Zhu, Y. Structural evolutions of metallic materials processed by severe plastic deformation. *Mater. Sci. Eng. R* **2018**, *133*, 1–59. [CrossRef]
22. Noda, M.; Hirohashi, M.; Funami, K. Low temperature superplasticity and its deformation mechanism in grain refinement of Al-Mg alloy by multi-axial alternative forging. *Mater. Trans.* **2003**, *11*, 2288–2297. [CrossRef]
23. Vang, J.; Kang, S.; Kim, H.; Horita, Z. Lamellae deformation and structural evolution in an Al-33%Cu eutectic alloy during equal-channel angular pressing. *J. Mater. Sci.* **2002**, *37*, 5223–5227.

24. Zhou, Q.; Wang, J.; Misra, A.; Huang, P.; Wang, F.; Xu, K. Atomistic study of fundamental character and motion of dislocations in intermetallic Al2Cu. *Int. J. Plast.* **2016**, *87*, 100–113. [CrossRef]
25. Zhou, Q.; Wang, J.; Misra, A.; Huang, P.; Wang, F.; Xu, K. Dislocations interaction induced structural instability in intermetallic Al_2Cu. *Comput. Mater.* **2017**, *24*, 1–7. [CrossRef]

materials

MDPI

Article

Investigation of the Influence of Open-Die Forging Parameters on the Flow Kinetics of AZ91 Magnesium Alloy

Grzegorz Banaszek [1], Teresa Bajor [2,*], Anna Kawałek [2] and Tomasz Garstka [1]

[1] Department of Materials Engineering, Faculty of Production Engineering and Materials Technology, Czestochowa University of Technology, 42-201 Czestochowa, Poland; grzegorz.banaszek@pcz.pl (G.B.); tomasz.garstka@pcz.pl (T.G.)
[2] Departmet of Production Management, Faculty of Production Engineering and Materials Technology, Czestochowa University of Technology, 42-201 Czestochowa, Poland; anna.kawalek@pcz.pl
* Correspondence: teresa.bajor@pcz.pl

Abstract: This paper presents the results of numerical tests of the process of forging magnesium alloy ingots (AZ91) on a hydraulic press with the use of flat and proprietary shaped anvils. The analysis of the hydrostatic pressure distribution and the deformation intensity was carried out. It is one of the elements used for determining the assumptions for the technology of forging to obtain a semi-finished product from the AZ91 alloy with good strength properties. The aim of the research was to reduce the number of forging passes, which will shorten the operation time and reduce the product manufacturing costs. Numerical tests of the AZ91 magnesium alloy were carried out using commercial Forge®NxT software.

Keywords: magnesium alloy AZ91; physical modelling; open die forging; flat anvils; shaped anvils

Citation: Banaszek, G.; Bajor, T.; Kawałek, A.; Garstka, T. Investigation of the Influence of Open-Die Forging Parameters on the Flow Kinetics of AZ91 Magnesium Alloy. *Materials* **2021**, *14*, 4010. https://doi.org/10.3390/ma14144010

Academic Editor: Ivo Schindler

Received: 23 June 2021
Accepted: 13 July 2021
Published: 17 July 2021

1. Introduction

The search for lightweight construction materials with favourable strength parameters, which has continued over several decades, has led scientists toward magnesium alloys [1–3]. The implemented environmental protection policy, the main goal of which is to reduce the weight of cars and fuel consumption, and to reduce the impact of greenhouse gases emitted by cars, is not without significance in this matter [4–7]. Magnesium alloys, being the lightest construction materials and showing good heat dissipation and vibration damping, are found to have more and more applications in the automotive industry. They are used to produce elements for operation at ambient temperatures, such as brackets, covers, or casings of modern cars [8–11]. The vast majority of products made of magnesium alloys are obtained mainly in extrusion and stamping processes and, less frequently, in rolling and forging processes.

However, forged products made of magnesium alloys deserve special attention due to their homogeneous microstructure and improved mechanical properties compared to elements made of cast alloys. Due to their properties, the products obtained in the forging process are also attractive to such industries as: shipbuilding, aviation, space, and electronics [12–14]. The unquestionable advantage of using open-die forging processes to deform magnesium alloys is the possibility of freely shaping the metal flow kinematics, including by controlling the shape and dimensional parameters of anvil working surfaces and the main parameters of extending operations, which is often impossible, e.g., in extrusion processes. It is also possible to forge magnesium alloys in differently-shaped anvils. The use of shaped anvils allows for the introduction of the intended nature of stresses and strains in the local areas of the forgings. Additionally, the advantage of this forging method is the reduction of the number of forging passes, which reduces the production costs of the final products [15].

The implementation of research in the field of designing forging technology requires a comprehensive approach to the research problem. A high variability of shaping parameters

(such as temperature and sequence of operations) and technological procedures (such as material rotation and deformation by means of anvils during the forging elongation operation, values of the set reductions, relative feed values, deformation speed, and shape and dimensional parameters of the anvil working surfaces) makes it extremely difficult to obtain forgings from high-quality magnesium alloys with a homogeneous microstructure throughout the entire volume. Due to the hexagonal, compact, crystallographic structure, magnesium alloys have limited plasticity and poor deformability at ambient temperature. They are also characterised by a high anisotropy of mechanical and plastic properties arising during the given plastic deformation. Due to these factors, there is an increase in demand for a technology for the production of magnesium alloys with better strength properties. Proper implementation of the open-die forging process in flat and shaped anvils of selected magnesium alloys requires not only special forging equipment but, most of all, necessary specialist knowledge in this field. Undertaking the research into the theoretical analysis of plastic forming of the AZ91 magnesium alloy is one of the stages of designing the technology of manufacturing finished products with good mechanical properties [15–19].

2. Test Objective and Scope

The aim of the paper was to determine the distributions of hydrostatic pressure and strain intensity in AZ91 magnesium alloy rods, shaped by open forging in flat and shaped anvils, based on model tests of these technological processes. The use of shaped anvils will reduce the number of forging passes and, at the same time, reduce the cost of manufacturing the product.

Modelling of the forging process was performed using the Forge®NxT software commercial software (version 2.0) Transvalor S.A., Biot, Sophia Antipolis cedex, France based on FEM, which allows for the determination of changes in the value of hydrostatic pressure and strain intensity in the plastically processed metal at any stage of the forging elongation operation. Based on the analysis of the results of numerical tests, assumptions for the technology of producing magnesium alloy bars by the open-die forging method in flat and shaped anvils will be developed.

The obtained test results should contribute to the improvement of the mechanical properties of the finished products through the appropriate selection of technological parameters of the open-die forging process in flat and shaped anvils.

The ranges of deformation, deformation speed, and temperature changes during the theoretical research were assumed on the basis of the characteristics of forging machines such as: PHM 250 T Żywiec, Poland or PWH-250R, Poland used in real forging processes and on the basis of literature data [15,20].

3. Materials and Methods

The material chosen for the tests was magnesium alloy AZ91 with chemical compositions as given in Table 1 [15].

Table 1. Chemical composition of the investigated alloy (%).

Alloy	Zn	Al	Si	Cu	Mn	Fe	Ni	Mg
AZ91	0.59	8.98	0.05	0.006	0.23	0.013	0.003	R

4. Determination of Rheological Properties of the Selected Magnesium Alloy

Knowledge of the characteristics describing the technological properties of the material is the basis for the correct conduct of the theoretical research and the design of new technological processes (or modification of existing ones). For each technological process of plastic working, a set of data that accurately describes the material's susceptibility to plastic forming should be defined [15].

For plastic working processes, the basic feature characterising the material's susceptibility to plastic forming is the flow stress $\sigma_{\mathbf{p}}$ and limit strain ε_g.

The flow stress σ_p, i.e., the stress necessary to initiate and continue plastic flow of metal under uniaxial stress conditions, is a function of strain (ε), strain rate ($\dot{\varepsilon}$), temperature (T) and history of strain.

During hot plastic working, processes resulting from the plastic deformation mechanism, material hardening, and thermally activated processes, as well as time-dependent phenomena leading to material weakening, occur in the material structure. Thus, it is relatively difficult to determine the technological plasticity characteristics of the material for the conditions of hot plastic working [15].

The values of flow stress σ_p in computer programmes intended for modelling plastic working processes by the finite element method are determined on the basis of the assumed flow stress function. The flow stress is described by the dependence in the form of $\sigma_p = (\varepsilon, \dot{\varepsilon}, T)$. Many functions are used for the mathematical description of changes in value σ_p depending on the strain ε, temperature T, and strain rate $\dot{\varepsilon}$. One of them is the Hansel–Spittel Equation (1) [21]. This dependence is frequently used to derive value σ_p in computer programmes for numerical modelling of plastic working processes [22]:

$$\sigma_p = Ae^{m_1 T} \varepsilon^{m_2} \dot{\varepsilon}^{m_3} \varepsilon^{\frac{m_4}{\varepsilon}} (1+\varepsilon)^{m_5 T} \varepsilon^{m_7 T} \dot{\varepsilon}^{m_8 T} T^{m_9} \quad (1)$$

where: $\sigma_{\mathbf{p}}$ is the flow stress, ε is the true strain, $\dot{\varepsilon}$ is the strain rate, T is the temperature, m_1–m_9 are coefficients characterising magnesium alloys.

In this paper, the rheological properties of the AZ91 magnesium alloy were determined on the basis of compression tests performed with a Gleeble 3800 metallurgical process simulator [22]. The Gleeble 3800 simulator makes it possible to carry out tests for a wide range of temperatures, corresponding to the actual conditions occurring in the analysed technological process [23]. Tests are carried out in a vacuum chamber at a constant temperature of the deformed sample. For plastometric tests, cylindrical samples with a diameter of 10 mm and a length of 12 mm are used (Figure 1a). The uniaxial compression test involves deformation of cylindrical samples between two well-lubricated planes. Given the ideal conditions, the compression of the samples should be isothermal. The area of interaction between the planes and the samples should have a zero value of the friction coefficient. Moreover, when the sample is compressed, no deformation consisting in losing its cylindrical shape should occur. Taking these conditions into account and assuming the invariability of the metal volume during the compression test, the determined dependencies of the actual stress on the actual deformation should be very similar to the conditions occurring in metal shaping in industrial processes.

The advantage of the uniaxial compression test at elevated temperature is that the data concerning the actual stress in relation to the actual deformation can be obtained for a much wider range of strains, compared to those tested, for example, in a tensile test.

The plastometric tests were conducted with the following parameters:

- Sample temperature: 200, 300, 400 °C,
- Strain rate: 0.1, 1, 10 s^{-1},
- True strain: max. 0.8.

The samples were heated at a constant rate of 5 °C/s, up to a preset temperature, held at this temperature for 20 s and then compressed [15]. The diagram for conducted tests is shown in Figure 1b.

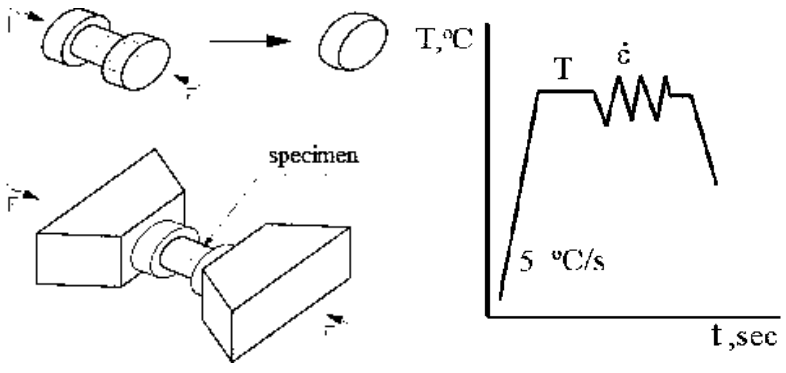

(**a**) (**b**)

Figure 1. Geometry and dimension of load (**a**); and thermal cycle of physical simulation (**b**) [15].

The dependencies between stress and actual deformation (Figure 2a,c) for the AZ91 magnesium alloy was developed on the basis of plastometric tests. The obtained test results were approximated in order to determine the coefficients of Equation (1) (Table 2).

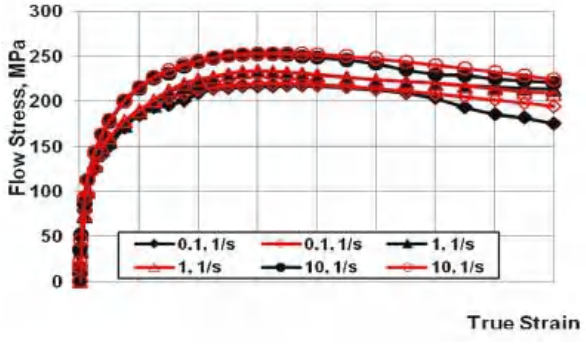

(**a**)

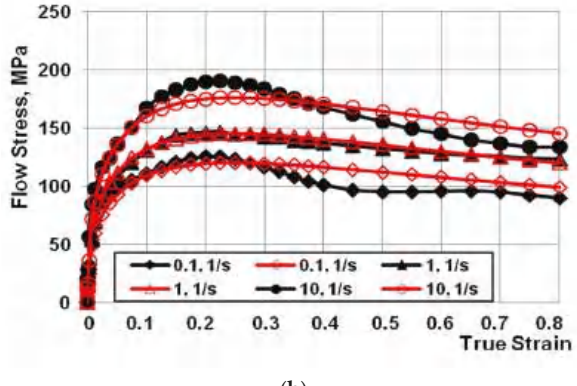

(**b**)

Figure 2. *Cont.*

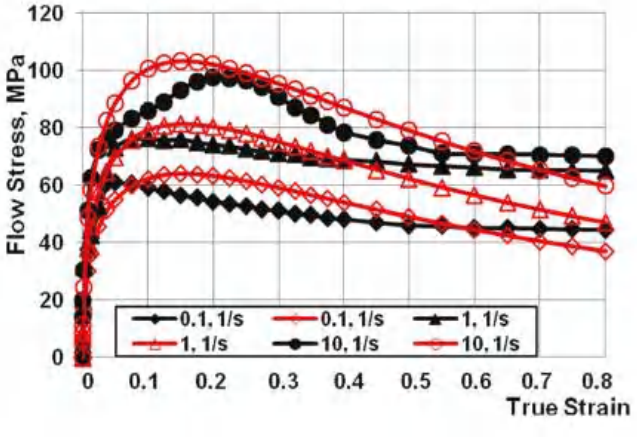

(**c**)

Figure 2. Work-hardening curves for the strain rate range of (0.1 s^{-1}–10.0 s^{-1}) at a temperature of: (**a**) 200, (**b**) 300, and (**c**) 400 °C. (Black indicates the experimental curves; red indicates the approximated curves) [15].

Table 2. Parameter values obtained from the approximation of Equation (1).

	A	m1	m2	m3	m4	m5	m7	m8	m9
AZ91	5985.99	−0.0116	0.37027	0.20062	-1.948×10^{-5}	−0.008	0.5807	0.00021	2.54972

Based on the data in Figure 2, it can be observed that, after reaching the critical deformation, the value of yield stress decreased with the increase of the actual deformation value, for the entire tested range of changes in temperature, deformation, and deformation rate. The decrease in the value of yield stress after reaching the maximum value is caused by the ongoing processes of dynamic healing. Dynamic processes of microstructure reconstruction are more intense at temperatures above 300 °C [15].

It is assumed that the coefficients of the approximating function (1) are sufficiently well-selected if the mean approximation error does not exceed 10%. After analysing the course of the actual curves and approximated curves presented in Figure 2, the approximation error was found to be less than 10%.

5. Research Methodology

The geometric shape and dimensions of the anvil deformation valley used to model the operation of elongation of an ingot made of an AZ91 magnesium alloy were selected on the basis of the literature and the authors' own research carried out at the Department of Plastic Processing and Safety Engineering of the Czestochowa University of Technology [24–33] and are presented in Figures 3 and 4.

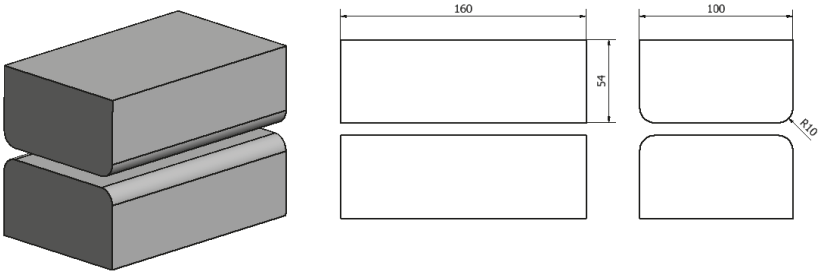

Figure 3. Shape and dimensions of flat dies used for AZ91 magnesium alloy forging [15].

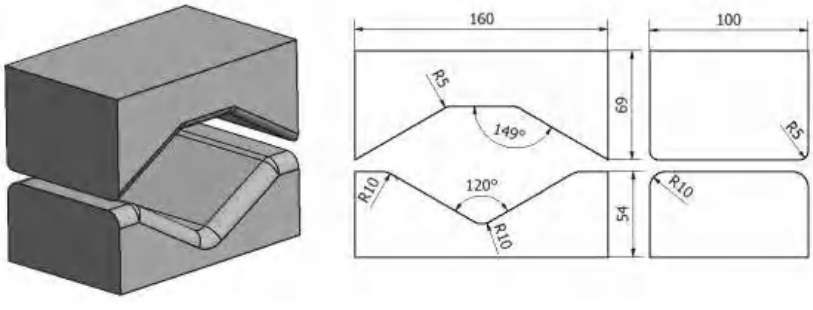

Figure 4. Shape and dimensions of rhombic-trapezoid dies used for AZ91 magnesium alloy forging [15].

The model charge for the numerical tests of the elongation process was an AZ91 magnesium alloy bar with diameter ϕ = 80 mm and length l = 80 mm. After the operations, the semi-finished product will have the following dimensions: 60 × 60 × 180. For numerical simulations, the number of nodes in the volume of the model charge was assumed to be 9116, while the number of tetrahedral elements was 41568.

Numerical modelling of the elongation operation process was performed using commercial software based on the Forge®NxT finite element method. This software allows for the thermomechanical simulation of, among others, plastic processing processes [34]. *Galerkin* equations were used for thermal calculations. The main technological parameters of the forging elongation operation were adopted on the basis of the authors' own research [15,24–28] and the literature [29–33]. The initial conditions during the simulation of the elongation operation were the feed speed of the upper anvil equal to v = 8 mm/s, while the lower anvil was assumed to be stationary.

Figure 5 shows a diagram of the operation of the AZ91 alloy rod elongation in flat anvils. Relative reduction of 40% was used in all forging passes in this operation. The forging passes were implemented in accordance with the forging direction indicated in Figure 5. The first three forging passes were carried out with a relative feed of 0.8, then the forging was rotated in the direction shown in Figure 5 by an angle of 90°, and then the anvils returned to the beginning of the forging (place of the Cartesian xyz coordinate system sketch). Later, three consecutive forging passes (strictly 4, 5, and 6) were performed, also with a density of 40% and a relative feed of 0.8.

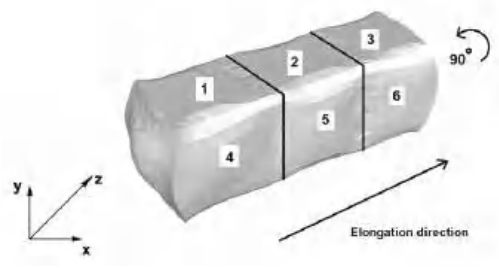

Figure 5. Flat die elongation process diagram [15].

Figure 6 shows a diagram of the operation of the AZ91 alloy rod elongation in the trapezoid and diamond anvils. In the first two forging passes, one side of the bar was forged with a relative reduction of 25% and a relative feed of anvils of 0.8, in accordance with the direction shown in Figure 6. The forging was rotated, as shown in Figure 6, by an angle of 90°, and the anvils returned to the beginning of the forging (sketch of the Cartesian xyz coordinate system). Then, two successive forging passes (marked as 3 and 4) were carried out with a relative reduction of 40% and a relative feed of 0.8. The shape of the anvils determines the value of the applied relative reduction in the first forging passes.

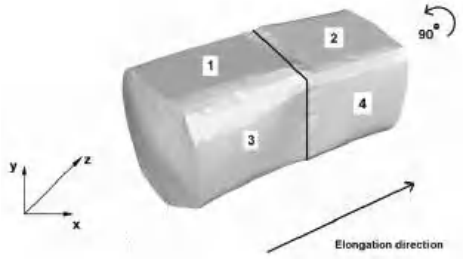

Figure 6. Trapezoid-rhombic die elongation operation diagram [15].

In the paper, to simulate the elongation operation, a thermo-viscoplastic model of the deformed body, which is based on the theory of large plastic deformations, was used. The value of the friction coefficient adopted during the tests was $\mu = 0.3$, in accordance with Coulomb's law.

It was assumed that the heat transfer coefficient between the anvils and the material is $\lambda = 5000\ W/m^2K$, while the heat transfer coefficient between the metal and the environment is equal to $\lambda = 10\ W/m^2K$. The ambient temperature and the anvil temperature were assumed to be equal to 25 °C.

The initial temperature of the charge before the elongation operations in its entire volume was assumed to be the same and equal to 400 °C.

6. Analysis of the Distribution of Hydrostatic Pressure Values during the Elongation Operation

Figures 7–14 show the distributions of hydrostatic pressure values obtained during numerical simulations of AZ91 magnesium alloy elongation in flat anvils.

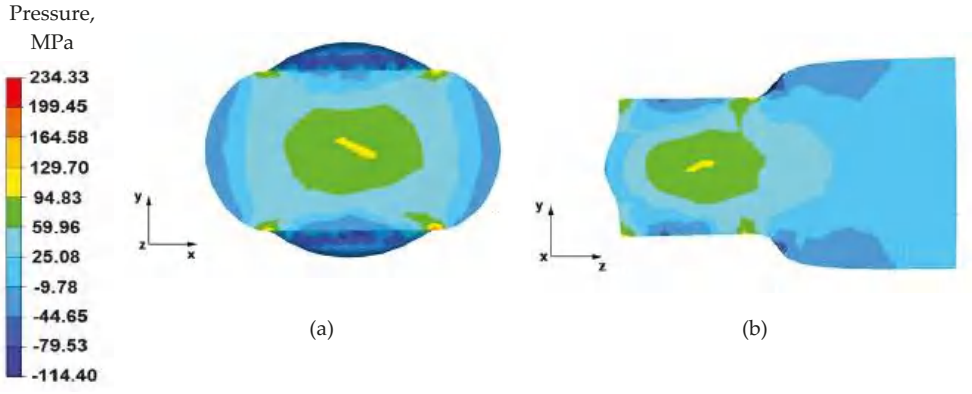

Figure 7. Distribution of the hydrostatic pressure of the AZ 91 alloy forging, deformed in the first pass with 40% reduction in flat anvils: (**a**) on the cross-section, (**b**) on the longitudinal section.

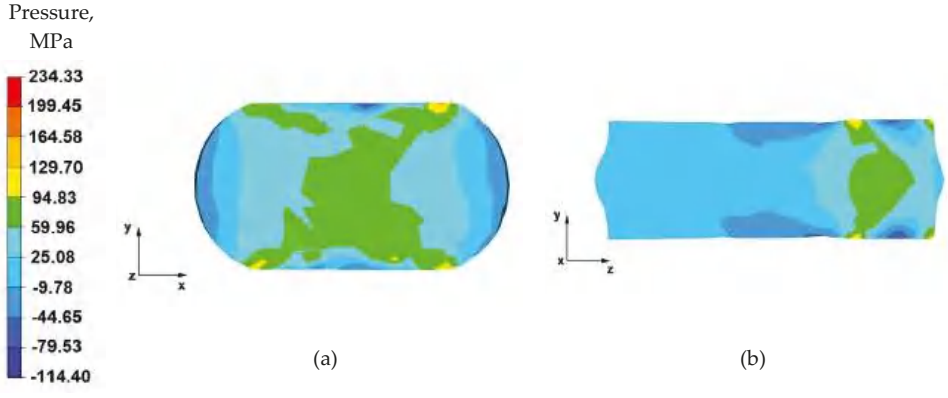

Figure 8. Distribution of the hydrostatic pressure of the AZ 91 alloy forging, deformed in the third pass with 40% reduction in flat anvils: (**a**) on the cross-section, (**b**) on the longitudinal section.

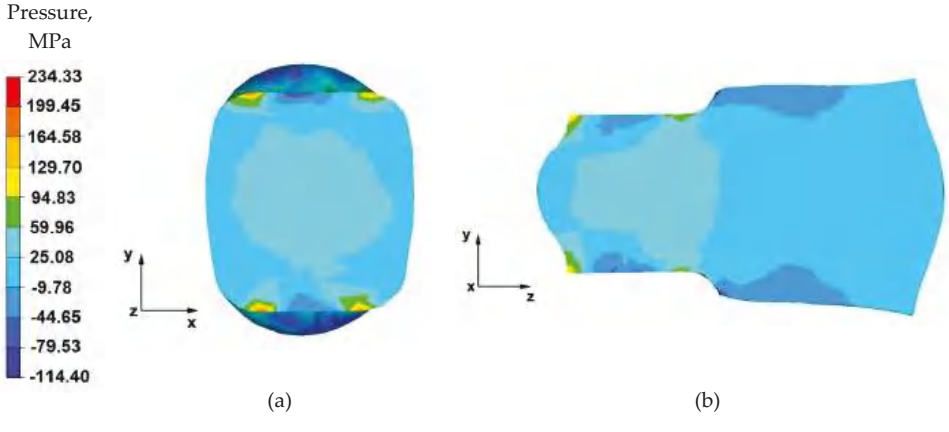

Figure 9. Distribution of the hydrostatic pressure of the AZ 91 alloy forging, deformed in the fourth pass with 40% reduction in flat anvils after slanting by 90°: (**a**) on the cross-section, (**b**) on the longitudinal section.

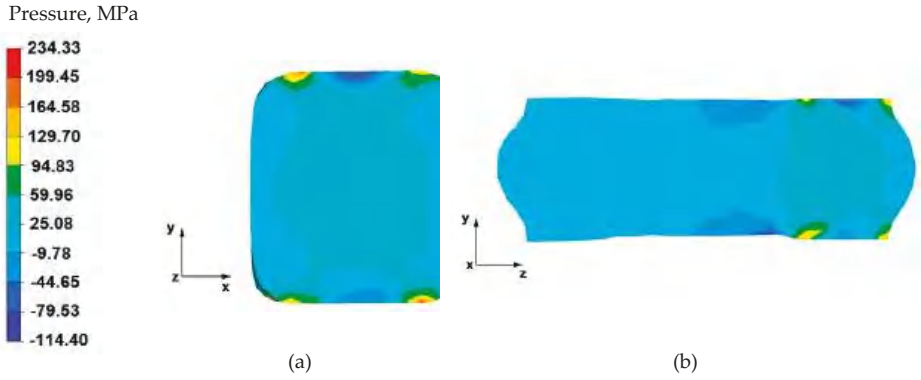

Figure 10. Distribution of the hydrostatic pressure of the AZ 91 alloy forging, deformed in the sixth pass with 40% reduction in flat anvils after slanting by 90°: (**a**) on the cross-section, (**b**) on the longitudinal section.

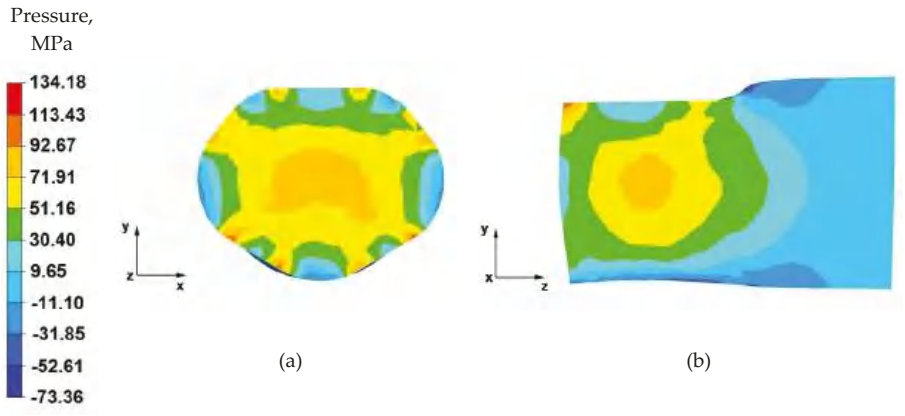

Figure 11. Distribution of the hydrostatic pressure of the AZ 91 alloy forging, deformed in the first pass with 25% reduction in trapezoid and diamond anvils: (**a**) on the cross-section, (**b**) on the longitudinal section.

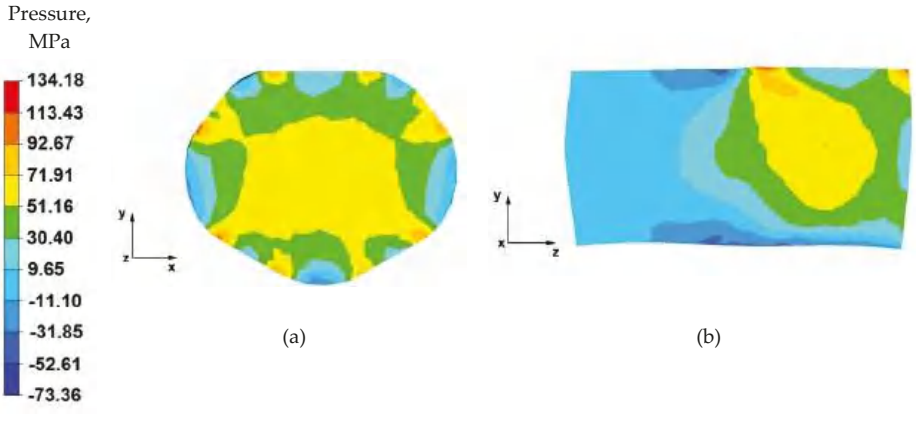

Figure 12. Distribution of the hydrostatic pressure of the AZ 91 alloy forging, deformed in the second pass with 25% reduction in trapezoid and diamond anvils: (**a**) on the cross-section, (**b**) on the longitudinal section.

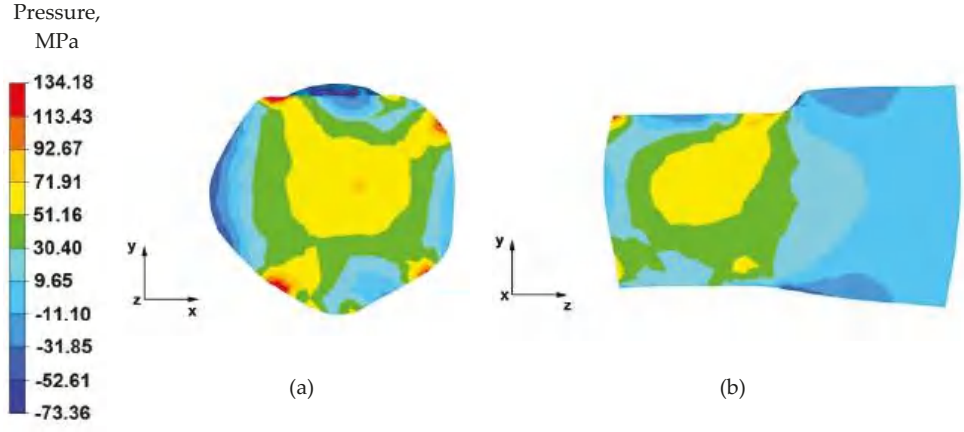

Figure 13. Distribution of the hydrostatic pressure of the AZ 91 alloy forging, deformed in the third pass with 40% reduction in trapezoid and diamond anvils after slanting by 90°: (**a**) on the cross-section, (**b**) on the longitudinal section.

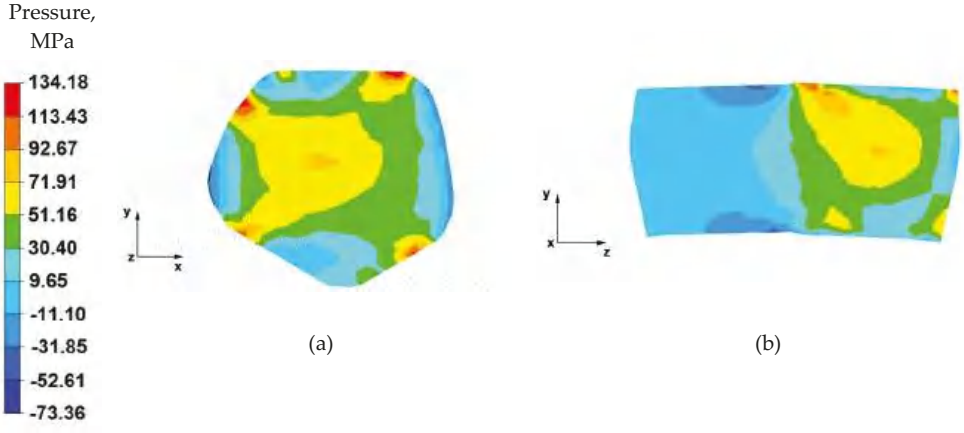

Figure 14. Distribution of the hydrostatic pressure of the AZ 91 alloy forging, deformed in the fourth pass with 40% reduction in trapezoid and diamond anvils after slanting by 90°: (**a**) on the cross-section, (**b**) on the longitudinal section.

From the data in Figure 7a showing the distribution of hydrostatic pressure on the cross-section in the first stage of the elongation operation in flat anvils, it follows that, on the cross-section of the forging under consideration, except for the outer zones, there are high values of hydrostatic pressure, which means good plastic processing of the charge material. The pressure forces caused by the effect of the lower and upper anvils compensate parallelly to the y-axis, resulting in high-pressure values ranging from 130 to 60 MPa. This means that the material was forged through, and it should be assumed that, for almost the entire section of the forging, the degrees of forging will have high values, which is a desirable phenomenon in good practice of applying the elongation operation.

Based on the analysis of the data presented in Figure 7b, it can be concluded that, in the deformation valley, there is high hydrostatic pressure with values in the range 130–25 MPa, due to the pressure of the anvils. This proves good forging in the areas along the forging axis. Negative values of hydrostatic pressure (−10–−80 MPa) can be observed in the zones at the contact surface of the deformed forging with the working surfaces of the anvils. The cause of negative hydrostatic pressure values are the friction forces at the

material–tool contact surfaces. This causes tensile stresses to occur in the near-surface layers of the forging. The occurrence of these stresses may cause delamination and cracking of the material.

From the data shown in Figure 8a, it follows that a similar hydrostatic pressure distribution was obtained as in the first pass (Figure 7a). A forging cross is visible, which is characteristic for the elongation operation in flat anvils. It is undesirable when striving to obtain uniform distributions of the values of strains and stresses in the entire volume of the forging or in local zones, while it is desirable when striving to achieve the forging of the material lying in the zones including the forging cross. The high value of hydrostatic pressure inside the forging indicates a good degree of plastic processing of the material practically throughout its cross-section, with the exception of the outer zones of the forging.

By analysing the data contained in Figure 8b, it can be concluded that there are high values of hydrostatic pressure in the place of the anvil's effect on the material. The pressure forces directed along the y-axis cause universal compression of the material, thus causing its plastic flow along the z-axis. The lack of hydrostatic pressure outside the deformation valley indicates the presence of high mean stress values with positive values, which causes the material to stretch.

From the data shown in Figure 9a, it follows that a uniform distribution of hydrostatic pressure values in the considered section of the forging was obtained. However, the values of this pressure are half the values for the cases shown in Figures 7a and 8a. The lower values of hydrostatic pressure are due to the use of a lower absolute reduction for this case. The obtained uniform distribution of hydrostatic pressure in the forging cross-section affects the achievement of uniform mechanical properties of the finished product.

Based on the data in Figure 9b, it can be stated that, in the deformation valley, the value of hydrostatic pressure is equal to 60 MPa, except for the areas located near the material–tool contact zones. For these areas, the hydrostatic pressure values were negative and ranged from -10 to -45 MPa. Outside the deformation valley, the pressure value was 25 MPa. Such a nature of the hydrostatic pressure value distribution proves good forcing through the material in the deformation valley.

From the analysis of the data shown in Figure 10a, it follows that the forging cross formed during the deformation indicates good forging in the last deformation stage, ending the elongation operation of the AZ 91 alloy. Apart from the near-surface zone, which will be removed in the machining process, the hydrostatic pressure values fluctuated within the range of 60–25 MPa. Such good material processing in the last stage of the forging guarantees a homogeneous structure, and thus, appropriate mechanical properties.

By analysing the data presented in Figure 10b and obtained for the last forging pass in this elongation operation, it can be stated that the material was processed uniformly both in the zones under the action of the anvils, as well as in the entire longitudinal section along the *z*-axis. The values of hydrostatic pressure in this area of the forging ranged from 60 to 25 MPa. Slight local disturbances, which did not affect the processing of the material in the entire volume of the forging, occurred in the zones of contact of the material with the tool. It is extremely difficult to obtain, on the longitudinal section of the elongated forgings, identical and yet the same sign of the stress values in the entire volume, when carrying out the elongation operation in flat anvils.

From the data in Figure 11a, it follows that, after the first stage of the elongation operation in the shaped anvils, the appropriate forging of the forging was obtained, in accordance with good forging practice, except for the outer zones. Such a degree of plastic processing of the material was achieved through the variable geometry of the anvils used to elongate the alloy. Their working surfaces caused the directions of the pressure and friction forces from the variable geometry of the upper trapezoid and lower diamond anvils to cross. In almost the entire cross-section of the forgings, high values of hydrostatic pressure in the range of 93–30 MPa were obtained.

By analysing the data in Figure 11b, it can be observed that there are high values of hydrostatic pressure in the metal in the anvil action zones. The analysis of the hydrostatic

pressure distribution on the longitudinal section of the forging shows that the AZ91 alloy core was forged through, which is very desirable in forging elongation operations, and not always achievable. There, the hydrostatic pressure values were within the range of 93–72 MPa. Good forging of the axial zone (in this case, along the *z*-axis) proves that good strength properties and good quality of the product made by hot elongation were obtained.

Based on the data in Figure 12a, it can be concluded that the nature of the hydrostatic pressure fields is similar to that obtained in the first forging pass (Figure 8). Similarly to the first forging pass, a good material processing was obtained, from which it can be concluded that the finished product will be characterised by good mechanical properties.

By analysing the data in Figure 12b, it can be stated that, apart from the zones of contact of the material with the lower diamond anvil, the material flows freely without touching the top of the working surfaces of the anvil. Due to the lack of deformation resistance in this zone, tensile stresses occur there (no hydrostatic pressure). Apart from this small local part of the forging, the material has good plastic processing (the hydrostatic pressure value is within the range of 72–30 MPa), ensuring that it is forged through. In subsequent forging passes, after the forging is rotated by 90°, it will be important to maintain such a degree of processing.

Figure 13a shows the distribution of the hydrostatic pressure on the cross-section of the forging forged in the third pass with 40% reduction in trapezoid and diamond anvils after slanting by 90°. After the forging was rotated, it was possible to apply a relative reduction of 40%. The implementation of such deformation ensures the maintenance of high values of hydrostatic pressure in the range of 93–51 MPa in almost the entire volume of the forging. The only zones with lower values of hydrostatic pressure are the local outer zones. Local zones with lower values of hydrostatic pressure will be levelled in the next stages of forging. It is important that the material is forged well in the entire volume of the forging in the initial elongation operations.

From the analysis of the data in Figure 13b, it follows that an appropriate character of the stress distribution in the deformation valley, consistent with the good forging practice of conducting the elongation operation, was obtained. In the anvil interaction zone, the deformed metal showed high values of hydrostatic pressure (72–51 MPa).

Based on the data shown in Figure 14a, it can be concluded that, in the last step of the elongation operation, good plastic processing of the material was also obtained. The obtained values of hydrostatic pressure in the metal on its cross-section were within the range of 113–51 MPa. Obtaining the desired state of stresses is the result of the crossing in the forging core of the pressure force vectors, resulting from the effect of the side walls of the working surfaces of shaped anvils on the metal. Such a deformation method leads to the all-round compression state in the material located in the deformation valley.

By analysing the data in Figure 14b, it can be stated that, along the metal's longitudinal section, there were high values of hydrostatic pressure, while outside the deformation valley, the value of hydrostatic pressure in the metal was small and amounted to about 10 MPa.

7. Analysis of the Effective Strain Distribution during the Elongation Operation

Figures 15–18 show the distribution of the effective strain values obtained during the numerical modelling of the operation of extending the AZ91 magnesium alloy ingot in flat and shaped anvils.

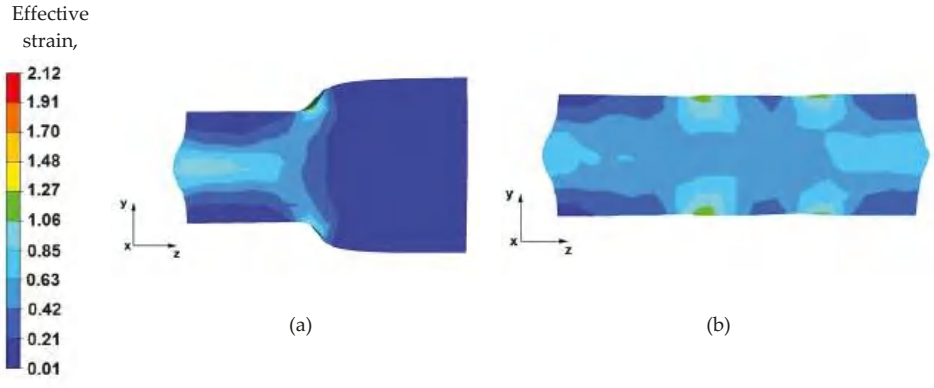

Figure 15. Distribution of the effective strain value on the longitudinal section of the AZ 91 alloy forging with 40% reduction in flat anvils (**a**) forged in the first pass, (**b**) forged in the third pass.

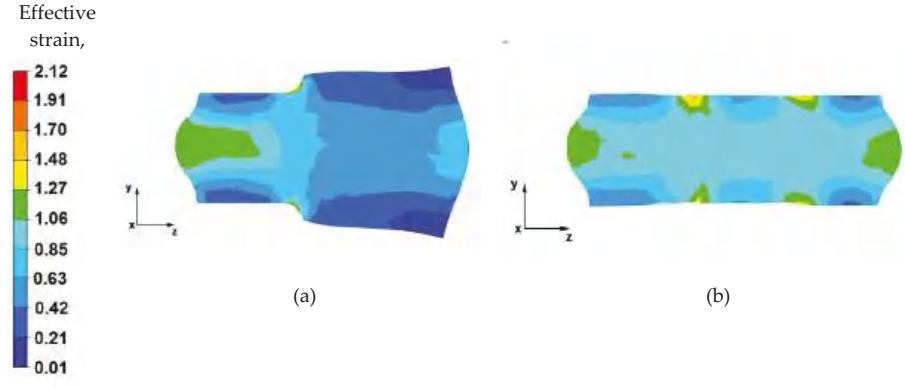

Figure 16. Distribution of the effective strain value on the longitudinal section of the AZ 91 forging, with 40% compression in flat anvils after slanting by an angle of 90°, (**a**) forged in the fourth pass, (**b**) forged in the sixth pass.

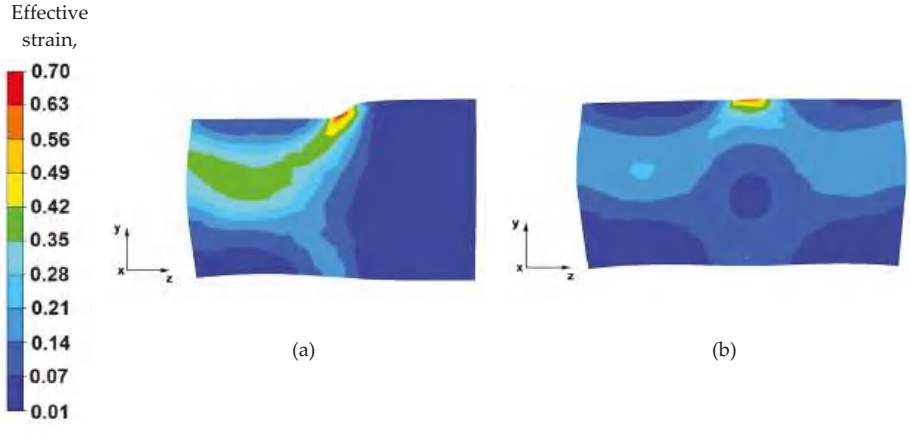

Figure 17. Distribution of the effective strain value on the longitudinal section of the AZ 91 alloy forging, with 25% reduction in trapezoid and diamond anvils, (**a**) forged in the first pass, (**b**) forged in the second pass.

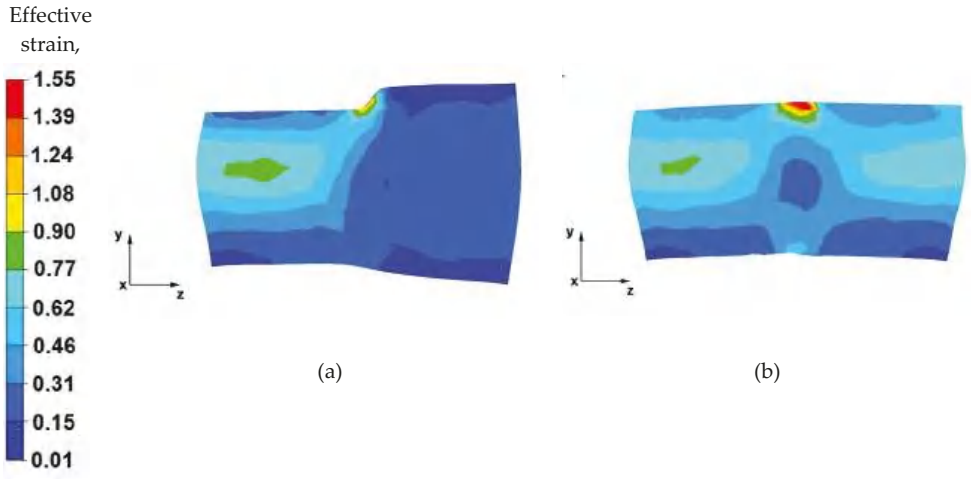

Figure 18. Distribution of the effective strain value on the longitudinal section of the AZ 91 forging, with 40% reduction in trapezoid and diamond anvils after slanting by 90°, (**a**) forged in the third pass, (**b**) forged in the fourth pass.

By analysing the data in Figure 15a, it can be concluded that, in the deformation valley, in the areas along the longitudinal axis of the forging, the material was forged evenly, and there are strains of the highest value (1.06–0.85). Hence, the flow of metal is also greatest in the axial zone. It can be seen that the forging core in the deformation valley is uniformly forged, which is particularly desirable in the elongation operation stages when the temperature of the forging is close to the initial temperature, and the deformation resistance is relatively low. This means that the value of the relative reduction (40%) was selected rationally and in accordance with good forging practice. Lower values of the reduction would not result in such good forging through the core, and reductions above 40% would cause forging cracks in the axial zones. A large intensification of deformations is also visible in the places of the upper and lower anvils' rounding, which is related to the deep penetration of the anvil side surfaces into the material. In the next stages of forging, after slanting, these places will be levelled.

Based on the analysis of the data contained in Figure 15b, it can be stated that the effective strain distribution on the longitudinal section, after the forging is completely forged to one side (i.e., before slanting), is even along its entire length. Uniform effective strain distribution proves the possibility of obtaining homogeneous mechanical properties of the finished product. Slight differences in the effective strain values occur in the places of successive relative anvil feeds. Otherwise, the subsurface zones will be removed in the subsequent machining steps.

By analysing the data shown in Figure 16a, it was observed that, after rotating the forging by an angle of 90°, the effective strain values in the forging core increased and fell within the range of 1.06–1.27. In the deformation valley, the material flows plastically along the *z*-axis in the opposite direction to the forging direction. The deformation intensity values in the zones under the direct influence of the anvils ranged from 0.63 to 0.42. Lower effective strain values on the contact surfaces of the material with the tools are a result of the higher deformation resistance caused by the friction forces occurring there.

From the data in Figure 16b, it can be concluded that there is a uniform effective strain distribution in the forged material. The occurrence of small areas with a higher effective strain value is related to the shifting of the anvils in the successive forging passes. Further areas of greater effective strain were observed in the front and rear parts of the forging, in the places of free metal flow along the *z*-axis, in the forging direction, and in the opposite direction. This metal flow pattern occurs in any elongation operation, especially

in flat anvils. The uniform effective strain values distribution over the entire volume of the forging can be obtained by the appropriate selection of the relative anvil feed value. In the analysed operation of the AZ91 magnesium alloy ingot elongation, the relative feed was assumed to be 0.8.

Based on the data shown in Figure 17a, it can be stated that the effective strain value is unevenly distributed along the longitudinal section of the forged alloy. The reason for this condition is the use of a relative reduction of a low value of 25%, due to the geometric shapes of the anvils which, in the first stages of forming the forgings, before turning by 90°, make it impossible to use larger reductions. Additionally, the use of two different anvils results in asymmetric plastic flow of the metal in the deformation valley. The values of the pressure and friction forces from the upper trapezoid anvil were greater, and the deformation valley from the side of the trapezoid anvil was also greater. Therefore, an uneven distribution of the effective strain values can be observed (0.35–0.29). In the deformation valley, from the side of the lower trapezoid anvil, the deformation intensity value was 0.17–0.060. On the basis of the conducted analysis, it can be concluded that the obtained effective strain distribution is unfavourable and is not compliant with good forging practice of conducting the elongation operation. This unfavourable effective strain distribution will be eliminated in the subsequent forging passes.

From the data in Figure 17b, it follows that, after the second forging pass, a more even distribution of the effective strain values was obtained on the longitudinal section of the forging. The effective strain values ranged from 0.44 to 0.22. Low strain values were related to the low relative reduction of only 25% due to the contact of the side surfaces of the anvils, as well as different shape and dimensional parameters of the anvils used.

By analysing the effective strain distributions shown in Figure 18a, it can be observed that good forging occurred in its central part. Under the action of the anvils, the metal flows freely in the opposite direction to the *z*-axis, while the near-surface zones of the forging are less forged because the plastic flow of the metal in these zones is blocked by the side surfaces of both the diamond and trapezoid anvils. The most important thing in forging elongation operations is the appropriate forging of the axial zone, which is not always possible to achieve in other elongation operations. However, in the analysed case, it was possible to achieve this.

Based on the analysis of the data presented in Figure 18b, it can be concluded that, after successive metal forging passes in shaped anvils, the effective strain value is two times lower in the zones where there is no anvil interaction (0.31) than in the zones of their impact (0.77). The use of shaped anvils in the elongation operation of the anvil shape affects the uniform distribution of the effective strain in the anvil interaction zones, while it is the cause of the uneven distribution of the effective strain in the places of subsequent forging passes. However, in the entire volume of the deformed metal, these places are few, and they do not significantly affect the mechanical properties of the finished product.

8. Final Conclusions

Based on the analysis of the results of numerical modelling of the elongation operation of the AZ91 magnesium alloy ingot in flat and shaped anvils, the following final conclusions were formulated:

- From an economic and technological point of view, it is rational to carry out the elongation operation of the AZ91 magnesium alloy ingot in trapezoid and diamond shape anvils designed by the authors. As a result of the use of shaped anvils in the elongation operation, it was possible to reduce the number of forging passes from six to four, compared to the technology for which flat anvils were used, obtaining the same shape and dimensional parameters of the finished forging.
- During the elongation operation in both flat and shaped anvils, an even distribution of hydrostatic pressure was obtained. The hydrostatic pressure values were 94–59 MPa during the elongation operation in flat anvils and 91–51 MPa in the shaped anvils, which means good material processing.

- Negative values of hydrostatic pressure (no hydrostatic pressure) during the elongation operation in flat anvils can be observed on the contact surfaces of the deformed forging with the working surfaces of the anvils. On the other hand, during the elongation operation in diamond and trapezoid anvils, negative values of hydrostatic pressure occur on the surface of contact of the upper trapezoid anvil with the material. The cause of the negative hydrostatic pressure values is the friction forces occurring in the material–tool contact zones, which cause tensile stresses in the near-surface layers of the forging. The occurrence of these stresses may cause delamination and cracking of the material.
- The uniform distribution of the deformation intensity value during the elongation operation of the model AZ91 magnesium alloy ingot was obtained both in diamond and trapezoid and flat anvils. The deformation intensity values obtained in the shape anvils were lower compared to the values obtained in the flat anvils. Slight differences in the deformation intensity values occurred in the boundary points between successive relative anvil feeds. However, material from these zones is removed in subsequent machining steps.
- For deformation of the AZ91 magnesium alloy in hot forging operations, it is recommended to use shaped anvils in the initial stages of the forging formation, while flat anvils should be used in the final stages of forming. The homogeneity of the deformation intensity distribution was observed for the following technological parameters: relative reduction in the range of 25–40%, relative feed 0.8, forging rotation angle 90°. The elongation operation was carried out by forging on one side.

Author Contributions: Conceptualization, G.B., T.B., A.K. and T.G.; methodology, G.B. and T.B.; validation, T.B., G.B., A.K. and T.G.; formal analysis, G.B., T.B., A.K. and T.G.; investigation, G.B. and T.B.; resources, T.B., A.K. and T.G.; data curation, T.B.; writing—original draft preparation, G.B., A.K., T.B. and T.G.; writing—review and editing, T.B., G.B. and A.K.; supervision, A.K. All authors have read and agreed to the published version of the manuscript.

Funding: This research received no external funding.

Institutional Review Board Statement: Not applicable.

Informed Consent Statement: Not applicable.

Data Availability Statement: Data sharing not applicable.

Conflicts of Interest: The authors declare no conflict of interest.

References

1. Song, J.; Sche, J.; Chen, D.; Pan, F. Latest research advances on magnesium and magnesium alloys worldwide. *J. Magnes. Alloys* **2020**, *8*, 1–41. [CrossRef]
2. Mordike, B.L.; Ebert, T. Magnesium: Properties—Applications—Potential. *Mater. Sci. Eng.* **2001**, *302*, 37–45. [CrossRef]
3. Yang, Z.; Li, J.; Zhang, J.; Lorimer, G.; Robson, J. Review on research and development of magnesium alloys. *Acta Metall. Sin.* **2008**, *21*, 313–328. [CrossRef]
4. Bettles, C.; Gibson, M. Current wrought magnesium alloys: Strengths and weaknesses. *JOM* **2005**, *57*, 46–49. [CrossRef]
5. Madaj, M.; Greger, M.; Karas, V. Magnesium-alloy die forgings for automotive applications. *Mater. Technol.* **2015**, *49*, 267–273. [CrossRef]
6. Esmaily, M.; Svensson, J.; Fajardo, S.; Birbilis, N.; Frankel, G.; Virtanen, S.; Arrabal, R.; Thomas, S.; Johansson, L. Fundamentals and advances in magnesium alloy corrosion. *Prog. Mater. Sci.* **2017**, *89*, 92–193. [CrossRef]
7. Gray, J.; Luan, B. Protective coatings on magnesium and its alloys—A critical review. *J. Alloys Compd.* **2002**, *336*, 88–113. [CrossRef]
8. Nie, J.F. Precipitation and hardening in magnesium alloys. *Metall. Mater. Trans.* **2012**, *43*, 3891–3939. [CrossRef]
9. Zeng, Z.; Stanford, N.; Davies, C.H.J.; Nie, J.F.; Birbilis, N. Magnesium extrusion alloys: A review of developments and prospects. *Int. Mater. Rev.* **2019**, *64*, 27–62. [CrossRef]
10. Papenberg, N.P.; Gneiger, S.; Weißensteiner, I.; Uggowitzer, P.J.; Pogatscher, S. Mg-alloys for forging applications—A review. *Materials* **2020**, *13*, 985. [CrossRef]
11. Braszczyńska-Malik, K. Discontinuous and continuous precipitation in magnesium-aluminium type alloys. *J. Alloys Compd.* **2009**, *477*, 870–876. [CrossRef]
12. Gann, J.A. Magnesium industry's lightest structural metal. *SAE Trans* **1930**, *25*, 620–641.

13. Polmear, I. Recent developments in light alloys. *Mater. Trans. JIM.* **1996**, *37*, 12–31. [CrossRef]
14. Polmear, I.; StJohn, D.; Nie, J.F.; Qian, M. *Light Alloys: Metallurgy of the Light Metals*, 5th ed.; Elsevier Butterworth-Heinemann: Oxford, UK, 2017.
15. Banaszek, G.; Bajor, T.; Kawałek, A.; Garstka, T. Analysis of the open die forging process of the AZ91 magnesium alloy. *Materials* **2020**, *13*, 3873. [CrossRef] [PubMed]
16. Dziubinska, A.; Gontarz, A.; Dziubinski, M.; Barszcz, M. The forming of magnesium alloy forgings for aircraft and automotive applications. *Adv. Sci. Technol. Res. J.* **2016**, *10*, 158–168. [CrossRef]
17. Shan, D.; Xu, W.; Lu, Y. Study on precision forging technology for a complex-shaped light alloy forging. *J. Mater. Process. Technol.* **2004**, *151*, 289–293. [CrossRef]
18. Hartley, P.; Pillinger, I. Numerical simulation of the forging process. *Comput. Method Appl. Mach.* **2006**, *195*, 6676–6690. [CrossRef]
19. Hawryluk, M.; Jakubik, J. Analysis of forging defects for selected industrial die forging processes. *Eng. Fail. Anal.* **2016**, *59*, 396–409. [CrossRef]
20. Skubisz, P.; Sińczak, J.; Bednarek, S. Forgeability of Mg–Al–Zn magnesium alloys in hot and warm close die forging. *J. Mater. Process. Technol.* **2006**, *177*, 210–213. [CrossRef]
21. Spittel, A.; Hensel, T. *Kraft-und Arbeitsbedarf Bildsamer Formgebungsverfahren*; VEB Deutscher Verlag für Grundstoffindustrie: Lipsk, Germany, 1978.
22. Dyja, H.; Sobczak, K.; Kawalek, A.; Knapinski, M. The analysis of the influence of varying types of shape grooves on the behaviour of internal material discontinuities during rolling. *Metalurgija* **2013**, *52*, 35–38.
23. Kawałek, A.; Rapalska-Nowakowska, J.; Dyja, H.; Koczurkiewicz, B. Physical and numerical modelling of heat treatment the precipitation-hardening complex-phase steel (CP). *Metalurgija* **2013**, *52*, 23–26.
24. Banaszek, G.; Berski, S.; Dyja, H.; Kawałek, A. Theoretical modelling of metallurgical defect closing-up processes during forming a forging. *J. Iron Steel Res. Int.* **2013**, *20*, 111–116. [CrossRef]
25. Banaszek, G.; Berski, S.; Dyja, H. Numerical analysis of the torsion stretch forging operation in asymmetrical anvils. *Metall. Min. Ind.* **2011**, *3*, 98–101.
26. Banaszek, G.; Dyja, H.; Berski, S. Choosing the forging parameters and tool shape from the point of view of quality improvement of forging. *Metalurgija* **2003**, *42*, 239–244.
27. Banaszek, G.; Szota, P. A comprehensive numerical analysis of the effect of relative feed during the operation of stretch forging of large ingots in profiled anvils. *J. Mater. Process. Technol.* **2005**, *169*, 437–444. [CrossRef]
28. Chen, K.; Yang, Y.; Shao, G.; Liu, K. Strain function analysis method for void closure in the forging process of the large-sized steel ingot. *Comput. Mater. Sci.* **2012**, *51*, 72–77. [CrossRef]
29. Cho, J.R.; Bae, W.B.; Kim, Y.H.; Choi, S.S.; Kim, D.K. Analysis of the cogging process for heavy ingots by finite element method and physical modeling method. *J. Mater. Process. Technol.* **1998**, *80–81*, 161–165. [CrossRef]
30. Lee, M.C.; Jang, S.M.; Cho, J.H.; Joun, M.S. Finite element simulation of pore closing during cylinder upsetting. *Int. J. Mod. Phys.* **2008**, *22*, 5768–5773. [CrossRef]
31. Park, C.Y.; Yang, D.Y. A study of void crushing in large forgings, estimation of bonding efficiency by finite element analysis. *J. Mater. Process. Technol.* **1997**, *72*, 32–41. [CrossRef]
32. Park, C.Y.; Yang, D.Y. Modelling of void crushing for large ingot hot forging. *J. Mater. Process. Technol.* **1998**, *67*, 195–200. [CrossRef]
33. Sińczak, J.; Majta, J.; Głowacki, M. Prediction of mechanical properties of heavy forgings. *J. Mater. Process. Technol.* **1998**, *107*, 166–173. [CrossRef]
34. Transvalor Solution: How to Run Forge 2008, Users Guide, Sophia Antipolis, France 2008. Available online: www.transvalor.com (accessed on 1 January 2021).

materials

MDPI

Article

The Analysis of Deformability, Structure and Properties of AZ61 Cast Magnesium Alloy in a New Hammer Forging Process for Aircraft Mounts

Anna Dziubińska *, Piotr Surdacki and Krzysztof Majerski

Faculty of Mechanical Engineering, Lublin University of Technology, 20-618 Lublin, Poland; piotr.surdacki@pollub.pl (P.S.); k.majerski@pollub.pl (K.M.)
* Correspondence: a.dziubinska@pollub.pl

Abstract: This article presents the analysis of the deformability, structure and properties of the AZ61 cast magnesium alloy on the example of a new forging process of aircraft mount forgings. It was assumed that their production process would be based on drop forging on a die hammer. Two geometries of preforms, differing in forging degree, were used as the billet for the forging process. It was assumed that using a cast, unformed preform positively affects the deformability of hard-deformable magnesium alloys and flow kinematics during their forging and reduces the number of operations necessary to obtain the correct product. Numerical analysis of the proposed new technology was carried out using DEFORM 3D v.11, a commercial program dedicated to analyzing metal forming processes. The simulations were performed in the conditions of spatial strain, considering the full thermomechanical analysis. The obtained results of numerical tests confirmed the possibility of forming the forgings of aviation mounts from the AZ61 cast magnesium alloy with the proposed technology. They also allowed us to obtain information about the kinematics of the material flow during forming and process parameters, such as strain intensity distribution, temperatures, Cockcroft–Latham criterion and forming energy. The proposed forging process on a die hammer was verified in industrial conditions. The manufactured forgings of aircraft mounts made of AZ61 magnesium alloy were subjected to qualitative tests in terms of their structure, conductivity and mechanical properties.

Keywords: magnesium alloys; deformation; hammer forging; aircraft mounts; FEM; industrial research; structure; mechanical properties

Citation: Dziubińska, A.; Surdacki, P.; Majerski, K. The Analysis of Deformability, Structure and Properties of AZ61 Cast Magnesium Alloy in a New Hammer Forging Process for Aircraft Mounts. *Materials* **2021**, *14*, 2593. https://doi.org/10.3390/ma14102593

Academic Editor: Ivo Schindler

Received: 31 March 2021
Accepted: 14 May 2021
Published: 16 May 2021

Publisher's Note: MDPI stays neutral with regard to jurisdictional claims in published maps and institutional affiliations.

1. Introduction

Lately, an increased interest in magnesium alloys has been noticeable [1–6], especially in aviation and the automotive industry [7–9]. Decreasing the structure mass has become a major priority in many branches of the industry. This is why magnesium-based elements made of light metal alloys are increasingly explored in machine construction [10].

However, magnesium is a reactive metal and very susceptible to corrosion, especially in environments containing chloride ions, limiting the application area of magnesium alloys. For this reason, it is necessary to protect the surface of magnesium components by applying additional paint coatings, conversion coatings or electrochemical coatings, or by using anodizing processes and vapor deposition of coatings [11–14].

In aviation, a wide range of construction elements is used, e.g., gearbox, engine, wing, hull plating, door, wheels, landing gear, cockpit panels and seat elements [15]. For example, in Boing 727 c.a. 1200 elements are made of magnesium. As far as the automotive is concerned, magnesium alloys are used in, among others, producing engines, bodywork, cylinder head covers, seat and sunroof frames and pedal support brackets and stems [7,16]. In particular, heat treatment of magnesium alloys is used in aerospace and automotive applications. This is important because high mechanical properties can

be achieved for critical aerospace and automotive parts. Annealing, supersaturation and aging of magnesium alloys are used [2,17–19].

Magnesium alloys are also found in household items. Using magnesium, the density, of which is 1.74 g/cm^3, allows to significantly decrease the product's weight, even by 30%. The factors limiting the usage of magnesium alloys include low corrosion resistance, flammability, lower strength, specific forming conditions due to a narrow range of temperature parameters and sensitivity to strain, which results in high-cost of metal forming and mechanical machining [8,20,21].

The magnesium alloys are the most widely used as-cast alloys [22–25]. This is conditioned by their availability on the market, well-developed casting technology and lower price. Unfortunately, the quality of the obtained castings in terms of their strength and functional properties is insufficient due to the occurrence of the following casting defects: heterogeneity of the structure, coarse grain structure, blisters, porosities, contraction cavities, femoral stems and other defects, which decrease the durability of the obtained castings.

The necessity of using castings is forced by the low availability of magnesium forgings, which would significantly increase the mechanical and functional properties of the final product and decrease the production cost. Despite the beneficial mechanical properties, using magnesium alloys for forming accounts for only 1% of the annual production of magnesium in the world, which is related to the limited plasticity of these magnesium alloys.

Metal forming of magnesium alloys proves even more difficult due to the narrow range of temperature parameters and sensitivity to the strain. Therefore, forming magnesium alloys is carried out in high-temperature on forging machines with low operating speeds while maintaining isothermal temperature conditions during deformation. Currently, the few companies that have implemented the technology of forging magnesium alloys on specialized hydraulic presses with tool heating systems include Otto-Fuchs and Weisensee Warmpressteile from Germany and KUMZ from Russia.

Some casting alloys are also formed, including by forging [26,27]. This way, products from castings have better mechanical and functional properties, which results in the uniformity and fragmentation of the casting structure. Standard shapes of billets available on the market are used for forging magnesium alloys, and the process is carried out in isothermal conditions on specialized presses equipped with heating systems. Low production capacities are caused mainly by the recommended forging technology on very slow presses, and using complicated heating installations mounted in the tooling contributes to high production costs and low attractiveness of products compared to, e.g., aluminum.

The die forging of magnesium alloys on forging equipment, such as forging hammers without specialized heating systems, would reduce production costs and increase productivity. Unfortunately, using standard shapes of castings for forging magnesium alloys, particularly hard-deforming, on traditional hammers does not guarantee correct forgings without cracks. Often the first cracks inside the material appear during the initial forging when forging is formed. Further processing of the forgings in the finishing impression reveals a defect in the form of cracks, which disqualifies the product. The solution to this problem could be using the ready-made preforms, which are cast to mirror the forgings as closely as possible. Theoretically, in terms of costs, using preforms obtained by the casting should be more advantageous than using billets, and consequently, should be an interesting alternative. In this case, the production process of the charge is shortened by the operations related to the extrusion of the billets themselves and the initial forging of the preforms. It seems that such a solution may also have several valuable advantages. The mechanical properties of the forgings obtained from the billets are comparable for both technologies, and in many cases, favor those cast due to their low anisotropy. There are, however, differences in the structure of the forgings made of ingot compared to using wrought billet forging. The forging made of an extruded billet receives in some sections a fibrous structure, which results in different values of strength properties depending on the direction of the fibers in the forging. In some cases, this may be disadvantageous from

the point of view of the distribution of the mechanical properties in the product. A more fragmented and homogeneous structure in the entire volume of the product favor forgings made of cast materials.

It was assumed that using a preform cast as close as possible to the shape of the forging in the plane of the die division would have a positive effect on the kinematics of metal flow, especially when deforming less deformable grades of magnesium alloys, which would allow obtaining a correct product without defects with a more precise shape and dimensions. By limiting the number of operations needed to produce the forging, greater material and energy savings can be achieved.

Therefore, it was considered advisable to test this concept and develop new technology for forging magnesium alloys from cast preforms. The AZ61 magnesium alloy with good strength properties, which is of interest to the aerospace and automotive industries, was selected for the study. The article analyses the deformability, structure and properties of the AZ61 cast magnesium alloy in the form of preforms used in the new hammer forging process of the forgings of the aircraft mounts.

2. Research Methodology

2.1. Assumptions of the New Technology and Numerical Simulations

The research concentrated on a new forming process of forging an aircraft mount (Figure 1a) manufactured from a billet in the form of a sand-cast preform from a high-strength AZ61 grade magnesium alloy. Currently, aircraft mounts presented in Figure 1b are manufactured by machining from cast elements or by multi-stage forging from wrought billet [28–31]. This technology is particularly time, labor, and energy-consuming. Moreover, it generates significant material waste, while the quality of the finished product is low. Among other manufacturing methods, there is a die forging of a wrought billet. In this method, limits to the usage occur since it is difficult to produce elements from less plastic magnesium alloys. The process is conducted in many stages (Figure 2a), leaving a significant stock allowance. Approximately 50% of the forging mass is technological waste created in several forging operations and numerous heating operations. In the die forging of mounts from less plastic magnesium alloys, it is often necessary to obtain additional dies for initial forging. This technology is also very material-, labor- and energy-consuming, as well as limitedly effective.

Figure 1. 3D models of the forging of aircraft mount from AZ61 alloy (**a**) and of the finished aircraft mount (**b**).

It was assumed that in the new process of forging an aircraft mount from AZ61 grade alloy, the geometry of the preform would be similar to the forging, especially in terms of the outline in the area of die division. Using a not-wrought preform positively influences the flow kinematics and deformability of the material during forging. Using a billet with precise/accurate dimensions in the form of cast preform allows reducing material waste compared to the process currently used in the industry, that is, forging from an extruded billet. The process is realized in one forging operation in a finishing die, using typical forging machines, die hammers and inexpensive tool heating methods (furnace, gas burner). It is also worth mentioning that using a ready-made cast forging for the forging process limits the number and duration of operations required for the forging to be obtained, which

influences the effectiveness and decreases the labor consumption of the process. Elements subjected to metal forming following the new technology are of better quality, resulting from a better macro- and microstructure, whereas its surfaces are smoother, which, in turn, enhance the functional and mechanical properties of the product compared to the ones made from cast only.

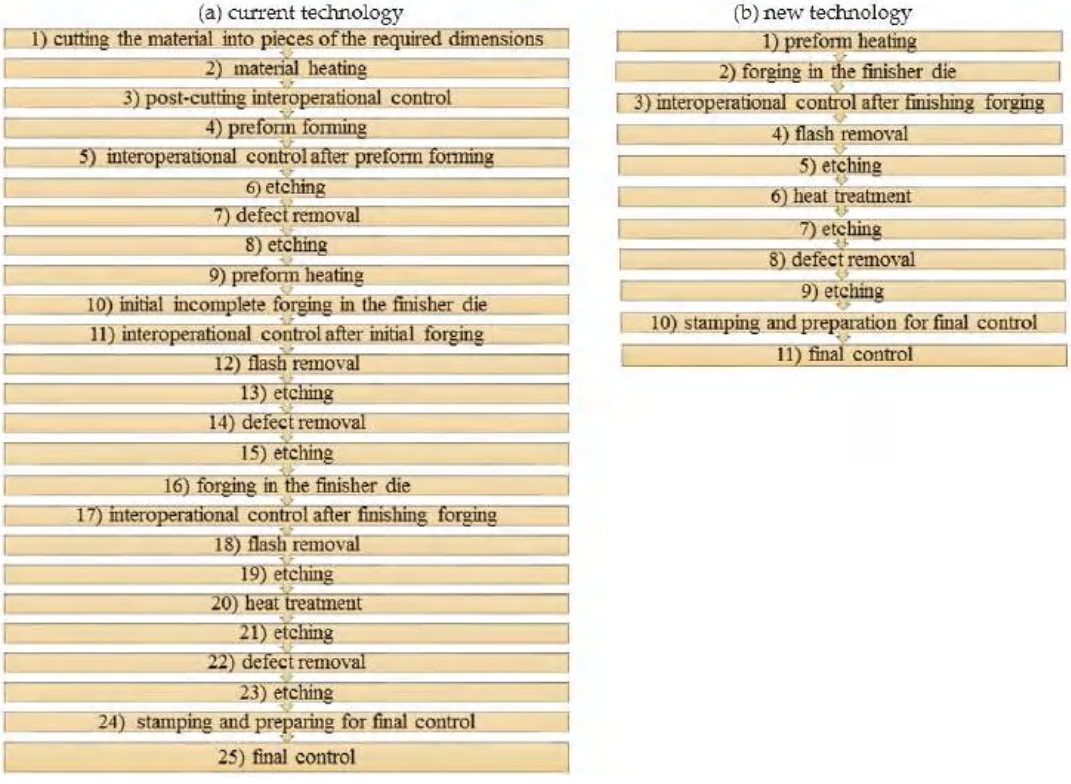

Figure 2. Scheme of the currently applied, multi-stage forging process for high-strength magnesium alloy from an extruded billet (**a**) and the new forming process (**b**).

The numerical analysis of forging the aircraft mount in a hammer from AZ61 grade alloy was performed using the finite elements method (FEM) in Deform 3D ver. 11.0 software (Scientific Forming Technologies Corporation, Columbus, Ohio, United States). FEM simulations were conducted with the spatial strain state and applying the full thermomechanical model. For the new process, two preforms geometries were designed, with a more and less significant forging degree, being the ratio of the height of the billet h_0 to the height of the deformed forging. The forgings differ mainly in height and thus in the degree of forging and the cross-sectional dimensions in the division plane. The degree of forging, i.e., the ratio of the height of the forging preform to the height of the forging product for the first variant was $h_I/h_0 = 38.5/28.5 = 1.35$, and for the second variant, $h_{II}/h_0 = 43.5/28.5 = 1.52$. The scheme of the geometry of the preforms and the forging is shown in Figure 3. It was assumed that the new forming process conducted from the cast preform with a smaller and higher forging ratio would be realized in one forging operation in the finishing impression. Figure 4 presents an exemplary forging process. It was assumed in the simulations that the preform-shaped billet is heated to 400 °C [32], whereas the die temperature during the process is constant and equal 250 °C [32]. The material was divided

into 150,000 tetragonal elements. The material model of the AZ61 magnesium alloy cast in the sand casts was developed based on its own plastometric tests on a DIL 805A/D strain dilatometer. The plastic strain was introduced to the program in table form and depends on the temperature in the range 240–440 °C, strain rate from 0.01 s^{-1} to 10 s^{-1} and strain values in the range 0–1.

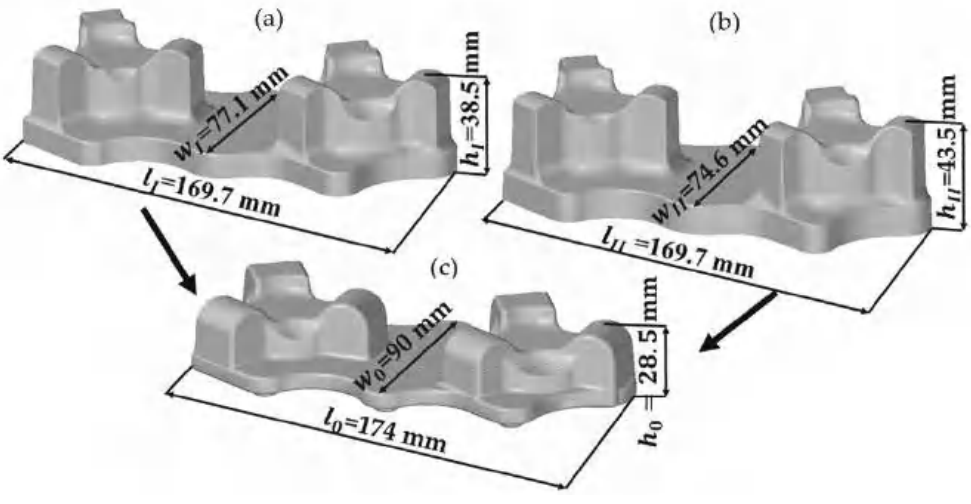

Figure 3. Model 3D of the parts: (**a**) variant I-preform with a smaller forging ratio, (**b**) variant II-preform with a higher forging ratio, (**c**) forging.

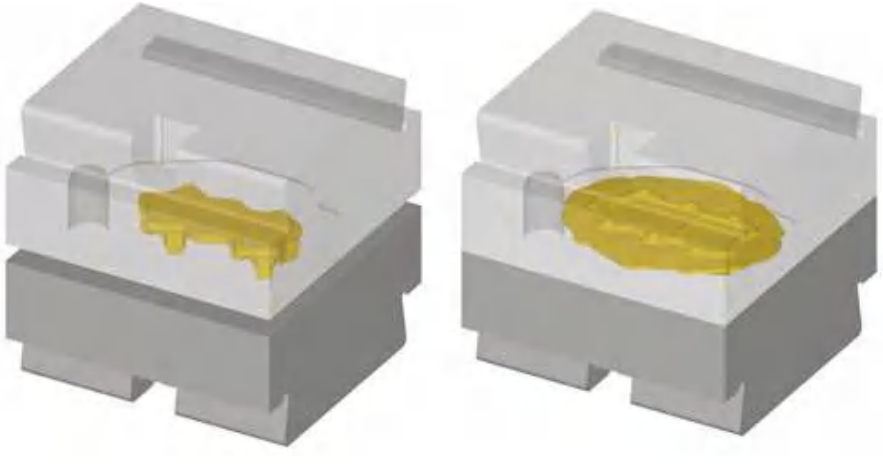

Figure 4. An exemplary process of forging an aircraft mount from AZ61 magnesium alloy, conducted in a die hammer for the preform with a smaller forging ratio: (**a**) beginning of the process, (**b**) end of the process.

The forging process for manufacturing magnesium alloy aircraft bracket is performed with a hammer described by the impact energy of 36 kJ and the weight of the dropping part of 1200 kg. The heat transfer coefficient between the workpiece and the environment was assumed to be 0.03 kW/m^2K and between workpiece and tools 4.5 kW/m^2K [33].

The friction conditions between the formed material and the tools were described with the constant friction model. The friction factor describing the contact between the AZ61 magnesium alloy and steel with graphite lubrication was set to m = 0.24 [34].

2.2. The Material Used for the Tests and the Conditions for the Experimental Tests for Forging of Aircraft Mounts Forgings

AZ61 magnesium alloy cast into sand molds was used for the experimental tests. The chemical composition of the AZ61 alloy is shown in Table 1. Preforms form-shaped casts (Figure 5) were made by NEOCAST Lightweight Metal Technologies (Cracow, Poland). All castings were subjected to the annealing by heating a furnace to the temperature T = 415 °C in a protective argon atmosphere, heating at T = 415 °C for 24 h, and then cooling in air. The annealing temperature was selected based on testing the hardness and microstructure of castings annealed at different temperatures.

Table 1. Chemical composition of AZ61 magnesium alloy used in the experiment (wt %).

Al	Zn	Mn	Fe	Si	Cu	Ni	Mg
5.8–7.2	0.4–1.5	0.15–0.5	max 0.005	max 0.10	max 0.05	max 0.005	rest

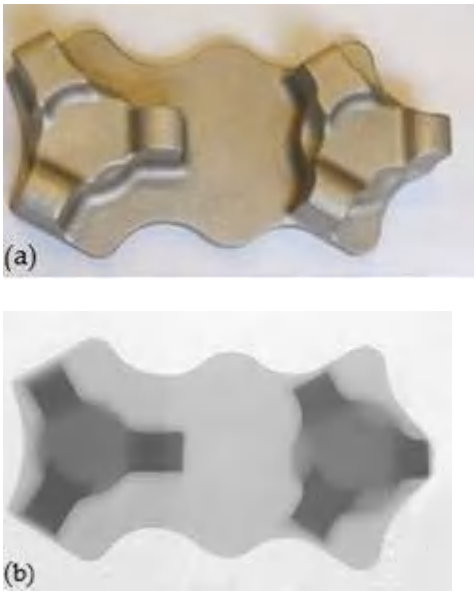

Figure 5. Cast preforms: (**a**) lower degree of forging, (**b**) X-ray of a preform.

The experimental tests of the new process of forming forgings of aircraft mounts from AZ61 alloy castings were carried out in industrial conditions at ZOP Co. Ltd. FORGING PLANT (Świdnik, Poland). All forging tests were performed on an MPM 3150 die hammer (Huta Zygmunt, Poland) (Figure 6a) using a set of dies shown in Figure 7 and the conditions assumed in computer simulations (Section 2.1). The dies were heated in the furnace to the temperature of 250 °C, and during the tests, their temperature was maintained using gas burners (Figure 6b). The preforms were heated to the forging temperature of 400 °C in a PEO-A1-type rotary electric furnace with forced air circulation (ELTERMA Świebodzin, Poland) (Figure 6c). After obtaining the appropriate thermal conditions, the preforms were forged in a single operation in a finishing impression (Figure 7). Correct forgings of aviation mounts were trimmed from the flash using a saw and then etched in five baths

with the parameters presented in Table 2. Then, the forgings were heat-treated in the form of supersaturation at T = 415 °C for 6 h and cooling in water and aging in temperature T = 175 °C for 24 h and cooling in air.

Figure 6. Machines used during tests in industrial conditions: (**a**) MPM 3150 drop hammer, (**b**) gas burner, (**c**) electric furnace.

Table 2. Conditions in the individual baths used for the etching process.

Bath	Conditions
I	Warm water, 50–70 °C
II	Cold water
III	Nitric acid aqueous solution HNO_3 (around 20–35%)
IV	Cold water
V	Sodium hydroxide aqueous solution NaOH (around 10%) 50–70 °C

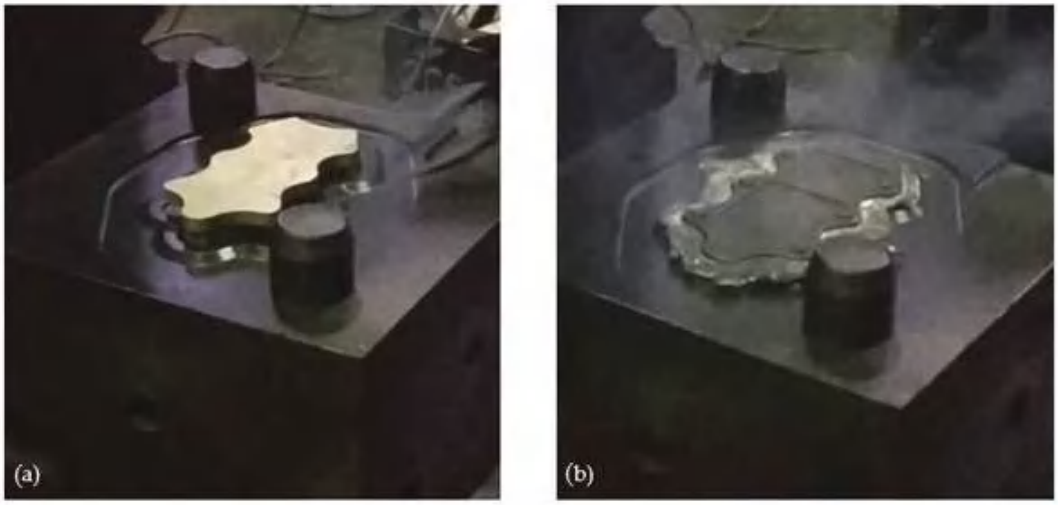

Figure 7. Forging in a finishing impression for a cast preform with a lower degree of forging: (**a**) start of the process, (**b**) end of the process.

2.3. Types of Qualitative Tests Performed for the Formed Forgings

To assess the quality of the formed AZ61 alloy forgings of aircraft mounts obtained during industrial tests, the structure, electrical conductivity and mechanical properties were tested. The macrostructure tests were carried out in the cross-section of the mounting rib (Figure 8) for cast preforms, homogenized cast preforms, forgings after forging as well as forgings after forging and heat treatment, respectively. First, cross-sections were made, which were subjected to the process of grinding and polishing. Initially, grinding was applied on a SiC-coated abrasive disc with a grain size of 400 for 3 min. Then, polishing with a diamond suspension of 9 μm was applied for 3 min. The next step was polishing using a diamond suspension with a grain size of up to 3 μm for 3 min. Then polishing was carried out with colloidal silica with a grain size of 0.05 μm for 3 min. Between each step, the samples were rinsed substantially with alcohol to counteract surface oxidation. After the polished sections were made, the samples were etched by immersion and gentle stirring for 5–15 s in a solution of 100 mL ethanol, 10 mL distilled water, 10 mL acetic acid, and 5 g picric acid etchant.

Microstructural examinations were carried out using the NIKON MA200 optical microscope (Tokyo, Japan). Quantitative microstructure analysis was performed using Image-Pro 10 software. The analysis was carried out both in the central and near-surface areas of the samples, as shown in Figure 8. The chemical composition analysis in micro-areas was carried out by the EDS method using a Phenom ProX scanning electron microscope equipped with a CeB_6 crystal source and an SDD-type EDS detector.

The next performed qualitative tests were tests of specific electrical conductivity. They were carried out to evaluate the structure of the material after forging and after heat treatment. Conductivity measurements were made on the metallographic polished sections analyzed during the microstructure tests. The conductivity of the samples was measured with a SIGMATEST model 2.069 (Ferster Instruments Incorporated, Pittsburgh, PA, USA). The measurements were made at an ambient temperature of 21 °C.

Strength tests were carried out on samples made of heat-treated cast preforms and on forgings of mounts. The geometry of the samples and the test procedure were following ISO 6892-1. A Shimadzu AG-X plus 20KN testing machine (Kyoto, Japan) was used for the tests, equipped with a longitudinal extensometer to measure deformations and to control the test speed in the feedback loop. The tests were carried out under controlled conditions

at 21 °C. The speed of the test was variable. In the elastic range, the strain was controlled using the signal from the extensometer, and the speed was 0.025%/s. In the range of plastic flow, the traverse displacement speed was 0.9 mm/min.

(a) (b)

Figure 8. Microstructure test areas, (**a**) preform, (**b**) forging.

Hardness measurements were made using the Vickers method with the Future-tech FM800 hardness tester (Future-Tech Corporation, Kawasaki, Japan). Measurements were made on the HV0.5 scale following PN-EN ISO 6507-1: 2006

3. Results and Discussion

3.1. Results of Numerical Simulations

The theoretical analysis results confirmed the possibility of forming the forging of the aircraft mount from AZ61 magnesium alloy from cast preforms of an assumed geometry. Figure 9 shows the correct shape of the forging from the FEM simulation. The formed elements are correct in shape, which confirms the proper design of the process and good deformability of the cast AZ61 magnesium alloy under the assumed temperature conditions and the assumed geometry of the preforms.

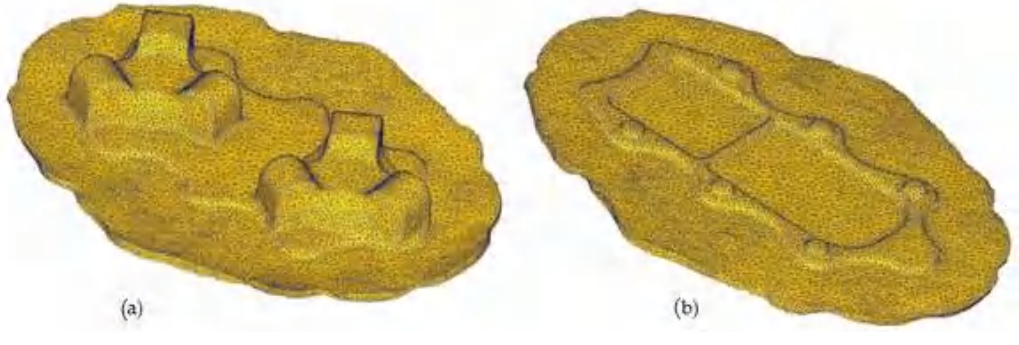

Figure 9. FEM-simulated shape of aircraft bracket forging: (**a**) top, (**b**) bottom.

The numerical analysis results also provided information on the important parameters of the process, such as strain intensity, distribution of temperature and Cockcroft–Latham damage criterion and the forming energy. The distribution of the effective strain in the

formed forging of the aircraft mount is shown in Figure 10. It can be observed that in both of the formed forgings (with smaller and higher forging degrees), the distribution of effective strain is similar and heterogeneous in the entire product. The highest values of this parameter occur in the surface areas of the bottom of the forging and in the flash, which is typical for die forging processes and for hammer forging.

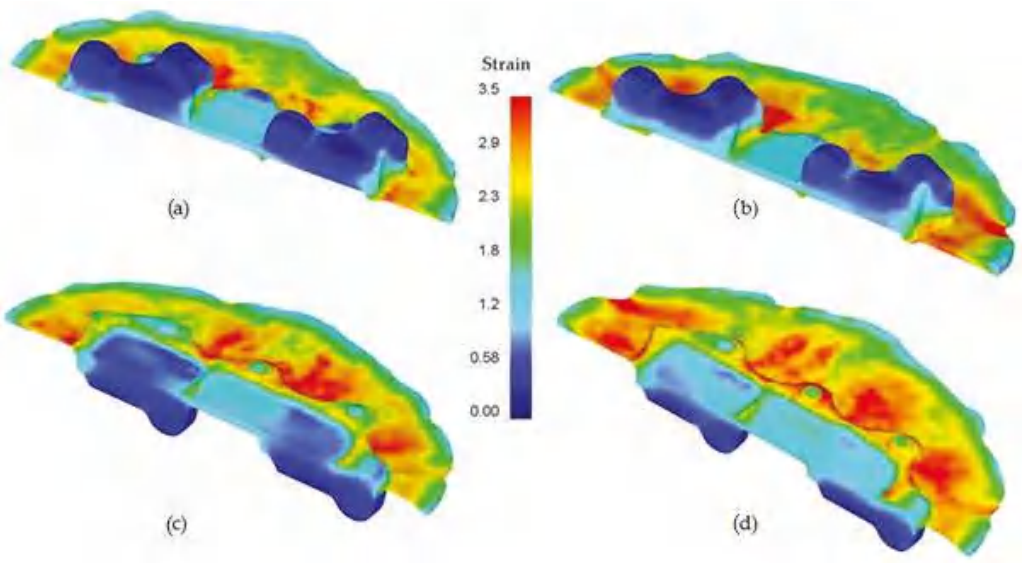

Figure 10. Distribution of the effective strain in the cross-section of the AZ61 aircraft mount: (**a**) lower degree of forging–top of the forging, (**b**) a higher degree of forging–top of the forging, (**c**) lower degree of forging–bottom of the forging, (**d**) higher degree of forging–bottom of the forging.

Additionally, the distribution of temperature in the formed forgings (Figure 11) was analyzed. It can be observed that in the areas of high strain, temperatures exceeding 410 °C occur for a preform of a lower degree of forging and around 420 °C for the other version of the preform. It is a typical distribution of those parameters in the die forging processes and does not negatively influence the quality of the products as the flash is removed. In other areas, temperatures do not exceed 400 °C.

Along with the analysis of the parameters discussed above, the risk of cracking in the forging was researched. For the theoretical analysis of this phenomenon, the Cockroft–Latham (C–L) failure criterion [35] in a modified form implemented in the Deform 3D program. This program determines the places at risk of cracking based on this criterion expressed by the formula:

$$\int_0^{\varepsilon_p} \frac{\sigma_{\max}}{\sigma_H} d\varepsilon = C_1 \quad (1)$$

where σ_{max}-maximum principal stress, σ_H-equivalent stress according to Huber's hypothesis, ε-strain intensity, C_1-integral value.

The C-L criterion assumes that when the work done by tensile stresses in uniform tension reaches a certain critical value $C_1 = C_{CL}$, plastic fracture of the material occurs. The results are shown in Figure 12. The distribution of the Cockcroft–Latham damage criterion indicates that the highest risk of cracking is on the circumference of the flash. This phenomenon remains following the industrial practice for hard-deformable materials, that is, among others, the AZ61 alloy. For this reason, radial cracks often occur on the circumference of the flash.

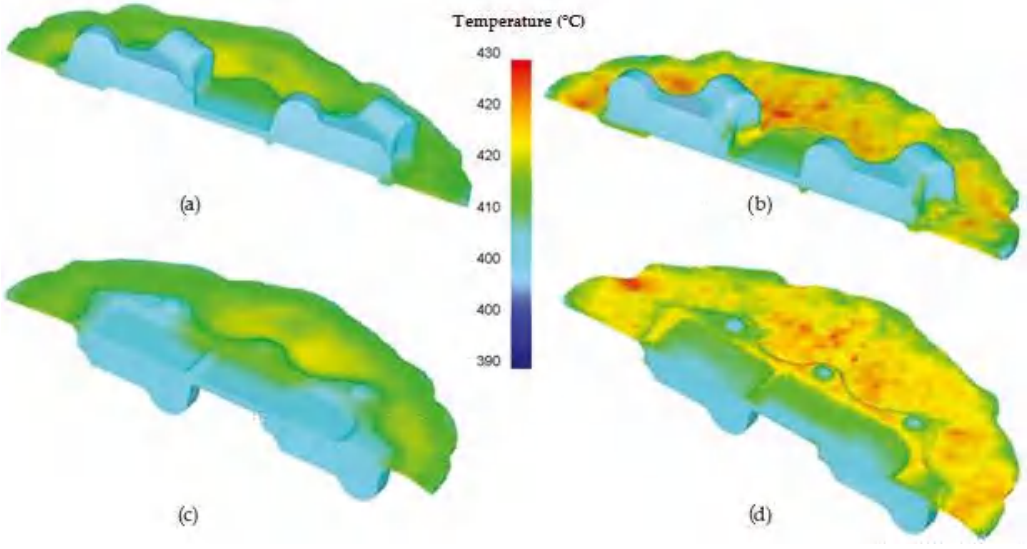

Figure 11. Distribution of temperature in the cross-section of the AZ61 aircraft mount: (**a**) lower degree of forging–top of the forging, (**b**) higher degree of forging–top of the forging, (**c**) lower degree of forging–bottom of the forging, (**d**) higher degree of forging–bottom of the forging.

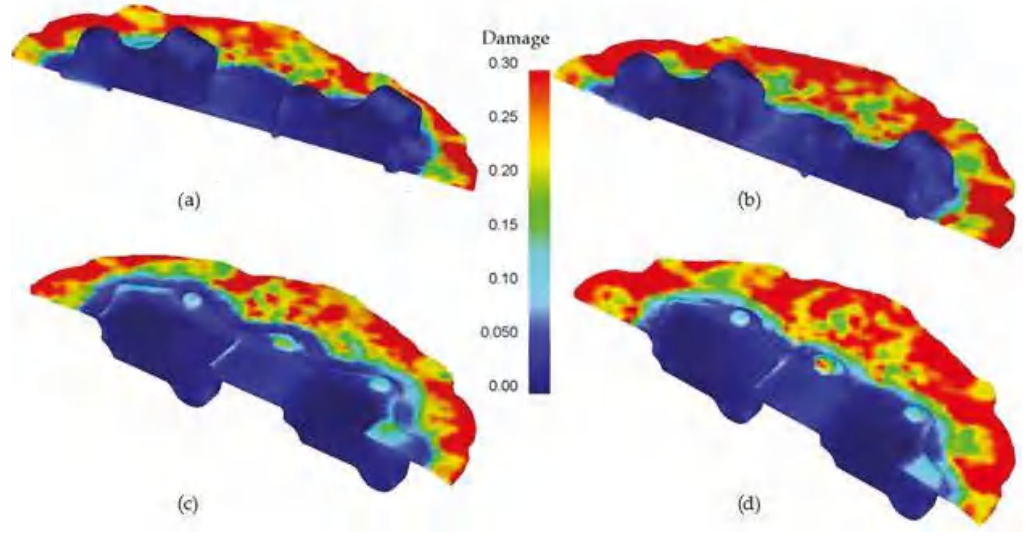

Figure 12. Distribution of the Cockcroft–Latham damage criterion in the axial section of the AZ61 aircraft forging: (**a**) lower degree of forging–top of the forging, (**b**) higher degree of forging–top of the forging, (**c**) lower degree of forging–bottom of the forging, (**d**) higher degree of forging–bottom of the forging.

FEM analysis allowed to determine the forming energy (Figure 13) occurring during forging in the die hammer in a finishing die from two designed preforms. The maximum energy needed to obtain the forging from the first (smaller) variant was approximately 21 kJ, and for the second variant, approximately 27 kJ. This justifies the conclusion that the hammer on which the process was carried out was appropriately selected.

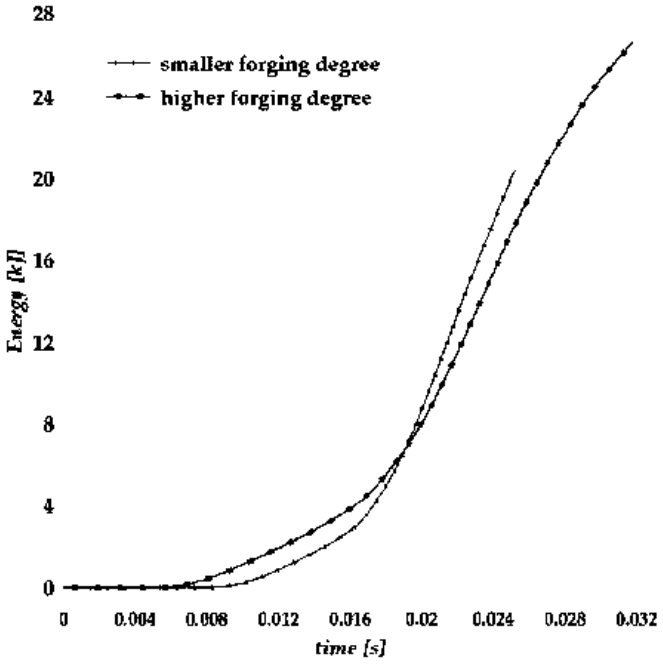

Figure 13. Scheme of the forging energy of the AZ61 aircraft mount forging for the two analyzed preforms.

Table 3 shows the comparative analysis performed in volume and material losses of forging from cast preforms with the technology of forging from an extruded rod. Forming the mount forgings from cast preforms was characterized by lower material consumption by about 47% for variant I and about 18% for variant II compared to the currently used forging technology directly from the rod.

Table 3. Comparison of the volume and material losses of forging from cast preforms with the technology of forging from an extruded rod.

Volumes and Material Loss Analyzed	Forging	Billet in the Form of Extruded Rod	Billet in the Form of Cast Preform Variant I	Billet in Form of Cast Preform Variant II
Volume (mm^3)	156,638.4	254,469	208,720.74	237,770.5
Volume of flash (mm^3)		97,830.6	52,082.34	81,132.1
Material loss (%)		62.5	33.3	51.8
Decrease in material loss (%)			47	18

3.2. The Results of Experimental Tests

The results of experimental tests carried out in industrial conditions confirm the good deformability of the AZ61cast magnesium alloy and the possibility of producing aircraft mounts from both geometry variants of the cast-shaped preforms. Figures 14 and 15 show the forgings obtained for both variants of the preforms: a lower degree of forging (Figure 14) and a higher degree of forging (Figure 15). After the visual inspection of the forgings obtained after trimming the flash and etching (Figures 14b,c and 15b,c), no laps or other surface defects were found, proving that the correct products were obtained.

Figure 14. Forging obtained for a preform with a lower degree of forging (variant I): (**a**) after forging, (**b**) top view after trimming, (**c**) bottom view after trimming.

Figure 15. Forging obtained for a preform with a higher degree of forging (variant II): (**a**) after forging, (**b**) top view after trimming, (**c**) bottom view after trimming.

3.3. The Results of Qualitative Research

Figures 16 and 17 show the reference area of the preform variant I cross-section; (a) as-cast, (b) homogenized, used to analyze the chemical composition in micro-areas. The figure shows the points where the microanalysis was performed. The measurement results are summarized in Table 4.

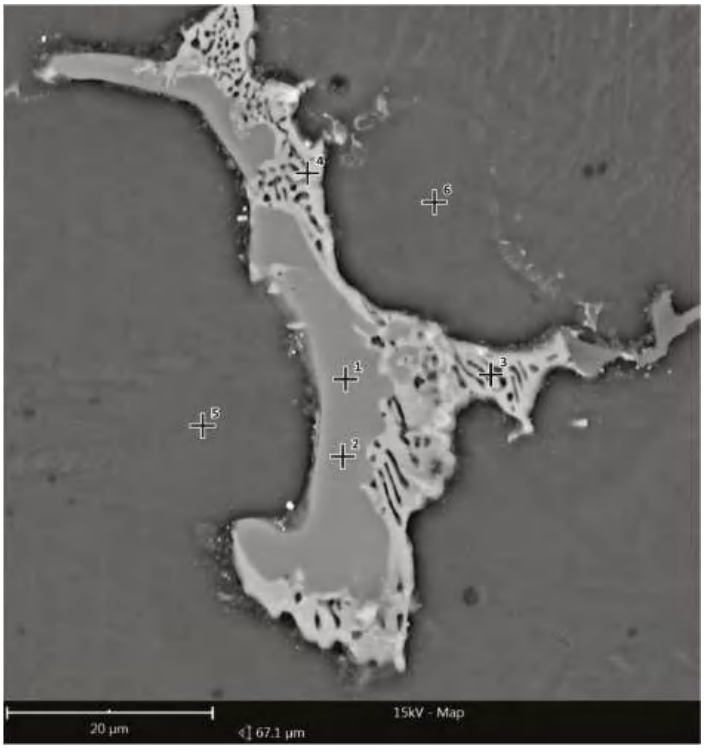

Figure 16. Reference second area of analysis marked on Figure 8 of the cast preform variant I cross-section used to analyze the chemical composition in micro-areas.

Table 4. Results of microanalysis of chemical composition by EDS method.

Scheme 1	Area	Element	Measurement Number			Mean (Weight Conc.)
			1	2	3	
Preform variant I as-cast	αMg matrix	Mg	89.45	89.33	-	89.39
		Al	7.38	7.09		7.24
		Zn	3.17	3.58		3.38
	β-Intermetallic	Mg	52.34	52.32	-	52.33
		Al	31.22	30.94		31.08
		Zn	16.44	16.74		16.59
	Eutectic	Mg	49.95	54.84	-	52.40
		Al	30.91	28.44		29.68
		Zn	19.14	16.72		17.93
Preform variant I as-castafter homogenization	Homogenized matrix	Mg	91.42	92.07	91.96	91.75
		Al	7.08	6.39	6.44	6.64
		Zn	1.50	1.55	1.61	1.55

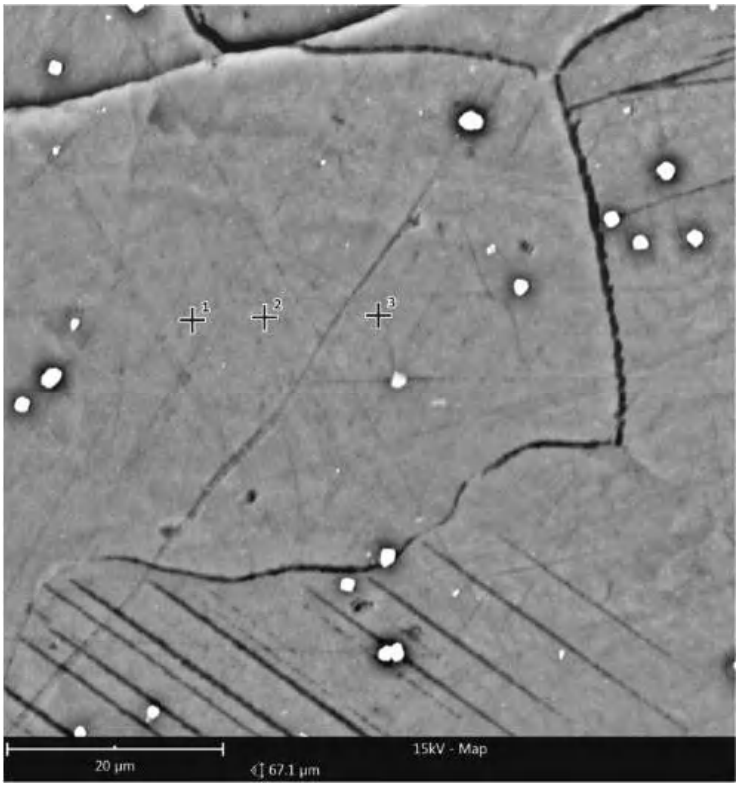

Figure 17. Reference second area of analysis marked on Figure 8 of the cast preform variant I cross-section after homogenization used to analyze the chemical composition in micro-areas.

The microanalysis results indicated a significant heterogeneity of the chemical composition of the preform in the as-cast state, which was characteristic of this type of alloy. Three basic regions were distinguished, regions of different composition: the zone of Mg solid solution with low content of alloying additives, precipitations of the intermetallic phase (most likely Mg17Al12) and eutectic regions. As a result of the homogenization process, the chemical composition became homogeneous and was close to the nominal one over the entire tested cross-section.

Based on studying the microstructure of the cast preforms in their raw state, the structures shown in Figures 18–21 were obtained.

All raw castings had a homogeneous structure throughout the tested cross-section. This structure was characteristic of this as-cast alloy and was dendritic. It consisted of chain precipitates of intermetallic phased, most of which were β phase (Mg17Al12) surrounded by eutectic precipitated. The alloy matrix was a solid solution of αMg. After homogenization of the castings, grain growth was visible, with the dissolution of most of the precipitates in the alloy matrix.

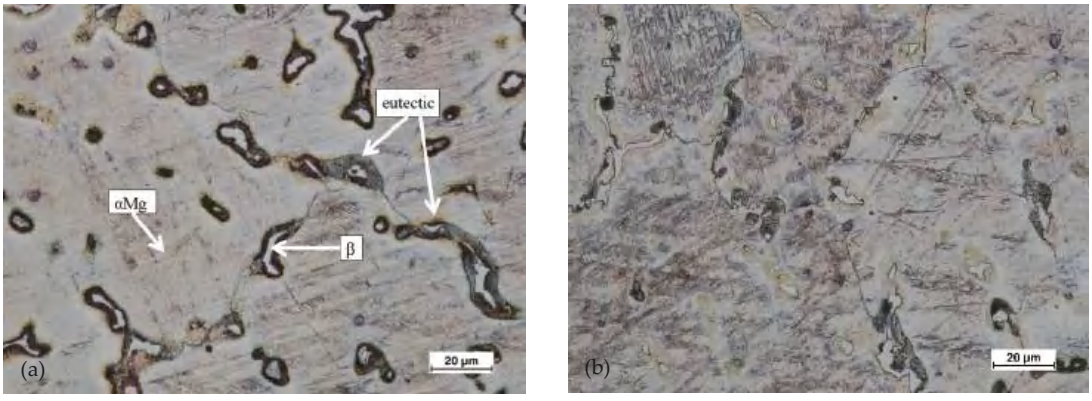

Figure 18. Microstructure for the cast preform, variant I: (**a**) first area of analysis marked on Figure 8, (**b**) second area of analysis marked on Figure 8.

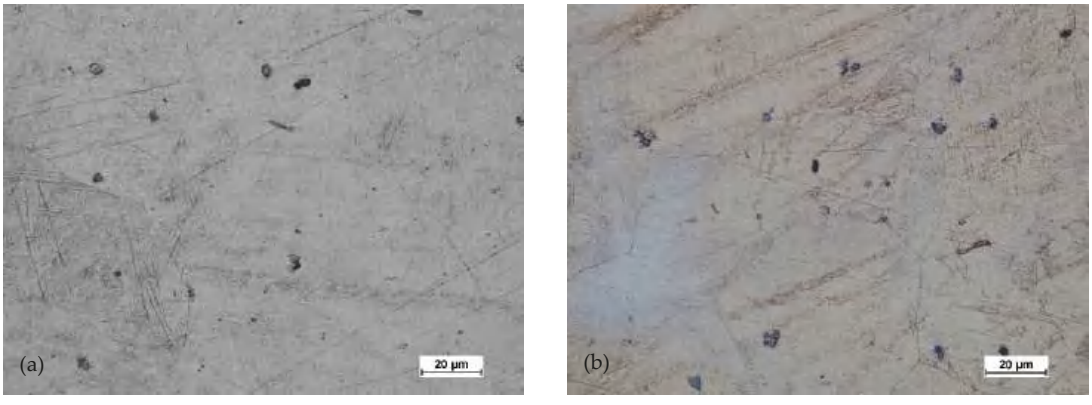

Figure 19. Microstructure for the cast preform, variant I after the homogenization process: (**a**) first area of analysis marked on Figure 8, (**b**) second area of analysis marked on Figure 8.

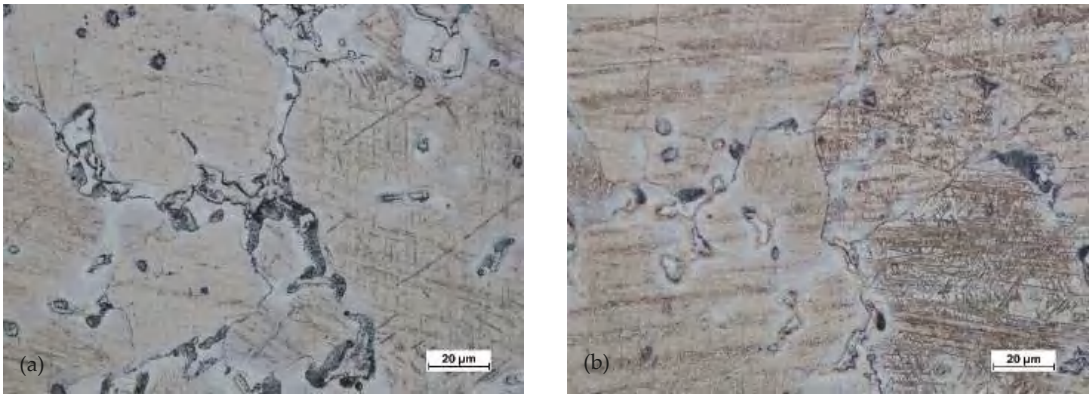

Figure 20. Microstructure for the cast preform, variant II: (**a**) first area of analysis marked on Figure 8, (**b**) second area of analysis marked on Figure 8.

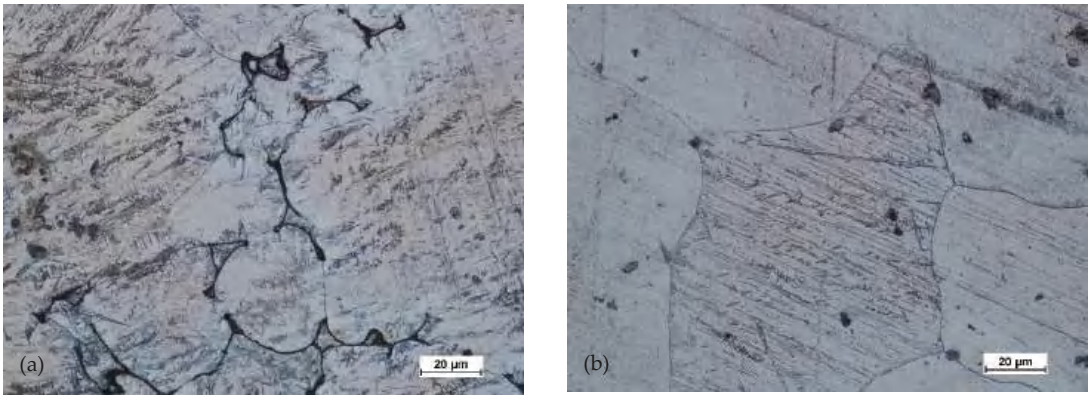

Figure 21. Microstructure for the cast preform, variant II after the homogenization process: (**a**) first area of analysis marked on Figure 8, (**b**) second area of analysis marked on Figure 8.

Figures 22–25 show the microstructures for forgings of aircraft mounts obtained in the forging process with a die hammer.

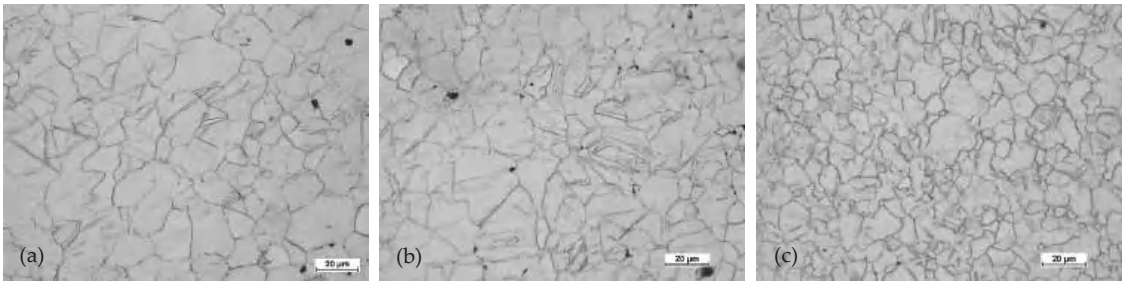

Figure 22. Microstructure for the forging obtained from the preform I: (**a**) first area of analysis marked on Figure 8, (**b**) second area of analysis marked on Figure 8, (**c**) third area of analysis marked on Figure 8.

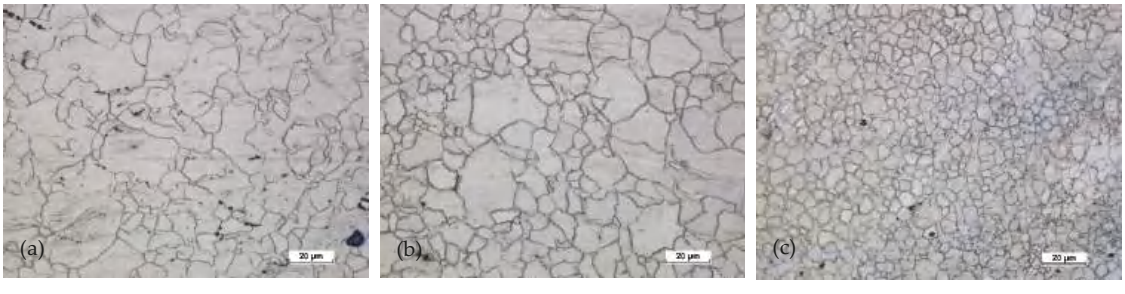

Figure 23. Microstructure for the forging obtained from the preform II: (**a**) first area of analysis marked on Figure 8, (**b**) second area of analysis marked on Figure 8, (**c**) third area of analysis marked on Figure 8.

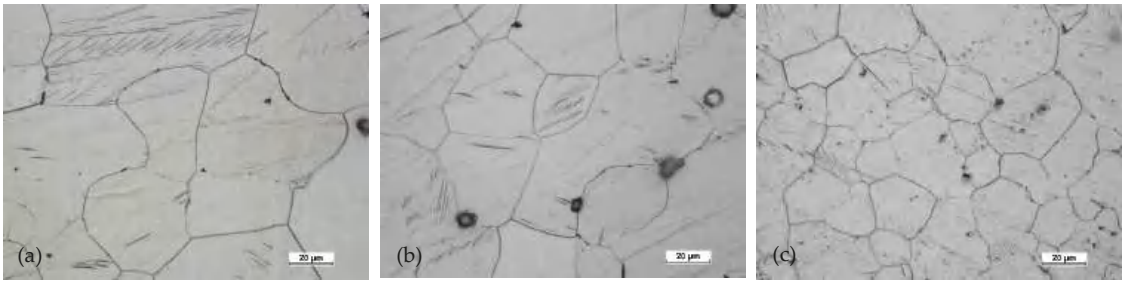

Figure 24. Microstructure for the forging obtained from preform I after forging and heat treatment: (**a**) first area of analysis marked on Figure 8, (**b**) second area of analysis marked on Figure 8, (**c**) third area of analysis marked on Figure 8.

Figure 25. Microstructure for the forging obtained from preform II after forging and heat treatment: (**a**) first area of analysis marked on Figure 8, (**b**) second area of analysis marked on Figure 8, (**c**) third area of analysis marked on Figure 8.

After the preform of the first variant was hammered, the microstructure had a significantly finer grain both in the central zone and near the surface. In the third area, with the highest intensity of deformation, the grain was the finest. The grain size was relatively uniform (for AZ61 magnesium alloy). The twin deformations were visible.

In the case of forging a higher preform (second variant), the situation was analogous. The greatest grain refinement occurs in the third area, and in areas 1 and 2, the grain sizes were less homogeneous compared to the lower preform. However, the difference was not significant. The grain size differences were acceptable. The shape of the grains in all studied areas indicated that the processes of dynamic recovery and recrystallization were significantly advanced. When comparing the structural homogeneity obtained in the considered variants of the preforms, it should be noted that, although the most favorable microstructure was obtained for area 3 of the preform II, the differences in individual areas were smaller in the case of the I variant preform. This may indicate that a high degree of forging promotes fragmentation and homogeneity. However, the differences in the individual areas indicate that the distribution of deformations in the II variant forging was less homogeneous.

Figures 24 and 25 show the microstructures of the forgings after forging and heat treatment.

After heat treatment, the grain regrowth was noticed. However, it was not as significant as after homogenization. Lenticular secondary precipitated were visible (discontinuous). In all areas, the grain size was similar, and its shape was regular.

A quantitative assessment of the microstructure was carried out in the areas analyzed on the surface of preforms and forgings. Table 5 summarizes the average values of the grain size in individual areas marked in Figure 8.

Table 5. Average grain size in the studied areas marked in Figure 8.

Sample	Mean Grain Size [μm^2] in Area:		
	1	**2**	**3**
Preform I as-cast	5300.6	-	-
Preform I after homogenization	2849.6		
Forging I	159.1	140.7	61.2
Forging II	108.8	101.1	25.3
Forging I heat-treated	1676.9	1216.6	561.3
Forging II heat-treated	793.3	1169.7	315.9

The as-cast grain size was significant, mainly due to undeveloped grain boundaries in the dendritic structure. The grain was still relatively large after homogenization. As a result of forging, the grain broke down, and due to recrystallization, the average grain size dropped significantly, especially in areas with high deformation value (3 area), as indicated by the results of numerical simulations. For the variant with a higher degree of deformation, the average grain size was smaller in all areas.

The use of heat treatment increased the grain size in all areas, particularly for variant I. The obtained results indicate that using high deformation values had a positive effect on the microstructure obtained at the end of the process.

Figures 26–30 show grain surface distributions for the analyzed areas marked in Figure 8.

The analysis of the grain size distribution in individual areas showed that in most cases, the smallest grains were the most numerous group and that there were single grains of a much larger size. In the case of forged samples, for variant I in areas 1 and 2, most of the grains had a surface area below 100 μm^2, and for area 3, below 60 μm^2. For variant II in areas 1 and 2, the values were analogous, and in area 3, most of the grains were smaller than 40 μm^2. After the heat treatment, the grain size increased and the differences in grain size in the individual areas reduced. Table 6 presents the results of measurements of the specific conductivity of the examined metallographic polished sections. The obtained resulted prove that after carrying out the heat treatment process in the form of homogenization on castings, the values of electrical conductivity decrease. Consequently, the increase in conductivity after the forging process from preforms could be detected. The highest conductivity for the considered variants of the process was shown by forgings after the forging and heat treatment, which verified that the heat treatment was carried out correctly.

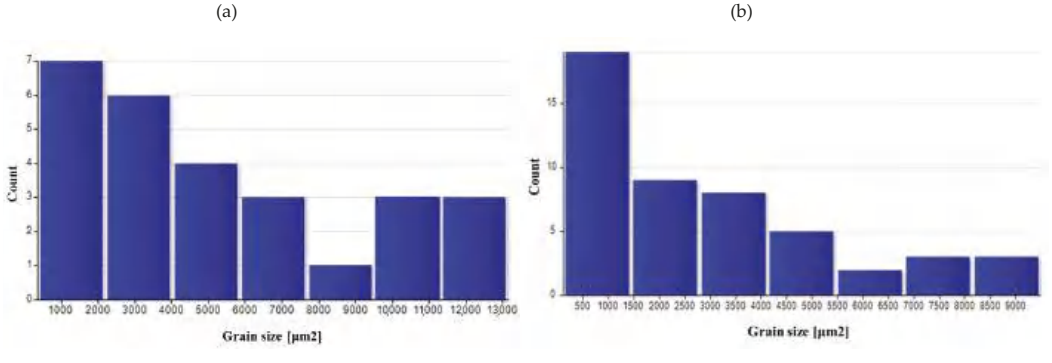

Figure 26. Grain surface distributions for the analyzed areas marked in Figure 8: (**a**) preform I as-cast in area 1, (**b**) preform I after homogenization in area 1.

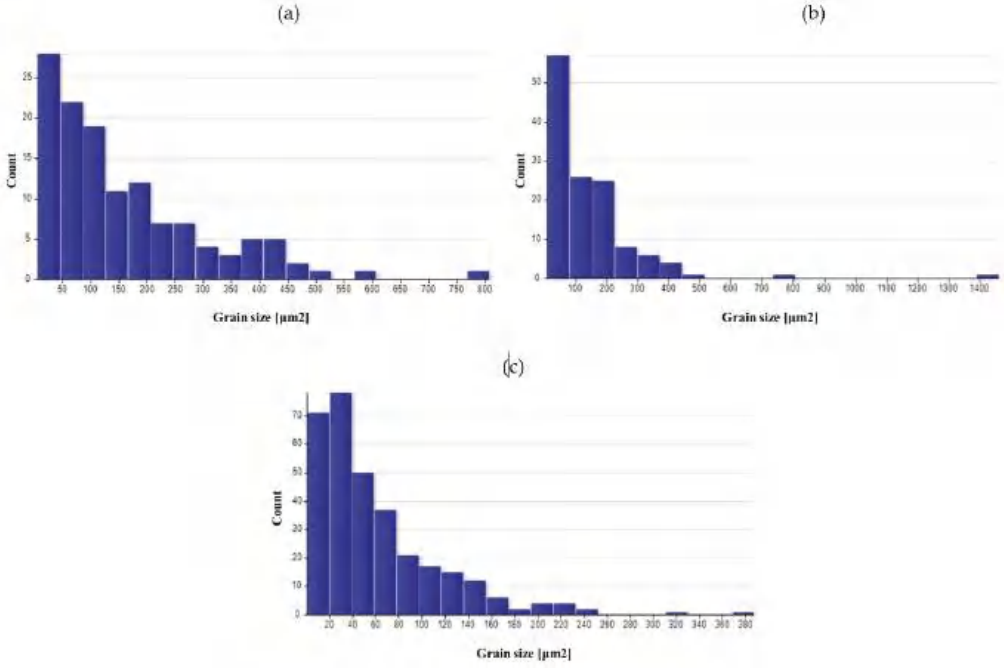

Figure 27. Grain surface distributions for the analyzed areas marked in Figure 8: (**a**) forging I area 1, (**b**) forging I area 2 (**c**) forging I area 3.

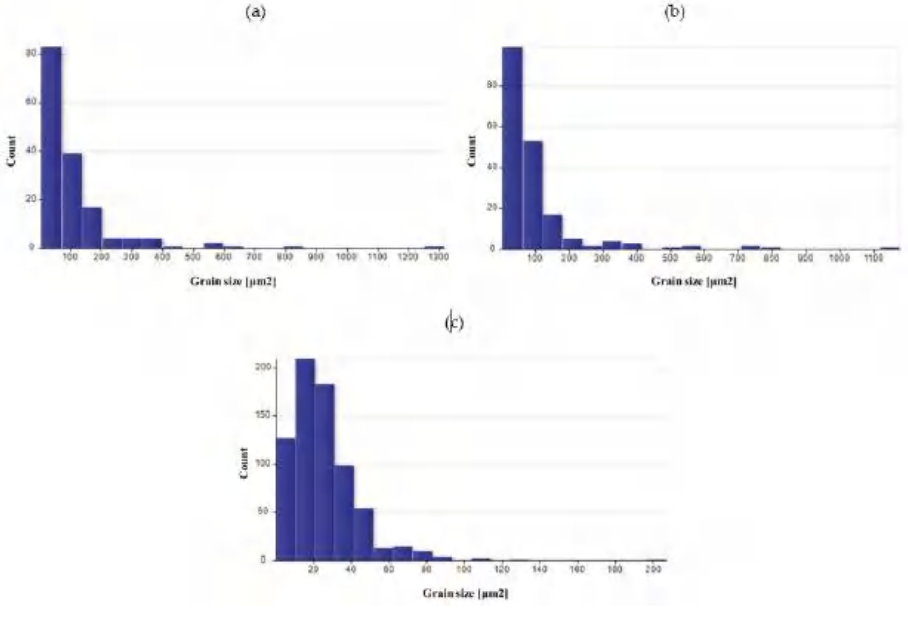

Figure 28. Grain surface distributions for the analyzed areas marked in Figure 8: (**a**) forging II area 1 (**b**) forging II area 2 (**c**) forging II area 3.

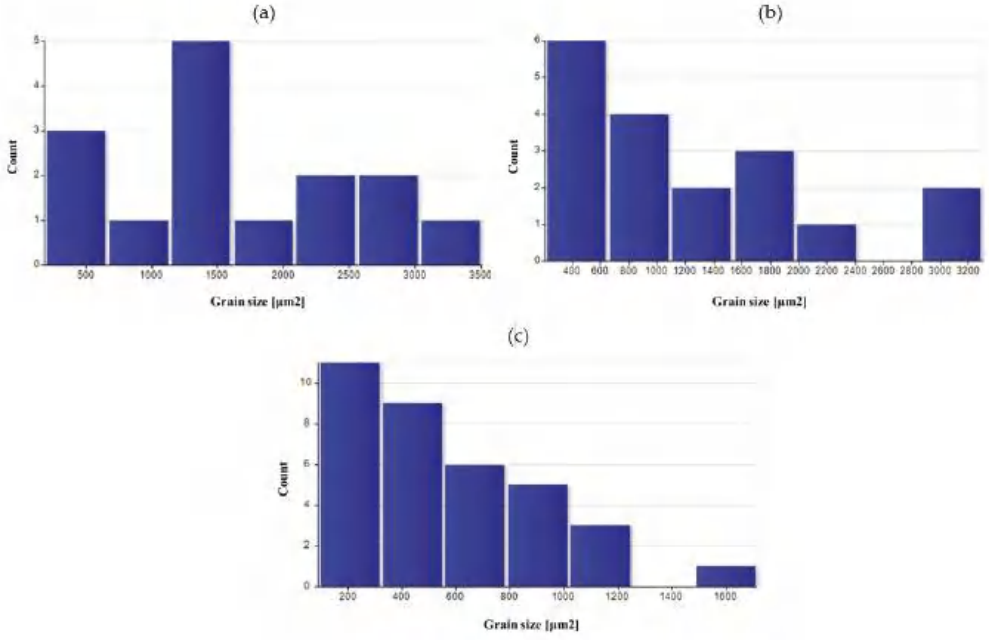

Figure 29. Grain surface distributions for the analyzed areas marked in Figure 8: (**a**) forging I heat-treated area 1, (**b**) forging I heat-treated area 2, (**c**) forging I heat-treated area 3.

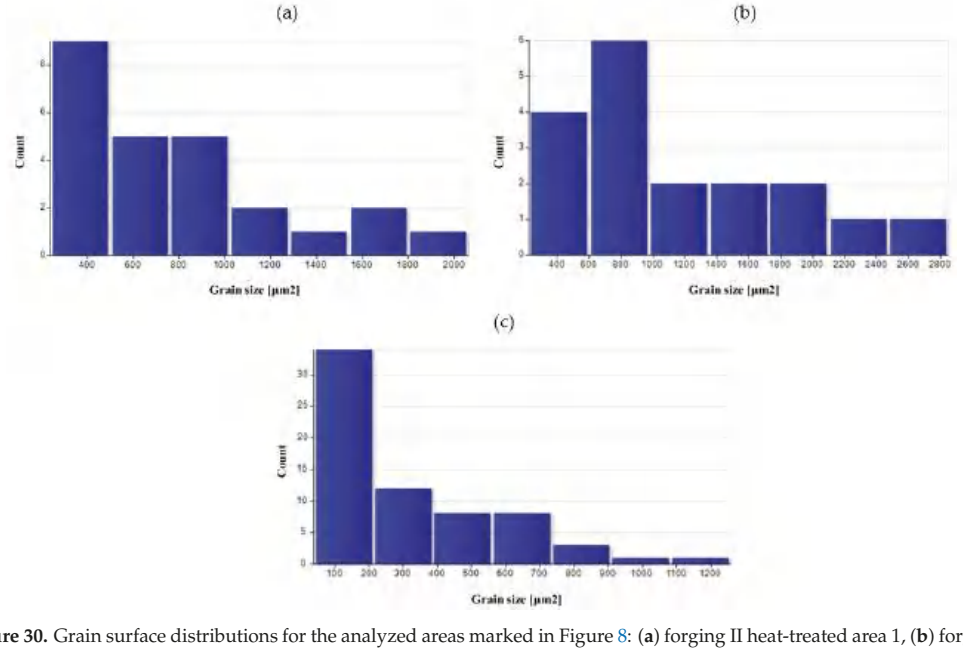

Figure 30. Grain surface distributions for the analyzed areas marked in Figure 8: (**a**) forging II heat-treated area 1, (**b**) forging II heat-treated area 2, (**c**) forging II heat-treated area 3.

Table 6. Results of specific conductivity s measurements and average grain diameter.

Sample	Measurement Number			Mean (MS/m)	Standard Deviation
	1	2	3		
Preform I after casting	8.17	8.12	8.4	8.22	0.15
Preform I after homogenization	7.46	7.39	7.46	7.43	0.04
Forging I after forging	8.39	8.52	8.39	8.43	0.07
Forging I after forging and heat treatment	9.05	8.58	9.01	8.88	0.26
Preform II after casting	9.01	9.92	8.97	8.99	0.09
Preform II after homogenization	7.86	7.76	7.80	7.80	0.05
Forging II after forging	8.28	8.62	8.00	8.30	0.31
Forging II after forging and heat treatment	9.05	9.10	8.97	9.04	0.06

Figure 31 shows example curves obtained during the static tensile test on the testing machine of samples made of AZ61 alloys. The analysis of the curves obtained in the static tensile test showed that the samples made of castings and subjected to the heat treatment process showed the smallest plasticity and tensile strength. The forgings after heat treatment were characterized by much higher strength and elongation. There were no significant differences between the samples forged using the lower and the higher preforms. The minimally higher values were in forging forged from a preform with a higher degree of forging.

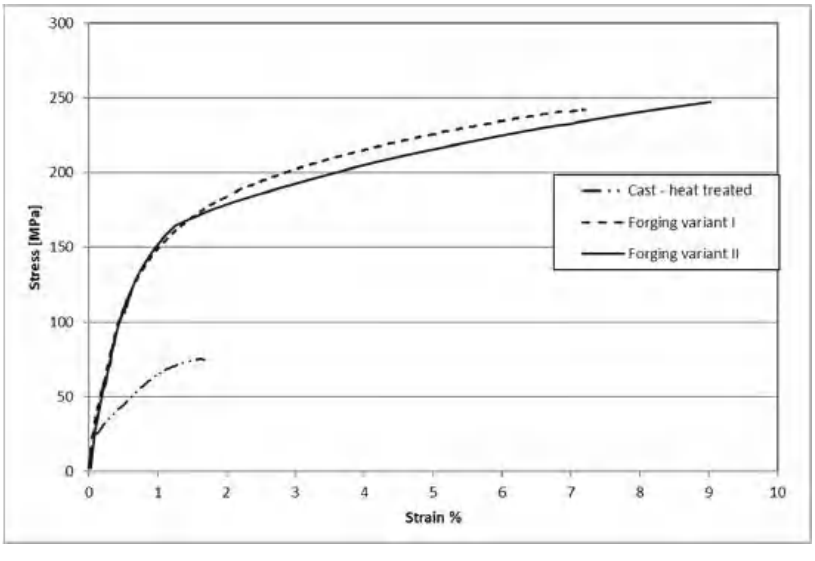

Figure 31. Example curves obtained during the static tensile test of samples made of AZ61 alloys.

Table 7 shows the results of measuring the hardness of samples made of AZ61 magnesium alloy for each of the tested variants. The hardness measurements show that in the case of AZ61 alloy, there was a slight but noticeable decrease in hardness after homogenization. As a result of forging, the hardness was increased to slightly lower than that of the casting. After thermal treatment, the hardness of the alloy increased significantly. No noteworthy differences were observed between the hardness of castings with different

geometries (preform I and preform II) when using different billet. Finally, the hardness of the hammer-forged forgings of the second variant turned out to be the highest.

Table 7. Results of hardness measurement for samples made of AZ61 alloy.

Sample	Measurement Number			Mean (HV05)	Standard Deviation
	1	2	3		
Preform I after casting	65.1	71.2	67.5	69.9	2.5
Preform I after homogenization	56.2	54.7	55.5	55.5	0.6
Forging I after forging	62.6	62.2	64.2	63.0	0.9
Forging I after forging and heat treatment	73.6	74.4	72.1	73.4	1.0
Preform II after casting	68.6	69.1	67.3	68.3	0.08
Preform II after homogenization	52.2	56.7	57.4	55.4	2.3
Forging II after forging	62.1	65.5	63.1	63.6	1.4
Forging II after forging and heat treatment	77.7	73.9	74.9	75.5	1.6

4. Summary and Conclusions

Based on the analyses conducted, the following conclusions were formulated:

- The objective of this study was to investigate the formability of AZ61 cast magnesium alloy using the example of an innovative technique for producing forging of aircraft mounts by hammer forging from cast preforms. The numerical and experimental results demonstrate that AZ61 cast magnesium alloy in sand molds has good formability in the hammer die forging process, and the proposed new forging method is a viable way of producing forgings of aircraft mounts with the required shape. The new method ensures considerable material and energy savings and higher properties of the product than previously applied techniques, consisting of forming aircraft mounts only from casts by machining operations.

The developed new technology of forging from preforms assumes greater production efficiency due to the shortening of the time of forging in one forging operation compared to the multi-stage forging from the extruded rod used in the industry.

- Structural studies have shown that the material's structure undergoes substantial evolution at different stages of the process. Homogenization results in obtaining a consistent initial structure for the die forging process. After forging, significant grain refinement was observed, which is not uniform throughout the forging volume, but the grain size differences are perfectly acceptable. Further heat treatment makes the grain sizes and shapes uniform and allows the alloy to be strengthened by secondary precipitation. The conducted tests and conductivity analysis confirm the observed evolution of the material's microstructure during the process. The detected decrease in hardness promotes forming, while its significant increase after heat treatment has a positive effect on the performance of forgings. Small differences in the values obtained for variants I and II may result, first of all, from the different cooling kinetics of castings with different volumes and the different degree of forging. Finally, variant II has higher mechanical properties and conductivity, but the differences are small. Comparing the maximum values of the strength and hardness properties of the new forging technology from forgings to the traditional rod forging technology, they are as follows: new technology-Rm = 250 MPa, HV = 75.5; bar forging-Rm = 292 MPa, HV = 65.7 [35].
- Lightweight magnesium alloys belong to the group of construction materials considered key importance for the future. Therefore, it is necessary to conduct further research developing the technique for manufacturing magnesium alloy products using

forging hammers that have significantly higher output capacity than hydraulic presses. The positive results of previous studies on the hammer forging process from AZ61 magnesium alloy-shaped cast preforms prove that the research should be continued for other workable magnesium alloys.

Author Contributions: Conceptualization, A.D., P.S., K.M.; methodology, A.D., K.M.; software, A.D., P.S.; investigation, A.D., P.S., K.M.; resources, A.D., writing—original draft preparation, A.D., P.S., K.M.; visualization, A.D., P.S., K.M.; All authors have read and agreed to the published version of the manuscript.

Funding: Project "The Design and Implementation of an Innovative Low-Waste Metal Forming Technology for High-Strength Light Metal Alloys Used in the Aircraft and Automotive Industry"; no. LIDER/10/0058/L-8/16/NCBR/2017. The total cost of the project: 1,200,000 PLN. The project is financed by the National Centre for Research and Development under the 8th edition of the LIDER Program.

Institutional Review Board Statement: Not applicable.

Informed Consent Statement: Not applicable.

Data Availability Statement: The data presented in this study are available on request from the corresponding author. The data are not publicly available due to protection of intellectual property.

Conflicts of Interest: The authors declare no conflict of interest.

References

1. Kainer, K. *Magnesium—Alloys and Technologies*; Wiley: Weinheim, Germany, 2003.
2. Papenberg, N.P.; Gneiger, S.; Weißensteiner, I.; Uggowitzer, P.J.; Pogatscher, S. Mg-Alloys for Forging Applications—A review. *Materials* **2020**, *13*, 985. [CrossRef] [PubMed]
3. Wu, Y.; Liu, J.; Deng, B.; Ye, T.; Li, Q.; Zhou, X.; Zhang, H. Microstructure, Texture and Mechanical Properties of AZ31 Magnesium Alloy Fabricated by High Strain Rate Biaxial Forging. *Materials* **2020**, *13*, 3050. [CrossRef] [PubMed]
4. You, S.; Huang, Y.; Kainer, K.U.; Hort, N. Recent research and developments on wrought magnesium alloys. *J. Mag. Alloys* **2017**, *5*, 239–253. [CrossRef]
5. Song, J.; She, J.; Chen, D.; Pan, F. Latest research advances on magnesium and magnesium alloys worldwide. *J. Mag. Alloys* **2020**, *8*, 1–41. [CrossRef]
6. Jayasathyakawin, S.; Ravichandran, M.; Baskar, N.; Anand Chairman, C.; Balasundaram, R. Mechanical properties and applications of Magnesium alloy—Review. *Mater. Today Proc.* **2020**, *27*, 909–913. [CrossRef]
7. Blawert, C.; Hort, N.; Kainer, K.U. Automotive applications of Mg and its alloys. *Trans. Indian Inst. Metal.* **2004**, *57*, 397–408.
8. Bohlen, J.; Letzig, D.; Kainer, K.U. New Perspectives for Wrought Magnesium Alloys. *Mater. Sci. Forum.* **2007**, *546–549*, 1–10. [CrossRef]
9. Kulekci, M.K. Magnesium and its alloys applications in automotive industry. *Int. J. Adv. Manuf. Technol.* **2008**, *39*, 851–865. [CrossRef]
10. Dziubinska, A.; Gontarz, A.; Zagorski, I. Qualitative research on AZ31 magnesium alloy aircraft brackets with a triangular rib produced by a new forging method. *Aircr. Eng. Aerosp. Technol.* **2018**, *90*, 482–488. [CrossRef]
11. Dehghanghadikolaei, A.; Ibrahim, H.; Amerinatanzi, A.; Elahinia, M. *Metals for Biomedical Devices*; 9—Biodegradable Magnesium Alloys; Woodhead Publishing: Cambride, UK, 2019; pp. 265–289.
12. Ibrahim, H.; Dehghanghadikolaei, A.; Advincula, R.; Dean, D.; Luo, A.; Elahinia, M. Ceramic coating for delayed degradation of Mg-1.2Zn-0.5Ca-0.5Mn bone fixation and instrumentation. *Thin Solid Films* **2019**, *687*, 137456. [CrossRef]
13. Xie, W.; Zhao, Y.; Liao, B.; Pang, P.; Wuu, D.; Zhang, S. Al–AlN composite coatings on AZ31 magnesium alloy for surface hardening and corrosion resistance. *Vacuum* **2021**, *188*, 110146. [CrossRef]
14. Heimann, R.B. Magnesium alloys for biomedical application: Advanced corrosion control through surface coating. *Surf. Coat. Technol.* **2021**, *405*, 126521. [CrossRef]
15. Dziubinska, A.; Gontarz, A.; Dziedzic, K. Qualitative research of AZ31 magnesium alloy aircraft brackets produced by a new forging method. *Arch. Met. Mater.* **2016**, *61*, 1003–1008. [CrossRef]
16. Gontarz, A.; Winiarski, G. Numerical and experimental study of producing flanges on hollow parts by extrusion with a movable sleeve. *Arch. Met. Mater.* **2015**, *60*, 1917–1921. [CrossRef]
17. Balaji, V.; Raja, V.B.; Palanikumar, K.; Ponshanmugakumar; Aditya, N.; Rohit, V. Effect of heat treatment on magnesium alloys used in automotive industry: A review. *Mater. Proc.* 2021. [CrossRef]
18. Davis, A.E.; Kennedy, J.R.; Lunt, D.; Guo, J.; Strong, D.; Robson, J.D. Preageing of magnesium alloys. *Mater. Sci. Eng.* **2021**, *809*, 141002. [CrossRef]

19. ASTM B661-12(2020). *Standard Practice for Heat Treatment of Magnesium Alloys*; ASTM International: West Conshohocken, PA, USA, 2020.
20. Hadasik, E.; Kuc, D. Plastic forming of magnesium alloys. *Met. Form.* **2013**, *19*, 131–146.
21. Kawalla, R. Magnesium and magnesium alloys. In *Processing of Metals, Plasticity and Structure*; Silesian University of Technology Publishing House: Gliwice, Poland, 2006.
22. Vargel, C. *Corrosion of Aluminium*; Elsevier: Oxford, UK, 2020.
23. Sakai, T.; Nakata, T.; Miyamoto, T.; Kamado, S.; Liao, J. Tensile creep behavior of a die-cast Mg–6Al-0.2Mn–2Ca-0.3Si (wt.%) alloy. *Mater. Sci. Eng. A* **2020**, *774*, 138841. [CrossRef]
24. Weiler, J.P. Exploring the concept of castability in magnesium die-casting alloys. *J. Magnes. Alloys* **2021**, *9*, 102–111. [CrossRef]
25. Kula, A.; Tokarski, T.; Niewczas, M. Comparative studies on the structure and properties of rapidly solidified and conventionally cast AM60 magnesium alloys. *Mater. Sci. Eng.* **2019**, *759*, 346–356. [CrossRef]
26. Wang, Q.; Zhang, Z.; Zhang, X.; Yu, J. Precision forging technologies for magnesium alloy bracket and wheel. *Trans. Nonfer. Met. Soc. China* **2008**, *18*, 205–208. [CrossRef]
27. Yang, Z.; Li, J.P.; Zang, J.X.; Lorimer, G.W.; Robson, J. Review on research and development of magnesium alloys. *Acta Met. Sin. (Engl. Lett.)* **2008**, *21*, 313–328. [CrossRef]
28. Gziut, O.; Kuczmaszewski, J.; Zagórski, I. Analysis of chip fragmentation in AZ91HP alloy milling with respect to reducing the risk of chip ignition. *Ekspolatacja i Niezawodn.-Maint. Reliab.* **2016**, *18*, 73–79. [CrossRef]
29. Kuczmaszewski, J.; Zagórski, I.; Dziubińska, A. Investigation of Ignition Temperature, Time to Ignition and Chip Morphology after the High-Speed Dry Milling of Magnesium Alloys. *Air. Eng. Aerosp. Technol.* **2014**, *88*, 1–11. [CrossRef]
30. Matuszak, J.; Zaleski, K. Edge states after wire brushing of magnesium alloys. *Air. Eng. Aerosp. Technol.* **2014**, *86*, 328–335. [CrossRef]
31. Nars, M.N.A.; Outeiro, J.C. Sensitivity Analysis of Cryogenic Cooling on Machining of Magnesium Alloy AZ31B-O. *Proc. Cirp* **2015**, *31*, 264–269.
32. Gontarz, A.; Drozdowski, K.; Dziubinska, A.; Winiarski, G. A study of a new screw press forging process for producing aircraft drop forgings made of magnesium alloy AZ61A. *Air. Eng. Aerosp. Technol.* **2018**, *90*, 559–565. [CrossRef]
33. Palaniswamy, H.; Ngaile, G.; Altan, T. Finite element simulation of magnesium alloy sheet forming at elevated temperatures. *J. Mater. Proc. Technol.* **2004**, *146*, 52–60. [CrossRef]
34. Gontarz, A.; Dziubińska, A.; Okoń, Ł. Determination of friction coefficients at elevated temperatures for some Al, Mg and Ti alloys. *Arch. Metall. Mater.* **2011**, *56*, 379–394. [CrossRef]
35. Cockcroft, M.G.; Latham, D.J. Ductility and the workability of metals. *J. Inst. Met.* **1968**, *96*, 33–39.

materials

MDPI

Article

Modeling of the Closure of Metallurgical Defects in the Magnesium Alloy Die Forging Process

Grzegorz Banaszek, Teresa Bajor *, Anna Kawałek and Marcin Knapiński

Faculty of Production Engineering and Materials Technology, Czestochowa University of Technology, 42-201 Czestochowa, Poland

* Correspondence: teresa.bajor@pcz.pl

Abstract: The article discusses the impact of hot forging elongation operations on the closure of metallurgical discontinuities such as middle porosity in selected magnesium alloys (AZ91) depending on the shape of the input used. Numerical modeling was carried out using the Forge®NxT 2.1 program based on the finite element method and laboratory modeling in order to bring about the closure of defects of metallurgical origin in deformed forging ingots. On the basis of the conducted research, optimal values of the main technological parameters of forging and appropriate groups of anvils to be used in individual stages of forging were proposed in order to eliminate metallurgical defects.

Keywords: magnesium alloy AZ91; physical modeling; forging; closure of discontinuities

Citation: Banaszek, G.; Bajor, T.; Kawałek, A.; Knapiński, M. Modeling of the Closure of Metallurgical Defects in the Magnesium Alloy Die Forging Process. *Materials* **2022**, *15*, 7465. https://doi.org/10.3390/ma15217465

Academic Editor: Ivo Schindler

Received: 19 September 2022
Accepted: 20 October 2022
Published: 25 October 2022

1. Introduction

The search for lightweight construction materials characterized by favorable strength parameters is still a leading topic among the scientific community. In the current political and economic situation, with turbulence in the energy market, reducing the weight of cars and fuel consumption and reducing the impact of greenhouse gases emitted by cars is an important element for consumers [1–3]. Magnesium alloys, as the lightest construction materials and showing good heat dissipation and vibration damping, are gaining and finding more and more applications in the automotive industry [4–12]. A large number of magnesium alloy products are obtained mainly in extrusion and stamping processes, less often in rolling and forging processes. We should pay attention to forged products made of magnesium alloys due to their homogeneous microstructure and improved mechanical properties compared with cast alloy elements. Designing forging technology requires a comprehensive approach to the research problem posed. High variability of shaping parameters such as: temperature; sequence of operations and technological treatments, for example, turning the material and applying deformations using anvils during forging elongation operations; values of applied reductions; relative feed values; deformation speed; and shape-dimensional parameters of the working surfaces of anvils makes obtaining forgings made of high-quality magnesium alloys with a homogeneous microstructure throughout the whole volume an extremely difficult matter. Due to the hexagonally compact crystallographic structure, magnesium alloys have limited plasticity and poor deformability at ambient temperature. The correct implementation of the free-forging process in flat and shaped anvils of selected magnesium alloys allows obtainment of a product with satisfactory final properties [13,14]. Shaping products by forging methods provides a method to close metallurgical discontinuities formed at the stage of production of the input material. In the case of forming high-quality products, especially in terms of the absence of metallurgical discontinuities, the application of the lengthening operation is, according to the authors, an innovative method of charge preparation, which enables their liquidation. The elongating operation in flat anvils creates such a state of stress that favors the welding of metallurgical discontinuities. The analysis of methods of closing metallurgical defects in the cross-section of forgings is presented in the works [15–21],

where it was shown that the closure of metallurgical defects in deformed forgings is influenced by the main parameters of the forging process, such as reduction, relative feed, charge temperature, and the shape and dimensions of anvils.

2. Test Objective and Scope

The aim of the study was to investigate the influence of elongation operations on the closure of metallurgical discontinuities of the middle porosity type depending on the shape of the applied input.

In order to realize the aim of the work set out in this way, the authors proposed that hot forging elongation operations should be carried out using flat anvil assemblies.

In order to achieve the goal of the proposed work, numerical studies of elongation operations in flat anvil assemblies for two geometric shapes of samples were carried out.

Modeling of elongation operations was performed using Forge®NxT 2.1 based on FEM, which allows tracking changes in temperature distributions, hydrostatic pressure, and strain intensity in the plastically processed magnesium alloy AZ91. The distributions of temperature values, hydrostatic pressure, and strain intensity over the cross-section of the deformed alloy after each forging pass were determined.

During tests of forging elongation operations, the results of plastometric tests on a given AZ91 alloy were used, on the basis of which stress–strain dependence diagrams of the actual alloy were developed and the coefficients of the plasticizing stress function were selected [13,14]. The ranges of deformation, deformation speed, and temperature changes during the theoretical research were assumed on the basis of the characteristics of forging machines used in real forging processes, and on the basis of literature data and the authors' own research carried out at the Department of Plastic Processing and Safety Engineering of the Czestochowa University of Technology [13–26].

In order to compare the results of numerical modeling with the actual laboratory process, the samples were deformed using the Gleeble 3800® metallurgical processes simulator. On the basis of the conducted research, an analysis of the influence of the geometric shape of the input on the welding of the modeled internal metallurgical discontinuity of the middle porosity type was carried out. Physical verification of the numerical model was also carried out to determine the structure of the forged magnesium alloy AZ91 in the discontinuity modeled zone and a comparison of this structure with the discontinuity zone.

The results of the tests should contribute to improving the structural and mechanical properties of AZ91 alloy bars through the appropriate selection of the shape of the feedstock.

3. Materials and Methods

The material chosen for the tests was magnesium alloy AZ91 with a chemical compositions as provided in Table 1.

Table 1. Chemical composition of the investigated alloy [%].

Alloy	Zn	Al	Si	Cu	Mn	Fe	Ni	Mg
AZ91	0.59	8.98	0.05	0.006	0.23	0.013	0.003	R

4. Methodology of Numerical Research

The elongation operation in flat anvils of four samples made of magnesium alloy AZ91 was analyzed. Two samples were in the shape of a cube measuring 10 × 10 × 10 mm, and two more were in the shape of a cylinder with a diameter of 10 mm and a length of 10 mm. In two samples of different shapes, an axial internal discontinuity was modeled by making a hole in the axes of the samples with a diameter of 2 mm equal to their length. For the purposes of numerical modeling, the sample model was made in the AutoCad 2009® computer program and the designed discontinuity was treated as the difference in volume between the sample and the discontinuity.

To model the elongation operation, a commercial computer program on PC FORGE®NxT 2.1 was used, which is a product of Transvalor Solution, based on the finite element method (FEM) [27]. This program allows for thermomechanical simulation of, among others, plastic processing. A detailed description of temperature, energy, strain, and deformation functions as well as thermomechanical and friction laws, used during the calculations, can be found in the papers [13,14,16]. Calculation of thermal properties was made by using the Galerkin equation, while the strengthening curves were approximated by the Hensel–Spittel equation [28]. In the paper, to simulate the elongation operation, a thermo-viscoplastic model of the deformed body, which is based on the theory of large plastic deformations, was used. To generate the grid of finite elements, tetrahedral elements with the base of triangles were used. In the generated model input, the number of nodes equal to 3369 was used for simulation, while the number of tetrahedral elements adopted for the simulation was 30,084. In addition, in the axial area where there was a modeled discontinuity due to the mesh compaction tool in the program, 9116 nodes were generated, which accounted for 58,726 elements. This was done in order to increase the accuracy of calculations and to more accurately illustrate the mechanism of discontinuity welding, which then affected the accuracy of the obtained results and the subsequent analysis of these results. The value of the coefficient of friction between the surface of the anvils and the deformed rod was determined to be $\mu = 0.3$ according to Coulomb's law. It was assumed that the heat transfer coefficient between the anvils and the material is h = 10,000 W/m^{2}K, while the heat transfer coefficient between the metal and the environment is equal to h = 10 W/m^{2}K. The ambient temperature was assumed to be equal to 20 °C, while the temperature of the anvils was equal to 300 °C. The initial temperature of the input before the elongation operations in its entire volume was assumed to be the same and equal to 400 °C. The feed speed of the upper anvil was equal to v = 8 mm/s, while the lower anvil was assumed to be stationary in all forging passages for all four samples. During numerical modeling, all four samples were deformed with a relative reduction of 35%, then rotated clockwise by an angle of 90° and deformed again with a reduction in the same value. The same boundary and initial conditions were assumed during physical modeling carried out in the Gleeble 3800® metallurgical processes simulator.

5. Analysis of Distributions of Temperature Values, Effective Strain, and Hydrostatic Pressure during the Elongation Operation of a Circular Sample

The results of the tests concerning the distribution of temperature values, effective strain, and hydrostatic pressure values during the elongation operation of samples with a circular cross-section made of magnesium alloy AZ91 are shown in Figures 1–11.

The data in Figure 1 show that in the axial zone of the sample, the temperature after deformation was 386 °C, it is a decrease of 14 °C compared with the initial forging temperature, which is 400 °C. In the areas to the right and left of the sample, the temperature was much higher at 388 °C. The material flowed freely in these zones, unrestricted by the working surfaces of the anvils, and despite contact with the environment at the assumed temperature of 20 °C, it did not cool significantly due to a large deformation work, which influenced maintaining the temperature close to the initial temperature. In the upper and lower part of the sample, along the *y*-axis, there was a temperature drop of 10 °C from the initial temperature. This was the result of heat transfer to the anvils, which were heated before being deformed to 300 °C. The anvils were heated to such a temperature that the heat flow from the sample toward the working surfaces of the anvils was not significantly large. In the actual conditions of industrial forging, the anvils are heated to a temperature range of 200–300 °C before the elongation operation, so that the forged material does not cool down too quickly in subsequent forging transitions. The first anvil transition is not heated because it maintains its temperature due to the flow of heat from the deformed material in subsequent transitions.

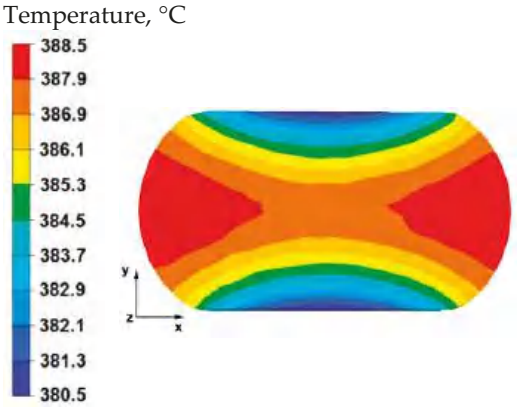

Figure 1. Distribution of temperature values on the surface of the cross-section of the sample with modeled discontinuity—after deformation with 35% reduction.

By analyzing the data presented in Figure 2, it can be stated that after rotating the sample by 90° and deforming again with a relative reduction of 35%, in the middle part of the sample along the *x* axis there was a temperature drop of 26 °C from the initial temperature. Despite the large work of deformation caused by the significant reduction, the temperature drop was due to the longer duration of the second forging transition. The longer duration of the second forging transition was associated with the rotation of the sample by an angle of 90°. In the zones of the material lying under the working surfaces of the anvils, a temperature equal to 367 °C was recorded, this is a decrease of 33 °C from the temperature at the beginning of forging process.

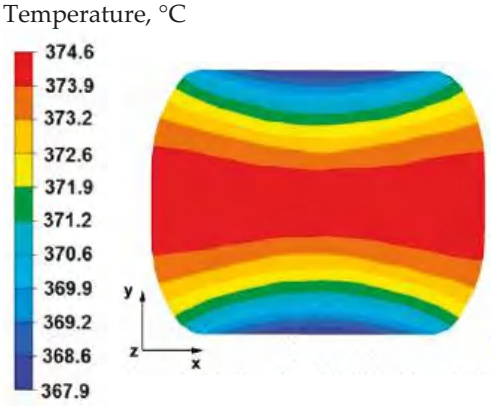

Figure 2. Distribution of temperature values on the surface of the cross-section of the sample with modeled discontinuity after rotation by 90° and re-deformation with 35% reduction.

Figures 3 and 4 compare the distributions of the effective strain after deformation of the sample with the modeled discontinuity (Figure 3) and without the modeled discontinuity (Figure 4). The data presented in these figures show that in the axial zone of the sample with modeled discontinuity, there was a disturbance in the deformation intensity distribution. This was due to the intensification of deformations within the welded discontinuity. The shape of the welded discontinuity (the hole inside the cylinder-shaped sample) influenced the different nature of the metal flow in the zone of its occurrence; it was related to different directions of the friction and pressure force vectors, which were initiated by a change in

the geometric shape of the welded discontinuity during the growing reduction that occurs during deformation. In the sample without discontinuities (Figure 4) this phenomenon was not observed, only the external shape of the deformed sample and the shape of flat anvils, which forced such and no other flow of the deformed alloy, were responsible for the directions of the vectors of friction forces and pressure. The deformation intensity values in the axial zone of the sample with discontinuity (Figure 3) ranged from 1.20 to 1.50, and in the same zone in the sample without discontinuities (Figure 4) were within the range of 0.70–0.90. In other zones outside the area of occurrence of the welded discontinuity in both cases, the distribution of the deformation value was of the same nature and its value was in the range of 0.19–0.62.

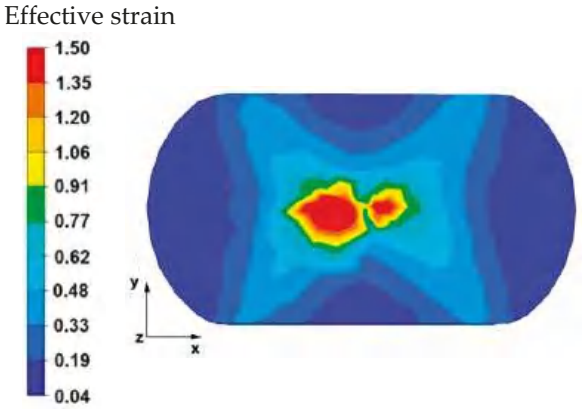

Figure 3. Distribution of the effective strain values on the surface of the cross-section of the sample with modeled discontinuity after deformation with 35% reduction.

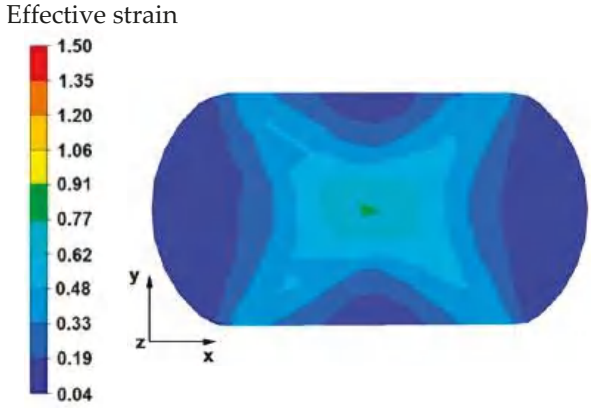

Figure 4. Distribution of the effective strain value on the surface of the cross-section of the sample without the modeled discontinuity after deformation with 35% reduction.

By analyzing the data in Figures 5 and 6, it can be stated that the distributions of the hydrostatic pressure values do not show such intense changes in the metal flow in the discontinuity zone compared with the sample without discontinuities (Figures 3 and 4). There is a difference in the axial zones of both samples, but the difference is not significant and amounts to 17 MPa. In other sample zones, the distribution of hydrostatic pressure values is the same, which indicates that the welded discontinuity in the axial zone does not affect the metal flow in the other zones of the deformed sample.

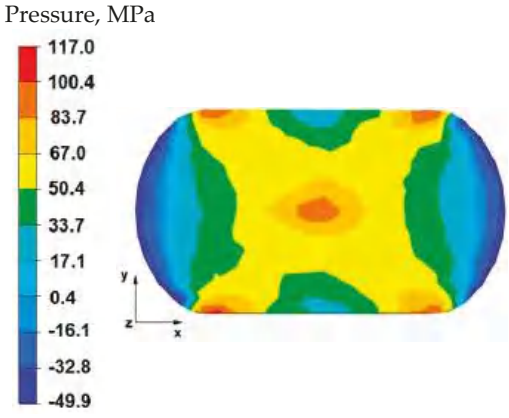

Figure 5. Distribution of hydrostatic pressure values on the surface of the cross-section of the sample with modeled discontinuity—after deformation with 35% reduction.

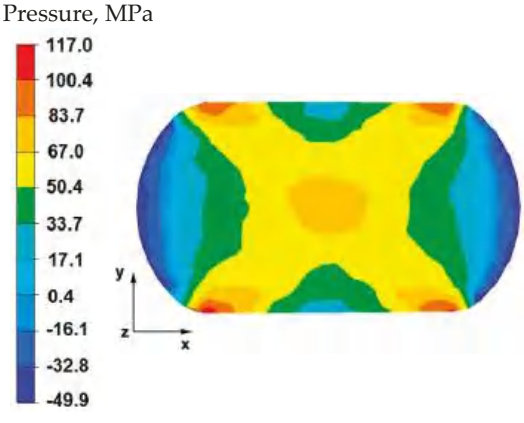

Figure 6. Distribution of hydrostatic pressure values on the surface of the cross-section of the sample without modelled discontinuity—after deformation with 35% reduction.

Based on the data shown in Figure 7, it can be stated that in the sample of the magnesium alloy AZ91 within the welded discontinuity, there is a different nature of the effective strain distribution. In the areas located on the right and left side of the discontinuity, there are large values of effective strain of the order of 1.50, and in the further distance, the values are in the range of 0.91–1.20. The data presented in Figure 7 show that the effective strain values reach the maximum values and these are compressive deformations. In the areas located in the upper and lower part of the welded discontinuity, the effective strain values are small and fluctuate in the range of 0.33–0.62, these are tensile deformations. In order to completely weld discontinuities, it is important to select the main technological parameters of forging operations and a shape of dies or anvils to ensure the greatest possible intensification of compressive deformations within the welded discontinuities during the deformation of forgings. Within the welded discontinuity, such a distribution of effective strain is undesirable where tensile deformations prevail. Such a deformation distribution blocks the process of welding discontinuities in forging processes and therefore the final product will settle defects in the form of unwelded discontinuities of the middle porosity type.

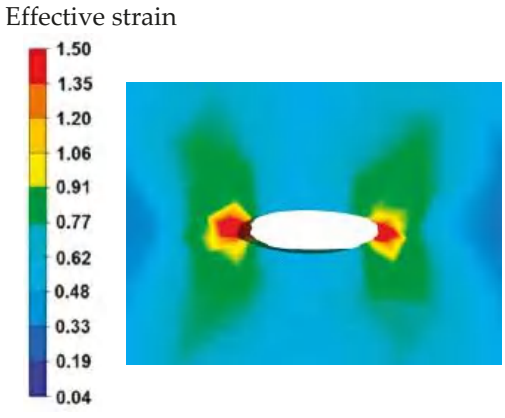

Figure 7. Distribution of effective strain values within the modelled discontinuity at a 20% reduction.

Figure 8 shows the distribution of hydrostatic pressure around the welded discontinuity during sample deformation at a reduction of 20%. The presented data show that in the areas on the right and left side of the welded defect, there is a high hydrostatic pressure with values from 83 to 117 MPa—these are compressive stresses. However, there is no hydrostatic pressure in the areas above and below the welded discontinuity. There are tensile stresses of 50 MPa, which is 50% lower than the values of compressive stresses (right and left side, 117 MPa). This distribution of hydrostatic pressure values is advantageous in terms of discontinuity welding. Equalization of the values of tensile and compressive stresses or higher values of tensile stresses in the welded discontinuity zone block their welding, therefore discontinuities in the final product in the form of middle porosity remain.

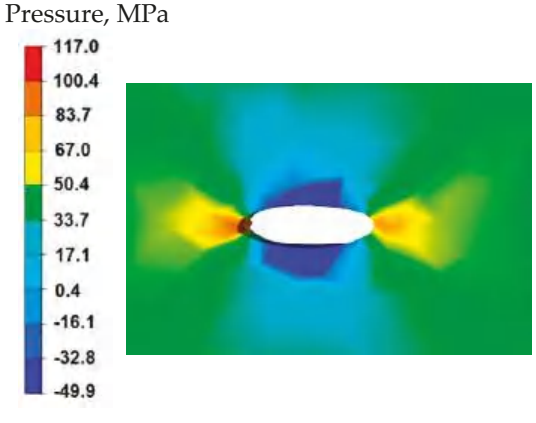

Figure 8. Distribution of hydrostatic pressure values within the modeled discontinuity at a 20% reduction.

Figure 9 shows an axonometric projection of a deformed sample with 35% reduction with a completely unheated discontinuity visible inside. A view of this discontinuity is shown due to the fact that in the figures showing the surface of the transverse cross-sections, this discontinuity is poorly visible. The presented discontinuity is not welded because the applied reduction was insufficient. The use of larger reductions was impossible because it is known from forging practice that the use of one-time reductions above 35% causes cracks in materials along the axis of deformed forgings.

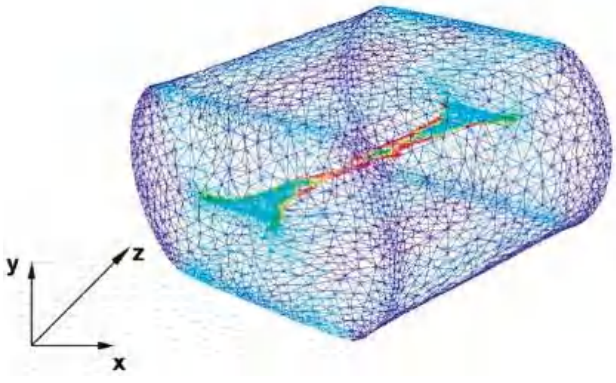

Figure 9. View of an unheated fully modeled discontinuity intended to simulate the central porosity inside a circular sample deformed with 35% reduction.

By analyzing the data in Figure 10, it can be stated that in the axial zone of the deformed sample and in areas slightly distant from the axial zone, the effective strain values were large and amounted to 1.50. During the second reduction, after prior rotation of the sample by 90°, the axial discontinuity was completely welded due to the high intensity of deformations occurring in this zone. In the area outside the axial zone of the deformed sample, different values of effective strain were recorded, ranging from 0.04 to 0.77.

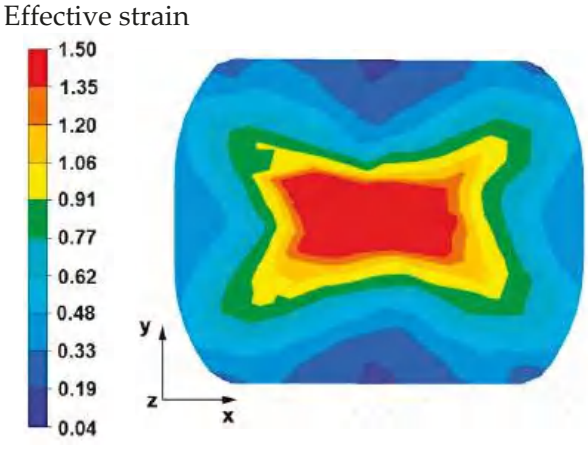

Figure 10. Distribution of the effective strain values on the surface of the cross-section of the sample with modeled discontinuity after rotation by 90° and re-deformation with 35% reduction.

The analysis of the data in Figure 11 shows that in the axial zone of the deformed sample, after the second reduction, the hydrostatic pressure values were in the range of 50–67 MPa and it was high enough to lead to complete welding of the discontinuity occurring there. In the area outside the axial zone, the hydrostatic pressure values were very small, and in some small areas, there was no hydrostatic pressure.

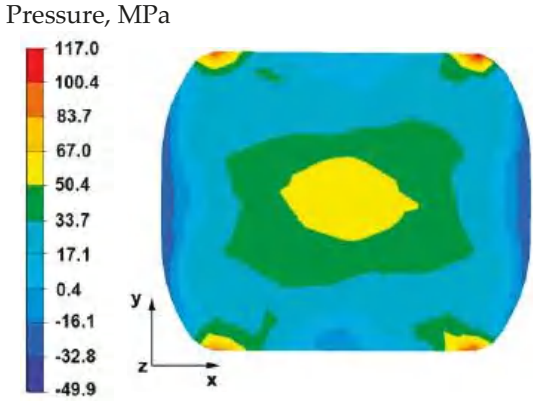

Figure 11. Distribution of hydrostatic pressure on the surface of the cross-section of the sample with modeled discontinuity after rotation by 90° and re-deformation with 35% reduction.

6. Distributions of Temperature, Effective Strain, and Hydrostatic Pressure Values on the Surface of the Cross-Section of the Deformed Sample with a Square Cross-Section Made of AZ 91 Magnesium Alloy

The test results on the distribution of temperature values, effective strain, and hydrostatic pressure values during the elongation operation of the AZ91 magnesium alloy square sample with modeled axial discontinuity are presented in Figures 12–17. The data obtained during the elongation of a sample with the same cross-section without the modelled discontinuity were not presented because the obtained data were identical to the data for a sample with discontinuity. This was due to the fact that for a sample with a square cross-section, a total discontinuity welding was obtained after the first final bend of 35%, so there were no differences in the nature of the obtained distributions.

The data in Figure 12 shows that in the middle area lying along the *x*-axis of the deformed sample, the temperature value was 378 °C and was lower by 22 °C than the initial value. In the tool–material contact zones, the temperature value was 371 °C. It is worth noting that after the first forging transition in a sample with a circular cross-section (Figure 1), the temperature drops were lower and amounted to about 15 °C and thus, in the axial zone, the drop was 14°, and at the point of contact the material–tool contact zone drop was 10°. The comparison of data provided in Figure 12 with the data from Figure 1 shows that the shape of the hot forging input material, especially the input material with small initial dimensions, has a large impact on the temperature distribution in the volume of forgings. During deformation, the cylinder-shaped forging cools down more slowly than the cube or cuboid-shaped forging. This is due to the different nature of heat transferring to the environment, and in particular, heat transferring to the anvils. The deformed cylinder-shaped sample in the initial phase of pressure on the flat anvils only has a point contact with the upper and lower anvils. In later stages of the operation, this contact gradually increases until it reaches the final reduction of 35%. After applying a 20% reduction, the entire upper and lower surface of the sample will be in contact with the anvils. As a result, there will be a smaller temperature drop in individual zones of the deformed sample when torn with a cube-shaped sample. For this sample, in the first phase of the operation, the upper and lower surfaces of the sample are in complete contact with the working surfaces of the anvils, hence a much greater temperature drop in the volume of the deformed sample occurs.

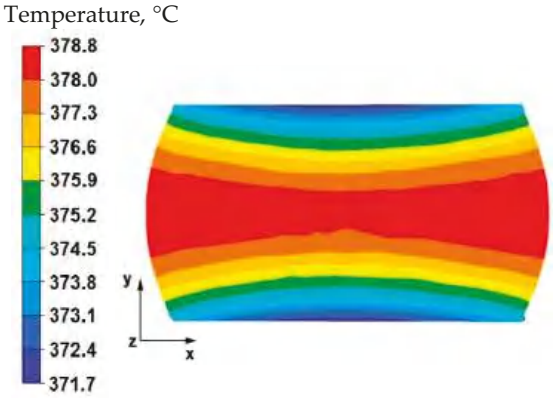

Figure 12. Distribution of temperature values on the surface of the cross-section of the sample with modeled discontinuity after deformation with 35% reduction.

By analyzing the data in Figure 13, it can be stated that in the central area of the sample lying along the *x*-axis, after the second reduction, the temperature was equal to 365 °C, which is a decrease of 35 °C from the initial temperature. In the tool–material contact zone, a temperature equal to 358 °C was recorded, which means that in these zones the temperature fell by 42 °C from the initial temperature.

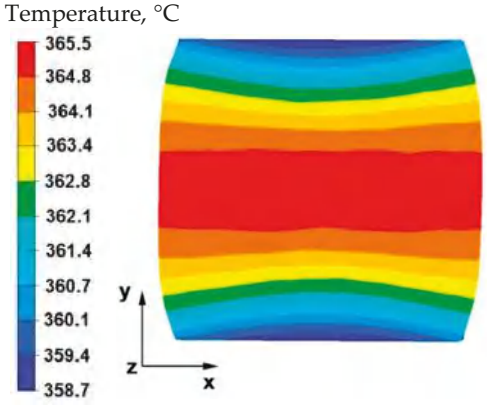

Figure 13. Distribution of temperature values on the surface of the cross-section of the sample with modeled discontinuity after rotation by 90° and re-deformation with 35% reduction.

Figure 14 shows the distribution of the effective strain values on the cross-sectional area of the sample after the first reduction. The data presented in this figure show that in the central area of the sample, the values of effective strain were obtained within the range of 0.62–1.06, while in the external areas, the values were obtained within the range of 0.04–0.77. The geometric shape and initial dimensions of the sample, deformed in the elongation operation in flat anvils, have not only a strict impact on the distribution of temperature values, but also on the distribution of the effective strain values, causing different directions of the vectors of friction forces and pressure, which are responsible for the kinematics of the flow of the magnesium alloy in question. In this case, the shape of the sample (cube) had a beneficial effect on the welding of the axial internal discontinuity because a magnesium alloy flow kinematics was obtained, which, after deformation with a 35% reduction, allowed the discontinuity to be welded in the first forging transition. This

was not achieved in the first forging transition with the same technological parameters and the same anvil of the sample in the shape of a cylinder.

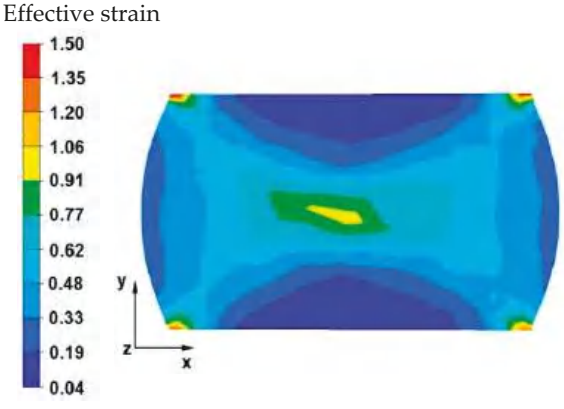

Figure 14. Distribution of the effective strain values on the surface of the cross-section of the sample with modeled discontinuity after deformation with 35% reduction.

The data in Figure 15 show that in the central area of the sample, large values of effective strain were obtained, which ranged from 1.35 to 1.50. If the metallurgical discontinuity was not welded in the first forging transition, the large value of the obtained deformations in the second transition would lead to the discontinuity being welded. In the outer areas of the sample, after the second transition, the effective strain values were very diverse in practically the entire range of values given in the legend. For the analyzed cross-sectional area of the sample, a forging cross is visible, characteristic for conducting a number of elongation operations in flat anvils, in particular for batch materials with a square or rectangle cross-section. This introduces large inequalities in the distribution of values, not only of deformations but also stresses, and not only in forged magnesium alloys, but also in many other alloys found in iron alloys. This is inevitable during forging of flat anvils, but the advantage of the described forging cross is the intensification of deformations and stresses in the axial forging zones where there is an axial discontinuity of the middle porosity type that is difficult to level in forging processes.

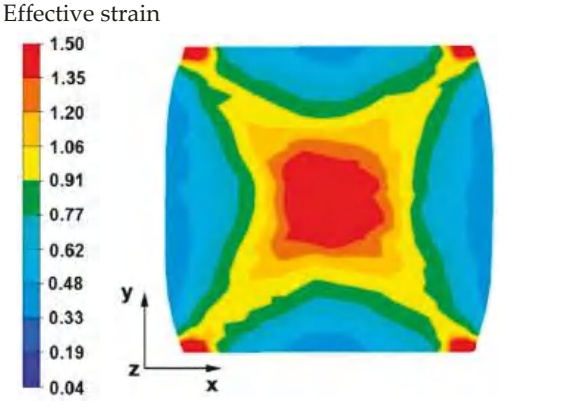

Figure 15. Distribution of the effective strain values on the surface of the cross-section of the sample with modeled discontinuity after rotation by 90° and re-deformation with 35% reduction.

By analyzing the data in Figure 16, it can be stated that in the central area of the sample there were high hydrostatic pressure values in the range of 67–117 MPa, while in the outer areas on the right and left side of the deformed sample, after the first forging transition, the hydrostatic pressure values were small and ranged from 0.4–17 MPa. In the axial zone of the sample, large hydrostatic pressure values occurred, which allowed the axial discontinuity to be welded. In this case, it was possible to ensure this due to the task of maximum applicable relative reduction with the use of flat anvils, which introduce stress intensification directed to the axis of the deformed material.

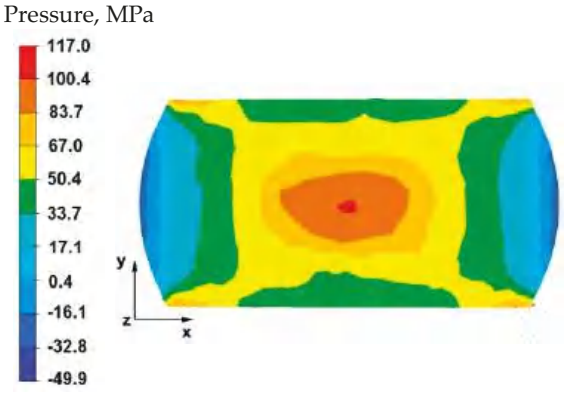

Figure 16. Distribution of hydrostatic pressure on the surface of the cross-section of the sample with modeled discontinuity after deformation with 35% reduction.

The data in Figure 17 shows that after rotating the sample by 90° and re-executing the relative reduction of 35%, in the internal area of the sample, small hydrostatic pressure values were recorded, which were in the range of 17–33 MPa. While in the areas located on the left and right side of the sample along the *x*-axis, the pressure values ranged from 0.4–12 MPa. After the sample was rotated and reduced once again with the same value, large hydrostatic pressure values were not obtained in the axial zone of the sample. Hence, it is important to determine the appropriate deformation parameters which make it possible to achieve complete welding of axial discontinuities in the initial stages of forging, where the material is still very plastic and the temperature in the sample axis is still close to the initial forging temperature.

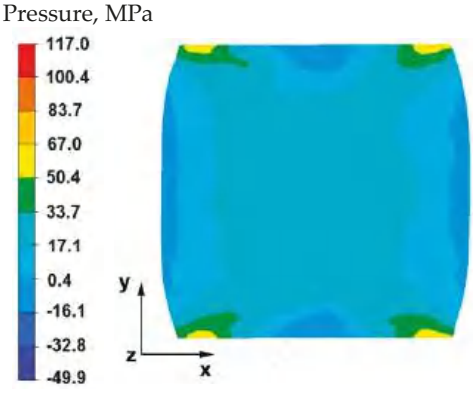

Figure 17. Distribution of hydrostatic pressure on the surface of the cross-section of the sample with modeled discontinuity after rotation by 90° and re-deformation with 35% reduction.

7. Physical Modeling of Closing Discontinuities in Forging Conditions in Flat Anvils

In order to verify the numerical tests of the material elongation process with artificially introduced axial discontinuity, physical simulations were carried out using the MaxStrain module of the Gleeble system. Two types of samples were used for the tests: with a square cross-section of 10 × 10 mm and with a circular cross-section with a diameter of 12 mm. In both samples, holes were made along the axis of the samples with a diameter of 2 mm. The holes were a model image of metallurgical axial discontinuities appearing in the cast input material intended for elongation operations. Figure 18 shows samples prepared for deformation.

The samples were heated to 400 °C, maintained at this temperature for 150 s, and then deformed in flat anvils with a 35% reduction, reducing the initial height from 10 mm to 6.5 mm (for a square section sample) and from 12 mm to 7.8 mm (for a circular section sample). After the set deformation, the samples were heated to a temperature of 400 °C, rotated by an angle of 90°, and then another deformation was set in such a way as to obtain a sample with a final height of 10 mm (for a sample with a square cross-section) and a height of 12 mm (for a sample with a circular cross-section) from the material expanded after the first deformation. In both cases, a constant anvil speed of 8 mm/s was used.

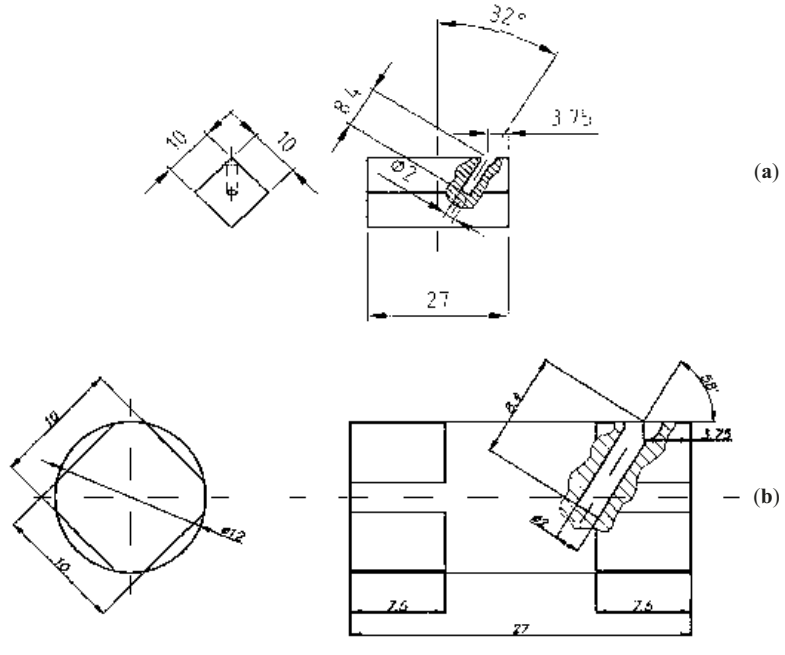

Figure 18. Samples prepared for the deformation process in the MaxStrain device: (**a**)—a sample with a square cross-section of 10 × 10 mm; (**b**)—a sample with a circular cross-section of 12 mm in diameter.

After deformation, the samples were cut in a plane perpendicular to their axis in the middle of their length. On the obtained cross-sections, metallographic micro-sections were prepared using the HNO_3 nitric acid reagent (65%) and C_2H_5OH ethanol (96%) digestion. The micro-sections were subjected to observation using optical microscopy and scanning electron microscopy. The aim of the observation was to analyze the structural changes in the material occurring during deformation in the area of the modeled discontinuity. Figures 19 and 20 show images from the optical microscope of the disclosed sample microstructures after deformation. Figure 19a shows a sample with a square cross-section in

which no artificial axial discontinuity was introduced, while Figure 19b shows a deformed sample in which there was initially an artificially introduced discontinuity. However, Figure 20a,b show analogous areas disclosed in a sample of a circular cross-section.

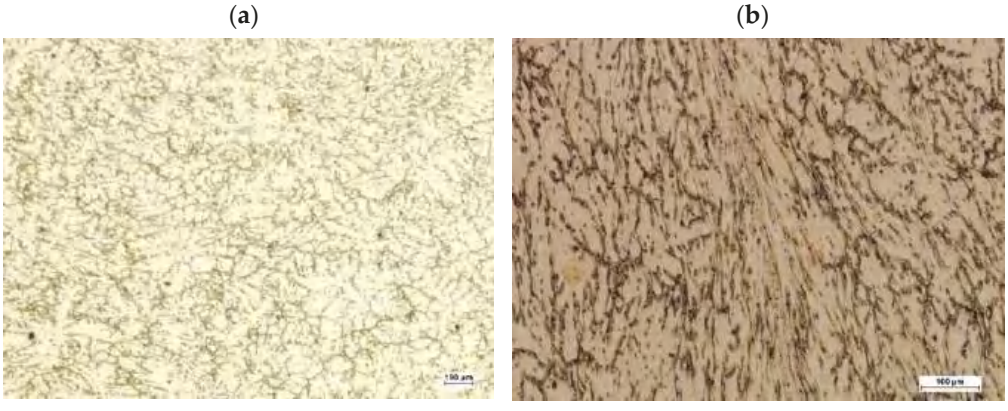

Figure 19. The disclosed microstructure of the sample with a square cross-section in the area of the axis after plastic deformation: (**a**)—sample without axial discontinuity; (**b**)—sample with artificially introduced axial discontinuity.

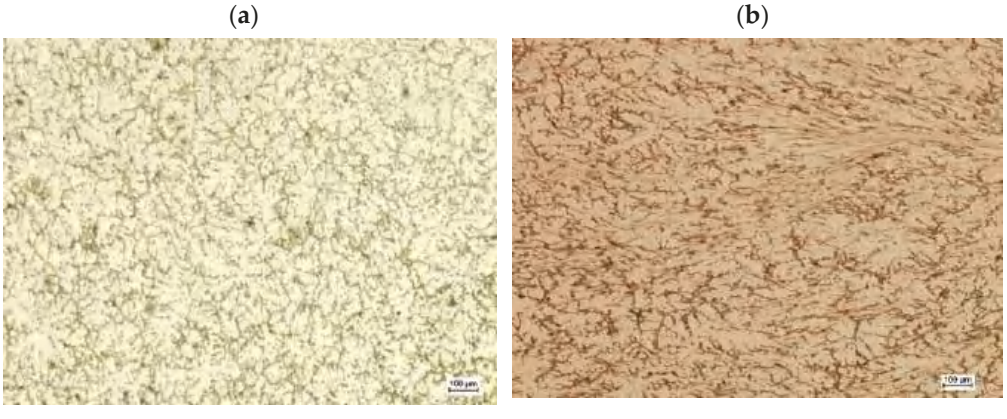

Figure 20. The disclosed microstructure of the sample with a circular cross-section in the area of the axis after plastic deformation: (**a**)—sample without axial discontinuity; (**b**)—sample with artificially introduced axial discontinuity.

Since the observation with the use of an optical microscope did not show discontinuities in the deformed samples, which indicates that during the plastic deformation the introduced axial discontinuity was closed, the microstructure of the material in the closed zone of the defect was additionally observed using a scanning electron microscope. Figures 21 and 22 show microstructure images obtained from SEM analysis for a closed discontinuity area at two different magnifications. Figure 21 shows the microstructure of a sample with a square cross-section, while Figure 22 shows a sample with a circular cross-section.

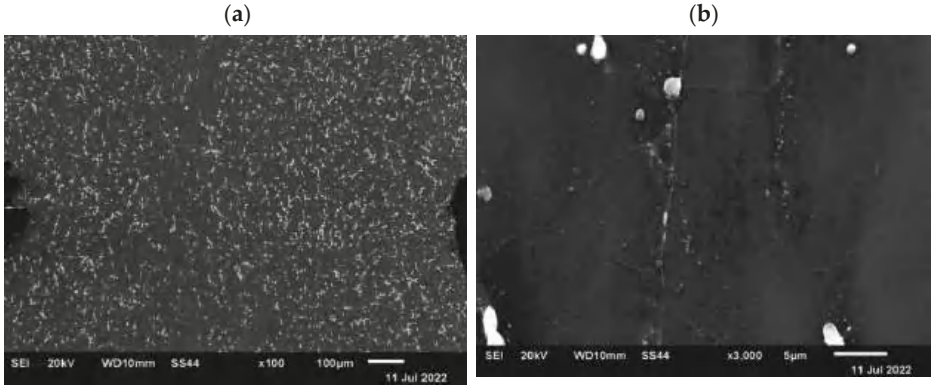

Figure 21. The microstructure of the sample with a square cross-section in the axis area after plastic deformation disclosed in the SEM analysis: (**a**)—magnification ×100; (**b**)—magnification ×3500.

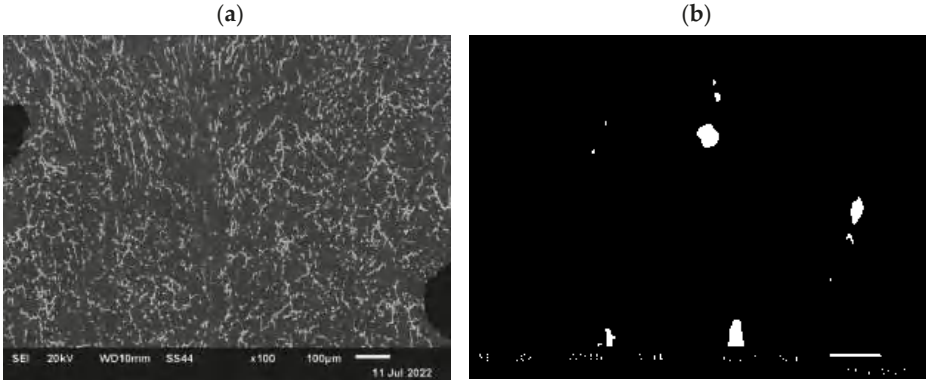

Figure 22. The microstructure of the sample with a circular cross-section in the area of the axis after plastic deformation disclosed in the SEM analysis: (**a**)—magnification ×100; (**b**)—magnification ×3500.

The conducted SEM analysis confirmed the previous observations carried out with the use of an optical microscope, which concluded that the deformation system used is sufficient to completely close the axial metallurgical discontinuity in the AZ91 alloy.

8. Conclusions

Based on the analysis of the results of the conducted research, the following final conclusions were drawn:

The geometric shape of the input material significantly affects the welding of the internal metallurgical discontinuity of the type of central porosity.

As a result of the conducted tests, it was found that the complete welding of the axial discontinuity was obtained in a cylinder-shaped sample after the first forging transition, while it was obtained in a cube-shaped sample after the second forging transition.

Large hydrostatic pressure values achieved during the elongation of the AZ91 magnesium alloy samples in the first two forging transitions positively affected the welding of metallurgical discontinuities.

The use of a single, possibly large relative reduction influences the formation of a deformed sample of stresses and compressive deformations in local areas, which are conducive to the sealing of axial discontinuity.

During the conducted physical research, the authors observed that in the range of temperatures of the deformation process, there was no cracking of the material in its local zones and no adhesion of the outer layers of the magnesium alloy to the working surfaces of flat anvils.

Author Contributions: Conceptualization, G.B., T.B., A.K. and M.K.; Data curation, G.B., T.B. and A.K.; Formal analysis, G.B., T.B. and M.K.; Funding acquisition, G.B.; Investigation, G.B., T.B. and M.K.; Methodology, G.B., T.B., A.K. and M.K.; Resources, T.B., A.K. and M.K.; Software, G.B. and M.K.; Supervision, A.K. and M.K.; Validation, T.B.; Visualization, G.B., T.B. and A.K.; Writing—original draft, G.B., T.B. and M.K.; Writing—review & editing, A.K. and M.K. All authors have read and agreed to the published version of the manuscript.

Funding: This research received no external funding.

Institutional Review Board Statement: Not applicable.

Informed Consent Statement: Not applicable.

Conflicts of Interest: The authors declare no conflict of interest.

References

1. Song, J.; Sche, J.; Chen, D.; Pan, F. Latest research advances on magnesium and magnesium alloys worldwide. *J. Magnes. Alloys* **2020**, *8*, 1–41. [CrossRef]
2. Mordike, B.L.; Ebert, T. Magnesium: Properties—Applications—Potential. *Mater. Sci. Eng. A* **2001**, *302*, 37–45. [CrossRef]
3. Yang, Z.; Li, J.; Zhang, J.; Lorimer, G.; Robson, J. Review on research and development of magnesium alloys. *Acta Metall. Sin.* **2008**, *21*, 313–328. [CrossRef]
4. Gray, J.; Luan, B. Protective coatings on magnesium and its alloys—A critical review. *J. Alloys Compd.* **2002**, *336*, 88–113. [CrossRef]
5. Nie, J.F. Precipitation and hardening in magnesium alloys. *Metall. Mater. Trans. A* **2012**, *43*, 3891–3939. [CrossRef]
6. Zeng, Z.; Stanford, N.; Davies, C.H.J.; Nie, J.F.; Birbilis, N. Magnesium extrusion alloys: A review of developments and prospects. *Int. Mater. Rev.* **2019**, *64*, 27–62. [CrossRef]
7. Papenberg, N.P.; Gneiger, S.; Weißensteiner, I.; Uggowitzer, P.J.; Pogatscher, S. Mg-Alloys for Forging Applications—A Review. *Materials* **2020**, *13*, 985. [CrossRef]
8. Braszczyńska-Malik, K. Discontinuous and continuous precipitation in magnesium–aluminium type alloys. *J. Alloys Compd.* **2009**, *477*, 870–876. [CrossRef]
9. Gann, J.A. Magnesium industry's lightest structural metal. *SAE Trans.* **1930/1931**, *25/26*, 620–641.
10. Polmear, I. Recent Developments in Light Alloys. *Mater. Trans. JIM* **1996**, *37*, 12–31. [CrossRef]
11. Polmear, I.; StJohn, D.; Nie, J.F.; Qian, M. *Light Alloys: Metallurgy of the Light Metals*, 5th ed.; Elsevier, Butterworth-Heinemann: Oxford, UK, 2017.
12. Dziubinska, A.; Gontarz, A.; Dziubinski, M.; Barszcz, M. The forming of magnesium alloy forgings for aircraft and automotive applications. *Adv. Sci. Technol. Res. J.* **2016**, *10*, 158–168. [CrossRef]
13. Banaszek, G.; Bajor, T.; Kawałek, A.; Garstka, T. Analysis of the Open Die Forging Process of the AZ91 Magnesium Alloy. *Materials* **2020**, *13*, 3873. [CrossRef] [PubMed]
14. Banaszek, G.; Bajor, T.; Kawałek, A.; Garstka, T. Investigation of the Influence of Open-Die Forging Parameters on the Flow Kinetics of AZ91 Magnesium Alloy. *Materials* **2021**, *14*, 4010. [CrossRef] [PubMed]
15. Lin, S.Y. Upsetting of Cylindrical Specimen Between Elastic Tools. *J. Mater. Process. Technol.* **1999**, *86*, 73–80. [CrossRef]
16. Park, C.Y.; Yang, D.Y. Modelling of void crushing for large-ingot hot forging. *J. Mater. Process. Technol.* **1997**, *67*, 195–200. [CrossRef]
17. Banaszek, G.; Berski, S.; Dyja, H.; Kawałek, A. Theoretical modelling of metallurgical defect closing-up processes during forming a forging. *J. Iron Steel Res. Int.* **2013**, *20*, 111–116. [CrossRef]
18. Chen, K.; Yang, Y.; Shao, G.; Liu, K. Strain function analysis method for void closure in the forging process of the large-sized steel ingot. *Comput. Mater. Sci.* **2012**, *51*, 72–77. [CrossRef]
19. Cho, J.R.; Bae, W.B.; Kim, Y.H.; Choi, S.S.; Kim, D.K. Analysis of the cogging process for heavy ingots by finite element method and physical modeling method. *J. Mater. Process. Technol.* **1998**, *80–81*, 161–165. [CrossRef]
20. Lee, M.C.; Jang, S.M.; Cho, J.H.; Joun, M.S. Finite element simulation of pore closing during cylinder upsetting. *Int. J. Mod. Phys.* **2008**, *22*, 5768–5773. [CrossRef]
21. Park, C.Y.; Yang, D.Y. A study of void crushing in large forgings, estimation of bonding efficiency by finite element analysis. *J. Mater. Process. Technol.* **1997**, *72*, 32–41. [CrossRef]
22. Banaszek, G.; Berski, S.; Dyja, H. Numerical analysis of the torsion stretch forging operation in asymmetrical anvils. *Metall. Min. Ind.* **2011**, *3*, 98–101.

23. Banaszek, G.; Dyja, H.; Berski, S. Choosing the forging parameters and tool shape from the point of view of quality improvement of forging. *Metalurgija* **2003**, *42*, 239–244.
24. Shan, D.; Xu, W.; Lu, Y. Study on precision forging technology for a complex-shaped light alloy forging. *J. Mater. Process. Technol.* **2004**, *151*, 289–293. [CrossRef]
25. Hartley, P.; Pillinger, I. Numerical simulation of the forging process. *Comput. Methods Appl. Mech. Eng.* **2006**, *195*, 6676–6690. [CrossRef]
26. Dyja, H.; Sobczak, K.; Kawalek, A.; Knapinski, M. The analysis of the influence of varying types of shape grooves on the behaviour of internal material discontinuities during rolling. *Metalurgija* **2013**, *52*, 35–38.
27. Transvalor Solution: How to Run Forge 2008, Users Guide, Sophia Antipolis, France 2008. Available online: www.transvalor.com (accessed on 15 May 2022).
28. Spittel, A.; Hensel, T. *Kraft-und Arbeitsbedarf Bildsamer Formgebungsverfahren*; Deutscher Verlag für Grundstoffindustrie: Lipsk, Germany, 1978.

materials

MDPI

Article

Investigation of Forging Metal Specimens of Different Relative Reductions Using Ultrasonic Waves

Ján Moravec [1,*], Peter Bury [2] and František Černobila [2]

[1] Department of Technological Engineering, Faculty of Mechanical Engineering, University of Žilina, Univerzitná 8215/1, 010 26 Žilina, Slovakia
[2] Department of Physics, Faculty of Electrical Engineering and Information Technology, University of Žilina, Univerzitná 8215/1, 010 26 Žilina, Slovakia; peter.bury@uniza.sk (P.B.); frantisek.cernobila@uniza.sk (F.Č.)
* Correspondence: jan.moravec@fstroj.uniza.sk; Tel.: +42-141-513-2764

Abstract: Forgings produced in industry are an irreplaceable basis for subsequent elaborating on machine tools. The quality of the semi-finished product produced by forging is a necessary prerequisite for ensuring the final quality of the final product because the forging can produce some defects. The presented paper is aimed at investigation of selected characteristics of forging steel specimens for various levels of their relative reduction. Ultrasound testing belongs to methods for investigation of structure changes, including defects. Experimental investigation, using both the attenuation and velocity measurements, verify that the reduction of specimens' material can have an effect on the propagation of ultrasound waves passing through the specimen body. The procedure of steel samples forging corresponds accordingly to the process of their hardening. The increase of toughness after relative reduction of forging in the range of 10–50% is with highest probability caused by the strength matrices development due to the relatively important deformation hardening. It is evident that the deformation hardening is almost the same after every 10% addition of relative reduction. Experiments are supplemented by Barkhausen noise detection and metallographic characteristics of the samples. While differences between the Barkhausen noise values are in principle relatively small and significant differences are only in the values of the position of the envelope, there is maximum coincidence with ultrasonic investigation.

Keywords: forging metal specimens; ultrasonic investigation; Barkhausen noise; hidden defects

Citation: Moravec, J.; Bury, P.; Černobila, F. Investigation of Forging Metal Specimens of Different Relative Reductions Using Ultrasonic Waves. *Materials* **2021**, *14*, 2406. https://doi.org/10.3390/ma14092406

Academic Editor: Radim Kocich

Received: 23 February 2021
Accepted: 29 April 2021
Published: 5 May 2021

1. Introduction

Metal beating is one of the basic forming processes, especially under dynamic loading. Hammering belongs to the field of forging and is the most common operation on impact machines (hammers, drop hammers, spindle presses, etc.). The beating itself takes only a few fractions of a second, which means that the process cannot be considered isothermal. In addition to its practical significance, beating is of fundamental importance for determining the mechanical properties under impact loading. Only the pressure test allows the tool to immediately hit the material. The theory of plastic deformation propagation, taking into account the influence of the deformation rate, the thermal effect, the actual course of the load and the final dimensions, is still under investigation. With sufficiently short samples, the propagation of plastic deformation can be neglected. Only short samples can be used for beating on conventional machines. It is known from practice that the maximum length of loose material that can be broken without deflection is l = 3d. When hammering, the height of the material always decreases. Various tests are applied to test forgings, such as checking the chemical composition of the material, checking the mechanical properties and structure of the forgings. These are commonly used tests in which forging errors can be detected. In particular, the following methods are used in practice to detect hidden forging defects:

- Assay of electromagnetic waves of different lengths;
- Test of magnetic and electrical phenomena—capillary tests;
- Magnetoinductive methods;
- Magnetographic method;
- Magnetic powder method;
- Magnetic fluorescence method;
- Radiation methods;
- X-ray defectoscopy;
- Ultrasound defectoscopy.

In the experimental part, attention was focused on ultrasonic waves and their attenuation.

Quantities characterizing the propagation of high-frequency acoustic waves (ultrasound) in solid materials can be determined from the investigation of dependence of both acoustic wave velocity and attenuation on individual variables describing investigated properties of existing materials. The relation of velocity and attenuation of ultrasonic waves to various properties referring to intrinsic structure of solid material can then enable their study by means of ultrasonic velocity and attenuation measurement. Among these properties, mainly mechanical (elastic, structural, etc.) properties of materials, which directly reflect their intrinsic structure, are considered [1,2].

Using the measurement of acoustic wave velocity that is in proportion to the root of ratio of elastic constants and density of investigated materials, we can receive information connected directly with interatomic forces or density. The ultrasonic wave attenuation very sensitively reflects material intrinsic structure, not only the type of structure but also the changes due to occurrence of defects (dislocations, grains, cracks etc.) Ultrasonic attenuation and velocity in metal materials depend on the method of preparation and further treatment, which can influence grain magnitude as well as the generation of some defects. The attenuation also reflects permanent changes in material arising due to its strain [3]. In the case of material with a grain structure, dislocations, cracks or other defects, the attenuation is caused by the dispersion, the frequency dependence of which depends on the rate of wavelength and mean defect size [4].

The issue is quite extensive and the number of papers devoted to the study of the material characteristics of forgings is large. The most important is [5]. The authors deal with ultrasound control used in non-destructive testing to detect cracks and other defects. It is an important publication and provides a good overview of the issue. Other contributions, such as [6,7], deal with large forged steel parts, testing the phase field by ultrasound in each directional reaction. The CIVA software package (EXTENDE S.A., Massy, France) was used to optimize the phase field. The three test samples described in the source [8] were taken from the material so that the UT indications were in the middle of the cross-section. The samples were then subjected to cyclic loading by applying tensile stresses of different magnitudes and different stress ratios. The experimental investigation in the article [9] confirms the challenges and the current shortcomings in the control of planned industrial components, where such microstructures are desirable in terms of their mechanical properties. Article [10] is an important and significant work, where the interaction between ultrasonic acoustic radiation and the microstructure of duplex stainless steel 2205 was studied. Samples were examined at 780 °C to promote precipitation of intermetallic phases. The UT response in each sample was measured, associated with the respective microstructural properties. Article [11] summarizes the results of research into the effect of sensitivity distribution of double transducer probes, which are often used in non-destructive ultrasonic testing of forgings. The sensitivity distribution measured in two directions, parallel and perpendicular to the separation plane of the dual sensor probe, was tested and analyzed. The approach presented in paper [12] combines the technique of focusing with synthetic aperture (SAFT) to accurately find and quantify small errors. The ultrasound inspection data obtained in the pulsed echo configuration are reconstructed using the synthetic binding application coupling (SAFT) technique. Document [13] investigated the relationship between changes in ultrasonic group and

phase velocity with the local properties of a forged and heat-treated large bainitic steel block. From the obtained data it is possible to find out the number and approximate location of small errors. Article [14] describes the development of a new piezoelectric machine operating in a continuous mode. The machine was used to investigate the very high cyclic fatigue (VHCF) properties of the VT3-1 alpha beta aviation titanium alloy. This is produced by two production technologies: forging and extrusion. Extruded titanium alloy has a higher torsional strength of VHCF compared to forging. Ultrasonic testing was used to evaluate the quality of the joints [15]. The basic rising process was chosen to investigate the forging. The good quality of the joint after forging was examined by a penetration test and optical microscopy. A reliable connection between the two materials is important for optimal stress transfer between the materials throughout the component. A special bending test was developed to determine the interfacial strength. The paper [16] describes the problem of the large size of the radial structure and the high mechanical power of the MP1000 miner spindle forging. The low efficiency and reliability of ultrasonic non-destructive tests make it difficult to detect uneven material in the forging process. The numerical finite element method itself, the simulation of the process of detecting ultrasonic errors of the spindle forging, is performed using software. To classify internal defects in the forging, the authors proposed a method [17] based on sample detection of errors obtained in ultrasonic tests. The reliability of the method is more than 75%. The authors also developed a program for the classification of internal defects in relation to the length and their location across the thickness and width of the forging. The pulse compression technique was applied in [18] for ultrasonic inspection of the forging. Currently, (some) authors have applied it in combination with the use of broadband ultrasonic transducers and broadband excitation signals. The methods are extended by applying distance gain size (DGS) analysis to the output pulse compression signal. The assessment and assessment of cracks [19] when deciding on suitability for use require an examination of the location and size of cracks in hazardous areas. An ultrasonic transducer is mainly used for such evaluation, but classical methods cannot accurately evaluate the forging, such as mainly wheel hubs.

It is also possible to make other contributions to the issue. In [20–22], the authors deal with the processing of ultrasonic field signals and [21] deals with the problem of velocities in steel blocks, which is very stimulating for the whole area of such research. In addition to these papers, there is also [22], where the authors present an interesting area of pulsed compression ultrasonic technology, where a detailed course of steel inspection is described. The following literature [23–28] deals with and presents in detail non-destructive evaluation systems with the application of ultrasound, so it is probably not necessary to discuss these articles in more detail. Article [25] describes the problem of the speed of ultrasonic waves as one of the suitable methods for investigating the properties of materials and forgings by non-destructive methods. The paper [27] focuses on the presented issue of large-scale parts [6,7,13]. In the paper [29], the authors dealt with a wide range of issues of analysis and research of texture issues in metals. The last contribution of this review is [30], which interestingly describes the issue of ultrasound in its application to complex and rugged surfaces of metal parts. The hot deformation behavior and pulse current assisted diffusion bonding (PCDB) behavior of sintered γ-TiAl-based alloy with near gamma microstructure were investigated for fabricating honeycomb structure via isothermal forging—PCDB route. Additionally, the mechanical property and structural morphology demonstrated that the best forging with parameter was forging at 1200 °C with a nominal strain rate of 10^{-3} s^{-1} subsequent to the effects of bonding [31]. In work [32], the influence of weak interface between particles and matrix on mechanical properties of metal matrix–ceramic reinforced composites is studied. Firstly, the samples made of coelectrodeposited Ni-SiC composites with 10% of SiC with poor interface bonding were prepared. Furthermore, the tensile test of samples was performed. The determined Young's v modulus was equal to 67 ± 8 GPa and the ultimate tensile strength to 230 ± 15 MPa.

In the presented paper, the samples are of simple shapes and it is not necessary to apply complicated procedures for the investigation of the investigated characteristics. The presented contribution is orientated toward analysis of changes of mechanical properties in steel samples that undergo forging with respect to the original non-forging sample. The structure changes of existing material were investigated for various relative reductions of forging deformation using both attenuation frequency dependence and ultrasound velocity measurements. Obtained results were also compared with results obtained by another method on the same samples, specifically by means of the characteristics of the samples using the Barkhausen noise method and metallographic observation of the sample material.

2. Ultrasonic Investigation

2.1. Experimental Details

Investigated material was chosen from non-operated steel of composition described in Table 1 and, from six sample series corresponding to six different material conditions, original non-forging sample (0) and five forging samples with relative reduction 10% (1), 20% (2), 30% (3), 40% (4) and 50% (5) were prepared. The relative reduction of forging steel samples was calculated using the relation

$$\Phi = \ln (h_0/h) \times 100\%, \quad (1)$$

where h_0 is the original height and h is the height after forging.

Table 1. Chemical impurities in investigated steel in %.

C Max.	*Mn* Max.	*Si* Max.	*P* Max.	*S* Max.
0.10	0.45	0.15	0.03	0.025

The logarithmic degree of beating for individual samples was assigned according to Table 2.

Table 2. Logarithmic degree ϕ of beating samples.

Sample	0	1	2	3	4	5
Logarithmic degree	0	1.02	1.58	1.094	1.175	1.335

The samples were subjected to a reduction ranging from 5% to 50%. One sample was uncompressed. The actual dimensions of the compressed samples and their reduction are shown in Table 3.

Table 3. Actual dimensions of rollers height after pressing (mm).

Sample	0	1	2	3	4	5
Height	12.85	12.15	11.18	10.25	8.80	6.75

Samples for the forging were prepared in the cylinder shape with diameter d = 13 mm and original height h = 12.85 mm. The velocity and attenuation of ultrasound were measured for ultrasonic wave propagated in the direction of cylinder axis and by that in deformation direction, but after grinding and polishing of both cylinder surfaces. The ultrasound pulses of six different frequencies from the range 5–30 MHz were generated by the quartz transducers using the Pulse Modulator and Receiver—MATEC 7700 (Northborough, MA, USA). The same quartz was used for receiving the reflected ultrasonic wave. The attenuation was measured using MATEC Attenuation Recorder 2470 A. All measurements were performed at room temperature. However, the higher frequencies of ultrasound (>30 MHz) due to the extremely high attenuation could not be used.

2.2. Experimental Results and Discussion

The results of velocity measurement for all investigated samples and for deformation directions in cylinder axis are shown in Figure 1.

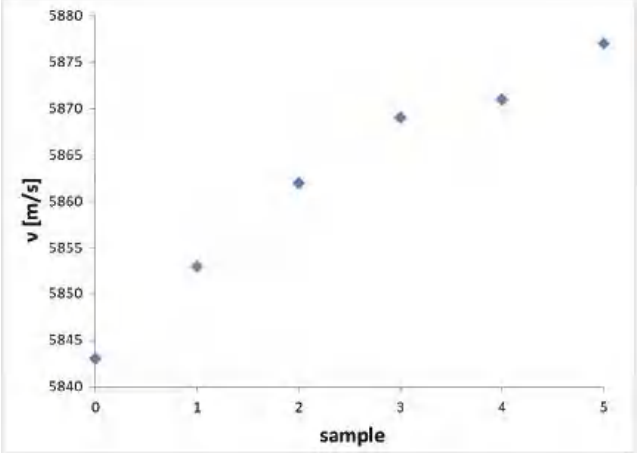

Figure 1. Values of ultrasonic velocity measured at frequency 12.2 MHz for forging samples with relative reduction 10% (1), 20% (2), 30% (3), 40% (4) and 50% (5), including non-forging sample (0).

The velocity measurements were made at frequency of 12.2 MHz with accuracy better then 2×10^{-3}. It is seen that the value of ultrasound velocity increases with increasing relative reduction up to sample *3* (30%) almost linearly and after that, there is only a small attenuation rise to sample *4* (40%), and then it continues again in the early trend to the last sample *5* (50%). Such behavior, also taking into account the increase of the density with increasing relative reduction, corresponds to the considerable increase of elastic constant. The procedure of steel samples forging corresponds accordingly to the process of their hardening. The increase of the toughness after relative reduction of forging in the range of 10–50% is with highest probability caused by the strength matrices development due to the relatively important deformation hardening. It is evident that the deformation hardening is almost the same after every 10% addition of relative reduction, excepting the mentioned rise between 30% and 40% of reduction, however.

The frequency dependences of ultrasonic attenuation measured for individual samples are illustrated in Figure 2. By contrast to velocity measurements, the development of frequency dependence of attenuation shows at first the increase of attenuation magnitude in the case of first deformed sample *1* (10%) in regards to the non-forging sample but is then followed with its decrease with increasing relative reduction. The decrease of ultrasonic attenuation with increasing relative reduction fully corresponds to velocity measurements and by that to the deformation hardening. Even the small rise of velocity between 30% and 40% of relative reduction corresponds to a small decrease of attenuation between the same samples. The fact that the initial increase of attenuation of sample *1* (10%) does not correspond to results of velocity measurement could be connected with some defect in creation after the first forging. As these defects do not influence the hardening process, they could affect the ultrasonic wave dispersion. Because the frequency dependence of attenuation can be described by the same function, except perhaps for the last one (50%), it practically confirms that the relative reduction caused by forging process at least to 40% does not create additional defects.

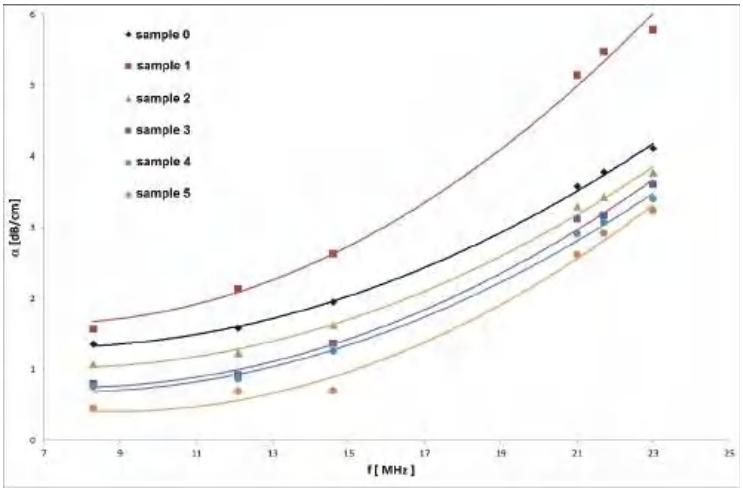

Figure 2. Frequency dependence of ultrasonic attenuation for the samples with different values of relative reduction, 0% (*0*), 10% (*1*), 20% (2), 30% (3), 40% (4) and 50% (50) measured in frequency range 8.2–23.1 MHz.

The results obtained by measurements of attenuation and velocity correlate considerably with results of authors' measurements obtained on the same samples, mainly by the Barkhausen noise detection and metallographic characteristics.

3. Investigation of Sample Characteristics Using Barkhausen Noise

3.1. Experimental Results

Another method used for the analysis of changes of mechanical properties in steel samples that undergo forging with respect to the non-forging sample is the Barkhausen noise method. The basic parameters used in this method were: magnetization frequency 125 Hz, voltage 5 V, serial sensor and Barkhausen noise in frequencies range from 10 to 1000 kHz. The obtained characteristics and dependences of the rollers are shown in Figures 3–10.

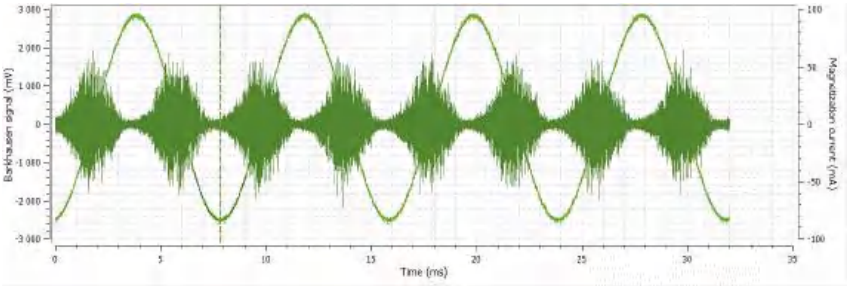

Figure 3. Sample No. 0—Barkhausen noise 339 mV—position of envelope maximum—10.58 a.u.—envelope extension (FWHM—full width at half maximum) 81.2 a.u.

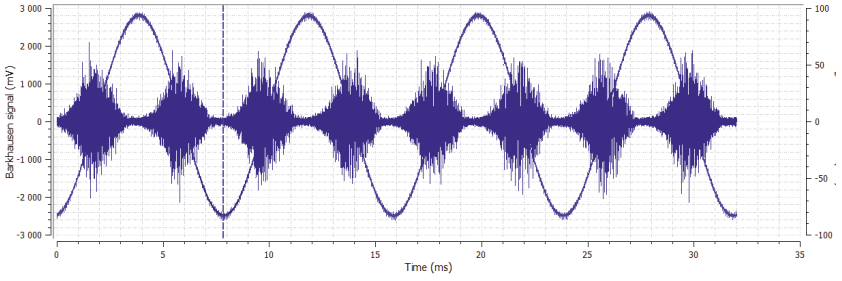

Figure 4. Sample No. 1—Barkhausen noise 334 mV—position of envelope maximum—8 a.u.—envelope extension (FWHM) 77 a.u.

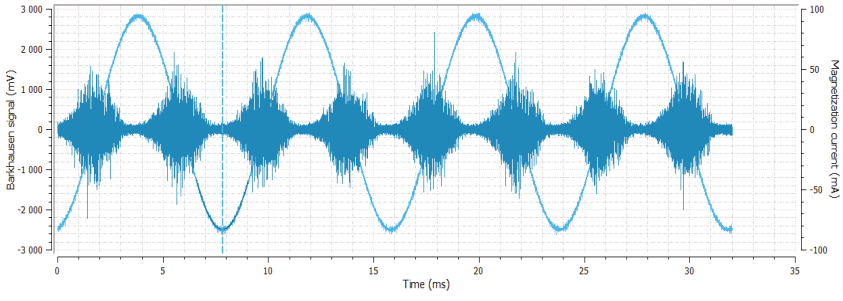

Figure 5. Sample No. 2—Barkhausen noise 300 mV—position of envelope maximum—7.8 a.u.—envelope extension (FWHM) 67 a.u.

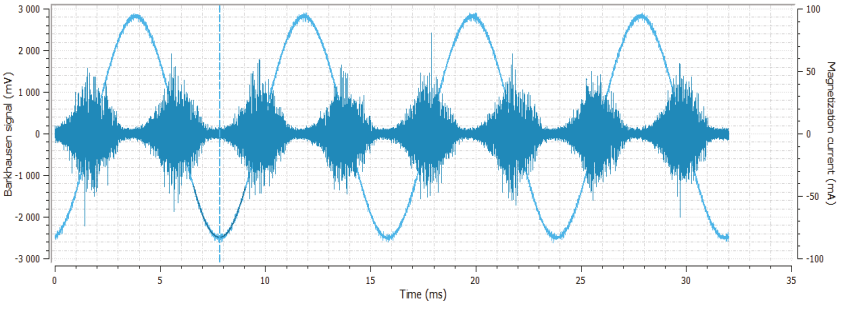

Figure 6. Sample No. 3—Barkhausen noise 344 mV—position of envelope maximum—7.16 a.u.—envelope extension (FWHM) 63 a.u.

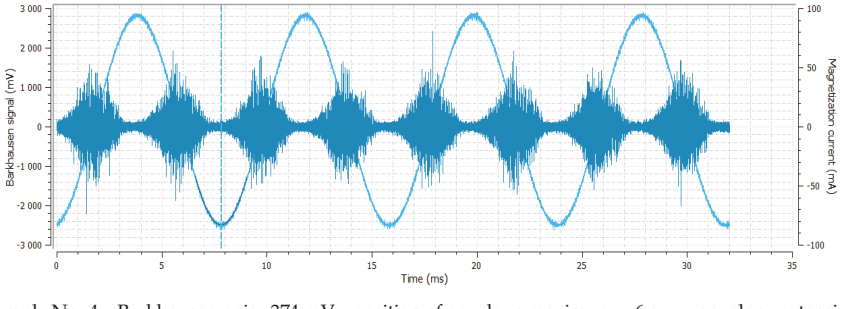

Figure 7. Sample No. 4—Barkhausen noise 374 mV—position of envelope maximum—6 a.u.—envelope extension (FWHM) 70.6 a.u.

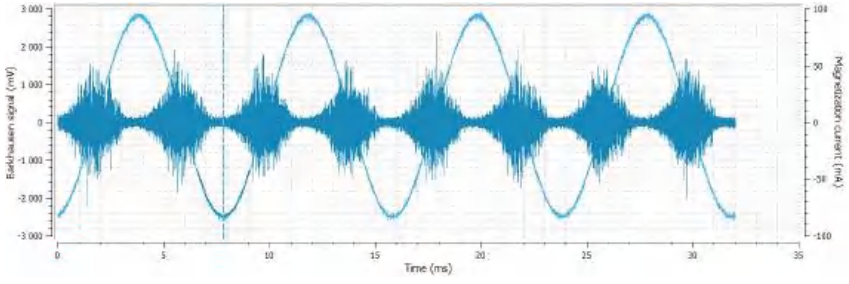

Figure 8. Sample No. 5—Barkhausen noise 340 mV—position of envelope maximum—7.7 a.u.—envelope extension (FWHM) 70.2 a.u.

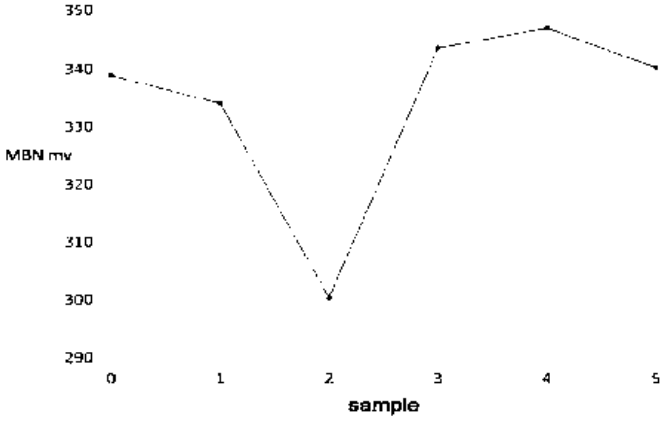

Figure 9. Dependence of rollers and MBN.

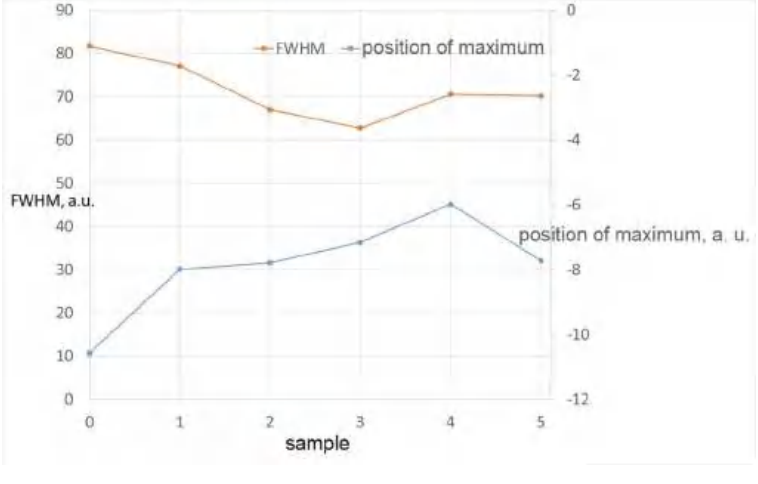

Figure 10. Dependence of rollers and position of maximum and FWHM.

3.2. Evaluation and Discussion of Barkhausen Noise Test

Magnetic parameters do not show a clear trend. Barkhausen noise (MBN) decreases slightly from roller no. 0 to roller no. 2 and consequently the values for the last three rollers no. 3 to 5 are higher compared to roller no. 2, around the value of 345 mV. The position of the envelope maximum (which usually corresponds to mechanical and magnetic hardness) as well as the width of the envelope at half its height (FWHM) also show an ambiguous trend. The differences between the Barkhausen noise values are in principle relatively small. Significant differences are in the values of the position of the envelope maximum. Overall, it can be said that the experimental Barkhausen noise data are essentially unsuitable for the characterization of these samples, or that it is now difficult to interpret these data, as the information from conventional destructive tests is not known.

4. Metallographic Observation

The attached pictures of sample microstructures obtained by metallographic microscope (Figure 11) show the surfaces of the investigated samples after their forging with respect to the original non-forging sample. The samples were cut in the longitudinal axis and etched. The surface is magnified 500× to make the structure of the material well observable. The marking of the individual samples is in accordance with the previous one. It is evident that the sample microstructure changes with increasing relative reduction. It can be seen that the samples' grains, including free space between them, are reduced in a way that corresponds to the increase of their compaction and/or hardening. However, it seems that after relative reduction 40% (e) the sample microstructure does not quite coincide with the described trend of structure changes, but this fact corresponds with ultrasonic investigation, primarily with the ultrasound velocity changes with increasing relative reduction.

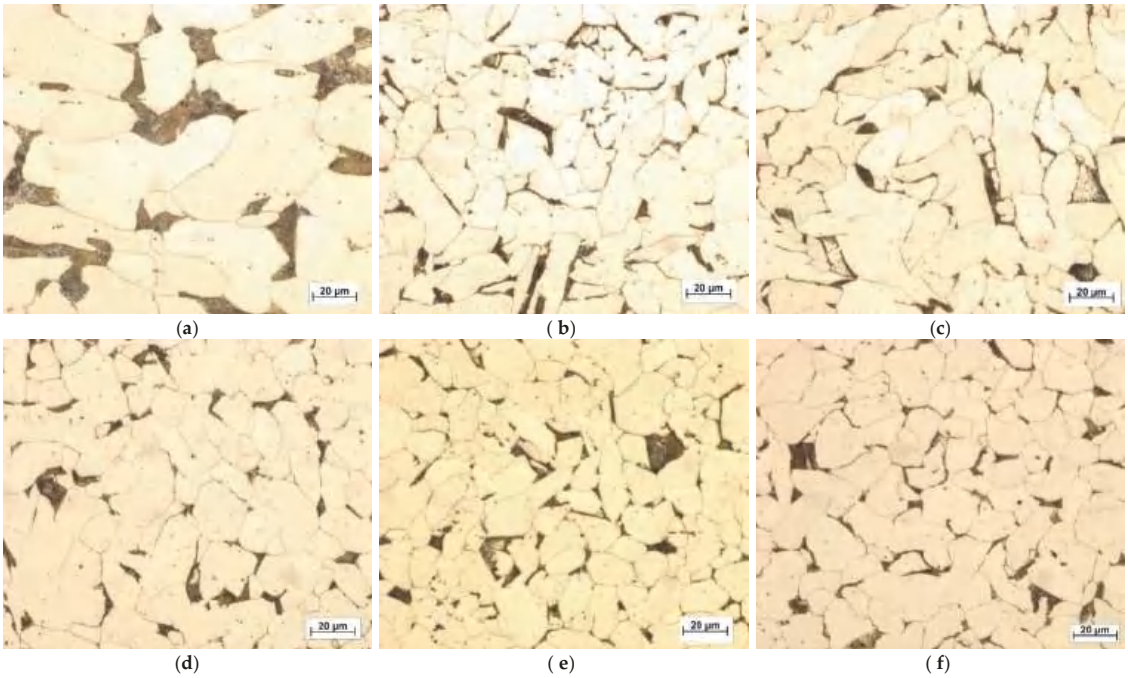

(**a**) (**b**) (**c**)

(**d**) (**e**) (**f**)

Figure 11. Microstructure of non-forging sample (**a**) and forging samples with relative reduction 10% (**b**), 20% (**c**), 30% (**d**), 40% (**e**) and 50% (**f**).

In the experimental part, attention was paid preferentially to the shape of transient waves and attenuation. The hardness of the samples remained at an overall low value and is supplemented for a complete view of the problems of the samples used. The hardness values are summarized in Table 4.

Table 4. The hardness of the forging samples.

Sample No.	Test 1 (HV)	Test 2 (HV)	Test 3 (HV)
1	131.6	136.8	133.2
2	140.4	142.8	134.9
3	124.4	128.8	129.4
4	127.1	129.5	126.9
5	131.5	136.2	136.5

5. Conclusions

In this contribution, the analysis of changes of mechanical properties in steel samples that undergo forging with respect to the original non-forging sample is presented. Experimental examining of ultrasound is proven to be a suitable and preferred method for determining the desired characteristics. The investigation of Barkhausen characteristics is given as a complementary method. The results are also supplemented by metallographic images of all samples. In conclusion, we can state that methods of ultrasonic attenuation and velocity measurement definitely recorded changes in steel bars that undergo 10–50% relative reduction caused by forging procedure of original steel samples. Experimental results show both velocity increases and attenuation decrease with increasing relative reduction which means that there is then a considerable increase of elastic constant that corresponds accordingly with the process of their hardening. The initial increase of ultrasound attenuation at the lowest value of relative reduction could be connected with some defect creation caused by the forging process at the beginning of the forging procedure and no additional defects, at least to 40% of reduction, are created. While differences between the Barkhausen noise values are in principle relatively small and significant differences are only in the values of the position of the envelope maximum, the pictures of the samples' microstructure obtained by metallographic microscope coincide well with ultrasonic investigation.

Author Contributions: Conceptualization, J.M. and P.B.; methodology, J.M.; software, J.M. and F.Č.; validation, J.M. and P.B.; investigation, J.M. and F.Č.; resources, J.M.; writing—original draft preparation, J.M. and P.B.; writing—review and editing, J.M. and P.B.; funding acquisition., J.M. All authors have read and agreed to the published version of the manuscript.

Funding: This work was supported by project S-102-0008/20-1.

Institutional Review Board Statement: Not applicable.

Informed Consent Statement: Not applicable.

Data Availability Statement: Not applicable.

Conflicts of Interest: The authors declare no conflict of interest.

References

1. Mason, W.P. *Physical Acoustics*; Academic Press: New York, NY, USA, 1966; Volume IV.
2. Papadakis, E.P. *Ultrasonic Instruments and Devices*; Academic Press: New York, NY, USA, 2001.
3. Truel, R.; Elbaum, C.; Chick, B.B. *Ultrasonic Methods in Solid State Physics*; Academic Press: New York, NY, USA, 1969.
4. Hamák, I. *Residual Lifetime of Girders M 140 after Long-Time Operation*; Order No. 222/2167; The Welding Research Institute Bratislava: Bratislava, Slovakia, 2000.
5. Senni, L.; Battaglini, L.; Burrascano, P.; Laureti, S.; Ricci, M. Industrial Applications: Ultrasonic Inspection of Large Forgings. In *Ultrasonic Nondestructive Evaluation Systems. Industrial Application Issues*, 1st ed.; Burrascano, P., Callegari, S., Montisci, A., Ricci, M., Versaci, M., Eds.; Springer: Cham, Switzerland, 2015; pp. 245–258.

6. Dupont-Marillia, F.; Jahazi, M.; Bellanger, P. Phased array inspection of large size forged steel parts. In Proceedings of the 44th Annual Review of Progress in Quantitative Nondestructive Evaluation, Provo, UT, USA, 16–21 July 2017.
7. Dupont-Marillia, F.; Jahazi, M.; Lafrenier, S.; Bellanger, P. Design and optimisation of a phased array transducer for ultrasonic inspection of large forged steel ingots. *NDT E Int.* **2019**, *103*, 119–129. [CrossRef]
8. Varfolomev, I.; Moroz, S.; Siegele, D.; Kadau, K.; Amann, C. Study on fatigue crack initiation and propagation from forging defects. *Procedia Struct. Integr.* **2017**, *7*, 359–367. [CrossRef]
9. Tranca, T.; Radu, J. Understanding and improving ultrasonic inspection of the forging titanium alloy. In Proceedings of the 9th European Workshop on Structural Health Monitoring, Manchaster, UK, 10–13 July 2018.
10. Barella, S.; Cecca, C.D.; Gruttadauria, A.; Mapelli, C.; Mombelli, D.; Da Rocha, C.F.; Strohaecker, T. Study on the microstructure influence in ultrasonic test in duplex forged components. In Proceedings of the 2nd International Conference Ingot Casting Rolling and Forging—ICRF 2014, Milan, Italy, 7–9 May 2014.
11. Kaczmarek, R.; Kaczmarek, K. The influence of sensitivity field of dual transducer probes on accuracy of discontinuity sizing and evaluation in terms of testing of forgings according to EN 10228-3. *Arch. Metall. Mater.* **2016**, *61*, 1677–1682. [CrossRef]
12. Fendt, K.T.; Mooshofer, H.; Rupitsch, S.J.; Ermert, H. Ultrasonic Defect Characterization in Heavy Rotor Forgings by Means of the Synthetic Aperture Focusing Technique and Optimization Methods. *IEEE Trans. Ultrason. Ferroelectr. Freq. Control* **2016**, *63*, 874–885. [CrossRef] [PubMed]
13. Dupont-Marillia, F.; Jahazi, M.; Lafrenier, S.; Bellanger, P. Influence of Local Mechanical Parameters on Ultrasonic Wave Propagation in Large Forged Steel Ingots. *J. Nondestruct. Eval.* **2019**, *38*, 1–9. [CrossRef]
14. Nikitin, A.; Bathias, C.; Palin-Luc, T. A new piezoelectric fatigue testing machine in pure torsion for ultrasonic gigacycle fatigue tests: Application to forged and extruded titanium alloys. *Fatigue Fract. Eng. Mater. Struct.* **2015**, *38*, 1294–1304. [CrossRef]
15. Förster, W.; Binotsch, C.; Awiszus, B.; Lehmann, T.; Műller, J.; Kirbach, C.; Stockmann, M.; Ihlemann, J. Forging of eccentric co-extruded Al-Mg compounds and analysis of the interface strength. In Proceedings of the 18th Chemnitz Seminar on Materials Engineering, Chemnitz, Germany, 10–11 March 2016.
16. Changan, H.; Linghui, K.; He, M. Design and research of UT inspection tool in flaw inspection of large-size forging shaft parts. In Proceedings of the 5th International Conference on Applied Materials and Manufacturing Technology, Singapore, 21–23 June 2019.
17. Nikitin, V.P.; Korotyshev, I.V.; Artyuchov, V.N.; Sinitsyn, E.O.; Kudrin, A.A. Classifying internal defects in forgings based on flaw-detection patterns obtained by ultrasound. *Metallurgist* **2008**, *52*, 366–370. [CrossRef]
18. Rizwan, M.K.; Senni, I.; Burrascano, P.; Laureti, S.; Goldammer, M.; Mooshofer, H.; Borgna, R.; Neri, S.; Ricci, M. Contextual Application of Pulse-Compression and Multi-frequency Distance-Gain Size Analysis in Ultrasonic Inspection of Forging. *J. Nondestruct. Eval.* **2019**, *38*, 1–13. [CrossRef]
19. Zhang, H.; Xu, C.; Xiao, D. Crack Assessment of Wheel Hubs via an Ultrasonic Transducer and Industrial Robot. *Sensors* **2018**, *18*, 4336. [CrossRef] [PubMed]
20. Rus, G.; Wooh, S.-C.; Callego, R. Processing of ultrasonic array signals for charactering defects. Part, I: Signal synthesis. *IEEE Trans. Ultrason. Ferroelectr. Freq. Control* **2007**, *54*, 2129–2138. [CrossRef] [PubMed]
21. Ali, M.G.S.; Elsayed, N.Z.; Eid, A.M. Ultrasonic attentuation and velocity in Steel standard refernce blocks. *Rom. J. Acoust* **2013**, *1*, 33–38.
22. Ricci, M.; Sennil, L.; Burrascano, P.; Borgua, R.; Neri, S.; Calderini, M. Pulse-compresion ultrasonic technique foe the inspection of forged steel with high atteunation. *Insight-Non-Destr. Test. Cond. Monit.* **2012**, *54*, 91–95. [CrossRef]
23. Fend, K.T.; Moosfer, H.; Rupitsch, S.J.; Ermert, H. Ultrasonic defect characterization in synthetic aperture focusing tecchnique and optimatization methods. *IEEE Trans. Ultrason. Ferroelectr. Freq. Control* **2016**, *63*, 874–885. [CrossRef] [PubMed]
24. Schmerr, L.; Song, J.S. *Ultrasonic Nondestructive Evaluation Systems*; Springer: New York, NY, USA, 2007.
25. Burrascano, P.; Callegari, S.; Montisci, A.; Ricci, M.; Versaci, M. (Eds.) *Ultrasonic Nondestructive Evaluation Systems: Industrial Application Issues*; Springer: New York, NY, USA, 2014.
26. Charles, D.N.; Alcheikh, W. *Handbuch of Nondestructive Evaluation*; Mc Graw Hill: New York, NY, USA, 2003; ISBN 9780070281219.
27. Dupont-Marillia, F.; Jahazi, M.; Lafreniere, S.; Bellanger, P. Influence of local mechanical properties of high strenght steel from large size forged ingot on ultarsonic wave velocities, review of Progress in Quantifave nondestructive Evaluation. *AIP Conf. Proc.* **2017**, *1806*, 090002.
28. Ruiz, N.; Ortiz, H.; Carrein, G.; Rubio, Z. Utilization of Ultrasonic Measurements for Determining the Variations in Microstructure of Thermally Degraded2205 Duplex Stainless Steel. *J. Nondestr. Eval.* **2009**, *28*, 131. [CrossRef]
29. Kurc-Lisiecka, A.; Ozgowicz, W.; Ratuszek, W.; Kowalska, J. Analysis of deformation Texture in AISI 304, Steel Sheets. *Solid State Phenom.* **2013**, *203–204*, 105–110.
30. Ma, H.W.; Zhang, X.H.; Wei, J. Research on an ultrasonic NDT system for complex surface parts. *J. Mater. Process. Technol.* **2002**, *129*, 666–670. [CrossRef]
31. Shi, C.; Lu, Z.; Zhang, K.; Deng, L.; Wang, C. Microstructure evolution and mechanical properties of γ-TiAl honeycombstructure fabricated by isothermal forging and pulse current assisted diffusion bonding. *Intermetalics* **2018**, *99*, 59–68. [CrossRef]
32. Jarzabek, D.M. The impact of weak inter facial bonding strength on mechanical properties of metal matrix-ceramic reinforced composites. *Compos. Struct.* **2018**, *2*, 352–362. [CrossRef]

materials

MDPI

Article

Analysis of the Extrusion Process of Aluminium Alloy Profiles

Teresa Bajor [1,*], Anna Kawałek [1], Szymon Berski [1], Henryk Jurczak [2] and Jacek Borowski [3]

[1] Faculty of Production Engineering and Materials Technology, Czestochowa University of Technology, 42-201 Czestochowa, Poland
[2] Albatros Ltd., ul. Południowa 36, 78-600 Wałcz, Poland
[3] Łukasiewicz Research Network—Poznań Institute of Technology, ul. Ewarysta Estkowskiego 6, 61-755 Poznań, Poland
* Correspondence: teresa.bajor@pcz.pl

Abstract: The paper presents an analysis of the results of numerical tests of the extrusion process of structural panels made of the 5xxx and 6xxx series aluminium alloys in a designed split die. The obtained products are intended for innovative superstructures of special car bodies. The main purpose of the research was the designed split die and numerical simulations and analysis of test results to determine the parameters of the extrusion process. The distribution of stress intensity, strain, strain rate, and temperature in the extruded metal was analysed for two different speeds of the punch movement. On the basis of the analysis of the distribution of stress values occurring in the extrusion process, the conditions enabling the real process of extrusion of the panel profile in industrial conditions in the designed split die were determined. It was shown that panel sections can be produced from ingots with a length of 770 mm on a press with a pressure of 35 MN (12″).

Keywords: extrusion; aluminium alloys; car bodies; plastometric tests; rheological properties; FEM modelling

Citation: Bajor, T.; Kawałek, A.; Berski, S.; Jurczak, H.; Borowski, J. Analysis of the Extrusion Process of Aluminium Alloy Profiles. *Materials* **2022**, *15*, 8311. https://doi.org/10.3390/ma15238311

Academic Editor: Ivo Schindler

Received: 6 November 2022
Accepted: 21 November 2022
Published: 23 November 2022

Publisher's Note: MDPI stays neutral with regard to jurisdictional claims in published maps and institutional affiliations.

1. Introduction

Aluminium alloy flat bars (panels) with various, often complex, structures, which are usually made by extrusion on presses, are common products in modern, lightweight structures. Extrusion is a widely used process in the production of long components with complex cross-sections. This technological method allows for obtaining unique shapes of products, which provides exceptional design opportunities for architects and designers [1–4]. Extrusion is one of the types of metal forming processes. During the extrusion process, the material placed in the container with the die, subjected to the pressure of the punch, flows out through the holes of the die and is elongated at the expense of reducing the cross-section.

Aluminium alloys with magnesium of the 5xxx series are intended for plastic working. At the same time, these alloys are characterised by high strength properties, thanks to which they are very frequently used in various types of structures. These kinds of alloys are also characterised by very good technological properties, such as high corrosion resistance, high strength, good weldability, and ease of shaping. Moreover, they have the lowest density of all aluminium alloys, which reduces the weight of a given element, device, or entire structure. As a result, they are used in various economic sectors, and their percentage share in material processing is constantly growing. Currently, aluminium alloys are the most widely used in transport due to their low weight. At the same time, they are characterised by high strength properties and very good corrosion resistance, even in aggressive environments. In the automotive industry, aluminium alloys are used both for structural elements (frame and body elements), as well as engine parts and accessories. The use of aluminium frames significantly reduces the weight of the means of transport, which makes it easier to control, because its centre of gravity is lowered, and the braking distance of the vehicle is shortened [5–7].

6xxx series aluminium alloys contain magnesium and silicon. A characteristic feature of this series of alloys is very high corrosion resistance and good plasticity. These alloys are widely used in construction, interior design, the automotive industry, furniture, electronics, lighting, load-bearing elements of trucks, buses, ships, cranes, wagons, bridges, and barriers, as well as in the mining, chemical, food and shipbuilding industries [8–11].

Aluminium alloys have also been used as an effective method to improve the corrosion resistance and formability of Mg alloys. Magnesium and its alloys, such as aluminium alloys, are used in the automotive and aerospace industries due to their low density, good mechanical properties, excellent electromagnetic shielding ability, and good recyclability. However, the practical use of Mg alloys is limited by their low corrosion resistance [12]. Authors have presented effective methods of joining various Al/Mg alloys, with these methods also including the hot extrusion method [12]. A review of the literature showed that using the hot extrusion method can combine different materials: 1060/6063 Al alloys. The first reason is that the split metal streams are fresh without oxidation and impurities. Secondly, the materials inside the welding chamber experience high temperature, high pressure, and an almost vacuum atmosphere, which is beneficial for solid bonding and microstructure improvement [13].

The corrosion resistance of aluminium alloys can be increased by using the anodising process [14–16]. This process consists in creating a coating on the aluminium surface, which increases resistance to various external factors, such as acid rain, sea water, or UV radiation. It is also an effective way to delay the aging of aluminium. Anodising significantly improves the aesthetic value of aluminium products.

The use of extrusion technology of new large-size aluminium profiles with a width of 200 to 600 mm will allow the introduction to the market of a new solution in the form of an innovative superstructure for special-purpose vehicles, characterised by a modular body structure made of aluminium alloy panels. Thus far, no such solution exists in which extruded aluminium panels (especially from 5xxx and 6xxx series alloys) are used to build superstructures of special-purpose vehicles. Currently, the bodies of special vehicles are based on steel structures combined with composite components or steel sheets. Plastic bodies have elements joined in the gluing technology, while traditional bodies based on steel and aluminium are most often joined by welding or riveting. The use of an innovative modular superstructure with wide panels made of aluminium alloys, as proposed by the authors, eliminates the current problems, such as: very limited recycling possibilities of plastic elements, the harmfulness of substances used in the manufacturing process, and the length of the production cycle, as well as the nuisance associated with the processes of joining elements. Certainly, there are many solutions on the market that use aluminium profiles with different groove shapes and mounting methods, but there are no solutions using such wide profiles. Thanks to the use of panels, the assembly and disassembly time of bodies can be significantly reduced; individual panels can be easily replaced, which is also a very important factor in the operation of special-purpose vehicles that work in difficult conditions; their components are frequently damaged. The use of an aluminium modular superstructure made of large-size aluminium panels will allow the reduction in the weight of the vehicle by about 10% in relation to bodies currently made of welded structural steel. Moreover, aluminium is a material that helps to reduce the amount of greenhouse gases emitted into the environment. This is carried out in two ways: thanks to the use of bodies made of aluminium panels, the load capacity of the vehicles is increased, which, in turn, leads to an increase in transport capacity and the possibility of transporting more goods; the weight of the vehicles is further reduced, which helps reduce fuel consumption [1,17–21].

2. Purpose and Scope of the Study

The development of deformation technology at the design stage gives indisputable benefits when planning the production process of new products. The use of modern IT tools enables a multi-faceted analysis of changes occurring during the manufacturing process of the finished product. The purpose of the study was to design a die and to

perform and analyse the results of numerical tests of the extrusion process of structural panels made of 5xxx and 6xxx series aluminium alloys intended for innovative construction of bodies of special-purpose vehicles. The influence of the following parameters of the extrusion process was analysed: distribution of strain intensity, distribution of temperature of the extruded alloy, distribution of strain rate, and distribution of stress intensity. The calculations were made using FEM for the three-dimensional state of deformation, taking the thermal phenomena occurring during the applied deformation scheme into account. Numerical modelling of the panel profile extrusion process was performed using the Forge®NxT software based on the finite element method [18,22–26]. The main focus of the FEM modelling process in Forge®NxT was the analysis of the distribution of the above-mentioned parameters during the extrusion of three Al alloys and the assessment of their suitability for the actual shaping process in a vertical hydraulic press with a container diameter of 12″ and a pressure of up to 3500 T.

3. Materials and Methods

The material chosen for the tests was aluminium alloys with chemical compositions as given in Table 1.

Table 1. Chemical composition of the investigated alloys [%].

Alloy	Si	Fe	Cu	Mn	Mg	Cr	Zn	Ti	Al
5074	0.224	0.14	0.007	0.465	3.44	0.002	0.002	0.018	R
6005	0.40	0.175	0.05	0.05	0.675	0.05	0.05	0.05	R
6082	0.95	≤0.18	≤0.02	0.50	0.95	≤0.03	≤0.02	≤0.02	R

Before the extrusion process modelling, plastic flow models for the three analysed alloys were developed: Al5754, Al6005, and Al6082. Plastic flow models were developed based on uniaxial compression tests performed with the Gleeble 3800 metallurgical process simulator. Plastometric tests were carried out for the following parameters:

- Temperature: 350 °C, 400 °C, 450 °C, 500 °C, and 550 °C.
- Deformation velocity: 0.01 s^{-1}, 0.1 s^{-1}, 1 s^{-1}, 10 s^{-1}, and 30 s^{-1}.
- Actual deformation: max. 1.15 for the GLEEBLE 3800 simulator.

The samples were heated at a constant rate of 5 °C/s to the desired temperature, held at this temperature for 20 s, and then deformed.

The results of plastometric tests were used to determine the coefficients of the yield stress function, which were used to simulate numerical extrusion processes in the Forge®NxT software. σ_p formula (1) was used to determine the value of the yield stress. Table 2 presents the values of the parameters A and m_1–m_9 used to define the value of plasticising stress σ_p for the three aluminium alloys [22].

Table 2. Parameter values A and $m_1 \div m_9$ used to define the σ_p value of Al alloys.

Al Alloys		Al5754	Al6005	Al6082
The values of the parameters obtained as a result of the approximation of Equation (1)	A	0.1900358	79.928099	9.561×10^{-7}
	m_1	−0.0074103	−0.0055896	−0.012197
	m_2	0.3359757	0.3994022	0.1363548
	m_3	−0.1777271	−0.0724108	0.1500382
	m_4	−0.0002228	-1.323×10^{-5}	−0.000265
	m_5	−0.0042127	−0.0013238	−0.0005808
	m_7	0.4302946	−0.4114212	0.0370012
	m_8	0.0007222	0.00043599	−2.658396
	m_9	1.6723026	0.42435319	3.8141389

The values of the parameters obtained as a result of the approximation of Equation (1).

$$\sigma_p = Ae^{m_1 T}\varepsilon^{m_2}\dot{\varepsilon}^{m_3}\varepsilon^{\frac{m_4}{\varepsilon}}(1+\varepsilon)^{m_5 T}\varepsilon^{m_7 T}\dot{\varepsilon}^{m_8 T}T^{m_9} \quad (1)$$

where: σ_p—plasticising stress; $\dot{\varepsilon}$—strain rate; T—temperature of the deformed material; ε—actual deformation, A; m_1–m_9—function coefficients.

Equation (1) is frequently used to derive value σ_p in computer software for numerical modelling of plastic working.

Modelling of the extrusion process was performed for each alloy with two different punch speeds. The main simulation parameters for all analysed alloys are presented in Table 3.

Table 3. Main parameters used in extrusion process for all Al alloys.

Extrusion Speed v, mm/s	Initial Temperature of Billet T, °C	Friction Coefficient between Die and Ingot, μ	Friction Coefficient between Punch and Ingot, μ	Heat Transfer Coefficient α, kg/(°C·s^{-3})	Extrusion Ratio, λ
3 6	485	0.4	0.07	10,000	48

In order to carry out the extrusion process of the section shown in Figure 1, a die had to be designed, thanks to which it would be possible to obtain panels with a width of s = 200 mm and a thickness of h = 35 mm from an ingot homogenised in the casting process with 770 mm in length and 305 mm in diameter. The section consists of three parts: connector (I), central part (II), and outer part (III), and it is a component of load-bearing structures used in the automotive industry. To carry out the extrusion process, a multi-port die was designed with bridges separating the extruded material in such a way to obtain an even plastic flow of the metal in the calibration zone of the die.

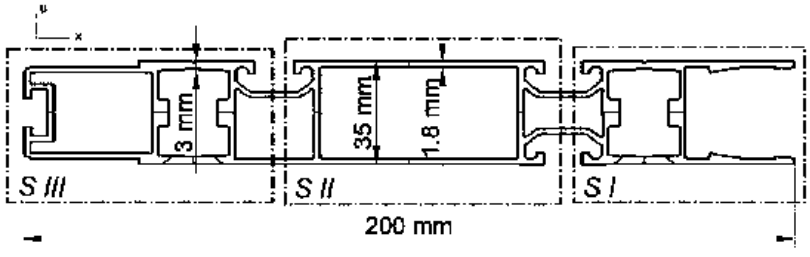

Figure 1. Panel section of an arm (component) for load-bearing structures used in the automotive industry with dimensions of 200 mm × 35 mm.

In this type of die, during metal deformation, both in the real process and during process modelling using the finite element method, metal deformation occurs in several characteristic stages, as shown on the example of a port die with longitudinal and transverse bridges in Figure 2.

In the first stage of the extrusion process, the metal in the container contacts the die and flows into the ports, where it is separated by port bridges, both transverse and longitudinal (Figure 2a).

From the data presented in Figure 2a, a local increase in the metal flow velocity can be observed. In the next stage (Figure 2b), the metal fills the ports and flows into the welding chamber. At this stage, the value of the metal flow velocity decreases. In the last step of the extrusion process, when the welding chamber is filled with metal, the value of the plastic flow velocity increases again and reaches a maximum when passing through the calibration zone.

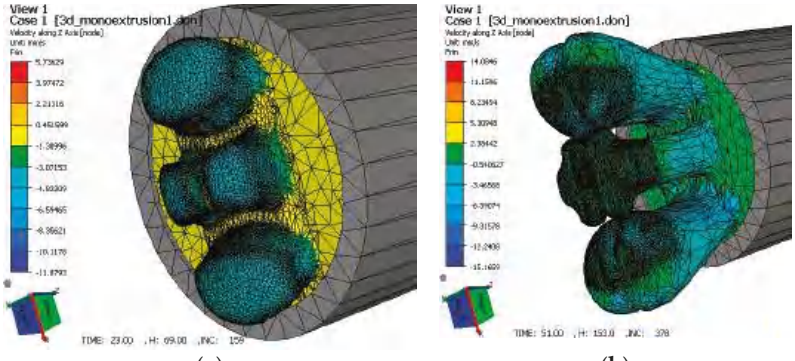

(**a**) (**b**)

Figure 2. Stages of metal deformation in port dies with separating bridges (edges), a core, and a welding chamber: (**a**) metal is separated in the core part of the die through port bridges; (**b**) metal flows into the welding and calibration zone through contact with the plate part of the die.

The metal flow kinematics in this type of die is determined by the distribution of the parameters that affect the plasticisation of the material, such as temperature, deformation, or strain rate. To obtain a section with the cross-section shown in Figure 1, a die was designed, the essential elements of which are shown in Figure 3.

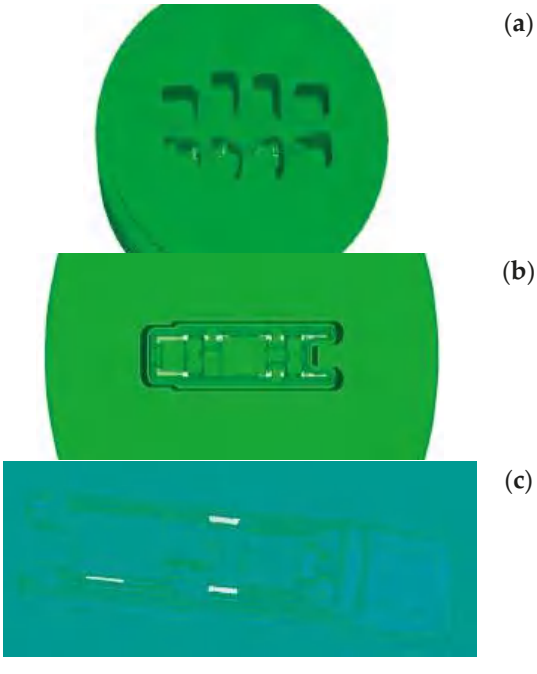

(**a**)

(**b**)

(**c**)

Figure 3. Die structure: (**a**) inlet part to the die with port opening; (**b**) two-stage calibration part of the die; (**c**) outlet part of the die, where the metal temperature stabilises after leaving the calibration zone (not used in the first modelling stage).

Due to the small wall thickness of the panel section (g = 1.8 mm, and the largest is g_{max} = 3 mm) in relation to its width (s = 200 mm) and the symmetrical arrangement of the

cutout, the analysis covered the distributions on the contact surface of the deformed metal with the die.

At the first stage of forming the section walls, deformation unevenness results from different metal flow velocities along the axis, which causes the formation of tongues (uneven shape of the beginning of the strand) and, therefore, the first stage of metal flowing out of the calibration part of the die was analysed.

The largest metal deformations during the extrusion process in this type of dies occur at two characteristic stages of the process. These are the stages in which the metal initially flows perpendicular to the axis of the ingot, and then, due to the shape of the die, the direction of its flow is forced to change to parallel to the axis of the ingot. Inner layers of the metal that are not in direct contact with the curved surface (edge) of the die have a slower flow velocity than those in direct contact with the surface of the tool. In these zones, there is a large velocity gradient, which causes areas of large deformation in the subsurface layers. Such a concentration of deformations in these zones is related to the tool geometry (edge rounding radius and edge inclination angle), which is not affected by the type of deformed material, the plastic resistance to metal flow resulting from the friction of external metal layers against the tool, and the internal friction depending on the material properties of the deformed metal.

During metal deformation in the designed die, there are two areas characterised by a high concentration of deformations. The first area is the zone where the metal flows from the container to the ports during metal separation. The second is a two-stage area of metal outflow from the welding chamber to the calibration part, where the panel profile is given the final shape. Modelling of the extrusion process of the panel section shown in Figure 1 was performed for three different 5xxx and 6xxx series Al alloys. Moreover, in order to adapt the modelled process to the real conditions of one of the industrial aluminium presses, the process was carried out for two punch speeds: 3 and 6 mm/s.

4. Analysis of Modelling Results of the Panel Profile Extrusion Process Using the Forge®NxT Software

4.1. Analysis of Strain Intensity Distributions

Figures 4–6 show the distribution of strain intensity during the process of extrusion of a panel section from three different Al alloys.

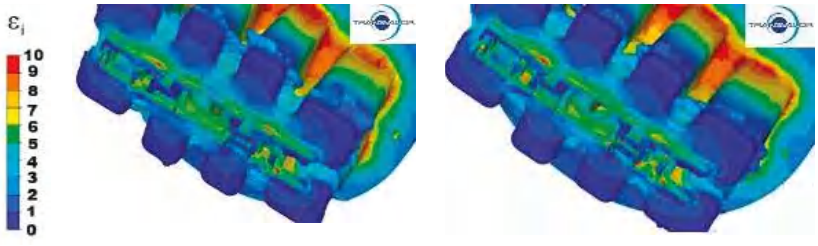

(**a**) (**b**)

Figure 4. Distribution of strain intensity—Al 5754 alloy: (**a**) punch feed speed 3 mm/s; (**b**) punch feed speed 6 mm/s.

For all tested materials and variants of the extrusion process, two areas with a high concentration of strain intensity can be observed. The differences result from the size of these areas and the value of deformations.

For 5754 aluminium at the punch speed v = 3 mm/s (Figure 4a) in the first area, the highest values of strain intensity are observed (ε = 10), mainly in the central metal zones of the base of the port walls (port entrances) and in small fragments in the contact area of the bridge surfaces with the port walls. By contrast, for the maximum values of deformation on the same surfaces, but for the 4 ports furthest from the axis of the ingot, the values of strain

intensity are, on average, between 8 and 9. In the second area, the highest strain intensity is observed at the edge of the second stage of cross-sectional reduction, in the places where the section wall is thickest, and in the corners of individual parts of the section. One can also observe a large unevenness in strain intensity in parts I and II, their value ranging from 5 to 9. The lowest values of strain intensity occur in the welding chamber, in the corners of the ports, where the metal has the lowest flow velocity and specific dead zones are formed. The same phenomenon occurs in the corners of the container, where the values of strain intensity are also very small.

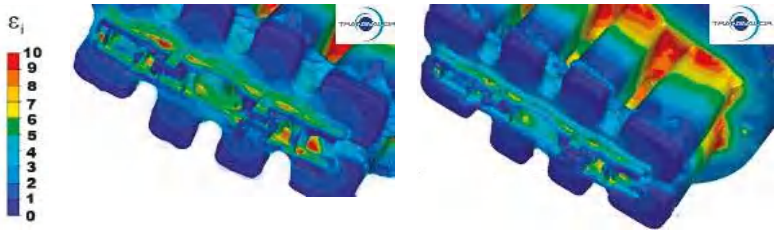

(**a**) (**b**)

Figure 5. Distribution of strain intensity—Al 6005 alloy: (**a**) punch feed speed 3 mm/s; (**b**) punch feed speed 6 mm/s.

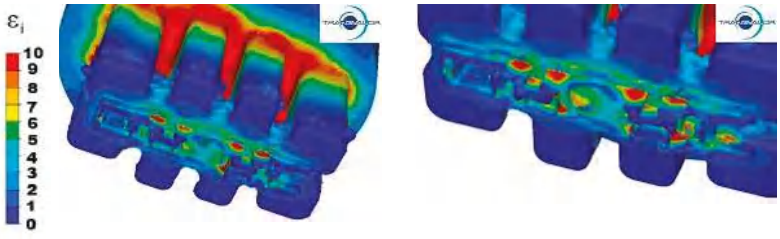

(**a**) (**b**)

Figure 6. Distribution of strain intensity—Al 6082 alloy: (**a**) punch feed speed 3 mm/s; (**b**) punch feed speed 6 mm/s.

Increasing the extrusion speed to 6 mm/s (Figure 4b) causes an increase in the zones with maximum values of strain intensity in the first area, and for the ports that are furthest from the axis of the ingot, strain intensity increases to the value of 10. However, in the second area, due to higher values of the metal flow velocity and the uniform flow of the metal along the axis of the ingot, the values of strain intensity range from 4 to 6.

For 6005 aluminium extruded with a punch speed of v = 3 mm/s (Figure 5a), the highest values of strain intensity equal to 10 were observed in the first area, mainly on the entire contact surface of the bridges with the metal and at the base of the walls of all ports. In the second area, the highest strain intensity is observed in the same places as for the Al 5754 alloy. However, the unevenness of the distribution of strain intensity is much greater, because the area with the greatest deformations is larger and in part III, it covers almost 50% of its length, while in parts I and II, the values of strain intensity vary in the range from 5 to 10. The lowest strain intensity occurs in the welding chamber in the corners of the ports and in the corners of the container, and its value is from 0 to 1.

For this Al alloy, an increase in the extrusion speed to 6 mm/s (Figure 5b) results in a more even distribution of the strain intensity in the second reduction stage, where the non-uniformity between strains is in range from 2 to 5, while in the first reduction stage, these irregularities are significant and in the range from 4 to 10. In all three parts (I–III), the maximum values of the strain intensity appear in the places where the profile walls are thickest, because in these places, the metal has a higher flow velocity than in the

neighbouring thin-walled zones. This difference in flow velocity causes large deformations in these places.

During the extrusion process of the 6082 aluminium alloy with the punch speed v = 3 mm/s (Figure 6a), it can be observed that in the first area, the zone of maximum deformation values is very extensive and virtually covers the entire area of the base of metal entry into the ports and reaches up to 20% of the height of the ports. In the second area, deformation unevenness is very high, and deformation values range from 2 to 10.

By increasing the extrusion speed of this alloy to 6 mm/s (Figure 6b), the area containing the deformation with maximum values extends to about 25% of the port length in the first area, and in the second area, the distribution of deformation in individual parts is almost the same as the distribution obtained for the punch speed of 3 mm/s.

On the basis of the tests carried out, it is found that the increase in the extrusion speed increases the strain intensity in specific zones. The distributions of strain intensity values obtained on the cross-section of the extruded profile depend on the thickness of the profile wall.

4.2. Analysis of Temperature Distribution in the Extruded Metal

The temperature distribution in the process of extrusion of sections depends strictly on the temperature conditions of the tools and their shape, as well as on the process conditions—in this case, extrusion speed and friction. Moreover, the material properties of the extruded metal are extremely important, as they significantly affect the plastic flow resistance of the metal during extrusion and have a significant share in the value of energy and strength parameters of the process. There are only few plants in Poland and in the world where it is possible to carry out the process of extrusion of this type of section, due to the need to use containers with large diameters and complicated shapes of dies, which results in a large energy expenditure, possible only in presses with very high pressures. Therefore, in the next stage of the study, an analysis of the temperature distribution during the process of extrusion of a panel section from three different Al alloys was carried out (Figures 7–9). Simulations of the extrusion process were carried out for two different punch speeds: 3 and 6 mm/s. The analysis of the temperature distribution was performed mainly in the calibration zone, i.e., in the area where the plastic metal flows out from the ports in the welding chamber zone to the calibrating strips.

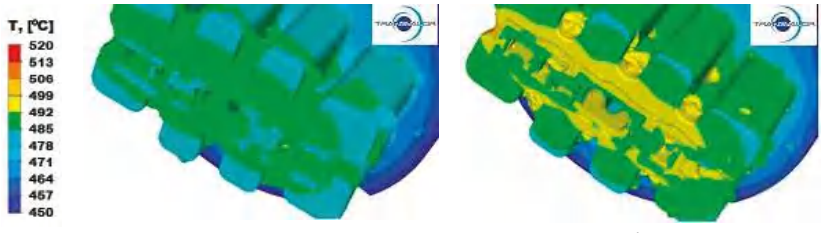

(**a**) (**b**)

Figure 7. Temperature distribution—Al 5754 alloy: (**a**) punch feed speed 3 mm/s; (**b**) punch feed speed 6 mm/s.

For the Al5754 alloy and the extrusion speed v = 3 mm/s (Figure 7a), the temperature values range from 485 °C to 492 °C. Higher temperature is observed in parts I and III, where the section has a thickened wall, where there is a less intense heat exchange with the surroundings, and where large deformations occur. Increasing the punch feed speed to 6 mm/s (Figure 7b) affects the unevenness of the temperature distribution in the individual parts, as well as in the entire volume of the die. The same temperature of approximately 492 °C occurs along the entire calibration strip in part II, while in part III, the temperature ranges from 492 °C to 499 °C. In part II, a temperature distribution from 488 °C on the

thickened wall to 499 °C on the free ends of the section can be observed. For this material (Figure 7b), the temperature in the corners of the ports in the welding zone drops to 480 °C.

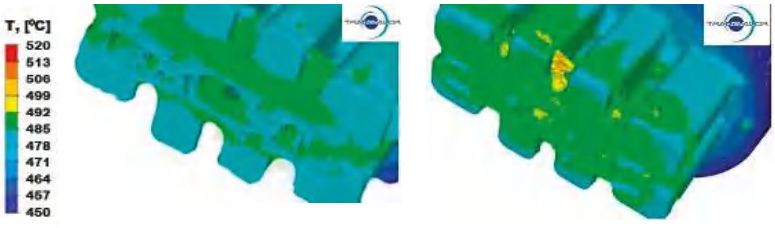

(**a**) (**b**)

Figure 8. Temperature distribution—Al 6005 alloy: (**a**) punch feed speed 3 mm/s; (**b**) punch feed speed 6 mm/s.

(**a**) (**b**)

Figure 9. Temperature distribution—Al 6082 alloy: (**a**) punch feed speed 3 mm/s; (**b**) punch feed speed 6 mm/s.

For aluminium 6005 extruded with a punch speed of v = 3 mm/s (Figure 8a), the temperature distribution is uniform for all parts and ranges from 478 °C to 485 °C. After increasing the punch feed speed to v = 6 mm/s (Figure 8b), the metal slightly cools down at the ends and reaches temperatures in the range of 478–485 °C, in relation to the temperature of the metal along the axis of the ingot in part II, where it reaches the temperature of 492 °C.

When extruding aluminium 6082 at a lower punch feed speed (Figure 9a), an even temperature is observed in the entire volume of the metal contained in the die in the range from 478 °C to 484 °C. Increasing the extrusion speed (Figure 9b) does not change the nature of its decomposition, but causes an increase by about 7 °C.

4.3. Analysis of the Distribution of Strain Rate

Modelling the extrusion process of a panel section in a die with a constant shape causes the metal in all variants of the process to have the same plastic deformation path, which means that extrusion speed (v) has the greatest impact on the distribution of strain rate values. The temperature of the deformed metal and its rheological properties also have a significant effect on the distribution of strain rate. Process analysis with the use of FEM enables assessing the sensitivity of the material to strain rate.

Numerical analysis of strain rate for the panel section extrusion process allowed for determining the value ranges of this parameter. For all analysed Al alloys and two tested punch feed rates, the intensity of the extrusion speed is in the range from 0 to 3 s^{-1}. This is the lower limit of the value of strain rate that occurs during the extrusion process. In the literature [27,28], it is assumed that for hydraulic presses, it is in the range from 3 to 10 s^{-1} and in mechanical presses, from 20–80 s^{-1}.

For alloy Al5754, the distribution of strain rate is shown in Figure 10a. Disregarding the values for erroneous mesh nodes (red—escape of nodes from the port), intensity strain and velocity are in the range from 0 to 1.5 s^{-1}. The greatest strain rate is observed in the

welding zone, where the metal filling the die changes its direction rapidly and the value of the plastic flow rate changes as well. The change in the flow direction is forced by the tool geometry and is limited in this area: by the die core, the edges of the ports, and the bridges (areas marked with a solid line). In this zone, the highest values of strain rate range from 0.3 to 1.2 s^{-1}, whereas in the zone of two-stage reduction of the cross-section of the metal flowing from the welding chamber to the calibration part (area marked with a dashed-dotted line), the values of strain rate range from 0.3 to 1.5 s^{-1}.

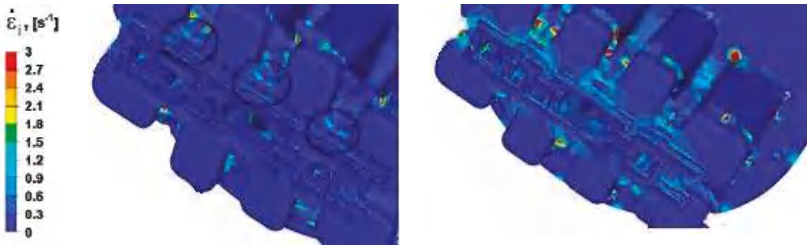

(**a**) (**b**)

Figure 10. The distribution of strain rate—alloy Al 5754: (**a**) punch feed speed 3 mm/s; (**b**) punch feed speed 6 mm/s.

When the extrusion speed is increased to 6 mm/s (Figure 10b), areas with higher values of strain rate are greater, and the maximum values of the average strain rate reach up to 2.1 s^{-1}.

In the process of extrusion of alloy Al 6005 deformed at a speed of v = 3 mm/s (Figure 11a), in the welding zones (marked in Figure 10a with a solid line), the distribution of strain rate is similar to the distribution obtained for alloy Al5754. There are areas of increased intensity of strain rate in the shape of cones, where the average values range from 0.3 to 0.9 s^{-1}; however, the distribution of strain rate is more uniform. An uneven distribution of strain rate can be noticed in the area of the two-stage reduction in the cross-section, where the values of strain rate are up to 2.1 s^{-1}.

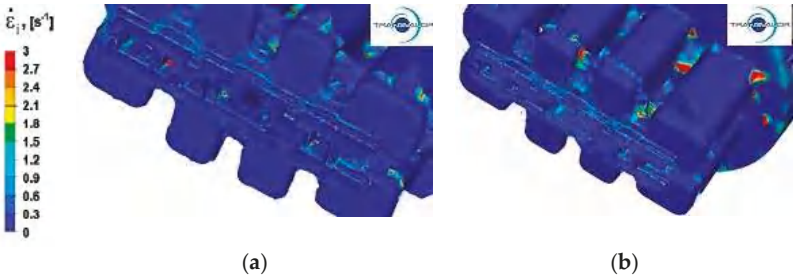

(**a**) (**b**)

Figure 11. The distribution of strain rate—alloy Al 6005: (**a**) punch feed speed 3 mm/s; (**b**) punch feed speed 6 mm/s.

Increasing the extrusion speed to v = 6 mm/s (Figure 11b) increases the maximum values of strain rate, which is about 3 s^{-1}. The average values of this parameter in the zone where the material exits from ports (for the area marked with a solid line in Figure 10a) are slightly higher than for the extrusion process with punch feed speed v = 3 mm/s and range from 0.3 to 1.2 s^{-1}. Similarly, comparing the metal flow during the extrusion process with velocity v = 3 mm/s, the area with an uneven distribution of strain rate is slightly larger in the zone of two-stage reduction of the cross-section (part II), and the value of strain rate increases to 2.4 s^{-1}. Zones with the highest values of strain rate occur at the height of the

cones of intense flow resulting from the zone where the metal passes from the port bridge to the calibration zone.

In the process of extrusion of alloy Al 6082, the areas with the highest values of strain rate occur when the aluminium flows into the port channels in the material separation zone, and the values of this parameter reach 3 s^{-1}. In part II also, in the first and second reduction stage, in the central part of the blank, the maximum values of strain rate appear (Figure 12a).

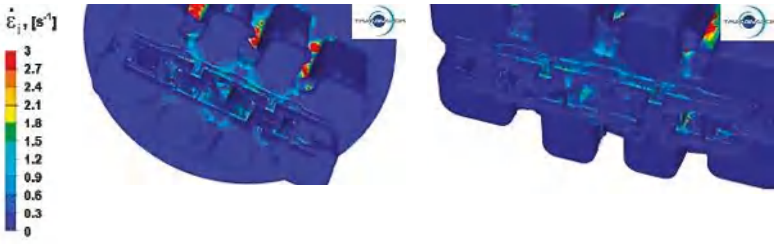

(**a**) (**b**)

Figure 12. The distribution of strain rate—alloy Al 6082: (**a**) punch feed speed 3 mm/s; (**b**) punch feed speed 6 mm/s.

By increasing the extrusion speed, it is possible to obtain the effect of a more even distribution of strain rate over the entire cross-section of the section, which is particularly visible in part I in the first reduction stage (Figure 12b).

4.4. Analysis of the Distribution of Stress Intensity

Figures 13–15 show the distribution of stress intensity for the three tested Al alloys and for two punch feed speeds during extrusion of a panel section.

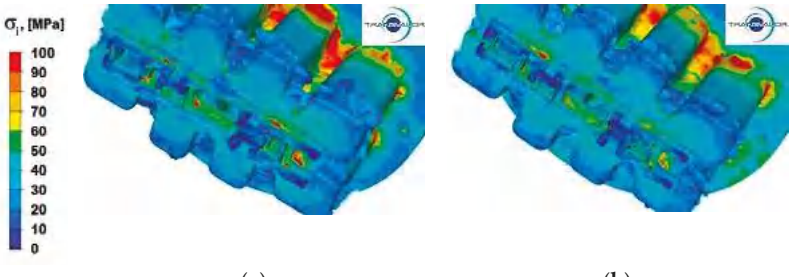

(**a**) (**b**)

Figure 13. Distribution of stress intensity—alloy Al 5754: (**a**) punch feed speed 3 mm/s; (**b**) punch feed speed 6 mm/s.

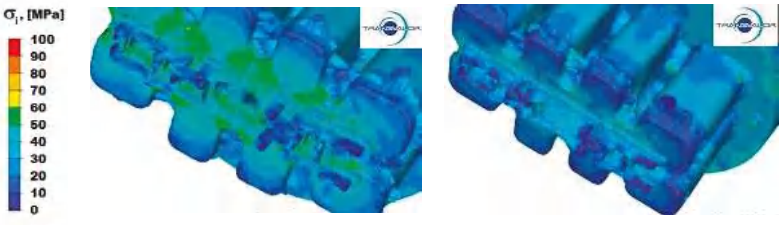

(**a**) (**b**)

Figure 14. Distribution of stress intensity—alloy Al 6005: (**a**) punch feed speed 3 mm/s; (**b**) punch feed speed 6 mm/s.

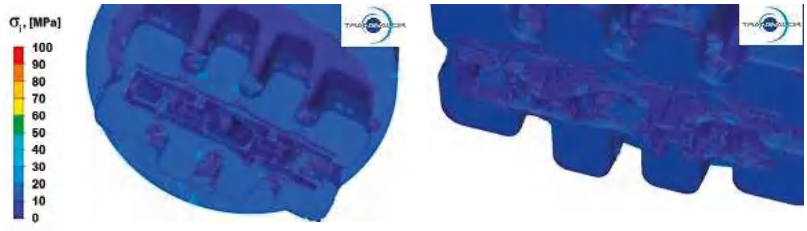

(**a**) (**b**)

Figure 15. Distribution of stress intensity—alloy Al 6082: (**a**) punch feed speed 3 mm/s; (**b**) punch feed speed 6 mm/s.

Figure 13a,b show the distribution of stress intensity during the alloy Al 5754 extrusion process deformed at two different punch feed speeds. From the data provided in these figures, it can be observed that for this Al alloy, the largest areas of maximum stress intensity occur in the places where the aluminium flows into the ports and on the edges separating the ports, whereas in the calibration zone, the maximum values of stress intensity occur only in single nodes of the second reduction stage.

In Figure 13b, showing the distribution of stress intensity during the extrusion process at a speed of 6 mm/s, it can be observed that increasing the extrusion speed results in a more uniform flow of the aluminium layers in the separation zone. It also includes small areas where the maximum values of stress intensity occur. By contrast, in the calibration zone, there is a slight increase in the value of stress intensity, both in the first and in the second reduction stage. It is especially visible in the axial zone (part II of the section—Figure 1), where the values of stress intensity increase from 20 to 60 MPa.

For aluminium 6005, the values of stress intensity in the same stage of the extrusion process in all characteristic areas are significantly lower than for alloy Al 5754. In the process of extruding the section with punch feed speed v = 3 (Figure 14a), the highest values of stress intensity occur in the calibration area (part II). It is especially visible in places where the distribution of strain rate (Figure 11a,b) includes cones of intense flow, and the values of stress intensity reach up to 60 MPa. In the reduction area in the first and second stage, there are different values of stress intensity from 20 MPa to 60 MPa. In the separation area (I), stress intensity is much lower and reaches a maximum of 40 MPa. By increasing the extrusion speed to 6 mm/s (Figure 14b) in area I (separation), the values of stress intensity slightly increase to about 50 MPa, whereas in part II, both in the first and second stage of reduction, the values of stress intensity are distributed more evenly than for the punch feed speed v = 3 mm/s and are in the range from 30 to 50 MPa. Apart from a greater uniformity of stress intensity, this alloy is not very sensitive to changes in strain rate.

Data in Figure 15 suggest that during the deformation of alloy Al 6082, the values of stress intensity both in the separation and calibration zones, as well as in the remaining area, are in the range from 10 to 30 MPa and slightly differ for both extrusion speeds tested.

Table 4 shows the values of punch pressure on the metal determined in the modelling process during the profile extrusion for all analysed alloys and the two punch feed speeds.

The data in Table 4 show that the highest values of the total pressure of the punch during the profile extrusion process occur for aluminium alloy 5754, and the lowest for 6082 alloy. Based on the presented results of numerical tests of the profile extrusion process, it can be concluded that it is possible to carry out the extrusion process of this product on a press with a pressure of 3500 T.

Table 4. Summary of values of the total punch pressure during profile extrusion.

Aluminium Alloy	The Speed of the Punch [mm/s]	Total Pressure [T]
5754	3	2500
	6	2800
6005	3	1200
	6	1300
6082	3	1100
	6	1300

5. Final Statements and Conclusions

Based on the theoretical analysis of the study results of the extrusion process of the Al alloy panel section, the following conclusions were formulated:

- Based on the obtained results, it is possible to define the conditions enabling the actual process to be carried out in an industrial plant in a designed split die.
- Taking the actual rheological properties of the analysed Al alloys during numerical modelling of the extrusion process into account will ensure an increase in the accuracy of calculations in relation to the actual technological processes.
- For all tested materials and variants of the extrusion process, two areas of high concentration of strain intensity can be observed. There are differences in the sizes of these areas and in the values of deformation.
- The conducted numerical tests show that the temperature increase in the deformed material is related to plastic deformation and the friction phenomenon occurring between the material and the die.
- The value of the pressing force during the process depends on the stage of the extrusion process. The first maximum local pressure force occurs when the material is separated by the port bridges, both transverse and longitudinal. In the next step, the metal fills the ports and flows into the welding chamber. At this stage, the value of the extrusion force drops slightly. As the sealing chamber is filled, the value of the extrusion force increases again and reaches its maximum when passing through the calibration zone.
- Based on the analysis of the distribution of values of force occurring in the extrusion process, it can be concluded that panel sections can be produced from ingots with a length of 770 mm using a press with a pressure of 35 MN (12″), because the maximum extrusion force does not exceed 30 MN.

Author Contributions: Methodology, T.B., S.B., H.J. and J.B.; Software, S.B.; Validation, T.B., A.K. and J.B.; Formal analysis, T.B., A.K. and S.B.; Investigation, T.B, S.B. and H.J.; Resources, H.J. and J.B.; Data curation, T.B., A.K. and S.B.; Writing—original draft, T.B. and S.B.; Writing—review & editing, A.K.; Visualization, T.B. and S.B.; Supervision, H.J.; Project administration, A.K., H.J. and J.B.; Funding acquisition, A.K. and J.B. All authors have read and agreed to the published version of the manuscript.

Funding: European Regional Development Funds: POIR.04.01.04-00-0016/17.

Institutional Review Board Statement: Not applicable.

Informed Consent Statement: Not applicable.

Acknowledgments: This work was supported by the project entitled Ultralight and high-strength modular structural panels for applications e.g., in the bodywork construction of special vehicles implemented under Measure 4.1 "Research and development work", Submeasure 4.1.4 "Application projects" of the Operational Programme Smart Growth 2014–2020 co-financed by the European Regional Development Funds, agreement No. POIR.04.01.04-00-0016/17.

Conflicts of Interest: The authors declare no conflict of interest.

References

1. Miller, W.S.; Zhuang, L.; Bottema, J.; Wittebrood, A.J.; De Smet, P.; Haszler, A.; Vieregge, A. Recent development in aluminium alloys for the automotive industry. *Mater. Sci. Eng. A* **2000**, *280*, 37–49. [CrossRef]
2. Luo, A.A. Recent advances in light metals and manufacturing for automotive applications. *CIM J.* **2021**, *12*, 79–87. [CrossRef]
3. Fridlyander, I.N.; Sister, V.; Grushko, O.E.; Berstenev, V.V.; Sheveleva, L.M.; Ivanova, L.A. Aluminum Alloys: Promising Materials in the Automotive Industry. *Met. Sci. Heat Treat.* **2002**, *44*, 365–370. [CrossRef]
4. Poole, W.J.; Wells, M.A.; Azizi-Alizamini, H.; Parson, N.C. Through process podelling of pxtrusion for AA3xxx alloys. *Mater. Sci. Forum* **2014**, *794–796*, 682–690. [CrossRef]
5. Siczek, K.S.K. Light solution in the Automotive Industry (Lekkie rozwiązania w przemyśle zamochodowym). *Autobusy* **2017**, *12*, 1311–1314.
6. Cortés, J.A.; Díez, L.; Cañete, F.J.; Sánchez-Martínez, J.J.; Entrambasaguas, J.T. Performance analysis of OFDM modulation on indoor broadband PLC channels. *EURASIP J. Adv. Signal Process.* **2011**, 78. [CrossRef]
7. Taub, A.; Krajewski, P.E.; Luo, A.; Owens, J.N. Yesterday, today, and tomorrow: The evolution of technology for structural materials over the last 50 years. *JOM* **2007**, *59*, 48–57. [CrossRef]
8. Polmear, I.; StJohn, D.; Nie, J.-F.; Qian, M. Wrought Aluminium Alloys. *Light Alloy.* **2017**, 157–263. [CrossRef]
9. Polmear, I.J. Recent developments in light alloys. *Mater. Trans. JIM* **1996**, *37*, 12–31. [CrossRef]
10. Hirsch, J. Recent development in aluminium for automotive applications. *Trans. Nonferrous Met. Soc. China* **2014**, *24*, 1995–2002. [CrossRef]
11. Mukhopadhyay, P. Alloy Designation, Processing, and Use of AA6XXX Series Aluminium Alloys. *Int. Sch. Res. Netw.* **2012**, *2012*, 165082. [CrossRef]
12. Chen, L.; Tang, J.; Zhao, G.; Zhang, C.; Chu, X. Fabrication of Al/Mg/Al laminate by a porthole die co-extrusion process. *J. Mater. Process. Technol.* **2018**, *258*, 165–173. [CrossRef]
13. Fan, X.; Chen, L.; Chen, G.; Zhao, G.; Zhang, C. Joining of 1060/6063 aluminum alloys based on porthole die extrusion process. *J. Mater. Process. Technol.* **2017**, *250*, 65–72. [CrossRef]
14. Martínez-Viademonte, M.P.; Abrahami, S.T.; Hack, T.; Burchardt, M.; Terryn, H. A Review on Anodizing of Aerospace Aluminum Alloys for Corrosion Protection. *Coatings* **2020**, *10*, 1106. [CrossRef]
15. Grillet, A.M.; Gorby, A.D.; Trujillo, S.M.; Grant, R.P.; Hodges, V.C.; Parson, T.B.; Grasser, T.W. Mechanical properties of anodized coatings over molten aluminum alloy. *J. Colloid Interface Sci.* **2007**, *317*, 264–274. [CrossRef]
16. Ziobro, G.; Richert, M.; Wiewióra, M. Influence of corrosion on mechanical properties and microstructure of 3XXX, 5XXX and 6XXX series aluminum alloys. *Metall. Foundry Eng.* **2017**, *43*, 291. [CrossRef]
17. Ángel, M.; Salaverría, P.; Rover, J. Intensive use of a aluminium in ar body construction. In Proceedings of the 12th European Automotive Congress, EAEC, Bratislava, Slovakia, 29 June–1 July 2009; pp. 1–15.
18. Dyja, H.; Tussupkaliyeva, E.; Bajor, T.; Laber, K. Physical Modeling of Plastic Working Conditions for Rods of 7xxx Series Aluminum Alloys. *Arch. Metall. Mater.* **2017**, *62*, 515–521. [CrossRef]
19. Peppas, A.; Kollias, K.; Dragatogiannis, D.; Charitidis, C. Sustainability analysis of aluminium hot forming and quenching technology for lightweight vehicles manufacturing. *Int. J. Thermofluids* **2021**, *10*, 100082. [CrossRef]
20. Raugei, M.; El Fakir, O.; Wang, L.; Lin, J.; Morrey, D. Life cycle assessment of the potential environmental benefits of a novel hot forming process in automotive manufacturing. *J. Clean. Prod.* **2014**, *83*, 80–86. [CrossRef]
21. Del Pero, F.; Delogu, M.; Berzi, L.; Dattilo, C.A.; Zonfrillo, G.; Pierini, M. ScienceDirect Sustainability assessment for different design solutions within the automotive field Sustainability assessment for different design solutions within the automotive field. *Procedia Struct. Integr.* **2019**, *24*, 906–925. [CrossRef]
22. Dyja, H.; Galkin, A.M.; Knapiński, M. *Rheology of Plastically Deformed Metals (Reologia Metali Odkształcanych Plastycznie)*; Wydawnictwo Politechniki Częstochowskiej: Czestochowa, Poland, 2010.
23. Lesniak, D.; Rękas, A.; Libura, W.; Zasadziński, J. Study of the deformability of 5xxx series aluminum alloys with high Mg content in a semi-industrial extrusion process. *Met. Form.* **2014**, *25*, 159–167. Available online: https://www.researchgate.net/publication/319873131 (accessed on 26 April 2022).
24. Bajor, T.; Kawałek, A.; Sawicki, S.; Laber, K.; Borowski, J. Influence of deformation conditions on the rheological properties of 6XXX series Al alloy. *Metall. Foundry Eng.* **2018**, *44*, 161. [CrossRef]
25. Kawałek, A.; Bajor, T.; Sawicki, S.; Krakowiak, M.; Jurczak, H. The effect of deformation conditions on the rheological properties of the Al 5754 alloy. *Metalurgija* **2020**, *1*, 43–46.
26. Kawałek, A.; Bajor, T.; Kwapisz, M.; Sawicki, S.; Borowski, J. NUMERICAL MODELING OF THE EXTRUSION PROCESS OF ALUMINUM ALLOY 6XXX SERIES SECTION. *J. Chem. Technol. Metall.* **2021**, *56*, 375–381.
27. Smith, E.H. *Mechanical Engineer's Reference Book*, 12th ed.; Elsevier: Amsterdam, The Netherlands, 1994.
28. Totten, G.E.; Tiryakioglu, M.; Kessler, O. *Encyclopedia of Aluminum and Its Alloys*; EBook, CRC Press: Boca Raton, FL, USA, 2018.

materials

MDPI

Article

Bonding of Al6061 by Hot Compression Forming: A Computational and Experimental Study of Interface Conditions at Bonded Surfaces

Brigit Mittelman [1,2,*], Michael Ben-Haroush [2], Ira Aloush [1], Linoy Mordechay [1] and Elad Priel [1,2,*]

[1] Department of Mechanical Engineering, Center for Thermo-Mechanics and Failure of Materials, Shamoon Collage of Engineering, Bee'r-Sheva 84100, Israel; sikora.ira92@gmail.com (I.A.); linoy1101@gmail.com (L.M.)
[2] Department of Materials, Nuclear Research Center Negev (NRCN), Bee'r-Sheva 84190, Israel; mikib789@gmail.com
* Correspondence: brigit@post.bgu.ac.il (B.M.); eladp@sce.ac.il (E.P.)

Abstract: In recent years, there has been a growing interest in composite components, which may be designed to provide enhanced mechanical and physical effective properties. One of the methods available to produce such components is joining by plastic deformation, which results in metallurgical bonding at the interface. However, the portions of the interface that are bonded and the inhomogeneity in the bonding strength achieved at the interface tend to be overlooked. In the present study, Al6061 beams were bonded, by hot compression (300–500 °C) to different degrees of reduction. The compression was followed by tensile debonding experiments and the revealed interface was microscopically characterized in order to determine the areas that were metallurgically bonded. The SEM characterization revealed that the actual bonded area is much smaller than the interface contact area. Thermo-mechanical finite element models of the compression stage were used to investigate the thermo-mechanical fields, which develop along the interface and influence the resulting bonding strength. The principal strain field patterns across the interface area were shown to be similar to the experimentally observed temperature-dependent bonding patterns. In addition, a quantitative criterion for bonding quality was implemented and shown to correlate with the experimental findings.

Keywords: bonding strength; compression; forming; Al6061; FE

Citation: Mittelman, B.; Ben-Haroush, M.; Aloush, I.; Mordechay, L.; Priel, E. Bonding of Al6061 by Hot Compression Forming: A Computational and Experimental Study of Interface Conditions at Bonded Surfaces. *Materials* **2021**, *14*, 3598. https://doi.org/10.3390/ma14133598

Academic Editor: Ivo Schindler

Received: 31 May 2021
Accepted: 23 June 2021
Published: 28 June 2021

1. Introduction

Modern engineering components used in the aerospace, automotive and nuclear industries are designed to function under greater operating loads and harsher environmental conditions [1,2]. This is possible due to the incorporation of new and innovative composite materials, which provide enhanced mechanical and physical effective properties [3]. One class of composite components are multi-layered components, in which dissimilar or similar materials are joined to create one metallic component [4–6]. Joining processes can be classified into the following two groups: mechanical joining (such as by using fasteners, and clinching), and joining that includes metallurgical bonding (such as welding and adhesive bonding) [7]. The use of aluminum alloys for structural component manufacturing for those industries is increasing, due to their characteristic high strength-to-weight ratio, excellent formability and corrosion resistance. Among the widely used aluminum alloys is Al 6061, which, in addition to the mentioned characteristics, is also heat treatable and weldable, making it useful for a wide range of industrial applications [8]. Metallurgical bonding is obtained by diffusion processes between parts with mutual interface. The diffusion process is governed by temperature, pressure, surface quality, and bonding time [9].

One of the methods that results in metallurgical bonding is joining by plastic deformation, or "cold welding", in which similar and dissimilar metals can be combined

without melting. This method enables bonding large surfaces together, as opposed to small bonded areas obtained in mechanical bonding methods, such as riveting and clinching. Joining by plastic deformation also enables joining a wide range of materials (dissimilar included), with less distortion and residual stresses, and with high process reliability. A comprehensive review on the advantages and limitations of various plastic joining methods is given in [10].

Commonly used joining processes by plastic deformation include cold and hot roll-bonding [4–6,11–13], co-extrusion [14,15], and compression [16–18]. The effectiveness of such multi-layered composites as load-bearing components highly depends on the interface strength between the different metallic layers [19,20]. There are various methods proposed in the literature for the quantification of bonding strength. In [5], the bond strength of hot-rolled Al–Mg–Al composites was investigated. The hot rolling was conducted at several pre-heated temperatures of 400–475°, with a single reduction pass of 60%, 70% or 80%. The average bond strength was estimated using dog-bone specimens cut in the rolling direction, with a maximum bond strength of 66 MPa reported for the lowest temperature and reduction utilized. In [4], the strength obtained in cold-rolled Al–St–Al strips was investigated. Thickness reductions of 10–65% were conducted, and the average bond strength was estimated using a peel test. It was reported that the increased reduction ratio resulted in a higher contact pressure and increased bond strength. The study in [4] reports two interesting findings. It was shown that increasing the roll speed, although it did not increase the contact pressure, resulted in an increase in the average bond strength. It was also reported that increasing the yield strength of the inner layer (using higher strength steel), although increasing the contact pressure, resulted in a lower bond strength. These findings may hint that interface deformation, rather than interface pressure, plays a critical role in bond formation. In a recent study, hot compression bonding of 2196 Al–Cu–Li alloys, at temperatures of 450–550 °C and an axial compression of 20–60% at different strain rates, was investigated [18]. Tensile specimens were machined from the compressed samples and tested, to estimate the average bond strength. The study defined two parameters to quantify the bond strength with respect to the original material strength and elongation. These are, in essence, a normalized maximum stress (max bond stress/max material stress) and normalized elongation (max bond elongation/max material elongation). It was shown that a scalar parameter, which is a function of temperature, strain, and stress values, can be correlated to the normalized bond strength. A similar approach was applied by the authors of this manuscript to define the bond criterion in hot-rolled Al–Al strips [21].

The main limitation of the various studies reported in the literature is the assumption that all of the interface is metallurgically bonded; this is not necessarily the case, as the thermo-mechanical fields that govern the formation of the metallurgical bond are usually inhomogeneous across the contact interface area [21]. This implies that the measured bond strength, which is computed as the peak load at debonding divided by the contact area, is only a crude estimation. For the design of optimal bonding processes, it is first necessary to determine how local thermo-mechanical field values, rather than global average values, influence the bond strength.

The goal of the current study is to correlate between the local thermo-mechanical fields that develop during hot compression bonding and the resulting metallurgically bonded areas. Tensile debonding experiments were conducted in order to expose the bonded interface, and characterize and quantify the areas that underwent metallurgical bonding. This analysis, in conjunction with finite element analysis, enabled correlation of the exposed bonded area to the thermo-mechanical fields, which develop during the bonding process.

The article is structured as follows: Section 2 describes the bonding and debonding experiments, metallurgical characterization, and finite element modeling. The experimental and finite element analysis results are described in Section 3. Section 4 is devoted to discussing the findings, and correlating between the thermo-mechanical fields and the

exposed surface areas. The summary and conclusions, as well as the plans for future expansion of the study, are given in Section 5.

2. Materials and Methods

To investigate the relation between the bonding surface and the thermo-mechanical fields that govern the bonding process, an experimental/computational methodology was utilized. First, compression experiments at different test temperatures were conducted in order to obtain metallurgical bonding between the specimens. To quantify the thermo-mechanical fields, which develop at the bonding interface, finite element modeling of the bonding tests was performed, verified and validated. Next, debonding experiments were conducted in order to both asses the interface bonding strength and to expose the bonded surfaces for metallurgical characterization.

2.1. Bonding and Debonding Experimental Setup and Metallurgical Charcterization

In the present study, beams of Al6061 were cut from a flat plate (cold rolled with surface quality N6) to approximate dimensions of 6.5 × 10 × 58 mm each. Hot compression tests were conducted in an MTS exceed system machine with maximal load of 300 KN, equipped with an environmental chamber of up to 550 °C. In order to create diffusion bonding using plastic forming, pairs of Al6061 beams were placed one on top of the other with overlap of 20 mm and compressed to different degrees of axial deformations under 300, 400 or 500 °C using a constant ram velocity of 1 mm/min (see Figure 1a). The non-overlapping part of the beams was intentionally left in order to enable consecutive tension tests for examining the debonding between the beams. The initial configuration of the beams in the compression tests is presented in Figure 1b. Special attention was given to collinear placement of the beams, one relative to the other. The specimen deformation during the bonding and debonding process was monitored using a high-resolution Manta G-319 camera. The time-dependent deformation patterns were subsequently used to validate the computational models as will be discussed later on.

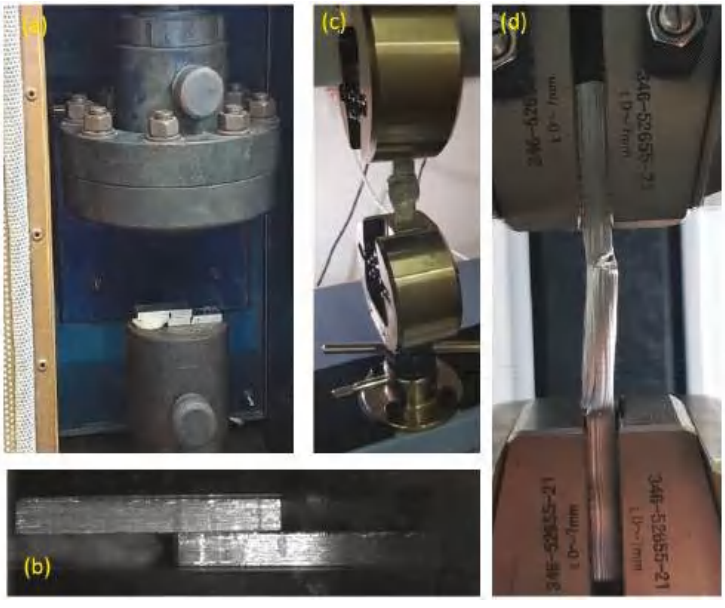

Figure 1. A specimen in the compression experimental system (**a**), and initial beam configuration in the compression tests, placed within the system (**b**). A specimen in the tensile machine (**c**), also shown from a side view inside the tensile grips (**d**).

In order to ensure that the system tools and the specimen had reached the target temperature (so that the experiment could be considered approximately isothermal), the furnace was held at the target temperature for 40 min. Then the two beams were placed on the lower pressing plate (with no pressure applied), and held for additional 20 min before beginning the compression.

The debonding tensile tests were conducted using a 10 kN Shimadzu electro-mechanical test machine. All tension experiments were conducted at room temperature (and after the specimens were completely cooled) with a loading rate of 1 mm/min, and all tests were conducted until failure. Following the debonding tests, a scanning electron microscope (SEM, JEOL JSM-7400F, Tokyo, Japan) was used to examine the exposed fracture surfaces and assess the different bonding zones.

2.2. Computational Modeling

As described in Section 2.1, the compression tests were performed within a furnace, which is a part of the MTS system. Special attention was given to ensure both system tools and the specimens had reached the target temperature. Since the experiments were conducted under low ram velocities, the heat generation due to plastic dissipation can be neglected and it may be assumed that the bonding process is isothermal. The computational models were developed using the commercial FE (finite elements) code ABAQUS using an explicit solver. The Al6061 was defined as an elasto-plastic material using the J_2 yielding criterion with isotropic hardening. The flow curves were characterized using compression tests on single-beam specimens, at all temperatures relevant to this study (25, 300, 400, and 500 °C). Since digital image data were used to track the displacement of the surfaces of the pressing plates in contact with the specimen, the elastic response of the tools became irrelevant and the pressing plates were defined in the FE model as rigid. A penalty-type contact constraint was specified between the beams (at the interface) and also between the beams and pressing plates. In the tangential direction a constant friction coefficient of 0.4 (at all temperatures) was defined. The friction coefficient between Al and steel was previously characterized by the authors in [22]. No penetration was allowed in the normal direction ("hard contact" definition). Due to symmetry, only half of the system was modeled as shown in Figure 2. The mesh was constructed using 8-nodal hexahedral elements, with reduced integration.

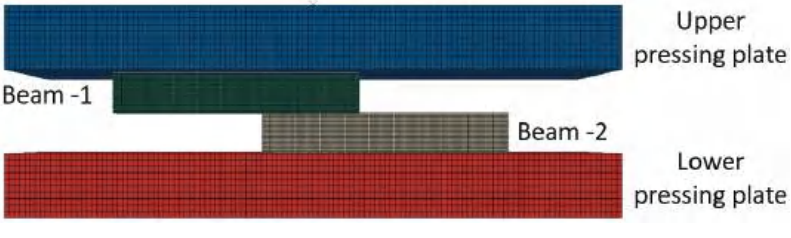

Figure 2. The geometry of the compression system represented in the model, with the 3D mesh used throughout this study (side view).

The experimentally measured displacement was prescribed as the boundary conditions on the upper pressing plate while the lower pressing plate was clamped. The computational models underwent standard convergence tests to verify the solution was converged with respect to element size and time step (see Appendix A).

3. Results

3.1. Determination of Al6061 Flow Stress

As was mentioned in Section 2.1, the system tools and the specimen were held at the target temperature for 40 and 20 min, respectively, before starting the compression, so that the experiment could be considered isothermal. However, since a wide range of

temperatures is considered in this work, characterization of the AA6061 flow stress at these temperatures is necessary for the computational study.

The flow stress of the material was characterized using compression tests of single-beam specimens, at 25, 300, 400, and 500 °C. An FE model was built for each of the test temperatures, and the flow stress was determined using the iterative approach detailed in [22]. The resulting stress–strain relations are provided in Table 1, in the following form: $\sigma = K \cdot \varepsilon^n + \sigma_{yield}$.

Table 1. The flow stress relation characterized for the examined Al6061 at different temperatures.

Specimen Temp. [°C]	**25**	**300**	**400**	**500**
Flow stress [MPa]	$325 \cdot \varepsilon^{0.75} + 225$	$55 \cdot \varepsilon^{0.8} + 88$	$10 \cdot \varepsilon^{0.75} + 42$	$10 \cdot \varepsilon^{0.8} + 10$

It can be seen from Table 1 that the flow stress decreases as the temperature increases, as expected. The strain hardening (represented by the slope of the stress–strain curve) is significant at room temperature and small at elevated temperatures. The strain hardening is also monotonically decreasing with increasing temperature. It should be noted that the constant representing the yield stress at different temperatures is similar to the values of the yield stress reported in the literature for Al6061-T6 and Al6061-T651 [23].

3.2. Compression Bonding Tests

The experimental program is presented in Table 2, along with the axial reductions obtained in the compression bonding stage.

Table 2. Compression bonding experimental parameters and dimensions of the specimens after the test.

Temperature [°C]	**Specimen No.**	**Reduction [%]**	**W_{avg} [mm]**	**L_{avg} [mm]**
300	AAA1	46.48	34.2	28.2
	AAA2	43.54	31.47	27.95
	AAA3	38.33	29.65	23.2
	AAA4	32.39	26.75	22.52
400	AAB2	49.45	34.5	26.50
	AAB3	43.39	31.50	25.56
	AAB4	34.29	28.98	23.70
	AAB5	25.02	25.60	21.50
500	AAC2	53.45	37.50	28.75
	AAC3	44.84	32.80	23.4
	AAC4	-	-	-
	AAC5	-	-	-

It can be seen from Table 2 that, at the smallest reductions, bonding was not achieved at 500 °C; however, it was achieved at 400 °C and 300 °C. The dimensions of the overlap area are indicated in Figure 3, using an example of specimen AAA2 after the compression.

The force–displacement curves obtained in the compression bonding tests, at 300, 400 and 500 °C, are presented in Figure 4 for the entire range of reductions examined. It can be seen that the curves obtained for the specimens that were compressed at the same temperature conditions are overlapping, as expected. Also, as the temperature increases the forces required to obtain the same amount of deformation decrease.

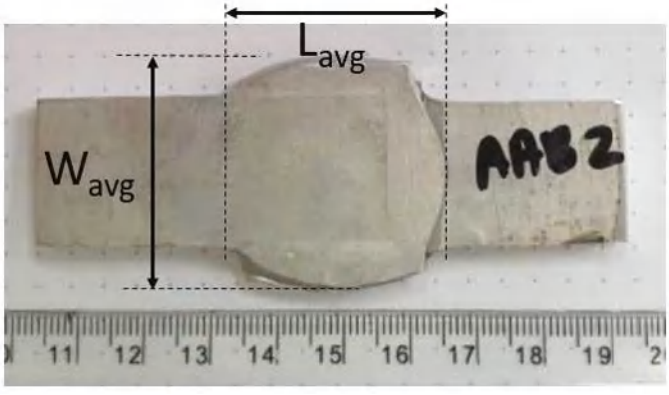

Figure 3. Representative measurements of the overlapping area.

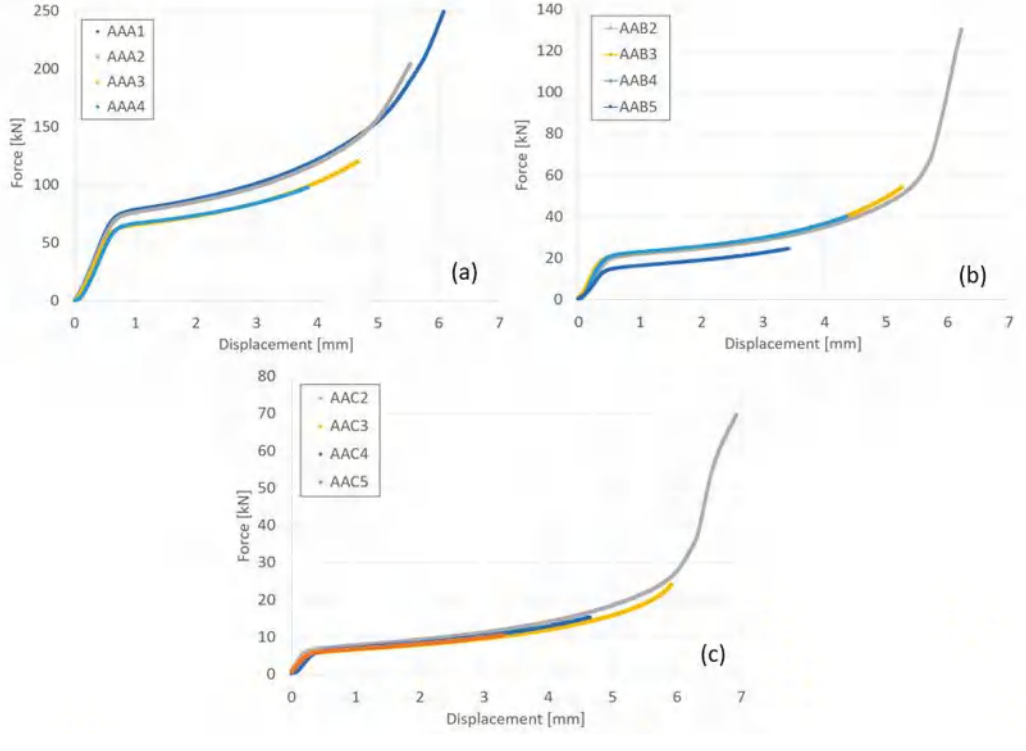

Figure 4. Force–displacement curves of the couples of Al6061 compressed at the following different temperatures: 300 °C (**a**), 400 °C (**b**), and 500 °C (**c**).

It should be noted that the differences in the force–displacement curves of the specimens AAA3,AAA4 compared to AAA1,AAA2 result from differences in the length of the overlap (see Figure 1) when positioning of the specimens in the furnace for the compression test (which was significantly smaller for specimens AAA3,AAA4).

3.3. Validation of the Finite Element Models

To validate the computational models, a comparison between the measured and computed values was performed. As an example, the results for the largest reduction at each tested temperature are presented in Figure 5.

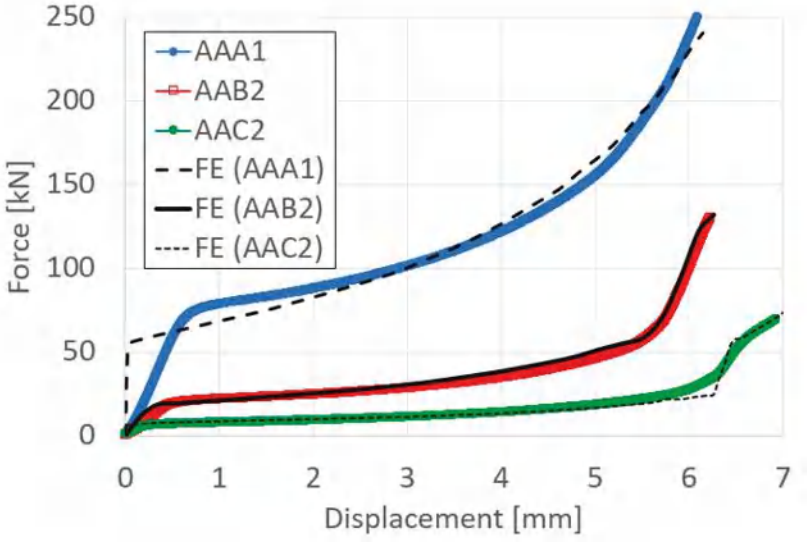

Figure 5. Experimental Vs computed force–displacement curves of the couples of Al6061 compressed at the following temperatures: 300 °C, 400 °C, and 500 °C.

Figure 5 demonstrates that the computational model is able to follow the experimental force–displacement curves. In addition to the force–displacement curve, the computed deformed specimen dimensions were compared to the experimentally obtained deformation. Representative examples are presented in the following Figure 6, which show that the deformation contours fit the experimentally obtained ones.

3.4. Debonding Experiments

As previously mentioned, the debonding experiments were conducted mainly in order to expose the bonded surfaces. Nevertheless, the shear stress required for delamination (which is equal to the bonding strength under shear) was roughly approximated by $\tau_{bonding} \approx F_{\max}/A_0$, where $F_{\max}$ is the maximum force obtained in the tension test and A_0 is the approximated overlapping area obtained in the compression stage (see Table 2 for the width and the length of the interface area measurement after compression). The results of the approximated $\tau_{bonding}$ are presented in the following Table 3. It is important to notice that the approximated $\tau_{bonding}$ is computed under the assumption that the entire overlapping area A_0 is bonded with the same strength, which may be a rough approximation. Furthermore, only a fraction of the overlapping area may be bonded, as discussed in the following section, which microscopically examines the interface after failure.

3.5. Macroscopic Charcterization Following Debonding Tests

Following the debonding of the beams by the tension test, the revealed interface has several distinguishable areas, which can be observed without any equipment. As can be seen from Figure 7, the same general pattern can be observed in the specimens that were bonded at different degrees of reduction (see Figure 7a–c), as well as at different temperatures. This macroscopic pattern resembled an eye, and included a rhombus-like area ("sclera", outlined on the specimen surface in blue in Figure 7), which contains a

round inner "iris" area (see Figure 7b). The macroscopic pattern is a bit different at 300 °C, where the region of the "sclera" resembles the letter "X" rather than a rhombus. In the specimens that were bonded at the same temperature, the macroscopic patterns are similar (however their dimensions change with different reductions).

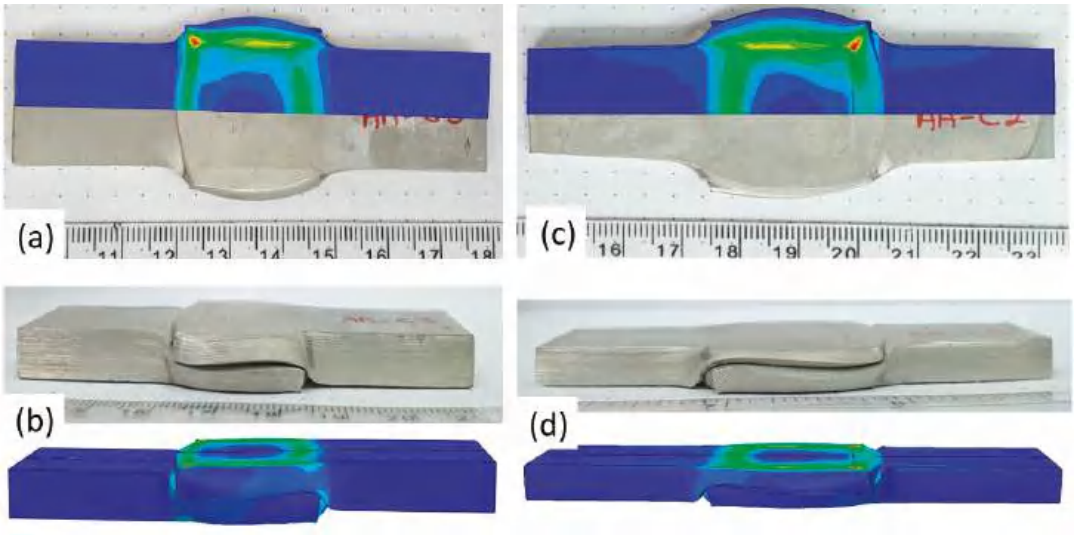

Figure 6. Upper (**a**) and side (**b**) view of specimen AAC3. Upper (**c**) and side (**d**) view of specimen AAC2.

Table 3. Approximated $\tau_{bonding}$ from force obtained in tension and area from the compression stage.

Temperature [°C]	Specimen No.	Actual Reduction [%]	$\tau_{bonding}$ [MPa]	Notes
300	AAA1	46.48	12.16	
	AAA2	43.54	11.19	
	AAA3	38.33	5.08	
	AAA4	32.39	4.26	
400	AAB2	49.45	10.89	
	AAB3	43.39	11.73	
	AAB4	34.29	8.28	
	AAB5	25.02	7.22	
500	AAC2	53.45	7.29	
	AAC3	44.84	7.50	
	AAC4	-	-	No bonding
	AAC5	-	-	No bonding

The division into different areas is thought to result from different surface textures at the interface, which differ in degrees of roughness compared with their surroundings, and therefore reflect light differently. The different areas were also examined microscopically, as discussed in the following subsection.

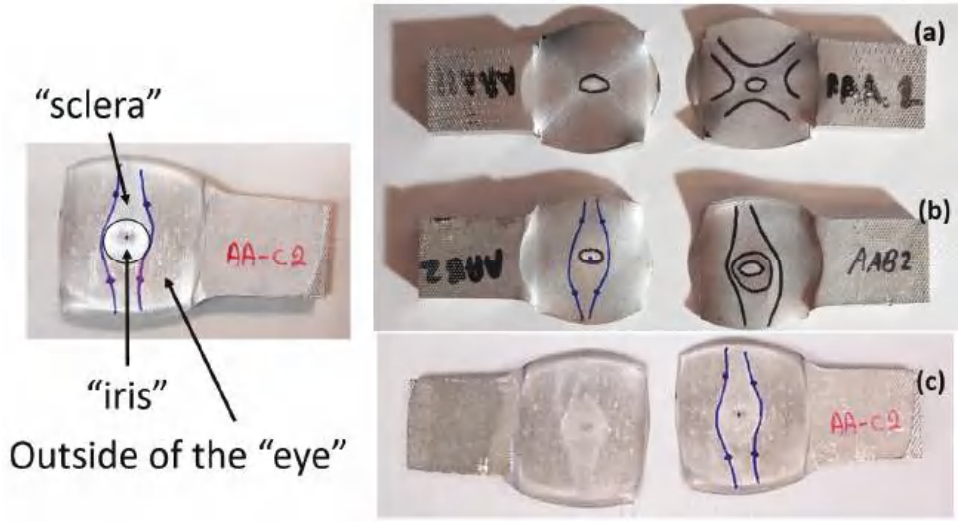

Figure 7. Examples of the interfaces revealed after debonding by a tension test. Specimen AAA1 (bonded at 300 °C, 46% reduction) (**a**) Specimens AAB2 (bonded at 400 °C, 49% reduction) (**b**), Specimen AAC2 (bonded at 500 °C, 53% reduction) (**c**).

3.6. Microscopic Charcterization Following Debonding

Based on the macroscopic observations presented in Figure 7, it was initially speculated that the interface eye-like pattern revealed by the debonding is a result of differences in textures, which have a microscopic as well as a macroscopic distinction (which causes the differences in light reflection).

The three areas—"iris", "sclera", and the outside of the "eye"—were examined using a SEM microscope, in specimens that were bonded at different temperatures (300 °C, 400 °C, 500 °C), and also ones that underwent different reductions at the same temperature. The different areas were magnified up to ×2500 in order to reveal differences in the textural characteristics at the microscopic level. Representative examples of each area are presented in the following Table 4. Those examples are of specimens that were bonded at different temperatures, but with a similar degree of reduction. Specimen AAA1 was bonded at 300 °C and 46.5% reduction, AAB2 was bonded at 400 °C and 49.5% reduction, and AAC3 was bonded at 500 °C and 45% reduction.

It can be seen from Table 4 that the microscopic features indicate a diffusional bond was created; however, not always along the entire interface. The presence of dimples, which are characteristic for ductile failure (of material bulk), are evidence for the diffusional bonding that took place during the compression stage. In general, deeper dimples will be correlated with a stronger diffusional bond. The interface microscopic features also depend on the debonding method, which was obtained by shear loading.

In the AAA1 sample, obtained at 300 °C, the "Iris" is covered with dimples of various degrees of depth, some of which appear to be quite deep and large, and others are shallower. Their round shape indicates that this area failed in tension. At the "sclera", only a part of the area is covered by dimples. At smaller magnifications (which are not included in Table 4), it seems the stripes of dimples concentrate in the vicinity of grain boundaries. In between the stripes of dimples the areas seem to resemble a brittle-like surface, with ripples that imply the presence of a mechanical bonding as well (in which case both sides of the interface grip each other through the irregularities in the surface). Outside of the "eye", the fracture surface is mostly brittle with visible grains (intergranular brittle fracture) and small patches of shallow dimples. Ripples indicating mechanical bonding are present throughout this area.

Table 4. SEM images of different areas of the interface after debonding, magnification ×2500.

	"iris"	"sclera"	Outside the "eye"
AAA1 (Bonded at 300 °C, 46.5% reduction)	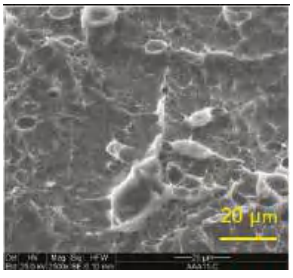	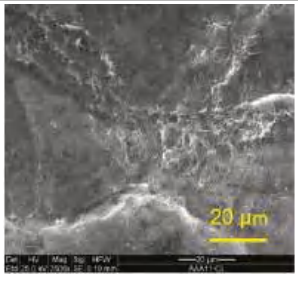	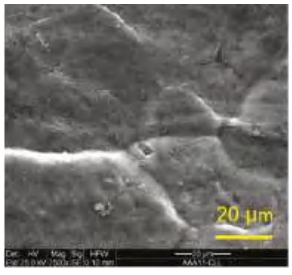
AAB2 (Bonded at 400 °C, 49.5% reduction)		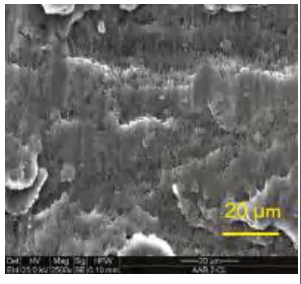	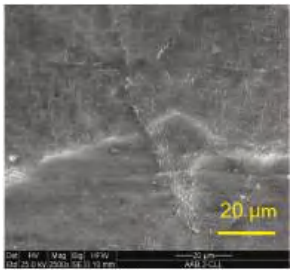
AAC3 (Bonded at 500 °C, 45% reduction)	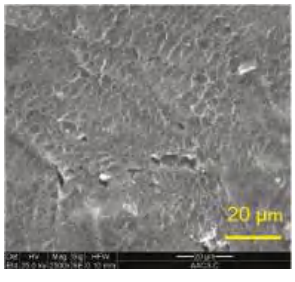	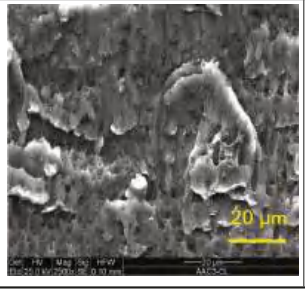	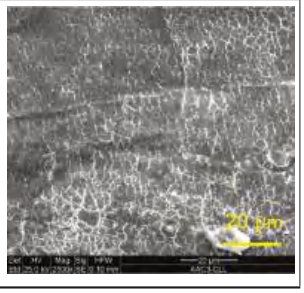

In the AAB2 sample, obtained at 400 °C, the "iris" is covered with very dense and deep dimples, indicating a strong diffusional bond. The dimples are slightly elongated, indicating that this area failed under a combination of tension and shear. The "sclera" is also mostly covered with dimples, which are very elongated as a result of the debonding process under shear. In between the dimpled area there are patches of tearing (cracking between primary voids), which create smooth surfaces. Outside of the "eye", the fracture surface is partially covered with very shallow dimples, indicating a considerably weaker diffusional bonding. The rest of the surface is smoother, with outlines of intergranular surfaces, indicating an intergranular brittle fracture. Ripples can also be detected, indicating mechanical bonding took place as well.

In the AAC3 sample, obtained at 500 °C, the "iris" is covered with shallow dimples, indicating a weak diffusional bonding. Their round shape indicates that this area failed primarily in tension. The "sclera" looks similar to the same area in 400 °C, mostly covered with elongated dimples as a result of the shear debonding; however, the dimples are larger compared with the 400 °C "sclera". Also present here are small areas of tear between the dimples. Outside of the "eye", the fracture surface is covered with dimples, mostly shallow, but some areas have deeper dimples. In contrast with the lower temperatures, this indicates the entire area outside the "eye" was bonded by diffusion, though shallow dimples indicate a weak bonding strength. The round shape of the dimples indicates

that this area failed mainly in tension. Underneath the dimples, ripples are also observed, indicating mechanical bonding took place as well.

The change in features obtained at similar reductions at different temperatures is assumed to result from the following two competing processes: the temperature-dependent diffusion on the one hand, and the temperature-dependent oxidation rate on the other, both of which increase with temperature. Before compression, the specimens are inserted into the furnace, and are held for an additional 20 min after arriving at the destination temperature. This allows time for the oxidation layer to build up. The oxidation rate in aluminum and its alloys is larger as the temperature increases [24]. In order to obtain diffusional bonding, the brittle oxidation layer needs to be broken in order to expose oxidation-free aluminum. The ram velocity is constant; however, since the strain distribution along the interface is non-uniform (see Section 4), the time required for achieving base metal-to-base metal contact will change at different areas along the interface. When such contact is achieved, the temperature is again an important factor for determining the diffusional bond strength, since the diffusion coefficient is exponentially dependent on temperature [9]. The local pressure also influences the diffusion coefficient (which increases with pressure), and by itself depends on the temperature, also through the flow stress. It seems, from the resulting interface in Table 4, that the strongest diffusion bonding was achieved at 400 °C. At 300 °C, the weaker bonding is probably due to the higher flow stress, which decreases the formability, whereas at 500 °C the weaker bonding is assumed to result from a thicker oxidation layer that has to be broken in order to enable base metal-to-base metal contact, which is required for the diffusion bonding to take place.

These results are conflicting with the approximated bonding strength in Table 3, which shows increasing strength with decreasing temperature. There are several causes for this inconsistency. One of them is that the simple calculation $\tau_{bonding} \approx F_{\max}/A_0$ assumes that the entire interface is bonded. We can see from Table 4 that this is not the case. Moreover, the microscopic features presented in Table 4 indicate that the bonding strength is not uniform along the bonded portions of the interface. In addition, the debonding process takes place at room temperature, after the specimens went through a heat treatment at different temperatures (300–500 °C, during pre-heating and compression). Since Al6061 is sensitive to heat treatments, the flow stress at room temperature will be different, which, in turn, also influences the resulting stress required for debonding. As mentioned in the introduction, there are several tests that are commonly used to determine the debonding force (such as peel or shear tests). Using a similar calculation, such as $F_{\max}/A_0$, on those tests overlooks the aforementioned considerations, thus leading to erroneous conclusions.

4. Correlation between Computed Thermo-Mechanical Fields and Microscopic Observations

In the previous section, the debonded interface was divided into three macroscopically distinguishable areas—the "iris", "sclera", and the outside of the "eye". In order to obtain a better understanding of the thermo-mechanical fields that influenced these macroscopic features and created the different surface textures, FE models of the specimens, compressed at 300 °C, 400 °C and 500 °C to different degrees of reduction, were created. Mechanical fields, such as the principal components of the strains and stresses, were examined along the interface. Out of those, the ones that create contours that resemble the contours of the "eye" are presented in Table 5, for several specimens. It is important to mention that the FE thermo-mechanical models were only of the compression stage (i.e., the stage of bonding creation), and the mechanical fields presented in Table 5 show the fields iso-contours when reaching the final reduction in the specific specimen.

Table 5 shows the iso-contours of strain fields of several specimens at the end of the compression test. Those include components of the principal strains and shear strain. The interface between the beams at the beginning of the test lies on the x–z plane, so at the beginning of the test, the maximal principal (largest tension) $\varepsilon 11$ component is εzz, the mid principal strain $\varepsilon 22$ is εxx, and the minimum principal strain $\varepsilon 33$ is the compression εyy.

Table 5. Mechanical fields from FE models of the bonding interface when reaching the specimen's final reduction.

Spec.	AAA1 (Bonded at 300 °C, 46.5% Reduction)	AAB2 (Bonded at 400 °C, 49.5% Reduction)
Macro image		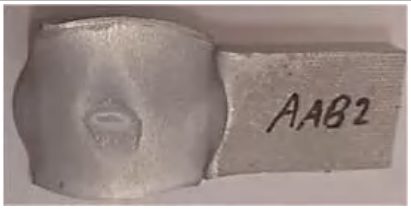
ε11 (Max. principal strain)	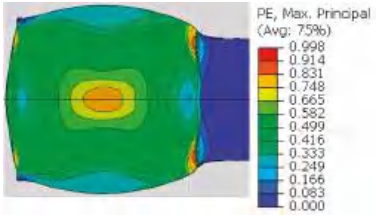	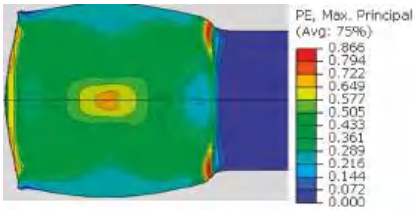
ε22 (Mid principal strain)	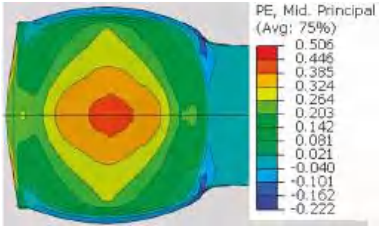	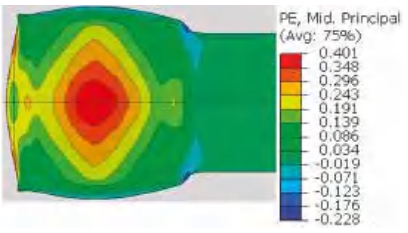
ε33 (Min. principal strain)	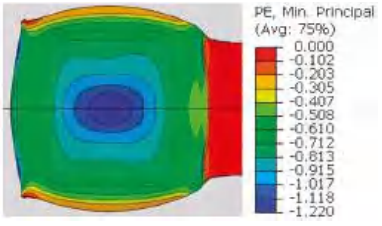	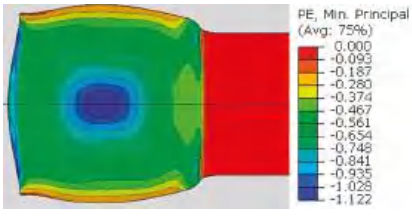
Spec.	AAC3 (Bonded at 500 °C, 45% reduction)	AAC4 (Bonded at 500 °C, 32% reduction)
Macro image		
ε11 (Max. principal strain)	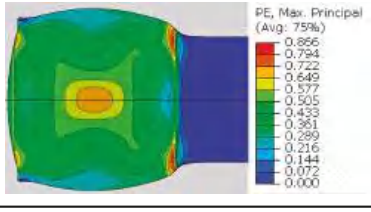	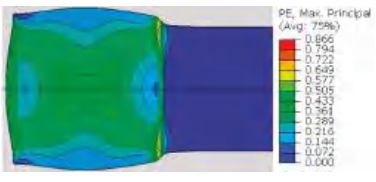

Table 5. *Cont.*

Spec.	AAA1 (Bonded at 300 °C, 46.5% Reduction)	AAB2 (Bonded at 400 °C, 49.5% Reduction)
ε22 (Mid principal strain)	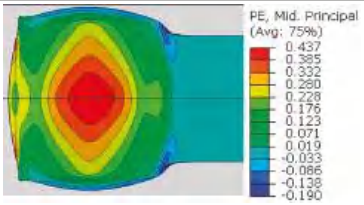	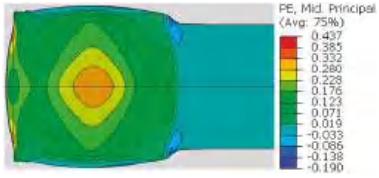
ε33 (Min. principal strain)	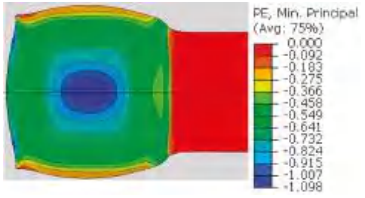	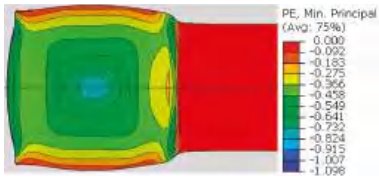

It can be seen from Table 5 that the macroscopic features that create the contour of the "eye" seem to be a superposition of the influences of the three principal strain components—the approximately in-plane tension components ε11 and ε22, and the compression ε33 (normal to the interface). The relative magnitude between the components determines the dominant features on the surface, which are connected to the principal strain component iso-contours. The shape of the "eye" seems to be dominated by the ε22 component. The "iris" seems to be associated with both ε11 and ε33. The "×" macroscopic pattern at 300 °C seems to be a result of a dominant ε11 component (which reaches higher values at 300 °C).

The specimens AAC3 and AAC4 are both specimens that were bonded at 500 °C, but reached different reductions—45% (AAC3) and 32% (AAC4). Contrary to similar reductions at 400 °C and 300 °C, bonding was not created in specimen AAC4 (the two beams did not hold together when removed from the furnace). Accordingly, there was no detectable macroscopic pattern on the interface. In Table 5, the scale of the mechanical fields is similar, so that they could be compared. The values of ε11, ε22, and ε33 across the interface are clearly smaller in specimen AAC4 than in AAC3. It is assumed that there is a certain degree of strain that has to be locally reached in order for the oxidation layer to be broken. These strains lead to surface exposure and enable the base metal-to-base metal contact required to create a diffusion bond between the surfaces [25]. The deformation of specimen AAC4 was apparently insufficient for this degree of local strain to be reached. Since the thickness of the oxidation layer is temperature (and time) dependent, this local strain required for bonding is temperature dependent as well. This is consistent with the experimental results, which show that bonding was obtained at similar and even smaller reductions, in compression tests at lower temperatures, in which the oxidation layer is expected to be thinner.

To quantify the influence of the thermo-mechanical fields on the bonding conditions, the scalar bonding quality criterion used in [18] was utilized, as follows:

$$J = \int_0^t k_0 \frac{\sigma_p}{\sigma_{eq}} \exp\left(\frac{RT}{Q}\right) \dot{\varepsilon}\, dt \tag{1}$$

where σ_p, σ_{eq} are the pressure and equivalent stress, respectively, $\dot{\varepsilon}$ is the stain rate, T [K] is the temperature, R [J/mol K] is the universal gas constant and Q [J/mol] is the activation energy for diffusion. The value of k_0 depends on the material and surface conditions. The bonding quality is assumed to increase for greater values of J, with some critical value J_{cr} denoting full metallurgical bonding. Unlike the study in [18], which utilized the average

values from the experiment, in the current study, the local values of J were evaluated using the computed time-dependent mechanical fields values. Average values of J in each of the regions of interest, shown in Figure 8, were computed (J was calculated in differential form at five nodal points in the FE model, sampling each area). The results are provided in Figure 9, where k_0 was taken as 1 and Q was taken as 124–144 [J/mol] for 300–500 °C, respectively.

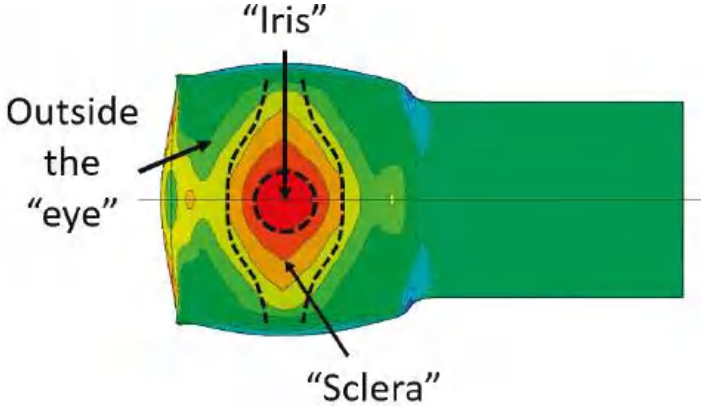

Figure 8. Areas of interest where the different values of bonding quality parameter J where computed.

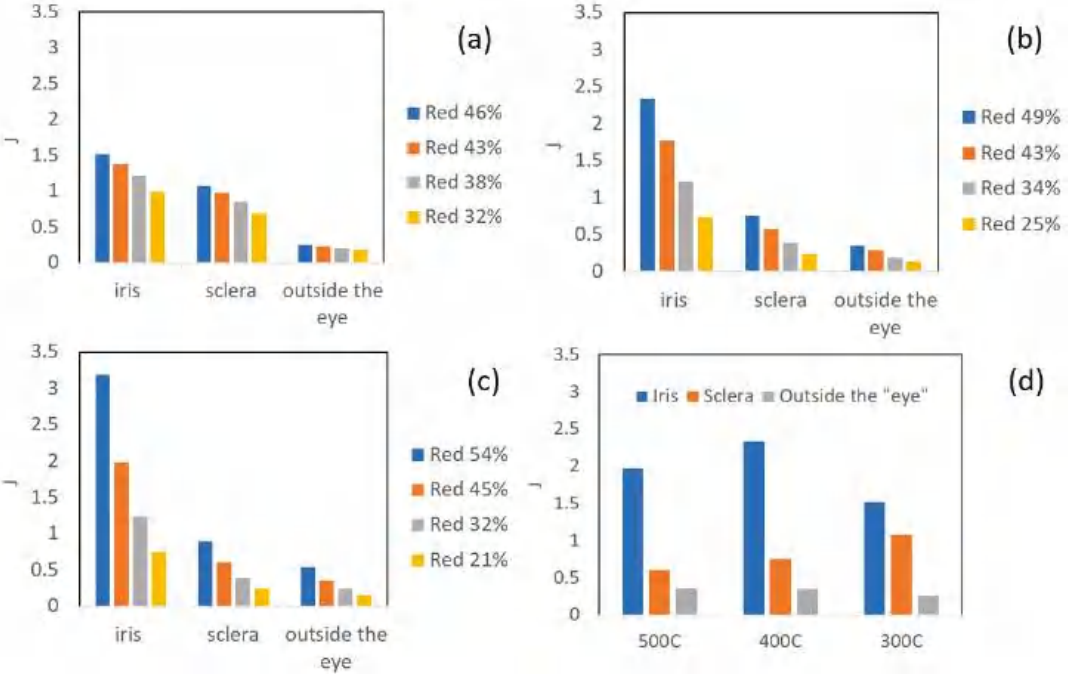

Figure 9. Comparison between bonding quality parameter J at the following temperatures: 300 °C (**a**), 400 °C (**b**), 500 °C (**c**) at different reduction values. J at different temperatures with similar reduction of about 45% (**d**).

It can clearly be seen in Figure 9a–c that the computed average values of J are considerably higher in the "iris" region, for all temperatures considered. The J value decreases in the "sclera" and in the area outside of the "eye". It can also be seen that the trend in J values between the different regions is maintained for all temperatures; however, the differences between the regions are greater as the temperature increases. It can be seen in Figure 9d that the average value of J in the "iris" is greater at 400 °C compared to the value at 500 °C. This correlates to the findings shown in Table 4, which show the highest density of dimples in the "iris" at 400 °C, compared to 500 °C and 300 °C. Figure 9d also shows that similar values of J outside the "eye" are obtained for 400 °C and 500 °C, with smaller values for 300 °C. These findings also correlate well with the metallurgical observation, which shows the presence of shallow dimples at 400 °C and 500 °C, and almost no evidence of metallurgical bonding at 300 °C. Nevertheless, the high value of J in the "sclera" at 300 °C, compared to 400 °C and 500 °C, does not seem to correlate with the metallurgical observations, since at 300 °C only a fraction of the area shows evidence of metallurgical bonding. Although the experimental/computational methodology presented in this study seems promising for identifying the relation between the interface conditions and the resulting bonding quality, more experimental data is required in order to determine the critical value of J for full metallurgical bonding in Al6061.

5. Summary and Conclusions

Experiments, in conjunction with finite element modeling and metallurgical characterization, were used to investigate the hot compression bonding of Al6061 beams. Temperatures of 300–500 °C and deformations of up to 60% were considered. Tensile debonding tests were conducted in order to expose which section of the interface was actually bonded, and to obtain what is commonly considered the bonding strength. SEM imaging was used to identify metallurgically bonded regions at the interface. It was revealed that the actual bonded area is much smaller than the interface contact area. This finding makes standard quantification of the bonding strength by $F_{\max}/A_0$ underestimate the true bonding strength. It was also shown that the bonded area follows a very distinct pattern, which is temperature dependent. The finite element modeling demonstrated that the principal plastic strain components, which develop across the interface, have similar patterns. The results from the finite element models were also used to compute a scalar bonding parameter J, which is deformation, temperature and time dependent. Good correlation was shown between the spatial distribution of the computed bonding parameter J and the microscopically observed inhomogeneity of the bonded areas across the interface. Future work will include modeling of the debonding experiments, using the cohesive zone approach to model the interface areas in order to provide a better understanding of the variations in bonding strength.

Author Contributions: Conceptualization, E.P. and B.M.; methodology, E.P., B.M., M.B.-H.; formal analysis, B.M., I.A., L.M., M.B.-H.; resources, E.P.; writing—original draft preparation, B.M., M.B.-H., I.A., L.M.; writing—review and editing, B.M., E.P.; supervision, E.P.; project administration, E.P.; funding acquisition, E.P. All authors have read and agreed to the published version of the manuscript.

Funding: This research was funded by the IAEC, Grant no.4300011151.

Institutional Review Board Statement: Not applicable.

Informed Consent Statement: Not applicable.

Data Availability Statement: The data presented in this study are available on request from the corresponding author.

Acknowledgments: The authors would like to thank Yosi Hadad and Yaniv Tzriker from the NRCN with assistance in specimen perpetration.

Conflicts of Interest: The authors declare no conflict of interest.

Appendix A. Verification of the Computational Models

To ensure that the discretization error is minimal, convergence tests were performed. An explicit solver was used with mass scaling, so the convergence was checked for both the mesh refinement (increasing number of degrees of freedom—DOFs) and for different values of mass scaling for the chosen mesh. The two compressed bars were uniformly meshed so that the elements had an aspect ratio of one, which was kept for all four degrees of mesh refinement. As a test case, convergence was checked at 400 °C after a 56% reduction in the bars (the largest reduction obtained in the tests). The pressure, the strain component at y direction (εyy), and the equivalent plastic strain (εeq) (all influencing the bonding strength) were extracted along the width, at the center of the contact area (see Figure A1), at the end of the compression (at maximum displacement). In addition, the force–displacement response was also examined. For the chosen value of mass scaling (100,000), it was ensured that throughout the compression process the kinetic energy was at least 100 times smaller compared with the internal energy. The mesh included about 3×10^5–1.3×10^6 DOFs, respectively, for the entire model. The mesh used throughout this work included about 5.7×10^5 DOFs, and a mass scaling value of 100,000. Figure A2 demonstrates that convergence was achieved for the chosen mesh. A similar examination was performed to ensure that the chosen mass scaling value also provides converged results.

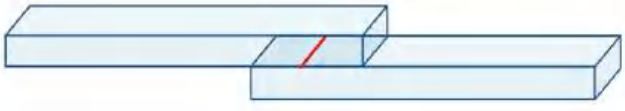

Figure A1. The two bars in contact before deformation. The red line indicates the path at the center of the contact area, along which the mechanical fields were extracted.

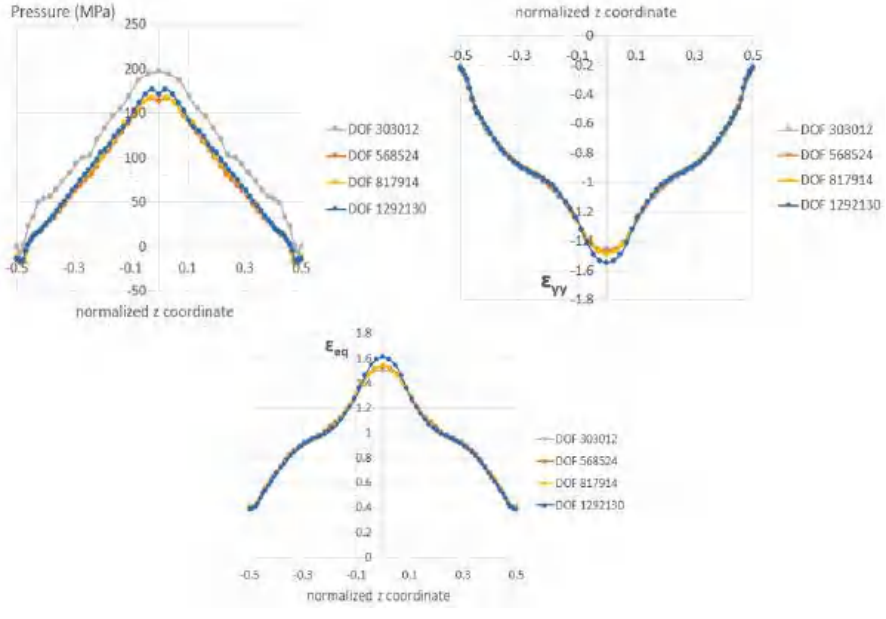

Figure A2. An example of a convergence test for the case of compression at 400 °C to 56% reduction. Here, for the chosen mass scaling value of 100,000, the mechanical fields (pressure—top, εyy—middle, and εeq—bottom) are examined for different degrees of mesh refinement.

References

1. Botelho, E.C.; Silva, R.A.; Pardini, L.C.; Renzende, M.C. A review on the development and properties of continuous Fiber/epoxy/aluminum hybrid composites for aircraft structures. *Mater. Res.* **2006**, *9*, 247–256. [CrossRef]
2. Goushegir, S.M.; Scharnagl, N.; Dos Santos, J.F.; Amancio-Filho, S.T. Durability of Metal-Composite Friction Spot Joints under Environmental Conditions. *Materials* **2020**, *13*, 1144. [CrossRef]
3. Samal, P.; Vundavilli, P.R.; Meher, A.; Mahapatra, M.M. Recent progress in aluminum metal matrix composites: A review on processing, mechanical and wear properties. *J. Manuf. Process.* **2020**, *59*, 131–152. [CrossRef]
4. Danesh Manesh, H.; Shahabi, H.S. Effective parameters on bonding strength of roll bonded Al/St/Al multilayer strips. *J. Alloys Compd.* **2009**, *476*, 292–299. [CrossRef]
5. Zhang, X.P.; Yang, T.H.; Castagne, S.; Wang, J.T. Microstructure bonding strength and thickness ratio of Al/Mg/Al alloy laminated composites prepared by hot rolling. *Mater. Sci. Eng. A* **2011**, *528*, 1954–1960. [CrossRef]
6. Hassan, M.; Ali, A.; Ilyas, M.; Hussain, G.; Ul Haq, I. Experimental and numerical simulation of steel/steel (St/St) interface in bi-layer sheet metal. *Int. J. Lightweight Mater. Manuf.* **2019**, *2*, 89–96. [CrossRef]
7. Lumley, R. *Fundamentals of Aluminum Metallurgy, Production Processing and Applications*, 1st ed.; Woodhead Publishing: Cambridge, UK, 2011.
8. Chunlei, G.; Yongdong, X.; Mengjun, W. Prediction of the flow stress of Al6061 at hot deformation conditions. *Mater. Sci. Eng. A* **2011**, *528*, 4199–4203. [CrossRef]
9. Helmut, M. *Diffusion in Solids: Fundamentals, Methods, Materials, Diffusion-Controlled Processes*, 2nd ed.; Springer: Berlin/Heidelberg, Germany, 2009; pp. 127–147.
10. Mori, K.I.; Bay, N.; Fratini, L.; Micari, F.; Tekkaya, A.E. Joining by plastic deformation. *CIRP Ann. Manuf. Technol.* **2013**, *62*, 673–694. [CrossRef]
11. Zinong, T.; Bing, Z.; Jun, J.; Zhiqiang, L.; Jianguo, L. A study on the hot roll bonding of aluminum alloys. *Procedia Manuf.* **2020**, *50*, 56–62. [CrossRef]
12. Ghalehbandi, S.M.; Malaki, M.; Gupta, M. Accumulative roll bonding—A review. *Appl. Sci.* **2019**, *9*, 3627. [CrossRef]
13. Clerico, P.; Mininger, X.; Prevond, L.; Baudin, T.; Helbert, A.L. Compromise between magnetic shielding and mechanical strength of thin Al/Steel/Al sandwiches produced by cold roll bonding: Experimental and numerical approaches. *J. Alloys Compd.* **2019**, *798*, 67–81. [CrossRef]
14. Kazanowski, P.; Epler, M.E.; Misiolek, W.Z. Bi-Metal rod extrusion-process and product optimization. *Mater. Sci. Eng. A* **2004**, *369*, 170–180. [CrossRef]
15. Priel, E.; Ungarish, Z.; Navi, N.U. Co-extrusion of a Mg/Al Composite Billet: A Computational Study Validated by Experiments. *J. Mater. Process. Technol.* **2016**, *236*, 103–113. [CrossRef]
16. Qing, T.; Xiu, L.; Qingsong, W. Diffusion bonding of Al6061 and Cu by hot isostatic pressing. *J. Wuhan Univ. Technol. Mater. Sci. Ed.* **2020**, *35*, 183–191.
17. Xie, B.; Sun, M.; Xu, B.; Wang, C.; Zhang, J.; Zhao, L.; Li, D.; Li, Y. Evolution of interfacial characteristics and mechanical properties for 316LN stainless steel joints manufactured by hot-compression bonding. *J. Mater. Process. Technol.* **2020**, *283*, 116733. [CrossRef]
18. Xu, X.; Ma, X.; Yu, S.; Zhao, G.; Wang, Y.; Chen, X. Bonding mechanism and mechanical properties of 2196 Al-Cu-Li alloy joined by hot compression deformation. *Mater. Charact.* **2020**, *167*, 110486. [CrossRef]
19. Lesuer, D.R.; Syn, C.K.; Sherby, O.D.; Wadsworth, J.; Lewandowski, J.J.; Hunt, W.H. Mechanical behavior of laminated metal composites. *Int. Mater. Rev.* **1996**, *41*, 169–197. [CrossRef]
20. Alkramifard, H.R.; Mirzadeh, H.; Parsa, M.H. Estimating interface bonding strength in clad sheets based on tensile test results. *Mater. Des.* **2014**, *64*, 307–309. [CrossRef]
21. Mittleman, B.; Guttmann, G.M.; Priel, E. A computational analysis of thermo-mechanical fields in hot roll bonding of aluminum validated by experiments. *J. Miner. Met. Mater. Soc.* **2019**, *72*, 718–728. [CrossRef]
22. Mittelman, B.; Priel, E.; Navi, N.U. A finite element study of thermo-mechanical fields and their relation to friction conditions in Al1050 ring compression tests. *J. Manuf. Mater. Process.* **2018**, *2*, 83. [CrossRef]
23. Nakamura, T.; Obikawa, T.; Yukutake, E.; Ueda, S.; Nishizaki, I. Tool temperature and process modeling of friction stir welding. *Mod. Mech. Eng.* **2018**, *8*, 78–94. [CrossRef]
24. Jeurgens, L.P.H.; Sloof, W.G.; Tichelaar, F.D.; Mittemeijer, J. Growth kinetics and mechanisms of aluminum-oxide films formed by thermal oxidation of aluminum. *J. Appl. Phys.* **2002**, *92*, 1649–1656. [CrossRef]
25. Bay, N. Cold pressure welding-The mechanisms governing bonding. *J. Eng. Ind.* **1979**, *101*, 121–127. [CrossRef]

MDPI
St. Alban-Anlage 66
4052 Basel
Switzerland
Tel. +41 61 683 77 34
Fax +41 61 302 89 18
www.mdpi.com

Materials Editorial Office
E-mail: materials@mdpi.com
www.mdpi.com/journal/materials

Academic Open
Access Publishing

www.mdpi.com

ISBN 978-3-0365-7745-6